Search for gravitational wave transient sources in LIGO-Virgo data

Marie-Anne Bizouard

LAL-059

Habilitation à diriger des recherches
présentée à l'Université Paris-Sud

Search for gravitational wave transient sources in the LIGO-Virgo data

---

Marie-Anne Bizouard

7 Décembre 2017

Jury:

Dr. Luc Blanchet	Examinateur
Prof. Erik Katsavounidis	Rapporteur
Prof. Sergey Klimenko	Examinateur
Dr. Frédérique Marion	Rapportrice
Prof. Giovanni Prodi	Rapporteur
Prof. Achille Stocchi	Président
Prof. Jo van den Brand	Examinateur

Contents

Prologue

Ce mémoire rassemble un certain nombre de travaux que j'ai menés depuis que j'ai rejoint la Collaboration Virgo en 1998. Dès sa création, le groupe Virgo du LAL avait développé un intérêt pour la recherche des signaux émis par les supernovae de type Ia, et c'est donc tout naturellement que j'ai commencé à travailler sur le sujet, qui englobent bien d'autres sources que les supernovae. Mais en 1998, Virgo n'est pas en opération. La construction des tunnels qui accueillent les deux bras de l'interféromètre n'a pas encore commencé. La priorité du groupe n'est donc pas la préparation de l'analyse des données, mais la mise en route du détecteur. Mes premières années dans Virgo seront donc dédiées à cette longue et lente mise en route. Le groupe du LAL avait en charge de nombreux développements: contrôle global de l'interféromètre, software généraux de contrôle de Virgo, contrôle commande du vide et du système d'injection laser. De ces années d'apprentissage et de travail sur le détecteur, rien ne sera dit dans ce mémoire. Seuls de bons souvenirs de travail d'équipe resteront à la postérité. Ce sera aussi le cas du développement des programmes d'analyse des données de Virgo pour la recherche des ondes gravitationnelles impulsionnelles dont j'ai pris la responsabilité à partir de 2002 et qui, faute de combattants, a périclité.

Le chapître 1 donne quelques rudiments sur les ondes gravitationnelles, le détecteur Virgo et résume l'état de la connaissance sur les sources d'ondes gravitationnelles impulsionnelles. Le chapître 2 résume plus de 60 ans de devélopements techniques qui ont abouti à la première observation de la fusion de deux trous noirs. L'histoire moderne de la recherche des ondes gravitationnelles est marquée par le rapprochement, dès 2004, des collaborations Virgo, LIGO et GEO (LIGO et GEO forment la LIGO Scientific Collaboration ou LSC). Cela aboutira en 2006 par un accord pour échanger et analyser les données ensemble. C'est en fait la naissance d'une nouvelle astronomie, car non seulement un réseau de trois interferomêtres permet d'augmenter la fraction du ciel couverte du réseau à tout moment, mais la localisation d'une source transitoire est aussi grandement améliorée. Ceci est fondamental pour les observations des sources dans les domaines optiques et gamma. Les données de Virgo et LIGO sont échangées et les analyses sont communes. L'avantage d'une recherche d'ondes gravitationnelles transitoires avec un réseau de détecteurs est illustré dans le chapître 3 à travers un papier qui comparent les performances de plusieurs programmes d'analyse propres à Virgo et la LSC et qui détermine le gain qu'apporte Virgo au réseau formé par les détecteurs LIGO. Cette étude, menée avec des données simulées, Gaussiennes et stationnaires, ne prend pas en compte les effets des bruits environnementaux qui génèrent une quantité phénoménale d'événements qui peuvent mimer un vrai signal d'ondes gravitationelles. Toute recherche de sources d'ondes gravitationnelles requière un travail important de compréhension de la qualité des données et de développement de vetos qui permettent de rejeter une large fraction de faux événements. Ce travail a commencé dès les premiers runs de mise en route de Virgo est résumé dans le chapître 4. Je donne des exemples de différentes sources de bruit qui ont été identifées dans les dernières prises de données de Virgo: C7: 5 jours de prises de données en septembre 2005 avec Virgo pour la première fois dans sa configuration finale (interférometre dont la puissance laser est recyclée). VSR1 est la première prise de données scientifiques: 136 jours du 18 mai au 1$^{\text{ier}}$ octobre 2007. La seconde prise de données scientifiques, VSR2, a eu lieu du 7 juillet 2009 au 9 janvier 2010 (186 jours). Une fois identifiée, il faut éliminer la source de bruit. Quand le problème ne peut être régler au niveau du détecteur, ou qu'il est identifié bien après la fin de la prise de données, il faut déterminer quelles périodes de données doivent être écartées afin de ne pas altérer la signification statistique d'un vrai événement[1]

J'ai mené la première recherche de sources impulsionnelles non modelisées dans Virgo avec les données prises en 2005 (C7). Cette analyse, faite avec les données d'un seul détecteur a été publiée dans Classical and Quantum Gravity [1]. La reproduction de l'article est inclue dans le chapître 3. L'analyse n'aurait pas pu aboutir sans un travail de fond de compréhension des données et le développement de vetos. En effet, les faux événements ne peuvent être éliminés en les comparant avec ceux d'un autre détecteur comme cela est fait quand on dispose des données de plusieurs détecteurs. J'ai résumé ce travail dans la note technique VIR-0013D-007 [2]. Avec K. G. Arun, nous avons estimé les performances de cette recherche de signaux courts pour détecter la fin de la coalescence de deux trous noirs massifs. Il

[1]Il est bon de rappeler que nous recherchons des signaux de très faible amplitude détectable avec un rapport sur bruit inférieur à 10.

s'agit d'une source très prometteuses d'ondes gravitationnelles puisqu'elle correspond à la première source découverte 10 ans plus tard, et nous avons profité des progrès des groupes de relativité numérique qui dans les années 2006-2007 ont rendu publique les premi'eres formes d'ondes simulées de la phase finale du plongeon de deux trous noirs. Cela nous a permis de tester l'efficacité du programme d'analyse à ces signaux. Bien que modeste (la sensibilité de Virgo en 2005 était loin d'égaler la sensibilité d'advanced LIGO en 2015), il s'agissait du premier résultat de recherche directe de la fusion de deux trous noirs massifs dans des données réelles avec un programme de recherche de signaux courts. Travail prémonitoire puisque GW150914 a été observé en ligne en 2015 grâce à un algorithme similaire mais bien plus performant. La note technique VIR-011A-08 [3] donne des détails sur la façon dont on a estimé les performances de cette analyse.

En mai 2007, Virgo dont la sensibilité était environ un ordre de grandeur moins bonne que les détecteurs LIGO[2] a pris 4,5 mois de données en coincidence avec la fin de la prise de données S5 de LIGO. À haute fréquence (au delà de 300 Hz), la sensibilité de Virgo et de LIGO était comparable. J'ai ainsi décidé de faire une recherche de sources courtes dans les données des quatre détecteurs du réseau Virgo-LIGO entre 300Hz et 5 kHz. Cette analyse a fait l'objet d'une contribution au papier qui résume l'ensemble de la recherche de sources courtes non modelisées dans les données prises en commun dans Virgo et LIGO [4]. Cette analyse est décrite plus en détails dans le chapître 3.

Entre 2010 et 2015, les prises de données se sont arrêtées pour l'installation et le démarrage des détecteurs de seconde génération: advanced Virgo et advanced LIGO. J'ai à cette époque là profité de mon séjour à Carleton College dans le Minnesotta pour travailler avec le groupe LSC de l'Université du Minnesota sur un nouvel algorithme dédié à la recherche de signaux transitoires de durée longue (plusieurs centaines de secondes). Avec Tanner Prestegard, principal dévelopeur de l'algorithme, nous avons analysé les données de LIGO prises en 2005 et 2010. La publication est reproduite dans le chapître 3.

Finalement, le chapître 3 contient aussi un papier qui traite de la possibilité de déterminer les paramêtres physiques de l'effondrement d'une étoile en supernova à partir du signal d'onde gravitationnelle détecté. Cette analyse Bayesienne est basée sur un catalogue de formes d'ondes qui est supposé bien représenter l'ensemble des paramêtres possibles de l'étoile en rotation. Il s'agit d'un travail auquel j'ai participé pendant mon séjour à Carleton College et dont C. Röever en était le principal investigateur.

Je voudrais profiter de cet espace pour remercier l'ensemble des collègues et étudiants de Virgo et LIGO avec qui j'ai eu le plaisir de travailler et qui ont contribué grandement à ce qui est présenté dans ce mémoire. En premier lieu mes collègues au LAL: S. Antier, N. Arnaud, K. G. Arun, V. Brisson, F. Cavalier, A. C. Clapson, V. Frey, P. Hello, P. Heusse, M. Davier, N. Leroy, T. Pradier, F. Robinet et M. Was. Ceux de la collaboration Virgo: L. Bosi, G. Guidi, F. Marion, D. Verkindt et A. Viceré. Et enfin les collègues de la LSC: T. Ballinger, N. Christensen, M. Coughlin, T. Isogai, V. Mandic, T. Prestegard, E. Thrane, E. Tucker et C. Röever.

Je n'oublie pas non plus les collègues qui m'ont formée ou avec qui j'ai travaillé sur le coté moins bling bling de cette recherche: C. Arnault, G. Barrand, F. Cavalier, B. Mansoux, D. Jouano, E. Jules et encore une fois Philippe Heusse.

Pour finir, je voudrais remercier les membres du jury, L. Blanchet, E. Katsavounidis, S. Klimenko, F. Marion, G. Prodi, A. Stocchi et J. van den Brand, qui m'ont fait l'honneur d'accepter de perdre quelques jours de leur précieux temps. Je dois aussi ici remercier mon collègue Nelson Christensen pour son sens léger de la pression. L'habilitation est un archaiisme du système académique Français qui non seulement ne sert à rien (dans le domaine de la Physique expérimentale, les chercheurs sont évalués sur leur production scientifique. Quel comité n'a jamais lu une habilitation?), mais contribue à discrimer "ceux qui l'ont" de "ceux qui ne l'ont pas", sans compter que le temps que ce processus prend, est du temps de recherche perdu. Définitivement perdu.

[2] l'horizon qui est la distance à laquelle un signal de coalescence d'étoiles à neutrons est détecté avec un signal sur bruit de 8 était de $\sim$ 30 Mpc dans LIGO Hanford et de $\sim$ 8 Mpc dans Virgo.

Chapter 1

Gravitational waves

1.1 Introduction

It has been nearly a century since Albert Einstein completed the general theory of relativity [5]. Since this time general relativity has been used to describe a host of interesting astrophysical phenomena: the precession of the perihelion of Mercury's orbit [6, 7, 8, 9], the bending of light (from the Sun itself [10] to galaxies serving as gravitational lenses [11]), the equivalence principle [9], gravitational redshift [12, 13, 14], frame dragging (LenseThirring precession) [15], light travel delay [16, 17, 18, 19], neutron stars [20, 21], black holes [20, 22], the precession and inspiral of compact binary systems [23], and the description of the evolution and expansion of the universe itself [24, 25].

Gravitational waves, predicted by Einstein's general theory of relativity [26, 27], are ripples in the fabric of space-time, which propagate at the speed of light. The acceleration of massive objects creates a disturbance that causes tidal gravitational fields to propagate away from this source at the speed of light. This is similar to how the acceleration of charged particles creates an electromagnetic wave, namely *light*. In essence, gravitational waves are the light of the gravitational force. Whereas electromagnetic light is easily absorbed or scattered, gravitational waves flow unimpeded from the most interesting locations of our universe, thereby potentially giving a picture of black hole formation or the earliest moments after the Big Bang. The existence of gravitational waves has been confirmed through the binary neutron star observations of J. Taylor and J. Weisberg [28, 23]. This is one way to observe gravitational waves. Among the other means to observe gravitational wave effects one can quote the timing residuals measurements of few very stable Galactic pulsars [29]. A gravitational wave passing between the pulsar and the observer on Earth will leave a modulating signature on the observed period of the pulsar. The CMB B-mode polarization in the cosmic microwave background is a signature of the presence of gravitational waves produced by primordial vacuum modes amplified by inflation [30, 31]. All these detection methods are making use of probes that are extra-terrestral and tackle very low frequency GWs. In the early fifties, Earth-based detectors have been proposed to detect gravitational waves generated by astrophysical compact objects. Joe Weber in the 1960's at University of Maryland built narrow-band resonant bar detectors sensitive to signal around 1 kHz. The use of laser interferometry decades later enlarged the frequency band by several orders of magnitude. Detectors on Earth are limited by the seismic noise below ~ 1 Hz. The natural path was to design space borne detectors able to cover the intermediate frequencies range. All the different observational techniques and the targeted GW sources spectrum are illustrated in Figure 1.1.

In addition to celebrating the centenary of general relativity and the prediction of gravitational waves, 2015 found itself to be the *Internation Year Of Light And Light-Based Technologies* [32]. While it may seem exotic to regard gravitational waves as a type of light (but in reality there is a one-to-one association between propagation gravitational waves and propagating electromagnetic waves), the laser interferometers that are used to detect gravitational waves are the most exquisite applications of electromagnetic radiation (namely the laser beams) used to probe physical phenomena.

There has been, and continues to be, a world-wide effort to observe gravitational waves [33, 34]. The first generation of ground-based interferometric gravitational wave detectors, LIGO [35], GEO [36] and Virgo [37, 38], have operated and taken data at their design sensitivities over the last few years. The data have been examined for the presence of gravitational wave signals. While no gravitational wave events have been found important astrophysical statements could be made [34]. The network of detectors has been upgraded since 2010 and extended. Advanced LIGO [39]

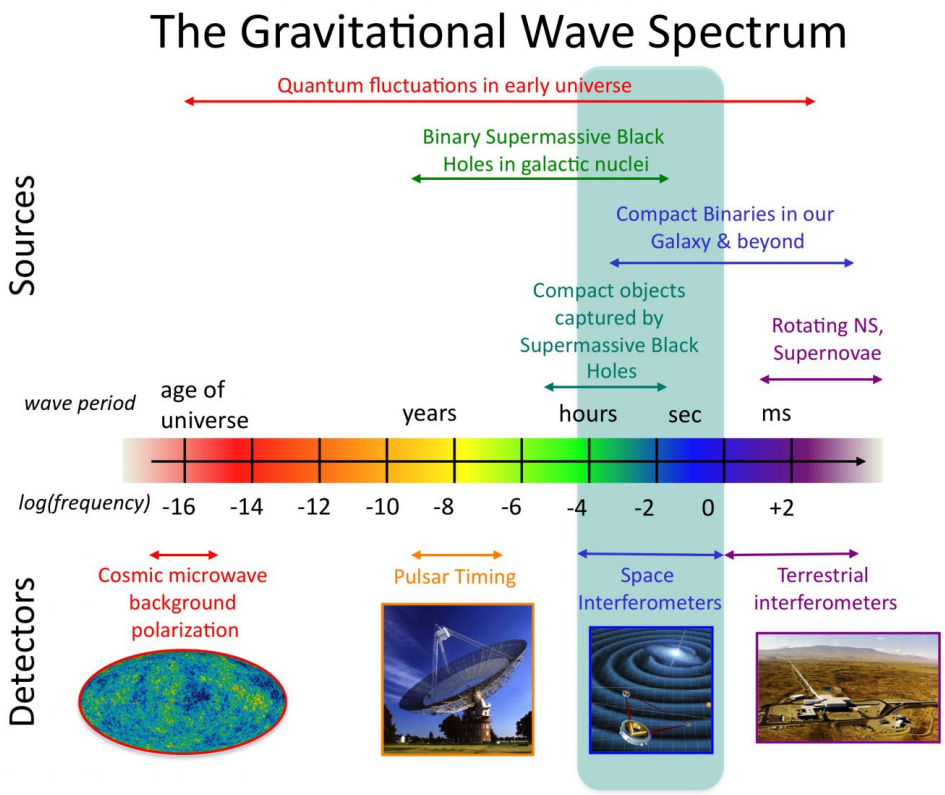

Figure 1.1: Gravitational wave spectrum, sources and detectors (credit NASA).

started observations in September 2015, leading to the first observations of gravitational waves emitted during the merger of two massive stellar mass black holes [40, 41]. Advanced Virgo [42] science operations should hopefully start in 2017. The Japanese detector KAGRA [43, 44] will commence observations after 2018. We now know that these second generation interferometric detectors have the sensitivity needed for a direct detection of an astrophysical source emitting gravitational waves. The next expected discovery should concern a binary system with at least one neutron star. The binary neutron stars inspiral distance range will reach 200 Mpc when upgraded detectors reach their design sensitivities circa 2020 [45]. The capability of the global network to determine accurately the sky location of the source is opening a new window on the Universe, where gravitational alerts will be used for quick electromagnetic follow-ups of the sources [46, 47].

1.2 From Newton to Einstein

Until the development of general relativity by Albert Einstein in 1915, Newton's description of gravitation held sway in the scientific world. However, as successful Newtonian gravitation was in describing the universe up to the end of the 19^{th} centrury, some cracks in the pillars of the theory were beginning to appear. As early as 1676, Ole Christensen Römer, then working at the Observatoire de Paris, recognized that the speed of light must be finite. Römer used the finite speed of light to explain a 10 minute delay in observing the predicted eclipse of Jupiter's moon Io. By 1862, Léon Foucault was able to obtain a speed of light that differs from today's accepted value by only 1.2×10^{-3} %[1]. Returning to Newtonian gravitation, a problem is that this theory predicts an instantaneous force of attraction

[1]Foucault's technique of bouncing light off of a rotating mirror, sending the beam to a distant fixed mirror which then retro-reflects the beam back to the rotating mirror, allowing the extraction of the speed of light from the angular displacement of the beam, is a technique

between two masses. If one mass moves, the change in position of one mass would be observed instantaneously by the second mass through the sudden change in the gravitational force.

Another concern with Newtonian gravitation pertained to the fact that the masses which appear when calculating the magnitude of the gravitational force are the same as the inertial masses. This is in contrast to the Coulomb force, where the electric charge of two objects affects the electric force between them, but their acceleration depends on their inertial masses. In Newtonian gravity there is no explanation or reason why the same mass should be responsible for both the strength of the gravitational force and the inertia, however this comes naturally within general relativity.

Finally, the slight inaccuracy in the ability to predict the precession of the orbit of Mercury was another problem of Newtonian gravity. Newtonian gravity had great success in predicting the orbits of the solar system planets, and gave a solid theoretical foundation to Kepler's Laws. There was also the success of predicting the existence of another planet due to anomalies in Uranus' orbit; this is how in 1846 Urbain Le Verrier (Observatoire de Paris) succeeded in calculating the location of this new planet, which then allowed Johann Gottfried Galle in Germany to first observe Neptune [48]. However the problem with Mercury's orbit provided no such success for describing the anomaly. In 1859 Le Verrier found that Newtonian gravity and perturbations from the known planets could not fully describe Mercury's precession; Le Verrier noted a discrepancy of 38 arc-seconds per century in the precession of the orbit of Mercury [49] (later measurements and calculations would fix the problem at 43 arc-seconds per century). It would not be until the development of general relativity that the full description of the orbital precession of Mercury could be fully explained.

The road to the successful construction of general relativity can be traced to the tremendous transformation that took place in the 19^{th} century with the development of a complete description of electromagnetic phenomena, culminating with Maxwell's equations. The full explanation of electromagnetic phenomena challenged physicists to understand the vacuum (and ultimately spacetime), and by the inherent nature of the equations, led to the Lorentz transformation. In 1864 James Clerk Maxwell was able to produce a full description of electricity and magnetism [50]. One of the concepts that was most disturbing to the physicists at the time was the displacement current. In 1826 André-Marie Ampère showed that an electric current produces a magnetic field. By 1861, Maxwell described how an electric field that was changing in time could also produce a magnetic field. In terms of current notation, the production of a magnetic field is captured in one of the Maxwell equations,

$$\nabla \times \mathbf{B} = \mu_0(\mathbf{J} + \epsilon_0 \frac{\partial \mathbf{E}}{\partial t}) \ , \tag{1.1}$$

where ϵ_0 is the permitivity of the vacuum and μ_0 is the permeability of the vacuum. Whereas the physical electric current density is represented by $\mathbf{J}$, the displacement current is $\epsilon_0 \frac{\partial \mathbf{E}}{\partial t}$. By the 1860's it was accepted that an electric current, namely moving electric charges, could produce a magnetic field. But with the displacement current, how would it be possible for a magnetic field to be created from the vacuum? Many physicists at the time refused to believe that the displacement current could exist unless the vacuum was filled with some material containing moving charges; certainly not from a void.

Further issues pertaining to the vacuum from Maxwell's equations caused consternation amongst 19^{th} century physicists. Specifically, Maxwell's equations predicted traveling electromagnetic waves. The same equations of Maxwell showed that these waves would travel at a speed of $v = 1/\sqrt{\epsilon_0 \mu_0}$. The speed of light is currently recognized to be $c = 1/\sqrt{\epsilon_0 \mu_0} = 299792458 \ m/s$. Physicists in the 19^{th} only had experience with waves that travel through a medium. The sound waves we hear travel through air, we can easily see waves in water, and seismic waves traveling through the Earth and can be felt and measured. The concept of a traveling wave that needed no medium was incomprehensible to 19^{th} physicists. Even Maxwell believed that there must be an *ether*, namely the medium in which the electromagnetic waves would propagate, but his equations did not provide any guidance as the composition of such an ether [51].

Even though Maxwell's equations predicted electromagnetic waves, it was not clear to the 19^{th} century physicists that this was *light*. Heinrich Hertz was critical in confirming the electromagnetic waves could be created and detected. Hertz was able to confirm the existence of electromagnetic waves by simultaneously creating and detecting them [52, 53]. By accident, Hertz discharged a capacitor through a wire loop, but a second loop nearby (but unconnected to the first loop) simultaneously produced an electrical field across its unconnected terminals. Through a series of further experiments Hertz was able to demonstrate that the electromagnetic (radio) waves that he created shared the same characteristics as light, namely, refraction, diffraction, polarization, and reflection. He also demonstrated that the electromagnetic waves were transverse. From his measurements Hertz was able to calculate a value for the speed of the electromagnetic waves, which was very close to the accepted value for the speed of light [54]. Hertz provided the

that is still used by University students around the world to accuately measure the speed of light for themselves.

important experimental evidence that the electromagnetic waves predicted from Maxwell's equations were actually the physical description of light.

Even with the important validation of electromagnetic waves by Hertz, and their description being contained within Maxwell's equations, physicists still struggled with the concept that these waves could propagate through the vacuum. There must be a medium for the electromagnetic waves, specifically the luminiferous ether. In 1887 Albert Michelson and Edward Morley developed and experiment to measure the speed of light with respect to the presumed ether [55]. Michelson and Morley hoped to measure the speed of the Earth with respect to the ether; the motion of the Earth being due to its motion around the Sun. Michelson and Morley used an interferometer in their experiment (which provides a nice historical link to how Virgo and LIGO are currently trying to detect gravitational waves). The premise of Michelson and Morley's experiment was that due to the motion of the ether the light in the two arms of the interferometer would take different times to travel their paths, which would cause different phase changes, and hence move the interference fringe at the output. Fig. 1.2 displays the experimental setup [55]. By floating the interferometer on a pool of mercury it was possible to re-orient the experiment, changing the orientation of the interferometer arms with respect to the apparent motion of the Earth through the ether. This experiment, and subsequent attempts by Michelson, provided no evidence for the existence of the ether. While the consequences implied by the experimental outcome did not sink in with physicists instantaneously, the result did eventually resonate with those that would pave the way toward the special theory of relativity.

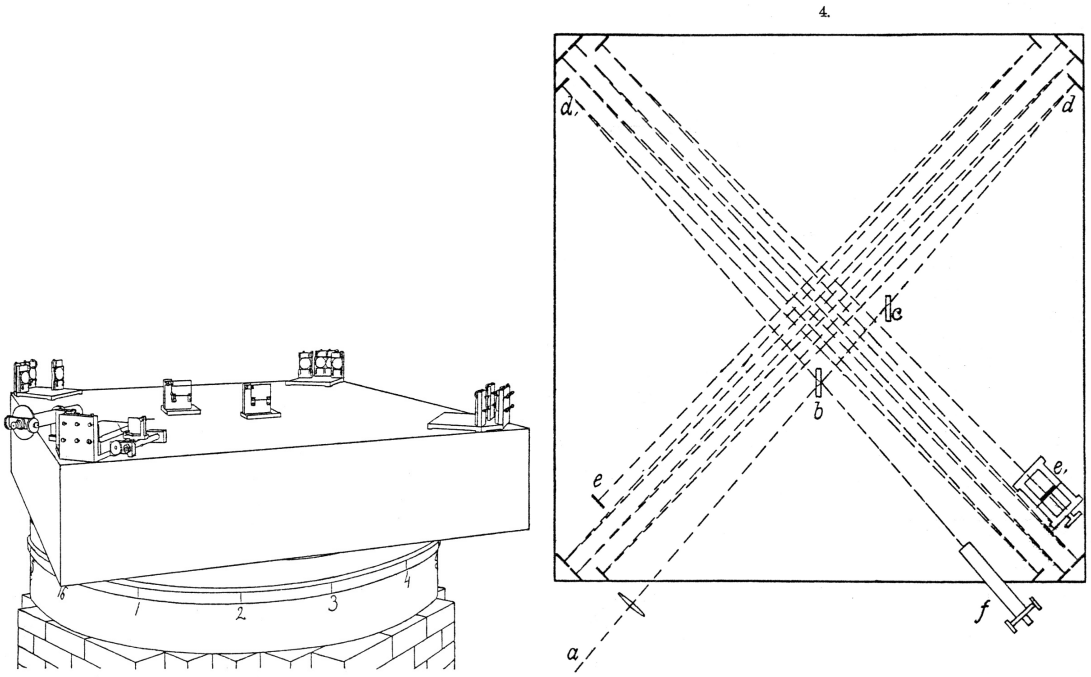

Figure 1.2: Michelson and Morley's interferometric setup. On the left is the sketch of the interferometer attached to a stone slab that floats on a pool of mercury. The sketch on the right displays the optical elements of the experiment, and the paths that the light takes [55].

The null outcome of the Michelson and Morley experiment forces a recollection of a previous *failed* experiment. In 1810 François Arago, conducted an experiment where he hoped to measure the difference in the velocity of light from a star when the Earth was moving at different velocities with respect to the star [56]. Arago was trying to confirm a prediction from Newton's corpuscular theory of light that when light enters a prism, the diffraction angle of the light depends on its speed. In this case the colors of light are determined by the speed of light. Arago mounted a prism at the end of a telescope. He then observed the deflection of light from particular stars in the morning and in the evening (when the direction of motion of the surface of the Earth, where the telescope was mounted, would change with respect to the stars). He also repeated the observations 6 months later when the orbit of the Earth about the Sun

would change the speed of the telescope with respect to the star. No difference in the deflection angle of the starlight was observed. 95 years later, with the development of special relativity, one could understand that the measured speed of light is always the same, regardless of the velocity of the observer with respect to the light source.

The 1890's saw a series of theoretical physics developments that tried to reconcile Maxwell's equations, the observations of Michelson and Morley, and the presumed existence (still) of the luminiferous ether. One of the main contributors to this effort was Hendrik Lorentz. Initially Lorentz attempted to explain electromagnetic waves in different reference frames that are moving relative to the ether [57, 58]. Lorentz developed the concept of *local time*,

$$t' = t - vx/c^2, \tag{1.2}$$

where t is the value of time for a clock at rest with respect to the ether, t' is the time value for a clock moving at a speed v with respect to ether along the positive x axis, and x is the distance (in the frame of the ether at rest) from the point where the two clocks were co-located when they had values of $t = 0$ and $t' = 0$. With this transformation Lorentz noted that Maxwell's equations maintain their form. Lorentz also used *length contraction*,

$$l = l_0\sqrt{1 - \frac{v^2}{c^2}}, \tag{1.3}$$

to try and explain the results of Michelson and Morley [59] (this had also been done by George FitzGerald in 1889 [60]). For length contraction according to Lorentz, l_0 is the length of an object at rest in the ether, while l is the length in the dimension parallel to the direction of motion for the object moving at speed v (c is the speed of light). In 1904 Lorentz published a paper that described electromagnetic phenomena in a covariant formulation [61]. Lorentz also provided the coordinate transformations (from which one can derive length contraction and time dilation) so that electromagnetic phenomena in inertial reference frames would be described by the exact same equations. Lorentz also provided how moving masses would see an increase in their inertial mass. This paper had a dramatic effect of the development of special relativity, serving as a source of motivation for Henri Poincaré and Albert Einstein.

Henri Poincaré, made tremendous contributions to the development of special relativity. In addition, in 1891, well before the development of general relativity, Poincaré stressed the need to use non-Euclidean geometry in the description of gravitation [62]. In 1898 he attempted to provide a physical interpretation to the local time that Lorentz had produced, and to address the important relativistic concept of simultaneity [63].

In 1902 Poincaré published a book containing a comprehensive description of almost all of the important topics in physics at the time; he also wrote extensively in the book about non-Euclidean geometries [64]. Poincaré allows himself to make various assumptions as to the standing of certain open issues in physics. For example, he states that there is no absolute time nor absolute space. With respect to time, he notes that we cannot talk events having time durations, not being simultaneous. In our modern language we would say that the duration of events, or simultaneity, are observer dependent. Finally, Poincaré reflects on the fact that there is no good reason to describe mechanics in Euclidean geometry; it might be less convenient to use non-Euclidean geometry, but it could be equally valid.

1905 was also an important and productive year for Poincaré. On June 5, 1905, Poincaré presented at the Académie des Sciences in Paris , "Électricité – Sur la dynamique de l'électron"; this was subsequently published in *Comptes Rendus* [65]. Here Poincaré described how the Lorentz transformations, along with rotations, form a group. In this paper Poincaré made a point of attributing these transformations to Lorentz, and in a subsequent publication he named the group after Lorentz as well. In addition, Poincaré clearly stated that Michelson's result implied that it was not possible to describe absolute motion with respect to an ether. Poincaré reported that, according to the Lorentz's assumptions, these transformations should apply to all forces, not just electromagnetism. Poincaré then spoke specifically about gravitation. In contrast to the implications of Newton's theory of gravitation where changes are propagated instantaneously, Poincaré believed that the effects of gravitational propagate at the speed of light (and in contrast to Laplace's assumption that gravitational effects propagate at a finite speed, but one faster than the speed of light). Poincaré also made the point that when a mass moves, the change in the gravitational field propagates out at the speed of light. He also remarked that the change in the gravitational field would be propagated out as a gravitational wave. Shortly following the Comptes Rendus paper, on July 23, 1905, Poincaré submitted a far more comprehensive paper describing these topics [66]. At the beginning of the paper Poincaré forcefully states the lack of experimental evidence of the absolute movement of the Earth is a general law of nature, which he coined to the *le Postulat de Relativité*. Poincaré further expanded on the postulate of relativity to note that even though the evidence for relativity was demonstrated based on electromagnetic phenomena, it should apply to the other forces in nature as

well. Poincaré studied the implications of this for gravitation, saying that the Lorentz transformations should apply to gravitation, and that the effect of a moving mass would be to have the change in the gravitational field propagate out via a gravitational wave at the speed of light.

The course of history now arrives in 1905 at the publication of Einstein's papers on special relativity; physicists around the world began to recognize that the laws of physics were forever changed. Einstein's first paper was submitted on June 30, 1905, and published on September 26 of the same year [67]. In it is the presentation of the principle of relativity, and the postulate that the speed of light is constant, regardless of the velocity of the body that emitted the light. Einstein notes that with these postulates one obtains the description of the electrodynamics of moving bodies (based on Maxwell's electrodynamics for bodies at rest), that there is no need for a luminiferous ether, and there is no requirement for an absolutely stationary space. In the same paper Einstein goes on to present what we now call the Lorentz transformations, derives the relativistic expression for the Doppler effect, and explains how energy of light can be transformed between different frames. It is interesting to note that Einstein has no citations in this paper.

Later that year, on September 27, 1905, Einstein submitted a second special relativity paper, which was subsequently published on November 21 [68]. Here Einstein presented the equivalence of mass and energy. Although the paper did not write the now famous expression $E = mc^2$ in this form, it is easily extracted from the summary of the paper.

The transition from the special relativity of 1905 to the general relativity of 1916 required an important contribution from Hermann Minkowski. In 1908 he presented his conclusion that space and time could not be discussed separately, but instead one needs to discuss spacetime [69]. Minkowski presented the Lorentz transformation via a geometrical interpretation. The spatial (x, y, z) and temporal (t) coordinates were interpreted as being the parts of a 4-vector. A spacetime diagram was presented for the first time, complete with worldlines. Finally, proper time (*Eigenzeit*), was defined for the first time,

$$d\tau = \frac{1}{c}\sqrt{c^2dt^2 - dx^2 - dy^2 - dz^2}, \tag{1.4}$$

where $\int d\tau = \tau$ is the proper time. This geometrical interpretation of special relativity opened the path for the geometrical interpretation of gravitation, namely general relativity [5].

1.3 General Relativity

The theory of general relativity is the modern description of gravitation. Newtonian gravitation was a remarkable accomplishment, but ultimately a more comprehensive theory was needed. General relativity has been demonstrated to explain phenomena on the scale of the solar system, to the universe as a whole. There are number of very good books to learn general relativity; see [70] for a summary. The general relativity material below will follow the presentation and notation of [71].

In physics it is natural to talk about forces, and how the accelerations produced from these forces lead to the consequent equations of motion. When comparing general relativity to the electro-weak, or strong forces, it is amazing to note the difference. With general relativity one needs to describe how a particle moves with respect to the space geometry, and not to some force. Particle trajectories are described in terms of motion in their geometry, or specifically their spacetime geometry.

What is fundamental to the motion of particles is the *metric* tensor. The metric describes the geometry of the spacetime that a particle is within. The Pythagorean theorem allows one to calculate the distance between two points; for a infinitesimal distance displacement dl in flat three-dimensional space one has

$$dl^2 = dx^2 + dy^2 + dz^2. \tag{1.5}$$

In this case we could also write

$$dl^2 = g_{ij}dx^i dx^j. \tag{1.6}$$

where the Einstein summation convention is implied, and the metric g_{ij} (let's not quible about the notational difference between a tensor and a tensor component) is given by

$$g_{ij} = \begin{pmatrix} 1 & 0 & 0 \\ 0 & 1 & 0 \\ 0 & 0 & 1 \end{pmatrix}. \tag{1.7}$$

Moving to special relativity, one must use the language of spacetime intervals. In the absence of matter or energy the spacetime (which will be the word used to represent the universe's three spatial and one temporal coordinates) is flat, and is described by what is known as the Minkowski metric. In this case, for the spacetime interval ds^2 we have

$$ds^2 = -c^2dt^2 + dx^2 + dy^2 + dz^2, \tag{1.8}$$

or

$$ds^2 = g_{\mu\nu}dx^\mu dx^\nu. \tag{1.9}$$

The flat spacetime represented by the Minkowski metric, which is given by $g_{\mu\nu} = \eta_{\mu\nu}$, or (with $c = 1$)

$$g_{\mu\nu} = \eta_{\mu\nu} = \begin{pmatrix} -1 & 0 & 0 & 0 \\ 0 & 1 & 0 & 0 \\ 0 & 0 & 1 & 0 \\ 0 & 0 & 0 & 1 \end{pmatrix}. \tag{1.10}$$

With general relativity spacetime is not necessarily flat. The 16 components of $g_{\mu\nu}$ can differ from those of $\eta_{\mu\nu}$. The major questions then become how to derive the metric in the presence of matter and energy, and how to predict the motion of particles when spacetime is not flat (i.e. not described by the Minkowski metric). Note that we assume that we live in a universe where $g_{\mu\nu} = g_{\nu\mu}$ (i.e. we assume that nonsymmetric gravitational theory [72] is not correct). Note that $g^{\gamma\alpha}$ is the inverse metric tensor, defined via $g^{\gamma\alpha}g_{\alpha\nu} = \delta^\gamma_\nu$ (the Einstein summation notation is assumed), where $\delta^\gamma_\nu = 1$ if $\gamma = \nu$ and $\delta^\gamma_\nu = 0$ if $\gamma \neq \nu$.

For now let us assume that there is some arbitrary structure to spacetime such that $g_{\mu\nu} \neq \eta_{\mu\nu}$. The information on the curvature of spacetime is contained within the metric. Because of the curvature particles will follow non-trivial trajectories. The *geodesic equation* provides the means to calculate a particle's position as a function of its proper time, τ as it moves along its worldline. To derive the geodesic equation one uses the extreme action principle to find the worldline of longest proper time, specifically

$$\frac{d}{d\tau}(g_{\gamma\mu}\frac{dx^\mu}{d\tau}) - \frac{1}{2}\partial_\gamma g_{\mu\nu}\frac{dx^\mu}{d\tau}\frac{dx^\nu}{d\tau} = 0, \tag{1.11}$$

where ∂_γ is shorthand for $\frac{\partial}{\partial x^\gamma}$. Like Newtonian gravity, one must specify two initial conditions (for example a location and the velocity at some initial time) in order to fully describe the location of the particle as a function of time; however with general relativity one must also know the metric as a function of spacetime $g_{\mu\nu}(x^\alpha)$. Hence with the geodesic equation the motion of any particle can be calculated, assuming that the metric is known.

The information of the curvature of spacetime is contained within the metric, and one uses Riemannian geometry to describe the curvature and related tensor quantities. The Christoffel symbol, $\Gamma^\alpha_{\mu\nu}$, is defined as

$$\Gamma^\alpha_{\mu\nu} \equiv \frac{1}{2}g^{\alpha\sigma}[\partial_\mu g_{\nu\sigma} + \partial_\nu g_{\sigma\mu} - \partial_\sigma g_{\mu\nu}] \ , \tag{1.12}$$

and it allows us to define an *absolute gradient* (derivative) operation that keeps the same form when using any coordinate system, namely its form is coordinate independent. The absolute gradient of a vector A^μ would be

$$\nabla_\alpha A^\mu \equiv \frac{\partial A^\mu}{\partial x^\alpha} + \Gamma^\mu_{\alpha\nu}A^\nu \ . \tag{1.13}$$

Note that with the Chistoffel symbol the geodesic equation can be written in a more compact form, namely

$$\frac{d^2x^\gamma}{d\tau^2} + \Gamma^\gamma_{\mu\nu}\frac{dx^\mu}{d\tau}\frac{dx^\nu}{d\tau} = 0 \ . \tag{1.14}$$

The Riemann tensor is defined in terms of the Christoffel symbols, namely

$$R^\alpha_{\beta\mu\nu} = \partial_\mu\Gamma^\alpha_{\beta\nu} - \partial_\nu\Gamma^\alpha_{\beta\mu} + \Gamma^\alpha_{\mu\gamma}\Gamma^\gamma_{\beta\nu} - \Gamma^\alpha_{\nu\sigma}\Gamma^\sigma_{\beta\mu} \ . \tag{1.15}$$

The Rienmann tensor is a useful quantity for predicting the trajectory of particles subjected to tidal effects, including those in and about the Earth. The Ricci tensor is then defined as

$$R_{\beta\nu} \equiv R^\alpha_{\beta\alpha\nu} \ , \tag{1.16}$$

and finally the curvature scalar is given by

$$R \equiv g^{\beta\nu} R_{\beta\nu} \ . \tag{1.17}$$

In order to derive the metric as a function of spacetime one must know the mass and energy distribution in the spacetime. The Einstein equation relates the curvature of spacetime to the mass, energy, and momentum present. For most of the 20^{th} century the Einstein equation was written as

$$R^{\mu\nu} - \frac{1}{2} g^{\mu\nu} R = 8\pi G T^{\mu\nu} \ , \tag{1.18}$$

where G is Newton's constant and $R^{\mu\nu} = R_{\alpha\beta} g^{\mu\alpha} g^{\nu\beta}$. The stress-energy tensor, $T^{\mu\nu}$ contains the information of the mass-energy and momentum density present in the spacetime. For example, a perfect fluid at rest would have

$$T^{\mu\nu} = \begin{pmatrix} \rho_0 & 0 & 0 & 0 \\ 0 & p_0 & 0 & 0 \\ 0 & 0 & p_0 & 0 \\ 0 & 0 & 0 & p_0 \end{pmatrix} \ , \tag{1.19}$$

where ρ_0 is the energy in the rest frame of the fluid, while p_0 is the pressure in the rest frame of the fluid. While Einstein personally waffled with the form of the equation, the late 1990's observations of distant Type Ia supernovae [73, 74] and the cosmic microwave background [75, 76, 25] indicated that the equation should instead be represented by

$$R^{\mu\nu} - \frac{1}{2} g^{\mu\nu} R + \Lambda g^{\mu\nu} = 8\pi G T^{\mu\nu} \ , \tag{1.20}$$

where Λ is the cosmological constant, or in terms of current jargon, the representation of *dark energy*. One can rewrite the Einstein equation with cosmological constant as,

$$\begin{aligned} R^{\mu\nu} - \frac{1}{2} g^{\mu\nu} R &= 8\pi G T^{\mu\nu} - \Lambda g^{\mu\nu} \\ &= 8\pi G (T^{\mu\nu} + T_v^{\mu\nu}) \ , \end{aligned} \tag{1.21}$$

where one can not talk instead of a cosmological constant, Λ, but a dark energy, represented by a stress energy tensor

$$T_v^{\mu\nu} = -g^{\mu\nu} \frac{\Lambda}{8\pi G} \tag{1.22}$$

and the vacuum energy density would be

$$\rho_v = T^{tt} = -g^{tt} \frac{\Lambda}{8\pi G} = \frac{\Lambda}{8\pi G} \ . \tag{1.23}$$

This also implies a pressure of the vacuum of

$$p_v = -\frac{\Lambda}{8\pi G} \ . \tag{1.24}$$

The observations from distant Type Ia supernovae [73, 74] and the cosmic microwave background [75, 76, 25] show that the universe's expansion is accelerating, implying the presence of a negative pressure. Parameter estimation on cosmic microwave background data [77, 76, 25] tells us that the vacuum energy density is $\Omega_\Lambda = 0.68$, where an energy density is expressed in terms of its ratio with the critical energy density necessary to close the universe, namely

$$\Omega \equiv \frac{\rho}{\rho_c} \tag{1.25}$$

where

$$\rho_c = \frac{3H_0^2}{8\pi G} \tag{1.26}$$

and H_0 is the current Hubble constant ($H_0 = 67.3\,\mathrm{kms}^{-1}\mathrm{Mpc}^{-1}$ [25]). When dealing with cosmological problems it is imperative to include the cosmological constant; for applications in and about a black hole, a particular galaxy, or our solar system, Λ can be ignored.

A classic example of a closed form solution is for the metric around a spherical mass distribution, namely the Schwarzschild solution. In this case the metric outside of the spherical mass is given by

$$g_{\mu\nu} = \begin{pmatrix} -(1-\frac{2GM}{rc^2}) & 0 & 0 & 0 \\ 0 & (1-\frac{2GM}{rc^2})^{-1} & 0 & 0 \\ 0 & 0 & r^2 & 0 \\ 0 & 0 & 0 & r^2 sin^2(\theta) \end{pmatrix} , \tag{1.27}$$

where M is the total mass, r is the radial coordinate (and not the proper radial distance), and θ and ϕ are the latitude and longitude coordinates. The spacetime interval is then

$$ds^2 = -(1-\frac{2GM}{rc^2})dt^2 + (1-\frac{2GM}{rc^2})^{-1}dr^2 + r^2 d\theta^2 + r^2 sin^2(\theta)d\phi^2 \ . \tag{1.28}$$

1.4 Linearized General Relativity

The Einstein equation is non-linear, and notoriously difficult to solve. Only a limited number of closed form solutions exist. As such, it is often more convenient to make some approximations and simplify the equations. In fact, by working to first order in pertubations to the flat space metric the corresponding equations of general relativity can be made linear. For example, we can write the metric as

$$g_{\mu\nu} \approx \eta_{\mu\nu} + h_{\mu\nu} \ , \tag{1.29}$$

where $h_{\mu\nu}$ is the small perturbation to the flat spacetime Minkowski metric. In order to appreciate the small scale of gravitational perturbations seen in the Schwarzschild metric, the term $\frac{2GM}{rc^2}$ in Eq. (1.28) gives the magnitude (h) of the scale of $h_{\mu\nu}$. At the surface of the Earth $h \approx 1.4 \times 10^{-9}$. At the surface of the Sun $h \approx 4.3 \times 10^{-6}$. Clearly for the environment about the surface of the Earth or the Sun the deviations from the flat Minkowski metric are very small. For comparison, consider a neutron star with a mass of 1.4 $M_\odot$ and radius of 10 km; in this case $h \approx 0.42$. The Schwarschild radius is what defines a black hole, namely when $\frac{2GM}{rc^2} = 1$; in that case the change from flat spacetime is significant.

In the case of studies pertaining to the detection of gravitational waves, using linearized general relativity will be more than adequate. Virgo and LIGO are searching for gravitational waves where the amplitude of the wave (and hence the perturbation) has $h < 10^{-20}$, certainly a small perturbation to flat spacetime. However the production of gravitational waves could certainly happen in an environment where the deviation from flat spacetime is significant.

An important topic for gravitational wave detection science concerns the prediction of gravitational wave signals. A comparison between predicted and detected signals is critical for the success of gravitational wave science and has been demonstrated by numerous GW150914 companion papers. Predicting how the changing distribution of mass and energy (represented by the stress energy tensor $T^{\mu\nu}$) affects perturbations at the location of a gravitational wave detector, $h_{\alpha\beta}$, is tremendously complicated; the use of appropriate approximation techniques and the assumption of *reasonable* conditions for the source mass-energy (limited velocities for the material, not excessive curvature to spacetime, etc.) can lead to simplified equations that are more tractable [78].

The coalescence of binary systems containing neutron stars and/or black holes have always been considered as the most promising source of gravitational wave signals for LIGO and Virgo. The prediction of the basic form of these signals (see below) is relatively straightforward [71, 20], but as the compact binary coalescing systems approaches merger the general relativistic effects become more significant. A perturbative method to iteratively make the prediction of the gravitational wave signal more accurate involves the use of *post-Newtonian expansion* [78]. For this technique a parameter is defined, $\epsilon \sim v/c$, where v represents the characteristic velocity of material moving within the source. Solutions to the complicated general relativistic equations are then done iteratively in powers of ϵ.Another approximation technique is called the post-Minkowskian method; here one still assumes that gravitational field is weak, but no assumptions are made on the velocity of the source material. Solutions are generated via the expansion in powers of Newton's constant G [78]. These techniques will be discussed in more detail below, especially when talking about the attempt to detect gravitational wave signals from compact binary coalescing systems by LIGO and Virgo.

1.5 Gravitational Wave Generation

Presented below is a brief summary of the general relativistic description of gravitational waves. This introduction to the topic follows the style and content of [71]. For a thorough review of gravitational wave physics, sources, and detection see also [79, 80, 81].

As previously mentioned, when discussing the gravitational waves that Virgo and LIGO aim to detect one can consider that the perturbation to spacetime from the gravitational wave is small. It is acceptable to use the weak field limit and write

$$g_{\mu\nu} \approx \eta_{\mu\nu} + h_{\mu\nu} \ , \tag{1.30}$$

where $h_{\mu\nu}$ is the metric perturbation. This approximation can then be inserted into the Einstein equation, Eq. (1.18). When working with the Einstein equation one only keeps terms proportionl to h (i.e. neglecting terms of order h^2 or higher), since for the gravitational waves searched for by Virgo and LIGO one has $h < 10^{-20}$. For example, the Riemann tensor can then be approximated as

$$R_{\alpha\beta\mu\nu} \approx \frac{1}{2}[\partial_\beta\partial_\mu h_{\alpha\nu} + \partial_\alpha\partial_\nu h_{\beta\mu} - \partial_\alpha\partial_\mu h_{\beta\nu} - \partial_\beta\partial_\nu h_{\alpha\mu}] \ . \tag{1.31}$$

In producing solutions for gravitational waves it is convenient to define the *trace-reversed metric tensor*, namely

$$H_{\mu\nu} \equiv h_{\mu\nu} - \frac{1}{2}\eta_{\mu\nu}h \ , \tag{1.32}$$

where $h = \eta^{\mu\nu}h_{\mu\nu}$ is the trace of $h_{\mu\nu}$. Note that the trace-reversed name is derived from the fact that $H = \eta^{\mu\nu}H_{\mu\nu} = -h$. The inverted equation is then

$$h_{\mu\nu} \equiv H_{\mu\nu} - \frac{1}{2}\eta_{\mu\nu}H \ . \tag{1.33}$$

As such, the Einstein equation can be reduced to

$$\partial^\beta\partial_\beta H^{\gamma\sigma} - \partial^\gamma\partial_\mu H^{\mu\sigma} - \partial^\sigma\partial_\mu H^{\mu\gamma} + \eta^{\gamma\sigma}\partial_\beta\partial_\mu H^{\mu\beta} = -16\pi G T^{\gamma\sigma} \ , \tag{1.34}$$

where $\partial^\beta = \eta^{\alpha\beta}\partial_\alpha$ and $H^{\alpha\beta} = \eta^{\alpha\mu}\eta^{\beta\nu}H_{\mu\nu}$.

Gauge transformations will further simplify the Einstein equation. In order to do so, one needs to consider a simple coordinate transformation,

$$x'^\alpha = x^\alpha + \xi^\alpha \ , \tag{1.35}$$

where $\xi^\alpha = \xi^\alpha(x, y, z, t)$ and $|\xi^\alpha| \ll 1$. In terms of the new coordinates one then has

$$h'_{\mu\nu} = h_{\mu\nu} - \partial_\mu\xi_\nu - \partial_\nu\xi_\mu \tag{1.36}$$

and

$$H'_{\mu\nu} = H_{\mu\nu} - \partial_\mu\xi_\nu - \partial_\nu\xi_\mu + \eta_{\mu\nu}\partial_\alpha\xi^\alpha \ . \tag{1.37}$$

Still working only with terms first order in h, the coordinate transformation does not change the Riemann tensor,

$$R'_{\alpha\beta\mu\nu} \approx R_{\alpha\beta\mu\nu} \tag{1.38}$$

which implies that the Einstein equation (to first order in h) will also not change. Therefore the coordinate transformations defined in Eq. (1.35) define a *gauge transformation*. An appropriate choice of gauge can further simplify the Einstein equation. For example, the *Lorentz gauge* is an example of where it is possible to find a particular gauge transformation where one will have

$$\partial_\mu H'^{\mu\nu} = 0 \ . \tag{1.39}$$

This convenient condition further simplifies the approximative form of the Einstein equation, Eq. (1.34), to the much more tractable form

$$\partial_\beta\partial^\beta H^{\mu\nu} = -16\pi G T^{\mu\nu} \tag{1.40}$$

and

$$\partial_\mu H^{\mu\nu} = 0 \tag{1.41}$$

(where the primes are now suppressed). Finally, it is still possible within the constraints of the Lorentz gauge to impose the additional gauge condition of

$$\partial_\beta \partial^\beta \xi^\mu = 0 \ . \tag{1.42}$$

When one considers gravitational waves it is natural to make associations with electromagnetic waves (i.e. light). Light is a transverse electromagnetic wave that propagates at c in the vacuum. Consider a gravitational phenomena propagating in the vacuum. When speaking of a vacuum it implies the absence of matter-energy density, so one would have $T^{\mu\nu}$. This would then further reduce the Einstein equation to the form (within the Lorentz gauge)

$$\partial_\beta \partial^\beta H^{\mu\nu} = [-\frac{\partial^2}{\partial t^2} + \nabla^2] H^{\mu\nu} = 0 \ . \tag{1.43}$$

A solution to this differential equation would clearly be that of a traveling wave, for example

$$H^{\mu\nu}(t,x,y,z) = A^{\mu\nu} cos(k_\beta x^\beta) = A^{\mu\nu} cos(\vec{k}\cdot\vec{r} - \omega t) \ . \tag{1.44}$$

The amplitude of the traveling wave is a constant matrix, $A^{\mu\nu}$. The requirement that the metric be symmetric also implies that $A^{\mu\nu} = A^{\nu\mu}$. By using the Einstein equation for gravitational waves in a vacuum, Eq. (1.43), one obtains the condition

$$k^\beta k_\beta = \eta_{\mu\beta} k^\mu k^\beta = 0 \ . \tag{1.45}$$

This wavevector equation is again reminiscent of electromagnetic waves, where $k^t = \omega$, and $\vec{k} = (k^x, k^y, k^z)$. In this case

$$\eta_{\mu\beta} k^\mu k^\beta = -\omega^2 + k^2 = 0 \ , \tag{1.46}$$

where $k^2 = \vec{k}\cdot\vec{k}$, which implies that the wave travels at a velocity of $v = \frac{\omega}{k} = 1$. Hence gravitational waves travel at the speed of light. The Lorentz gauge condition, Eq. (1.41), implies that $k_\mu A^{\mu\nu} = \eta_{\alpha\mu} k^\alpha A^{\mu\nu} = 0$, which then implies that the effect of the gravitational wave is transverse to the propagation direction; this is again analogous to electromagnetic waves. The other gauge condition, Eq. (1.42), will further help to simplify an expression for $A^{\mu\nu}$. The coordinate transformation $\xi^\mu = B^\mu sin(k_\sigma x^\sigma)$ satisfies gauge condition expressed in Eq. (1.42). Applying the coordinate transformation will mean that the wave amplitude matrix will transform as

$$A'^{\mu\nu} = A^{\mu\nu} - k^\mu B^\nu - k^\nu B^\mu + \eta^{\mu\nu} k_\alpha B^\alpha \ . \tag{1.47}$$

An appropriate choice of the B^μ terms will allow one to assign $A'^{t\mu} = A'^{\mu t} = 0$ and $A'^\mu_\mu = \eta_{\mu\nu} A'^{\mu\nu} = 0$ (and we again henceforth drop the primes). The final result is that the wave amplitude matrix is now transverse and traceless. The gravitational waves described in this way will be said to be in a transverse-traceless gauge. Since this solution for the trace-reversed metric tensor, Eq. (1.32) is traceless ($A^\mu_\mu = H^\mu_\mu = 0$), in the transverse-traceless gauge the metric perturbation and the trace-reversed metric tensor are equivalent, or $h^{TT}_{\mu\nu} = H^{TT}_{\mu\nu}$.

A gravitational wave with angular frequency ω traveling in the $+\hat{\mathbf{z}}$ direction will be used as an example. In terms of the cartesian coordinate system, $k^\beta = [\omega, 0, 0, \omega]$, or equivalently $k_\beta = [-\omega, 0, 0, \omega]$. Eq. (1.41) then implies

$$k_\nu A^{\nu\mu} = -\omega A^{t\mu} + \omega A^{z\mu} = 0 \tag{1.48}$$

which then gives $A^{t\mu} = A^{z\mu}$. But since it has already been determined that $A^{t\mu} = 0$ then $A^{z\mu} = 0$. Finally, by the traceless condition $A^\mu_\mu = 0$, and the already established $A^{tt} = A^{zz} = 0$, it follows that $A^{xx} + A^{yy} = 0$. The only possible remaining non-zero term for $A^{\mu\nu}$ are $A^{xx} = -A^{yy}$ (traceless condition) and $A^{xy} = A^{yx}$ (by symmetry of the metric). For this example of a graviational wave traveling in the $+\hat{\mathbf{z}}$ direction it is clear that the wave can be described by two polarizations,

$$A^{xx} = -A^{yy} = A_+ \tag{1.49}$$

and

$$A^{xy} = A^{yx} = A_\times \ , \tag{1.50}$$

or

$$A^{\mu\nu} = A_+ \begin{pmatrix} 0 & 0 & 0 & 0 \\ 0 & 1 & 0 & 0 \\ 0 & 0 & -1 & 0 \\ 0 & 0 & 0 & 0 \end{pmatrix} + A_\times \begin{pmatrix} 0 & 0 & 0 & 0 \\ 0 & 0 & 1 & 0 \\ 0 & 1 & 0 & 0 \\ 0 & 0 & 0 & 0 \end{pmatrix} \ . \tag{1.51}$$

In order to work with the metric $g_{\mu\nu} = \eta_{\mu\nu} + h_{\mu\nu}$ one needs $A_{\mu\nu} = \eta_{\mu\alpha}\eta_{\mu\beta}A^{\alpha\beta}$, and it can easily be shown that

$$A_{\mu\nu} = A_+ \begin{pmatrix} 0 & 0 & 0 & 0 \\ 0 & 1 & 0 & 0 \\ 0 & 0 & -1 & 0 \\ 0 & 0 & 0 & 0 \end{pmatrix} + A_\times \begin{pmatrix} 0 & 0 & 0 & 0 \\ 0 & 0 & 1 & 0 \\ 0 & 1 & 0 & 0 \\ 0 & 0 & 0 & 0 \end{pmatrix} . \tag{1.52}$$

The two matrices in Eq. (1.52) represent the two possible polarizations of gravitational waves, and are referred to as the *plus* (+) and *cross* (×) polarizations.

Now that the form of the gravitational wave has been defined, the obvious question is what effect it might have on a massive test particle. The obvious place to start is with the geodesic equation, Eq. (1.14). Consider a particle at rest, thereby having a *4-velocity*

$$u^\alpha = \frac{dx^\alpha}{d\tau} \approx [1, 0, 0, 0] . \tag{1.53}$$

A plane wave gravitational wave traveling in the $+\hat{\mathbf{z}}$ direction will be incident on the particle,

$$h^{TT}_{\mu\nu} = A_{\mu\nu} cos(kz - \omega t) , \tag{1.54}$$

where $A_{\mu\nu}$ is represented by Eq. (1.52). Using Eq(1.12) it is straightforward to show that the only meaningful Christoffel symbols would be Γ^γ_{tt}, and then

$$\begin{aligned} \Gamma^\gamma_{tt} &= \frac{1}{2} g^{\gamma\sigma}[\partial_t g_{t\sigma} + \partial_t g_{\sigma t} - \partial_\sigma g_{tt}] \\ &\approx \frac{1}{2}\eta^{\gamma\sigma}[2\partial_t h^{TT}_{t\sigma} - \partial_\sigma h^{TT}_{tt}] \\ &= 0 . \end{aligned} \tag{1.55}$$

This result would seem to imply that the particle will experience no acceleration due to the gravitational wave, and hence will not move. However the particle is co-moving with the coordinate system, so one must be careful in drawing conclusions. What will be more informative is to calculate the physical distance between particles.

Consider a circular ring of particles in the $x - y$ plane at $z = 0$; the ring radius is R. A gravitational wave, as defined by Eq. (1.54) is incident on the particles. As a first example, the gravitational wave will be linearly polarized in the plus polarization ($A_\times = 0, A_+ \neq 0$). The coordinate difference between a particle on the ring and the origin is $\Delta x = Rcos(\theta)$ and $\Delta y = Rsin(\theta)$. The physical distance between the particle and the origin would then be

$$\begin{aligned} \Delta s^2 &= g_{\mu\nu}\Delta x^\mu \Delta x^\nu = (\eta_{\mu\nu} + h^{TT}_{\mu\nu})\Delta x^\mu \Delta x^\nu \\ &= (\eta_{\mu\nu} + A_{+\mu\nu})cos(\omega t)\Delta x^\mu \Delta x^\nu \\ &= (\eta_{xx} + A_+ cos(\omega t))(Rcos(\theta))^2 + (\eta_{yy} - A_+)cos(\omega t))(Rsin(\theta))^2 \\ &= R^2[1 + A_+ cos(\omega t)(cos^2(\theta) - sin^2(\theta))] \\ &= R^2[1 + A_+ cos(\omega t)cos(2\theta)] , \end{aligned} \tag{1.56}$$

which then implies

$$\begin{aligned} \Delta s &= R[1 + A_+ cos(\omega t)cos(2\theta)]^{1/2} \\ &\approx R[1 + \frac{1}{2}A_+ cos(\omega t)cos(2\theta)] . \end{aligned} \tag{1.57}$$

A similar derivation for the cross polarization ($A_+ = 0, A_\times \neq 0$) gives

$$\Delta s \approx R[1 + \frac{1}{2}A_\times cos(\omega t)sin(2\theta)] . \tag{1.58}$$

Consider first the effect of the plus polarization gravitational wave, Eq. (1.57); initially at $t = 0$ the particle on the positive x-axis ($\theta = 0$) will have a larger physical distance from the origin than the particle on the positive y-axis. As the wave evolves in time the particle on the positive y-axis will acquire a larger physical distance than the particle

on the positive x-axis. One axis expands while the other contracts. The expansion and contraction for the cross polarization is the same, except that effect is rotated by $\theta = \pi/4$ from that of the plus polarization. This is displayed in Fig. (1.3).

The effect of a gravitational wave resembles that of a tidal gravitational force; in one dimension there is an acceleration inward while it is outward in the opposite dimension. A gravitational wave also produces a *strain* on spacetime. Consider the particle on the positive x-axis ($\theta = 0$), subjected to the plus-polarization gravitational wave. In the absence of a gravitational wave the distance to the origin is R, while with the gravitational wave the distance is $R[1 + \frac{1}{2}A_+ cos(\omega t)]$. Strain is defined to be the ratio of the change in length, ΔL, over length L. Hence the strain on spacetime from the plus-polarization gravitational wave is

$$\frac{\Delta L}{L} = \frac{\frac{R}{2}A_+ cos(\omega t)}{R} = \frac{1}{2}A_+ cos(\omega t) \ . \tag{1.59}$$

From this one can see that in trying to detect a gravitational wave of a given amplitude A_+ a change in length ΔL will be easier to measure if the total unperturbed length L is longer. This fact will be critically important when discussing kilometer arm length detectors, such as Virgo or LIGO.

Gravitational waves, similar to electromagnetic waves, carry energy and momentum. Consider once again a plus-polarization wave traveling in the $+\hat{\mathbf{z}}$ direction,

$$h_+(t, z) = h_{xx}^{TT} = -h_{yy}^{TT} = A_+ cos(kz - \omega t) \ . \tag{1.60}$$

It can be shown that the energy density of this wave is given by

$$T_{tt}^{GW} = \frac{\langle \dot{h}_+ \dot{h}_+ \rangle}{16\pi G} \ , \tag{1.61}$$

where the brackets $\langle\rangle$ signify an average over many wavelengths and $\dot{h}_+$ represents the time derivative of the gravitational wave

$$\dot{h}_+ = -\omega A_+ sin(kz - \omega t) \ . \tag{1.62}$$

The cross-polarization gravitational wave would have a similar energy density

$$T_{tt}^{GW} = \frac{\langle \dot{h}_\times \dot{h}_\times \rangle}{16\pi G} \ , \tag{1.63}$$

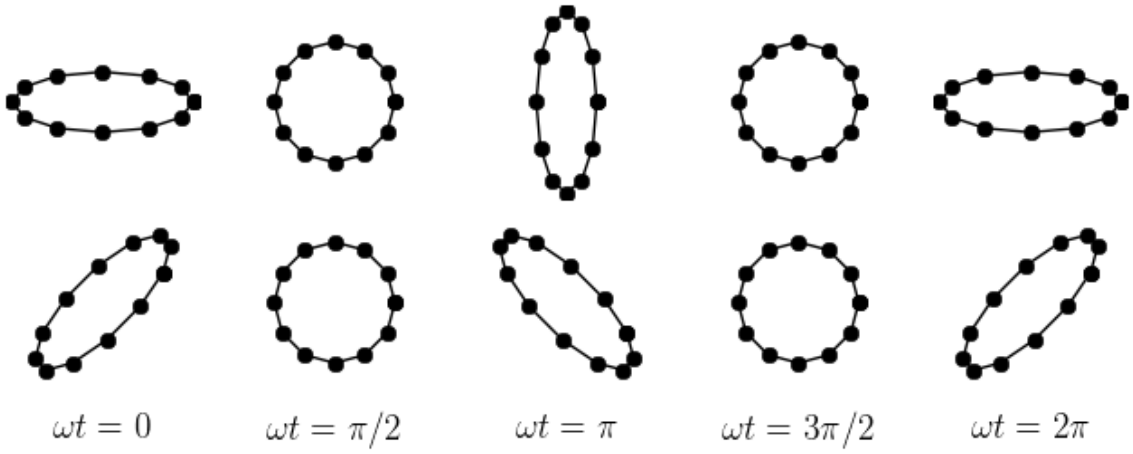

Figure 1.3: Examples of the response of a ring of particles floating in space (located in the $z = 0$ plane) to a plus-polarization gravitational wave (top), and a cross-polarization gravitational wave (bottom). The gravitational waves are defined by Eq. (1.54).

where $h_\times = h^{TT}_{xy} = h^{TT}_{yx}$. For a general gravitational wave with both polarizations present the energy density would be

$$T^{GW}_{tt} = \frac{\langle \dot{h}_+ \dot{h}_+ + \dot{h}_\times \dot{h}_\times \rangle}{16\pi G} = \frac{\langle \dot{h}^{TT}_{jk} \dot{h}^{TTjk} \rangle}{32\pi G} \ . \tag{1.64}$$

The gravitational wave energy per unit time per unit area, or the flux Ψ, is an important quantity to know. This will relate the gravitational wave power of a distant source to what is possible to observe with detectors on Earth. Consider the gravitational wave to be flowing directly into a surface of area A. In time Δt the volume occupied by the wave will be $V = Ac\Delta t$. The total energy, E, in gravitational waves in this volume will be

$$E = \rho A c \Delta t \tag{1.65}$$

where the energy density $\rho = T^{GW}_{tt}$. Hence the flux is given by

$$\Psi = \frac{E}{A\Delta t} = \frac{\rho A \Delta t}{Ac\Delta t} = \rho c \ . \tag{1.66}$$

Therefore with $c = 1$,

$$\Psi = T^{GW}_{tt} \ . \tag{1.67}$$

One can again make the analogy to electromagnetism when trying to describe the production of gravitational waves. In classical electromagnetic theory, an accelerated charge will produce *light*, or an electromagnetic wave. Accelerated mass will produce gravitational waves. The lowest multipole moment for electromagnetic waves is the dipole moment; there is no monopole radiation. A positive and a negative charge separated by some distance constitute an electric dipole. On the other hand, the is no negative mass in general relativity, only positive. Hence the lowest order multipole moment for the production of gravitational waves is the quadrupole.

The *reduced quadrupole moment* is defined as

$$\mathcal{I}^{jk} = \int_{src} \rho (x^j x^k - \frac{1}{3}\eta^{jk} r^2) dV \tag{1.68}$$

where the superscripts j and k run over the three spatial-dimensions, ρ is the mass-energy density of the signal source, and the integral is over the volume containing the source.

Consider some distribution of mass-energy that is changing with time. One can calculate the reduced quadrupole moment, $\mathcal{I}^{jk}$ in terms of some convenient coordinate system about the source. If there is acceleration within that mass-energy distribution then it is possible for gravitational waves to be produced. In terms of the coordinate system that is used to construct the reduced quadrupole moment, the gravitational waves that would propagate in the $+\hat{\mathbf{z}}$ direction would be

$$\begin{aligned} h^{xx}_{TT} &= \frac{G}{R}(\mathcal{I}^{xx} - \mathcal{I}^{yy}) \ , \\ h^{yy}_{TT} &= \frac{G}{R}(\mathcal{I}^{yy} - \mathcal{I}^{xx}) \ , \\ h^{yx}_{TT} &= h^{xy}_{TT} = \frac{2G}{R}\mathcal{I}^{xy} \ , \end{aligned} \tag{1.69}$$

where R is the distance to the source. In addition to the unique direction specified by the $+\hat{\mathbf{z}}$ direction, one also needs to have the general solution for the propagation of gravitational waves in any direction (as represented by the transvers and traceless gravitational wave solution in that direction). Call $\hat{\mathbf{n}}$ the unit vector that represents the general direction of propagation of the gravitational wave. Then the metric perturbation for the gravitational wave propagating in the $+\hat{\mathbf{n}}$ direction will be

$$h^{jk}_{TT} = \frac{2G}{R}(P^j_m P^k_n - \frac{1}{2}P^{jk}P_{mn})\ddot{\mathcal{I}}^{mn} \ , \tag{1.70}$$

where the tranverse-traceless projection operator is

$$P^j_m \equiv \delta^j_m - n^j n_m \ . \tag{1.71}$$

For convenience one can refer to the transverse-traceless part of the reduced quadrupole moment, or

$$I^{jk}_{TT} \equiv (P^j_m P^k_n - \frac{1}{2} P^{jk} P_{mn}) I^{mn} \ . \tag{1.72}$$

The flux of energy in gravitational waves was defined in Eq. (1.64) and Eq. (1.67), but now it can be expressed in terms of the changing reduced quadrupole moment of the source,

$$\Psi = \frac{G}{8\pi R^2} \langle \dddot{I}^{jk}_{TT} \dddot{I}^{TT}_{jk} \rangle \tag{1.73}$$

By integrating over all directions it is then possible to express the gravitational wave luminosity from the source,

$$L_{GW} = -\frac{dE}{dt} = \frac{G}{5} \langle \dddot{I}^{jk} \dddot{I}_{jk} \rangle \ . \tag{1.74}$$

We will now consider the case of compact (neutron stars and black holes) binary systems. Two point masses, m_1 and m_2 are separated by a distance D, and orbiting about one another at angular frequency ω. The distance of m_1 from the system's center of mass is r_1, while m_2 is separated from the center of mass by r_2; note that $r_1/r_2 = m_2/m_1$, and $r_1 + r_2 = D$. The coordinate system will be such that the orbital plane will coincide with the $x-y$ plane ($z = 0$). The phase of the orbit is defined by an arbitrary choice of $t = 0$ such that m_1 will be found on the positive $\hat{\mathbf{x}}$ axis while m_2 will be found on the negative $\hat{\mathbf{x}}$ axis. As such, the locations of the masses during the orbit will be

$$\begin{aligned} x_1 &= r_1 cos(\omega t) \\ y_1 &= r_1 sin(\omega t) \\ x_2 &= -r_2 cos(\omega t) \\ y_2 &= -r_2 sin(\omega t) \ . \end{aligned} \tag{1.75}$$

From this and Eq. (1.68) one can derive the reduced quadrupole moment,

$$I^{jk} = \frac{1}{2} M \eta D^2 \begin{bmatrix} \frac{1}{3} + cos(2\omega t) & sin(2\omega t) & 0 \\ sin(2\omega t) & \frac{1}{3} - cos(2\omega t) & 0 \\ 0 & 0 & 1 \end{bmatrix} \ , \tag{1.76}$$

where the total mass is $M = m_1 + m_2$ and

$$\eta = \frac{m_1 m_2}{M^2} \ . \tag{1.77}$$

Gravitational waves traveling in the $+\hat{\mathbf{z}}$ direction can now be found from Eq. (1.69),

$$h^{jk}_{TT} = -\frac{4GM}{R} \eta D^2 \omega^2 \begin{bmatrix} cos(2\omega(t-R)) & sin(2\omega(t-R)) & 0 \\ sin(2\omega(t-R)) & -cos(2\omega(t-R)) & 0 \\ 0 & 0 & 0 \end{bmatrix} \ , \tag{1.78}$$

where the $(t - R)$ expresses how the wave will be observed at a retarded time a distance of R away form the source. Note that this gravitational wave is circular polarized; the amplitudes A_+ and $A_\times$ are the same, but their phase differs by $\pi/2$. The gravitational waves' frequency is twice that of the orbital frequency. In order to find the gravitational waves propagating in other directions one would use Eq. (1.70). For example, a gravitational wave propagating in the $+\hat{\mathbf{x}}$ direction (i.e. in the plane of the orbit) would be

$$h^{jk}_{TT} = \frac{2GM}{R} \eta D^2 \omega^2 \begin{bmatrix} 0 & 0 & 0 \\ 0 & cos(2\omega(t-R)) & 0 \\ 0 & 0 & -cos(2\omega(t-R)) \end{bmatrix} \ , \tag{1.79}$$

which is linearly polarized ($A_+ \neq 0$ but $A_\times = 0$). This would be the procedure to find the gravitational waves to lowest post-Newtonian [78] order. Post-Newtonian expansion would lead to additional terms that would contribute to the amplitude and phase of the gravitational wave.

For this binary system the gravitational wave luminosity can be derived from Eq. (1.74), or

$$L_{GW} = -\frac{dE}{dt} = \frac{32(GM)^2\eta^2 D^4\omega^6}{5g} \ . \tag{1.80}$$

By conservation of energy, the emission of gravitational waves will result in the diminishment of the energy of the binary system. By the Virial theorem, the total (kinetic plus potential) energy of the binary system is

$$E = -\frac{Gm_1m_2}{2D} = -\frac{1}{2}M(GM\omega)^{2/3}\eta \ . \tag{1.81}$$

The orbital decay (decreasing orbital period $T = 2\pi/\omega$) can be derived from Eq. (1.80) and Eq. (1.81),

$$\frac{dT}{dt} = \frac{dT}{d\omega}\frac{d\omega}{dE}\frac{dE}{dt} = -\frac{192\pi}{5}\eta(GM\omega^{5/3}) \ . \tag{1.82}$$

Note that the minus sign implies that as time evolves, the orbital period T decreases while the orbital frequency ω (and hence the gravitational wave frequency at 2ω) increases.

The existence of gravitational waves were confirmed initially through the observations of the decay of the binary pulsar PSR 1913+16 [82] by Joseph Taylor and Joel Weisberg. The 1993 Nobel Prize was awarded to Joseph Taylor and Russell Hulse for the discovery of PSR 1913+16. The tremendous agreement between the predictions of general relativity and 30 years of radio observations of PSR 1913+16 can be seen in Fig. 1.4. But the spectacular discovery of GW150914 the first merger of two ~ 30 $M_\odot$black holes on 2015 September 14^{th} in the LIGO detectors data has opened up a new window on the universe in addition to definitevely confirmed the existence of gravitational waves. More details on the discovery is given in section 2.5.1.2.

General relativity can also be used to predict gravitational waves from other astrophysical sources, such as pulsars and core collapse supernovae, cosmic strings, or the phase transitions during the Big Bang era. These systems are much more complex than the compact binary coalescence, but tremendous theoretical work has led to gravitational wave predictions that Virgo and LIGO hope to verify [84, 85, 86, 87, 88].

1.6 Sources

With the exception of a few searches, all sources of gravitational waves targeted by ground based gravitational wave detectors are of astrophysical origin. In general relativity, gravitational waves are emitted by the non spherical motion of mass, and propagate at the speed of light as ripples on the spacetime metric. Gravitational waves manifest themselves as tidal forces, stretching the distance between nearby geodesics in one direction and squeezing them in the transverse direction. The gravitational wave amplitude scales as the inverse of the distance to the source, but in order to be detectable by ground based gravitational wave detectors, the source must be massive and compact. That is the reason why among all known astrophysical objects, neutron stars and black holes are the brightest potential sources of gravitational waves.

What does the gravitational wave waveform look like? How much energy is emitted? Is the emission continuous or transient? How often does a source emit gravitational waves? All these questions depend on the gravitational wave emission process, that can drive back the astrophysical object to stability by decreasing the non spherical mass motion (for instance rotating neutron stars) or to instability (for instance binary neutron star coalescences). The distance to which we can detect gravitational wave sources depends also on the detector sensitivity and its frequency bandwidth. In the following we will limit ourself to descriptions of the main sources that emit in the frequency band of our detectors from $\sim 10\,\text{Hz}$ to $10\,\text{kHz}$ and explain why different techniques are used to maximize the chance of discovery.

1.6.1 Compact Binary Coalescence

Compact binary systems are composed of neutron stars (BNSs), black holes (BBHs), or a neutron star and a black hole (NSBH). As observed with the binary system PSR 1913+16 [83], GWs are emitted as the two objects slowly spiral toward one other before the final plunge.

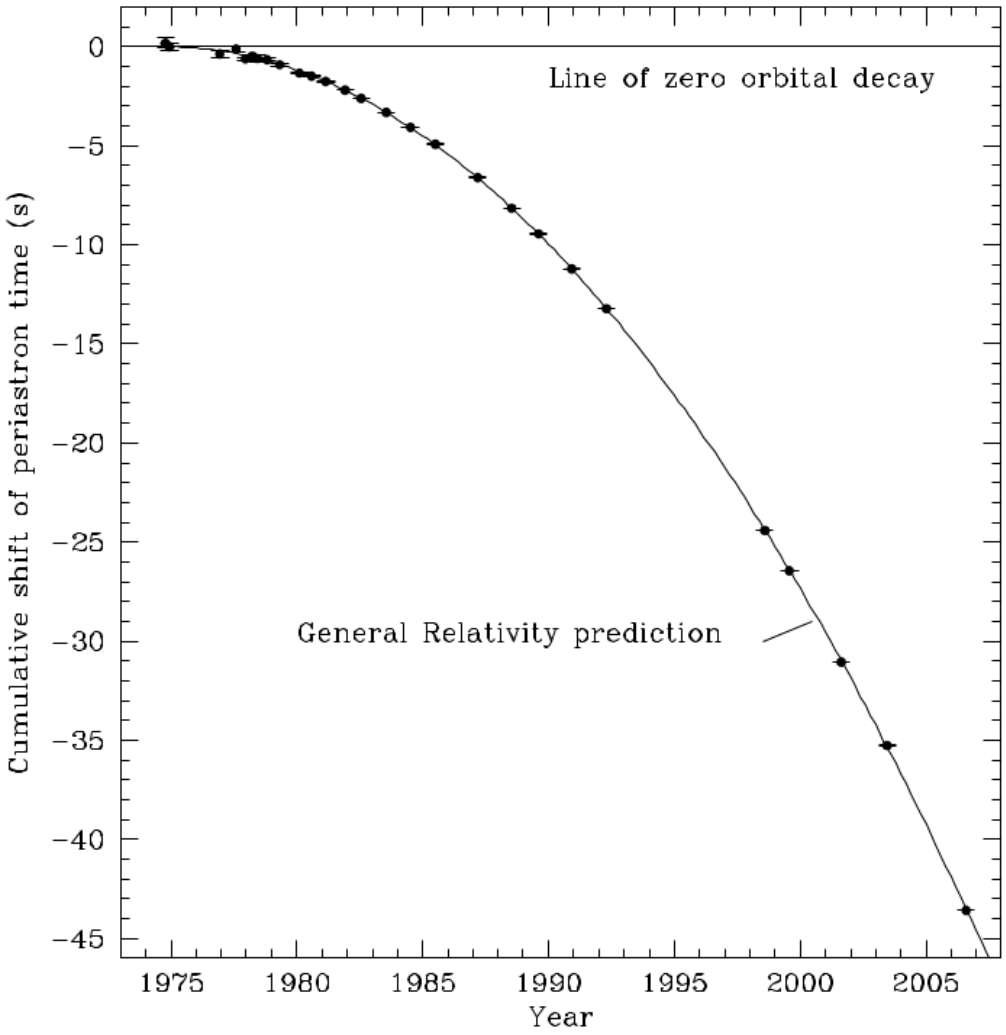

Figure 1.4: The orbital decay of PSR 1913+16 caused by the loss of energy by gravitational wave emission. The parabolic curve depicts the predicted (via general relativity) shift of the periastron time relative to an unchanging orbit. The data points represent the measurements summarized in [83], with error bars that are too small to easily see. This figure is from [83] and by courtesy of Joel Weisberg.

While binary systems spiral inwards over billions of years, only the signal from their last instants is detectable by the ground based interferometric detectors; a few minutes to a few seconds before the merger, when the GW frequency is sufficiently high to fall in the detectors' observational bandwidth. The inspiral phase is well described by analytical post-Newtonian theory until the system reaches the innermost stable circular orbit [78]. Beyond this orbit strong gravitational forces dominate and the two bodies merge in a fraction of a second, forming a single black hole that reaches equilibrium through quasi-normal mode GW emission (ring-down phase). A BNS inspiral signal will have many cycles in the frequency bandwidth of the LIGO, GEO and Virgo detectors. For systems with total mass > 100 $M_\odot$ the frequency corresponding to the inner most stable circular orbit is lower than the lowest frequency of the LIGO and Virgo detectors, and only the merger and ring-down phases will be visible by these detectors for systems of total mass up to 450 $M_\odot$.

Even if BNS systems had been observed [89], until the discovery of GW150914 there were doubts cast on the existence of stellar mass binary black holes (BBHs). There were only theoretical arguments, based on stellar evolution models, that stellar mass BBHs and NSBH systems exist [90, 91, 92]. For almost the same reasons, there is as yet no conclusive evidence that intermediate mass black holes (systems with total mass between 100 and 450 $M_\odot$) exist in appreciable numbers, but recent observations of the hyper luminous X-ray source HLX-1 support the hypothesis of an intermediate mass BH formed after the collision of a dwarf galaxy with a more massive galaxy [93]. Intermediate mass black holes are supposed to form from a stellar BH accreting matter from another compact companion. They might also be the end-product of very massive first generation stars (population III stars) formed in galaxy nuclei [94]. Another scenario is the runaway merging of young massive stars in dense stellar clusters [95]
The GW inspiral signal depends on the physical parameters of the binary system: masses, spins and eccentricity. Accurate waveforms can be constructed for signals from the inspiral phase of compact binaries that include effects of spins (see [96] and references therein), and thus matched filtering based searches are possible. For isolated systems it is generally admitted that the binary systems' orbit will have time to become circular before entering the detector's sensitivity band, so eccentricity can be neglected. Spin is also neglected for low mass binaries, which we expect not to affect detection efficiency. Only recently the merger phase of some binary configurations has been numerically simulated (see [97, 98, 99] and references therein). A number of waveforms including inspiral, merger and ring-down phases, without spin have been constructed and used in searching for binary systems with total mass up to 100 and 450 $M_\odot$ [100, 101]. However, these waveforms are subject to large uncertainties for mass ratios $> 4{:}1$. Neglecting spin also introduces losses in detection efficiency for intermediate mass black holes searches, and despite the tremendous efforts of the numerical relativity community, template-banks of fully spinning waveforms with spin precession for any mass ratio are not yet available. All in all, matched filtering searches are limited to systems of total mass smaller than 100 $M_\odot$ and the higher mass parameter space is covered by un-modelled generic transient searches focusing on the merger and ring-down phases (~ 1 s long signals).

Once a compact binar coalescence is detected in the data, the most accurate waveforms are required to estimate as accurately as possible the parameters of the source. If one includes all possible objects' spin orientation 15 parameters must be estimated. Bayesian inference methods have been developed for more than 15 years [102]. They all need the most accurate waveforms. For BBH systems, the numerical relativity predictions are extremely useful as the Einstein equations during the merger phase can only be solved numerically. Numerical relativity predictions allow to calibrate the analytical waveforms during the merger phase [103].

1.6.2 Continuous Waves

Rotating neutron stars with time varying quadrupole moments radiate GWs through different emission mechanisms. Among these, non axisymmetric deformations are considered the most reliable mechanism, at least for isolated systems. These deformations in the crust can be generated by elastic stress [104, 105] or by magnetic fields [106]. Mechanisms other than crustal distortions include GW driven instabilities of normal oscillation modes (r-mode [107] and f-modes Chandrasekhar-Friedman-Schutz [108] instabilities), or free precession, when the star's rotational axis does not coincide with its symmetry axis. In such a case, the emission of GWs is long-lasting and quasi-monochromatic. For most isolated neutron stars, the star is slowly spinning down because of the GW back reaction and the electromagnetic radiation (pulsars).

In the case of non axisymmetric deformations, the gravitational wave frequency is twice the spin frequency and the amplitude of the emitted GWs is proportional to the deformation which is expressed in terms of the ellipticity ϵ[2]

[2] $\epsilon = \frac{I_{xx} - I_{yy}}{I_{zz}}$, where the Is are the moments of inertia of the star and the spin axis is assumed to lie in the $z-$direction.

of the distorted object. Predictions for ϵ are highly uncertain. The maximum deformation that a crust can support depends on the neutron star equation of state through the shear modulus of the inner crust and on the crust's structure (crystalline or amorphous), through its breaking strain [109]. Possible breaking strain values span several orders of magnitude, the largest ones ($\sim 10^{-1}$) corresponding to perfect crystals. Shear modulus values of the inner crust also span a few orders of magnitude, with solid strange-quark star models yielding the highest shear modulus values. Adding it all up, the maximum values of the ellipticity range from several 10^{-7} to a few 10^{-4}.

But what are the ellipticity values in actual pulsars? This question does not have a clear-cut answer and it cannot be dismissed that a certain fraction of neutron stars have negligible axial quadrupole moment. This is supported by observations of extremely low period derivatives of millisecond pulsars that indicate that these recycled pulsars have little equatorial asymmetry ($\epsilon < 10^{-8}$). Simulations of isolated spinning neutron star populations including gravitational and electromagnetic torques [110] provide insight into the type of constraints that even non-detections of continuous GW signals will place on neutron star population parameters in the advanced detector era.

Accreting neutron stars in binary systems have a natural way to maintain large crust deformations, through the accretion spot. In fact it has been suspected for a long time that GW emission could balance the accretion torque and explain why spin frequency of known accreting neutron stars are never approaching the breaking limit [104, 111]. However the actual search for signals from binary systems is significantly complicated by the additional unknown orbital parameters that one would need to search over [112].

1.6.3 Stochastic Gravitational Wave Background

A cosmological and astrophysical stochastic background of GWs (SGWB) is expected from the incoherent superposition of GWs emitted by many sources. Cosmological sources include amplification of quantum vacuum fluctuations during inflation [30], electro-weak phase transitions [87], pre Big Bang models [113, 114] and cosmic (super-)strings [115, 88, 116]. Most of these processes took place in the early stages of the universe making GWs a unique way to probe primordial evolution. An astrophysical SGWB may be generated by the concurrent emission of a large population of sources such like compact binary coalescence and merger, core collapse supernovae or rotating neutron stars (see for [117] for a discussion on the implications of the measured BBHs rate by LIGO-Virgo for the stochastic gravitational wave background).

A SGWB is described in terms of the GW energy density

$$\Omega_{GW}(f) = \frac{f}{\rho_c}\frac{d\rho_{GW}}{df} \tag{1.83}$$

where ρ_c is the critical energy density of the universe and $d\rho_{GW}$ is the GW energy density contained in the frequency range f to $f + df$. Predictions on Ω_{GW} as well as indirect phenomenological and experimental bounds are illustrated in Figure 1.5 which is taken from [118]. The most stringent bound comes from Big Bang nucleosynthesis (BBN) and cosmic microwave background (CMB) measurements, and it depends on the number N_ν of neutrino families at the time of the BBN [84]:

$$\Omega_{BBN} = \int \Omega_{GW}(f) d\ln f < 1.1 \times 10^{-5}(N_\nu - 3) \tag{1.84}$$

Primordial nucleosynthesis provides an upper bound $N_\nu - 3 < 1.4$. The CMB data can be used to derive a limit on the maximal SGWB energy density at the time of photon decoupling

$$\Omega_{CMB} = \int \Omega_{GW}(f) d\ln f < 2.0 \times 10^{-6} \tag{1.85}$$

for homogeneous (non-adiabatic) initial conditions [119], and

$$\Omega_{CMB} = \int \Omega_{GW}(f) d\ln f < 1.7 \times 10^{-7} \tag{1.86}$$

for adiabatic initial conditions [120]. These are the phenomenological upper bounds that can be directly compared to LIGO-Virgo measurements. So far the best upper limit set by LIGO and Virgo is

$$\Omega_{GW} = \int \Omega_{GW}(f) d\ln f < 5.6 \times 10^{-6} \tag{1.87}$$

in the 41.5 – 169.25 Hz band [121, 122].

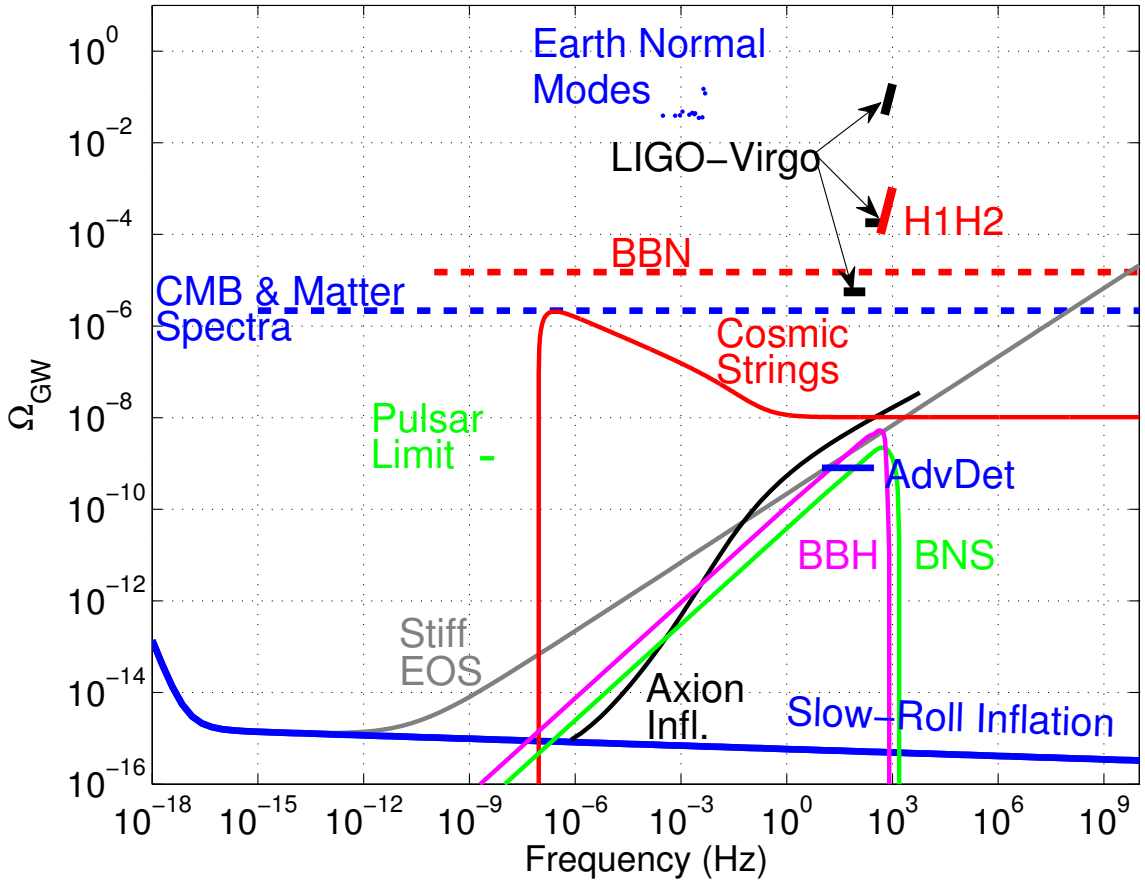

Figure 1.5: Comparisons of different SGWB search upper limits on the GW spectrum Ω_{GW} and indirect bounds [118].

1.6.4 Gravitational Wave Bursts

Short-lived, or transient, GW signals are thought to be generated in a variety of circumstances. In some cases, for instance the gravitational collapse of a massive star, or the coalescence of two neutron stars, GW emission is associated with EM radiation or neutrino radiation. In other cases, the scenarios are more speculative and refer to objects that have never been observed as, for example, cosmic strings. If historically, core collapse supernova was the most promising gravitataional wave burst source, a large number of scenarios and GW emission mechanisms are now considered. The parameter space has thus grown over the years and is no more restricted to very short duration signal (of the order of few milliseconds), but includes transient GWs lasting few minutes or days in the most extreme cases.

1.6.4.1 Massive Star Core Collapses

Massive star core collapses have been considered as one of the most promising sources of GWs for ground based detectors. The different mechanisms involved in stellar collapse have been studied for more than 40 years, and GW emission is now predicted in different phases: it is anticipated during the collapse itself through the aspherical bulk mass motion (core bounce phase). In the post-bounce phase, convection instabilities inside and above the proto-neutron star can develop, driven by entropy gradients, neutrino heating and standing accretion shock instability (SASI) mechanisms (see [86, 123] and references therein). These phenomena may produce GWs lasting up to few seconds. After a supernova explosion or a collapsar (black hole formation) a certain fraction of the ejected material can fall back, heating the proto-neutron star and exciting oscillation modes that generate GWs (g-mode pulsations and r-mode instabilities). Furthermore, when a black hole is formed, accretion-induced ringing may generate GWs. Current state-of-the-art numerical simulations take into account many non axisymmetric effects in 3D, attempt to model micro-physics (neutrino transport, electron capture, realistic equation of state), and include rotational dynamics and magnetic fields [124]. Still, we are quite far from having a complete catalogue of all possible waveforms. For instance, GWs emitted during the core bounce exhibit a sharp peak in the waveform for most of the initial conditions and energy up to a few 10^{-8} $M_{\odot}c^2$ can be emitted [125], but the exact signal shape depends on the rotational profile and the nuclear equation of state [126]. Consequently, for the searches, we consider only the generic broad features of the waveforms in the literature.

1.6.4.2 Pulsar Glitches and Magnetic Flares

Some pulsars occasionally show sudden discontinuities (glitches) in their EM activity followed by gradual recoveries that may last days or years. These glitches correspond to a sudden change (for most of them an increase) of the rotational frequency. Soft Gamma-ray Repeater (SGR) flares [127], anomalous X-ray pulsars (AXPs) as well as radio glitches are examples of this and are thought to be consequences of star-quakes or of angular momentum transfer between a solid crust and a more rapidly rotating loose component of the neutron star interior [109]. During such glitches normal modes (mainly f-modes) could be excited and generate GWs.

1.6.4.3 Cosmic Strings

Cosmic strings predicted in symmetry-breaking phase transitions [128], or cosmic super-strings in string theory inflation models, may, if they exist, form a dynamical network that loses energy mainly through GW emission. Cosmic strings interact (crossing themselves and reconnecting) forming closed loops. A fraction of these loops oscillate relativistically because of their tension (energy per unit length), and shrink by emitting GWs. This is expected to form a stochastic background of GWs that are red shifted since their emission [129]. Besides, string interactions are expected to generate GW bursts that could be detected individually. This may happen when strings inter-commute, forming string shape discontinuities (kinks) that propagate along the string. When loops are formed, some part of the string can reach speed-of-light velocity (cusps) that may produce strong GW bursts [130]. The GW amplitude depends on the tension of the string. The (super-)string density depends on the loop size, the string tension and an additional parameter, the reconnection probability, which in the case of super-strings is smaller than 1.

1.6.4.4 Rotational instabilities

Most massive stars are likely to rotate slowly, making proto-neutron stars with birth spin periods of $\sim 10 - 100$ ms. On the other hand, those formed during the merger of two neutron stars are most likely rapidly spinning, with birth

spins of $\mathcal{O}(1\,\mathrm{ms})$ and rotational kinetic energy of up to $10^{52}\,\mathrm{erg}$ [131]. The outer region of the proto-neutron star is strongly differentially rotating while the inner core is uniformally rotating. Magnetorotational instabilities and/or hydrodynamic shear instabilities will act to redistribute angular momentum toward uniform rotation. The subsequent nonaxisymmetric deformation may lead to significant, though short-term $\tau \lesssim 1\,\mathrm{s}$, GW emission [86, 132].

When the ratio of rotational kinetic to gravitational energy, $T/|W|$, exceeds certain value, the axisymmetric shape may be destorted to a more energetically-favorable triaxial shape, corresponding to a spinning bar that is an ideal GWs emission shape. At $T/|W| \gtrsim 0.14$, a secular gravitational-radiation reaction may start, leading to nonaxisymmetric deformation. The timescale depends on many factors but is estimated to be $\mathcal{O}(1\,\mathrm{s})$. The secular instability has the potential of lasting for $\sim 10 - 100\,\mathrm{s}$ [133].

1.6.4.5 r-modes

r-modes or Rossby modes are quasi-toroidal oscillations that only appear in rotating stars and are caused by the Coriolis force acting as restoring force along the surface. Their periods are on the same order as the stars rotation. r-modes in neutron stars are unstable to growth at all rotation rates by gravitational-radiation reaction via the secular Chandrasekhar-Friedman-Schutz instability [107, 134]. r-modes emit GWs with $f_{\mathrm{GW}} = 4/3\,(\Omega_{\mathrm{NS}}/2\pi)$ at the lowest order (quadrupole), where Ω_{NS} is the neutron star angular velocity. The amplitude is rather small ($h << 10^{-24}$ at 20 Mpc) and depends on Ω_{NS} and the neutron star density. r-modes are expected to be a source of very-long-lasting quasi-continuous GW emission, though long GW transients may be also possible [135]. Interestingly, potential astrophysical sources of GWs from r-modes are accreting neutron stars in low-mass X-ray binaries [104]).

1.6.4.6 Accretion disk instabilities

In the long GRB collapsar scenario, the central engine consists of a black hole surrounded by an accretion disk/torus [136]. The inner part of the disk is likely to be sufficiently hot to be neutrino cooled while the outer regions are cooled inefficiently and form a thick accretion torus [137]. A variety of (magneto)-hydrodynamic instabilities may occur in the disk/torus leading to the emission of GWs.

Piro and Pfahl [137] considered gravitational instability of the outer torus leading to fragmentation. Multiple fragments may collapse to a single big dense fragment of up to $\sim 1 M_{\odot}$ that then travels inward either by means of effective viscosity and/or GW emission. In both cases, the inspiral will last $\mathcal{O}(10 - 100\,\mathrm{s})$, making it a prime candidate source for a long GW transient.

Van Putten has proposed an extreme "suspended – accretion" scenario in which the central black hole and the accretion torus are dynamically linked by strong magnetic fields [138, 139, 140]. In this picture, black hole spin-down drives both the actual GRB central engine and strong magnetoturbulence in the torus, leading to a time-varying mass quadrupole moment and, thus, to the emission of GWs. Van Putten postulated, based on a simple energy argument, branching ratios of emitted GW energy to electromagnetic energy of $E_{\mathrm{GW}}/E_{\mathrm{EM}} \gtrsim 100$ and thus, $E_{\mathrm{GW}} \sim \mathrm{few} \times 10^{53}\,\mathrm{erg}$. These numbers are perhaps unlikely to obtain in nature, but the overall concept of driven magnetoturbulence is worth considering.

Chapter 2

Gravitational waves detection

The quest to detect gravitational waves has been hindered in many ways, but the importance of gravitational wave detection has been recognized to be of paramount importance. First and foremost, the production of gravitational waves is difficult. As noted in Chapter 1, the leading order term in production is the quadrupole; in order for there to be effective gravitational wave generation it is necessary to have very large asymmetric mass distributions moving at relativistic velocities [141]. In addition, if we refer to the formula for the production of gravitational waves in terms of the reduced mass quadrupole moment, Eq.(1.69), and also re-inserting c, the gravitational wave strain amplitude is proportional to G/c^4. A consequence of this is that it will be impossible to produce terrestrial sources of gravitational waves that could potentially be detected. In order to detect gravitational waves of sufficient amplitude one is dependent on cataclysmic astrophysical phenomena[1]. But this shows the importance of gravitational wave detection; it will provide information on calamitous gravitational events, and display physical processes that would be obscured electromagnetically.

2.1 A little bit of history

Historically (at least for the better part of the 20^{th} century) it was not the weakness of gravitational waves that produced the most doubt about gravitational wave detection, but the existence of gravitational waves themselves. Even Einstein struggled with the existence of gravitational waves. In his initial 1916 treatise on general relativity [26] the existence of gravitational waves seemed obvious (especially because of comparisons to electromagnetic radiation), although there were flaws in the calculation. Einstein's 1918 paper [27] resolved the previous problems (aside from a factor of 2 error [141]) and the picture painted for the existence of gravitational waves seemed clear. However, Einstein (along with his assistant Nathan Rosen) subsequently wavered on whether gravitational waves existed. A fascinating interplay between Einstein and Rosen and a *Physical Review* referee (who, as it turned out, was the cosmologist Howard Percy Robertson) led Einstein and Rosen to write in their 1937 article [142] that gravitational waves did not exist. After the referee report (and further discussions with Robertson and Leopold Infeld in a collegial context) [143] Einstein changed his mind and wrote positively about the existence of gravitational waves. In retrospect, this proved to be an early and difficuly encounter with coordinate singularities in general relativity [143].

Arthur Eddington also contributed greatly to the understanding and believability of gravitational waves. Eddington corrected [144] improper assumptions and errors that Einstein had made [26, 27] in his description of gravitational waves [9]. Eddington was also able to describe the difference between *real* gravitational wave modes, namely those that carry energy, and *fictitious* modes that are due to a poor choice of coordinates [144, 141, 9] (which Eddington described as propagating at "the speed of thought" [144]). This confusion between different modes, in addition to Eddington's wry comment, led to confusion as to the existence of gravitational waves and whether they can be detected; however Eddington's presentation does make clear which modes are real and carry energy as they propagate [144, 141, 9].

There did not seem to be much doubt about the existence of gravitational waves for Lev Landau and Evgeny Lifshitz. Their original 1939 Russian edition of *The Classical Theory of Fields* [145] contains descriptions of gravitational waves. In fact, their presentation of gravitational waves is (not surprisingly) concise and correct [146].

[1] The strain amplitude diminishes as the inverse of the distance

2.1.1 The 1957 Chapel Hill conference

Probably the most decisive moment in the debate over the existence and detectability of gravitational waves occurred at the 1957 Chapel Hill conference [147]. It was through work and discussions leading up to, and at the conference itself, that the question of whether a gravitational wave detector (in principle) could be constructed was resolved. The description of the resolution of the detection question within the context of the 1957 Chapel Hill conference is nicely and concisely presented in [148].

From the Chapel Hill conference came a description of a thought experiment (the so-called *sticky bead argument*) that shows that gravitational waves contain energy and could be detected. The attribution as to who came up with this argument is not clear, but credit can be distributed between Hermann Bondi, Felix Pirani, and Richard Feynmann who, at the end conference, formally presented the sticky bead argument (which to him seemed to be an obvious physical argument free of the problems and hinderances of tensor calculus [146]). Feynman's presentation apparently was a summation of previously presented material during the conference [147, 148], but its clarity was essential to turn on minds. The crux of the argument is that if one puts two beads on a stick, where the stick is perpendicular to the direction of propagation of the gravitational wave, as the wave propagates by, the stick will be held firm by the atomic and molecular forces while the beads will move with respect to each other. If there is friction between the beads and the stick (and why wouldn't there be?), then heat will be generated. Clearly the source of this energy is ultimately the gravitational wave [146]. Pirani's work [149, 150], and his presentation at the conference[2] had an especially high impact on those who were thinking about actually constructing a real gravitational wave detector [147, 148]. He demonstrated that the relative acceleration of particle pairs (and not the acceleration of a single particle, which would seem not to move when a particle's position is fixed in a coordinate system) can be associated with the Riemann tensor (Eq. 1.15). While his presentation did not say that non-zero components of the Riemann tensor were due to gravitational waves, it was apparently clear to a number of attendees of the conference that gravitational waves would produce this sort of effect. The existence of gravitational waves now seemed obvious, and a path toward detection had been started. In introductory general relativity textbooks it is now standard to show the association between tidal forces and the Riemann tensor [71]. Immediately after the Chapel Hill conference Hermann Bondi published [151] a paper that presented a varient of the sticky bead argument showing that gravitational waves exist and carry energy.

An important attendee of the Chapel Hill conference was Joseph Weber. In an exchange with Bondi it appears that Weber was truly moving from the sticky bead thought experiment toward a real experiment; Weber was now trying to imagine how he could calculate the effect of gravitational waves on matter in the lab [148, 147]. Also in attendance at the Chapel Hill conference was John Wheeler. Weber, an experimentalist trained as an electrical engineer decided in the mid-1950's that he wanted to dedicate his experimental skills toward experiments in general relativity. Consequently he spent time doing research with Wheeler in 1955 at Princeton, then in 1956 in Leiden when Wheeler went there for a sabbatical [148]. Upon leaving the conference, Weber and Wheeler published an article (which may have been started before the Chapel Hill conference [148]) that explains why gravitational waves are real [152]. With respect to the confidence in being able to detect gravitational waves, Weber makes the comment,

"In 1958 I was able to prove, using Einstein's equations that a gravitational wave would change the dimensions of an extended body." [153]

In [154] Weber does explain how masses will be deformed by a gravitational wave, and uses the example of two masses held together by a spring to model a mass quadrupqole detector. Weber then goes to imagine the effect of a gravitational wave on a macroscopic piezoelectric crystal; some of the components of the Riemann tensor would be derived by monitoring the voltages at different points on the surface of the crystal. In this paper Weber also speculates that it would be possible to generate gravitational waves in the lab that could be detected via

"... electrically induced stresses in crystals. These give approximately a seventeen-order increase in radiation over a spinning rod of the same length as the crystal." [154]

While this speculation that an extraordinary amount of gravitational waves could be generated was not correct, this is an important paper through the description of a mass quadrupole detector. As will be described below, the most effective Weber detectors were not piezoelectric crystals, but large mass quadrupoles (bars) where the gravitational wave excited the fundamental mode (it should be noted that the bar-detectors used piezoelectric transducers mounted on the surface of the detector to transform a bar's mechanical excitations into electric signals). Clearly the 1957

[2] titled "Measurement of Classical Gravitational Fields".

Chapel Hill conference had a great effect on Weber, and by the 1960s the era of real gravitational wave detection had begun.

2.1.2 The first gravitational wave detectors: Weber bars

By 1966 Joseph Weber had initiated the era of experimental searches for gravitational waves, and had constructed a gravitational wave detector [155]. The detector was a cylinder of aluminum, 150 cm in length and 61 cm in diameter. A gravitational wave would excite the bar's lowest order compression mode, which in this case corresponded to a frequency of 1657 Hz. This would then be the frequency where the detector had its best strain sensitivity for the detection of gravitational waves. Weber noted that at this frequency the detector could be sensitive to gravitational wave signals from supernovae or binary neutron star coalescence from sources within our Galaxy. The bar was suspended via a vibration isolation system within a vacuum. Quartz strain gauges were the transducers that turned the mechanical signal into an electrical signal. Weber claimed that the strain sensitivity of the detector was a few parts in 10^{16} [155].

Weber eventually placed five similar detectors at the University of Maryland, and one 1000 km away at Argonne National Lab. By 1969 Weber claimed "Evidence for Discovery of Gravitational Radiation" [156]. The data from Argonne was sent back to Maryland via a telephone line. Considering the complex data acquisiting sytems that operate today, it is quaint to note that, "Pen and ink recorders with event markers record coincidences on all charts" [156]. Weber was essentially looking for coincidences around the fundamental frequency of the bars, ~ 1.6 kHz. Weber reported over 20 statistically significant coincident (between Maryland and Argonne detectors) events for an 81 day observing period, with no preferred direction in the sky for the potential sources. Weber also claimed that his seismometers showed no evidence for the presence of seismic events, and shielding would eliminate a common source of electromagnetic noise. The amplitude of the events reported by Weber implied a flux of gravitational wave energy of 10^4 ergs cm^{-2} s^{-1} — which is an extremely small value given all known extragalactic bright sources —, and a gravitational wave energy density within the observing bandwidth of 10^{-32} g cm^{-3}. In a subsequent paper [157] Weber reinforces his detection claim by comparing his detection statistics with what is achieved when the data from the Maryland and Argonne detectors was *time-shifted*[3] from one another by 2 s. Weber then published a further analysis of his data [158] that claimed that there was an observed excess of events when the detectors were optimally aligned with the Galactic center. A simple calculation by Weber then gives the amazing result that these events would imply that 1000 $M_\odot c^2$ in energy per year is being converted into gravitational waves.

Weber's results generated much notice and interest in the physics world [159, 160, 161]. People were surprised by the magnitude of the gravitational wave events claimed by Weber, and the physics community accepted the results as valid, although with caveats that they would need to be verified [159, 160, 161]. By 1972 a number of others had constructed gravitational wave bar detectors similar to Webers [162], and there was no confirmation of Weber's results. Not only did this detectors not observe gravitational waves, but they also implemented careful calibration procedures that includes artificial signal injection (via electrostatic stimulation of the bar) [159]; this was a process that Weber had negelected to do. It should be noted that this is a procedure that is critical for Virgo and LIGO, and one that gives credence to the sensitivities of the current signal search pipelines.

Peter Kafka and Schnupp [163, 164] implemented a technique that is presently used in all Virgo and LIGO signal searches, namely the *time slide*. Their data came from bar detectors, similar to Weber's, located in Munich, Germany, and Frascati, Italy. They analyzed their data, looking for coincident events, but implement 40 different artificial time delays between the two data streams. Having the statistical distribution of coincident events from the time slides, they then looked for coincident events in the *zero lag* data. No statistically significant events (as compared to the time slide results) were observed. Interestingly, there observation period overlapped with times when Weber was also observing and claimed results [165]. Certainly by the mid to late 1970's there was great doubt about Weber's gravitational wave detection claims [159].

The technology for the gravitational bar detectors evolved quickly. William Fairbank and his group at Stanford implemented an aluminum bar detector that was cooled to 4.2 K, and used Superconducting Quantum Interference Devices, or *SQUIDS* as transducers for converting the mechanincal motion of the bar detector into an electrical signal [166]. Their bar detector had a resonant frequency of 842 Hz, and at this frequency their gravitational wave strain sensitivity was 10^{-18}. Initially as a single detector they were unable to make detection observation claims. However, they were soon joined by similar detectors at Louisiana State University and Rome, and a niobium bar at Western Australia. Coincidence observations proved to be difficult in the 1980s due to experimental problems [159].

[3]This concept of a time-shift will play an important roll in determining the statistical significance of events seen in Virgo-LIGOs data.

For example, the network of cryogenic bar detectors were not observing at the time of SN1987a. As the cryogenic bar detectors did continue to operate through the 1990s and beyond, no credible gravitational wave events were observed [167].

2.1.3 Interferometric gravitational wave detectors

The idea of using a Michelson interferometer to detect gravitational waves is almost as old as Weber's bar detector. In 1962 two Soviet physicists, V.I. Pustovoit and M.E. Gertsenshtein, noted that the use of a Michelson interferometer would be a possible means to detect gravitational waves over a frequency range that was broader than the Weber bars [168, 169]. In addition, the authors noted that the interferometers would have a sensitivity that would potentially be better than the Weber bars. An L-shaped Michelson interferometer would also be ideal for detecting the stain on spacetime from a gravitational wave [159].

In the early 1960s Weber and his student, Robert Forward, also considered using a Michelson interferometer to detect gravitational waves [170, 159]. After completing his PhD with Weber, Forward worked with Hughes Research Laboratories. It was at Hughes that Forward first constructed a Michelson interferometer to be used as a gravitational wave detector [170]. Forward attributes the conception of the idea for constructing an interferometric detector, and one that would have a better response to a broader range of signal frequencies, to a conversation he had with Weber in 1964 [170]. Part of the motivation to develop a broad band detector was to look for a gravitational wave signal around 60 Hz from the Crab Pulsar [170]. Forward also gives credit to US astronaut Philip Chapman and Rainer Weiss for help with the design of the interferometer [170]. Weiss had started his long carreer in experimental gravitational radiation during his postdoctoral stay at Princeton (1962) working with Robert Dicke. Dicke was interested to experimentally test Einstein theory and alternative ones like tensor-scalar theories of gravitation. After 2 years spent at Princeton building gravimeter to test potential Earth excitation by scalar waves, Weiss returned to MIT in 1965 where he was assigned to teaching relativity and naturally the question of which predictions of general relativity could be measureable lead Weiss to re-read Pirani's 1956 papers. It became rather clear for Weiss that the laser technology progresses had provided a more efficient way to measure the energy deposited by the gravitational waves than Weber's device. Where Pirani had imagined to put a "spring" between the the test masses, a continuous measurement of the distance between free test masses would reveal most directly the physical characteristics of the Riemann tensor.

This first interferometer built by Forward was contained on a single table-top, with the end mirrors fixed in mirror mounts. In this configuration the mirrors would not be free to move, hence it would not be possible to detect a gravitational wave. Still by driving one of the mirrors with a piezo-electric crystal Forward and his team could measure the displacement sensitivity of the detector. With 160 μW of input laser power ($\lambda = 632.8$ nm) the interferometer was demonstrated to have a postition sensitivity of $x(f) = 1.3 \times 10^{-14}$ m Hz$^{-1/2}$ for frequencies above 1 kHz, whereas the expected shot noise level was $x(f) = 1.06 \times 10^{-14}$ m Hz$^{-1/2}$ [170]. Forward noted that the measurement was limited by acoustic and ground noise, even though the experiment resided on a steel table that was itself supported by a multistage vibration isolation system consisting of some combination of springs, brass plates, rubber and inner tubes [170]. Forward noted that:

"The best system sensitivity was achieved on the inner tube supported steel table in a quiet room. Attempts to achieve equally good results on the other systems were not successful, indicating once again that vibration isolation is still an art rather than a science" [170].

This last statement is especially noteworthy considering the time and scientific imput that has been dedicated by Virgo and LIGO in designing their current vibration isolation systems.

Forward and his team then constructed a more advanced interferometer, and one that could in principle detect gravitational waves [171]. This time they used a HeNe laser of 35 mW input power (of which only $10mW$ reached the photodetectors), and an interferometer arm-length (a simple configuration where the laser beam traveled down and back one time) of 4.25 m. The end mirrors in the Michelson interferometer were nominally free to move for frequencies above 1 kHz (they were mounted in support blocks that were reported to have allowed free motion for frequencies between 1 kHz and 20 kHz). The interferometer had an arm-length displacement sensitivity of about 10^{-14} m Hz$^{-1/2}$ [170] in the 1 – 20 Hz band, or a strain sensitivity of roughly 10^{-16} (roughly the same as the bar interferometers at the same time in the early 1970s) [171].

At the time Forward was implementing an interferometric gravitational wave detector, Rainer Weiss at MIT produced a thorough investigation into not only how a Michelson interferometer could be used to detect gravitational

waves, but also a systematic and comprehensive investigation into the noise sources that would constrain such a measurement [172]. In his paper[4] Weiss is quick to note that he has been influenced by the seminal work of Pirani [149]; through this work Weiss was motivated to use interferometric techniques to measure the relative position of free masses, and thereby infer characteristics of the Riemann tensor. The newly invented laser also provided a means to accurately measure the relative position of free masses. It is interesting to see that, like Forward, Weiss also acknowledges the ideas developed by Philip Chapmann. Finally, Weiss was also motivated to develop a gravitational wave detector with a broadband frequency response because of the recent discovery of pulsars, and especially the Crab Pulsar which would be producing gravitational waves at about 59.7 Hz.

In [172] Weiss proposed the construction of a Michelson interferometer. However, as opposed to Forward's design where the laser beam traveled down the arms of the interferometer once, Weiss proposed a system where the laser beam would bounce back and forth multiple times in the interferometer, thereby increasing the effective arm-length (and increasing the strain sensitivity of the detector). This is known as a Herriott optical delay line system [173]. While optical delay lines are not being used by LIGO or Virgo (Fabry-Perot cavities are being used), it is fascinating to see the number of ideas introduced by Weiss in 1972 that are of paramount importance for LIGO and Virgo today. Weiss proposed an interferometer where the light would be frequency modulated with Pockel cells, and that would then be used to hold the output on a fixed fringe via a servo system. The masses of the interferometer arms would be vibrationally isolated, but free to move at the frequencies of interest of the detector [172].

In what could be considered as the most important part of Weiss' presentation [172], he systematically listed and quantified the most important noise sources in an interferometric gravitational wave detector. These noise sources included amplitude noise on the laser source (including shot noise), frequency noise of the laser source, thermal noise in the masses and their suspension systems, radiation pressure noise from the laser light, seismic noise, noise due to residual gas in the vacuum system housing the interferometric detector, cosmic ray noise, gravitational-gradient noise, and residual electric and magnetic field noise. This comprehensive description of a realistic broadband interferometric gravitational wave detector initiated the experimental effort that has led to the present day LIGO and Virgo detectors [159].

Following Weiss and Forward pioneering work, several groups in Europe built multi-meter longs interferometer prototypes. The goal was to make prototypes that demonstrated the technology needed to construct kilometer length interferometers. Albrecht Rüdiger, Rolland Schilling and Walter Winkler in Garching created a 3 m arm length detector in the late 1970s [174], and a 30 m detector ten years after [175]. Ron Drever and Jim Hough in Glasgow built in the early 1980s a 10 m prototype [176]. At the same time, Weiss and his team at MIT built laser interferometric gravitational wave detector with a Herriott optical delay line system and 1.5 m length arms. The Garching interferometers were also Herriott delay lines, while the Glasgow detector used resonant optical cavities [177, 178], an idea by Ron Drever (then at Glasgow, before moving to Caltech). These Fabry-Perot cavities have the light bounce back and forth a number of times, but in a resonant fashion within an optical cavity. A similar interferometer, albeit with 40 m arms, was then constructed at Caltech in the late 1980s [179]. Fabry-Perot cavities were eventually incorporated into the design of LIGO and Virgo. The work on these prototypes was absolutely critical in establishing the technology needed for LIGO [180]. Similarly in the 1980s, the work on lasers, laser stabilization and interferometer optics in Orsay, France, plus the research on vibration isolation systems in Pisa, Italy, helped to create Virgo [181].

In France, after the attempt to build a suspended in vaccum aluminium bar led by Sylvano Bonazzola at the Observatoire de Paris Meudon (1971 – 1974) a small group led by Gérard Petiau joined later by Philippe Tourrenc were charged to study the gravitational wave detection case. These theoritical studies (1975 – 1981) concluded that optical methods would provide the most efficient means to detection gravitational waves. At that time Philippe Tourrenc convinced general relativity theorists, quantum optics theoriticians and experimental opticians to discuss jointly the gravitational waves search by interferometry. A small group composed notabily of Philippe Tourrenc, Thibault Damour, Serge Reynaud, Christian Bordé, Antoine Heidman, Nathalie Deruelle, Alain Brillet and Jean-Yves Vinet led the first theoritical and experimental studies[5]. In the late seventies, during a post-doctoral stay at the University of Colorado Boulder, Alain Brillet met Peter Bender who transmitted him the excitement for gravitational waves detection with laser interferometry. When he came back to France, Brillet established contacts with the European experimental teams as well as Rai Weiss's group at the MIT. He produced, in 1983, the first cost estimate of a kilometric interferometer. In 1985 Alain Brillet met Adalberto Giazotto at the Marcel Grossman conference in Rome. After many years of experience with bar detectors seismic isolation, Giazzoto's group was prototyping seismic

[4]This is actually an unpubished MIT report document.

[5]funded by DRET (Direction de la recherche et des études techniques of the Defense ministry).

isolation systems for the large optics of a future interferometer gravitational wave detector in Italy. They decided to join their efforts and start working on the Virgo project, whose main particularities was the use of Nd:YAG lasers and the low-frequency seismic isolation. The project was formally presented in may 1989 to CNRS and INFN and was approved by the INFN and CNRS board of trustees in September 1993 and April 1994 respectively[6].

Given the size and the technological challenge that a km-long arm interferometer represents, only two projects would take birth in the eighties. Located near Pisa, Italy, Virgo was funded by France and Italy national agencies. LIGO in the USA has been proposed by Ron Drever, Rainer Weiss and Kip Thorne. The NSF funded in May 1990 the construction of two detectors: one in Livingston, Louisiana state, and another one in Hanford, Washingston state. It took more than one decade to create the infrastructures and to build and commission the detectors. German and United Kingdom groups got funded to build a 600-m arm-lenght laser interferometer in Hannover, Germany (1995) [182]. In the last 20 years, the GEO detector has been very useful to develop and test advanced technology for LIGO and Virgo [183]. Finally, the Institute for Cosmic Ray Research (ICRR) of the University of Tokyo started also in 1995 a 300 m long arm laser interferometer similar to LIGO and Virgo design. The TAMA project stopped data taking in 2003 as its goal was to develop advanced techniques needed for a 3-km arm-length interferometer (KAGRA) which is under construction [184].

2.2 Present day gravitational wave detection

The Weber bars and the initial laser interferometers were examples of gravitational wave detection at relatively high frequencies, namely in the kHz range. The era of the bar detectors has essentially passed. Present ground based laser interferometric gravitational wave detectors (such as Virgo and LIGO) are searching for signal from 10 Hz up to 10 kHz. However, there are a number of other methods that are presently being proposed or implemented in order to observe gravitational waves in other frequency regimes.

2.2.1 Interferometers in space

There is much to be gained, in principle, by putting a gravitational wave interferometer in space. Since the gravitational wave strain amplitude h produces a strain on space of $\Delta L/L$, the detector's sensitivity can be dramatically improved by using the vast possibilities of empty space and make L as large as possible. In addition, there will be no need to construct a vacuum system in space. A detector in space would escape numerous noise sources that plague ground based detectors: human made noise, seismic noise, and gravity gradient noise.

The idea to construct a gravitational wave detector in space came in the 1980s [185], similar to when the kilometer length ground based interferometers were conceived. LISA [186]) and DECIGO [187] are two examples of spaced based gravitational wave detectors that are being planned.

The Laser Interferometer Space Antenna (LISA) was originally conceived as a joint NASA-ESA project that would search from gravitational waves from 0.03 mHz to 0.1 Hz. The plan for LISA was to measure changes in the separation between test masses in three spacecraft (the three spacecraft forming an equilateral triangle) that are separated by 5×10^6 km [188]. This distance is too great for proper interferometry to be used. Each spacecraft will have two optical systems with an angle of 60^o between them. Each of the LISA spacecraft was to have two separate lasers that can be phase-locked so as to behave like the beam-splitter of a Michelson interferometer. On the spacecraft and at the end of each arm (subtended by a laser beam) will be a freely floating test mass, and these are the masses that will be monitored.

At the frequencies where LISA would be most sensitive it would observe a host of binary star systems in the Milky Way, binary supermassive black hole systems throughout the universe, and the stochastic gravitational wave background from the Big Bang.

In 2011 NASA withdrew from the LISA project. The ESA is continuing with the LISA concept, but slightly rescaled. It is referred to as the *evolved* Laser Interferometer Space Antenna, or eLISA [189]. The separation for the spacecraft in eLISA is now 10^6 km. While there will still be three spacecraft, there will now only be one pseudo-interferometer, as opposed to the three that were originally planned for LISA. The central (and center of the interferometer) spacecraft is referred to as the *mother*, while the two other spacecraft (at the end of the interferometer

[6]This information comes from a brief historical summary in the "Rapport de prospective" written in 2003 by the Commission Interdisciplinaire 47 of the CNRS coordinated by Jean-Yves Vinet.

arms) are the *daughters*. Beginning of 2017, in response to the L3 launch opportunities of the ESA Cosmic Vision Programme, the LISA consortium has submitted a proposal in which the original three spacecraft constellation was back [190]. The proposal has been selected in June 2017. The three LISA spacecraft will orbit about the sun while remaining in a near-equilateral triangular formation. The goal will be to keep the spacecraft at nearly constant distance from the Earth. The spacecraft will be at a distance of up to 70×10^6 km from the Earth; this is the outer limit for possible communication with the spacecraft. The LISA observing frequency band will be 0.1 – 100 mHz. The hope is that the best strain sensitivity for LISA will be $h(f) = 6 \times 10^{-22}\,\mathrm{Hz}^{-1/2}$ at 5 mHz [190]. The current plan is for LISA to launch in 2032 [7]

Another ambitious proposed gravitational wave detector in space is the Japanese project DECI-Hertz interferometer Gravitational wave Observatory, or DECIGO [187]. The ultimate goal of DECIGO would be to have four clusters of spacecraft that would be in orbits about the sun. Each cluster would consist of three spacecraft, 1000 km apart from one other; the individual cluster configuration resembles that of the original LISA design, but with a smaller arm-length. Since the arm-lengths are not so large it will be possible (within an individual cluster) to measure the relative displacements with three pairs of Michelson interferometers with Fabry-Perot cavities in their arms. The hope is that the ultimate strain sensitivity of DECIGO will be around $10^{-23}\,\mathrm{Hz}^{-1/2}$ in the frequency band of 0.1 – 10 Hz.

This frequency band is important. The confusion limiting background noise from compact binaries in our galaxy is expected to be low at frequencies above 0.1 Hz. The sensitivity of DECIGO is predicted to be sufficient for the detection of gravitational waves created by coalescences of intermediate mass black hole binaries. If the DECIGO is as good as predicted then the coalescences of black hole binaries of 1000 $M_\odot$ at $z = 10$ would produce an event with a signal-to-noise ratio of order 1000. In addition, it is also claimed that DECIGO will be able to detect stochastic background of gravitational wave in the frequency band of 0.1 – 1 Hz at the level of to $\Omega_{GW} = 2 \times 10^{-15}$. The current plan is that the DECIGO mission will be in the air and acquiring data in the 2020s [187].

2.2.2 Pulsar Timing

Within a decade of the discovery of pulsars in the late sixties, it was recognized that these exotic astrophysical objects might serve as tools to detect another exotic astrophysical phenomenon: gravitational waves [191, 192, 193]. The time of arrival of a pulse is modified if a gravitational wave passes between the pulsar at emission and the Earth at reception. Those gravitational waves will, of course, affect the time of arrivals not only from a single pulsar, but for time of arrivals from pulsars from all directions in the sky. Many of the noise sources that limit the precision of pulsar timing are not correlated for different pulsars and different directions. It was understood from the beginning, therefore, that the best hope for detecting gravitational waves this way lay in using an array of pulsars in different sky directions [29].

The concept of detection via such a pulsar timing array is now entering the realm of practicality, or at least plausibility, at the same time that Earth-based laser interferometers, LIGO and Virgo, are making their first detection, and at a time that plans for spacebased interferometers are moving haltingly forward. These three approaches address very different ranges of gravitational wave frequency, Earth-based around 100 Hz, space-based around 10^{-3} Hz, and pulsar timing arrays below 10^{-7} Hz (with a peak sensitivity around 10^{-8} Hz to 10^{-9} Hz), so gravitational wave detection with each approach would bring very different information about the Universe and its contents [29].

Within the pulsar community there has been the formation of collaborations that will use pulsar timing in order to try and observe gravitational waves: the Parkes (PPTA) [194], the North American (NANOGRAV) [195], and European (EPTA) groups [196], together with their international collaboration in the International Pulsar Timing Array (IPTA) [197]. In addition, the Square Kilometer Array [198] (Australia/South Africa) will also contribute to the pulsar timing array. There is the hope within the pulsar timing array community that they can detect gravitational waves within five years, most plausibly a stochastic background of gravitational waves from binary supermassive black holes. Whether that hope can be fulfilled depends for one thing on achieving a timing precision of several tens of nanoseconds. The barriers to this are both in the Earth telescopes and their electronics and in the heavens, especially the inherent noise in the pulsar mechanism and the extent to which the effects of the interstellar medium can be mitigated. Pulsar timing arrays could achieve a gravitational wave characteristic strain sensitivity of about 10^{-16}, a noise power spectral density of $10^{-12}\,\mathrm{Hz}^{-1/2}$, and an ability to measure a stochastic background of gravitational waves at the level of $\Omega_{GW}h^2 \approx 10^{-14}$; all at 10^{-9} Hz [199].

[7] The 2015 GW discovery has brought back strong arguments in favor of the initial 3 spacecraft LISA configuration.

Pulsar timing array success also depends on the cooperation of nature, cooperation beyond providing strong gravitational wave sources. The more pulsars available, the bigger the array and the better the chances are of gravitational wave detection. But only around 1% of the known pulsars have acceptable features for achieving the needed timing accuracy. A search for gravitational waves therefore involves a current search for more pulsars. If more pulsars can be found, if improved data algorithms are found for dealing with the interstellar medium, if better electronic backends are developed, and if enough time is available on big radio telescopes around the world, gravitational waves will be detected by pulsar timing arrays within five years. These are all big "Ifs" however the future of the pulsar timing array will be important to watch [29].

2.2.3 Atom Interferometers

It is clear that interferometers using light will be important devices for observing gravitational waves. However from quantum mechanics we know that massive particles also exhibit wave-like characteristics. As such, recently there has been much research into the applicability of using atom interferometers as a means to observe gravitational waves [200, 201].

Instead of monitoring test masses, like the mirrors within Virgo and LIGO, the atom interferometers would try to detect gravitational waves using freely-falling atoms as the test masses. Light pulses impinge on atoms from directions 180^o apart. Tuned to the atomic resonance, the light pulses would put the atoms in superposition states, between the ground state and a particular excited state. The atom interferometers propose to cancel problematic laser frequency noise by the use of a differential measurement between separate two atom interferometers. Considering two neighboring atom interferometers, the laser beams will interact with both of them and therefore any noise from the laser will be common mode. Between the observation of the two neighboring atom interferometers, a subtraction of the phase will diminish the common noise while keeping the gravitational wave signal [201].

Studies indicate that ground based atom interferometers (with an arm-length of 4 km, like LIGO's) would achieve a strain sensitivity of $10^{-18}\,\mathrm{Hz}^{-1/2}$ for frequencies between 1 Hz and 10 Hz. The ground based interferometers would not suffer from the low frequency seismic noise that troubles Virgo and LIGO since the atoms will be freely falling in a vacuum. A space based atom interferometric gravitational wave detector (with an arm-length of 10^3 km) is claimed to have a strain sensitivity between $10^{-19}\,\mathrm{Hz}^{-1/2}$ and $10^{-20}\,\mathrm{Hz}^{-1/2}$ for frequencies between 10^{-2} Hz and 1 Hz [200, 201]. The field of atom interferometric gravitational wave detection is relatively young, and it will be extremely interesting to see how this detection method plays out in the future.

2.3 Ground based interferometric detectors

In 2011 Virgo [37] and LIGO [202] completed observations for gravitational waves using their initial designs. With the goal to increase their strain sensitivity by a factor of about 10, advanced LIGO [39] came on-line in 2015, while advanced Virgo [203] begin observations in 2017. In addition, the Japanese detector, KAGRA [43, 44], should commence with its observations around 2018. There is also a plan for the construction of a third LIGO detector, but this one would be located in India [204]. In the 2020s there should be an extensive world-wide network of second generation detectors. This has important implications for signal detection [39, 203], signal reconstruction [126, 205], parameter estimation [206], and signal source location on the sky [45, 207, 208, 209].

2.3.1 The LIGO-GEO-Virgo ground based gravitational detector network

The LIGO-GEO-Virgo network was composed of five long-arm detectors located in the United States and in Europe: LIGO has two 4-km arm-length detectors at two sites (Washington and Louisiana) [34]. In addition, until 2007, there was also a 2 km interferometer at the LIGO Washington site. Virgo is a 3-km arm-length interferometer located near Pisa (Italy). Finally, the 600-m arm-length GEO detector is located near Hannover (Germany). The optical configurations of the LIGO and Virgo detectors are very similar (laser power recycled Michelson interferometers with an additional mirror at the beginning of each arm to form Fabry-Perot cavities in the arms to increase the effective light travel distance), while GEO is a signal and power recycled Michelson interferometer with folded arms (see [81] and references therein).

The LIGO, GEO and Virgo detectors went through many years of commissioning before they reached their design sensitivities. Sensitivity is usually quantified by the noise spectral density as illustrated in Figure 2.1. For many

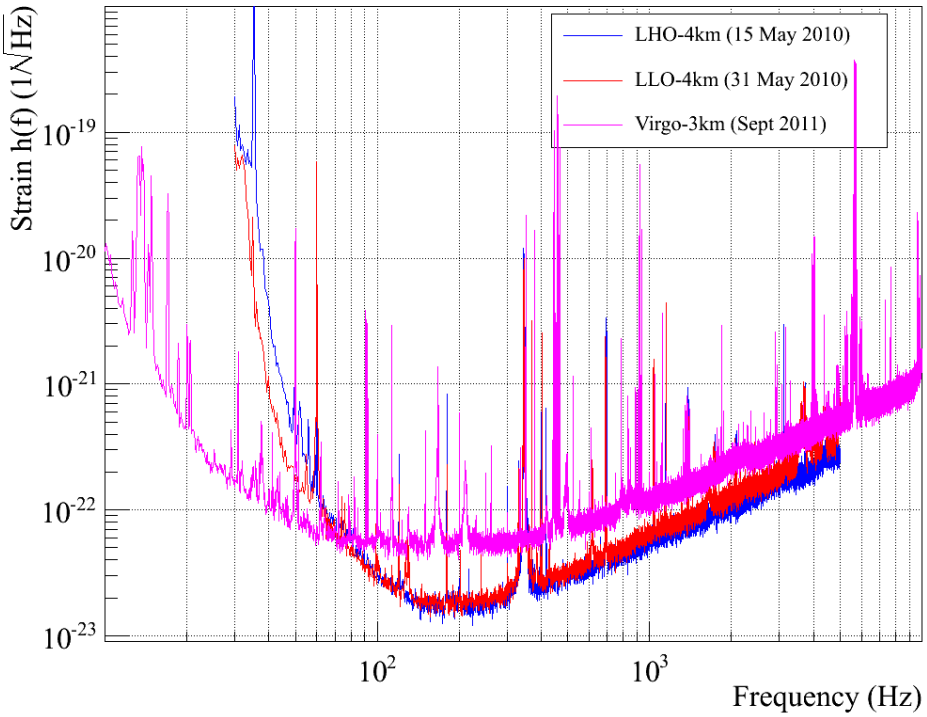

Figure 2.1: The best LIGO and Virgo sensitivities during the initial observational era.

gravitational wave searches, the most relevant aspect is the volume of the Universe that can be observed times the duration of the observation. The detection volume depends on the amount of gravitational wave energy emitted and the frequency bandwidth of the signal. When the signal waveform is known, one can compute the distance at which a signal headed toward the detector can be detected with a SNR of 8 [8]. This allows one to monitor the constant evolution of the detector's sensitivity for some of the most promising sources such as BNS systems (the best sensitivity distance (horizon) for BNS ever reached by the LIGO and Virgo detectors was 49.3, 47.2 and 23.2 Mpc respectively [210]). Yet, on a very short period of time, the detector's sensitivity can be severely affected by a transient noise increase (glitch) due to an external disturbance (thunder, airplane, ...), or a failure, for example, of the control loops that maintain the suspended optics in their optimal positions. In a transient gravitational wave search glitches produce an excess of background events with respect to what Gaussian noise would give. This impairs the transient gravitational wave search performance. Moreover, as visible in Figure 2.1, hundreds of permanent monochromatic noise features are present in the data. Noise lines are especially problematic when their frequencies overlap with the frequency of a promising rotating neutron star. Understanding all the couplings between the external noise sources and the gravitational wave strain amplitude signal allows the detectors' commissioning teams to find a way to get rid of the noise sources or at least reduce the coupling. The other cure consists of flagging the periods of time that should not be analyzed and the ones that have high probability to contain fake gravitational wave events (vetoes) [211, 212, 213].

Vetoing the noisy periods is one way to reduce the excess of background events. The other way is to demand that the gravitational wave signal to be visible in at least two interferometers (coincident analysis when only the arrival time of the event is considered or coherent analysis when data are summed up taking into account the antenna response of each to a source coming from a specific sky position). This assumes that noises in each detector are uncorrelated. In searching for a stochastic gravitational wave background cross-correlating the output of two detectors requires also that detectors' noises are uncorrelated. A network of widely separated detectors provides this advantage, except that

[8] In the case of Gaussian noise, an SNR 8 event is very unlikely to be due to noise

it can be still sensitive to magnetic resonances formed inside the spherical cavity formed by the surface of the Earth and the ionosphere (Schumann resonances are excited by lightning strikes all around the world) [214]. These magnetic features have been found coherent in LIGO/Virgo data and magnetometer data recorded at the different sites. The resonant structures show broad peaks at 8, 12, 21, ... Hz [215].

Having a network of widely separated interferometers is also required in order to identify the astrophysical parameters of the source of a transient gravitational wave signal. The rapid measurement of the position on the sky of the putative source must be accurate for optical/X-ray/γ-ray telescopes to point to the right position for quick observations after the prompt gravitational wave emission is detected.

Considering only the timing information, if only two separated detectors are available, the source is localized on an annulus. With three detectors, the sky area is restricted to two regions, mirror images in the plane formed by the three detectors [216, 208, 209, 217, 207]. More and more sophisticated methods have been developed (see [218] and references therein) to especially account for the correlation between all source parameters or the waveform uncertainty. Yet, using only the timing information gives a zeroth order approximation of what the LIGO-GEO-Virgo network is able to achieve. The timing accuracy of a single detector depends on the event SNR ρ and the effective bandwidth σ_f of the signal in the detector:

$$\sigma_t = \frac{1}{2\pi\rho\sigma_f} \tag{2.1}$$

For a $\rho \sim 10$ and $\sigma_f \sim 100\,\mathrm{Hz}$ signal, σ_t is $\sim 0.1\,\mathrm{ms}$. In the case of the LIGO-GEO-Virgo network this leads to sky area of up to tens of square degrees for signals in $100 - 300\,\mathrm{Hz}$ regions [219, 220]. Such poor sky localization is a limitation for pointing instruments such as optical telescopes whose field of view is generally much smaller than a few square degrees.

2.3.2 Virgo and advanced Virgo

A number of CNRS laboratories in France, and INFN laboratories in Italy initially proposed the Virgo Project, and subsequently created the Virgo Collaboration. A bilateral agreement between CNRS and INFN led to the construction of Virgo in Cascina, Italy. In 2000, CNRS and INFN decided to create the European Gravitational Observatory (EGO) consortium to manage the construction and the operation of Virgo and promote gravitational waves research in Europe. Subsequently Dutch, Hungarian and Polish groups have joined the Virgo Collaboration.

The Virgo interferometer demonstrated its success as part of the first generation of kilometer length gravitational wave detectors [37]. It reached its design sensitivity, and although no gravitational wave signal was detected, Virgo data (along with LIGO [202] data) was used to set important astrophysical upper limits [33, 34]. The best strain sensitivity achieved by initial Virgo is displayed in Figure 2.2

Since 2007, LIGO [202], GEO [183] and Virgo [37] have been pooling their data and carrying out their searches jointly. In 2007 LIGO was about to conclude its 5^{th} science (S5) run, while Virgo had just started its first science run (VSR1). Since then, another one-year-long joint science run took place in 2009 – 2010 (S6, VSR2 and VSR3). In late 2010, the LIGO detectors shut down for advanced LIGO installation. Virgo continued commissioning through late 2011 and improved its low-frequency sensitivity ($< 60\,\mathrm{Hz}$) by a factor of 3. A joint run with the GEO detector was conducted in the summer of 2011 (S6 for GEO and VSR4 run for Virgo).

Advanced Virgo [203] is the continuation of the Virgo Project, and is an upgrade of the initial Virgo detector [37]. It is designed to have a sensitivity an order of magnitude better than that of initial Virgo. An increase of ~ 10 in strain sensitivity corresponds to an increase in the detection rate of ~ 1000. Advanced Virgo, along with advanced LIGO [39] and subsequently KAGRA [44], will be part of the international network of detectors that should soon make direct observations of gravitational waves. A comprehensive description of advanced Virgo can be found in [203]. Advanced Virgo will come on-line in 2016 – 2017. The expected sensitivity of advanced Virgo, along with its main noise sources, can be seen in Figure 2.9. Before discussing the sources of limiting noise, we will see in the next section how such a kilometric laser interferometer detector can detector GWs.

2.3.3 How do interferometric gravitational wave detectors work?

Figure 2.3 shows the optical layout of a simple Michelson interferometer. The beam splitter and the end mirrors are suspended by wires, and effectively free to move in the plane of the interferometer. We will now choose a coordinate system where the beam splitter and the end mirrors are fixed (TT gauge coordinates system). The coordinates origin

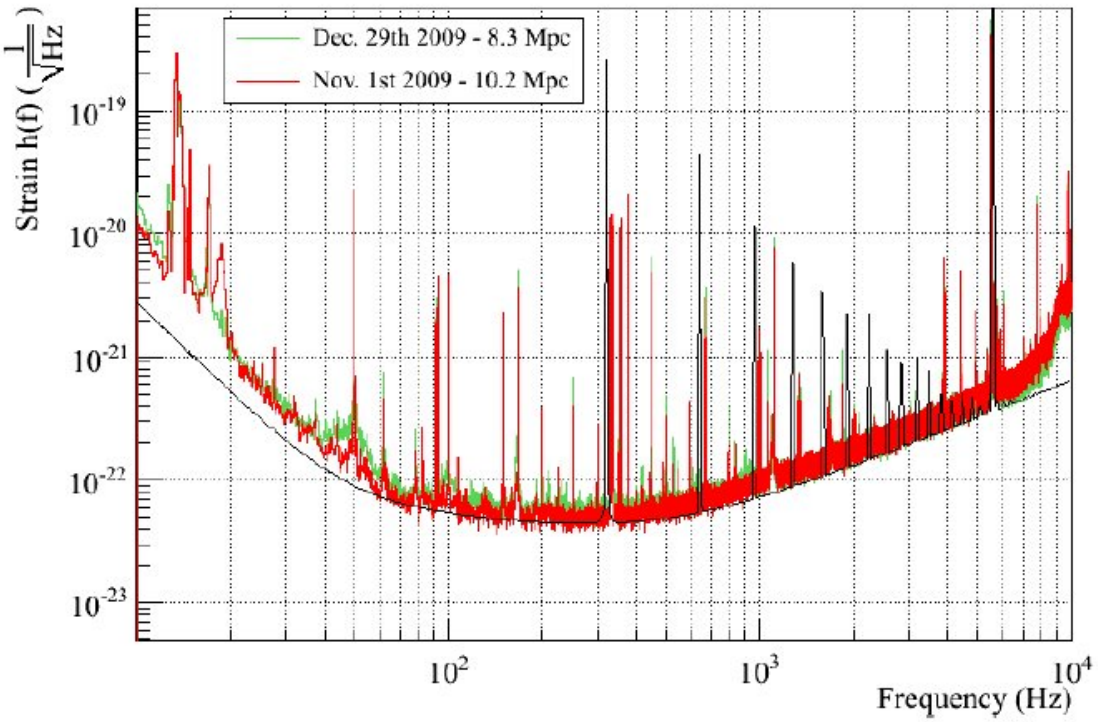

Figure 2.2: An example of the strain sensitivity achieved by Virgo [37]. The red trace (November 2009) gives an binary neutron start inspiral range (averaged over all angles) of 8.3 Mpc, while the green trace (from December 2009) gives an inspiral range of 10.2 Mpc. The initial Virgo design strain sensitivity is given by the black curve.

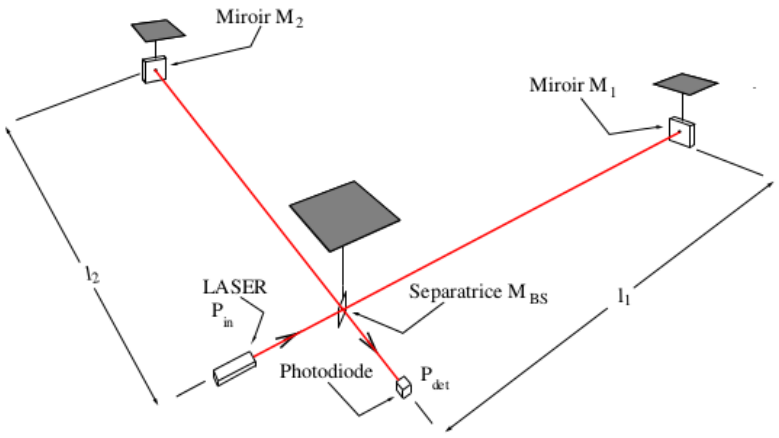

Figure 2.3: The basic Michelson interferometer. Light enters the interferometer from one port of the beam splitter, and half the light travels down each arm. The photodetector receives light exiting the dark port of the interferometer and hence the signal. This is where the dark fringe signal is produced.

is at the beam splitter and the arms along the **x** and **y** axes have lengths L_1 and L_2 that are roughly equal on a kilometer scale. With a laser of wavelength λ incident on the beam splitter, the electric field seen by the photodetector is

$$\Psi_{det} = \Psi_{in} r_{BS} t_{BS} (r_1 e^{2ikL_1} + r_2 e^{2ikL_2}), \tag{2.2}$$

where r_{BS} and t_{BS} are the reflectivity and the transmittivity of the beam splitter, r_1 and r_2 are the reflectivity of the end mirrors, $k = 2\pi/\lambda$ and Ψ_{in} is the electric field at the beam spliter. The light power exiting the dark port of the interferometer is thus

$$P_{out} = P_{in} r_{BS}^2 t_{BS}^2 (r_1^2 + r_2^2)(1 + Ccos(2k(L_2 - L_1)), \tag{2.3}$$

where P_{in} is the laser power impinging the beam splitter and the contrast C

$$C = \frac{2r_1 r_2}{r_1^2 + r_2^2} \tag{2.4}$$

quantifies the asymetries in reflectivities of the two arms. The amplitude of the light leaving the interferometer depends on the difference in the phase accumulated by the light travelling in the two arms. The interferometer operates with the condition that in the absence of excitation (noise or GW) the light exiting the dark port is null. Let's now see how a GW passing by will modify the laser power at the photodetector. For simplicity, we consider a plus polarized GW incoming from the **z** direction. In the TT gauge[9] the spacetime interval between two neighboring points connected by a light ray remains null

$$\begin{aligned} 0 = ds^2 = g_{\mu\nu} dx^\mu dx^\nu &= (\eta_{\mu\nu} + h_{\mu\nu}) dx^\mu dx^\nu, && (2.5)\\ &= -c^2 dt^2 + (1 + h_{11}(t)) dx^2 \quad \text{for the arm along x}, && (2.6)\\ &= -c^2 dt^2 + (1 + h_{22}(t)) dy^2 \quad \text{for the arm along y}, && (2.7)\\ & && (2.8) \end{aligned}$$

We can calculate the phase shift generated by the passing GW,

$$\Delta\phi = \frac{2\pi}{\lambda}(2L_x - 2L_y), \tag{2.9}$$

where L_x and L_y are the optical paths in the arms along the **x** and the **y** direction respectively. Using Eq. (2.6) we have

$$L_x = \int cdt = \int_0^L \sqrt{1 + h_{11}(t - \frac{x}{c})} dx \approx \int_0^L (1 + \frac{1}{2} h_{11}(t - \frac{x}{c})) dx, \tag{2.10}$$

A photon will travel one arm in $\sim 10\,\mu$s which is much shorter than the typical duration of the signals searched in the $10 - 10^4$ Hz sensitive band. We can thus consider that $h_{11}(t)$ does not vary during the light travel of a photon. Using $h_{11}(t) = -h_{22}(t) = h^+(t)$, Eq. (2.10) becomes

$$L_x \approx L_1 + \frac{1}{2} L_1 \; h^+(t). \tag{2.11}$$

Similarly, for the other arm we have

$$L_y \approx L_2 - \frac{1}{2} L_2 \; h^+(t). \tag{2.12}$$

Eqs (2.11) and (2.12) are telling that the distance between two free falling points (distance between the beam splitter and the end mirror) will vary when a GW is passing by and this variable is proportional to the amplitude of the GW

$$\frac{\Delta L}{L} \propto h^+ \tag{2.13}$$

The phase shift induced by the passing GW is thus approximated to

$$\Delta\phi = \frac{2\pi}{\lambda}(L_1 + L_2) h^+(t). \tag{2.14}$$

[9] In the TT gauge the coordinates are marked by the position of free falling objects.

This shows that a measure of the phase shift is a direct measure of the GW strain amplitude. For a signal amplitude of 10^{-21}, the phase shift is of order 10^{-11} rad which is extremely small. From Eq. (2.14) we could conclude that we can increase the phase shift induced by a GW by increasing the arms length. This is not true as the approximation made in Eq. (2.10) assumes that $2\pi f_{GW} L/c << 1$. In other words the response of a Michelson interferometer as function of the gravitational wave frequency is not constant.

We now need to consider the most general case of a GW with arbitrary direction and polarization and a description in the detector frame that corresponds to what is measured[10]. In the (**x**,**y**,**z**) frame attached to the source (where **z** is the GW propagation direction) the Minkowski metric perturbation expressed in the TT gauge is

$$h^{\mu\nu}(t) = \begin{pmatrix} 0 & 0 & 0 & 0 \\ 0 & h^+(t) & h^\times(t) & 0 \\ 0 & h^\times(t) & -h^+(t) & 0 \\ 0 & 0 & 0 & 0 \end{pmatrix} \tag{2.15}$$

Let us consider the effect of this coming wave on the detector. In other words, we want to know how the end mirrors move with respect to the beam splitter. In the TT gauge coordinate system, a particle initially at rest will remain at rest. Yet, when one measures the distance between two arm cavity mirrors, we use the coordinate system of a local inertial frame whose origin coincides with the geodesic of one of the mirror[11]. In this frame coordinate distances/time are proper distances at the first order in coordinates. In the frame (**X**,**Y**,**Z**) attached to the detector with **X** and **Y** axes aligned along the two arms[12] the variation of the distance between the end mirrors is given by the geodesic deviation equation [222] assuming the distance between masses is small compared to the GW wavelength

$$\frac{d^2\xi^\alpha}{d\tau^2} = \frac{d^2\xi^\alpha}{dt^2} = R^\alpha_{\mu\nu\beta}\ U^\mu\ U^\nu\ \xi^\beta \tag{2.16}$$

where ξ^α is the vector connecting two geodesics, U^μ is the four velocity vector of a mirror and $R^\alpha_{\mu\nu\beta}$ is the Riemann tensor which is gauge invariant. Keeping all quantities at first order in $h^{\mu\nu}$, and considering two masses separated by L_x along the **X** axis we have $U^\alpha = (1,0,0,0)$ and $\xi^\alpha = (0, L_x, 0, 0)$. Eq. (2.16) then becomes

$$\ddot{\xi}^\alpha = R^\alpha_{00\beta}\ \xi^\beta = R^\alpha_{00x}\ L_x = -R^\alpha_{0x0}\ L_x \tag{2.17}$$

As Eq. (2.17) is gauge invariant, we can use the expressions of the Riemann tensor in the TT gauge (see Eq. (1.31))

$$R^x_{0x0} = R_{x0x0} = -\frac{1}{2}\ddot{H}^{TT}_{xx} \tag{2.18}$$

$$R^y_{0x0} = R_{y0x0} = -\frac{1}{2}\ddot{H}^{TT}_{xy} \tag{2.19}$$

$$R^y_{0y0} = R_{y0y0} = -\frac{1}{2}\ddot{H}^{TT}_{yy} \tag{2.20}$$

$$\tag{2.21}$$

where H^{TT}_{ij} is the metric perturbation tensor in the detector frame. We finally obtain the equations that govern the change in the length of the **X** arm when a GW is passing by

$$\ddot{\xi}^x = \frac{1}{2}\ddot{H}^{TT}_{xx} L_x \tag{2.22}$$

$$\ddot{\xi}^y = \dot{\xi}^y = 0 \tag{2.23}$$

For the mirror located at $\xi^\alpha = (0, 0, L_y, 0)$ the displacement along the **Y** direction is given by

$$\ddot{\xi}^y = \frac{1}{2}\ddot{H}^{TT}_{yy} L_y \tag{2.24}$$

$$\ddot{\xi}^x = \dot{\xi}^x = 0 \tag{2.25}$$

[10]The previous demonstration was made in the TT gauge coordinates system which is not appropriate for measurements.

[11]This frame is also called the Fermi coordinate system. In this frame the effect of the passage of a GW is a displacement of the test masses.

[12]In [221], Schutz and Tinto consider the most general case where the angle between the detectors can be different from 90°. In this case it is convenient to have the **X** axis bisects the angle between the two arms. Here we consider arms angle to be 90° and **X** and **Y** axes align along the arms.

Eqs (2.22) and (2.24) can be solved perturbatively in H_{ij}. At zero order we have $\xi^i = L_i$. At the first order $\xi^i = L_i + \frac{1}{2}H_{ii}^{TT}\ L_i$. The relative length change of one arm is thus defined at first order in H_{ij} as

$$\frac{\delta L}{L} = \frac{1}{2}H_{ii}^{TT} \tag{2.26}$$

The difference between the relative length changes of the two arms, also called gravitational wave signal $s(t)$ is thus

$$s(t) = \Delta[\frac{\delta L}{L}] = \frac{1}{2}(H_{xx}^{TT} - H_{yy}^{TT}) \tag{2.27}$$

The expressions of the metric perturbation tensor in the detector frame are obtained from Eq. (2.15) applying three rotations that transform the source frame into the detection frame. This three rotations operation to pass from the source to the detector frames is described by the following orthogonal matrix

$$M = \begin{pmatrix} cos\psi cos\phi - cos\theta sin\phi sin\psi & cos\psi sin\phi + cos\theta cos\phi sin\psi & sin\theta sin\psi \\ -sin\psi cos\phi - cos\theta sin\phi cos\psi & -sin\psi sin\phi + cos\theta cos\phi cos\psi & sin\theta cos\psi \\ sin\theta sin\phi & -sin\theta cos\phi & cos\theta \end{pmatrix} \tag{2.28}$$

where θ, ϕ and ψ are the Euler's angles displayed in Figure 2.4. Note that ψ corresponds to the polarization angle of the gravitational wave. It corresponds to a rotation around the $\mathbf{z}$ axis. θ and ϕ are the usual spherical polar coordinates of the direction of the wave progagation axis as measured in the detector's frame. Dropping all indices we have

$$H(t) = {}^{t}M\ h(t)M \tag{2.29}$$

Eq. (2.27) can be written as

$$s(t) = F^{+}(\theta,\phi,\psi)h^{+}(t) + F^{\times}(\theta,\phi,\psi)h^{\times}(t) \tag{2.30}$$

where the antenna pattern functions F^+ and $F^\times$ are

$$F^{+}(\theta,\phi,\psi) = \frac{1}{2}(1+cos^2\theta)cos2\phi cos2\psi - cos\theta sin2\phi sin2\psi \tag{2.31}$$

$$F^{\times}(\theta,\phi,\psi) = \frac{1}{2}(1+cos^2\theta)cos2\phi sin2\psi + cos\theta sin2\phi cos2\psi \tag{2.32}$$

$$\tag{2.33}$$

These antenna pattern functions displayed in Figure 2.5 show the response of the detector to the two gravitational wave polarizations. The root mean square of the two polarization-averaged antenna pattern is showing a rather uniform response for all sky directions. If the sky coverage of an gravitational wave detector is not uniform, it covers a large fraction of the sky.

Coming back to the output of the Michelson interferometer shown on Figure 2.3 we will now consider the effect of the deviation of the arm's lengths due to a GW passing by (considering only one GW polarization)

$$L_1 \rightarrow L_1 + \frac{1}{2}L_1 h^{+} \tag{2.34}$$

$$L_2 \rightarrow L_2 - \frac{1}{2}L_2 h^{+} \tag{2.35}$$

Assuming $h^+ << 1$ Eq. (2.3) becomes

$$P_{out} = P_{in}r_{BS}^2 t_{BS}^2 (r_1^2 + r_2^2)(1 + Ccos(2k(L_2 - L_1) + Ckh^{+}(L_1 + L_2)sin(2k(L_2 - L_1)), \tag{2.36}$$

$$= P_{Michelson} + \delta P_{GW}, \tag{2.37}$$

where $P_{Michelson}$ is given by Eq. (2.3) and $\delta P_{GW} = \frac{P_{in}}{2}r_{BS}^2 t_{BS}^2 (r_1^2 + r_2^2)Ckh^{+}(L_1 + L_2)sin(2k(L_2 - L_1))$. The output light power of a Michelson interferometer is a function of the phase shift between its arms, and is recorded using a

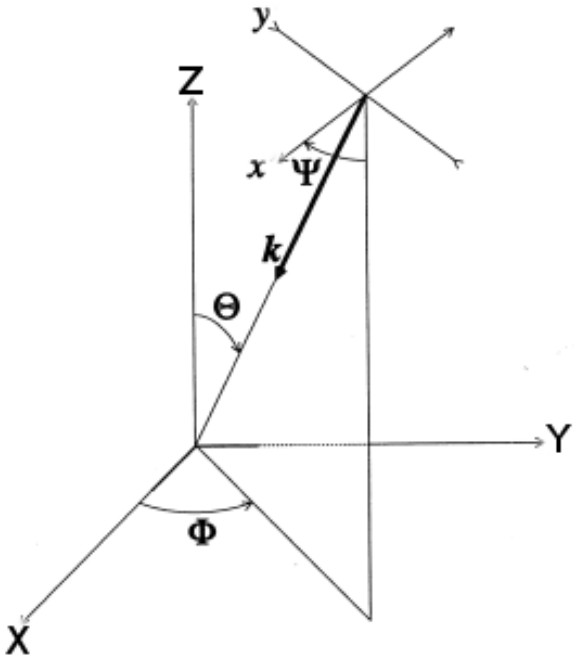

Figure 2.4: Source frame (**x**,**y**,**z**) and detector frame (**X**,**Y**,**Z**) representations. The sky location angles (θ and ϕ) and the polarization angle ψ are shown.

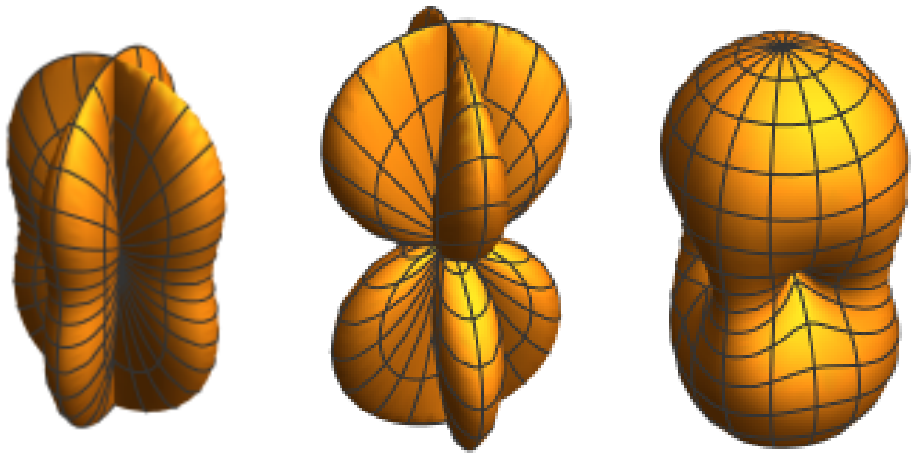

(a) (b) (c)

Figure 2.5: F^+ (a) and $F^\times$ (b) antenna pattern functions as a function of sky direction for a fix polarization angle (ψ=0). (c) is the root mean square of the two polarization antenna patern functions.

set of photodiodes. From the recorded power, after proper calibration, one can extract the detector strain amplitude time series [223]

$$\begin{aligned} d(t) &= n(t) + s(t), & (2.38)\\ &= n(t) + F^{+}(\theta,\phi,\psi)h^{+}(t) + F^{\times}(\theta,\phi,\psi)h^{\times}(t), & (2.39) \end{aligned}$$

where $n(t)$ is the detector noise time series.

2.3.4 Advanced Virgo optical configuration

Although most of the research work presented in this document has been mostly done with the Virgo and LIGO instruments, we will take the example of advanced Virgo [203] to describe the main features of a laser interferometer gravitational wave detector. Figure 2.6 illustrates the main elements that transform a Michelson interferometer into a gravitational wave detector.

In the previous section, we have considered a simple Michelson detector (Figure 2.6a) to explain the detection principle. However, the initial Virgo and LIGO interferometers were more sophisticated, and used a heterodyne detection strategy. If E_0 is the amplitude of the electric field from the laser, and assuming the use of a 50 – 50 transmission beam splitter, the electric field (neglecting unimportant common phase shifts) for the light incident on the photodetector would be

$$\begin{aligned} E_{out} = \frac{E_0}{2}(e^{i\delta\phi_1} - e^{i\delta\phi_2}) \approx i\frac{E_0}{2}(\phi_1 - \phi_2)\ , \\ = iE_0\frac{2\pi}{\lambda}(2L_1 - 2L_2)\ . \end{aligned} \tag{2.40}$$

The laser light for initial Virgo [37] and initial LIGO [202] was phase modulated at a frequency in the MHz regime. With this method, the deconvolved current from the photodiode that detects light at the interferometer output is proportional to the phase acquired by the light, namely

$$I \propto \frac{2\pi}{\lambda}(L_1 - L_2)\ . \tag{2.41}$$

A gravitatinal wave of optimal polarization normally incident upon the interferometer plane makes one arm decrease in length while the other increases. The Michelson interferometer acts as a gravitational wave transducer; the change in arm-length results in more light exiting the interferometer dark port.

An interferometer's sensitivity increases with arm length, but geographical and financial constraints limit the size of the arms. If there could be some way to bounce the light back and forth to increase the effective arm-length it would increase the detector performance. Fabry-Perot cavities at resonance have a storage time of

$$\frac{2L}{c(1-\sqrt{R_1R_2})}\ , \tag{2.42}$$

where R_1 is the power reflectivity of the front mirror of the Fabry-Perot cavity while R_2 is the end mirror's power reflectivity. Figure 2.6b shows the system of a Michelson interferometer with Fabry-Perot cavities. This gravitational wave interferometer design was proposed and tested in the late 1970s by Ron Drever [178]. The far mirror R_2 has a very high reflectivity ($R_2 \approx 1$) in order to ultimately direct the light back towards the beam splitter. The front mirror reflectivity R1 is such that advanced Virgo's effective arm-length is increased from $L = 3\,\text{km}$ to $L_{eff} = 846\,\text{km}$ [13]

The optical properties of the mirrors of the Fabry-Perot cavities must be exquisite in order to achieve success. The advanced Virgo mirrors were tested, and the root mean squared surface uniformity is less than 0.5 nm, scattered light is less than 100 parts per million (ppm), and absorption, including coating, is less than 0.4 ppm at 1064 nm for the end mirrors.

The advanced Virgo input mirrors for the Fabry-Perot cavity arms will have radii of curvature 1420 m, while the end mirrors radii of curvature will be 1683 m; this results in a beam radii (with $\lambda = 1.06\,\mu$ m) of 48.7 mm at the

[13] The effective length is given by $2\mathcal{F}/\pi$ where $\mathcal{F}$ is the finesse of the arm Fabry-Perot cavity (443 for advanced Virgo).

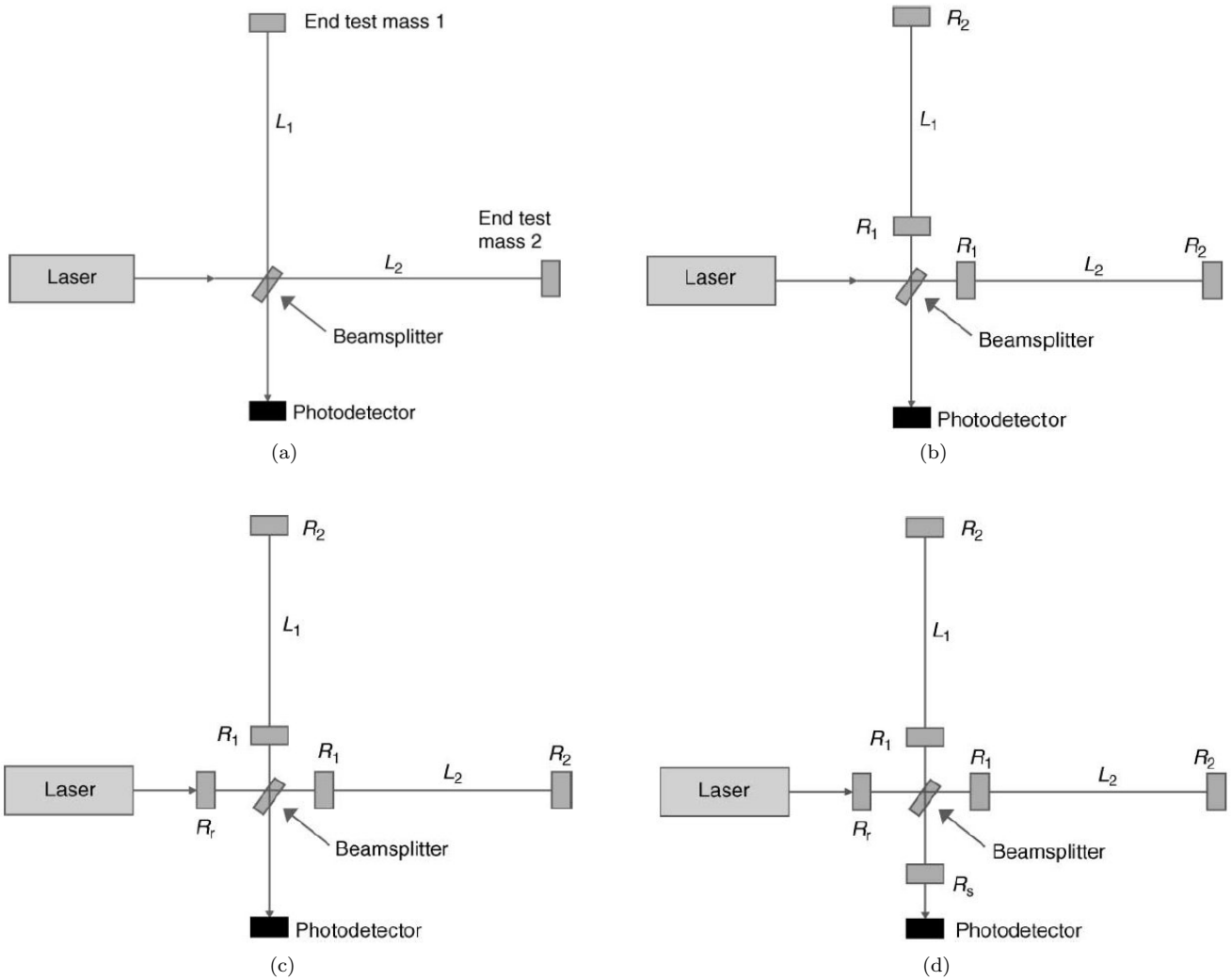

Figure 2.6: Transformation of a Michelson interferometer into a dual recycled interferometer with Fabry-Perot cavities.
(a): The basic Michelson interferometer. Light enters the interferometer from one port of the beam splitter, and half the light travels down each arm. The photodetector receives light exiting the dark port of the interferometer and hence the signal. This is where the dark fringe signal is produced.
(b): A Michelson interferometer with Fabry-Perot cavities in each arm. Light enters the interferometer from one port of the beam splitter, and half the light travels down each arm. The light is *stored* in the cavities, thereby increasing the effective arm-lengths of the interferometer. The front cavity mirrors have reflectivities of R_1, while the end mirrors have reflectivities of $R_2 \approx 1$. By using Fabry-Perot cavities advanced Virgo will increase its effective arm-lengths by a factor of 141 [203].
(c): A power recycled Michelson interferometer with Fabry-Perot cavities in each arm. Normally light would exit the interferometer through the light port and head back to the laser. Installation of the recycling mirror with reflectivity R_r sends the light back into the system. A Fabry-Perot cavity is formed between the recycling mirror and the first mirror (R_1) of the arms. For advanced Virgo this strategy will increase the power circulating in the interferometer by a factor of 28 [203].
(d): A signal recycled and power recycled Michelson interferometer with Fabry-Perot cavities in each arm. Normally light containing the gravitational wave signal would exit the interferometer through the dark port of the beam splitter and head to the photodetector. Installation of the signal recycling mirror with reflectivity R_s sends the light back into the system. The phase of the light acquired from the gravitational wave will build up at a particular frequency determined by the reflectivity R_s.

input mirror and 58 mm at the end mirror. The high power circulating in the interferometer, especially within the Fabry-Perot cavities, will cause thermal lensing; this has been observed in initial Virgo [224] and initial LIGO [35]. Thermal compensation is an integral part of the advanced Virgo [203] and advanced LIGO [39] design. To maintain the arm-cavity mode structure, it will be necessary to control the radius of curvature of all test masses within $\pm$ 2 m from the initial radius of curvature. An advanced Virgo test mass (and therefore a Fabry-Perot mirror) can be seen on the right in Figure 2.7.

The noise sources that inhibit the interferometer performance are discussed below. However, let us consider one's ability to measure the relative phase between the light in the two arms. The Heisenberg uncertainty relation for light with phase ϕ and photon number N is $\Delta\phi\ \Delta N \sim 1$. For a measurement lasting time τ using laser power P and frequency f, the number of photons of wavelength λ is $N = P\lambda\tau/hc$, and with Poisson statistics describing the light $\Delta N = \sqrt{N} = \sqrt{P\lambda\tau/hc}$. Therefore,

$$\Delta\phi\ \Delta N = \frac{2\pi}{\lambda}(2\Delta L)\sqrt{P\lambda\tau/hc} = 1\ , \tag{2.43}$$

where $\Delta L = L_1 - L_2$. This implies that

$$\Delta L = \frac{1}{4\pi}\sqrt{\frac{hc\lambda}{P\tau}}\ . \tag{2.44}$$

This is the demonstration of the *shot noise* limit of the Michelson interferometer. With more light power the interferometer can measure smaller distance displacements and achieve better sensitivity. The plan for advanced Virgo is to have 175 W exiting the laser ($\lambda = 1.06\,\mu$ m), with 125 W actually making it to the entrance of the interferometer (more on the interferometer input optics below). However, there is a nice trick one can use to produce more light circulating in the interferometer, namely power recycling. Figure 2.6c displays the power recycling interferometer design. The interferometer operates such that virtually none of the light exits the interferometer dark port, and the bulk of the light returns towards the laser. An additional mirror, R_r in Figure 2.6c, recycles the light. For advanced Virgo, recycling will increase the effective light power by another factor of 28. The higher circulating light power therefore improves the sensitivity.

There is one additional modification to the interferometer system that can further improve sensitivity, but only at a particular frequency. A further Fabry-Perot system can be made by installing what is called a signal recycling mirror; this would be mirror R_s in Figure 2.6d. Imagine light in arm 1 on the interferometer that acquires phase as the arm expands due to the gravitational wave. The traveling gravitational waves oscillation will subsequently cause arm 1 to contract while arm 2 expands. If the light that was in arm 1 could be sent to arm 2 while it is expanding, then the beam would acquire additional phase. This process could be repeated over and over. Mirror R_s serves this purpose, with its reflectivity defining the storage time for light in each interferometer arm. The storage time defined by the cavity formed by the signal recycling mirror, R_s, and the mirror at the front of the interferometer arm cavity, R_1, determines the resonance frequency. Signal recycling will give a substantial boost to interferometer sensitivity at a particular frequency, and will eventually be implemented in all the main ground based interferometric detectors.

The Virgo and LIGO interferometers are infinitely more complex than the relatively simple systems displayed in the figures of this manuscript. Figure 2.8 presents an aerial view of the Virgo site at Cascina, Italy (near Pisa). The magnitude of the 3-km system is apparent.

2.3.5 Noise sources and interferometer sensitivity

If the interferometers are to detect distance displacements smaller than $\Delta L \sim 10^{-18}$ m then they must be isolated from a host of deleterious noise sources. Seismic disturbances should not shake the interferometers. Thermal excitation of components will affect the sensitivity of the detector and should be minimized. The entire interferometer must be in an adequate vacuum in order to avoid fluctuations in gas density that would cause changes in the index of refraction and hence modification of the optical path length. The laser intensity and frequency noise must be minimized. The counting statistics of photons influences accuracy. As an illustration the expected noise sensitivity for the advanced Virgo is displayed in Figure 2.9, along with the sum of the expected noise sources.

In an ideal situation the interferometer sensitivity will be limited by the counting statistics of the photons. A proper functioning laser will have its photon number described by Poisson statistics, or shot noise; if the mean number of photons arriving per unit time is N then the uncertainty is $\Delta N = \sqrt{N}$, which implies an interferometer displacement

Figure 4 from F Acernese et al 2015 Class. Quantum Grav. 32 024001

Figure 2.7: Advanced Virgo optics. Left: The power recycling substrate (35 cm in diameter, left) beside the beam splitter of 55 cm in diameter. Right: One of the Fabry-Perot cavity mirrors, which also serves as a test mass for the gravitational wave detector [203].

.

Figure 2.8: A view of the gravitational wave detector, Virgo, from the air. Located in Cascina, Italy, outside of Pisa, the magnitude of the experiment is apparent with its 3 km interferometer arms.

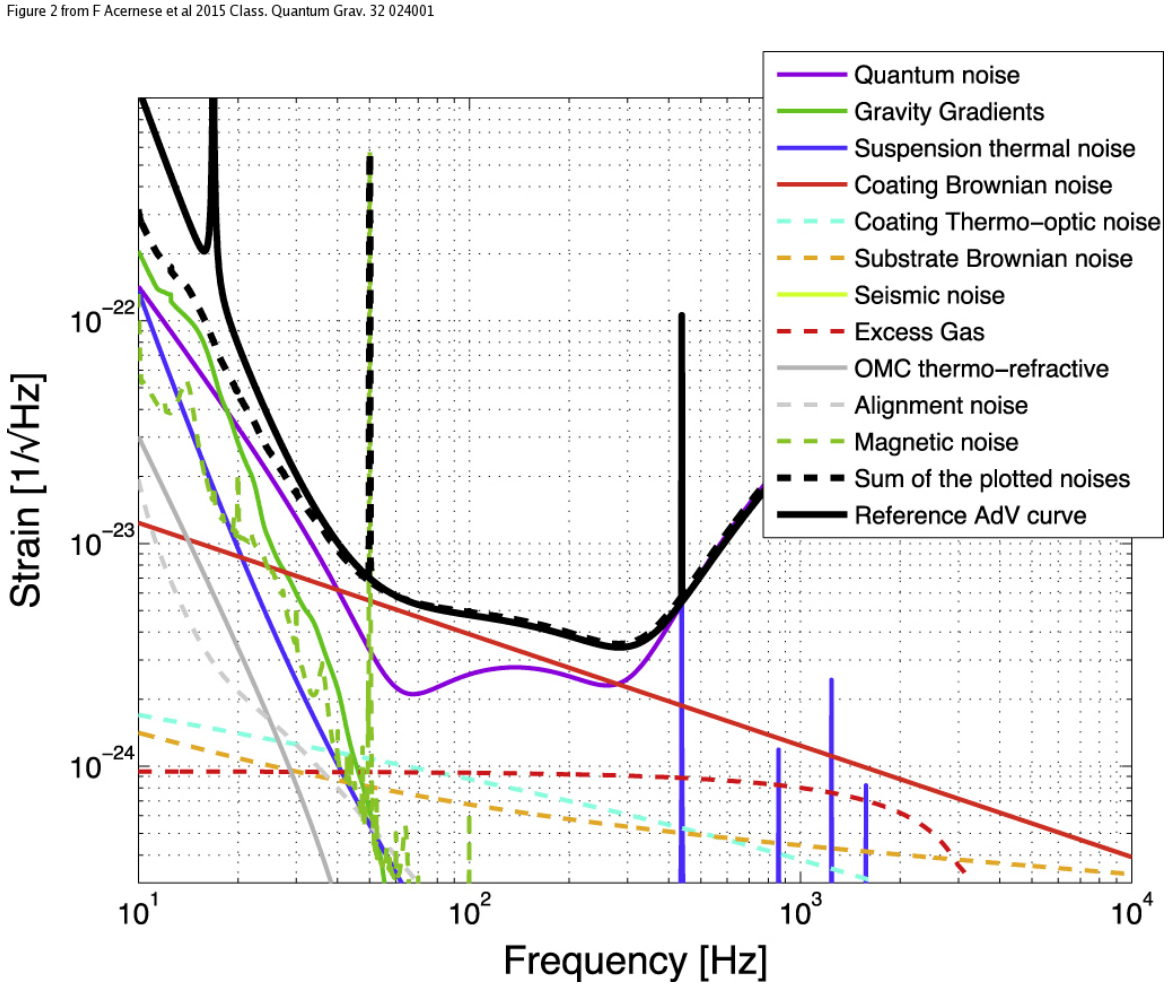

Figure 2.9: The predicted advanced Virgo sensitivity due to the expected noise sources. This has been calculated for the configuration optimized for binary neutron star detection with 125 W of input into the interferometer laser power [203].

sensitivity for ΔL given by Eq. 2.44, or a noise spectral density of

$$\Delta L(f) = \frac{1}{4\pi}\sqrt{\frac{hc\lambda}{P}}\ , \tag{2.45}$$

which has units of $m/\sqrt{Hz}$.

Note also that the sensitivity increases as the light power increases. The reason for this derives from the statistics of repeated measurements. The relative lengths of the interferometer arm-lengths could be measured, once, by a photon. However, the relative positions are measured repeatedly with every photon from the laser, and the variance of the mean decreases as $\sqrt{N}$, where N is the number of measurements (or photons) involved. The uncertainty in the difference of the interferometer arm-lengths is therefore inversely proportional to photon number, and hence the laser's power. In terms of strain sensitivity this would imply

$$h_{shot}(f) = \frac{1}{4\pi L}\sqrt{\frac{hc\lambda}{P}}\ , \tag{2.46}$$

which has units of $1/\sqrt{Hz}$.

This assumes the light just travels down the arm and back once. With Fabry-Perot cavities the light is stored, and the typical photon takes many trips back and forth before exiting the system. In order to maximize light power the end mirrors ($R_2 \sim 1$) and the strain sensitivity is improved to

$$h_{shot}(f) = \frac{1}{4\pi L'}\sqrt{\frac{hc\lambda}{P}}\ , \tag{2.47}$$

where

$$L' = \frac{L(1-R_1)}{(1-\sqrt{R_1 R2})^2} \approx \frac{L(1+\sqrt{R_1})}{1-\sqrt{R_1}}\ . \tag{2.48}$$

As the frequency of the gravitational waves increases the detection sensitivity will ultimately decrease. If the gravitational wave causes the interferometer arm-length to increase, then decrease, while the photons are still in the arm cavity, then the phase acquired from the gravitational wave will be washed away. This is the reason why interferometer sensitivity decreases as frequency increases, and explains the high-frequency behavior seen in Figure 2.9. Taking this into account, the strain sensitivity is

$$h_{shot}(f) = \frac{1}{4\pi L'}\sqrt{\frac{hc\lambda}{P}}\Big(1+\Big(\frac{4\pi L' f}{c}\Big)^2\Big)^{1/2}. \tag{2.49}$$

If the gravitational wave is to change the interferometer arm-length then the mirrors that define the arm must be free to move. In systems like Virgo fibers (made of fused silica [14] for advanced Virgo [203]) suspend the mirrors; each mirror is like a pendulum. While allowing the mirrors to move under the influence of the gravitational wave is a necessary condition, the pendulum itself is the first component of an elaborate vibration isolation system. Seismic noise will be troublesome for the detector at low frequencies. The spectral density of the seismic noise is about $(10^{-7}/f^2)$ m Hz$^{-1/2}$, for frequencies above 1 Hz. A simple pendulum, by itself, acts as a motion filtering device. Above its resonance frequency the pendulum filters motion with a transfer function like $T(f) \propto (f_0/f)^2$. Detectors such as advanced Virgo will have a pendulum with resonant frequencies of about $f_0 \approx 0.6$ Hz; The various second generation gravitational wave detectors (advanced Virgo [203], advanced LIGO [39], KAGRA [43, 44]) have different vibration isolation designs. The mirrors in these interferometers will be suspended in elaborate vibration isolation systems, which may include multiple pendulum and isolation stacks. The mirror suspension chain used in advanced Virgo, is shown on figure 2.10. This so called Superattenuator is composed of an inverted pendulum fixed to the ground, and a series of wires and mechanical filters attached to the top of the inverted pendulum. Their purpose is to filter the ground motion by repeatedly applying the $(f_0/f)^2$ factor to all degrees of freedom, horizontal for the inverted pendulum and fibers and vertical for the mechanical filters which are basically vertical springs. The resonant frequencies of these stage are in the 10 mHz – 2 Hz range well below the intended sensitive band 10 Hz – 10 kHz and

[14] as of mid 2016, advanced mirrors are suspended with steel wires due to an unexpected fused silica suspension breaking mechanism attributed to dust contamination.

the quality factors are rather low ($Q < 100$) [203]. A damped oscillator increase the root mean square motion by Q, for this reason low quality factors are chosen in the filtering chain in order to keep the integrated motion (dominated by the low frequency part) small. Seismic noise, and the induced gravity gradient noise, will be the limiting factor for interferometers seeking to detect gravity waves in the tens of hertz range, as can be seen in the sensitivity curve presented in Figure 2.9.

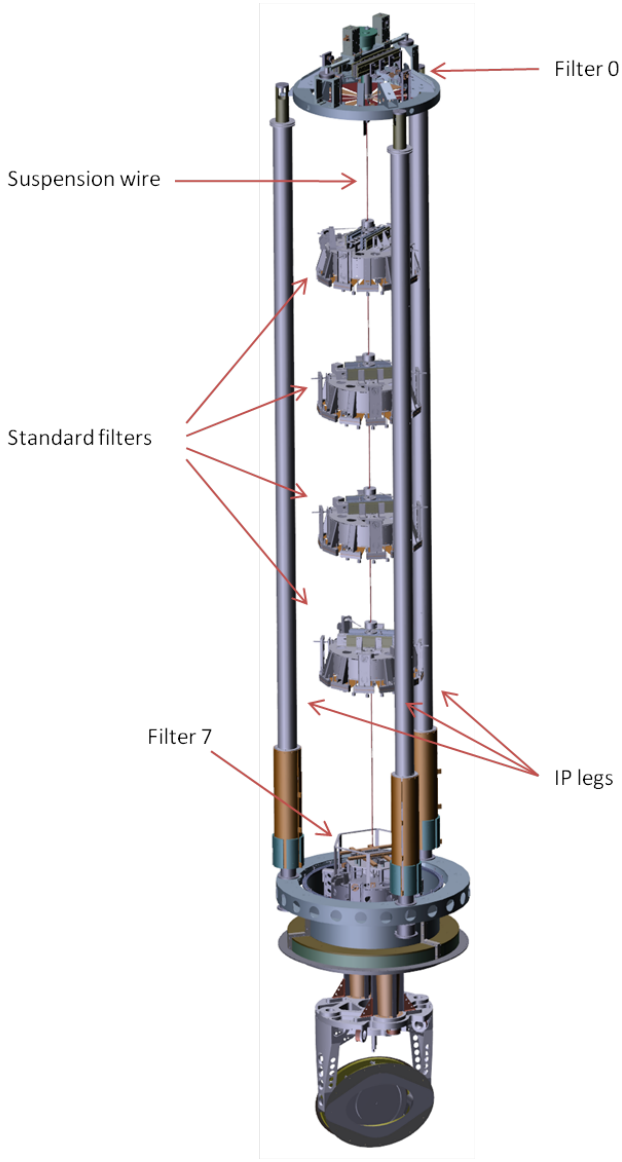

Figure 2.10: Schematics of the advanced Virgo Superattenuator [203]. It is composed of an inverted pendulum fixed to the ground, and a series of wires and mechanical filters attached to the top of the inverted pendulum. The purpose of this chain is to isolate the mirror suspended at the bottom of the apparatus from the ground motion.

Due to the extremely small distance displacements that these systems are trying to detect it should come as no surprise that thermal noise is a problem. This noise enters through a number of components in the system. The two most serious thermal noise sources are the fibers suspending the mirrors in the pendulum, and the mirrors themselves (the mirror coatings and the fused silica of the test mass itself for advanced Virgo [203]). Consider the fibers; there are a number of modes that can oscillate (i.e. violin modes). At temperature T each mode will have energy of $k_B T$,

but distributed over a band of frequencies determined by the quality factor (or Q) of the material. Low-loss (or high-Q) materials work best; for the violin modes of the wires there will be much noise at particular frequencies (in the hundreds of Hz). The mirror is a cylindrical object, which will have normal modes of oscillation that can be thermally excited. Advanced Virgo will have test masses composed of fused silica, which is typical for optical components. The Qs for the internal modes are greater than 2×10^6. It is interesting to note that KAGRA, which will be operating at a temperature of 20 K, will be using test masses composed of sapphire [225, 226]. The mirror coatings will also be an important and limiting source of thermal noise for advanced Virgo and advanced LIGO [227, 228]. This is another reason that KAGRA will be cooling the test masses of their interferometer [226]. Note from Figure 2.9 [203] that in the extemely important band from 80 Hz to 400 Hz advanced Virgo will be limited by the coating thermal noise; this will also be true for advanced LIGO [39].

With the laser interferometric gravitation wave detectors the laser is of paramount importance. Advanced Virgo will commence with a medium-power laser that is a Nd:YVO4 oscillator ($\lambda = 1.06\,\mu$m) that amplifies a 20 W injection-locked laser; this will then provide a power of 60 W. As demonstrated above, the sensitivity of the detector improves with increase laser light power. However, the laser can also introduce other noise. The frequency noise of the laser can couple into the system to produce length displacement sensitivity noise in the interferometer. With Virgo arm-lengths of 3 km, it will be impossible to hold the length of the two arms absolutely equal. The slightly differing arm spans will mean that the light sent back from each of the two Fabry-Perot cavities will have slightly differing phases. As a consequence, great effort is made to stabilize the frequency of the light entering the interferometer.

For advanced Virgo a multi-stage control system will be used for the frequency stabilization. Different references will be used, which include a rigid Fabry-Perot cavity and even the differential arm-length of the interferometer itself. The advanced Virgo laser, in the absence of frequency stabilization, would have frequency noise in the kHz $\mathrm{Hz}^{-1/2}$ range. In order to meet sensitivity and detection goals advanced Virgo will need to stabilize the frequency noise to the μHz $\mathrm{Hz}^{-1/2}$ range [203]. The stabilization of the laser's power level is also critical to the low noise performance of an interferometric gravitational wave detector. To minimize the deleterious effects laser power fluctuations, interferometric gravitational wave detectors typically operate on the dark fringe, but the DC readout method [229, 230] used by advanced LIGO requires an offset from a purely dark fringe. The design plan for advanced Virgo is to have the relative intensity noise of the laser-power fluctuations in the range of $10^{-9}\,\mathrm{Hz}^{-1/2}$ [203].

The spatial quality of the light going to the advanced Virgo interferometer is cleaned with by a mode-cleaner cavity. The ultimate goal of advanced Virgo will be to provide 125 W of TEM_{00} light after the input mode cleaner. Advanced Virgo will use a triangular array of mirrors (all suspended); the triangular cavity will have a length of 143.424 m and a finesse of 1200. The entire input optics arrangement for advanced Virgo is quite complicated. A diagram showing all of the components is displayed in Figure 2.11.

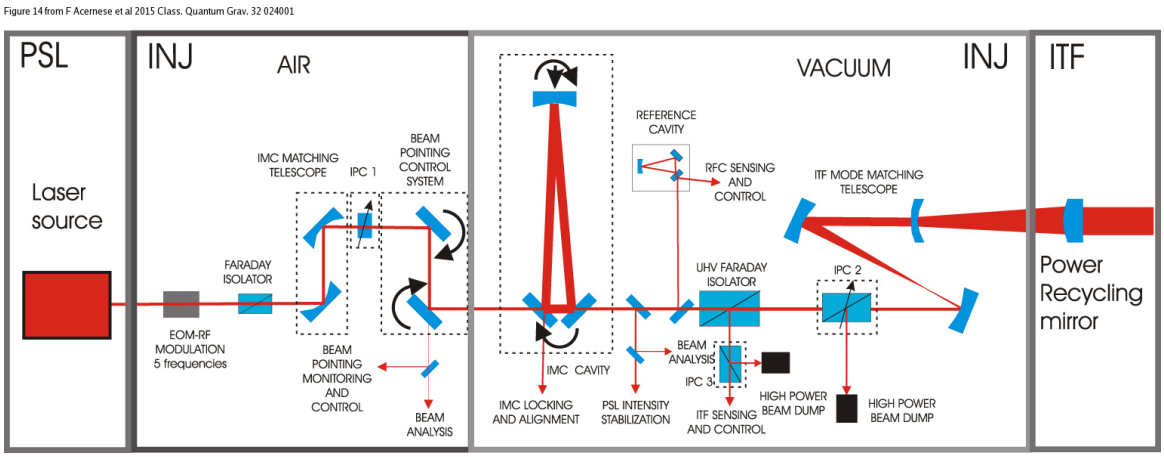

Figure 2.11: A display of the input optics layout for advanced Virgo [203].

Another important source of noise concerns the radiation reaction on the mirrors. Photons carry momentum, and when they reflect off of the suspended mirrors of Virgo or LIGO they impart momentum. When advanced Virgo sends

200 W into the interferometer, ultimately 650 kW of light power will be circulating within the Fabry-Perot cavities in each interferometer arm. This immense number of photons, coupled with the fact that the photon arrival times are random (Poisson statistics) means that radiation reaction noise will be important. This can be seen in the low frequency component of the quantum noise in Figure 2.9. The low frequency radiation reaction noise, plus the high frequency shot noise, combine to create the total quantum noise in the interferometer. While this quantum noise seems to be an unavoidable noise source, quantum states of light (namely *squeezed states of light*) can reduce this noise. This reduction of noise was demonstrated by LIGO after their S6 run [231] where squeezed light reduced the noise below the shot noise level for frequencies above 150 Hz; for higher frequencies a 2.15 dB (28%) reduction in the shot noise was observed [231]. The GEO-600 gravitational wave detector now uses squeezed light continuously, and has achieved an impressive 3.7 dB reduction in the shot noise level [183]. The use of quantum states of light is one of the ways that Virgo and LIGO hope to reduce their noise in the years to come.

2.4 Extending the network: multi-messenger astronomy

Many sources of gravitational waves are expected to be observable through other messengers, such as electromagnetic (EM) emission (from radio waves up to γ-rays) and neutrinos [34]. Many instruments are observing the sky at all wavelengths but photons are scattered, absorbed and delayed by the matter surrounding the astrophysical object while gravitational waves provide un-distorted information from the onset of the cataclysmic event. Gravitational wave emission usually happens first, and gravitational waves carry different information as gravitational waves are driven by the bulk motion of matter rather than the differential distribution of charges of the source.

Being able to observe different radiation from the progenitor of a GRB would solve a 40 year long enigma [232] on the exact nature of the GRB progenitor and the radiation mechanisms. GRBs are the brightest EM phenomena in the Universe and are likely associated to cataclysmic stellar events with a typical energy release of 10^{51} ergs. Long GRBs are related to the core collapse of massive stars [233, 234]. Short GRBs are thought to be generated when a BNS or a NS-BH merge forming a black hole and a dense accretion disk [235, 236]. The recent short GRB 130603B observations [237] bring additional support to this hypothesis through the kilo-nova model. A small fraction of short GRBs may come from Soft Gamma Repeater (SGR) giant flares [238]. In this case, only galactic SGRs would be observable by ground based interferometric detectors (even the second generation) as the maximum energy emitted by SGR giant flares in gravitational waves is $\sim 10^{46} - 10^{49}$ erg [239, 240].

GRBs, as well as micro-quasars [241] and magnetars [242, 243], have been proposed as high energy neutrino (HEN) emitters. The recent IceCube results seem to confirm the existence of extra-terrestrial HEN [244]. Besides, during supernova core collapse low energy neutrinos and gravitational waves are emitted deep inside the core and would provide insight in supernova mechanism, not accessible from EM waves which are emitted in optically thin regions far from the core. Moreover, the coincident detection of gravitational waves and low energy neutrinos in the absence of any EM counterpart would provide evidence for the existence of so called failed supernovae, which could occur at a rate comparable with that of visible supernovae [245].

For sources for which the gravitational wave signature is not fully predictable (for instance core collapse supernovae) the observation of other messengers predicted to be emitted during the same cataclysmic event will certainly add confidence to a potential gravitational wave observation. Because neutrinos, electromagnetic and gravitational wave detectors have uncorrelated backgrounds, electromagnetic or neutrino information can improve the gravitational wave search sensitivity as the search can be restricted to a small time interval and sky area [246, 247]. In the case of triggered GRB searches, the sensitivity is improved by a factor 2 [247]. However many interesting astrophysical objects may be missed because current telescopes observe only a small fraction of the sky at any time.

Although the sky coverage by a gravitational wave detector is not uniform, the worldwide gravitational wave detector network offers good sky coverage, and as soon as a gravitational wave transient event is detected, the sky position will be passed on to telescopes for investigations. Long and short GRB afterglow signals peak a few minutes after the prompt electromagnetic/gravitational wave emission. For core collapse supernovae, the afterglow peaks a few hours up to one day after the gravitational wave emission. Recent studies of the effect of high opacity in the kilo-novae light curves show a broad emission in the near infra-red peaking after a few days and lasting $\sim$ 1 week [248, 249]. The use of gravitational wave event alerts is complementary to the triggered gravitational wave search and requires a localization of the source in quasi real time with a good accuracy, which is still challenging for the LIGO-Virgo network.

2.5 Selected results

The first generation of ground-based interferometric gravitational wave detectors, LIGO, GEO and Virgo, have operated over a decade and taken data at their design sensitivities for a few years. The data has been examined for the presence of gravitational wave signals. Presented here is a brief summary of the most significant results. The network of detectors is currently being upgraded and extended. Advanced LIGO with its two upgraded detectors already took $\sim$ 4 months of data in 2015 that lead to the discovery of the first stellar-mass black hole merger events.

2.5.1 Gravitational wave transient search results

The signals from the targeted gravitational wave signal sources are either well described (compact binary systems, cosmic strings, black hole and neutron star desexcitation) or poorly known (core collapse supernovae, fallback accretion on neutron stars) [34]. Search techniques are adapted to each case (matched filtering or excess power) but here we are interested in signals that are visible during a rather short time interval (between few milliseconds up to few hundred of seconds). Until September 2015, as no gravitational wave transient signal had been discovered in LIGO, GEO nor Virgo data, we were just reporting upper limits on the rate of gravitational wave events or on the amount of energy released that could be compared to the rather uncertain astrophysical predictions. For core collapse supernovae (type II and Ib/c) observations yield a very approximative rate of 3 events per century per galaxy [250]. Compact binary system coalescence rates span 1 or 2 orders of magnitude uncertainty in each direction from the most likely value. These rates are based on observations of binary neutron stars in our galaxy or on simulations (population synthesis) of systems involving stellar-mass black holes [251] whose existence, with companion masses lower than $15M_{\odot}$, was mainly infered from X-ray binary system observations [252]. The observation of the rather high mass binary black hole merger GW150914 in September 2015 in advanced LIGO data has not only demonstrated that gravitational waves do exist but stellar-mass black holes exist and binary black hole system can merge within the Hubble time. In the following we briefly summarize the state of the art of GW transient searches in LIGO/Virgo/GEO data.

2.5.1.1 all-time/all-sky searches

The search for compact binary systems with LIGO-GEO-Virgo data covered a total mass range between 2 $M_{\odot}$ and 450 $M_{\odot}$ [34]. Because within this range, the different phases (inspiral, merger and ring-down) have very different contribution to the SNR and the waveforms have specific complexity, the template bank of waveforms used in the matched filtering searches are different according to the mass ranges. The waveform depends on the chirp mass of the binary $\mathcal{M}_c = \frac{(m_1 m_2)^{3/5}}{(m_1+m_2)^{1/5}}$, the symmetric mass ratio $\eta = \frac{m_1 m_2}{(m_1+m_2)^2}$ and the angular momentum of the compact objects $S_{1,2}$ that enters in the definition of the dimensionless spin parameter $\chi_{1,2} = \frac{cS_i}{Gm_{1,2}^2}$. The effect of spin on the waveform depends also on the ratio between the component objects masses. Parameters which affect the overall amplitude and phase of the signal as observed in the detector are maximized over in the matched-filter search, but can be more precisely recovered through full parameter estimation analysis [253, 254]. The search's parameter space is therefore defined by the limits placed on the compact objects masses and spins[15]. The minimum black hole mass is taken to 1 $M_{\odot}$ consistent with the smallest known masses of neutron stars [255]. There is no known maximum black hole mass, however beyond a total mass of $\sim$ 100 $M_{\odot}$, the merger and ringdown phases dominate the SNR because of the detector low frequency cut off, the search is thus split into two mass ranges:

- Total mass smaller than 100 $M_{\odot}$: To model black hole binary systems with total mass larger than 4 $M_{\odot}$, the effective-one-body (EOB) formalism [256, 257] is considered. It combines results from the Post-Newtonian approach [38, 51] with results from black hole perturbation theory and numerical relativity [CITE] to model the complete inspiral, merger and ringdown waveform. The search has recently introduced waveform models that assume the spins of the merging objects are aligned with the orbital angular momentum. Observations of X-ray binary systems indicate that astrophysical black holes may have near extremal spins [42]. For binary components with masses larger than 2 $M_{\odot}$, the spin magnitude of the search is limited to less than 0.9895. For lighter object the spin magnitude is limited to 0.05.

[15] Over the years the template bank has grown in complexity. The most recent feature is the inclusion of the angular momentum parameter (spin) in the waveforms.

- Total mass between 100 $M_\odot$ and 450 $M_\odot$: For binary systems of higher mass, only the merger and ring-down phases will be observable in the detectors' frequency band. That is the reason why with early LIGO data of 2004, a ring-down search has been carried out yielding an event rate upper limit of 3.2×10^{-5} Mpc^{-3} yr^{-1} for binary total mass between 100 and 400 $M_\odot$ [258]. With the most recent data (2005 – 2007), a search for intermediate mass black hole systems in the total mass range 100 and 450 $M_\odot$ and with mass ratio up to 1:4 has been performed. This search does not rely on a specific waveform model but coherently combines the data from the different detectors and looks for excess power in a time-frequency representation [101]. The largest effective range, 241 Mpc, is achieved for an $88 + 88$ $M_\odot$ system and in this masses range the rate upper limit is 1.3×10^{-7} Mpc^{-3} yr^{-1}. The upper limit on the event rate, averaged over all considered masses, is 9×10^{-7} Mpc^{-3} yr^{-1} which is just an order of magnitude higher than the most constraining rate upper limit. As globular clusters (GC) are the most likely hosts of intermediate mass black holes, the event rate can be converted into a limit on the astrophysical source density: 3×10^{-6} GC^{-1} yr^{-1}. This is still 3 orders of magnitudes higher than the astrophysical predictions [251], which is anyway rather uncertain as the formation of intermediate mass black holes is still under debate.

For un-modelled and much shorter (<1s) gravitational wave signals, several robust algorithms have been developed over the years [207, 259, 260, 261]. These algorithms have also demonstrated their ability to detect stellar-mass black hole binary systems (see section 2.5.1.2). For generic un-modelled short transient signals, a coherent multi-purpose multi-purpose transient signal search (coherent WaveBurst) has been carried out. This search showed that for a source at 10 kpc emitting around 150 Hz, a 50% efficiency detection can be reached if the source emits at least 2.2×10^{-8} $M_\odot c^2$ of gravitational radiation [262]. Upper limits on the rate of different types (ad-hoc waveforms) of events in the frequency range between 64 Hz to 5 kHz, as a function of signal amplitude at the Earth were derived. For signals strong enough (root-sum-square strain amplitude $h_{rss} \sim$ several 10^{-20} $\frac{\mathrm{strain}}{\sqrt{\mathrm{Hz}}}$) the rate upper limits all tend toward 1.4 events per year. The results can be recast as limits on the rate density of gravitational wave bursts assuming a source of gravitational wave energy isotropically distributed[16]. For instance for sources emitting 10^{-2} $M_\odot c^2$ around 150 Hz, the rate is bound to 6×10^{-3} Mpc^{-3} yr^{-1}.

Finally, a dedicated search for gravitational waves from cosmic super-string cusps has been performed in LIGO-Virgo data. It has not revealed any gravitational wave signal and upper limits on the event rate have been set and used to exclude portions of the cosmic strings parameter space (string tension, loop size and reconnection probability) as shown in Figure 2.12. This direct search yields the best exclusion limits in the small loop regime (10^{-4} – 10^{-8}) [263].

2.5.1.2 Discovery of the first binary black hole mergers

At the very beginning of the O1 run, on September 14 2015, GW150914, a rather strong transient signal (SNR$\sim$ 23) corresponding to the last instants of the coalescence of two black holes has been observed in advanced LIGO Hanford and Livingston data [40]. It has been observed with the un-modelled search pipeline coherent WaveBurst [259] less than 3 minutes after the data was acquired and then confirmed by the dedicated matched-filter searches (PyCBC [264] and GstLAL [265]) and another un-modelled search pipeline oLIB [261]. The false alarm probability is estimated to be less than 1 event in 1.7×10^6 years, corresponding to a significance greater than $5.3\,\sigma$. GW150914 is a near-equal mass black hole binary system whose source frame masses are 36^{+5}_{-4} $M_\odot$ and 29^{+4}_{-4} $M_\odot$ at 90% credible level [266]. The final black hole mass is 62^{+4}_{-4} $M_\odot$ meaning that $3^{+0.5}_{-0.5} M_\odot c^2$ was emitted in gravitational waves during the merger. The luminosity distance of the source is 420^{+150}_{-180} Mpc, corresponding to a redshift of ~ 0.09. On October 12, 2015, LVT121012 a second, less significant ($1.9\,\sigma$) but likely binary black hole event has been recorded[17]. The component masses are less precisely estimated, 23^{+18}_{-6} $M_\odot$ and 13^{+4}_{-5} $M_\odot$, as the luminosity distance is estimated at 1000^{+500}_{-500} Mpc. On December 26, 2015 another highly significant gravitational wave event GW151226 was observed with a SNR of 13 and a false alarm rate of less than 1 event in 1.7×10^6 years (more than 5.3 σ). The components masses are lower (14^{+8}_{-4} $M_\odot$ and 8^{+2}_{-3} $M_\odot$). The final black hole is found to be 21^{+6}_{-2} $M_\odot$ in mass and the luminosity distance 440^{+180}_{-190} Mpc.

The distribution of the BBH event candidates' SNR obtained by one of the matched-filtering search (PyCBC) is shown in Figure 2.13. All event source parameters are estimated using Bayesian inference methods assuming an

[16] This is a rough estimate when the distances are within our local universe.

[17] Because the event candidate significance is low, it has not been renamed GW151012

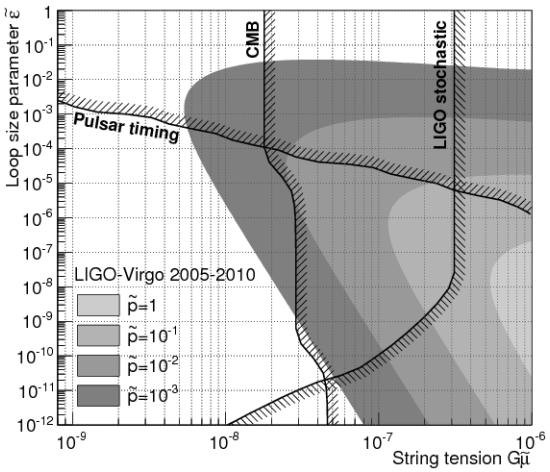

Figure 2.12: Constraints on the modified cosmic string parameters $G\tilde{\mu}$, $\tilde{\epsilon}$ and $\tilde{p}$. The grey regions, corresponding to 4 reconnection probability values, are excluded at 90% confidence level. Other constraints derived from a contribution of cosmic strings to the gravitational wave stochastic background for $\tilde{p} = 10^{-3}$ are shown. $G\tilde{\mu}$, $\tilde{\epsilon}$ and $\tilde{p}$ are redefined cosmic string parameters absorbing unknown parameters that are sometimes arbitrarily set to 1 [263].

astrophyiscal origin [266]. Many parameters are correlated and thus weakly constrained. For instance the luminosity distance and orbital plane inclination angle. The main properties of the three BBH events are given in Table 2.1.

The posterior probabilities of the component masses for the 3 events is given in Figure 2.14. The binary component masses of all three systems lie within the range expected for stellar-mass balck holes. The least massive BH is the secondary of GW151226, which has a 90% credible lower bound that $m_2 \geq 5\,\mathrm{M}_\odot$. This is above the expected maximum neutron star mass of $\sim 3\,\mathrm{M}_\odot$ [268]. The range of inferred component masses overlaps with those for stellar-mass BH measured through X-ray observations, but extends beyond the $\sim 16\,\mathrm{M}_\odot$ maximum of that population [269, 270].

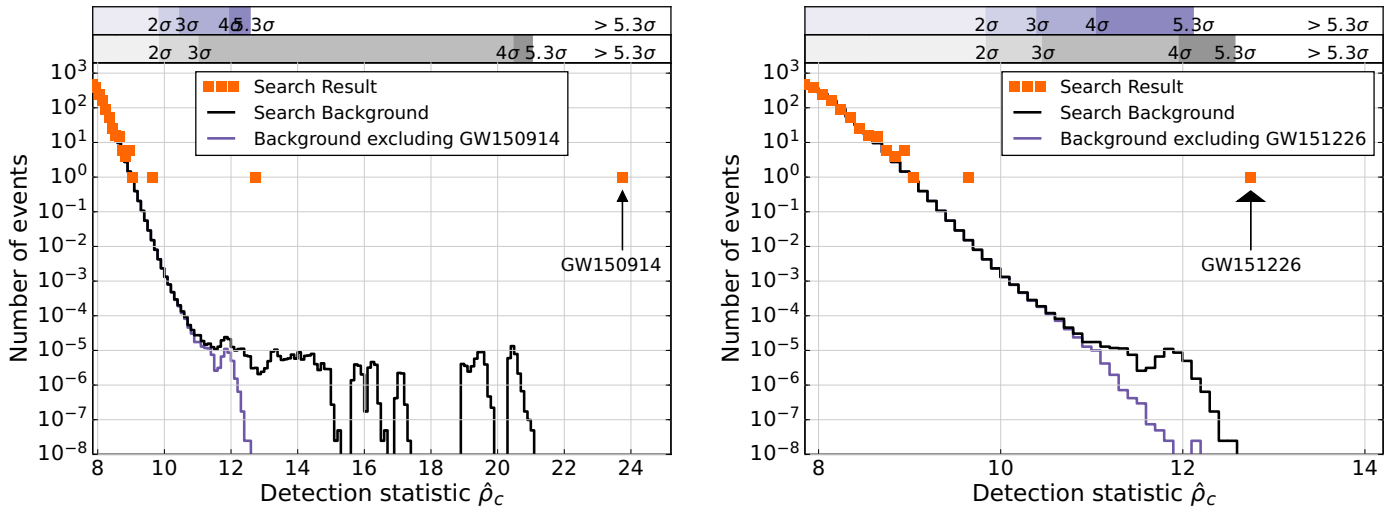

Figure 2.13: Search results from one of the matched filtering search (PyCBC [264]). The first plot shows the result with the full background. GW150914 is more significant than any background event in the data. When this contribution from GW150914 is removed, GW151226 is more significant than the remaining background, with a significance of $5.3\,\sigma$. LVT151012 is identified with a significance of $1.9\,\sigma$, and this is relatively unaffected by the removal of the background from the two most significant events [267].

Because of the masses' smaller values, the signal from GW151226 persists in the LIGO frequency band for approximately 5 seconds, increasing in frequency and amplitude over 150 cycles from 20 to 600 Hz. In comparison, only ~ 8 cycles have been observed between 35 and 150 Hz for GW150914. This allows GW151226 to show stronger evidence for a positive value of the effective spin than GW150914. In other words, there is good evidence that at least one component of GW151226 has a positive spin magnitude. The spin magnitude of the primary black hole is constrained to be less than 0.8 with 90% probability. There are two main effects that the BH spins $\mathbf{S_1}$ and $\mathbf{S_2}$ have on the phase and amplitude evolution of the GW signal. The spin projections along the direction of the orbital angular momentum $\mathbf{L}$ affect the inspiral rate of the binary. In particular, spin components aligned (anti-aligned) with $\mathbf{L}$ increase (decrease) the number of orbits from any given separation to merger with respect to the non-spinning case. Given the limited SNR of the observed signal, it is difficult to untangle the full degrees of freedom of the individual BHs spins. However, the dominant spin effect is well encoded in the projection of the components' spins onto the orbital angular momentum

$$\chi_{eff} = \frac{c}{G}\left(\frac{\mathbf{S_1}}{m_1} + \frac{\mathbf{S_2}}{m_2}\right).\frac{\mathbf{L}}{M}, \tag{2.50}$$

which takes values between -1 (both BHs have maximal spins anti-aligned with respect to the orbital angular momentum) and +1 (maximal aligned spins). The remaining in-plane spin components χ_p[18] lead to precession of the spins and the orbital plane, which in turn introduces modulations in the strain amplitude and phase as measured at the detectors. $\chi_p = 0$ corresponds to an aligned-spin (non-precessing) system, and $\chi_p = 1$ to a binary with the maximum level of precession. Waveforms including double precessing and double non-precessing spins have been considered. Results are reported in Figures 2.15 and 2.16 for GW150914 and GW151226. Not much can be said about the alignment of the spins, but we can rule out that both objects have large aligned spins.

Sky localization from a GW detector network is primarily determined by the measured delay in the signal arriving at the sites, with additional information coming from the signal amplitude and phase. For a two-detector network, the sky localization forms a characteristic broken annulus. Adding additional detectors to the network would improve localization abilities [271]. The 90% credible region for sky localization is $220\,\mathrm{deg}^2$ for GW150914, $860\,\mathrm{deg}^2$ for GW151226, and $1580\,\mathrm{deg}^2$ for LVT151012. As expected, the sky area is larger for quieter events. The sky area scales inversely with the square of the SNR.

[18]The leading order in the PN expansion expression is given in [267].

Event	Time (UTC)	FAR (yr^{-1})	FAP	$\mathcal{M}$ ($\mathrm{M}_\odot$)	m_1 ($\mathrm{M}_\odot$)	m_2 ($\mathrm{M}_\odot$)	χ_{eff}	D_{L} (Mpc)
GW150914	14 September 2015 09:50:45	$< 5.8 \times 10^{-7}$	7×10^{-8} ($> 5.3\,\sigma$)	28^{+2}_{-2}	36^{+5}_{-4}	29^{+4}_{-4}	$-0.06^{+0.14}_{0.14}$	420^{+150}_{-180}
GW151226	26 December 2015 03:38:53	$> 6.0 \times 10^{-7}$	7.5×10^{-8} ($> 5.3\,\sigma$)	$8.9^{+0.3}_{-0.3}$	$14.3^{+8.2}_{-3.7}$	$7.5^{+2.3}_{-2.3}$	$0.21^{+0.2}_{0.1}$	440^{+180}_{-190}
LVT151012	12 October 2015 09:54:43	0.44	0.05 ($1.9\,\sigma$)	15^{+1}_{-1}	23^{+18}_{-6}	13^{+4}_{-5}	$0.0^{+0.3}_{0.2}$	1000^{+500}_{-500}

Table 2.1: Parameters of the three most significant events in O1 (two detections and a probable one). The false alarm rate (FAR) and false alarm probability (FAP) given here were determined by the PyCBC pipeline. The values for the second and third events are calculated after the more significant events are removed from the background. The source-frame chirp mass $\mathcal{M}$, component masses $m_{1,2}$, effective spin χ_{eff}, and luminosity distance D_{L} are determined using a parameter estimation method that assumes the presence of a coherent compact binary coalescence signal starting at 20 Hz in the data. Quoted uncertainties include both the 90% credible interval and an estimate for the 90% range of systematic error determined from the variance between waveform models [267].

GW150914 is genuinely the first astrophysical object where strong-field dynamics of gravitation are at play. With the peak of the waveform occurring at a frequency of ~ 150 Hz, the part of the coalescence just before merger, as well as the merger-ringdown regime, could be studied in considerable detail, as described in [272]. This allowed for checks of the consistency between masses and spins during inspiral and ringdown, as well as parameterized tests of the waveform as a whole. Even though not much of the early inspiral was in the detectors' sensitive band, interesting bounds could be placed on departures from general relativity in the post-Newtonian coefficients up to 3.5PN. Since the source of GW151226 merged at ~ 450 Hz, it provides the opportunity to probe the post-Newtonian inspiral with many more waveform cycles, albeit at relatively low SNR. Especially in this regime, it allows for further tightening of the bounds on violations of general relativity.

For GW150914, the post-Newtonian coefficients showed moderately significant ($2\ -2.5\,\sigma$) deviations from their GR values of zero [272]. By contrast, the posteriors of GW151226 tend to be centered on the GR value. As a result, less offset is present in the combined posteriors. The merger-ringdown parameters have also been tested. For GW150914, this regime corresponded to frequencies of $f \in [130, 300]$ Hz, while for GW151226 it occurred at $f \gtrsim 400$ Hz. As expected, the posteriors from GW151226 are not very informative for these parameters, and the combined posteriors are essentially determined by those of GW150914. In summary, GW151226 makes its most important contribution to the joint posteriors in the post-Newtonian inspiral regime, where both offsets and statistical uncertainties have significantly decreased, in some cases to the $\sim 10\%$ level. A inspiral-merger consistency test is not meaningful for GW151226 since very little of the signal is observed in the post-merger phase. Likewise the SNR of GW151226 is too low for a useful residual subtraction test to be performed.

Finally, considering GW150914, one could constrain the rate of binary black hole coalescences in the local Universe. Assuming naively that all BBHs in the universe have the same masses and spins as this event, and assuming that the BBH merger rate is constant in the comoving frame, a 90% credible range of $2\ -\ 53\,\mathrm{Gpc}^{-3}\mathrm{yr}^{-1}$ has been derived. Incorporating all 3 triggers that pass the search threshold, accounting for the uncertainty in the astrophysical origin of each trigger, and considering different component mass distributions, a more realistic estimate is: $8\ -\ 250\,\mathrm{Gpc}^{-3}\mathrm{yr}^{-1}$.

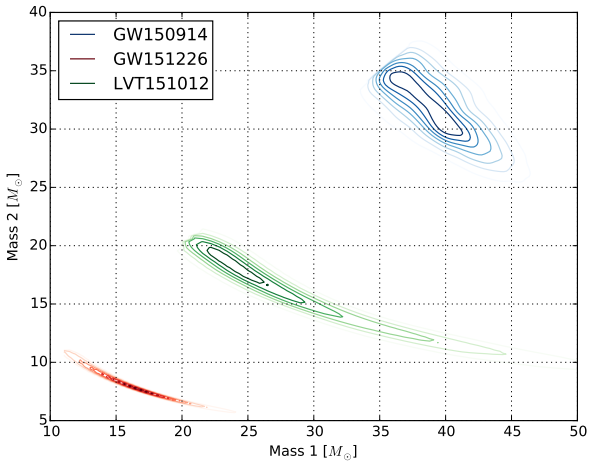

Figure 2.14: Posterior probability densities of the source-frame component masses m_1 and m_2 for the three events GW150914, GW151226 and LVT151012. We use the convention that $m_1 \geq m_2$, which produces the sharp cut in the two-dimensional distribution. For GW151226 and LVT151012 the curving degeneracy traces lines of constant chirp mass ($\mathcal{M} = 8.9^{+0.3}_{-0.3}\,\mathrm{M}_\odot$ and $\mathcal{M} = 15^{+1}_{-1}\,\mathrm{M}_\odot$ respectively) [267].

2.5.1.3 Triggered searches

Short GRBs are thought to be associated with the coalescence of NS-NS or NS-BH systems [34]. Long GRBs have been associated with massive star core collapse [273]. Although in both cases gravitational wave emission is expected, GRB red shift measurements show that the majority of GRB progenitors are at cosmological distances, well beyond the reach of LIGO-GEO-Virgo detectors. However a few GRBs have been measured at much closer distances: The closest is GRB 980425 associated to SN 1988bw at 36 Mpc [274] and the lowest firm redshift short GRB 080905A has been associated to an host galaxy at z$\sim$0.12 [275]. This and the existence of a class of sub-luminous long GRBs indicate that there is chance that a gravitational wave signal may be detectable in association with a GRB trigger. That is the reason why all recorded GRBs since 2003 (when at least two detectors are taking data [19]) have been examined for the presence of gravitational waves. Both binary inspirals and unmodelled gravitational wave transient types of searches are considered [276, 277, 278, 279, 280, 281]. Most of the GRB records are provided by the Swift and Fermi satellites [278] but GRBs from the InterPlanetary Network seen in 2005 – 2010 have also been considered [276]. No associated gravitational wave signals have been found. The Swift and Fermi GRB search excludes the existence of progenitors within a certain distance from Earth, which is different for every GRB, assuming an emission of $10^{-2}\,\mathrm{M}_\odot\mathrm{c}^2$ at 150 Hz in gravitational waves. The median exclusion distance for this set of GRBs is 17 Mpc. From the null results of the binary coalescence signal searches the corresponding median exclusion distance values are 16 Mpc and 28 Mpc for NS-NS and NS-BH systems respectively. If one assumes that all GRB progenitors emit the same amount of gravitational waves, the set of GRBs can also be considered as a whole. Constraints on the cumulative number of GRBs (including also IPN GRBs) as function of the red shift are shown in Figure 2.17 where a constant co-moving density rate of GRBs up to a cosmological distance beyond which all GRBs are at infinity is assumed. Extrapolations at the foreseen advanced gravitational wave detectors' sensitivities reach red shift values in the range of current short GRBs observations. For long GRBs, one needs to assume a rather optimistic gravitational wave emission ($10^{-2}\,\mathrm{M}_\odot\mathrm{c}^2$) in order to reach observed red shifts.

It is also interesting to underline that gravitational wave observations are able to exclude certain galaxy associations for two short GRBs, GRB 051103 [282] and GRB 070201 [283] (under the hypothesis that these GRBs were due to BNS mergers). The position obtained by the interplanetary network of satellites for GRB 051103 had a $3-\sigma$ error region overlapping with the outer disk of the M81 galaxy (3.63 Mpc). GRB 070201's position was 1.1 degree away from the center of Andromeda-M31 (770 kpc). A gravitational wave binary coalescence signal from either M81 or M31 would have been well within the sensitivity reach of the LIGO detectors. The absence of a gravitational wave

[19] this represents $\sim$ 350 GRBs

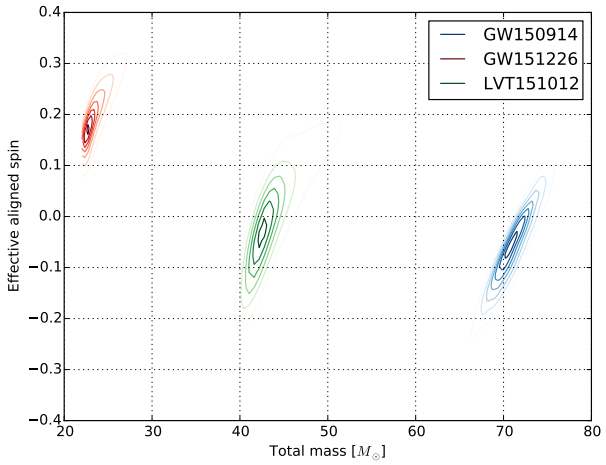

Figure 2.15: The effective spin of the inspiralling components of the three events GW150914, GW151226 and LVT151012 against their total mass [267].

detection excludes, with high confidence, the association between the GRBs and a BNS merger in their apparent host galaxies. However it is not possible to exclude SGR giant flares in the apparent host galaxies as the progenitors of these observed short GRBs ($\sim 15\%$ of the short GRBs are assumed to be SGRs [238]).

Times around the X-ray emission episodes of 6 galactic SGRs and anomalous X-ray pulsars [127] have been considered for un-modelled gravitational wave searches. The amount of gravitational wave energy and the mechanism of emission are still poorly understood. However, some theoretical models predict a gravitational wave energy emission as large as $10^{48} - 10^{49}$ ergs [240]. Among all magnetars that have emitted X-rays when LIGO, Virgo and GEO were taking data, SGR 1806−20 discovered in 2004 [284] was the most energetic transient observed in our galaxy ($\sim 4 \times 10^{46}$ ergs). No specific waveforms were assumed in the search, and 90% upper limits on the amount of gravitational wave energy emitted by the 6 magnetars have been set considering white noise bursts with frequencies ~ 100 Hz as representative of gravitational wave signals from low frequency oscillation modes and considering damped sinusoids with frequencies > 1 kHz as representative of gravitational wave signals from f-modes. The most constraining upper limit has been obtained for SGR 0501−4516 (1 kpc): it ranges from 3×10^{44} ergs to 1×10^{47} ergs for un-modelled low frequency gravitational wave emission and for f-mode damped sinusoid waveforms with 1090 Hz central frequency, respectively [285, 286]. It is interesting to note that values around 10^{45} ergs are comparable to the EM energy of giant flares[20]. Furthermore, the f-mode limit of 1×10^{47} ergs is in the range predicted by [240].

The Vela pulsar is one of the pulsars, within the LIGO-GEO-Virgo frequency bandwidth, with the least stable spin phase evolution. A sudden increase of its the rotation velocity is observed a few times a year. This could be due to star-quakes that adjust the crust of the neutron star or rearrangement of the interior material, and are expected to excite normal mode oscillations that may emit gravitational waves. On August 12^{th} 2006 a glitch amounting to a relative increase of the rotational frequency of 2.6×10^{-6} was measured. This glitch happened when the two co-located LIGO detectors at Hanford were taking data. A search was performed for ring-down gravitational wave waveforms from the quadrupolar (spherical harmonic order $\ell = 2$) f-mode oscillations with frequencies between 1 and 3 kHz and damping times between 50 and 500 ms. No gravitational wave signal was observed and a 90% confidence level upper limit on the peak strain amplitude of ring-down signals has been set between 6.3×10^{-21} and 1.4×10^{-20}, depending on which of the $2\ell + 1$ harmonics is excited. This peak strain value corresponds to a gravitational wave energy range of 5×10^{44} ergs to 1.3×10^{45} ergs [287].

Finally, let us mention gravitational wave searches triggered by high energy neutrino (HEN) observations. HENs may be emitted by various phenomena in association with gravitational waves (for instance GRBs and SGRs). Although these scenarios also involve EM emission that is already used as trigger for targeted gravitational wave searches, it is not excluded that there might be joint gravitational wave-HEN emission without a visible EM counterpart (for

[20]It is however unknown whether electromagnetic and gravitational wave energies are correlated.

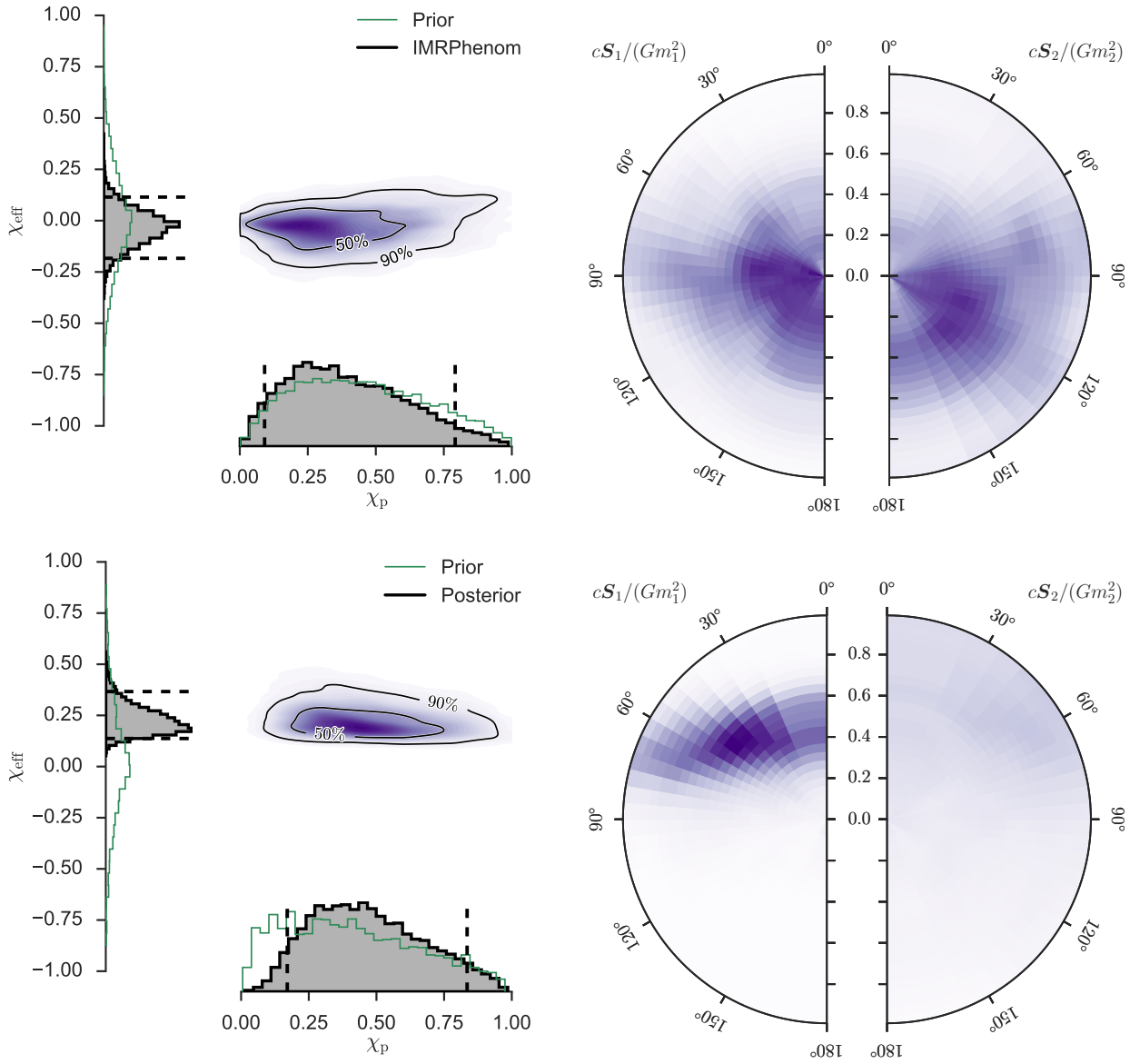

Figure 2.16: Right: The effective spin of the inspiralling components of GW150914 (top) and GW151226 (bottom) against the in-plane spin projection. Righht: Posterior density functions for the dimensionless spins $\chi_{1,2}$ relative to the normal to the orbital plane **L [266].**

example associated with choked GRBs). The first gravitational wave search triggered by HEN candidates was carried out using HEN triggers from the Antares experiment on S5/VSR1 gravitational wave data [288]. More recently IceCube triggers have been considered in coincidence with LIGO-Virgo data recorded between 2005 and 2010 [289]. A specific search for GW150914 BBH merger event has been carried out with IceCube-ANTARES triggers [290]. The astrophysical significance of all these null results is limited, however this is the first ever gravitational wave-HEN search and it paves on the way for searches in the advanced gravitational wave detector era.

2.5.1.4 Low latency searches

Two prototype low latency gravitational wave transient searches have been carried out for a few months before the initial LIGO shutdown [34]. The goal was to test pipelines, and the sending of alerts to a set of partners with a latency lower than 1 hour. Partners included Swift, optical telescopes (TAROT, ROTSE III, QUEST, the Palomar Transient Factory, Pi of the Sky, the TAROT/Zadko Telescope, SkyMapper and the Liverpool Telescope[21]) and a radio array (LOFAR [292]). 14 gravitational wave triggers with source sky localization were sent out and 9 of them were followed up [219, 220]. Note that none of the gravitational wave triggers showed evidence to be a genuine astrophysical event as the false alarm rate threshold was rather high (.25 per day). For 8 gravitational wave triggers, optical telescope images were analyzed. No optical transients were identified with a convincing association with any of these candidates [291].

The O1 run has been the first opportunity for the LIGO-Virgo collaboration to realize a scientifically sounded electromagnetic follow-up of the first candidate events whose astrophysical original was highly likely. The events' properties (significance, time and sky maps) were shared with 63 teams of observers covering radio, optical, near-infrared, X-ray, and gamma-ray wavelengths with ground- and space-based facilities[22]. The follow-up observations have been carried out by 25 teams via private Gamma-ray Coordinates Network Circulars [47]. As these events turned out to be binary black hole mergers, there was little expectation of a detectable electromagnetic signature. Among all reported results, only the Fermi-GBM team reported a rather faint transient source signal above 50 keV, 0.4 s after the GW event was detected, with a false alarm probability of 0.0022. This weak transient lasting 1 s does not appear to be connected with other previously known astrophysical, solar, terrestrial, or magnetospheric activity [293].

2.5.2 Continuous wave searches

Isolated asymmetric neutron stars are expected to emit quasi-monochromatic gravitational waves with a slowly decreasing frequency (spin-down) [34]. Because the wave is observed over long time intervals, modulations have to be considered (Doppler frequency modulation generated by the relative motion between the source and the detector location on Earth and amplitude modulation due to the non-uniform sensitivity of the detector across the sky).

If all parameters are known (frequency, frequency derivatives and source sky position) all demodulation effects can be removed and the gravitational wave signal is simply a sinusoidal that can be easily integrated over time to amplify the SNR[23]. The expected gravitational wave amplitude of all known pulsars is weak and the chance of detection is actually very small when one compares the searches' strain sensitivity to the spin-down limit. The spin-down limit is the strain amplitude calculated as if all observed rotational kinetic energy loss were due to gravitational waves. For most neutron stars falling in the LIGO-Virgo frequency bandwidth and whose frequency evolution is known, the spin-down limit is well below what searches are sensitive to. The Vela and the Crab pulsars are the two most notable exceptions.

Actually the most interesting searches for continuous gravitational waves aim at discovering new systems that are spinning at the right frequency for ground based gravitational wave detectors and are bumpy enough and close enough to be detected. The main challenge is the size of the parameter space to be spanned: position, frequency and spin-down terms, if the system is isolated, and also orbital parameters for systems in binaries. The search becomes computationally prohibitive when one tries to add coherently the data over longer and longer time intervals. Instead, at the price of a small sub-optimality, hierarchical methods are used for the search of all-sky/all-time continuous gravitational waves.

In the absence of gravitational wave candidate, upper limits on the intrinsic gravitational wave strain amplitude h_0 are derived. If the emission is due to non axisymmetric deformations then [294]

$$h_0 = \frac{16\pi^2 G}{c^4}\frac{\epsilon I f^2}{r} \tag{2.51}$$

where I is the moment of inertia, ϵ the ellipticity, f the gravitational wave frequency and r the distance of the source. If one knows the distance to the putative source, as in the case of searches that target known objects, upper limits on h_0 may be recast as upper limits on the ellipticity at a fixed nominal value of I (typically chosen as $10^{38}\, kg\, m^2$).

[21] See [291] for references.

[22] Four alerts were actually sent to partners. GW150914, LVT151012 and GW151226 were among these alerts and another trigger that turned out to be of noise origin.

[23] The real situation is a bit more complicated because of unknown other parameters (polarization angle, inclination angle, phase) that can be maximized over.

- Targeted searches (known position and frequency):

  The ephemerides of many pulsars are regularly updated thanks to optical, X-ray and γ-ray pulsar observations. They are used in known pulsar gravitational wave searches to determine the putative signals' Doppler and amplitude modulations [294, 295, 296, 297]. Since the first continuous gravitational wave search carried out in 2002 LIGO data targeting one pulsar (J1939+2134 [298]), a total of 195 known pulsars have been studied and thanks to sensitivity improvements and longer data sets, upper limits have improved over time [299, 300, 301, 302, 303]. With the most recent LIGO and Virgo data the lowest strain amplitude upper limit is 2.2×10^{-26} achieved for PSR J1804−2717 and the lowest limit on the ellipticity is 6.7×10^{-8} for PSR J2124−3358. For seven young pulsars the spin-down limit is approached within a factor 5. The h_0 upper limit values from gravitational wave observations are more constraining than the spin-down limits for two young pulsars: the Crab pulsar (f_{rot}=29.78 Hz) and the Vela pulsar (f_{rot}=11.2 Hz). For the Crab the 95% confidence upper limit on the strain amplitude is 2.0×10^{-25}, yielding a 2% upper limit value on the fractional rotational energy loss through gravitational wave emission [304, 301]. For Vela the strain amplitude limit is 1.1×10^{-24}, bounding to less than 33% the amount of rotational energy [302] lost in gravitational waves. Although the non-detection is not unexpected since the ellipticity values corresponding to the spin down limits are rather high (a few 10^{-5} and 10^{-4} for the Crab and Vela pulsars respectively), the constraints on the fraction of energy loss in gravitational waves are informative measurements that could not be obtained by other means. A narrow band search around Crab and Vela frequencies with VSR4 Virgo data have beaten as well the spin-down limit for these two pulsars [303] All results are represented in Figure 2.18.

- Directed searches (known position but unknown frequency):
  Most of the neutron stars are not observed as pulsars, but some location in the sky shows strong evidence for the presence of a non-pulsing neutron star which may be a strong gravitational wave emitter. This is for instance the case of the supernova remnant Cassiopeia A ($\sim$ 3.4 kpc) which is suspected to host a compact central object born less than 400 years ago. Under the assumption that its spin frequency evolution has been largely governed by gravitational wave emission, an indirect limit h_0^{age} on the gravitational wave strain amplitude which only depends on the age of the object can be compared to the search results. LIGO 2005 – 2007 data have been searched over a 200 Hz wide frequency band and 95% confidence upper limits on the strain amplitude beat the h_0^{age} indirect limit (7×10^{-25} at 150 Hz). Limits on neutron star ellipticity (4×10^{-4} at 100 Hz), and r-mode amplitude (5×10^{-3} at 300 Hz) were also derived [305]. A more recent search (using 2009 – 2010 enhanced LIGO data) targetting nine young supernova remnants including Cassiopeia A, has improved the upper limits by almost a factor 2[306]. These limits beat the indirect limits from energy conservation but are within the theoritical predictions for the ellipticities and the r-mode amplitudes.

  The low mass X-ray binary Sco X-1 (2.8 kpc), the brightest X-ray source in the Galaxy, is also an interesting potential gravitational wave emitter as the detection of continuous gravitational waves from this system would allow testing of the torque balance mechanism of accreting neutron stars. However, the rotation frequency of Sco X-1 is unknown making the search over frequency, spin-down and orbital parameters computationally very challenging. Because of this, a simplified search (20 Hz wide frequency band using only few hours of the most sensitive LIGO 2003 data) has been performed. The upper limit on the strain amplitude is few orders of magnitude higher than the torque balance prediction, which is $\sim 3 \times 10^{-26}$ for a source emitting gravitational waves at 540 Hz [307]. Ten days of LIGO 2005 – 2007 data have been analyzed over a larger frequency bandwidth (50 – 550 Hz)[24]. Upper limits have been improved by up to a factor 2.3 reaching 8×10^{-25} at 150 Hz (assuming a binary orientation prior as given by the electromagnetic information) [310].

  The Sagittarius A* radio source cluster at the Galactic center is expected to host $\sim$ 100 radio pulsars within 0.02 pc distance. A dedicated search for continuous gravitational waves sensitive to sources within few pc around Sagittarius A* has been performed with LIGO 2005-2007 data. No candidates have been found for frequency from 78 to 496 Hz. The 90% confidence upper limits on the gravitational wave strain amplitude of sources at the Galactic center are 3.35×10^{-25} for frequencies near 150 Hz [302]. Similarly, the Orion spur region has been

[24] New and improved Sco X-1 limits from a cross-correlation search and from a stochastic directional search in O1 data are now available in [308, 309]

searched for continuous waves sources in the 2009 – 2010 LIGO data. No candidates have been reported and upper limits are derived [311].

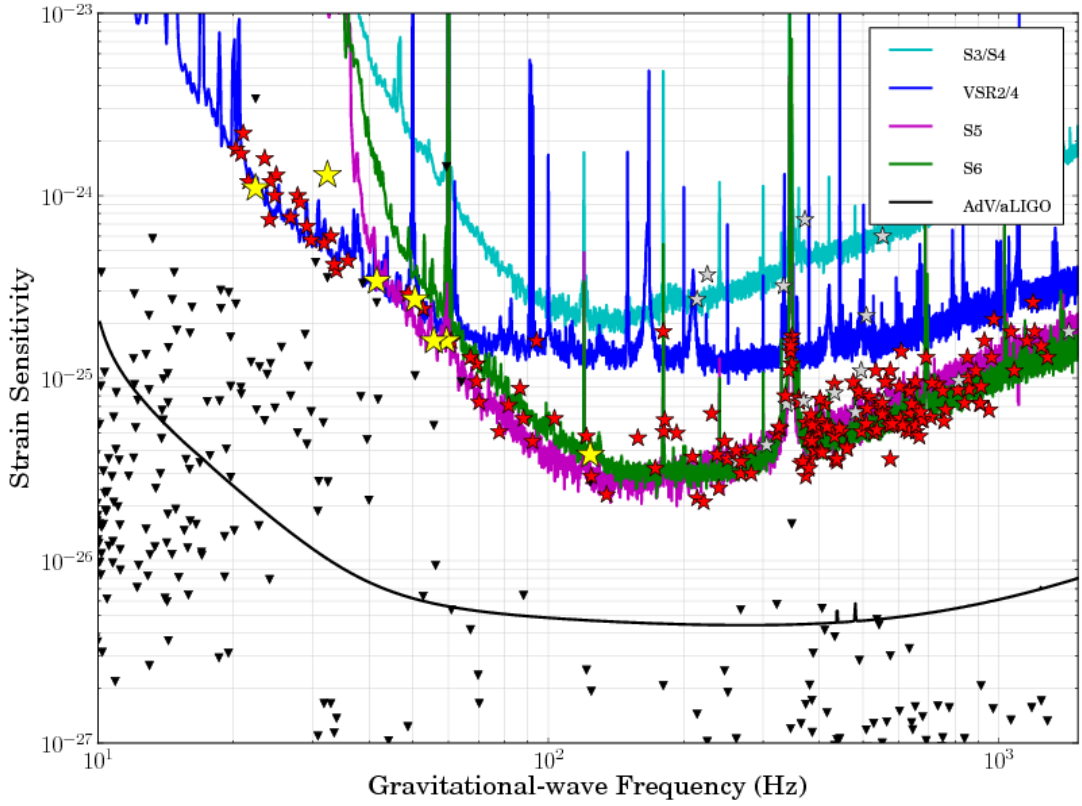

Figure 2.18: The 95% confidence strain amplitude upper limits are represented by star symbols (★) for 195 pulsars from the LIGO and Virgo S3/S4, S5, S6, VSR2 and VSR4 runs. The seven most interesting pulsars are represented by the large yellow stars. The small lighter colored stars represent results from S3/S4 and S5 data. The curves give an estimate of the strain sensitivities of these runs. The AdV/aLIGO straight curve assumes a joint analysis of two equally sensitive advanced LIGO detectors and the advanced Virgo detector operating at their full design sensitivities with one year of coherent integration. The ▼ give the spin-down limits for all (non-Globular Cluster) pulsars, based on values taken from the ATNF catalog and assuming the canonical moment of inertia.

- All-sky, all-frequency searches (objects not previously known):
  As already described, all-sky, all-frequency searches for unknown neutron stars are the most promising continuous gravitational wave searches but also the most challenging. As an illustration, one should remember that the volunteer-driven distributed computing project Einstein@home [312] was launched initially in 2005 to provide enough computing power for all-sky continuous searches extended to high frequency (up to 1200 Hz). Isolated unknown neutron stars have been searched for in LIGO and Virgo data with several searches [313, 314, 315, 316, 317, 318], and Virgo data were also considered especially important to complete the search for signals at low frequency [319]. In [320] one reports the first low frequency all-sky search of continuous gravitational wave signals conducted on Virgo VSR2 and VSR4 data. The search covered the full sky, a frequency range between

20 Hz and 128 Hz. All methods implement a hierarchical scheme where in the first step short segments of data are analyzed coherently. The results are then combined incoherently in different ways. For each of the searches the parameter space is different but all results are consistent and the best 90% CL upper limit is 5.5×10^{-25} at 171 Hz in agreement with the expected sensitivity of the analysis [318]. The reach of the search extends to a few kpc around 150 Hz. To be complete, one should mention that a search for continuous gravitational waves from neutron stars in binary systems has been performed in the most recent data of LIGO and Virgo providing interesting upper limits for frequency between 20 and 520 Hz [321, 322]. The most sensitive 95% confidence upper limit obtained on gravitational wave strain is 2.3×10^{-24} at 217 Hz, assuming the source waves are circularly polarized. Although this search has been optimized for circular binary orbits, the upper limits obtained remain valid for orbital eccentricities as large as 0.9.

2.5.3 Stochastic gravitational wave background searches

To search for a stochastic background signal, gravitational wave strain amplitudes of a pair of detectors are cross-correlated assuming noises are not correlated [34]. With four detectors, up to 6 pairs can be considered. The search sensitivity of each pair of detectors depends on the noise power spectrum of each detector and on the observing geometry (detectors' location and orientation and spatial distribution of the background). Having co-located and co-aligned detectors, like the two Hanford LIGO detectors, maximizes the search sensitivity over the full frequency band of the detectors, but taking into account correctly the presence of correlated noise that could cancel, corrupt or mimic the measurement of a stochastic background is a serious issue. On the contrary the LIGO Hanford and Livingston pair presumably do not have correlated noise[25] and benefit from their good relative alignment that yields good sensitivity in the low frequency region where the detectors' sensitivity is the highest. At higher frequencies ($>$ 500 Hz), pairs involving Virgo and one of the LIGO detectors have the highest sensitivity because of the distance aand Virgo orientation. Most of the theoretical signal models in the LIGO-Virgo frequency band are characterized by a simple power law spectrum with index α, $\Omega_{GW}(f) = \Omega_\alpha (f/f_r)^\alpha$, where f_r is an arbitrary reference frequency. For cosmological sources the stochastic background is assumed to be isotropic and the spectrum to be flat. On the other hand, for astrophysical sources it makes sense to search a background with a spatial distribution, as if it was coming from a point in the sky. The isotropic search carried out in the 41.5 – 169.25 Hz frequency band with LIGO S5 data of this pair of detectors set a direct upper limit on Ω_0 at 95% confidence level of 6.9×10^{-6} [122]. A stochastic background of this strength would contribute 9.7×10^{-6} to the total energy density. This limit hence beats the BBN and CMB bounds (see Figure 1.5). It also constrains values of the cosmic string free parameters (string tension μ and loop size ϵ) not excluded by any other experiments in the very small loop regime; $G\mu < 5 \times 10^{-8}$ for $\epsilon < 2 \times 10^{-11}$ for a string reconnection probability of 10^{-3}. The analysis of the LIGO S6/Virgo VSR2-VSR3 data has slighlty improved (by ya factor $\sim$2) these limits. The frequency range has also been extended (41.5 – 1726 Hz) [323]. Isotropic stochastic background searches using LIGO and Virgo pairs allowed us to set an upper limit on $\Omega_3 < 0.33$ at 900 Hz [324] which improves a limit set by LIGO Livingston and the ALLEGRO bar detector ($\Omega_{\rm GW}(915{\rm Hz}) < 1.02$) [325].

The sensitivity of searches based on cross-correlation depends, among other things, on the separation between the detectors: the smaller the separation, the better the sensitivity is. That's one of the main reasons why two co-located interferometers were sharing the same vaccum chamber at Hanford until 2010. However, co-located detectors are also expected to suffer from correlated noise that may bias the backgrund noise estimation. [326] reports the search for stochastic background signal in the two Hanford detectors in the 2005 – 2007 data. It especially adresses the difficulties to identify and measure the noise contribution to the measurement. Only upper limits at high frequencies, 460 – 1000 Hz, are reported: Ω_3 is contrained to be lower than 7.7×10^{-4} at 900 Hz.

Searches for point-like or more extended sources have been conducted over the same data, producing upper limits on the strain amplitude in each 0.25 Hz wide frequency bin. Three specific directions (the nearby low-mass X-ray binary Sco X-1, the galactic center and SN 1987A) have been studied, but no indication of a stochastic source has been found [327].

[25] See however the discussion on Schumann resonances in section 2.3.1

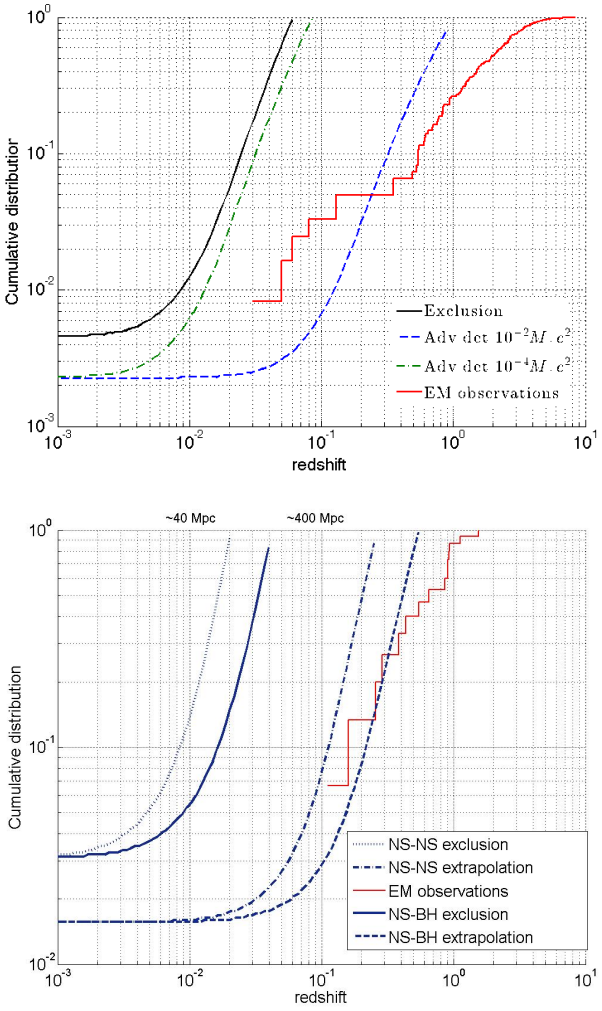

Figure 2.17: Cumulative distribution 90% confidence level exclusion as function of red shift from the analysis of 508 long GRBs (top) and 69 short GRBs (bottom) for different hypothesis on the GRB progenitors (smooth curves). The dashed curves are extrapolations assuming a factor 10 in sensitivity is brought by advanced LIGO-GEO-Virgo detectors. The red stairs show the cumulative distribution of measured redhsifts for GRBs [276].

Chapter 3

Searching for transient gravitational-waves

3.1 Summary of 10 years of searches

Transient sources of gravitational waves have always been considered the most promising source. And among all of them, binary neutron stars coalescence is the standard candel of the interfermetric gravitational wave detectors. But surprisingly, the very first gravitational wave event detected on Earth, recorded for a fraction of a second in the LIGO detectors in September 2015 [40], has been emitted from a binary system formed of two rather large mass black holes. This is the first time where one has witnessed a binary black hole system by observing the moment before it merges into a single black hole. Although compact binary systems are emitting gravitational-waves for millions of years, what is detectable is a rather short signal lasting from a few minutes up to a fraction of a second depending on the component masses, corresponding actually to the very last instant of the coalescence, the plunge of the two compact objects and the ring down of the newly born black hole. Neutron stars and black hole binary systems gravitational emission is now known with an extreme accuracy in different regimes and approximations as it can simply be reduced to the resolution of the two-body movement equation in general relativity. Yet, most approximation techniques fail at predicting the wave emitted when the two objects merge. This was known to be accessible only by solving the Einstein equations numerically. After four decades of developments and attempts, the numerical relativist community came in 2005 with stable long-term simulations of black hole inspiraling around each other, merging and decaying to a stationary black hole [328]. Soon after the 2005 breathrough made by Franz Pretorius many numerical groups produced more and more accurate waveforms which are used to develop semi-analytical solutions that are used in data analysis [329, 330, 331, 332, 333, 334]. Such level of solution accuracy is not yet reached for most of the other sources of transient signals where the presence of matter renders the waveform prediction an extremely complicated problem. As one of the next possibly discovered source of transient gravitational-waves one should mention massive stars core collapse that can end up into a supernova or a black hole. More and more accurate waveforms obtained by numerical simulations are available, but they are not used directly for detection. They are used to extract some information about the source.

Depending on how precisely are known the gravitational waves the design of the filtering of the transient searches will make use of the waveforms themselves. More exactly, when a bank of waveforms or templates can be generated easily in a timely manner (meaning waveforms are described analytically), the matched filtering is the optimal filtering technique. Sources such as compact binary systems, cosmic string kinks and cusps, neutron star resonant modes or black hole desexcitation ring-down belong to this category. Yet, there are two limitations: the accuracy of the analytical waveform models may depend on the source parameters. For compact binary mass ratio larger than a few units, waveform errors start to be the dominant source of systematic errors. The second limitation is the size of the parameter space which can make the template bank analysis computationnally impossible. Beyond the two masses, the most important parameters for a compact binary system are the component angular momenta (spins). For black hole binary spins must be considered as single black holes observations indicate they likely have rather large spins (see for instance Table 1 in [335]). Other parameters such as the orbital eccentricity are still not considered in

2016 matched filtering compact binary searches, spins are still assumed to be aligned or anti-aligned along the orbital angular momentum. This may lead to sub-optimal searches for binary black hole systems searches.

To search for all the other sources of transient gravitational waves and to cover part of the parameter space that may escape the dedicated matched filtering compact binary searches as explained above, alternative filtering techniques have been in used since the early times for ground based gravitational detectors. It includes time-frequency transforms, matched filtering with sine Gaussian waveforms, or cross-correlation. All methods have this in common that they make very few assumptions about the time and frequency behavior of the expected signal. Initially, these unmodelled transient searches focused on very short signals. The emblematic source was the few milli-seconds signal (burst) emitted when a massive star core collapses and bounces back. In a decade of developments [336, 337, 338, 339, 340, 341, 342, 343] the parameter space covered by these pipelines and their complexity has considerably increased while keeping their robustness against unknown source features. In the next section I'm summarizing my main contributions to the search of transient signals in Virgo and LIGO data in the last decade.

3.2 Transient search main contributions

When Virgo engineering run data started to be available in 2004, I cut my teeth with a single detector search with the 7^{th} commissioning Virgo run (C7). This heavily relied on a thorough understanding of the quality of the data. This was also an excellent opportunity to plunge into detector characterization activities (see chapter 4) with other colleagues. I used the filtering algorithm EGC developed by André-Claude Clapson, graduate student at LAL in 2003 – 2006. EGC correlates a single detector strain amplitude with complex exponential Gaussian template bank to generate time-frequency map of energy pixels that are then clusterized by an algorithm developed as well by André-Claude [260, 339]. At that time, in 2006, the first binary black hole simulated waveforms were available. With K.G. Arun, post-graduate at LAL, we asked John Baker's group at NASA Goddard Space Flight Center to provide us with binary black hole waveforms that we used in the analysis of the C7 Virgo data to estimate the sensitivity of a short transient search to binary stellar-mass black hole systems. Given the C7 data sensitivity, the shortness of the data set and the use of only one detector strain amplitude, we knew this would be a scope limited search. But this was the first complete all-sky short transient search in Virgo and the first search making use of numerical relativity binary black hole waveforms. A full transcript of the paper [1] is given in section 3.3.

It was known since the bar experiments transient signal searches that one needs more than one detector to reduce significantly the excess of rather loud triggers due to non Gaussian detector noise (glitches)[1]. Using the fact that glitches show up randomly in each detector[2], asking that a transient signal is seen simultaneously in at least two detectors allows to reduce the number of background triggers, and especially background triggers carrying a lot of energy or having some properties similar to the expected signal[3]. In 2005 while the LIGO detectors were engaged in their 2-years long fifth scientific run and Virgo was still being commissioned, the two collaborations decided to joint their effort to search gravitational waves in four detectors. I joined the initial LSC-Virgo working group for burst searches which main goal was to compare the performance of the LSC and Virgo pipelines and establish the best strategy to analyze data in coincidence for a set of non-aligned gravitational wave detectors. We especially show that, in the case of a comparable sensitivity network of detectors, to maximize the sky coverage of a potential source, one has interest to consider all pairs of detectors instead of asking for triple coincidence between all detectors. The gain in efficiency is $\sim$20%. A full transcript of the paper [344] is given in section 3.3.

In 2007, the Virgo detector was approaching its design sensitivity after 5 years of commissioning. The first scientific Virgo run (VSR1) started in July 2007 while LIGO was still taking data. In total $\sim$ 68 days of coincident data with 4 interferometers has been collected. I searched for burst signals in these data using the EGC pipeline adapted for a coincident search with four strain amplitude streams. Results have been compared with the two other pipelines coherent

[1] The reduction of the background triggers in the C7 search demanded months of work fully dedicated to detector characterization. The same level of scrunity would not have been possible for a longer data set. Furthermore the longer the data set is, the higher is the probability to have a source of glitches whose origin remains unknown. An all-time transient search requires more than one detector for assessing a discovery

[2] The case of correlated noise between detectors, though rather rare, is seriously currently studied in advanced detectors and has been systematically excluded so far in all observations.

[3] Anti-chirping waveforms are not rare in gravitational wave detector strain amplitude, corresponding to relaxing phenomena. Chirping is more seldom but not totally unlikely

waveburst (cWB) and the Omega pipeline. No signals were found by any of these pipelines and upper limits on the event rate were published in [4]. The was the first real experience of a complete all-sky short transient multi-detector search. The EGC results are included in the LSC-Virgo collaboration paper whose manuscript is given in section 3.3. The main lessons learned were that Virgo, because of its lower sensitivity compared to the LIGO detectors (a factor $\sim$ 2 – 3 worse than LIGO Hanford), added little to the pair formed by LIGO Hanford and LIGO Livingston. The other key factor in the search was the glitch rate. When the glitch rate in one detector starts to be large compared to the other detectors' rate, any network combination including this interferometer will produce an excess of triggers. This is not necessarily an handicap (what counts is the rate of the loudest glitches in fact) but when it is coupled with a low sensitivity, it made Virgo which is in addition non-aligned with the LIGO detectors almost useless in this all-sky search. The other lesson drawn from this search was that the EGC search sensitivity was limited by loud glitches in one of the detectors that passed the coincidence test that used only the trigger time and frequency information. These triggers were constituting an irreducible background that was from mimicking a genuine signal. Indeed, looking at their time-frequency shape in each detector, it was frustratingly obvious that these coincident triggers were just due to glitches in each detector. Asking for a bit of coherence between the detectors was needed to get rid of them. Furthermore, even with this improvement, it became more and more clear than EGC would not do better than cWB; both pipelines were covering the same parameter space and EGC was inherently less efficient for stochastic signals (modelled by band limited white noise). For all the reasons, I decided not to continue the development of the EGC pipeline.

Almost at the same period, I took advantage of a long-term stay at Carleton College to work with colleagues expert in Bayesian inferance methods to estimate the parameters of a massive star core collapse progenitor identified by its emission of gravitational waves. We have shown that data from interferometric gravitational wave detectors can be used to provide useful information on the mass of the progenitor model, precollapse rotation, and the nuclear equation of state. For this, we used a waveform library generated by H. Dimmelmeir's (the latest numerical simulations of rotating stellar core collapse models in general relativity including micro-physics and neutrino transport effects), and from it create an orthogonal set of eigenvectors using principal component analysis. Bayesian inference techniques are then used to reconstruct the associated gravitational wave signal that is assumed to be detected by an interferometric detector. Posterior probability distribution functions are derived for the amplitudes of the principal component analysis eigenvectors, and the pulse arrival time. A full transcript of the paper [126] is given in section 3.3.

Before advanced LIGO and advanced Virgo started to take data, I decided to join a newly formed search team targetting intermediate duration transients. This old idea was to cover a part of the un-modelled transient search parameter space which was not covered so far: any signals lasting from few seconds to days. It bridges the short transient to the continuous waves searches. Anecdotally, the effort started in the background stochastic group, to search for localized astrophysical sources contributing to the gravitational wave background. As often, no precise models can be directly used as most sources of long GW transients are associated with extremely complex dynamics and hydrodynamic instabilities following the collapse of a massive stars core in the context of core collapse supernovae [124, 86, 345]. Soon after core collapse and the formation of a protoneutron star, convective and other fluid instabilities (including standing accretion shock instability) may develop behind the supernova shock wave as it transitions into an accretion shock. Long-duration GW signals are expected from these violently aspherical dynamics, following within tens of milliseconds of the short-duration GW burst signal from core bounce and protoneutron star formation. Given the turbulent and chaotic nature of postbounce fluid dynamics, one expects a stochastic GW signal that could last from a fraction of a second to multiple seconds, and possibly even longer [346, 347, 348]. After the launch of an at least initially successful explosion, fallback accretion onto the newborn neutron star may spin it up, leading to nonaxisymmetric deformation and a characteristic upward chirp signal (700 Hz – few kHz). In the collapsar model for long GRBs [136], a stellar-mass black hole forms, surrounded by a massive, self-gravitating accretion disk. This disk may be susceptible to various nonaxisymmetric hydrodynamic and magnetohydrodynamic instabilities which may lead to fragmentation and inspiral of fragments into the central black hole [137, 349]. In an extreme scenario of such accretion disk instabilities (ADIs), magnetically suspended accretion is thought to extract spin energy from the black hole and dissipate it via GW emission from nonaxisymmetric disk modes and fragments [138, 139]. The associated GW signal is potentially long lasting (10 – 100 s) and predicted to exhibit a characteristic downward chirp. Finally, in magnetar models for long and short GRBs [234, 350], a long-lasting post-GRB GW transient may be emitted by a magnetar undergoing rotational or magnetic nonaxisymmetric deformation [133, 351].

Most of these sources may not be associated with an electromagnetic signal that can be used to target which part of the sky and data set to search for a signal. Thus an all-sky search pipeline has been developed starting from the STAMP[4] algorithm [345] by two graduate students Tanner Prestegard (Universiity of Minnesota) and Samuel Franco (LAL). The pipeline is described in [352]. The first long transient search in real data (covering LIGO data from 2005 to 2010) has been reported in [353]. The search targets gravitational wave transients of duration 10 – 500 s in a frequency band of 40 – 1000 Hz, with minimal assumptions about the signal waveform, polarization, source inclination and direction, or time of occurrence. All candidate triggers were consistent with the expected background and we set 90% confidence upper limits on the rate of long-duration gravitational wave transients for different types of gravitational wave signals. For signals from black hole accretion disk instabilities, we set upper limits on the source rate density of the order 10^{-5} – $10^{-4}\, Mpc^{-3}yr^{-1}$ at 90% confidence. These are the first results from an all-sky search for unmodeled long-duration transient gravitational waves. A full transcript of the paper [353] is given in section 3.3.

3.3 Search publications

[4]STAMP stands for Stochastic Transient Analysis Multiple-detector Pipeline.

Class. Quantum Grav. **26** (2009) 085009 (30pp) doi:10.1088/0264-9381/26/8/085009

Gravitational wave burst search in the Virgo C7 data

F Acernese[1ac], M Alshourbagy[2ab], F Antonucci[3a], S Aoudia[4], K G Arun[5], P Astone[3a], G Ballardin[6], F Barone[1ac], L Barsotti[2ab], M Barsuglia[7], Th. S Bauer[8a], S Bigotta[2ab], S Birindelli[4], M-A Bizouard[5], C Boccara[9], F Bondu[4], L Bonelli[2ab], L Bosi[10a], S Braccini[2a], C Bradaschia[2a], A Brillet[4], V Brisson[5], H J Bulten[8ab], D Buskulic[11], G Cagnoli[12a], E Calloni[1ab], E Campagna[12ac], B Canuel[6], F Carbognani[6], L Carbone[10a], F Cavalier[5], R Cavalieri[6], G Cella[2a], E Cesarini[12ab], E Chassande-Mottin[7], S Chatterji[3a], N Christensen[6], A-C Clapson[5], F Cleva[4], E Coccia[13ab], M Colombini[3b], C Corda[2ab], A Corsi[3a], F Cottone[10ab], J-P Coulon[4], E Cuoco[6], S D'Antonio[13a], A Dari[10ab], V Dattilo[6], M Davier[5], R De Rosa[1ab], M Del Prete[2ac], L Di Fiore[1a], A Di Lieto[2ab], M Di Paolo Emilio[13ad], A Di Virgilio[2a], V Fafone[13ab], I Ferrante[2ab], F Fidecaro[2ab], I Fiori[6], R Flaminio[14], J-D Fournier[4], S Frasca[3ab], F Frasconi[2a], L Gammaitoni[10ab], F Garufi[1ab], E Genin[6], A Gennai[2a], A Giazotto[2a,6], M Granata[7], V Granata[11], C Greverie[4], G Guidi[12ac], H Heitmann[4], P Hello[5], S Hild[15], D Huet[6], P La Penna[6], M Laval[4], N Leroy[5], N Letendre[11], M Lorenzini[12a], V Loriette[9], G Losurdo[12a], J-M Mackowski[14], E Majorana[3a], N Man[4], M Mantovani[6], F Marchesoni[10a], F Marion[11], J Marque[6], F Martelli[12ac], A Masserot[11], F Menzinger[6], C Michel[14], L Milano[1ab], Y Minenkov[13a], S Mitra[4], J Moreau[9], N Morgado[14], M Mohan[6], A Morgia[13ab], S Mosca[1ab], B Mours[11], I Neri[10ab], F Nocera[6], G Pagliaroli[13ad], C Palomba[3a], F Paoletti[2a,6], S Pardi[1ab], A Pasqualetti[6], R Passaquieti[2ab], D Passuello[2a], G Persichetti[1ab], F Piergiovanni[12ac], L Pinard[14], R Poggiani[2ab], M Punturo[10a], P Puppo[3a], O Rabaste[7], P Rapagnani[3ab], T Regimbau[4], F Ricci[3ab], A Rocchi[13a], L Rolland[11], R Romano[1ac], P Ruggi[6], B Sassolas[14], D Sentenac[6], B L Swinkels[6], R Terenzi[13ac], A Toncelli[2ab], M Tonelli[2ab], E Tournefier[11], F Travasso[10ab], G Vajente[2ab], J F J van den Brand[8ab], S van der Putten[8a], D Verkindt[11], F Vetrano[12ac], A Viceré[12ac], J-Y Vinet[4], H Vocca[10a], M Was[5] and M Yvert[11]

[1] INFN, sezione di Napoli[a]; Università di Napoli 'Federico II'[b], Complesso Universitario di Monte S. Angelo, I-80126 Napoli; Università di Salerno[c], Fisciano, I-84084 Salerno, Italy
[2] INFN, Sezione di Pisa[a]; Università di Pisa[b]; I-56127 Pisa; Università di Siena[c], I-53100 Siena, Italy
[3] INFN, Sezione di Roma[a]; Università 'La Sapienza'[b], I-00185 Roma, Italy
[4] Département Artemis, Observatoire de la Côte d'Azur, CNRS, F-06304 Nice, France
[5] LAL, Université Paris-Sud, IN2P3/CNRS, F-91898 Orsay, France
[6] European Gravitational Observatory (EGO), I-56021 Cascina (Pi), Italy
[7] AstroParticule et Cosmologie (APC), CNRS: UMR7164-IN2P3-Observatoire de Paris-Université Denis Diderot-Paris VII-CEA : DSM/IRFU, France
[8] National institute for subatomic physics[a], NL-1009 DB; Vrije Universiteit[b], NL-1081 HV, Amsterdam, The Netherlands
[9] ESPCI, CNRS, F-75005 Paris, France
[10] INFN, Sezione di Perugia[a]; Università di Perugia[b], I-6123 Perugia, Italy

[11] Laboratoire d'Annecy-le-Vieux de Physique des Particules (LAPP), IN2P3/CNRS, Université de Savoie, F-74941 Annecy-le-Vieux, France
[12] INFN, Sezione di Firenze[a], I-50019 Sesto Fiorentino; Università degli Studi di Firenze[b], I-50121 Firenze; Università degli Studi di Urbino 'Carlo Bo'[c], I-61029 Urbino, Italy
[13] INFN, Sezione di Roma Tor Vergata[a]; Università di Roma Tor Vergata[b], Istituto di Fisica dello Spazio Interplanetario (IFSI) INAF[c], I-00133 Roma; Università dell'Aquila[d], I-67100 L'Aquila, Italy
[14] Laboratoire des Matériaux Avancés LMA, IN2P3/CNRS, F-69622 Villeurbanne, Lyon, France
[15] School of Physics & Astronomy University of Birmingham B15 2TT, UK

Received 20 January 2009, in final form 9 March 2009
Published 1 April 2009
Online at stacks.iop.org/CQG/26/085009

Abstract
A search for gravitational wave burst events has been performed with the Virgo C7 commissioning run data that have been acquired in September 2005 over 5 days. It focused on unmodeled short duration signals in the frequency range 150 Hz to 2 kHz. A search aimed at detecting the GW emission from the merger and ring-down phases of binary black hole coalescences was also carried out. An extensive understanding of the data was required to be able to handle a burst search using the output of only one detector. A 90% confidence level upper limit on the number of expected events given the Virgo C7 sensitivity curve has been derived as a function of the signal strength, for unmodeled gravitational wave searches. The sensitivity of the analysis presented is, in terms of the root sum square strain amplitude, $h_{rss} \simeq 10^{-20}$ Hz$^{-1/2}$. This can be interpreted in terms of a frequentist upper limit on the rate $\mathcal{R}_{90\%}$ of detectable gravitational wave bursts at the level of 1.1 events per day at a 90% confidence level. From the binary black hole search, we obtained the distance reach at 50% and 90% efficiency as a function of the total mass of the final black hole. The maximal detection distance for non-spinning high and equal mass black hole binary system obtained by this analysis in C7 data is $\simeq 2.9 \pm 0.1$ Mpc for a detection efficiency of 50% for a binary of total mass 80 $M_{\odot}$.

PACS numbers: 04.80.Nn, 04.30.Tv, 95.30.Sf, 95.85.Sz

(Some figures in this article are in colour only in the electronic version)

1. Introduction

Virgo [1] is a 3 km long arm power-recycled Michelson interferometer located near Pisa, Italy, whose goal is to detect gravitational waves (GW) emitted by astrophysical sources extending out past the Virgo cluster. The commissioning of the detector started in 2003 and regular data taking campaigns have been organized after each important milestone. The last commissioning run (C7) took place in September 2005 and lasted for 5 days. The best achieved sensitivity was $h \simeq 7 \times 10^{-22}$ Hz$^{-1/2}$ at 300 Hz. The Virgo design sensitivity at this frequency is expected to be better by an order of magnitude assuming that 10 W enters into the interferometer. However, during the C7 run, Virgo was running with a reduced light power, 0.7 W, because the backscattering in the mode-cleaner cavity of the light reflected by the recycling mirror

prevented the control of the interferometer at full power. Despite the reduced sensitivity, several GW searches have been carried out using this data set in order to set up and tune the pipelines developed in Virgo: the search of the coalescence of neutron stars [2], the search of continuous wave sources [3], a joint Virgo, AURIGA, EXPLORER and NAUTILUS GW search [4], a targeted GW burst search associated with the long GRB 050915a [5], and the search of GW burst signals that is reported in this paper.

The category of gravitational wave bursts includes all possible signals whose duration is short, less than a few hundreds of milliseconds. Many violent astrophysical phenomena will be accompanied by an emission of GW burst. If these events happen sufficiently close by, the ground based gravitational detectors will be able to observe these short duration GW bursts. There are many candidate GW burst sources. These include massive star core collapse [6–11], the merging phase of coalescing compact binary systems forming a single black hole (BH) [12–15], BH ring down [16], astrophysical engines that generate gamma-ray bursts (GRB) [17], neutron star oscillation modes and instabilities [18] or cosmic string cusps and kinks [19]. Some of these sources are well modeled, but not all, and as such a burst pipeline is built by making very few assumptions about the nature of these waveforms. The theoretical event rates for many of these sources are quite uncertain.

Binary black hole (BBH) mergers are an interesting source for GW burst searches. The typical event rate for these sources is 1 Myr^{-1} per galaxy [20, 21] and is still highly uncertain given the lack of direct observational evidence for the existence of BBH systems, unlike the double neutron star systems. Though these sources are routinely searched for by the inspiral phase prior to merger using matched filtering techniques, an independent search focusing on the merger and ring-down GW emission, which is dominant for high mass binaries [12], may bring additional confidence[16]. A search of this type was first attempted with the LIGO S2 data [22]; this used the then-available numerical relativity waveforms from the Lazarus project as a model of BBH mergers. However the estimates obtained were projected as order of magnitude estimates due to the nonrobusteness of the waveforms used. Though the burst searches do not have as large of a distance reach as an inspiral search, it will be interesting to understand the implications of a BH binary search from a burst perspective, especially because a burst search is sensitive to the merger and ring-down phase of a BBH coalescence. Among the three phases of inspiral, merger and ring down, for the BBH most of the energy is released in the highly relativistic phase of merger, that is difficult to model by analytic approximation methods. But recently numerical relativity simulations have made significant advances in generating the waveforms for all the three phases of the binary evolution (see [23] and references therein).

In this paper, we report on an all-sky burst search for unmodeled waveforms and BBH mergers without using any prior information on the expected waveform. This concerns all short duration ($\ll$1 s) signals having energy in the best sensitivity frequency band of the C7 data, 150–2000 Hz. This search has been performed using the data of only one interferometer which does not allow one to perform timing coincidence to eliminate spurious events in one of the detectors, as was done in the burst searches performed using the LIGO detectors [22, 24, 25] and the bar detectors [26]. However, a similar one-detector burst search has already been carried out with the data from the TAMA detector [27]. The C7 run data has been used for extensive analysis of the Virgo noise; this is a fundamental step in the path toward performing a GW burst search with only one detector. Indeed, numerous sources of noise generate, in the interferometer's GW strain amplitude channel, transient events which mimic GW burst events; environmental noise, such as acoustic noise, has been found at the origin of many of them.

[16] Template based searches for binary black hole sources using different waveforms which capture the different phases, including merger and ring down, are now applied to analyze the LIGO and Virgo data.

Non-stationary data can also generate an excess of short duration events. Such phenomena have been found, examined, and understood in the C7 data. These studies allowed us to define the pre-processing and post-processing steps needed in order to optimize the performance of the GW burst pipeline used in this analysis.

The outline of this paper is as follows. In section 2 we describe the main features of the Virgo detector, emphasizing the operating characteristics during the C7 run that played a role in understanding the quality of the data. In section 2.2 we describe how we select the data periods that have been used for this analysis. The burst pipeline used in this analysis is described in section 3. In section 3.4 the main results on the C7 data characterization needed in order to understand and to suppress the sources of glitches are summarized; this includes the veto strategy used against identified sources of noise. Section 4 gives the results of the search in the C7 data. Section 5 explains how the analysis sensitivity has been estimated considering different types of possible GW burst waveforms. We especially considered in this paper BBH merger and ring-down numerical waveforms [28]. Section 6 gives the upper limits obtained at 90% of confidence level on the number of events as a function of the signal strain amplitude. We finally conclude this paper with an astrophysical interpretation of the present GW burst search.

2. Virgo during the commissioning run C7

2.1. Detector status

The Virgo detector [29] is a power-recycled Michelson interferometer with 3 km long arms that each contain a Fabry–Perot cavity. All mirrors are suspended from the so-called superattenuator [30], whose goal is to reduce drastically above 10 Hz the seismic noise transferred to the instrument. A 20 W Nd:YAG laser is used to illuminate the interferometer. The laser light is modulated in phase at the frequencies $\simeq$22 and 6 MHz; this technique permits the GW strain to be detected at the modulation frequency where the laser power fluctuation is much smaller than in the interferometer bandwidth. The beam is spatially filtered with a 144 m long triangular input mode-cleaner cavity before being injected into the main interferometer. The laser frequency is pre-stabilized in order to acquire the control of the different optical cavities, but to reach the extreme sensitivity targeted by Virgo an enhanced control of the laser frequency noise is required; it has to be reduced by several orders of magnitude. This is the role of the so-called *second stage frequency stabilization* which is engaged during the cavities' lock acquisition [31]. The beam entering the interferometer is divided by the beam splitter (BS) into two beams that are injected into the 3 km long arm cavities. Apart from the mirrors' losses, all light fed-in by the injection system subsequently returns to it. The power-recycling (PR) mirror, with a reflectivity of 92%, reflects the out-going light back to the main interferometer. Together with the Michelson interferometer the power-recycling mirror forms a Fabry–Perot-like cavity in which the light power is resonantly enhanced, thereby improving the shot noise limit. The Michelson interferometer is held on the dark fringe, and the GW strain signal is expected in the beam at the dark port, which leaves the vacuum via the so-called detection bench. The detection bench is a suspended table accommodating several optical components. The beam coming from the BS passes through an output mode cleaner, a 3.6 cm long rigid cavity. The main output beam is detected by a pair of InGaAs photodiodes. Useful signals are obtained by detecting the light in the transmission of the arm cavities and in reflection of the power-recycling cavity (B2 photodiode). The GW signal that results from a detuning of the carrier resonance in the arms is extracted from the dark port channel, demodulated and then sampled at 20 kHz. This signal is digitized and filtered.

The control of the interferometer consists in maintaining the laser light resonant in the optical cavities and the output port tuned on the dark fringe, defining its working point. More precisely, the carrier must be resonant in all cavities while the sidebands must be resonant in the central cavity but anti-resonant in the arms. Despite the good seismic noise attenuation provided by the superattenuator, feedback controls are mandatory in order to keep the interferometer locked on the right working point. In addition to the control of the longitudinal degrees of freedom of the cavities, the mirrors must be kept aligned with respect to each other. This is the so-called auto-alignment control (AA). If uncontrolled, the angular degrees of freedom of the suspended optics distort the cavity eigen modes. This causes power modulation of the light fields; furthermore, long term drifts will make the longitudinal control impossible after a certain amount of time, and misalignments increase the coupling of other noise sources into the dark port. This has been a major problem in the C7 data analysis (see section 3.4). In actuality, during C7 not all of the mirrors were under AA control; the arm input mirrors and the injection bench were only controlled locally.

To convert the signal received on the dark port into a measure of GW strain one needs to calibrate the residual arm-length difference; this includes at low frequencies the effect of the control loop keeping the cavities in resonance. The loop correction signals are subtracted from the dark port signal that is then converted into a strain via knowledge of the optical gain of the feedback control loops. This gain may vary depending, for instance, on the alignment drifts of the optical elements. To monitor the variation, some sinusoidal signals (four between 100 and 110 Hz, and four between 350 and 360 Hz) are applied on the end-arm mirrors and the amplitude of the lines are measured. Another important aspect of the GW strain reconstruction is the good knowledge of the transfer function of the actuator chain which is used to control the mirrors. Actually, during the C7 run, the calibration procedure was not as accurate as it is now. For instance, the frequency dependence of the digital to analog converter transfer function was not taken into account in the reconstruction of the GW strain amplitude channel $h(t)$. This yielded a systematic error on $h(t)$ which has been estimated to be 40% [32].

Moreover, during C7 Virgo was running with a 700 mW laser beam entering the interferometer in order to avoid instabilities due to the backscattering of light into the mode-cleaner cavity reflected by the recycling mirror. The problem has since been fixed during a shutdown carried out just after the C7 run. This reduced power light limited the sensitivity at high frequencies. Figure 1 displays and compares the progress achieved on the sensitivity curve since the beginning of the Virgo commissioning. At high frequencies (>300 Hz), the sensitivity was limited by the shot noise and the laser frequency noise. At low frequencies (<100 Hz) the longitudinal and angular controls of the mirrors are the main limitation; the electronic noise of the actuator and/or the sensor introduced by the control loops induce a displacement of the mirror which is well above the fundamental noise floor.

2.2. C7 data set

After the lock acquisition is completed, the interferometer state is set to *science mode*. The science mode duty cycle maintained by Virgo during C7 was 66%. The data was split into 53 data blocks, or segments, spanning over the 5 days. A minimal duration of 10 min has been required for a segment. In order to define the start and end time of the data segments of good quality for the search for burst GW events we considered all the known instrumental effects that influence and spoil the output of the burst pipeline. For example, the last 10 s of each segment has been removed because many signals, including the GW strain channel, start oscillating and thereby cause the loss of lock. Another problem concerns the excitation of some thermal resonances of the last stage of the suspension (violin modes) when attempting

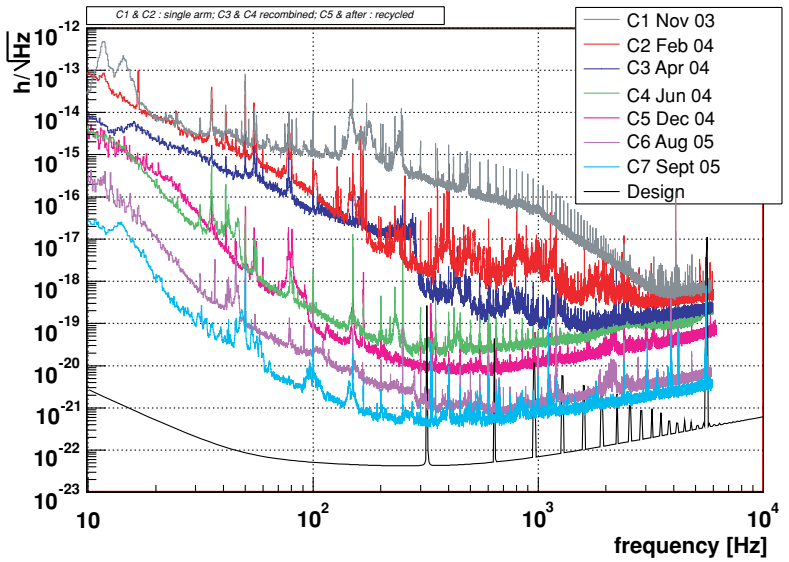

Figure 1. Sensitivity curves obtained between 2003 and 2005 during the commissioning of the Virgo detector before the 2005 shutdown. The black curve is the Virgo nominal sensitivity curve which has been computed assuming a 10 W laser.

to lock the interferometer. The decay time of these resonances has been determined, and for each segment we suppressed the beginning until the amplitude of the resonance having the longest decay time has been decreased by 90%. The reduction of the size of the data segments (hereafter called *science segments*) due to these data quality criteria amounts to 8%. In addition, some signals have been artificially injected into the GW strain channel during C7 by applying a force on the input mirror of one of the interferometer arm's Fabry–Perot cavity. These are the so-called hardware injections. The hardware injection signals are used in this analysis to test that the vetoes against external sources of noise that were implemented do not suppress any potentially real GW events (see section 3.4.4). The hardware injection periods were not considered for the GW burst search. Taking into account the application of the data quality criteria and the hardware injection periods, the duty cycle is finally reduced from 66% to 55%. This corresponds to a total duration of 2.51 days.

3. Description of the burst search pipeline

3.1. Overview

The GW burst pipeline that has been used in this search is composed of several parts that allow us to select and analyze all segments of Virgo data and eliminate, as much as possible, the artifacts in the detector output that could mimic a GW event. The core of the pipeline is the GW detection statistic, described in section 3.3, that is applied on pre-selected segments of data of good quality. This results in lists of triggers. As we are dealing with non-Gaussian and non-stationary data, many of these triggers are due to instrumental effects. The next step consists of identifying all the sources of noise disturbances that pollute the detector output, and then define vetoes to be applied *a posteriori* on the trigger lists. This step in this pipeline

is playing an important role as we cannot suppress these artifacts by requesting coincidence with another detector. We provide details on how the vetoes have been defined and which sources of noise they help in suppressing.

3.2. Data selection

Instrumental problems and environmental conditions have been identified that temporarily affect the detector sensitivity for a GW burst search. In a pre-selection step, we discard the periods where the detector operation is not optimal. To do so, we have defined a list of data quality flags (DQ) that highlight the intervals of malfunctioning. Among the DQ flags, some pertain to the saturation of the photodiodes and/or actuator signals that are used to keep the interferometer locked to its operating point. The analog electronics of the control loop that maintains the laser frequency noise below the requirements was sometimes also saturating. That then induces incorrect control signals and consequently a misbehaving GW strain amplitude. An excess of events was found when the GW strain $h(t)$ reconstruction process was facing a problem, for instance when the calibration lines were buried in the noise. When this happens the $h(t)$ reconstruction program sets a DQ flag stored in the data stream. Sometimes during C7 a few frames or channels were missing due to some failure of the data acquisition system. That produces a hole in the continuous time series. The burst pipelines manage properly with the presence of holes in a segment, but to accurately compute the effective duty cycle we have defined a DQ flag pertaining to this issue. Finally, it has been found that when an aircraft is flying above the interferometer at a relatively low altitude acoustic and/or seismic noise couples into the dark fringe beam and induces a strong effect in $h(t)$ that is detected by the burst pipelines. The band limited RMS of some acoustic probes (located in the end arm buildings) were monitored to detect the airplanes. All these DQ segments have been combined into a single list, taking into account possible overlaps. The dead time induced by the application of these DQ flags on triggers list was only 0.8%, of the total duration which is acceptably low.

3.3. Event trigger generation: exponential Gaussian correlator

Different pipelines have been developed to search for GW bursts. Many of them [33–36] rely on a common principle i.e., the detection of clusters of excess energy in a time-frequency representation of the data. The pipeline we use in this analysis follows the same idea; we refer to it as the exponential Gaussian correlator (EGC) as it been described in [37], but here we give a short summary.

The time-frequency plane can be tiled using a lattice of sine Gaussian waveforms i.e.,

$$\Phi(t) = \exp\left(-\frac{1}{2}\left(\frac{t}{\tau_0}\right)^2\right) \mathrm{e}^{2\pi \mathrm{i} f_0 t}, \tag{1}$$

where the values of the central frequency f_0 and typical duration τ_0 can be chosen in such way as to optimize the coverage of the plane. The idea is to consider the above waveforms as typical burst transients and to search for them using a matched filtering technique. For this reason, we designate $\Phi(t)$ as a template waveform. The EGC computes the cross-correlation of the data with the templates, namely

$$C(t) = \frac{1}{N}\int_{-\infty}^{+\infty} \frac{\tilde{x}(f)\tilde{\Phi}^*(f)}{S(f)} \mathrm{e}^{2\pi \mathrm{i} f t}\, \mathrm{d}f, \tag{2}$$

where $\tilde{x}(f)$ and $\tilde{\Phi}(f)$ are the Fourier transforms of the data and template, and $S(f)$ is the two-sided power spectral density of the noise. N is the normalization factor of the templates defined as

$$N = \sqrt{\int_{-\infty}^{+\infty} \frac{|\Phi(f)|^2}{S(f)}\,\mathrm{d}f}, \tag{3}$$

For the present analysis, the power spectral density has been estimated over data segments of 600 s duration. To define the template lattice, the parameterization using the quality factor $Q_0 = 2\pi\tau_0 f_0$ instead of the duration τ_0 is preferred. Using the algorithm of [38], we tile the parameter space (f_0, Q_0) with a minimal match of 99%. The parameter ranges 150 Hz $\leqslant f_0 \leqslant$ 2 kHz and $2 \leqslant Q_0 \leqslant 16$ correspond to the frequency band of best sensitivity for Virgo during the C7 run. This generates 420 templates; the shortest and longest ones have 0.31 ms and 34 ms duration.

The quantity $\rho = \sqrt{2 \times |C|^2}$ is the signal-to-noise ratio (SNR), which we use as a detection statistic. It depends on the analysis time t, the template frequency f_0, and quality factor Q_0. It thus defines a three-dimensional representation map of the data [37] in which we search for a local excess as compared to typical noise fluctuations.

We first apply a low threshold (SNR of 3.3) to the map. We form clusters with the surviving pixels of energy $|C_i|^2$ with a two pass procedure. The pixels are grouped into clusters using the Hoshen–Kopelman algorithm [39]. Once the cluster is formed, all pixels that have a SNR lower than 5 are removed. Then, all clusters overlapping in time or separated by less than 50 ms are grouped together once again. We produce the final list of triggers by requesting that the cluster SNR $\left(\sqrt{2 \times \sum |C_i|^2}\right)$ is larger than 11.3. This choice for the threshold is a good compromise between not having too many triggers and not losing too much detection efficiency.

The triggers' information is extracted from the clusters. The peak time, peak frequency and the trigger SNR are defined by the pixel that has the highest SNR. The duration and the frequency bandwidth of the trigger take into account all the pixels in the cluster. The timing resolution of EGC has been estimated for different kinds of waveforms [37, 40]. For most signals used in the benchmark test, the timing resolution of EGC is smaller than 1 ms for SNR of 10, but it can be as large as a few ms.

3.4. Vetoes

The search for GW burst events presented here was carried out on real data that are non-Gaussian and non-stationary. This prevents the use of theoretical estimates of the expected false alarm rate. In contrast, the background rate must be extracted from the data itself. In the multi-detector context, the background can be estimated by computing the rate of (purely accidental) coincidences between trigger lists that were time shifted with random delays [22, 25]. We cannot resort to such a procedure in the case of this study since we only have the Virgo C7 data set at our disposal. There is a need to initially identify, in an thorough way, all the sources of noise that generate large SNR triggers that can mimic GW burst events; these types of noise events have to be suppressed before we try to estimate the background event number.

We define a methodology that guarantees that we do not discard any true GW event as long as they do not coincide with a bad quality data period. Initially, there was the study of all the sources of noise that generate large SNR triggers, or more generally an excess of triggers, and the construction of vetoes to suppress these triggers. The study was performed on a subset of the C7 dataset (the playground segment) chosen arbitrarily before starting the GW burst

search, in order to avoid bias. Our main concern in the veto development process was to minimize the dead time introduced by the data quality selection, while assuring a high level of noise trigger rejection. To perform the background studies and develop the veto strategy we used the longest C7 science segment; this segment was 14 h in duration (22% of the whole dataset used for the GW burst search).

Several transient detection algorithms (excluding EGC in order to avoid bias) have been applied to the playground dataset to identify and characterize the sources of noise that generate the high SNR triggers that mimic a GW burst event. Mean filter searches for an excess in a moving average computed on whitened data [41]. Peak correlator is a matched filter using Gaussian waveform templates [41]. The wavelet detection filter is based on a multi-resolution time-frequency transform applied on whitened data [5]. Results of these pipelines have been compared to ensure that all sources of transient events have been discovered. These detection algorithms search for a short duration excess of energy, but using different methods. All of the trigger lists show a rather large excess of events compared to expectation from Gaussian noise; there was a definite excess of large SNR triggers.

Two categories of large triggers have been identified; the first one corresponds to short glitches correlated to a glitch also present in an auxiliary channel. These auxiliary channels include the available environmental monitoring and control loop signals (see section 3.4.1). The second category of glitches have been found to be due to the so-called 'bursts of bursts' that we describe in section 3.4.2. Specific vetoes against these two sorts of glitches have been developed as explained in section 3.4.3.

3.4.1. Origin of the short duration glitches. To veto all periods of data during which instrumental or environmental problems occurred and generated a glitch in the GW channel data, one first needs to figure out which auxiliary channels are the most sensitive to these particular sources of noise. The by-eye scanning of the loudest events observed in the playground dataset already gave hints to potentially useful auxiliary channels. However we subsequently performed a systematic analysis using many channels recorded by Virgo and using the mean filter pipeline.

We have found that three channels were particularly interesting for vetoing glitches in the GW strain amplitude channel $h(t)$. It has been seen that many high SNR burst events are coincident in time with the realignment of the quadrant photodiodes by some stepping motors. These quadrant photodiodes, used for the interferometer automatic alignment system, are located at the output of the interferometer, on the same optical bench hosting the photodiodes used to detect the interferometer dark port signal. The stepping motors were generating very loud acoustic and mechanical noise that coupled into the dark fringe beam nearby. Each time a quadrant photodiode is moved there is a large increase in the signal measured by an accelerometer probe located on the detection bench. When the quadrant photodiodes were not re-aligned (horizontal and vertical positions remain constant) the RMS of the accelerometer probe signal remained low. The rate of the quadrant photodiodes' realignment was not constant over the run; initially the alignment occurred every 3 s, but this was then reduced to every 300 s at the end the C7 run after the discovery of the problem (the parameters of the process responsible for the quadrant photodiodes realignment have subsequently been changed to diminish this problem). This acoustic/mechanical noise generated glitches in the GW strain amplitude channel whose frequency content was around 550 Hz. Due to the fact that the excess of acoustic noise could last up to 1 s, which is long for a glitch finding algorithm, we used the RMS computed over 100 ms of data from an accelerometer located on the detection bench instead of the mean filter triggers to create a veto (called 'Seismic' in the writing below). This allowed a more precise definition of the GPS time of the maximum of the excess of

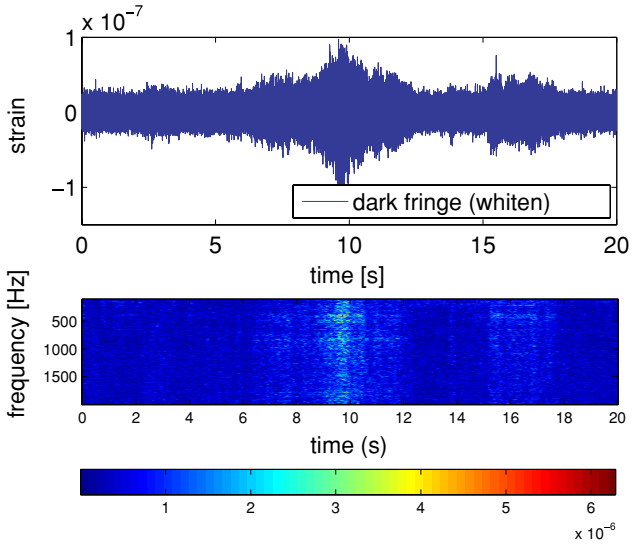

Figure 2. An example of a burst of bursts (BoB) around $t \simeq 10$ s. The upper plot shows the whitened interferometer dark port channel amplitude as a function of time, while the bottom plot is the corresponding spectrogram.

noise. This source of glitches has been found to be dominant in the playground dataset, but other (and rarer) types of glitches have also been found in the C7 data. Indeed, events in the second stage frequency stabilization system correction signal were observed in coincidence with $h(t)$ glitches. Some remaining loud glitches discovered in the GW strain amplitude channel have been found to be coincident in time with a dip in the power of the beam reflected by the interferometer toward the laser as recorded by the so-called B2 photodiode. The light impinging on the B2 photodiode is sensitive to the power-recycling cavity length change. The origin of the power dips have not been understood, but the effect on the GW strain amplitude was demonstrated and the safety of this veto using an optical auxiliary channel has been carefully studied, and is discussed below. To define an event by event veto for the two latest categories of glitches we used the mean filter triggers. These vetoes are hereafter referred to as 'SSFS' and 'B2'.

3.4.2. Bursts of bursts. We noted that the burst triggers were not uniformly distributed over time but seemed to show up in bunches lasting up to a few seconds. These events have been called bursts of bursts (BoB). Figure 2 shows the whitened GW strain channel's amplitude and its spectrogram during a data period that contains a burst of bursts.

The spectrogram shows that the event has a broadband frequency content contrary to most of the events caused by external disturbances. This broadband spectral signature provided clues that helped to identify the BoBs as local increases of the noise level due to an increase of the coupling factor between the frequency noise (which is only a factor 2 lower than the shot noise at high frequency for C7) and the interferometer's dark port channel. The presence of a peak around $T \simeq 27$ s in the correlogram of the burst events (see figure 3) provided evidence that the residual angular motion of the mirrors could be playing a role. Indeed, 27 s corresponds to the period of a mechanical resonance between the two last stages of the Virgo suspension that, if excited, may induce mirror angular degrees of freedom motion [42]. It turns

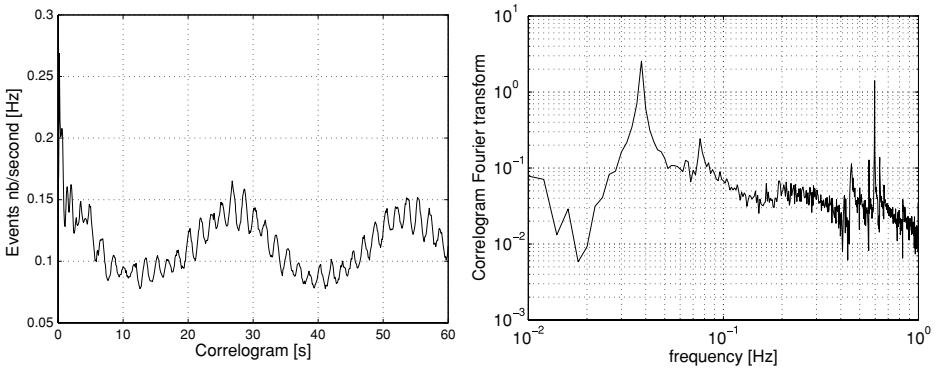

Figure 3. Left: the correlogram of the triggers found by the EGC pipeline in the C7 dataset. A peak around $T \simeq 27$ s is present, with a replica at 54 s. A 0.6 Hz modulation is also visible, and this frequency corresponds to the pendulum mode of the last stage of the Virgo suspension. Right: the Fourier transform of the correlogram. The 37 mHz mechanical resonance between the two last stages of the Virgo suspension is clearly visible.

out that the mirrors' alignment control system was not optimally working during C7 and the angular tilts of the mirrors induced an increase of the coupling of the laser frequency noise with the dark port amplitude. The BoB events represent a rather large fraction of the burst triggers in C7, as can be seen in figure 3, where the number of triggers in the correlogram fluctuates by up to ∼50%. This is also visible by the height and width of the 37 mHz peak in the Fourier transform of the correlogram. The BoBs contribute partly to the highest SNR triggers, but mainly to the moderate SNR values.

These non-stationary noise periods must be eliminated from the analysis since they generate an excess of noise triggers and they correspond to periods where the Virgo sensitivity is degraded compared to the norm. To identify those periods we used the band limited RMS of the dark port channel amplitude around 1111 Hz, which is the frequency of the line injected to measure the laser frequency noise component in the dark port channel. This line allows one to measure the common mode noise level in the GW strain amplitude, and especially the laser frequency noise. Actually, measuring the height of the line allows one to monitor the variation of the common mode coupling factor [43]. We computed the band limited RMS of the dark port channel amplitude around 1111 Hz over 10 Hz (1106–1116 Hz), at a sampling rate of 20 Hz. The high values of the band limited RMS correspond to periods where the non-stationary excess of noise is large. That allowed us to define the '1111 Hz' veto.

3.4.3. Veto parameters tuning. Once the channel and filter have been identified, one needs to tune the parameters of the veto, namely the threshold and the duration of the vetoed window around the time of the glitch. The parameters are adjusted to maximize the veto significance, keeping the dead time (i.e., percentage of vetoed science time) below a reasonable value. The significance is defined as the ratio of the number of triggers (presumed to be instrumental glitches) that the procedure vetoes by the square root of the number of triggers it would accidentally veto if there is no physical link between the glitches of the auxiliary channel and $h(t)$.[17] The significance measures the excess of coincident events in standard deviation units.

[17] The significance $= \frac{N-n}{\sqrt{n}}$ where N is the number of coincidences and n is the estimation of accidental events assuming Poisson statistics.

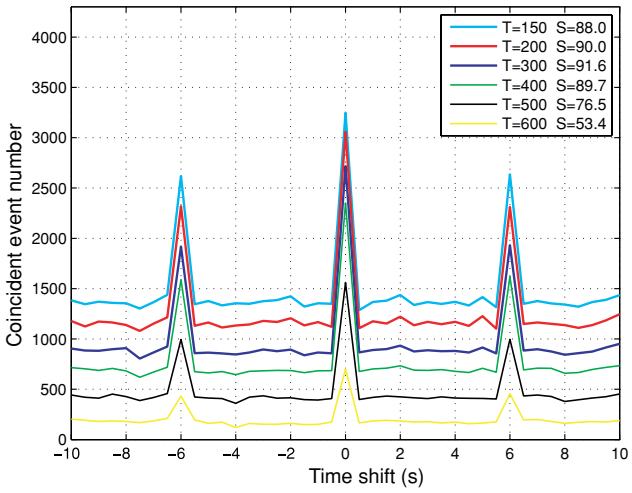

Figure 4. Number of coincident triggers between the GW strain amplitude and the auxiliary channel that has been used to define the Seismic veto, as a function of the time shift introduced in the Seismic veto list. The different curves have been obtained for different threshold values (T). *S* is the significance. The peaks correspond to the stepping motor that have been activated each 6 s during the playground dataset. The different curves have been obtained for various values of the threshold applied on the auxiliary channel RMS. The maximal value of the significance is obtained for a threshold of $T = 300$.

We used the GW strain amplitude triggers of the EGC pipeline to tune the vetoes as we wanted an optimal background rejection for this analysis. The rate of accidental coincidence was measured by artificially time shifting the list of auxiliary glitches while the number of vetoed triggers is obtained for the zero-lag. We vary the threshold on the auxiliary channel output (SNR or RMS) and the duration of the veto window. For each value we compute the dead time, the efficiency (fraction of EGC triggers that are vetoed) and the use percentage of the veto (fraction of auxiliary channel triggers that veto an EGC trigger). A good veto must have a high use percentage [44]. The size of the veto window must be larger than the peak time difference in order to conservatively veto the region around the glitch, and can be as large as the total duration of the auxiliary channel trigger. Values from 100 ms up to 600 ms have been tested.

Figure 4 shows the number of coincident triggers between the GW strain amplitude and the auxiliary channel that has been used to define the Seismic veto, as a function of the time shift introduced in one of the lists. In this case, the auxiliary channel triggers are the RMS of the channel computed at 10 Hz. Different values of the threshold have been tested (from 150 up to 650 by steps of 50). The maximal value of the significance is obtained for a threshold of 300. The threshold is confirmed by the fact that below this value the veto efficiency reaches a plateau. The choice of the duration of the veto window is based on a compromise between a high use percentage and a low dead time for the value of the threshold chosen. We checked that the optimal value, 500 ms, matches the width of the time difference between the auxiliary channel RMS and the EGC triggers.

The same procedure has been applied to tune the parameters of the 'SSFS' and 'B2' vetoes using the playground dataset. Some differences, compared to the Seismic case should be noted. For these two vetoes, built on the triggers generated by the mean filter glitch finding algorithm,

Table 1. Definition and parameters of the four event by event vetoes that have been developed and tuned for this analysis.

Veto	Auxiliary channel quantity	Threshold tuning method	Threshold	time window
1111 Hz	Band RMS (computed at 20 Hz)	Dead time	12	Period above the threshold +/-300 ms
Seismic	RMS (computed at 10 Hz)	Significance	300	500 ms (fixed)
SSFS	SNR of the mean filter triggers	Significance	6	Mean filter trigger duration - minimal value: 300 ms
B2	SNR of the mean filter triggers	Significance	10	Mean filter trigger duration - minimal value: 300 ms

we used the information of the trigger duration to define the veto duration, in addition to a fixed minimal window size. For the 1111 Hz veto, the duration of the window was defined by the time when the band RMS was above the threshold. The veto duration was then symmetrically enlarged. Given the nature of the BoB events (high EGC trigger multiplicity and rather noisy periods) we could not use the significance to optimize the threshold as it leads to setting the threshold at a very low value corresponding to an unacceptable large dead time. Instead, we set the threshold such that the dead time remained below 20%. We checked that this choice assures that the veto was able to suppress a large fraction of the BoB events. The veto definitions and the chosen parameters are reported in table 1.

3.4.4. Veto safety. The safety of a veto is of fundamental importance as we do not want to inadvertently eliminate any real GW event. Vetoes based and dedicated to suppress coincident glitches in the GW strain amplitude channel must be safe with respect to real GW events. The DQ flags and vetoes which suppress deleterious periods of data can be potentially unsafe since the source of noise is independent of the effect of a real GW impinging upon the detector. In contrast, we must be sure that a veto based on an auxiliary channel that has some glitches remains silent when a real GW event is passing through the detector. More precisely, environmental channels such as acoustic or seismic probes are expected to be safe, whereas vetoes constructed on optical or interferometer control channels may be unsafe, since a GW event will generate a change in photodiode signals that can be used within the feedback loop of some control systems. To test the safety of an auxiliary channel, one can examine the periods where hardware injections of fictitious GW signals are inserted into the interferometer. A deterministic force applied on the north input (NI) mirror, induces a variation of the length of the north arm Fabry–Perot cavity which then mimics the effect of a real GW on the interferometer. During C7 there were two periods of hardware injections, and these included two different type of burst waveforms: 60 Sine Gaussian ($f = 920$ Hz, $Q = 15$ and $f = 460$ Hz, $Q = 15$), and 33 Gaussian ($\sigma = 1$ ms). Both of these signals were injected with a SNR of 15 using a sensitivity curve taken just before the run started (the real SNR of the hardware injections is somehow different due to the sensitivity variation during the run). The critical point concerns the safety of the SSFS and B2 vetoes, which could in principle be unsafe. None of the hardware injection signals have been vetoed by the Seismic, SSFS and B2 vetoes. This establishes that our vetoes were safe. The anti-BoB veto 1111 Hz which was built using directly the gravitational wave channel was, by construction, unsafe for GW burst event whose frequency content is around 1111 ± 5 Hz. We could not check that the veto was unsafe for these signals using the hardware injections as no signal with enough amplitude in this frequency range has been injected, but we should consider that the GW burst analysis

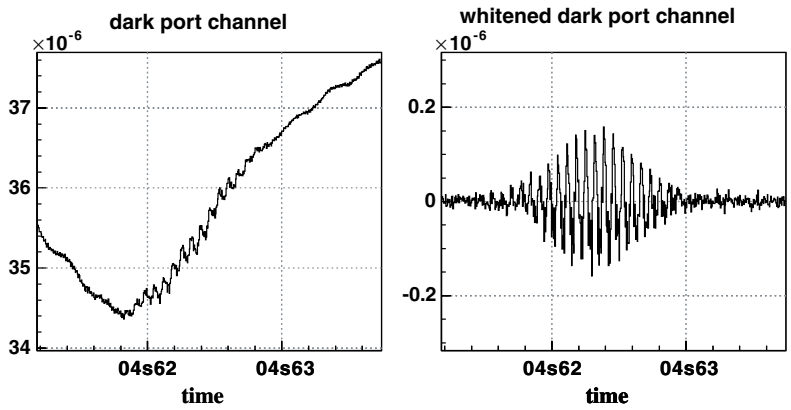

Figure 5. Time series in the dark port channel (left) and the whitened dark port channel (right) of the loudest event detected by the EGC pipeline in the search for GW bursts in the C7 data. This event was seen with a SNR of 69.7 at a frequency about 1466 Hz.

presented here is insensitive for GW signals in the 1106–1116 Hz frequency band. Besides, the safety of a veto assumes that its dead time remains small. This is the case for all the vetoes used in this analysis except the 1111 Hz veto whose large dead time (16.1%) might suppress a real GW burst event. The anti-BoB veto 1111 Hz suppressed two hardware injections, which is less than what we could foresee given the large dead time of this veto.

4. Output of the GW burst search pipeline

4.1. First results

We have generated the veto lists for the full C7 data set applying the tunings that have been defined using the playground segment as explained in section 3.4.3. After applying the vetoes on the whole dataset, the remaining largest SNR triggers were studied in order to assess their compatibility with a GW burst signal. At this stage, we ended up with a single rather large SNR event that has been subsequently thoroughly studied. This very peculiar event has been observed outside the playground segment. Only one event of this type has been found in the full run, at least with such a SNR. It looks like a Sine Gaussian signal, as shown in figure 5, with a SNR of 69.7, for one of the Sine Gaussian templates ($f = 1466$ Hz, $Q = 15.5$, $\sigma = Q/\Pi f =$ 3.4 ms); all environmental channels have been checked around this period using different glitch finding algorithms. Nothing suspected was found in any of the channels. However, the event was visible in the other phase of the demodulated dark port signal. We concluded that this event could not have been generated by a GW burst, but more likely could be due to an experimental problem, not occurring in the chosen playground segment. Indeed, the modulation phase angle was tuned such that the effect of a GW crossing the interferometer was contained in one demodulated phase (ACp) of the dark port signal, while the other (ACq) should not be perturbed. This observation lead us to develop an event-by-event veto (called 'PQ') based on the ratio of the SNR of time coincident triggers in the two demodulated phase signals as proposed in the literature [45–47]. Despite the fact that such a kind of events have not been found in the playground segment as a significant source of loud noise events, we

decided to develop this veto and to apply it on the full data set. The other loudest high SNR events have been found compatible with BoB-like events.

4.2. Necessity of an a posteriori veto

The in-phase signal contains *a priori* the GW strain amplitude, provided that the demodulation phase is well tuned. An error in the demodulation phase induces a small coupling of the GW signal with the quadrature channel. However, the ratio of the GW energy seen in the two phases is expected to remain high. The ratio is expected to be proportional to $\frac{1}{\sin(\delta\phi)}$, where $\delta\phi$ is the error on the demodulation phase [46]. Unfortunately we do not know precisely the value of $\delta\phi$ during C7. A real GW event will be seen with a SNR in ACp much higher than in ACq. In contrast, ACq will be sensitive to glitches in signals which are related to common mode noise. It may happen that some source of noise can affect both quadrature signals with similar strength. This is especially the case for a dust particle crossing the laser beam before the output dark port photodiode where the beam is especially small in width. A key point of such a veto is to assure that no real GW events would be suppressed, and therefore one would need to develop a veto with a rather good security factor. To do so, we used the hardware injections to verify safety and develop the characteristics of this veto.

EGC triggers have been generated for the dark port ACp and ACq channels and all events with SNR above 5 were considered. We then required time coincidence between the two sets of triggers using a window of ± 10 ms. No coincidence in frequency has been required. The hardware injection signals were detected in the ACp triggers with an efficiency of 98%. Unfortunately during C7, the injected SNR was not, on average, very large and consequently the signal energy in the ACq channel could not be expected to be very high (below the pipeline threshold at SNR $= 5$). Among the 91 detected hardware injections only five had a coincident trigger in the ACq phase channel within 10 ms; this tends to indicate that a large fraction of the GW energy would be contained in the ACp channel as expected; this is displayed in figure 6. The ratio between the SNR detected in the two demodulation phase channels in coincidence is

$$\kappa = \frac{\mathrm{SNR}_{\mathrm{ACp}}}{\mathrm{SNR}_{\mathrm{ACq}}}. \tag{4}$$

The very low event statistics (five events detected simultaneously in ACp and ACq) encourages us to stay conservative when defining the PQ veto parameters. We checked that the use of a ± 10 ms window limits the accidental coincidence event rate to 0.2 over the period of the hardware injections (assuming a Poisson trigger rate). This excludes the fact that we have more than one accidental association with an ACq trigger for the fix burst hardware injections as shown in figure 6. In this figure, the strange and unique high SNR event is totally isolated from the rest of the events. This event has $\kappa \simeq 0.42$ and a SNR in the ACq channel of 141; these facts totally exclude the possibility that this event has been generated by a real GW.

The goal of the PQ veto is to suppress high SNR events in the ACq channel that induce a transient in the dark port channel amplitude. That is why it is reasonable to consider only large SNR ACq triggers. A threshold is applied on the SNR of the ACq triggers ($\mathrm{SNR}_{\mathrm{ACq}}$). The other veto parameter threshold pertains to the ratio κ. We did not try to optimize these two parameters, but rather we keep a conservative attitude with respect to the hardware injection signals' position in the two-dimensional plane that shows the SNR of both quadratures for the coincident triggers (see figure 6). The veto list segments have been defined as the periods during which $\mathrm{SNR}_{\mathrm{ACq}} > 8$ and $\kappa < 1$. All burst hardware injection signals pass these conditions with a safety factor since they are all below the $\kappa = 2$ line. The starting and ending

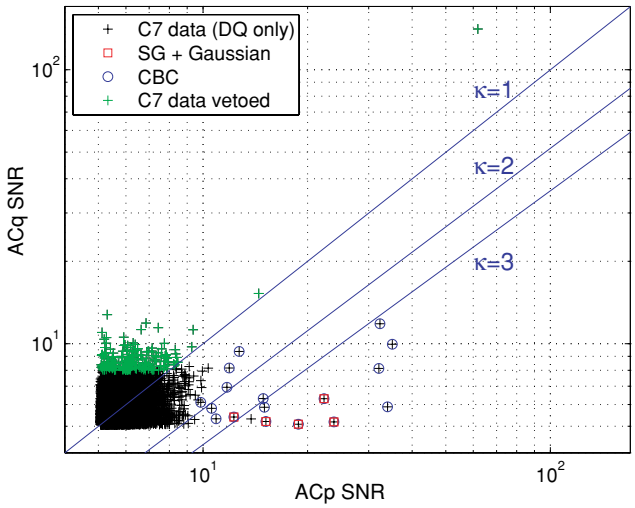

Figure 6. SNR of the coincident EGC triggers in the two quadrature demodulated channels of the output dark port signal: ACp (in phase) and ACq (in quadrature). The time coincidence window of the triggers seen in the two channels is 10 ms. The Seismic, SSFS, B2 and 1111 Hz vetoes have already been applied. The peculiar event appears very isolated with respect to the other triggers with its ACq SNR of 141. The hardware injection signals, which were seen in both of the two demodulation phase channels, are indicated by the circles for burst-like signals and by the squares for the compact binary coalescence (CBC) signals.

Table 2. Dead time of the different vetoes that have been found useful. The values are computed for the full C7 dataset.

Veto name	Seismic	SSFS	B2	PQ	1111 Hz	All vetoes
Dead time	3.75%	2.6%	0.03%	0.07%	16.1%	21.2%

times of the veto segments are given by the ACq trigger times. The dead time of the PQ veto is 0.07%, which is very acceptable.

4.3. Final results

Table 2 gives the dead time of the five event-by-event vetoes which have been used in this analysis. The total dead time amounts to 21.2% taking into account overlapping veto segments. This is a rather high value, mainly because of the presence of the non-stationary excess of noise due the looseness of the mirror's angular degree of freedom control during C7.

Figure 7 shows the triggers' SNR distribution obtained from the full C7 data set, after having applied consecutively the five vetoes (note that the highest SNR event is off of the scale of the plot). The four anti-glitch vetoes (Seismic, SSFS, B2 and PQ) suppress 10.6% of the total number of triggers and play an important role for the large SNR (>10) events since 51.3% of them are eliminated. The anti-BoB veto is critically important, and its efficiency on EGC triggers is impressive; 45.6% of the remaining triggers are eliminated, and 97.6% of the remaining loudest ones (SNR >10). Figure 8 shows the SNR of the remaining triggers as a function of their frequency. The application of all these vetoes allows us to reduce, by

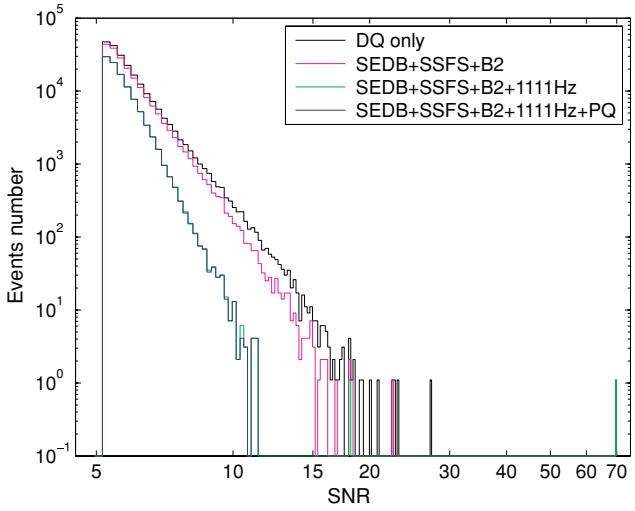

Figure 7. SNR distribution of the triggers obtained on the GW strain amplitude channel by EGC after applying all vetoes on the full C7 data set.

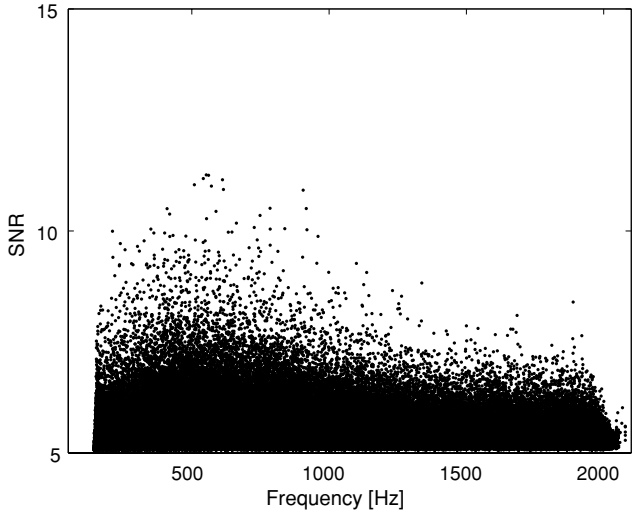

Figure 8. SNR as a function of the frequency of the triggers obtained on the GW strain amplitude channel by EGC after applying all vetoes on the full C7 data set. The distribution around 2 kHz is due to the templates' placement; some Sine Gaussian templates have a central frequency which can slightly exceed 2 kHz.

a factor 2, the number of events for all EGC triggers above SNR = 5. 98.8% of the EGC events above SNR >10 were eliminated. 21 triggers above SNR = 10 remain at the end. The loudest has a SNR of 11.26, and although it was not vetoed, it seems to be due to a short period non-stationary Virgo noise increase. We have determined that it is not a gravitational

wave event, but rather a BoB event. It has the same frequency content as the BoB events but its amplitude was not large enough to be suppressed by the anti-BoB veto.

5. GW burst search analysis sensitivity

5.1. Generation of the injected waveforms

The GW burst search presented in this paper is intended to be efficient for all waveforms as long as they have energy concentrated in time and frequency in the range 150–2000 Hz. However, since the Virgo sensitivity is not constant over this frequency band, the detection efficiency for a given signal strength will depend on the frequency of the signal. In order to assess the sensitivity of the detector to dissimilar kinds of signals at different frequencies, we used simulated waveforms of diverse types. These were added to the Virgo GW strain amplitude (software injection) and analyzed by the EGC pipeline, similar to how the C7 triggers were produced. These injected signals were randomly distributed in time during the C7 run, assuring a minimal separation of 60 s [48].

The waveforms investigated in this analysis were of two types. One group consisted of ad hoc waveforms, such as Sine Gaussians and Gaussians, whose detection efficiency is expected to depend mainly on the central frequency, bandwidth and duration of the waveform. On the other hand, to test the efficiency of this analysis to detect BBH merger and ring-down GW signals we used waveforms provided by numerical relativity simulations [49]. We also used a signal pertaining to a star core collapse, referred to as A1B2G1, from the supernova simulation catalog available in [50].

The amplitude of the GW associated with an astrophysical source depends on the distance of the source from the Earth. To quantify the strength of a GW burst, we used the root sum squared of the strain amplitude at the earth without folding in the detector antenna pattern

$$h_{rss} = \sqrt{\int (|h_\times(t)|^2 + |h_+(t)|^2)\,\mathrm{d}t}, \tag{5}$$

where h_+ and $h_\times$ are the two GW polarizations that we express below for the different cases relevant to our analysis. For a binary BH waveform h_{rss} is computed assuming a null inclination angle for the orbital plane.

5.1.1. Sine Gaussian and Gaussian waveforms. For the Sine Gaussian and Gaussian signals, the detection efficiency is expected to depend mainly on the central frequency, bandwidth and duration of the waveform. For these signals the strain sensitivity $h(t)$ of the detector can be written as

$$h(t) = F_+(\theta, \phi, \Psi)h_+(t) + F_\times(\theta, \phi, \Psi)h_\times(t), \tag{6}$$

where $F_\times$ and F_+ are the antenna response functions characterized by the source position (θ, ϕ) and polarization angle Ψ relative to the detector [51]. Specifically, for Sine Gaussian injections we used circular polarized waveforms described by

$$h_\times(t) = h_0\,\mathrm{e}^{-2(\pi f_0 t/Q_0)^2}\sin(2\pi f_0 t), \qquad h_+(t) = h_0\,\mathrm{e}^{-2(\pi f_0 t/Q_0)^2}\cos(2\pi f_0 t). \tag{7}$$

The typical duration of a Sine Gaussian signal depends on the parameter Q_0 and the central frequency f_0 as $\frac{Q_0}{2\pi f_0}$. Several values of f_0 ranging from 100 Hz up to 1797 Hz and $Q_0 = 3$, 8.9 and 9 were used. Their narrow-band feature allows the testing of the pipeline performance in a given frequency region.

For Gaussian injections, we used linearly polarized waveform given by

$$h_+(t) = h_0\, \mathrm{e}^{-t^2/\tau^2}, \tag{8}$$

$$h_\times = 0, \tag{9}$$

where τ is the width of the signal. Gaussian waveforms are of interest in the GW burst search because many predicted signals associated with core collapse GW emission just after the bounce have large peak structures. We chose the values of τ to lie between 0.1 and 6 ms. In the case of linearly polarized Gaussians, the angles θ, ϕ have been randomly chosen. For the circularly polarized Sine Gaussians the randomization has been done over the angles θ, ϕ and Ψ.

5.1.2. Astrophysical waveforms. For the core collapse signals, we have chosen only one waveform produced by a core collapse 3D simulation conducted with numerical general relativistic techniques in order to estimate, with a physical model, the detection efficiency for a realistic supernova GW signal. This signal corresponds to the case of a stiff equation of state, a small initial differential rotation and a moderate rotational kinetic energy [50]; this leads to a waveform with a large negative peak followed by a ring-down phase (regular collapse). More up-to-date simulations [52–54] using hydrodynamical models with realistic nuclear equations of state, deleptonization and progenitor models from stellar evolutionary calculations tend to confirm the general features of the regular core collapse. In this present study we are not interested in the details of the waveform. The waveform is linearly polarized and the simulations have been done similarly to the Gaussian signals.

With the recent breakthroughs in the field of numerical relativity (NR), many groups have been able to simulate the evolution of binary BHs through three stages: inspiral, merger and ring down [14, 49, 55]. These waveforms have been shown to be consistent with the already existing analytical results using post-Newtonian and BH perturbation theories [56–59] for the inspiral and ring-down phases, respectively. Furthermore, despite the differences in the numerical methods employed, gauges chosen, and methods adopted to evolve the systems, qualitatively the results from all groups show good agreement [60]. All these provide a motivation to use these results from a data analysis perspective. Many such attempts have already been made to search the three phases of the binary black hole evolution using NR outcomes [56, 61, 62]. We apply these results from the point of view of a GW burst data analysis and use the NR waveforms to assess the efficiency of the EGC burst pipeline to detect the BBH merger. For this application we used the numerical relativity (NR) simulations of the non-spinning, equal mass BBHs provided by the Goddard Space Flight Center group [49]. The injected waveforms were GW strains from the leading $l = 2, m = 2$ spin-weighted spherical harmonics from the simulations. These waveforms had (approximately) three cycles of inspiral, followed by merger, and then a ring down.

Unlike the ad hoc waveforms or the linearly polarized case of SN waveforms, one has to include the effect of the orbital inclination angle ι for the BBH merger waveforms. Equation (6) should be rewritten in order to include the effect of orbital inclination as

$$h(t) = F_+(\theta, \phi, \psi)A_+(\iota)h_+(t; \iota = 0) + F_\times(\theta, \phi, \psi)A_\times(\iota)h_\times(t; \iota = 0), \tag{10}$$

where F_+ and $F_\times$ are the usual antenna pattern functions, $A_+ = -\frac{1}{2}(1 + \cos^2 \iota)$, $A_\times = -\cos \iota$ and $h_+(t; \iota = 0)$ and $h_\times(t; \iota = 0)$ are the polarizations for the situation of zero inclination angle ι. In this case, the simulated waveforms are generated by randomizing all four angles involved. The NR waveforms for the BBH mergers in the total mass range 5 $M_\odot$–150 $M_\odot$ were injected into the C7 data in order to calibrate the detection efficiency of the pipeline to these types of mergers. The range of masses chosen for the injection was decided in accordance with the sensitivity of the C7 run.

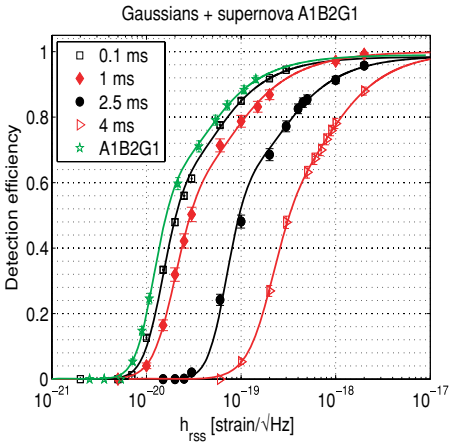

Figure 9. Detection efficiency of the search analysis as a function of the signal strength h_{rss} at earth for the Gaussian waveforms (with τ specified in the legend) and one core collapse simulated waveform (A1B2G1). The efficiencies were computed for sources at random sky locations. The error bars take into account only the statistical error on the detection efficiency.

5.2. Detection efficiency of the GW burst search with the software injections

We applied the same data quality criteria (DQ and vetoes) on the trigger list containing the waveform injections. The detection efficiency is defined as the fraction of injected signals reconstructed with a SNR larger than 11.3 corresponding to the loudest event found in the C7 data triggers. As the veto dead time is rather large, the vetoed periods have not been considered when computing the detection efficiency. Figures 9, 10 and 11 show the detection efficiency as a function of h_{rss} for each family of waveforms. The error on the efficiency data points takes into account only the statistical error. To estimate the values of h_{rss} at efficiency 50% and 90% the four parameters of an asymmetric sigmoid function have been fitted to the data points. The efficiency $\epsilon(h_{rss})$ is defined as follows:

$$\epsilon(h_{rss}) = \frac{\epsilon^{\max}}{1 + r^{\mathrm{mid}\,\alpha(1+\beta\tanh(r^{\mathrm{mid}}))}}, \tag{11}$$

where $\epsilon_{\max}$ is the maximal efficiency obtained for strong signals (it should tend to unity). r^{mid} is the ratio $h_{rss}/h_{rss}^{\mathrm{mid}}$ where h_{rss}^{mid} is the strain amplitude at half height, i.e., we have $\epsilon\left(h_{rss}^{\mathrm{mid}}\right) = \epsilon^{\max}/2$. α and β are respectively the slope and the asymmetry of the sigmoid function. The parameters were estimated by minimizing a χ^2 function. $\epsilon^{\max}$ is constrained to remain smaller than unity. For signals for which $\epsilon^{\max}$ does not reach unity, we checked that this is due to a fraction of signals with an injected SNR smaller than the threshold of 11.3. This is especially the case for the Gaussian and the A1B2G1 core collapse simulated waveforms, as expected. Indeed, as the frequency content of the Gaussian signals is maximal at low frequency, for a fixed h_{rss} and a random sky position, we expect a non-negligible fraction of low SNR Gaussian signals.

As expected for the Gaussian signals, the performance decreases as the width τ of the Gaussian increases. For τ greater than 4 ms, the detection efficiency is already quite poor, as shown in figure 9. Note that the results obtained for the supernova signal A1B2G1 are very similar to the Gaussian with $\tau = 0.25$ ms (see table 4); this is not surprising as the

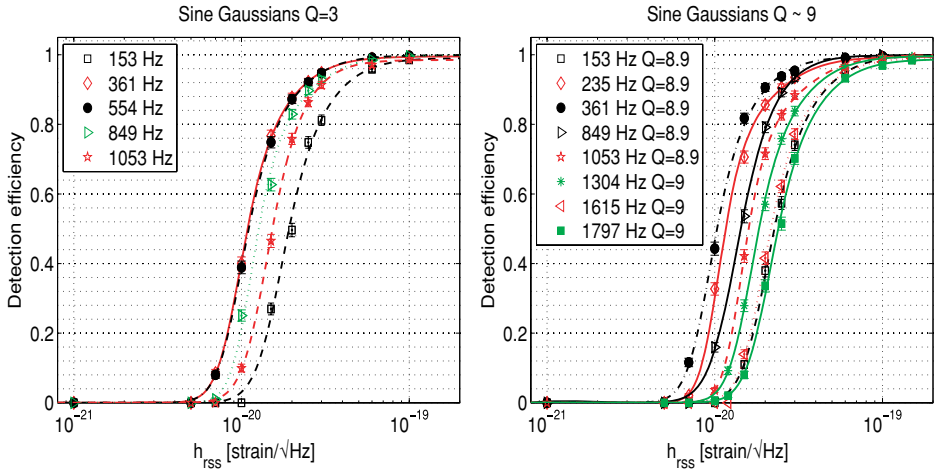

Figure 10. Detection efficiency of the search analysis as a function of the signal strength h_{rss} at earth for Sine Gaussian waveforms with different central frequencies f_0 and for two different values of the Q_0 factor: left $Q_0 = 3$, right $Q_0 \sim 9$. The efficiencies were computed for sources at random sky locations. The error bars take into account only the statistical error on the detection efficiency.

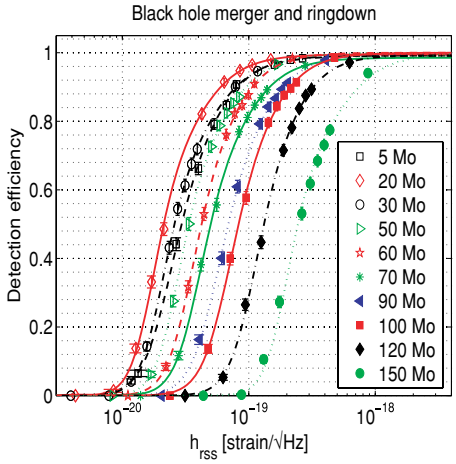

Figure 11. Detection efficiencies from the search analysis as a function of the signal strength h_{rss} for the BBH merger and ring-down waveforms for different BH total masses (but where the two individual component masses are equal). The efficiencies were computed for random polarization, inclination angles and sky positions. The error bars take into account only the statistical error on the detection efficiency.

A1B2G1 signal has a large amplitude peak whose width is approximately 0.35 ms. Figure 10 shows the detection efficiency of the analysis obtained with the Sine Gaussian waveforms; the performance follows the trend of the C7 Virgo noise floor shown in figure 1, which is expected for a signal well localized in frequency, such as a Sine Gaussian.

Table 3. h_{rss} corresponding to 50% and 90% efficiency in units of 10^{-20} strain $\mathrm{Hz}^{-1/2}$ obtained for the ad hoc Sine Gaussian waveforms. The efficiencies were averaged over the full C7 data set for random sky positions. The symbol—means that no simulated waveforms were available. The symbol (*) indicates that we used simulated waveform with $Q = 9$ instead of 8.9.

	50% efficiency		90% efficiency	
f_0 (Hz)	$Q = 3$	$Q = 8.9$ or 9	$Q = 3$	$Q = 8.9$ or 9
100	4.5	10.6	9.1	21.7
153	1.9	2.3	3.9	4.6
235	1.2	1.2	2.3	2.5
361	1.1	1.0	2.2	2.0
554	1.1	1.1	2.3	2.3
849	1.3	1.4	2.6	2.6
945	–	1.5(*)	–	2.9(*)
1053	1.5	1.6(*)	2.8	3.6(*)
1172	–	1.8(*)	–	3.6(*)
1304	–	1.8(*)	–	3.8(*)
1451	–	1.9(*)	–	3.7(*)
1615	–	2.2(*)	–	4.5(*)
1797	–	2.4(*)	–	5.1(*)

The performance obtained for the BBH merger waveforms for a total mass M from 5 $M_\odot$ up to 150 $M_\odot$ (displayed in figure 11) were not as good as for the Sine Gaussian signals. The best $h_{rss}^{50\%}$ was achieved for $M = 20M_\odot$ with $h_{rss}^{50\%} \simeq 2.2 \times 10^{-20}$ $\mathrm{Hz}^{-1/2}$. That was at least two times worse than the best Sine Gaussian result. The merger frequency can be approximated by the empirical formula [13, 25], deduced from figure 8 in [63]

$$f_{\mathrm{merger}} \simeq \frac{15\mathrm{kHz}}{M}, \tag{12}$$

where M is the mass (in units of solar mass) of the final BH formed after merger. M is smaller than the sum of the initial BH masses. For $M = 20$ $M_\odot$ this corresponds to 750 Hz, which is well inside the frequency range of the search. In contrast, for masses above 100 $M_\odot$, f_{merger} is smaller than 150 Hz, which is the lower frequency boundary of this search. The EGC pipeline for this kind of waveform is still able to catch the ring-down part of the signal, which has an appreciable contribution to the SNR, while the performance for a Sine Gaussian at the f_{merger} frequency would hardly be detectable. For the low mass signal the drop of performance is explained by the fact that the frequency at the merger exceeds the upper frequency boundary of this search, and moreover, the equivalent Q is expected to be larger than 16 (the upper value chosen in this search).

The value of h_{rss} corresponding to 50% and 90% of efficiency ($h_{rss}^{50\%}$ and $h_{rss}^{90\%}$) have been determined using the fitted sigmoid functions and are given in tables 3, 4 and 5 for Sine Gaussians, Gaussians, Supernova and BBH merger signals, respectively. The best value of $h_{rss}^{50\%}$, 1.05×10^{-20} $\mathrm{Hz}^{-1/2}$, was obtained with the Sine Gaussian of frequency $f_0 = 361$ Hz and $Q_0 = 9$; this signal is 15 times higher than the noise floor at this frequency. Note that bad performance obtained for the 100 Hz Sine Gaussian is expected since the lower frequency range of the search was 150 Hz. Moreover the C7 sensitivity is quite poor below 150 Hz.

The quality of the fitting procedure has been controlled by checking that χ^2 of the fitting function remains close to unity within at maximum a factor 3. Increasing the error on the efficiency by up to a factor 3 does not change the result on h_{rss} to within 1%. The statistical error on $h_{rss}^{50\%}$ and $h_{rss}^{90\%}$ have been computed using the covariance matrix of the efficiency

Table 4. h_{rss} corresponding to 50% and 90% efficiency in units of 10^{-20} strain $\mathrm{Hz}^{-1/2}$ for the Gaussian waveforms of different widths and one core collapse simulated waveform (A1B2G1). The efficiencies were averaged over random sky position.

τ (ms)	50% efficiency	90% efficiency
0.1	2.1	15.9
0.25	1.8	11.6
0.5	1.8	12.7
1.0	2.9	24.4
2.5	9.6	79.0
4.0	32.4	242.0
A1B2G1	1.63	12.4

Table 5. h_{rss} corresponding to 50% and 90% efficiency in units of 10^{-20} strain $\mathrm{Hz}^{-1/2}$ for the BBH numerical relativity waveforms. The total mass of the system varies from 5 $M_{\odot}$ up to 150 $M_{\odot}$.

Total mass ($M_{\odot}$)	50% efficiency	90% efficiency
5	3.0	8.2
10	2.3	5.6
20	2.1	6.0
30	2.6	7.9
40	3.0	8.0
50	3.4	9.6
60	4.2	10.7
70	5.0	14.6
80	5.8	14.8
90	6.9	18.7
100	8.3	21.3
120	13.2	32.4
150	24.5	74.4

curves; for the Sine Gaussian and BBH waveforms the error on $h_{rss}^{50\%}$ was below 1.3%. Note that for $h_{rss}^{90\%}$ the errors were higher, between 6% and 13%. For the Gaussian and core collapse waveforms the uncertainty is on average larger, indicating that the quality of the fitting was worse. The errors are between 1% and 4% for all the Gaussians, except for the Gaussian with $\tau = 4$ ms for which the error on $h_{rss}^{50\%}$ reaches 11%. However, the biggest uncertainty on the $h_{rss}^{50,90\%}$ values comes from the error on the GW strain ampliude calibration, which is of 40%. Including the systematic error due to the calibration uncertainty leads to an error on $h_{rss}^{50,90\%}$ between 40% and 43%.

6. Search results

6.1. Event rate and GW strength upper limits

From section 4 we can assert that we have not observed any GW event with a SNR above 11.3, corresponding to the loudest event SNR. Knowing the detection efficiency as a function of the signal strength for different kinds of signals, we can now derive a 90% confidence level (CL) upper limit on the event rate that depends on the strength of the signal. Using the loudest

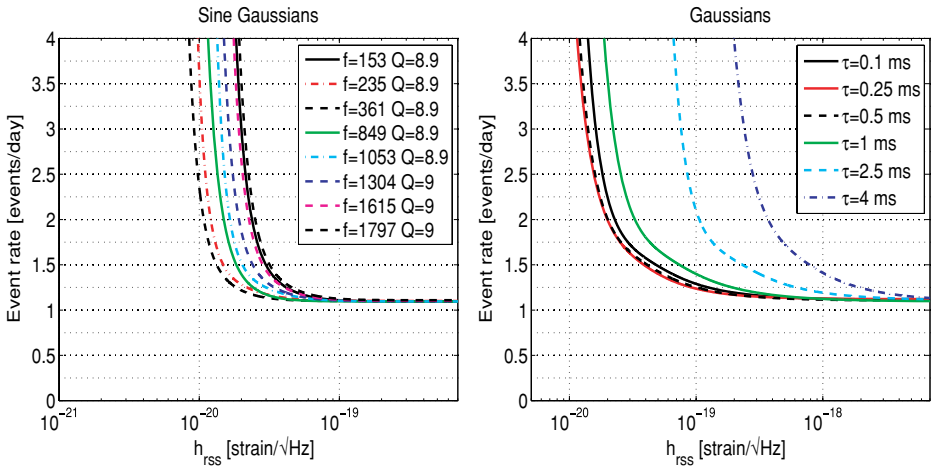

Figure 12. Event rate as a function of the h_{rss} exclusion plots at 90% confidence level obtained in the Virgo C7 data. The left plot corresponds to GW burst events that can be modeled by a Sine Gaussian with a Q of 8.9 or 9 for frequencies, f, covering the most promising part of the C7 frequency range. The right plot corresponds to GW burst events that can be modeled by a peak of different widths, τ, from 0.1 ms up to 4 ms.

event statistic as described in [64], the 90% CL exclusion on the event rate of a signal detected with an efficiency of $\epsilon(h_{rss})$ is given by

$$\mathcal{R}^{90\%}(h_{rss}) = \frac{-\ln(1-0.9)}{T\epsilon(h_{rss})}, \tag{13}$$

where $T \simeq 2.1$ days is the effective observation time for the C7 run (veto times have been subtracted from the total analyzed time). The results are given in figure 12 for the Sine Gaussian waveforms (Q $\sim$ 9) and the Gaussian waveforms.

As expected for strong signals, the exclusion rate reaches the asymptotic value of $\frac{-\ln(1-0.9)}{T} \simeq 1.1$ events per day whatever the signal type. We can exclude at 90% confidence level a GW event rate $\mathcal{R}_{90\%}$, assuming 100% detection efficiency, of 1.1 events per day for $T \simeq 2.1$ days of observation. On the other hand, depending on the characteristics of the signals the exclusion rate, when the signal becomes weak, is rather different. The vertical asymptotic value in figure 12 gives an indication of how the sensitivity of the search depends on a given frequency for the Sine Gaussian, or on the width of the Gaussian waveform. The exclusion results for Sine Gaussian waveforms with $Q = 3$ (from 153 Hz up to 1053 Hz only) are very similar to the Sine Gaussian results with $Q = 9$.

6.2. Astrophysical interpretation

In the previous section we determined the sensitivity of the C7 data analysis to different potential GW burst sources in terms of h_{rss}. This can be translated into an astrophysical estimate on the amount of GW energy emitted by a source or the distance reach, depending on the type of sources we consider. For simplicity we have assumed in our ad hoc waveform simulations that the emission is isotropic, although this may not be the case for a real

astrophysical signal. In the case of a Sine Gaussian waveform with a central frequency f_0 and quality factor $Q \gg 1$, one obtains for the GW energy emitted by the source [65, 66]

$$E_{\rm GW} \simeq \frac{r^2 c^3}{4G}(2\pi f_0)^2 h_{\rm rss}^2, \tag{14}$$

where r is the (non-cosmological) distance to the source. Similarly, for a Gaussian waveform, the emitted GW energy is

$$E_{\rm GW} \simeq \frac{r^2 c^3}{4G}\frac{1}{\tau^2} h_{\rm rss}^2, \tag{15}$$

where τ is the width of the Gaussian.

The above expressions can be used to derive an astrophysical sensitivity with the present C7 data analysis in different ways. For sources at a fixed distance, an estimate on the emitted GW energy can be obtained by using the smallest value of $h_{rss}^{50\%}$. Conversely, if we know the energy emitted in GWs, this information can be used to infer the maximum distance up to which such an event could have been observed by Virgo with an efficiency larger than 50%. In what follows we discuss these various possibilities, quantifying the detectability of supernova events and BBH merger events where the nature of waveforms and the energy of emission are known through the numerical simulations.

6.2.1. Detectability of an arbitrary burst GW event close to the galactic center. Considering the Sine Gaussian and Gaussian waveforms that give the best results in terms of $h_{rss}^{50\%}$, we can compare the estimation of the maximal GW energy emitted by a hypothetical GW burst source in the vicinity of the galactic center, assuming a distance of 10 kpc. With the 361 Hz Sine Gaussian we obtained $h_{rss}^{50\%}$ of 1.05×10^{-20} Hz$^{-1/2}$, which translates into an energy of $\sim 3 \times 10^{-5} M_\odot c^2$. For a Gaussian waveform, the most favorable case corresponds to $\tau = 0.25$ ms and $h_{rss}^{50\%} \simeq 1.79 \times 10^{-20}$ Hz$^{-1/2}$; the associated energy is $\sim 2.8 \times 10^{-4} M_\odot c^2$. Hence the most optimistic limit on the energy differs almost by an order of magnitude between the Gaussian and Sine Gaussian waveforms, while the detection performance in terms of h_{rss} is only two times worse for a Gaussian with respect to a Sine Gaussian.

6.2.2. Detectability of supernova events. We now consider the predictions on the GW energy produced by the collapse of a stellar iron core to form a neutron star. It is assumed that the progenitor star rotates fast enough to generate sufficient deformation. We do not consider here the GWs generated after the core collapse by the development of an oscillation of the proto-neutron star lasting a few hundred of milliseconds [10] since we did not expand the search for corresponding high Q oscillating signals. A few hundred of milliseconds at a frequency around 700 Hz corresponds to a Q of a few hundred. Using the core collapse waveform A1B2G1 injected into the data to determine the efficiency for that particular signal, we can derive the distance reach corresponding to 50% of efficiency as we do for the BBH waveforms; the distance is 0.15 kpc. However, this waveform might not be representative of the overall core collapse bounce waveforms. Indeed, depending on the progenitor model parameters (mass, rotation rate, equation of state) the GW energy prediction can vary by several orders of magnitude [53]: $3 \times 10^{-10}\ M_\odot\ c^2 < E_{GW} < 7 \times 10^{-8}\ M_\odot\ c^2$ with a peak frequency which can be as high as 800 Hz. However, these recent simulations [53] seem to indicate that the waveforms are rather generic regardless of the dynamic of the collapse (pressure dominated or centrifugal bounce). Even in the case of centrifugal bounce, the waveforms exhibit a positive pre-bounce followed by a negative peak, but the typical frequency is lower than in the case of a uniform differential rotation for which the typical frequency is around

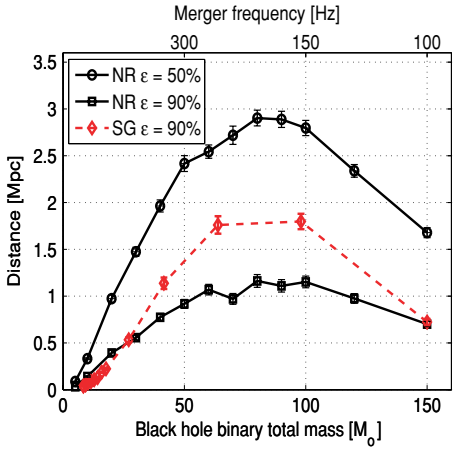

Figure 13. Detection distance of the black hole binary source with efficiency of 90% and 50% as a function of the total mass of the system. The curves with circles and squares have been obtained by estimating the EGC pipeline detection efficiency to numerical relativity black hole binary waveforms. The curve with diamonds was derived from the results obtained with Sine Gaussian waveforms assuming that the waveform when the two black holes merge resembles a Sine Gaussian. The error bars take into account only the statistical error on the detection efficiency.

700 Hz. For instance, if one considers the model with a 20 $M_\odot$ progenitor mass, a moderate differential rotation value ($A = 1000$ km) and a moderate initial rotation rate ($\beta = 0.5\%$) [53], $E_{GW} \simeq 2.32 \times 10^{-8}\ M_\odot$ and the characteristic frequency is 715 Hz using the equation of state provided by Shen [67]. We should not specifically assume that supernova GW signals are monochromatic waveforms like Sine Gaussians. They do not look like Gaussians either (they are more localized in frequency than Gaussian). Taking the $h_{rss}^{50\%}$ value for the $\tau = 0.5$ ms Gaussian (that roughly corresponds to the width of the peak of the considered waveform), we obtain a maximal distance range of 0.18 kpc. Using the Sine Gaussian expression, and using the $h_{rss}^{50\%}$ for a central frequency 715 Hz we obtain a distance of 0.12 kpc. For the A1B2G1 waveform used in this paper, and considering a radiated energy of $E_{GW} \simeq 2.13 \times 10^{-8}\ M_\odot\ c^2$ computed using equation (5) of [7], we obtain a distance of 0.12 kpc whatever the assumption made on the waveform (Gaussian of $\tau = 0.35$ ms or a Sine Gaussian of $f_0 = 650$ Hz). These numbers indicate the order of magnitude of the maximal detection distance we have reached during Virgo's C7 run. This achieved distance is somewhat small, and we expect to gain at least one order of magnitude with Virgo data acquired during more recent observation runs.

6.2.3. Distance reach for binary black hole mergers. From the detection efficiency results obtained with the BBH waveforms in section 5.2, one can derive a distance at which EGC is able to detect a signal with 50% or 90% efficiency, respectively $d^{50\%}$ and $d^{90\%}$. These values have been extracted from the results of the fits of the detection efficiency as a function of the distances for which the BBH sources have been simulated. An asymmetric sigmoid function has been used and the errors on $d^{50\%}$ and $d^{90\%}$ have been estimated as they have for $h_{rss}^{50\%}$ and $h_{rss}^{90\%}$. Figure 13 shows the $d^{50\%}$ and $d^{90\%}$ detection distances as a function of the total mass of the system. $d^{90\%}$ gives an indication of the average distance range up to which this search could have been able to detect a BBH source. With the present choice of threshold on

the SNR, our search is sensitive to BBH mergers in the mass range 20 $M_\odot$–150 $M_\odot$ up to a distance of 1–3 Mpc (0.5–1 Mpc) for 50% (90%) detection efficiency. The distance reach is maximum for a BBH of total mass 80–90 $M_\odot$. In the C7 sensitivity band, this mass range corresponds to signals where the merger part is dominant. Besides, for a mass higher than 100 $M_\odot$, the merger frequency (given by equation (12)) is below the frequency lower bound studied in the analysis (150 Hz). This fact adds to the degraded C7 run sensitivity below 150 Hz, and explains why the distance reach for the high mass waveforms is decreasing.

This bound on the distance can, in principle, be translated into an upper limit on the event rate, assuming a Gaussian distribution of BBH masses around 80 $M_\odot$. This analysis would require combining a model for the galaxies, their blue light luminosity distribution as a function of distance and mass, along with the antenna pattern of the detector; this has been proposed in [68] for the LIGO detectors. But given the limited volume of the universe that the present search is capable of sampling, we postpone this more complete analysis until we analyze the most recent Virgo data with its improved sensitivity. Moreover, the results have been obtained only for non-spinning equal mass binary systems.

An alternative way of deriving the distance reach for BBH mergers is to assume that the merger and ring-down phases of the BBH waveforms resemble Sine Gaussians and use the results obtained from the Sine Gaussian waveforms to derive the detection distance. In order to use Sine Gaussians to model the BBH mergers, we approximate the NR waveforms to be Sine Gaussians with peak frequency f_0 equal to the frequency at the merger ($f_{\rm merger}$) of the NR waveforms using equation (12) following [25]. It should be noted that this definition of $f_{\rm merger}$ is only approximate. Besides, it is not obvious how to assign a precise value of Q to the Sine Gaussian that approximates a BBH waveform. However, taking into account the typical duration τ of the 'merger' part of the waveform and using the relation, exact for a Sine Gaussian, $\tau = Q/(2\pi f_0)$, one could deduce that the Q is between 10 and 20 for the high mass BBH and as large as 40 for the low masses. This is larger than the boundary of Sine Gaussian templates bank used in this analysis. Hence, we may suspect that for the low mass ($<$20 $M_\odot$) the EGC pipeline is not optimally reconstructing the SNR of the NR waveforms. However, it is straightforward to show that $h_{rss}^{50\%}$, the quantity which is used in the derivation, does not depend on Q for Sine Gaussians as long as Q is sufficiently large (table 3 confirms this). For all these reasons, in the discussion that follows, we consider a Sine Gaussian with $Q \sim 9$. In order to determine the distance reach one should make an assumption on the total energy emitted by the source and on the source emission pattern. According to NR simulations [63], $\sim$3.5% of the total rest mass energy would be radiated away as GWs. Following [25], we can use equation (14) and the values of h_{rss} in table 3 to derive the distances up to which such BBH merger events could be observed with an efficiency of 50% or 90%. The results for the distance reach at an efficiency of 90% are presented in figure 13 together with the distance reach obtained using NR waveforms at the same detection efficiency. At intermediate masses and frequencies the distance reach obtained when BBH mergers are modeled with SG waveforms is about 60% larger than that obtained when more realistic NR waveforms are used. A detailed comparison of the two waveforms shows that this difference is partly due to the broader spectral distribution of the NR waveform for which part of the signal energy falls out of the detector and analysis bandwidth. The remaining difference is due to the EGC pipeline, which by construction matches more efficiently with the SG waveforms.

7. Conclusion

In this paper, we have reported on a search for short duration GW bursts in the Virgo C7 data from within the 150 Hz–2 kHz frequency band; this corresponds to the best sensitivity

achieved by Virgo during the C7 run. This search, carried out using the output of only one GW detector, required first the understanding and then the possibility of vetoing all identified sources of noise. Special care has been taken to assure ourselves that the procedure does not suppress a GW event, and that the dead time remains small. Unfortunately, the non-stationary data features prevent a search during vetoed time periods, which amounts to an accumulated dead time of 20.2%. Though this rather large dead time limits the astrophysical interest of the search, it has been possible to calculate a sensitivity for various GW burst sources. The best sensitivity that has been reached in terms of the square root of the strain amplitude at 50% of efficiency, $h_{rss}^{50\%}$, was 1.1×10^{-20} $\mathrm{Hz}^{-1/2}$ at 361 Hz, a frequency region where Virgo's sensitivity was optimal. If one considers the whole set of waveforms studied in this paper, the sensitivity lies between 10^{-20} and 10^{-19} $\mathrm{Hz}^{-1/2}$. However, one should note that the error on the sensitivity can be as large as 40% due to uncertainties in the calibration of the strain amplitude. Those numbers can be compared to GW burst searches carried out with LIGO detectors during the S2 data taken in 2003 [22]. Indeed, the C7 Virgo sensitivity is comparable to that of 4 km LIGO detectors during their S2 run; Virgo during C7 was a little bit more sensitive above 500 Hz and a bit less below. Not surprisingly, the search sensitivity obtained with C7 Virgo data is similar to LIGO S2 results for the same kind of waveforms: $h_{rss}^{50\%}$ having values between 10^{-20} and 10^{-19} $\mathrm{Hz}^{-1/2}$.

Besides the search of unmodeled GW burst waveforms, we have shown using recently computed numerical relativity waveforms that burst pipelines can be used efficiently to search for BBH merger GW emission. In the case of non-spinning equal mass system, a distance reach of 2.9 Mpc for 80 $M_{\odot}$ total mass has been inferred from the C7 data assuming an efficiency of 50%. This mass range corresponds to when the BH merger part of the signal dominates over the inspiral part. That also corresponds to a frequency region where ground base interferometers achieve their best sensitivity. It is interesting to note that the sensitivity in the merger dominated frequency range is up by roughly a factor of 10 in the most recent Virgo data (acquired in the later half of 2007). This would correspond to a distance reach up to 30 Mpc (12 Mpc) at 50% (90%) efficiency. This distance reach improvement is not enough to tackle regions where the number of galaxies becomes interesting given the expected BBH event rate. Further upgrades, like Advanced Virgo, may be needed to have a reasonable probability of detection. Despite that, and given the improvement of the Virgo sensitivity in the low frequency region, we will expand the EGC pipeline parameter space to explore more efficiently from this region. Though matched filtering with a bank of templates, including inspiral, merger and ring-down phases, might have a better detection efficiency for BBH mergers, it is important to complement the search with other techniques not based on tailored matched filtering but using generic templates, such as Sine Gaussians. This approach could provide a method that would be more robust at finding increasingly complicated signals that depend on a larger number of astrophysical parameters from the sources, such as a black hole's spin in the case of a black hole–neutron star system.

Finally, one should add that the recent Virgo data taking (VSR1) will be analyzed in coincidence with LIGO S5 data. That is especially interesting in the high frequency region (>600 Hz) where the sensitivity of the four detectors are all limited by shot noise. This network of four non-aligned interferometers with comparable sensitivity should be able to detect the GW signal emitted by a supernova anywhere in the galaxy.

Acknowledgments

The authors thank H Dimmelmeier for fruitful discussions and providing the new core collapse waveforms. We thank the numerical relativity group at NASA Goddard Space Flight Center

for sharing the results of their binary black hole simulations with us. We also want to thank B Kelly for valuable discussions about these waveforms.

References

[1] Acernese F *et al* (Virgo Collaboration) 2007 *Class. Quantum Grav.* **24** S381
[2] Acernese F *et al* (Virgo Collaboration) 2007 *Class. Quantum Grav.* **24** 5767
[3] Acernese F *et al* (Virgo Collaboration) 2007 *Class. Quantum Grav.* **24** S491
[4] Acernese F *et al* (Virgo, ROG and AURIGA Collaborations) 2008 *Class. Quantum Grav.* **25** 205007
[5] Acernese F *et al* (Virgo Collaboration) 2008 *Class. Quantum Grav.* **25** 225001
[6] Zwerger T and Mueller E 1997 *Astron. Astrophys.* **320** 209
[7] Dimmelmeier H, Font J A and Mueller E 2002 *Astron. Astrophys.* **393** 523
[8] Ott C D *et al* 2004 *Astrophys. J.* **600** 834
[9] Shibata M and Sekiguchi Y I 2004 *Phys. Rev.* D **69** 084024
[10] Ott C D *et al* 2006 *Phys. Rev. Lett.* **96** 201102
[11] Ott C D 2009 *Class. Quantum Grav.* **26** 063001
[12] Flanagan E E and Hughes S A 1998 *Phys. Rev.* D **57** 4535
[13] Baker J G *et al* 2006 *Phys. Rev.* D **73** 104002
[14] Pretorius F 2005 *Phys. Rev. Lett.* **95** 121101
[15] Campanelli M *et al* 2006 *Phys. Rev. Lett.* **96** 111101
[16] Kokkotas K D and Schmidt B G 1999 Quasi-normal modes of stars and black holes *Living Rev. Rel.* **2** 12–22 http://www.livingreviews.org/lrr-1999-2
[17] Meszaros P 2006 *Rep. Prog. Phys.* **69** 2259–322
[18] Ferrari V, Miniutti G and Pons J A 2003 *Class. Quantum Grav.* **20** S841
[19] Damour T and Vilenkin A 2005 *Phys. Rev.* D **71** 063510
[20] Postnov K A and Yungelson L R 2006 The evolution of compact binary star systems *Living Rev. Rel.* **6** 36–8 http://www.livingreviews.org/lrr-2006-6
[21] O'Shaughnessy R, Kim C, Frakgos T, Kalogera V and Belczynski K 2005 *Astrophys. J.* **633** 1076
[22] Abbott B *et al* (LSC) 2005 *Phys. Rev.* D **72** 062001
[23] Pretorius F 2007 *Relativistic Objects in Compact Binaries: From Birth to Coalescence* ed Colpi (Berlin: Springer) arXiv:0710.1338
[24] Abbott B *et al* (LSC) 2004 *Phys. Rev.* D **69** 102001
[25] Abbott B *et al* (LSC) 2007 *Class. Quantum Grav.* **24** 5343–69
[26] Astone P *et al* 2003 *Phys. Rev.* D **68** 022001
[27] Ando M *et al* (TAMA Collaboration) 2005 *Phys. Rev.* D **71** 082002
[28] Baker J G *et al* 2007 *Phys. Rev.* D **75** 123024
[29] Acernese F *et al* (Virgo Collaboration) The Virgo detector *NIM* unpublished
[30] Braccini S *et al* (Virgo Collaboration) 2005 *Astropart. Phys.* **23** 557
[31] Acernese F *et al* (Virgo Collaboration) 2008 *Astropart. Phys.* **30** 29–38
[32] Rolland L 2008 Private communication
[33] Anderson W G *et al* 2001 *Phys. Rev.* D **63** 042003
[34] Klimenko S and Mitselmakher G 2004 *Class. Quantum Grav.* **21** S1819
[35] Guidi G M *et al* 2004 *Class. Quantum Grav.* **21** S815
[36] Chatterji S *et al* 2004 *Class. Quantum Grav.* **21** S1809
[37] Clapson A-C *et al* 2008 *Class. Quantum Grav.* **25** 035002
[38] Arnaud N *et al* 2003 *Phys. Rev.* D **67** 102003
[39] Hoshen J and Kokelman R 1976 *Phys. Rev.* B **14** 3438
[40] Beauville F *et al* 2008 *Class. Quantum Grav.* **25** 045002
[41] Arnaud N *et al* 2003 *Phys. Rev.* D **67** 062004
[42] Acernese F *et al* (Virgo Collaboration) 2004 *Class. Quantum Grav.* **21** S425
[43] Flaminio R, Gouaty R and Tournefier E Virgo technical document, VIR-NOT-LAP-1390-313
[44] Christensen N, Shawhan P and González G (for the LIGO Scientific Collaboration) 2004 *Class. Quantum Grav.* **21** S1747
[45] Koetter K, Heng I, Hewitson M, Strain K, Woan G and Ward H 2003 *Class. Quantum Grav.* **20** S895–902
[46] Hanna C R (for the LSC Collaboration) 2006 *Class. Quantum Grav.* **23** S17–22
[47] Christensen N (for the LSC Collaboration) 2005 *Class. Quantum Grav.* **22** S1059–68
[48] Caron B *et al* 1999 *Astropart. Phys.* **10** 369

[49] Baker J G *et al* 2006 *Phys. Rev.* D **73** 104002
[50] http://www.mpa-garching.mpg.de/rel_hydro/
[51] Christensen N 1992 *Phys. Rev.* D **46** 5250
[52] Dimmelmeier H *et al* 2007 *Phys. Rev. Lett.* **98** 251101
[53] Dimmelmeier H *et al* 2008 *Phys. Rev.* D **78** 064056
[54] Ott C D *et al* 2007 *Phys. Rev. Lett.* **98** 261101
[55] Bruegmann B *et al* 2004 *Phys. Rev. Lett.* **92** 211101
[56] Buonanno A, Cook G B and Pretorius F 2007 *Phys. Rev.* D **75** 124018
[57] Baker J G *et al* 2007 *Phys. Rev. Lett.* **99** 181101
[58] Berti E *et al* 2007 *Phys. Rev.* D **76** 064034
[59] Hannam M *et al* 2008 *Phys. Rev.* D **77** 044020
[60] Baker J G *et al* 2007 *Class. Quantum Grav.* **24** S25–31
[61] Ajith P *et al* 2007 *Class. Quantum Grav.* **24** S689–700
[62] Pan Y *et al* 2008 *Phys. Rev.* D **77** 024014
[63] Baker J G *et al* 2006 *Phys. Rev.* D **73** 104002
[64] Brady P R, Creighton J D E and Wiseman A G 2004 *Class. Quantum Grav.* **21** S1775
[65] Shapiro S L and Teukolsky S A 1983 *BlackHoles, White Dwarfs and Neutron Stars* (New York: Wiley)
[66] Riles K LIGO technical document, LIGO-T040055-00-Z
[67] Shen H *et al* 1998 *Prog. Theor. Phys.* **100** 1013
[68] Kopparapu R K *et al* 2008 *Astrophys. J.* **675** 1459

IOP PUBLISHING CLASSICAL AND QUANTUM GRAVITY

Class. Quantum Grav. **25** (2008) 045002 (32pp) doi:10.1088/0264-9381/25/4/045002

A comparison of methods for gravitational wave burst searches from LIGO and Virgo

F Beauville[1], M-A Bizouard[2], L Blackburn[3], L Bosi[4], L Brocco[5], D A Brown[6,7], D Buskulic[1], F Cavalier[2], S Chatterji[6], N Christensen[8,9], A-C Clapson[2], S Fairhurst[7], D Grosjean[1], G Guidi[10], P Hello[2], S Heng[11], M Hewitson[11], E Katsavounidis[3], S Klimenko[12], M Knight[8], A Lazzarini[6], N Leroy[2], F Marion[1], J Markowitz[3], C Melachrinos[3], B Mours[1], F Ricci[5], A Viceré[10], I Yakushin[13] and M Zanolin[3]
(The joint LSC/Virgo working group)

[1] Laboratoire d'Annecy-le-Vieux de Physique des Particules, Chemin de Bellevue, BP 110, 74941 Annecy-le-Vieux Cedex, France
[2] Laboratoire de l'Accélérateur Linéaire, IN2P3/CNRS-Université de Paris XI, BP 34, 91898 Orsay Cedex, France
[3] LIGO—Massachusetts Institute of Technology, Cambridge, MA 02139, USA
[4] INFN Sezione di Perugia and/or Università di Perugia, Via A Pascoli, I-06123 Perugia, Italy
[5] INFN Sezione di Roma and/or Università 'La Sapienza', P le A Moro 2, I-00185 Roma, Italy
[6] LIGO—California Institute of Technology, Pasadena, CA 91125, USA
[7] University of Wisconsin–Milwaukee, Milwaukee, WI 53201, USA
[8] Carleton College, Northfield, MN 55057, USA
[9] European Gravitational Observatory (EGO), Via E Amaldi, I-56021 Cascina, Italy
[10] INFN Sezione Firenze/Urbino Via G Sansone 1, I-50019 Sesto Fiorentino; and/or Università di Firenze, Largo E Fermi 2, I-50125 Firenze and/or Università di Urbino, Via S Chiara 27, I-61029 Urbino, Italy
[11] University of Glasgow, Glasgow, G12 8QQ, UK
[12] University of Florida–Gainesville, FL 32611, USA
[13] LIGO Livingston Observatory, Livingston, LA 70754, USA

Received 20 June 2007, in final form 28 November 2007
Published 31 January 2008
Online at stacks.iop.org/CQG/25/045002

Abstract

The search procedure for burst gravitational waves has been studied using 24 h of simulated data in a network of three interferometers (Hanford 4 km, Livingston 4 km and Virgo 3 km are the example interferometers). Several methods to detect burst events developed in the LIGO Scientific Collaboration (LSC) and Virgo Collaboration have been studied and compared. We have performed coincidence analysis of the triggers obtained in the different interferometers with and without simulated signals added to the data. The benefits of having multiple interferometers of similar sensitivity are demonstrated by comparing the detection performance of the joint coincidence analysis with LSC and Virgo only burst searches. Adding Virgo to the LIGO detector network can increase by 50% the detection efficiency for this search. Another advantage of a joint LIGO–Virgo network is the ability to reconstruct the source sky position. The reconstruction accuracy depends on the timing

measurement accuracy of the events in each interferometer, and is displayed in this paper with a fixed source position example.

PACS numbers: 04.80.Nn, 07.05.Kf

(Some figures in this article are in colour only in the electronic version)

1. Introduction

The recent progress in the commissioning of gravitational wave interferometric detectors raises the possibility for performing joint data analysis between different collaborations. Indeed, the LIGO (two 4 km and one 2 km) [1] interferometers are at their design sensitivity, while the Virgo (3 km) interferometer's sensitivity is approaching its design expectations [2]. Moreover, efforts are currently being conducted in order to increase the duty cycle of each interferometer, and this will provide extended joint data-taking periods.

Gravitational wave (GW) burst events are characterized by their short duration (a few ms) and the absence of reliable theoretical predictions for their waveforms. The sources of GW burst events are numerous: massive star core collapse [3–6], the merging phase of coalescing compact binary systems forming a single black hole [7–10], black hole ring-down [11], astrophysical engines that generate gamma-ray burst [12] and even neutron star oscillation modes and instabilities. Newly born rapidly rotating neutron stars may emit GWs at the frequencies of the quasi-normal modes during the star's first minutes, and are expected to emit damped sinusoidal waveforms [13]. More exotic sources are possible, such as GW bursts emitted by cosmic strings [14]. Except for a few sources, the burst waveforms are poorly known and their amplitude is rather low. In this study, we did not consider well-modeled waveforms whose search is optimally done using matched filtering techniques. We concentrate on sources emitting poorly known waveforms.

It has been long acknowledged [17, 18] that GW burst detection can be enhanced by using information contained in a network of detectors spread around the world. Due to the time shortness of the burst GW and their weakness, we are obliged to work with quite high false alarm rates in each interferometer. With such a configuration, it is necessary to use a network of interferometers to reduce the false alarm rate (FAR). This is also the only way to disentangle a real GW burst event from transient noise events with sufficient confidence. Several methods and strategies can be used. There exist two categories of network data analysis: coincidence and coherent filtering. In the first approach, each interferometer data stream is analyzed, providing a list of event triggers. Triggers from the different interferometers are then compared to check if they are consistent with a real GW burst source. A coherent analysis uses all interferometer information by combining the input data streams or the filtered data streams into one single stream. The coincidence analysis is simpler to apply than the coherent analysis since it does not require the exchange of the detector data streams; this technique has been commonly used [19, 20]. On the other hand, the coherent analysis is expected to be, *a priori*, more powerful than the coincidence approach since a depreciated signal in a single interferometer can contribute to the global network output [18]. In this investigation, we focused on the coincidence analysis, trying to study all different aspects (including source location) since it is the simplest method to initially apply to multi-detector data. A similar comparison study for a coherent search is also underway for the LIGO–Virgo network.

The LSC burst search pipeline already performs coincidence analysis using LIGO's two well-aligned 4 km interferometers, and its 2 km interferometer. In addition, several joint searches with other detectors using real data have been done or are underway; an initial joint LIGO–TAMA coincidence search using real data has been reported in [21]. Joint searches for LIGO–GEO and LIGO–AURIGA [22] are underway. Similar efforts are carried out for binary inspiral GW searches. In the study presented in this paper, we analyze the potential benefits of a combined LIGO–Virgo detector network burst search; our study here is conducted using simulated data. This network is composed of three detectors of similar sensitivity. In actuality, having similar sensitivity plays a crucial role in the performance of a network (that is the reason why we did not consider the LIGO Hanford 2 km interferometer in this study. In addition, it could not be used to eliminate fake events due to environmental noise sources or detector artifacts since this study is carried out with the simulated data and not the real data). Nevertheless, while the LIGO detectors have the same orientation being separated by only 3000 km, the Virgo detector orientation and its distance with respect to the LIGO detectors imply that the Virgo and LIGO detectors do not have a maximal sensitivity simultaneously for the same region of the sky. Actually they are somewhat 'orthogonal'. It is then important to determine the gain of a coincidence search in such a network with respect to a search conducted using only the LIGO detectors. Note that a similar comparison study for the inspiral GW search has been carried out [23].

The paper is organized as follows. Section 2 contains a description of the characteristics of the data used for this analysis, including both the noise and source waveforms; these are the data that have been used for studying the different pipelines and the coincidence analysis. Section 3 summarizes the performance of seven different burst filters considered in this joint data analysis [24]. After having defined a benchmark, we evaluate and compare the intrinsic performance of each filter, and characterize each pipeline as is applied on both the LIGO and Virgo data streams. We address, at the end of this section, the issue of the burst signals' parameter space coverage by the different pipelines. We show, using simulated burst waveforms of different types, that the description of a burst GW with a few statistical parameters is not complete. We have investigated several strategies to carry out a coincidence analysis, taking into account that the three detectors do not have the same sensitivity with respect to the sky location for a particular source. The requirement for detecting a source in all the interferometers greatly decreases the FAR, but the detection efficiency may also drop drastically if the source is located in a region of the sky for which at least one detector has poor antenna response. We find that, for this particular network of detectors, requiring detection by any two of the three detectors gives an improved detection efficiency compared to the triple-coincidence detection at the same false alarm rate. Section 4 gives a summary of what can be achieved in such a network applying the different filters used by the two detector teams. We consider a source located at a fixed sky location (in the direction of the galactic center). We show the performance gain when adding a third interferometer of similar sensitivity but not well aligned with the first two. We have also estimated the gain of adding the event frequency information in the coincidence analysis. The benefits and disadvantages of a logical combination of filtered output obtained for each of the detector data streams (the so-called 'AND' and 'OR' analysis) have been investigated too and are summarized in section 5. Working with three interferometers spread over the world allows one to estimate the source sky location. In this study, we apply a method developed in Virgo [25] for estimating the source location. As an elementary building block of an all-time, all-sky search, we decided to look for a source that emits from a fixed location in the sky. The burst 'repeater' source was placed at the center of the Galaxy and the performance modulation due to the Earth's rotation has been studied with 24 h of simulated data. These results are given in section 6. Our results

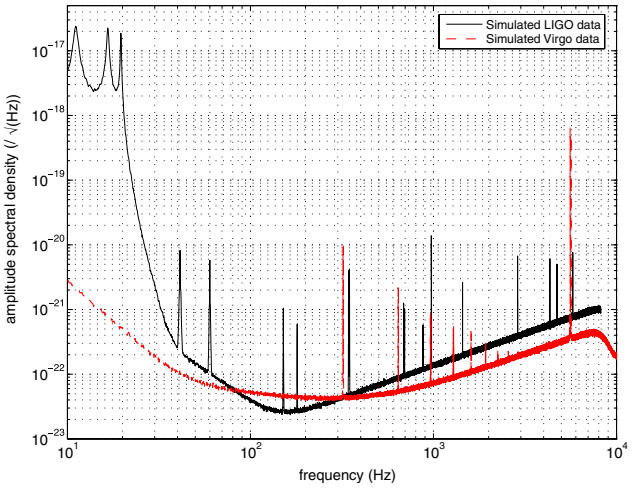

Figure 1. The LIGO (solid line) and Virgo (dashed line) simulated noise spectrum used in this study. The distortion close to the Nyquist frequency in the Virgo spectrum is due to the use of a low-pass filter applied before down-sampling the Virgo data generated at 40 kHz down to 20 kHz.

are summarized in section 7. Finally, one should note that, after a one year shutdown (for maintenance associated with further improving the detectors' sensitivity) starting in October 2007, the LIGO and Virgo detectors will be jointly operated as part of a single network.

2. Data set

2.1. Interferometer noise modeling

Simulated noise data streams have been generated for the LIGO Hanford (H1), LIGO Livingston (L1) and Virgo (V1) interferometers independently using the LSC [26] and Virgo [27] simulation tools. In both cases, a stationary and colored noise model has been used such as to reproduce the design sensitivity curve of the LIGO and Virgo interferometers as shown in figure 1. This includes thin thermal resonances (wire violin modes and mirror thermal noise) as foreseen in each detector; a Gaussian thermal noise modeling has been used for the Virgo noise generation, while a random phase modulation technique has been used for the LIGO noise simulation. The LIGO noise also includes lines due to electrical power supply (non-Gaussian process). In Virgo, the 50 Hz harmonics lines are subtracted in the main reconstructed gravitational wave strain applying a deterministic algorithm using an auxiliary channel which monitors the power supply of Virgo [28]. Two data sets have been produced. Initially, 3 h of H1 and V1 noise were created and used to characterize the burst filters and cross check the consistency of the different pipelines used in the LSC and Virgo. Then, 24 h of noise data have been produced for H1, L1 and V1 interferometers. These 24 h long data streams have been used for the coincidence analysis presented in this paper.

2.2. Signals

2.2.1. Waveforms and parameter space. Because many gravitational wave burst sources are currently not modeled in sufficient detail to allow matched filtering, most gravitational wave

Table 1. Boundaries of the parameter space for the burst signals studied. Time duration, peak frequency and bandwidth are the three parameters that have been chosen to describe the main features of expected burst signal waveform.

	Duration ($\Delta\tau$)	Peak frequency (ϕ)	Frequency bandwidth ($\Delta\phi$)
Minimum value	0.5 ms	50 Hz	5 Hz
Maximum value	50 ms	2000 Hz	1000 Hz

burst detection algorithms are designed to be insensitive to the details of the waveforms, and search through broad time and frequency ranges. However, in order to carry out a comparison of the different filters, we decided to use in this study three statistical variables as proposed in [29] to parametrize a burst signal. These three parameters are the time duration ($\Delta\tau$), the frequency bandwidth ($\Delta\phi$) and the peak frequency (ϕ) of the signal as defined using the first and second moments of the signal energy distribution in the time and frequency domains. Actually, the definition of the time duration and frequency bandwidth used in this paper differs from the one proposed in [29]: they are defined by the interval containing 50% of the signal energy, dropping 25% of the signal energy on both sides of the distribution. Note that $\Delta\phi$ and $\Delta\tau$ are constrained by some uncertainty relation [29, 30]:

$$\Delta\tau\,\Delta\phi > \frac{\Gamma}{4\pi}, \qquad \Gamma = 0.59\ldots. \tag{1}$$

This equation (also known as the Heisenberg–Gabor uncertainty relation) indicates that a signal cannot have arbitrarily small duration and bandwidth simultaneously.

The range values of those three quantities define a parameter space inside which the burst filters have to be as efficient as possible. The boundaries have been chosen taking into account theoretical predictions available in the literature and by the noise spectra shown in figure 1. They are given in table 1.

In order to fully characterize our burst filters, it is necessary to evaluate their performance using just a few waveforms that have different features and are well spread over the parameter space. We have used three different families of waveforms. First, the broadband Gaussian signals are of interest because many predicted core collapse simulation waveforms do have large peak structures corresponding to the bounce. Sine-Gaussian waveforms are narrowband signals that allow one to test a given frequency region. Finally, more complex waveforms predicted by the core collapse simulation, as described in [4], have been used; we have chosen two of them obtained with different assumptions on the model parameters. In both cases, the equation of state of the ideal gas is stiff, but in one case the differential rotation is small leading to type I (regular collapse) waveform (large negative peak followed by a ring-down phase). In the second case, the initial state is characterized by a rapidly rotating star with a large differential rotation producing a type II waveform characterized by multiple bounce collapse. The eight chosen waveforms, whose parameters are given in table 2, are represented in figure 2. Their frequency spectra are shown in figure 3.

The normalization of the signals can be done either by fixing the intrinsic signal strength (h_{rss}) or by the intrinsic signal-to-noise ratio (SNR) of the signal seen in a detector. The latter quantity is more suitable if one wants to compare a filter's performance in interferometers with different sensitivity. On the other hand, in the case of a network analysis, it is mandatory to consider a source of a given intrinsic amplitude. This quantity is defined by

$$h_{\mathrm{rss}} = \sqrt{\int_{-\infty}^{\infty} |h(t)|^2\,\mathrm{d}t}. \tag{2}$$

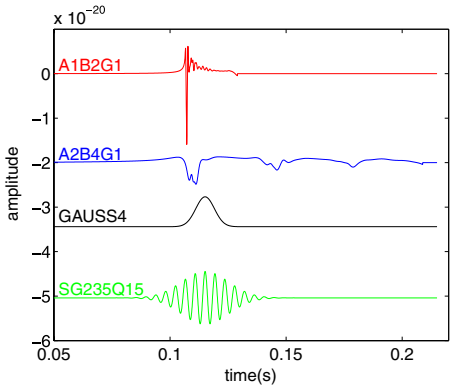

Figure 2. Waveform families of burst sources used in this study to estimate the performance of the different pipelines. DFM A1B2G1 and DFM A2B4G1: gravitational wave emitted during core collapse simulated by Dimmelmeier, Font and Mueller [4]. GAUSS4: Gaussian peak. SG235Q15: sine-Gaussian signal.

Table 2. Definition and parameter values of the eight waveforms used to estimate the burst filters' performance. For the DFM A1B2G1 and DFM A2B4G1 signals, the A, B and G parameters are defined in [4]. Information in the far-right column indicates whether the signal was used in the coincidence analysis described in section 4.

Name	Time domain formula	Parameter value	Coincidence
GAUSS1	$h(t) = \alpha \exp\left(\frac{-(t-t_0)^2}{2\sigma^2}\right)$	$\sigma = 1$ ms	Yes
GAUSS4		$\sigma = 4$ ms	Yes
SG235Q5	$h(t) = \alpha \exp\left(\frac{-2(t-t_0)^2\pi^2 f^2}{Q^2}\right)$	$f = 235$ Hz, $Q = 5$	No
SG235Q15	$\times \cos(2\pi f(t - t_0))$	$f = 235$ Hz, $Q = 15$	Yes
SG820Q5		$f = 820$ Hz, $Q = 5$	No
SG820Q15		$f = 820$ Hz, $Q = 15$	Yes
DFM A1B2G1		$A = 1, B = 2, G = 1$	Yes
DFM A2B4G1		$A = 2, B = 4, G = 1$	Yes

The intrinsic SNR seen in a detector is given by the SNR of a matched filter

$$\rho = 2\sqrt{\int_0^\infty \frac{|h(f)|^2}{S_h(f)}\,\mathrm{d}f}, \tag{3}$$

where $S_h(f)$ is the one-sided power spectrum of the detector noise.

For the estimation of the pipelines' performance given in section 3, we have considered that the detectors are optimally oriented with respect to the source (no antenna patterns have been considered).

The free parameters of the different pipelines studied here have been chosen such as to maximize the detection efficiency of the eight chosen waveforms. In section 3.4, we address the issue of a possible dependence of the pipeline parameters' tuning upon the waveforms considered. For that purpose, we have extended the set of waveforms, and studied a larger set of core collapse simulated waveforms (50). We have also added 50 waveforms which fill the region of the parameter space outside the 'minimal uncertainty' region. They are generated using band-passed white noise.

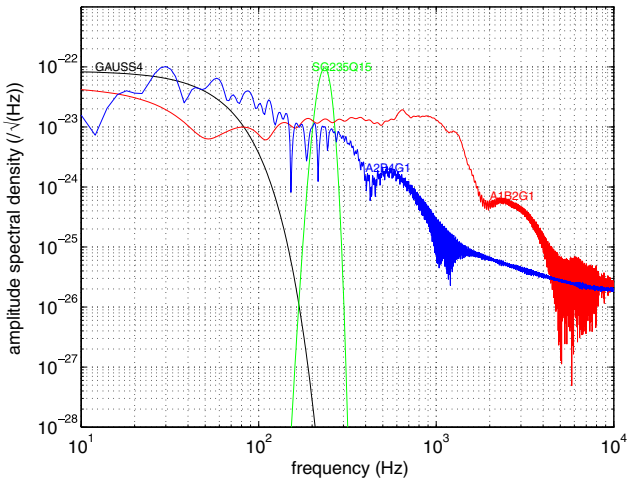

Figure 3. Spectrum of the waveform families of burst sources used in this study to estimate the performance of the different pipelines. DFM A1B2G1 and DFM A2B4G1: gravitational wave emitted during core collapse simulated by Dimmelmeier, Font and Mueller [4]. SG235Q15: sine-Gaussian signal. GAUSS4: Gaussian peak. All waveforms have been normalized such that $h_{\rm rss} = 3.59 \times 10^{-22}\sqrt{\rm Hz}$. This value corresponds to a SN source located at 10 kpc emitting a A1B2G1 waveform.

2.2.2. Coincidence analysis injections. For the coincidence analysis described in sections 4–6, we located the source in the direction of the galactic center. The waveforms are linearly polarized, with the polarization angle uniformly distributed. In addition to the unknown polarization angle, the response of the detector to a GW depends on the sky position of the source. A source of constant intrinsic emission strength located in the direction of the galactic center would emit signals whose amplitude measured by a detector would then vary over 24 h as shown in figure 4. We have used 24 h of simulated data in order to study, on average, the effect of the Earth's rotation on the detection performance. Due to the use of non-astrophysical waveforms (with the exception of supernova core collapse), we cannot use the distance to fix the strength of the signal. We have then normalized the six waveforms such that over 24 h there is only one injected event seen with a SNR of 10 or greater in all the three detectors. For the supernova core collapse, this scaling corresponds to a distance of 4.8 kpc for DFM A1B2G1 and 3.6 kpc for DFM A2B4G1.

3. Burst search methods and their performance

In this investigation, we have studied different burst detection algorithms. We compared their performance in order to determine if they cover the variety of possible astrophysical waveforms. Indeed, before performing a network analysis with some of them it is important to know how they behave individually. For each filter, we measure its detection efficiency as a function of the false alarm rate. Then, the arrival time of the signal in each interferometer has to be determined with very good accuracy (of the order of 1 ms) in order to be able to reconstruct the position of the source in the sky. In the following, we briefly describe the different pipelines used in this study. It is important to note that some of these filters require whitened data. This pre-processing stage is performed both for the LSC and Virgo pipelines

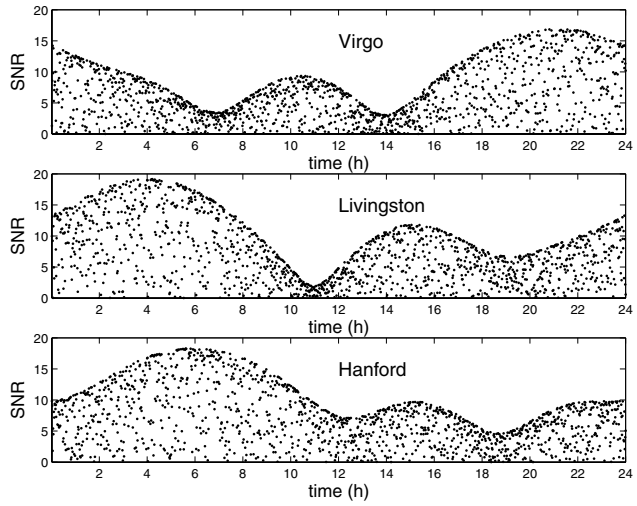

Figure 4. Signal-to-noise ratios of DFM A1B2G1 signals emitted by a source located in the direction of the galactic center over 24 h. The SNRs were computed for the H1, L1 and V1 detectors, taking into account their antenna pattern at the signal arrival time (note the envelope of the distributions). In this study, the source is polarized with the polarization angle uniformly distributed; this produces the distribution of values inside the envelope.

using a linear predictive error filter. These have been developed in each collaboration, see for instance [31, 33].

3.1. Pipeline description

We utilized search methods operating in the time and time–frequency domains. In addition, correlator filters were also applied. Two of these pipelines (KW and QT) have been developed in the LSC, while the others have been developed in the Virgo.

3.1.1. Excess power methods.

- *Power filter (PF).* PF [32] searches on whitened data for a power excess using different time analysis windows and different frequency bands chosen such that the product of the frequency width and the time duration remains constant. In order to cover the parameter space, five time windows have been chosen: 64, 128, 256, 512 and 1024 bins for the LIGO and Virgo data; the bin size is defined as the sampling time for the data, which is $1/16\,384$ s for LIGO and $1/20000$ s for Virgo. The windows duration is hence a little different for the two data sets because of the different data sampling rates. The PF has been tuned, in this study, to cover all frequencies between 40 Hz and 2000 Hz. In the time–frequency plane, the PF statistics are derived by taking the logarithm of the spectrogram.
- *Kleine Welle (KW).* KW searches for excess signal energy in the dyadic wavelet decomposition of a whitened time series. The wavelet transformation is evaluated at distinct scales (which is directly related to frequency) and involves stretching and contracting a mother wavelet (in this case the *Haar* wavelet) by the scale factor before using it to filter the time series [33]. In this study, the frequency range covered by KW

was from 64 Hz to 1064 Hz for the H1 and L1 data, and from 78 Hz up to 1250 Hz for the V1 data. As the input time series is whitened by the use of a linear predictive filter prior to the wavelet decomposition, the wavelet coefficients calculated at each scale follow a Gaussian distribution and are normalized to unity variance. KW identifies events in the time series by clustering large-amplitude coefficients which are nearby in time and scale.

3.1.2. Time domain filters.

- *Mean filter (MF).* MF searches for an excess in a moving average computed on the whitened data. Ten different analysis windows, with durations varying from 0.5 ms up to 10 ms, are used. The moving stride of each window is 1 bin. It has been shown that the analysis window size has to be matched with the duration of the signal to have the best detection result [18]. Note that the MF behaves like a low-pass filter and, given the choice of the windows' size, the MF could not explore the frequency domain beyond 1 kHz. A threshold is applied on each analysis window output, producing triggers which may overlap. They are then clustered if they coincide within a time window equal to 12 times the size of the analysis window. This value corresponds to the optimal signal efficiency for the chosen threshold (SNR $>$ 4) obtained on simulated Gaussian data in which signals, such as the ones used in this study, have been injected. Finally, note that no information about signal frequency is provided.
- *Alternative linear filter (ALF).* The ALF aims at detecting large slopes associated with peaks in the data in ten moving analysis windows whose duration varies between 0.5 ms and 15 ms. The moving stride of each window is 1 bin. The frequency range that ALF can explore is below 1 kHz. A straight line is fit to the data in an analysis window. The two non-independent fit results, namely the line slope and the offset value, are then combined quadratically to define the ALF statistics. Concerning the optimal analysis window size to detect a peak, it has been shown that the window size has to be 30% larger than the duration of the peak. This effect is due to the noise standard deviation which is reduced if the computation is done over a larger window [34]. The pipeline of ALF is identical to that of the MF filter concerning the events clusterization.

3.1.3. Correlator filters.

- *Peak correlator (PC).* This is a matched filter using the Gaussian waveform templates [15]. The Gaussian templates have been chosen such that the minimum match is better than 99% for the Gaussian peaks whose σ is between 0.2 ms and 6 ms (eight templates). That corresponds to a maximum frequency of about 900 Hz. Note that the PC has been implemented using the Welch overlapping scheme [35] which optimizes the computing cost in the case of small template size. The events obtained after thresholding are then clustered using only time coincidence information.
- *Exponential Gaussian correlator (EGC).* The complex exponential Gaussian correlator produces a time–frequency representation of the data by applying the correlation relation for a list of templates of the same family,

$$\Phi_{f_0,Q_0}(t) = \mathrm{e}^{-2(\pi f_0/Q_0)^2 t^2}\, \mathrm{e}^{\mathrm{i}2\pi f_0 t}, \tag{4}$$

with f_0 and Q_0 being the central frequency and the quality factor of the template, respectively.

Template selection relies on a tiling algorithm valid for any two-parameter matched filter bank [36]. Two tiling zones have been defined in order to optimize the visibility of non-oscillatory waveforms, while covering a large range of periodic signals with a reduced

number of templates (122). The first zone covers $10 \leqslant f \leqslant 1000$ Hz and $1 \leqslant Q_0 \leqslant 3$, while the second spans $150 \leqslant f \leqslant 1000$ Hz and $1 \leqslant Q_0 \leqslant 17$. The event duration covered is from 0.2 ms to 50 ms. Because the frequency coverage is redundant, templates are grouped in frequency bands 50 Hz wide, where they are ordered by decreasing quality factor. Events are then identified as local energy excesses. More details can be found in [37].

- *Q-transform (QT).* QT is a multi-resolution search for statistically significant signal energy in the time–frequency plane [33]. It is equivalent to a matched filter search for sinusoidal Gaussian bursts with unknown phase in the whitened data stream. The data are first whitened by the linear predictive filtering. The resulting whitened data are then projected onto an over-complete basis of the Gaussian-windowed complex exponentials within a targeted range of frequency and Q (the ratio of frequency to bandwidth). For this study, the Q-transform was tuned to search the frequency range from 64 Hz to 1024 Hz and the Q-range from 3.3 to 22 corresponding to an event duration range from 0.5 ms up to 50 ms. Candidate events are then described by the most significant set of non-overlapping time–frequency tiles that exceed a specified significance threshold.

Note that while the QT and EGC filters look similar, they are actually implemented differently. The noise normalization is done externally for QT, while EGC performs matched filtering. The event extraction is different; EGC includes all neighboring templates, while QT prunes overlapping templates.

3.2. Event trigger definition

Each of the burst search filters applies a threshold on the filter output. The filter output is either defined as an energy in a time–frequency grid or as a SNR in the time domain. This is performed for several values of the parameters (frequency band, window size, template). For time–frequency methods, all nearby pixels are clustered and the energy of the cluster is defined as the sum of the energy of the pixels according to a well-defined prescription developed in each of the methods. After thresholding, we obtain a collection of events defined by a start time, an end time, a peak time and the corresponding maximum filter output. In addition, filters designed for providing localization in the frequency domain (QT, KW and EGC) yield an estimation of the event bandwidth and the peak frequency, corresponding to the frequency of the template with the highest SNR.

Almost all the burst filters deal with several analysis windows, templates or time–frequency planes. In the case of a signal, several nearby templates or time–frequency planes are expected to trigger, corresponding (in actuality) to the same event. All burst pipelines thus apply an event clustering algorithm that gathers all primary defined events corresponding to the same signal event. The clustering algorithm usually depends on the filter type: time–frequency, correlators and time domain filters.

3.3. Detection performance

One way to quantify the detection potential of a burst search filter is through the determination of receiver operator characteristic (ROC) curves for each filter and for each family of waveforms. The ROC curve shows the filter detection efficiency versus the false alarm rate (FAR). The FAR is usually a free parameter which is fixed differently with each interferometer data set according to the type of analysis; a discovery search requires one to have very few false alarms in order to select golden events which are then studied deeply in detail (waveform, frequency content, arrival time consistency), while to better understand the

Table 3. Necessary ρ for 50% efficiency at FAR = 0.01 Hz for H1 (up) and V1 (bottom) data. The symbol '–' means that the performance was too poor to be estimated.

	PF	KW	QT	PC	EGC	MF	ALF
H1							
A1B2G1	6.7	7.5	6.5	5.1	5.1	7.3	6.7
A2B4G1	7.4	7.7	6.4	5.8	6.9	7.0	6.6
GAUSS1	6.2	7.0	5.5	4.9	5.6	6.7	6.1
GAUSS4	7.2	8.0	5.6	4.9	5.9	7.7	6.4
SG235Q5	7.7	6.9	5.1	6.1	5.8	7.5	7.0
SG235Q15	10.5	8.6	5.1	–	6.0	10.6	9.9
SG820Q5	5.9	7.4	5.2	–	6.0	8.2	6.9
SG820Q15	5.6	9.1	5.1	–	5.8	11.6	9.7
V1							
A1B2G1	5.9	7.1	6.6	5.6	5.3	6.1	6.0
A2B4G1	6.6	7.5	6.8	5.8	6.5	6.3	6.0
GAUSS1	5.9	6.5	5.9	4.9	5.5	6.0	5.7
GAUSS4	7.3	8.4	7.0	5.2	5.7	6.2	5.6
SG235Q5	6.6	6.9	5.2	6.6	5.5	7.5	6.9
SG235Q15	8.9	8.8	5.1	–	5.7	11.7	9.8
SG820Q5	5.7	7.5	5.1	–	5.7	8.6	7.1
SG820Q15	5.7	9.3	5.3	–	5.6	15.9	10.2

statistical properties of the background noise (gaussianity, stationarity) it is necessary to have a large FAR. Moreover, in a network analysis with non-correlated noise in the interferometers, a simple coincidence analysis reduces the final FAR by a few orders of magnitude with respect to the single-interferometer FAR (which can be chosen rather high). This is demonstrated in section 4. The ROC curves for the eight test-case waveforms have been computed for all burst filters and for different values of the strength of the signal. In particular, we checked the consistency of the results obtained with the H1 and V1 data. In the following, we summarize the main results about the ROC curves estimated for a FAR varying from 10^{-4} Hz (one false alarm per 3 h) to 10^{-1} Hz (a single-interferometer FAR which can be easily handled in a network coincidence analysis). Figure 5 shows the ROC curves (using the H1 data) for four of the eight waveforms: A1B2G1, SG235Q5, GAUSS1 and SG820Q15. They have been obtained for a signal injected with an intrinsic SNR of 7 (see equation (3)). This SNR value emphasizes the performance differences; with a higher value, for many pipelines the efficiency saturates at 100% over the full FAR range. Table 3 gives the values of a signals' intrinsic SNR necessary to have a detection efficiency of 50% at a fixed FAR of 0.01 Hz. These values have been obtained by fitting the curve of efficiency versus the signal h_{rss} with an asymmetric sigmoid function, as defined in [20].

The first comment about these numbers is that filters perform differently according to the waveforms. There is no one filter that performs better than all of the others when considering such a variety of waveforms. One can also note that the largest performance spread corresponds to sine-Gaussian signals, as shown in figure 5. The QT and EGC have rather constant and good performance for all the tested waveforms, and as expected perform very well for all sine-Gaussian waveforms. One can, however, remark that QT performs slightly better than EGC on the test-case sine-Gaussian signals, especially for the H1 data. This is partly due to the fact that QT is using an over-complete template bank, and also due to different event extraction for QT and EGC. Moreover, one should note that EGC explores the low-frequency region more effectively than QT (the lowest frequency of EGC is 10 Hz, while QT starts at

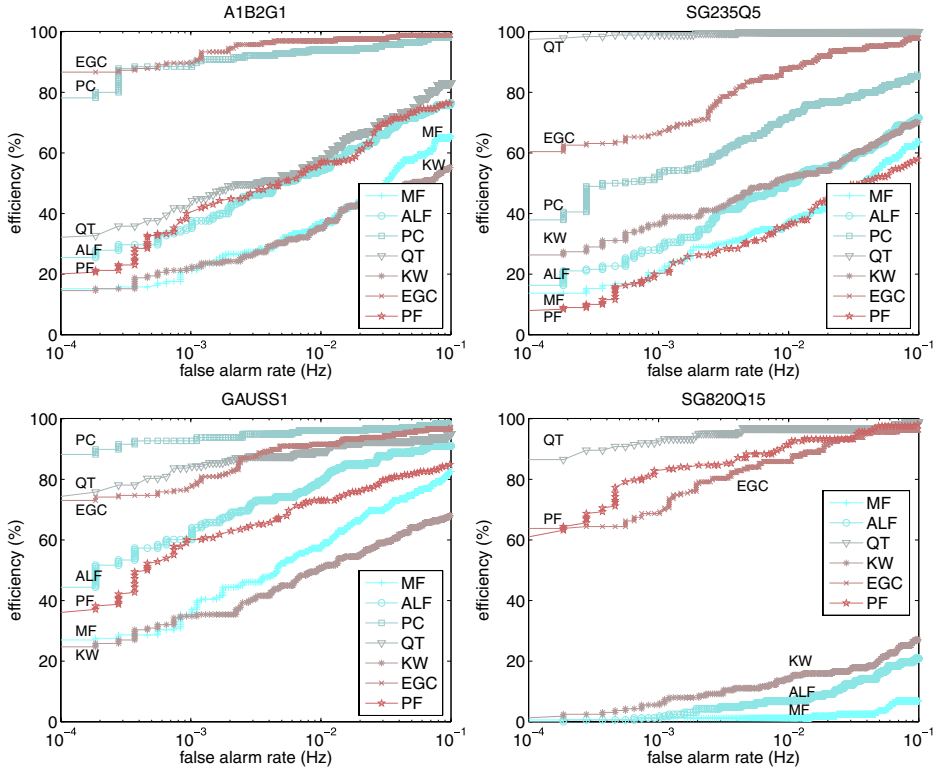

Figure 5. ROC curves obtained from the bank of filters studied using four different waveforms (DFM A1B2G1, SG235Q5, GAUSS1 and SG820Q15). The signal waveforms have been injected into H1 noise with an intrinsic SNR of 7.

64 Hz). That explains why EGC obtains a better performance on Gaussian signals for the V1 data.

The relative low efficiency of KW with respect, for instance, to the QT pipeline is partly due to the fact that QT is using an over-complete template bank, and to the fact that the Haar function basis does not optimally span the region at high Q. Moreover, KW has a totally orthogonal basis. The test-case signal's SNR is most likely spread over several wavelet functions. The KW clustering algorithm tries to recover as much signal as possible, but cannot be as efficient as an optimal matched filter (as extra noise is introduced).

The other filters have less consistent results. This is especially true for the case of MF, ALF and PC. For instance MF, which averages the data for a given duration, has a poor (expected and observed) performance on sine-Gaussian signals. For Q constant, MF's performance decreases as the frequency increases; at a fixed frequency, MF's performance decreases as Q increases because the number of cycles increases. An equivalent argument explains the poor performance of ALF and PC for sine-Gaussian waveforms. If the intrinsic strength of the signal is spread over many cycles, ALF is strongly disabled whatever the size of the analysis window. Conversely, PC and ALF perform well for signals whose waveform is peak-like (the DFM and Gaussian waveforms). PC is, *a priori*, an optimal filter for Gaussian peaks. PF's performance is rather constant; it obtains intermediate performance on the DFM and Gaussian

signals. For sine-Gaussian signals, PF is usually very competitive but, as can be seen in figure 5, this is not the case for the SG235Q5 signal. This loss of efficiency is due to the choice, done *a priori*, of the frequency windows in which the power is calculated. The frequency region around 235 Hz is split over two windows.

It is also interesting to note some differences in the results obtained with the H1 and V1 data for signals having the same SNR, as reported in table 3. The difference never exceeds a maximum of 25%, and is different from one pipeline to another; QT and PC perform better with the H1 data, while the other pipelines perform slightly better on the V1 data. The difference depends also on the waveforms; the largest difference is found for the GAUSS4 signal. The bad performance of QT on the GAUSS4 signal for V1 compared to H1 data is due to the fact that the amplitude of the GAUSS4 signal is lower in V1 than in H1 data. Indeed, this signal has its main frequency content at very low frequency (below 100 Hz as shown in figure 3). The waveforms are normalized for V1 and H1 such that their SNR is constant in both detectors. Since the Virgo PSD is lower at low frequency than LIGO's PSD, the overall amplitude of the GAUSS4 waveform is lower for V1 compared to H1. But, since the QT low-frequency cutoff (64 Hz) is the same for V1 and H1, QT will recover a smaller fraction of SNR of this signal in V1 compared to H1.

3.4. Waveform robustness results

In this study, the parameters of the algorithms have been chosen in order to cover a large fraction of the parameter space defined in section 2.2.1. However, many of the pipelines actually use parameters which have been tuned for real data analysis in the LSC or Virgo burst searches. The performance of the pipelines, described above, have been estimated using eight waveforms spread over the parameter space. In order to test the robustness of the pipelines' performance to a wider set of burst waveforms spread over the signal's parameter space, we have computed the efficiencies for all pipelines at a given FAR using 100 waveforms chosen randomly as follows:

- Fifty waveforms produced by core collapse simulations (SN) extracted from [3–5].
- Fifty band-passed white noise (WN) signals: white noise is filtered in frequency and then a Gaussian window is applied in the time domain in order to limit the duration of the signal.

The band-passed white noise signals have been considered in this study in order to easily span the parameter space, especially in the region of high-frequency and large-frequency bandwidth. The parameters of the waveforms are given in the appendix. Figure 6 shows the pipelines' efficiency obtained for a FAR of 0.001 Hz with the V1 data, represented in the two-dimensional plane defined by the central frequency and the time–frequency volume (the product of the duration with the frequency bandwidth). An important point concerns the location of the different families of waveforms; although the three parameters, based on the moments of the distribution of the signal energy in the time and frequency domains, obey the uncertainty relation (see equation (1)) that explain the borders of the plots, the different signal families do not populate exactly the same region of the parameter space. The core collapse signals (SN) are all concentrated in a region for which the central frequency is lower than 700 Hz, while the frequency bandwidth can be as large as 600 Hz, and the time duration is well spread over the full range. The band-passed WN signals cover the full parameter space, as defined in section 2.2.1. Note that the very low bandwidth WN signals look like sine-Gaussian signals (a Gaussian window is applied in the time domain on all filtered white noise waveforms in order to limit the duration).

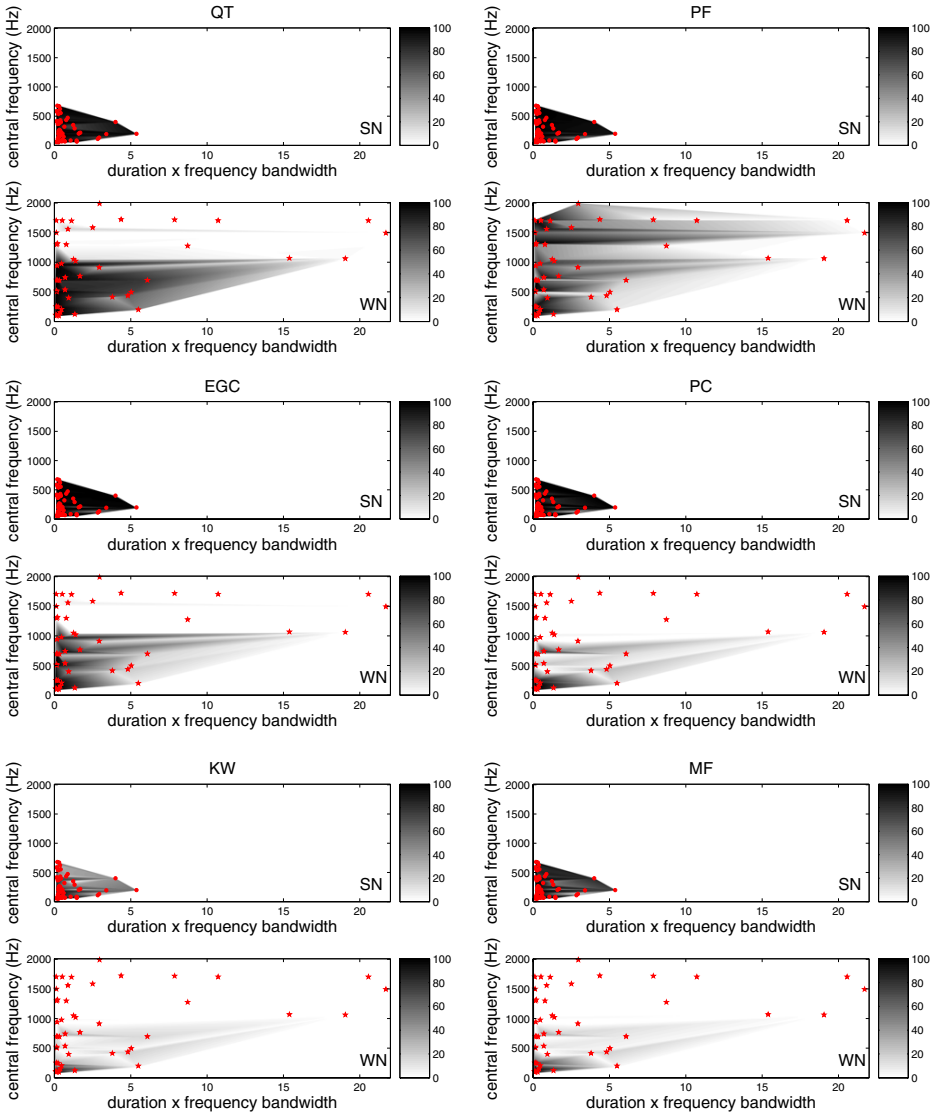

Figure 6. Pipeline efficiencies obtained for two families of waveforms: SN (top) and WN (bottom). The efficiency of six pipelines (ALF pipeline is not represented here, but is very similar to MF) is shown in the two-dimensional plane of the central frequency versus the time–frequency volume. The efficiency has been computed using the Virgo noise data for a FAR of 0.001 Hz and a signal SNR of 10.

One can note that the overall parameter space coverage performances obtained by the different pipelines are not identical. PF is the only pipeline which has been configured, in this analysis, to include data in the 1–2 kHz range in its analysis. Naturally, a pipeline that has been tuned to cover the full parameter space has a higher FAR at a given efficiency. This can be translated into an efficiency drop of a few percent for a given FAR for all signals.

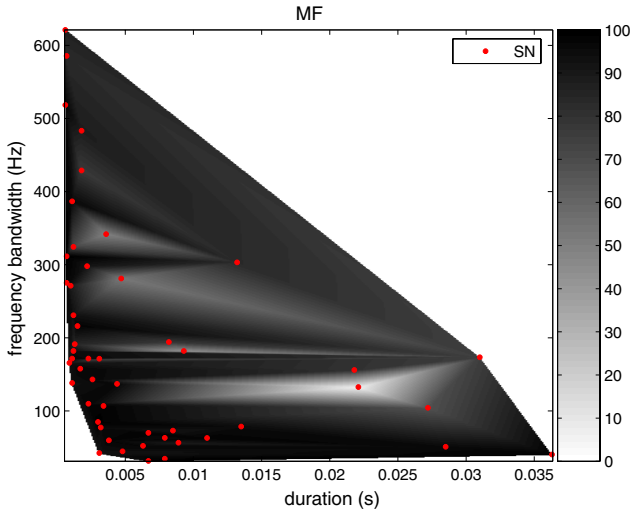

Figure 7. MF pipeline efficiencies obtained for 50 SN waveforms as a function of the duration and bandwidth of the signal. The efficiency has been computed for a FAR of 0.001 Hz and the signal SNR is 10.

The performance of the other detection pipelines drops above 1 kHz. It should be mentioned that for MF, ALF and PC the tuning is intrinsically limited; the only free parameter of these pipelines is the time duration of the signal, thereby limiting the frequency domain exploration. KW is the filter for which the performance gets worse as the time–frequency volume increases. Actually, as already mentioned in section 3.3, because of the choice of the Haar function basis the KW performance drops for long-duration signals. One can also note that all pipeline performances are maximum in the region of low or moderate time–frequency volume where the actual SN signals are located. All the pipelines obtain their best performance on the SN signals and fail mostly at detecting the WN signals. Concerning the very low bandwidth signals which look like sine-Gaussians, QT performs very well as expected, while the EGC efficiency is not as good for sine-Gaussian signals with very low-frequency bandwidth. EGC is expected to be an optimal filter for sine-Gaussian, as is QT. The loss of efficiency is due to the choice of template placement for EGC, which is non-optimal in the region of the parameter space populated by those particular sine-Gaussian signals.

Focusing on the SN family, one can see that all pipeline performances drop for a particular SN signal, although they all maintain a very high efficiency for the others. For instance, the MF efficiency decreases to 6% for this one SN signal, while it remains always above 75% for the 49 other SN signals, and even better for similar signals in the parameter space neighborhood, as shown in figure 7. This efficiency drop is primarily explained by the peculiarity of the shape of this core collapse simulated signal, which does not show any peak usually associated with core bounce but rather rapid oscillations. This particular signal corresponds to a rapid collapse for which the first peak usually present in the SN signals is strongly suppressed (non-rotating model). The waveform of this SN signal is shown in figure 8. This example suggests that the three parameters used to describe a gravitational burst event are not complete. This fact is even clearer when one considers the WN signal results; in the region of the SN signals, the overall performance of all pipelines on WN is lower than for SN signals. Moreover, for

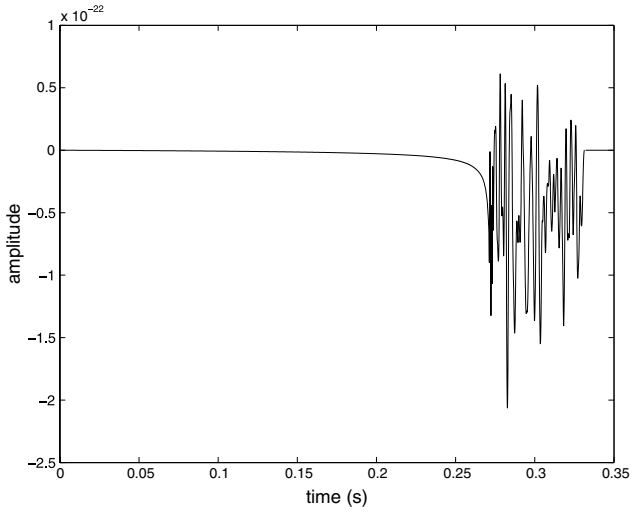

Figure 8. The waveform of the simulated SN signal (extracted from [5] and labeled as s15nonrot in the appendix) for which the efficiency of all pipelines is low compared to other SN signals close to it in the parameters space defined in this study.

all pipelines, there is a region, inside the SN area (for central frequency between 400 Hz and 500 Hz), where the efficiency drops to a very low value for WN signals, while there are some SN events with identical parameters for which the efficiency is close to 100%. This indicates again that the various pipelines are taking into account some signal shape information that might be badly modeled with the three parameters used for this study. But this present study is limited by the number of waveforms tested.

3.5. Timing accuracy

It is crucial to accurately estimate the arrival time of a signal in each gravitational wave detector in order to perform an interferometer network coincidence analysis, reconstruct the source sky location, and to perform a coincidence analysis with other messengers (neutrinos, gamma-ray bursts, etc). It is especially important to prove that we are able to determine the arrival time of a signal in each of the interferometers with an accuracy that is much better than the time of flight of a signal between two interferometers (10 ms between the LIGO interferometers, and 27 ms between the Virgo and LIGO interferometers). For the bank of burst filters investigated, we have studied the statistical properties of the signal arrival time estimators that can be built for each of the filters. The most natural and convenient definition of the signal arrival time is the time for which the amplitude is maximum. Taking this definition, an estimator for determining the signal arrival time has been defined based upon the filter statistics. Those estimators can be biased and/or can have different intrinsic accuracy depending on the waveform of the signal. We report in table 4 the bias and the standard deviation of the distribution of the difference between the true arrival time and the estimated arrival time obtained for each waveform injected each 60 s in the V1 3 h data stream. The signal strength was SNR $= 10$ and the detection efficiency was fixed by a common FAR of 0.1 Hz for all waveforms.

Table 4. Standard deviation and bias of the signal arrival time (in ms) obtained by estimators built from the burst filters. The values have been obtained for the different test-case waveforms selected at a false alarm rate of 0.1 Hz for the V1 data. The signal SNR is 10. When the efficiency is low, it has not been possible to estimate all the quantities for the PC filter estimator.

	PF	KW	QT	PC	EGC	MF	ALF
Standard deviation							
A1B2G1	0.05	0.5	0.2	0.04	0.03	0.05	0.3
A2B4G1	0.7	2.6	1.4	0.2	0.4	0.5	2.2
GAUSS1	1.2	1.4	0.8	0.1	0.2	0.8	1.5
GAUSS4	2.7	4.3	2.3	0.3	0.7	0.6	3.2
SG235Q5	1.4	0.9	0.9	1.2	0.5	1.3	1.1
SG235Q15	4.8	3.3	2.5	–	1.6	4.4	4.1
SG820Q5	0.2	0.3	0.2	–	0.2	0.3	0.3
SG820Q15	0.6	1.1	0.7	–	0.5	1.3	1.1
Bias							
A1B2G1	0.2	0.3	−0.1	−0.05	−0.06	0.03	0.1
A2B4G1	1.9	4.9	−1.7	−1.3	−1.4	2.1	0.7
GAUSS1	1.7	3.4	−0.05	−0.01	0.01	2.3	1.7
GAUSS4	4.1	10.7	−0.4	−0.03	−0.03	3.4	6.4
SG235Q5	0.6	1.3	−0.07	0.02	0.02	0.7	0.7
SG235Q15	1.1	0.8	0.06	–	0.1	0.2	0.6
SG820Q5	0.2	0.2	−0.01	–	0.01	0.1	0.1
SG820Q15	0.2	0.3	−0.04	–	0.03	0.3	0.2

As expected, the estimator built with the peak correlator filter output (PC) has a very good accuracy (less than 0.3 ms) and almost no bias for all signals which concentrate their energy in one peak (the Gaussian and DFM A1B2G1 signals). The best accuracy is obtained on the DFM A1B2G1 signal for all estimators. This is due to the small width of the DFM A1B2G1 peak (a width of 0.25 ms, compared with the 2.35 ms width of GAUSS1). Nevertheless, it has not been possible to characterize the arrival time estimator of PC on sine-Gaussian signals due to its very low efficiency. For the DFM A2B4G1 waveform, the bias and standard deviation of all estimators are rather large compared to other DFM waveforms due to the presence in the waveform of three peaks of decreasing amplitude separated by 5 ms. The energy of DFM A2B4G1 is more spread out in the time–frequency plane, decreasing the localization ability for all filters. For sine-Gaussian waveforms, the QT, EGC and PF estimators obtain the best time accuracy; they are the most efficient filters for detecting these signals. It is obvious that there is a direct relation between a low-efficiency filter and poor time accuracy estimator (see, for instance, PC or MF on sine-Gaussian waveforms), but an efficient filter does not necessarily allow one to build a good estimator of the arrival time (see, for example, ALF on Gaussian peak waveforms).

The large bias (up to 6.4 ms for ALF) of the time domain filters, KW and PF estimators, is explained partly by the whitening process applied to the data. Indeed, as shown in figure 9 for V1, the whitening filter strongly distorts a Gaussian waveform. The whitening can transform a Gaussian peak into a bipolar waveform due to the spectral power shape. As a consequence, the filter triggers on one peak or another depending on noise fluctuations. The whitening distortion effect is important for the signals that have a large SNR content at low frequency, such as the Gaussian signals. The distortion is even stronger in the case of H1 noise since the power spectrum is higher in the low-frequency region (the effect of the whitening process is then larger in this region). For instance, the MF estimator bias for a 4 ms Gaussian peak

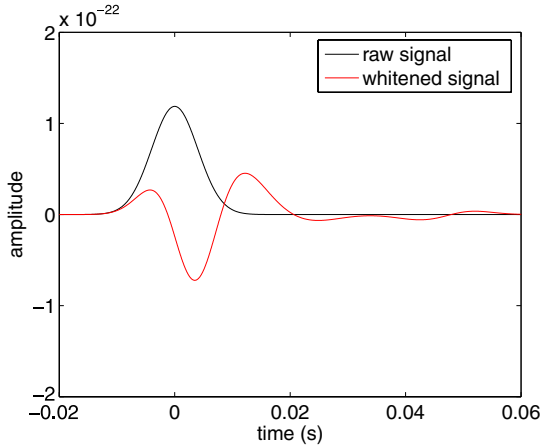

Figure 9. The effect of the V1 whitening pre-processing filter applied on a Gaussian pulse of 4 ms width (GAUSS4).

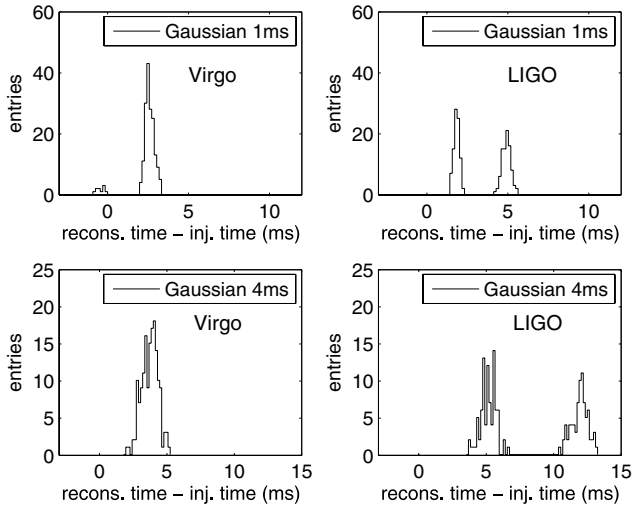

Figure 10. Distributions of the difference between the reconstructed arrival time of a Gaussian signal (the width of 1 ms and 4 ms) and the injected value. These distributions were created using the MF timing estimator on the V1 and H1 data.

increases from 3.4 ms to 8.3 ms and its standard deviation from 0.9 ms to 3.4 ms, as shown in figure 10. Moreover, the whitening algorithm used by the PF, MF and ALF pipelines was not a nonzero phase filter. It thus introduces an additional time delay that adds to the bias due to waveform distortion. This delay depends on the power spectrum and the waveform. Finally, it is important to note that for many waveforms the arrival time estimation accuracy for a signal of intrinsic SNR of 10 can be as good as 1 ms. The standard deviation of the arrival time estimation scales roughly inversely with the signal SNR [38].

4. Coincidence analysis

4.1. Description

As shown in section 3, the FAR of the burst signal filters will remain quite high if we do not want to miss the rare astrophysical event. For example, a DFM A1B2G1 signal of $\rho = 6$ can be observed with a detection efficiency between 30% and 75%, but with a 0.01 Hz FAR leading to 864 false alarm events per day. Furthermore, the FAR for burst searches on real data tend to be much higher than those on Gaussian stationary data. One way to significantly reduce the FAR while keeping the detection efficiency above, say 50%, is to request that the arrival times of signals in the detectors be compatible with the travel time of the wave between interferometer locations. This assumes, of course, that detector noise fluctuations are not correlated. It also requires the timing error to be less than the travel time of the wave which is the case for all pipelines (except maybe KW for Hanford–Livingston coincidence, see table 4). In the case of a source of unknown position, the signal arrival time difference must be less than the maximum travel time Δ_{12} between two detectors. If the source position is known (for example, a detected optical counterpart) one can use the exact travel time of the signal between the detectors. However, this constraint does not provide a large false alarm reduction.

In this study, the source has been located in the direction of the galactic center, while we are performing an all-sky blind search using only the timing information (the use of the frequency characteristics has been studied separately). Assuming that the trigger time distribution follows a Poisson distribution, the FAR of a coincidence analysis, performed with two interferometers' output, is given by the product, $fa_1 \cdot fa_2 \cdot 2\Delta_{12}$, where fa_i are the FARs in the detector pipelines and Δ_{12} is the maximum travel time of a signal from one detector to the other. If we consider a single experiment FAR of 0.1 Hz, the double experiment coincidence analysis FAR is around 0.2 mHz (for $\Delta_{12} = 10$ ms). However, if a detector in the network is not well aligned with respect to the others, the signal may be not visible in at least one detector, even with a high single interferometer FAR. It is thus important in the given network (the Hanford, Livingston and Virgo observatories) to study how the different network configurations compare. Hence we consider coincidence between these three interferometers (three-fold coincidence), and coincidence between two detectors among the three (two-fold coincidence). We also consider the combination of the two-fold coincidences in order to cope with the misalignment of the LIGO–Virgo detector network.

4.2. Two-fold and three-fold analysis

The seven pipelines have been applied on the three data streams in which six different waveforms were injected each minute (the maximum rate to avoid any bias of the pipeline output estimation due to the presence of too many signals in the data segment). The source of given $h_{\rm rss}$ is located in the direction of the galactic center and its polarization angle is varied randomly as explained in section 2.2.2. We produced event lists corresponding to a rate of false alarm events of 0.1 Hz. The efficiencies obtained by the pipelines for the six waveforms are reported in table 5.

4.2.1. Coincidence analysis. Starting from the generated list of events (FAR is 0.1 Hz), each pipeline looked for two-fold and three-fold coincidences. The coincidence time windows applied for a blind search take into account the maximum light travel time between pairs of interferometers and the maximum timing accuracy (bias and standard deviation) obtained for the test-case waveforms given in table 4. Using the results presented in table 4, we

Table 5. Detection efficiencies (in percent) obtained by the seven pipelines for a source located in the galactic center for a FAR of 0.1 Hz. The efficiencies have been estimated for each detector data stream: Hanford (H1), Livingston (L1) and Virgo (V1). In this study, the source emits signals regularly over 24 h (one emission each minute with the random polarization angle as explained in section 2.2.2); we tested six different waveforms. The pipelines' efficiencies thus take into account the modulation of the signal strength due to the antenna pattern of each detector at a given time. The best, worst and average efficiencies are also given.

	A1B2G1			A2B4G1			GAUSS1			GAUSS4			SG235Q15			SG820Q15		
	H1	L1	V1	H1	L1	V1	H1	L1	V1	H1	L1	V1	H1	L1	V1	H1	L1	V1
PF	42	42	49	49	48	47	66	62	50	28	29	57	35	38	31	42	42	63
KW	37	38	44	50	48	42	61	58	47	23	25	52	50	50	33	19	21	48
QT	46	45	48	59	56	46	72	68	50	40	43	52	71	67	53	48	47	65
PC	55	54	54	65	62	55	77	72	58	53	54	72	–	–	–	–	–	–
EGC	57	55	56	54	53	48	72	68	53	40	42	66	67	64	50	41	41	65
MF	40	40	51	53	52	51	64	61	50	27	29	63	38	41	23	10	11	33
ALF	43	43	52	57	55	52	68	63	53	36	39	68	42	43	25	16	19	44
Mean	46	45	51	55	53	49	69	65	52	35	37	61	43	43	31	25	26	45
Min	37	38	44	49	48	42	61	58	47	23	25	52	0	0	0	0	0	0
Max	57	55	56	65	62	55	77	72	58	53	54	72	71	67	53	48	47	65

conservatively assumed an error of 10 ms for all pipelines and for all signals. The event compatibility is tested using the estimated arrival times t_V, t_L and t_H of an event in each of the three detectors. For the two-fold coincidence analysis, the time difference in one of the three considered detector pairs must obey

$$|t_H - t_L| < \Delta_{HL}, \quad \text{for a H1–L1 two-fold coincidence analysis,} \tag{5}$$

$$|t_H - t_V| < \Delta_{VHL}, \quad \text{for a H1–V1 two-fold coincidence analysis,} \tag{6}$$

$$|t_L - t_V| < \Delta_{VHL}, \quad \text{for a V1–L1 two-fold coincidence analysis,} \tag{7}$$

where $\Delta_{HL} = 20$ ms and $\Delta_{VHL} = 38$ ms are the time windows of coincidence for the H1–L1 pair and for the H1–V1 or L1–V1 detector pairs, respectively. For the three-fold coincidence analysis, conditions (5)–(7) must be fulfilled simultaneously.

4.2.2. FAR estimation. It has been verified that the FAR does not depend on the pipeline but only depends on the coincidence time window that is applied for the given network configuration following the formula given in section 4.1. This supports the hypothesis that the event triggers for all pipelines are distributed according to a Poisson distribution. The FAR has been estimated precisely for each pipeline using the trigger list obtained from noise; in order to cope with the expected low number of false alarm events per day, especially in the case of the three-fold coincidence (most of the pipelines end up with 0 or 1 false alarm event), we have increased artificially by 10 000 times the duration of the simulation. We do this by time shifting, by a step of 1 s, the event arrival time obtained from noise data streams. In practice, for a two-fold coincidence analysis, we consider the two trigger lists and add to the arrival time of all the events of one list an offset of 1 s. We perform the coincidence and determine the number of coincident events and then we repeat the operation but adding an offset of 2 s, etc. Note that the events of a N s time-shifted stream that are in the last N s are moved to the beginning of the time-shifted stream such that the duration of the two streams in coincidence is always identical to 24 h. A 1 s time shift is long enough (the typical event duration is much smaller than 1 s) to be sure of having different triggers list each time we add

Table 6. Detection efficiencies (in percent) obtained from the seven pipelines for a source located in the galactic center for a double coincidence search between a pair of interferometers. The efficiency has been estimated for each combination: Hanford–Livingston (HL), Hanford–Virgo (HV) and Livingston–Virgo (LV). The two-fold coincidence analysis has been done using events list obtained for a FAR of 0.1 Hz in each detector. The FAR of each two-fold coincidence involving Virgo is 7.5×10^{-4} Hz and 4×10^{-4} Hz for the Hanford–Livingston two-fold coincidence analysis (for all pipelines).

	A1B2G1			A2B4G1			GAUSS1			GAUSS4			SG235Q15			SG820Q15		
	HL	HV	LV	HL	HV	LV	HL	HV	LV	HL	HV	LV	HL	HV	LV	HL	HV	LV
PF	29	15	17	34	17	18	48	28	27	18	12	14	24	5	9	28	22	22
KW	25	10	13	34	15	17	43	22	24	13	9	10	35	9	14	11	4	6
QT	31	16	18	40	22	22	53	32	31	28	16	19	53	33	32	33	27	26
PC	38	25	25	50	32	30	59	42	38	38	35	36	–	–	–	–	–	–
EGC	40	27	27	38	21	21	54	35	33	28	21	24	50	29	29	28	22	22
MF	26	14	17	37	22	22	47	27	27	17	14	16	28	4	9	4	1	3
ALF	29	17	18	40	25	24	50	32	30	23	20	22	31	6	11	9	4	7
Mean	31	18	19	39	22	22	51	31	30	24	18	20	32	12	15	16	11	12
Min	25	10	13	34	15	17	43	22	24	13	9	10	0	0	0	0	0	0
Max	40	27	27	50	32	30	59	42	38	38	35	36	53	33	32	33	27	26

Table 7. Detection efficiencies (in percent) obtained from the seven pipelines for a source located in the galactic center for a three-fold coincidence search between the Hanford, Livingston and Virgo interferometers. The coincidence analysis has been done using events list obtained for a FAR of 0.1 Hz in each detector. The three-fold coincidence FAR is 3×10^{-6} Hz for all pipelines.

	A1B2G1	A2B4G1	GAUSS1	GAUSS4	SG235Q15	SG820Q15
PF	9	10	17	7	3	13
KW	6	9	13	4	6	2
QT	9	12	21	9	22	17
PC	14	19	30	23	–	–
EGC	16	12	23	13	19	13
MF	8	13	17	8	3	–
ALF	9	14	20	12	3	2
Mean	10	13	20	11	8	7
Min	6	9	13	4	0	0
Max	16	19	30	23	22	17

an additional 1 s offset. We checked that similar results are obtained with a longer time offset. For the three-fold analysis, a similar action is done on two of the three trigger lists; a 1 s offset is added to one of the trigger lists, and a 2 s offset is added to the other. That guarantees that at each step we perform coincidence analysis with trigger lists as if we had simulated new data streams.

For a two-fold coincidence search, the FAR is $(7.5 \pm 0.1) \times 10^{-4}$ Hz for a pair involving the Virgo (7.6×10^{-4} Hz expected), and $(4.03 \pm 0.03) \times 10^{-4}$ Hz for the Livingston–Hanford pair (4.1×10^{-4} Hz expected). For the three-fold coincidence, the FAR is $(3.07 \pm 0.03) \times 10^{-6}$ Hz (3.04×10^{-6} Hz expected).

4.2.3. Two-fold, three-fold and combined two-fold analysis. In tables 6 and 7, we give the detection efficiencies obtained for the two-fold coincidence and the three-fold coincidence analysis, respectively. It is interesting to note that for a given waveform the three-fold coincidence efficiencies of the pipelines differ significantly. The maximum (30%) and average

Table 8. Detection efficiencies (in percent) obtained by the seven pipelines for a source located in the galactic center for a double coincidence search between pairs of interferometers. The two-fold coincidence analysis has been done using event lists compiled such that the two-fold coincidence false alarm rate is 10^{-6} Hz. The efficiency has been estimated for each combination: Hanford–Livingston (HL), Hanford–Virgo (HV) and Livingston–Virgo (LV).

	A1B2G1			A2B4G1			GAUSS1			GAUSS4			SG235Q15			SG820Q15		
	HL	HV	LV	HL	HV	LV	HL	HV	LV	HL	HV	LV	HL	HV	LV	HL	HV	LV
PF	23	9	11	29	10	13	43	18	20	13	5	7	15	1	4	22	12	15
KW	19	5	9	27	7	11	38	12	16	9	3	5	29	4	9	7	2	4
QT	25	8	12	35	12	16	48	22	22	22	9	12	48	25	25	26	16	18
PC	33	15	18	39	20	20	53	32	30	30	23	24	–	–	–	–	–	–
EGC	35	18	20	31	11	14	47	24	24	20	13	15	43	19	21	21	10	14
MF	20	7	10	30	12	15	40	15	18	10	6	8	18	–	3	–	–	–
ALF	23	8	12	34	14	16	43	20	22	16	11	14	21	1	4	4	–	2
Mean	25	10	13	32	12	15	45	20	22	17	10	12	25	7	9	11	6	8
Min	19	5	9	27	7	11	38	12	16	9	3	5	0	0	0	0	0	0
Max	35	18	20	39	20	20	53	32	30	30	23	24	48	25	25	26	16	18

(20%) values obtained for GAUSS1 are low due to the non-optimum alignment of the three detectors. On the other hand, we end up with a FAR which is easily manageable, with less than one false alarm per day. This number is not achievable by any individual interferometer search. However, requiring coincidence among three interferometers that are not optimally aligned might not be the best strategy, compared to a two-fold coincidence search using Hanford and Livingston, which are well aligned. Note that, as expected, the efficiency of the Livingston–Hanford pair is always higher than any pair involving Virgo. Among the two other pairs, Virgo–Hanford is the worst due to the least optimal antenna response overlap. The results of the two-fold coincidence, given in table 6, indicate that on average the efficiency can be up to 70% higher than in the three-fold coincidence case, but the FAR remains high (a few 10^{-4} Hz). We thus estimate the efficiency of the two-fold coincidence analysis at the FAR of the three-fold coincidence analysis to be 10^{-6} Hz. The results are summarized in table 8. The two-fold efficiency is higher than the three-fold efficiency (comparison done at the same FAR) and, of course, the Hanford–Livingston pair is always favored compared to any pair including the Virgo detector. One can also require the detection of events in one of the three pairs of interferometers. The main advantage of this strategy is to reduce the FAR because of the coincidence constraint, while recovering events which are located in a sky zone for which only two detectors are sensitive. The results are summarized in table 9 for all pipelines. The combined two-fold coincidence analysis has been done using event lists obtained for a FAR of 10^{-6} in each pair of detectors, such that the combined two-fold analysis FAR is 3×10^{-6} Hz; it is the sum of the FAR of the two-fold coincidence from which the events that are actually common to the three pairs of interferometers must be subtracted two times. This number of events is given by the three-fold FAR which is at least three orders of magnitude lower than the two-fold FAR, and then can therefore be neglected; this can be directly compared to the three-fold coincidence FAR (which was used to make table 7) of 3×10^{-6} Hz.

4.3. Coincidence searches using the frequency information

Some of the burst pipelines (QT, PF, KW and EGC) are able to estimate the characteristics of the events in the frequency domain. Specifically, these are the frequency bandwidth (defined by $f_{\min}$ and $f_{\max}$) and the peak frequency (f_{peak}) which corresponds to the template

Table 9. Detection efficiencies (in percent) obtained by the seven pipelines for a source located in the galactic center requiring that at least one pair of interferometers among the three detects the signal. This combined two-fold coincidence analysis has been done using event lists obtained for a FAR of 10^{-6} Hz in each pair of detectors, such that the combined two-fold analysis FAR is 3×10^{-6} Hz identical to the three-fold analysis.

HL ∪ HV ∪ LV	A1B2G1	A2B4G1	GAUSS1	GAUSS4	SG235Q15	SG820Q15
PF	33	39	60	19	19	34
KW	26	36	52	14	38	11
QT	35	48	66	32	67	40
PC	56	67	76	55	–	–
EGC	52	43	66	32	60	32
MF	28	43	55	17	20	–
ALF	33	47	60	28	25	6
Mean	38	46	62	28	33	18
Min	26	36	52	14	0	0
Max	56	67	76	55	67	40

or wavelet coefficient that has the highest SNR. The peak frequency is thus not necessarily in the middle of the frequency bandwidth. Those coincidence searches whose results are given in section 4.2 considered only the timing information. The QT pipeline used in the LSC is actually performing a combined coincidence search requesting timing and frequency coincidence. It has been shown [33] that the QT coincidence search pipeline can reach a better efficiency (of a few percent) for the same FAR when using the frequency information. It is worth mentioning that the time and frequency coincidence performed in the LSC QT pipeline is done before the event extraction; this results in pruning overlapping templates. In this study, the time and frequency coincidence is done using event lists.

In this study, we tried to estimate the benefit of adding the frequency information to a coincidence search. For this, we used the trigger lists generated for each interferometer at 0.1 Hz, and applied the same timing coincidence plus a constraint on the overlap of the bandwidth of the triggers:

$$f^i_{\max} > f^j_{\min} \quad \text{if} \quad f^i_{\min} < f^j_{\min} \qquad \text{or} \qquad f^j_{\max} > f^i_{\min} \quad \text{if} \quad f^i_{\min} > f^j_{\min}, \tag{8}$$

where i and j are the indices of two of the three detectors. We estimated the efficiencies of the three pipelines on the test-case signals for the two-fold and three-fold coincidence searches and compared them to the results given in tables 6 and 7 (time-only coincidence). The efficiencies obtained were very similar (with a loss lower than 1%) to those obtained for the time-only coincidence search. The FAR is reduced, but in a rather moderate way depending on the pipelines: a factor of 0.67 for EGC and KW, a factor of 0.4 for PF and a factor of 0.2 for QT for the three-fold coincidence search. The FAR reduction factors are given in table 10 for the different network configurations.

In addition, we have also tried to use the peak frequency information instead of the bandwidth in order to determine if events are coincident in the frequency domain. The event frequency compatibility test is then

$$\left| f^i_{\text{peak}} - f^i_{\text{peak}} \right| < \Delta f, \tag{9}$$

where Δf has been varied such as the efficiency remains constant compared to a time-only coincidence analysis. The FAR reduction was found to be slightly higher compared to the bandwidth overlap coincidence constraint. This is especially the case for PF, for which the FAR of a three-fold coincidence is reduced by a factor 0.08 compared to the time-only coincidence, keeping for all test-case waveforms the same efficiency. But for the other

Table 10. FAR (in Hz) obtained by the four burst pipelines that estimate the frequency characteristics of the events in this study (QT, PF, KW and EGC). The results are given for a time-only coincidence search and for the time-and-frequency coincidence search. In the latter case, one requests that the frequency bandwidth of events overlaps.

Network	VH	VL	HL	VHL
FAR (time-only) QT PF KW and EGC	7.6×10^{-4}	7.6×10^{-4}	4.0×10^{-4}	3.0×10^{-6}
FAR (time and frequency) QT	3.2×10^{-4}	3.2×10^{-4}	1.7×10^{-4}	4.9×10^{-7}
Reduction factor QT	0.4	0.4	0.4	0.2
FAR (time and frequency) PF	5.0×10^{-4}	5.0×10^{-4}	2.6×10^{-4}	1.2×10^{-6}
Reduction factor PF	0.7	0.7	0.7	0.4
FAR (time and frequency) KW	6.2×10^{-4}	6.2×10^{-4}	3.4×10^{-4}	2.0×10^{-6}
Reduction factor KW	0.8	0.8	0.9	0.7
FAR (time and frequency) EGC	6.2×10^{-4}	6.2×10^{-4}	3.7×10^{-4}	2.2×10^{-6}
Reduction factor EGC	0.8	0.8	0.9	0.7

pipelines (QT, KW and EGC), the signal efficiency drops by at least 10% absolute for some of the waveforms (mainly the large bandwidth signals such as A1B2G1 or GAUSS1). Indeed, for large bandwidth signals, these pipelines fail to estimate precisely the peak frequency, which hence seems not to be a robust enough parameter to be used for a time-and-frequency coincidence pipeline (to maintain the efficiency to the time-only coincidence value, it was mandatory to increase Δf such that no FAR reduction was observed); an exception to this is the PF pipeline.

4.4. Comparisons and detection strategy discussion

In the previous sections, we have estimated the efficiency of seven pipelines for different search strategies: three-fold, two-fold and combined two-fold coincidence. We have first shown that the performance of some of the pipelines depends strongly on the waveform. The extreme case is reached by the correlator PC which performs very well for the DFM and Gaussian waveforms, but fails at detecting the sine-Gaussian waveforms. On the other hand, the EGC and QT pipelines' performance remains very high for all kinds of waveforms. The PF and KW pipelines have similar performance whatever the waveform, but perform on average a bit less efficiently.

The two-fold coincidence results show that one can decrease the FAR from 0.1 Hz (8640 events per day) to a few 10^{-4} Hz (30 events per day), while maintaining a detection efficiency at an acceptable level. The best performances are, of course, obtained from the Hanford–Livingston pair; these efficiencies are, on average for all pipelines, 0.15 lower than the individual interferometer pipeline efficiencies working at a 0.1 Hz FAR. The efficiency of the HV or LV combination is approximately two-thirds of the HL efficiency, due to the different alignment of LIGO and Virgo. To reduce the FAR significantly, one has to request a three-fold coincidence; we then end up with two false alarm events per week. However, due to the non-optimum alignment of the three interferometers, the detection efficiency drops to 10–20% on average for the test-case waveforms. To overcome the problem of the non-optimum alignment of the three interferometers, while keeping a very low number of false alarm events, the best strategy seems to be such as to request the detection of an event in at least one of the three pairs of detectors (combined two-fold coincidence). We have seen that, for the same FAR (two events per week), the efficiency is three times higher, on average, compared to a three-fold coincidence search. The best performing pipeline efficiency is then between 40% and 76%, depending on the waveform for two false alarm events per week.

Moreover, comparing the two-fold coincident search obtained with the Hanford–Livingston pair to the combined two-fold coincidence, we have shown that, on average for all waveforms, the detection efficiency is increased by 50% by adding Virgo to the Hanford–Livingston network (we have checked that the two-fold coincidence Hanford–Livingston efficiencies for a FAR of 3×10^{-6} Hz are very similar to those given in table 8 for a FAR of 10^{-6} Hz. The difference is at maximum as high as 0.02). If we consider the results of the two-fold combined search in table 9, QT and EGC are the two best performing pipelines over the six test-case waveforms. The others have the main drawback of performance depending on the waveforms.

In addition, the figure of merit of the time-only coincident search can be improved if one requires that coincident events have similar frequency characteristics. We have seen that the reduction of the false alarm events actually depends, from one pipeline to another, on the frequency estimation of the event bandwidth. One can expect to reduce the false alarm event number by up to a factor 0.08 without losing any efficiency in the most favorable case (PF pipeline).

5. Combination of filters

In section 3, the detection potential of several pipelines has been compared using a few test-case waveforms. We have seen that a pipeline's performance is different from one waveform to another, and there is the indication that the pipelines are complementary and can cover the full range of tested waveforms. Conversely, for a given signal, it could be interesting to determine if all pipelines detect the same events. We would expect a gain of the detection efficiency by combining different filters' output. Of course, merging (OR analysis) the trigger lists of different pipelines increases the FAR. If the pipelines all detect the same events, it would then be more interesting to request that the filters' combination keep only the events seen by all the considered filters (AND analysis). But in that case, the detection probability will always be dominated by the filter that is least sensitive. We could however expect that the pipelines are not sensitive to the same noise events and hence see a reduction of the FAR. In this study, we have considered the 120 possible combinations given 7 pipelines, from 2 filters up to the 7 filter combination. To fairly compare the results, we need to derive the ROC curves and compare them to the single pipeline curves.

We started by using the seven pipelines' trigger lists provided for the eight test-case waveforms injected into the V1 and H1 data sets (optimal orientation) with a SNR of 5 and 10, and for 3 FAR (0.1 Hz, 0.01 Hz and 0.005 Hz). We chose identical FAR for all filters for the sake of simplicity, while they might not correspond to the optimal choice. Next, from the single method trigger lists we produced a new set of triggers; a single gravitational wave burst candidate was created via the merger of triggers that were overlapping or temporally closer than 0.1 s. This condition was introduced in order to account for the maximum timing error of the filters without merging triggers due to noise with real signal ones (we start from triggers lists computed at a maximum FAR of 0.1 Hz). The non-merged triggers are simply added to the new list for the OR analysis. These prescriptions allowed us to compute both the FAR for the combination of triggers as well as the efficiency. Then, for each type of combination (two filters, three filters, etc) we keep the one having the best ROCs. In such a way we can, at the end, compare the six combined ROCs with the seven pipelines' ROC.

The main conclusion of this analysis is that no combination shows a ROC consistently better than the best single method ROC, for all waveforms. As expected, the AND analysis helps at reducing the FAR, but the efficiency decrease is too large to provide any real gain. The result is robust with respect to the injection signal SNR and the choice of interferometer.

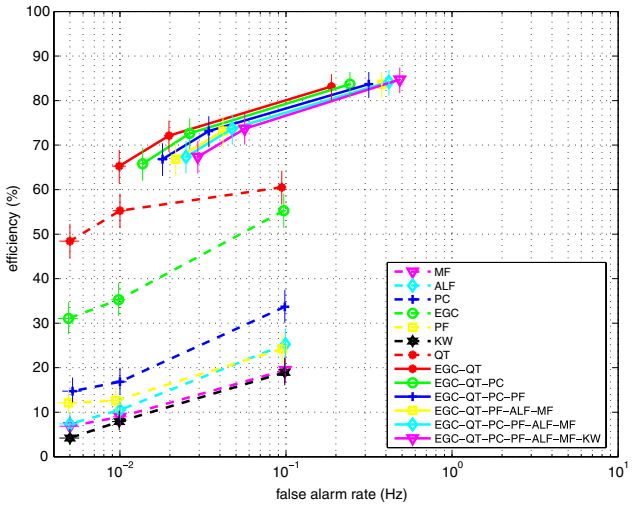

Figure 11. Three operating points for single methods and the best performing combination of methods in the V1 data for an injected sine-Gaussian SG235Q5 with a SNR of 5. The OR analysis obtained its best performance on this sine-Gaussian test-case waveform. The vertical error bars have been computed with a binomial fit and the horizontal ones by Poisson statistics. It can be noted that adding new methods to the EGC–QT combination only translates the ROC horizontally. This means that in this case adding methods increases the number of false alarms but not the number of observed injections.

Occasionally, for a specific waveform, like the sine-Gaussian SG235Q5 (as shown in figure 11), the OR combination of the two best pipelines mildly improves the ROC; the relative efficiency gain is between 10% and 30% depending on the FAR. But, this improvement depends on the waveform; for the A1B2G1 and GAUSS4 signals the performance is as good as the best pipeline, or even worse. In figure 11, we can also note that actually QT performs best on sine-Gaussian SG235Q5, and combining QT with EGC increases the detection efficiency from 55% (QT only) to 65% (QT or EGC) at a FAR of 10^{-2} Hz. Since these results do not encourage the combination of methods, we decided not to pursue it for the network study where only combinations of interferometers' configurations have been thoroughly studied.

6. Source sky location reconstruction

6.1. Introduction

In addition to the increase of the detection probability of a burst gravitational wave, the other significant advantage of the LIGO and Virgo detector network is to provide the possibility to estimate the position of the source on the sky. It is well known [39] that a minimum of three detectors is mandatory in order to determine the source sky position, even if an ambiguity remains between two positions symmetric with respect to the plane defined by the three detectors. So, the LIGO–Virgo network is the first step toward gravitational wave astronomy that includes source localization. The source coordinates on the sky are right ascension (α) and declination (δ). A method [25] has been developed for estimating the source position using only the arrival time t_i of the gravitational wave in each detector, and its associated arrival time error σ_i. This method has the advantage of being fast and independent of the pipeline.

Three-fold coincidence search events found by the seven pipelines in the 24 h of data with a FAR of 3×10^{-6} Hz have been considered in this sky location study. A comparison of the source reconstruction accuracy of each pipeline is presented below.

6.2. Method

Each burst pipeline provides a list of three-fold coincidence events defined by the arrival time and the event SNR reconstructed in the three detectors. We then have to estimate the arrival time error for each event. In this study, for the sake of simplicity, we have taken the following relation that is exact for a Gaussian signal of half-width 1 ms detected by PC [38]:

$$\sigma_i = \frac{1.4}{\mathrm{SNR}_i}\mathrm{ms}. \tag{10}$$

It should be noted that, in general, the burst pipelines can determine, event-by-event, the error of the arrival time, for instance, by taking into account the results given in section 3.5. We have checked that the results weakly depend on the error parametrization given in (10) as the result is primarily constrained by the arrival time values. To estimate α and δ a least-square minimization has been used. Our χ^2 function is defined by

$$\chi^2 = \sum_{i=1}^{n} \frac{\left(t_i - \left(t_0 + \Delta_i^{\mathrm{Earth}}(\alpha, \delta)\right)\right)^2}{\sigma_i^2}, \tag{11}$$

where t_0 is the arrival time of the gravitational wave at the center of the Earth and $\Delta_i^{\mathrm{Earth}}(\alpha, \delta)$ is the delay between the center of the Earth and the ith detector at a given sidereal time (and only depends on α and δ). First of all, this definition of the χ^2 function allows the fitting of uncorrelated data, while the usual reconstruction using two time differences between detector implies variables with correlated errors deserving a more difficult treatment. By introducing t_0, there is no reference detector D_1 used to compute timing differences. The second advantage is that the network is not limited to three detectors, and the addition of other detectors is straightforward. Nevertheless, this method requires that the event be seen by all the detectors above a given threshold, whereas coherent methods do not need this first selection step.

6.3. Results

Figure 12 shows an example of the reconstructed source coordinate distributions using the 24 h of simulated data. It has been obtained using 456 GAUSS1 events detected by the PC pipeline. These distributions include the effect of modulation due to the Earth's rotation over 24 h, which then induces some variation of the event arrival time errors. The errors on α and δ are about 1° (respectively, 0.7° and 1°). Table 11 gives a summary of angular reconstruction obtained for each pipeline on all waveforms studied. As expected, the estimation accuracy is mainly dependent on the arrival time measurement accuracy. In this case the correlator pipelines (PC and EGC) and QT produce the best results. The achieved precision depends also on the considered waveform. The best accuracy is obtained for waveforms which have rather simple shape, such as clearly defined peak (like DFM A1B2G1 or GAUSS1). In contrast, when the waveforms become more complex (DFM A2B4G1, sine-Gaussian), all the pipelines that make very few assumptions on the exact waveform (MF, ALF, PF, KW) fail at precisely locating the source. QT and EGC perform, as expected, the best for sine-Gaussian signals. One should also note that pipelines having a large timing bias have a poor source reconstruction estimation, due to the fact that the bias is mainly different in each detector. We have seen that bias is predominantly due to the use of nonzero phase whitening filtering. Since LIGO

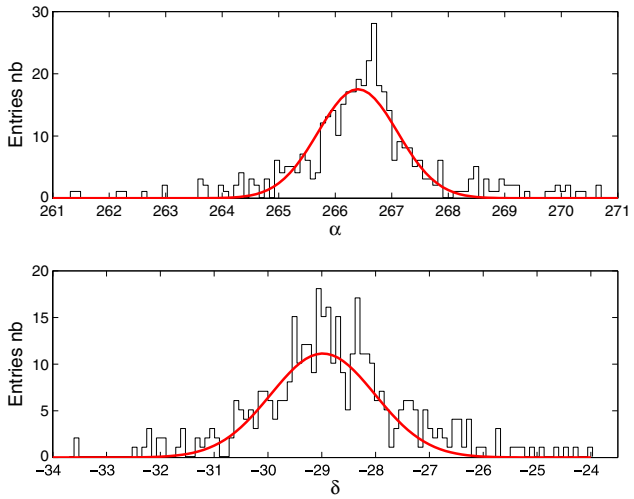

Figure 12. Distribution of source coordinates α and δ (in degrees) obtained for a GAUSS1 waveform detected with the PC pipeline in the LIGO–Virgo network. The source has been placed in the direction of the galactic center and emits signals regularly over 24 h. The curve is the result of a Gaussian fit of the data.

and Virgo have different power spectrum shapes the bias is different. That tends to prove that the source position determination should be somehow decoupled from the detection problem. Once good candidates are detected, techniques including more information (for instance rough waveform estimation as needed by Markov Chain Monte Carlo algorithms [23]) should be used to estimate the source position.

7. Summary

In this study, we have compared different pipelines developed both in the LSC and Virgo for the search for unmodeled gravitational wave bursts. For both Virgo and LIGO data sets, we have evaluated the pipeline's performance and validated their ability to detect a signal. Among all the seven pipelines studied, we have especially shown that some are more efficient than others. We have demonstrated the benefits of a LIGO–Virgo combined search for the detection of a signal; adding Virgo to the Hanford–Livingston interferometer network can increase the detection efficiency by 50% (without increasing the false alarm rate). We have shown that the combined two-fold coincident search is three times more efficient than a three-fold coincident search (for the same expected number of false alarm events). In contrast, combining the filters' trigger lists obtained on the same data stream does not improve the detection potential of the burst analysis. The second advantage of the LIGO–Virgo network is its capability to locate a source. We have shown that in the most favorable case we can expect to reconstruct the source position with a precision of the order of 1° for both the right ascension and the declination. The position determination performance is not as good when the waveform is complex in structure. It would be interesting, in the near future, to compare the performance obtained by the combined two-fold coincident search to coherent searches [40] using the same network of interferometers, as well as their respective performance to reconstruct the source position [17].

Table 11. Reconstructed source coordinates obtained by the burst pipelines using the method described in section 6.2 for the different waveforms studied. Standard deviation are also given. The galactic center is located at (266.4°, −28.98°). The number of three-fold coincident events used to determine the sky position is also given.

		A1B2G1	A2B4G1	GAUSS1	GAUSS4	SG235Q15	SG820Q15
	α	265.0 ± 4.0	260.3 ± 1.9	263.0 ± 7.0	250.0 ± 14.0	258.0 ± 29.0	266.0 ± 5.0
PF	δ	-28.0 ± 7.0	-27.0 ± 8.0	-29.0 ± 13.0	-13.0 ± 21.0	-15.0 ± 33.0	-28.0 ± 10.0
	#	126	138	255	104	37	184
	α	265.0 ± 5.0	264.7 ± 9.0	265.0 ± 8.0	265.0 ± 22.0	264.0 ± 29.0	266.0 ± 6.0
KW	δ	-26.5 ± 9.0	-26.0 ± 13.0	-25.0 ± 12.0	-29.0 ± 23.0	-15.0 ± 32.0	-27.0 ± 10.0
	#	93	159	227	61	102	38
	α	266.0 ± 1.5	264.0 ± 6.0	266.0 ± 4.0	268.0 ± 13.0	266.0 ± 11.0	267.0 ± 3.0
QT	δ	-28.8 ± 4.6	-28.0 ± 12.0	-28.5 ± 8.0	-25.0 ± 17.0	-25.0 ± 16.0	-29.0 ± 6.0
	#	134	179	300	131	318	238
	α	266.5 ± 0.5	266.7 ± 1.3	266.4 ± 0.7	266.6 ± 2.0		
PC	δ	-29.0 ± 0.6	-29.1 ± 2.3	-29.0 ± 1.0	-29.1 ± 3.6	–	–
	#	240	273	456	334		
	α	266.3 ± 0.3	265.6 ± 3.0	266.2 ± 1.0	266.7 ± 3.0	265.0 ± 9.0	267.1 ± 3.0
EGC	δ	-28.9 ± 0.4	-29.2 ± 7.0	-29.0 ± 1.7	-28.1 ± 6.0	-28.7 ± 13.0	-29.0 ± 4.5
	#	223	172	338	193 ?	269	191
	α	266.5 ± 0.5	261.3 ± 1.3	263.7 ± 8.0	258.5 ± 18.0	263.0 ± 30.0	
MF	δ	-29.0 ± 0.6	-27.3 ± 4.0	-30.2 ± 14.0	-10.0 ± 22.0	-24.0 ± 29.0	–
	#	112	182	243	115	41	
	α	265.5 ± 1.8	258.0 ± 14.0	260.1 ± 1.7	258.0 ± 3.0	260.0 ± 23.0	264.0 ± 10.0
ALF	δ	-27.0 ± 5.0	-25.9 ± 20.0	-29.4 ± 7.0	-17.0 ± 10.0	-27.0 ± 28.0	-28.0 ± 10.0
	#	132	208	288	175	50	32

The next step of this work is to analyze test sets of real data from LIGO and Virgo. This will bring forward other issues to be studied, such as the examination and handling of the quality of the data in a combined search. One of the key issues will be the non-stationarity of the data sets (the increase of the noise during short periods, for instance due to seismic activity) that can produce higher FAR than what has been optimally considered in this study. That could have an impact especially on the combined two-fold coincidence analysis FAR. Another aspect of the GW burst search is the glitches present in the real interferometer data. If a careful analysis is undertaken in order to understand the origin of the glitches, and thereby allowing one to suppress most of them, then dedicated techniques to distinguish real GW burst signal from noise transients could be used [41].

Acknowledgments

LIGO Laboratory and the LIGO Scientific Collaboration gratefully acknowledge the support of the United States National Science Foundation for the construction and operation of the LIGO Laboratory and for the support of this research. NC also acknowledges the support of the Fulbright Scholar Program. Virgo is supported by the CNRS (France) and INFN (Italy). Support was also provided by the MIT-France alliance award.

Appendix. Parameters used for the robustness test

Table A1 provides the parameters associated with the waveforms used in this study. These are the signals that were used to test the coverage of the GW parameter space by the burst search pipelines in section 3.4.

Table A1. Parameters of the 100 waveforms used to test the robustness of the different burst pipelines: 50 waveforms are simulated core collapse, while the 50 other (WN) are filtered white noise bursts. DFM waveforms (Newtonian or relativistic simulation) are taken from [4], BO waveforms (Newtonian) are taken from [5] and ZM (Newtonian) waveforms are extracted from [3]. The peak frequency, bandwidth and duration of the signals have been computed as explained in section 2.2.1.

Name	Peak frequency (Hz)	Bandwidth (Hz)	Duration (s)
DFM (New.) A1B2G1	365.3	182.1	0.0012
DFM (New.) A4B1G1	429.5	324.4	0.0012
DFM (New.) A4B5G5	138.1	84.9	0.0030
DFM (Rel.) A3B1G1	552.5	585.5	0.0007
DFM (Rel.) A3B2G1	433.3	428.9	0.0018
DFM (Rel.) A3B2G2	622.3	621.1	0.0006
DFM (Rel.) A3B4G2	77.9	52.3	0.0063
DFM (Rel.) A4B4G5	67.3	63.1	0.0110
DFM (Rel.) A1B3G2	670.1	518.4	0.0006
DFM (Rel.) A4B5G4	69.7	63.2	0.0079
DFM (Rel.) A4B1G1	288.8	281.2	0.0047
DFM (Rel.) A4B1G2	349.8	341.8	0.0036
DFM (Rel.) A3B3G2	83.7	78.7	0.0135
DFM (Rel.) A4B2G2	201.1	194.3	0.0082
BO s11A1000B0.3	197.0	109.9	0.0023
BO s11A50000B0.6	59.0	31.6	0.0067
BO s11A500B0.4	92.2	56.6	0.0089
BO s11A1000B0.4	81.6	44.7	0.0048
BO s15A500B0.4	74.8	73.0	0.0085
BO s15A1000B0.3	239.8	157.7	0.0017
BO s15A1000B0.6	51.3	34.6	0.0079
BO s15nonrot	133.4	132.7	0.0221
BO s20A50000B0.1	417.1	138.2	0.0011
BO s20A500B0.2	202.2	171.4	0.0031
BO s20A50000B0.2	401.7	171.5	0.0011
BO s20A50000B0.5	267.0	216.2	0.0015
BO s20nonrot	217.0	181.9	0.0093
BO s20A1000B0.4	83.0	50.9	0.0285
BO s25A500B0.2	198.0	173.3	0.0310
BO s20A1000B0.5	63.3	40.4	0.0363
BO s20A500B0.1	394.1	271.2	0.0010
ZM (New.) A1B1G3	550.3	311.4	0.0007
ZM (New.) A2B5G4	74.0	70.0	0.0067
ZM (New.) A4B2G5	395.2	386.6	0.0011
ZM (New.) A2B5G5	55.2	42.3	0.0031
ZM (New.) A3B4G3	112.4	59.7	0.0038
ZM (New.) A3B4G4	147.3	137.0	0.0044
ZM (New.) A2B2G3	588.3	165.7	0.0009
ZM (New.) A3B4G5	102.9	77.3	0.0032
ZM (New.) A3B2G1	193.0	156.0	0.0218
ZM (New.) A4B1G1	399.3	303.1	0.0132
ZM (New.) A1B3G1	110.1	104.3	0.0272
ZM (New.) A2B3G2	218.0	143.0	0.0026
ZM (New.) A3B2G2	370.3	230.8	0.0012
ZM (New.) A3B2G4	678.6	275.2	0.0007
ZM (New.) A4B1G4	535.0	191.4	0.0013
ZM (New.) A3B2G5	318.7	297.9	0.0022
ZM (New.) A4B1G5	473.3	483.3	0.0018

Table A1. (Continued.)

Name	Peak frequency (Hz)	Bandwidth (Hz)	Duration (s)
ZM (New.) A3B3G2	163.9	106.9	0.0034
ZM (New.) A4B2G2	248.9	171.6	0.0023
WN	155.3	171.6	0.0023
WN	200.6	176.0	0.0312
WN	101.1	21.7	0.0059
WN	97.2	10.4	0.0125
WN	100.6	8.1	0.0175
WN	97.0	10.8	0.0272
WN	110.1	43.8	0.0023
WN	121.6	78.8	0.0170
WN	118.3	99.5	0.0027
WN	206.1	193.9	0.0024
WN	250.2	43.1	0.0028
WN	248.3	7.6	0.0186
WN	247.2	55.7	0.0044
WN	398.0	39.6	0.0236
WN	413.6	200.8	0.0189
WN	437.0	400.9	0.0120
WN	495.2	320.6	0.0157
WN	503.6	11.0	0.0137
WN	503.0	9.0	0.0170
WN	519.3	41.6	0.0035
WN	535.7	118.9	0.0059
WN	766.4	541.2	0.0031
WN	696.4	553.8	0.0110
WN	699.7	7.6	0.0193
WN	695.2	85.4	0.0026
WN	693.8	16.2	0.0204
WN	742.3	443.6	0.0016
WN	943.4	16.2	0.0110
WN	976.4	178.8	0.0026
WN	912.7	203.9	0.0144
WN	1020.0	375.3	0.0037
WN	1049.1	31.9	0.0393
WN	1068.9	455.2	0.0338
WN	1062.5	577.2	0.0330
WN	1299.8	8.5	0.0181
WN	1300.0	32.8	0.0237
WN	1316.1	105.3	0.0020
WN	1276.6	353.4	0.0247
WN	1498.0	25.1	0.0051
WN	1586.1	439.9	0.0057
WN	1559.6	354.4	0.0025
WN	1494.2	716.4	0.0303
WN	1704.2	22.0	0.0054
WN	1703.7	34.2	0.0150
WN	1723.2	309.8	0.0141
WN	1718.8	455.2	0.0173
WN	1704.4	649.7	0.0165
WN	1704.4	642.5	0.0320
WN	1699.2	45.9	0.0244
WN	1991.7	164.3	0.0180

References

[1] Abbott B *et al* (the LIGO Scientific Collaboration) 2006 *Class. Quantum Grav.* **23** S51–6
[2] Acernese F *et al* (the Virgo Collaboration) 2006 *Class. Quantum Grav.* **23** S63–9
[3] Zwerger T and Mueller E 1997 *Astron. Astrophys.* **320** 209
[4] Dimmelmeier H, Font J A and Mueller E 2002 *Astron. Astrophys.* **393** 523
[5] Ott C *et al* 2004 *Astrophys. J.* **600** 834
[6] Shibata M and Sekiguchi Y I 2004 *Phys. Rev.* D **69** 084024
[7] Flanagan E E and Hughes S A 1998 *Phys. Rev.* D **57** 4535
[8] Baker J *et al* 2006 *Phys. Rev.* D **73** 104002
[9] Pretorius F 2005 *Phys. Rev. Lett.* **95** 121101
[10] Campanelli M *et al* 2006 *Phys. Rev. Lett.* **96** 111101
[11] Kokkotas K D and Schmidt B G 1999 Living Rev. Rel. http://www.livingreviews.org/lrr-1999-2
[12] Meszaros P 2006 *Rep. Prog. Phys.* **69** 2259–322
[13] Ferrari V, Miniutti G and Pons J A 2003 *Class. Quantum Grav.* **20** S841
[14] Damour T and Vilenkin A 2005 *Phys. Rev.* D **71** 063510
[15] Arnaud N *et al* 1999 *Phys. Rev.* D **59** 082002
[16] Ott C *et al* 2006 *Phys. Rev. Lett.* **96** 201102
[17] Gursel Y and Tinto M 1989 *Phys. Rev.* D **40** 3884
[18] Arnaud N *et al* 2003 *Phys. Rev.* D **68** 102001
[19] Astone P *et al* 2003 *Phys. Rev.* D **68** 022001
[20] Abbott B *et al* (the LIGO Scientific Collaboration) 2005 *Phys. Rev.* D **72** 062001
[21] Abbott B *et al* (the LIGO Scientific Collaboration and the TAMA Collaboration) 2005 *Phys. Rev.* D **72** 122004
[22] Poggi S *et al* 2006 *J. Phys. Conf. Ser.* **32** 198–205
[23] Beauville F *et al* 2008 Detailed comparison of LIGO and Virgo inspiral pipelines in preparation for a joint search *Class. Quantum Grav.* **25** 045001
[24] Beauville F *et al* 2005 *Class. Quantum Grav.* **22** S1293
[25] Cavalier F *et al* 2006 *Phys. Rev.* D **74** 082004
[26] The LSC programs are in the LSC Algorithm Library Applications software package LALAPPS http://www.lsc-group.phys.uwm.edu/daswg/projects/lalapps.html
[27] Caron B *et al* 1999 *Astropart. Phys.* **10** 369
[28] Buskilic D *et al* 2000 *Int. J. Mod. Phys.* D **9** 263–7
[29] Sutton P J 2007 Characterising the space of gravitational-wave bursts *LIGO Document* LIGO-PO70139-00-Z
[30] Flandrin P 1993 *Temps-Fréquence* (Paris: Ed. Hermes)
[31] Cuoco E *et al* 2001 *Class. Quantum Grav.* **18** 1727–51
[32] Guidi G *et al* 2004 *Class. Quantum Grav.* **21** S815–20
[33] Chatterji S *et al* 2004 *Class. Quantum Grav.* **21** S1809–18
[34] Pradier T *et al* 2001 *Phys. Rev.* D **63** 042002
[35] Welch P D 1967 *IEEE Trans. Audio Electroacoust.* **15** 70
[36] Arnaud N *et al* 2003 *Phys. Rev.* D **67** 102003
[37] Clapson A-C *et al* 2008 *Class. Quantum Grav.* **25** 035002
[38] Arnaud N *et al* 2003 *Phys. Rev.* D **67** 062004
[39] Boulanger J L *et al* 1989 *Astron. Astrophys.* **217** 381
[40] Klimenko S *et al* 2005 *Phys. Rev.* D **72** 122002
[41] Chatterji S *et al* 2006 *Phys. Rev.* D **74** 082005

All-sky search for gravitational-wave bursts in the first joint LIGO-GEO-Virgo run

J. Abadie,[29] B. P. Abbott,[29] R. Abbott,[29] T. Accadia,[27] F. Acernese,[19a,19c] R. Adhikari,[29] P. Ajith,[29] B. Allen,[2,77] G. Allen,[52] E. Amador Ceron,[77] R. S. Amin,[34] S. B. Anderson,[29] W. G. Anderson,[77] F. Antonucci,[22a] M. A. Arain,[64] M. Araya,[29] K. G. Arun,[26] Y. Aso,[29] S. Aston,[63] P. Astone,[22a] P. Aufmuth,[28] C. Aulbert,[2] S. Babak,[1] P. Baker,[37] G. Ballardin,[12] S. Ballmer,[29] D. Barker,[30] F. Barone,[19a,19c] B. Barr,[65] P. Barriga,[76] L. Barsotti,[32] M. Barsuglia,[4] M. A. Barton,[30] I. Bartos,[11] R. Bassiri,[65] M. Bastarrika,[65] Th. S. Bauer,[41a] B. Behnke,[1] M. G. Beker,[41a] A. Belletoile,[27] M. Benacquista,[59] J. Betzwieser,[29] P. T. Beyersdorf,[48] S. Bigotta,[21a,21b] I. A. Bilenko,[38] G. Billingsley,[29] S. Birindelli,[43a] R. Biswas,[77] M. A. Bizouard,[26] E. Black,[29] J. K. Blackburn,[29] L. Blackburn,[32] D. Blair,[76] B. Bland,[30] M. Blom,[41a] C. Boccara,[15] O. Bock,[2] T. P. Bodiya,[32] R. Bondarescu,[54] F. Bondu,[43b] L. Bonelli,[21a,21b] R. Bonnand,[33] R. Bork,[29] M. Born,[2] S. Bose,[78] L. Bosi,[20a] B. Bouhou,[4] S. Braccini,[21a] C. Bradaschia,[21a] P. R. Brady,[77] V. B. Braginsky,[38] J. E. Brau,[70] J. Breyer,[2] D. O. Bridges,[31] A. Brillet,[43a] M. Brinkmann,[2] V. Brisson,[26] M. Britzger,[2] A. F. Brooks,[29] D. A. Brown,[53] R. Budzyński,[45b] T. Bulik,[45c,45d] A. Bullington,[52] H. J. Bulten,[41a,41b] A. Buonanno,[66] O. Burmeister,[2] D. Buskulic,[27] C. Buy,[4] R. L. Byer,[52] L. Cadonati,[67] G. Cagnoli,[17a] J. Cain,[56] E. Calloni,[19a,19b] J. B. Camp,[39] E. Campagna,[17a,17b] J. Cannizzo,[39] K. C. Cannon,[29] B. Canuel,[12] J. Cao,[32] C. D. Capano,[53] F. Carbognani,[12] L. Cardenas,[29] S. Caudill,[34] M. Cavaglià,[56] F. Cavalier,[26] R. Cavalieri,[12] G. Cella,[21a] C. Cepeda,[29] E. Cesarini,[17b] T. Chalermsongsak,[29] E. Chalkley,[65] P. Charlton,[10] E. Chassande-Mottin,[4] S. Chatterji,[29] S. Chelkowski,[63] Y. Chen,[7] A. Chincarini,[18] N. Christensen,[9] S. S. Y. Chua,[5] C. T. Y. Chung,[55] D. Clark,[52] J. Clark,[8] J. H. Clayton,[77] F. Cleva,[43a] E. Coccia,[23a,23b] C. N. Colacino,[21a] J. Colas,[12] A. Colla,[22a,22b] M. Colombini,[22b] R. Conte,[72] D. Cook,[30] T. R. C. Corbitt,[32] N. Cornish,[37] A. Corsi,[22a] J.-P. Coulon,[43a] D. Coward,[76] D. C. Coyne,[29] J. D. E. Creighton,[77] T. D. Creighton,[59] A. M. Cruise,[63] R. M. Culter,[63] A. Cumming,[65] L. Cunningham,[65] E. Cuoco,[12] K. Dahl,[2] S. L. Danilishin,[38] S. D'Antonio,[23a] K. Danzmann,[2,28] V. Dattilo,[12] B. Daudert,[29] M. Davier,[26] G. Davies,[8] E. J. Daw,[57] R. Day,[12] T. Dayanga,[78] R. De Rosa,[19a,19b] D. DeBra,[52] J. Degallaix,[2] M. del Prete,[21a,21c] V. Dergachev,[68] R. DeSalvo,[29] S. Dhurandhar,[25] L. Di Fiore,[19a] A. Di Lieto,[21a,21b] M. Di Paolo Emilio,[23a,23c] A. Di Virgilio,[21a] M. Díaz,[59] A. Dietz,[27] F. Donovan,[32] K. L. Dooley,[64] E. E. Doomes,[51] M. Drago,[44c,44d] R. W. P. Drever,[6] J. Driggers,[29] J. Dueck,[2] I. Duke,[32] J.-C. Dumas,[76] M. Edgar,[65] M. Edwards,[8] A. Effler,[30] P. Ehrens,[29] T. Etzel,[29] M. Evans,[32] T. Evans,[31] V. Fafone,[23a,23b] S. Fairhurst,[8] Y. Faltas,[64] Y. Fan,[76] D. Fazi,[29] H. Fehrmann,[2] I. Ferrante,[21a,21b] F. Fidecaro,[21a,21b] L. S. Finn,[54] I. Fiori,[12] R. Flaminio,[33] K. Flasch,[77] S. Foley,[32] C. Forrest,[71] N. Fotopoulos,[77] J.-D. Fournier,[43a] J. Franc,[33] S. Frasca,[22a,22b] F. Frasconi,[21a] M. Frede,[2] M. Frei,[58] Z. Frei,[14] A. Freise,[63] R. Frey,[70] T. T. Fricke,[34] D. Friedrich,[2] P. Fritschel,[32] V. V. Frolov,[31] P. Fulda,[63] M. Fyffe,[31] M. Galimberti,[33] L. Gammaitoni,[20a,20b] J. A. Garofoli,[53] F. Garufi,[19a,19b] G. Gemme,[18] E. Genin,[12] A. Gennai,[21a] S. Ghosh,[78] J. A. Giaime,[34,31] S. Giampanis,[2] K. D. Giardina,[31] A. Giazotto,[21a] E. Goetz,[68] L. M. Goggin,[77] G. González,[34] S. Goßler,[2] R. Gouaty,[27] M. Granata,[4] A. Grant,[65] S. Gras,[76] C. Gray,[30] R. J. S. Greenhalgh,[47] A. M. Gretarsson,[13] C. Greverie,[43a] R. Grosso,[59] H. Grote,[2] S. Grunewald,[1] G. M. Guidi,[17a,17b] E. K. Gustafson,[29] R. Gustafson,[68] B. Hage,[28] J. M. Hallam,[63] D. Hammer,[77] G. D. Hammond,[65] C. Hanna,[29] J. Hanson,[31] J. Harms,[69] G. M. Harry,[32] I. W. Harry,[8] E. D. Harstad,[70] K. Haughian,[65] K. Hayama,[2] J.-F. Hayau,[43b] T. Hayler,[47] J. Heefner,[29] H. Heitmann,[43a] P. Hello,[26] I. S. Heng,[65] A. Heptonstall,[29] M. Hewitson,[2] S. Hild,[65] E. Hirose,[53] D. Hoak,[31] K. A. Hodge,[29] K. Holt,[31] D. J. Hosken,[62] J. Hough,[65] E. Howell,[76] D. Hoyland,[63] D. Huet,[12] B. Hughey,[32] S. Husa,[61] S. H. Huttner,[65] D. R. Ingram,[30] T. Isogai,[9] A. Ivanov,[29] P. Jaranowski,[45e] W. W. Johnson,[34] D. I. Jones,[74] G. Jones,[8] R. Jones,[65] L. Ju,[76] P. Kalmus,[29] V. Kalogera,[42] S. Kandhasamy,[69] J. Kanner,[66] E. Katsavounidis,[32] K. Kawabe,[30] S. Kawamura,[40] F. Kawazoe,[2] W. Kells,[29] D. G. Keppel,[29] A. Khalaidovski,[2] F. Y. Khalili,[38] R. Khan,[11] E. Khazanov,[24] H. Kim,[2] P. J. King,[29] J. S. Kissel,[34] S. Klimenko,[64] K. Kokeyama,[40] V. Kondrashov,[29] R. Kopparapu,[54] S. Koranda,[77] I. Kowalska,[45c] D. Kozak,[29] V. Kringel,[2] B. Krishnan,[1] A. Królak,[45a,45f] G. Kuehn,[2] J. Kullman,[2] R. Kumar,[65] P. Kwee,[28] P. K. Lam,[5] M. Landry,[30] M. Lang,[54] B. Lantz,[52] N. Lastzka,[2] A. Lazzarini,[29] P. Leaci,[2] M. Lei,[29] N. Leindecker,[52] I. Leonor,[70] N. Leroy,[26] N. Letendre,[27] T. G. F. Li,[41a] H. Lin,[64] P. E. Lindquist,[29] T. B. Littenberg,[37] N. A. Lockerbie,[75] D. Lodhia,[63] M. Lorenzini,[17a] V. Loriette,[15] M. Lormand,[31] G. Losurdo,[17a] P. Lu,[52] M. Lubinski,[30] A. Lucianetti,[64] H. Lück,[2,28] A. Lundgren,[53] B. Machenschalk,[2] M. MacInnis,[32] M. Mageswaran,[29] K. Mailand,[29] E. Majorana,[22a] C. Mak,[29] I. Maksimovic,[15] N. Man,[43a] I. Mandel,[42] V. Mandic,[69] M. Mantovani,[21c] F. Marchesoni,[20a] F. Marion,[27] S. Márka,[11] Z. Márka,[11] A. Markosyan,[52] J. Markowitz,[32] E. Maros,[29] J. Marque,[12] F. Martelli,[17a,17b] I. W. Martin,[65] R. M. Martin,[64] J. N. Marx,[29] K. Mason,[32] A. Masserot,[27] F. Matichard,[34,32] L. Matone,[11] R. A. Matzner,[58] N. Mavalvala,[32] R. McCarthy,[30] D. E. McClelland,[5] S. C. McGuire,[51] G. McIntyre,[29] D. J. A. McKechan,[8] M. Mehmet,[2] A. Melatos,[55] A. C. Melissinos,[71] G. Mendell,[30] D. F. Menéndez,[54] R. A. Mercer,[77] L. Merill,[76] S. Meshkov,[29] C. Messenger,[2] M. S. Meyer,[31] H. Miao,[76] C. Michel,[33] L. Milano,[19a,19b]

[54]*The Pennsylvania State University, University Park, Pennsylvania 16802, USA**
[55]*The University of Melbourne, Parkville VIC 3010, Australia**
[56]*The University of Mississippi, University, Mississippi 38677, USA**
[57]*The University of Sheffield, Sheffield S10 2TN, United Kingdom, USA**
[58]*The University of Texas at Austin, Austin, Texas 78712, USA**
[59]*The University of Texas at Brownsville and Texas Southmost College, Brownsville, Texas 78520, USA**
[60]*Trinity University, San Antonio, Texas 78212, USA**
[61]*Universitat de les Illes Balears, E-07122 Palma de Mallorca, Spain**
[62]*University of Adelaide, Adelaide, SA 5005, Australia**
[63]*University of Birmingham, Birmingham, B15 2TT, United Kingdom**
[64]*University of Florida, Gainesville, Florida 32611, USA**
[65]*University of Glasgow, Glasgow, G12 8QQ, United Kingdom**
[66]*University of Maryland, College Park, Maryland 20742 USA**
[67]*University of Massachusetts - Amherst, Amherst, Massachusetts 01003, USA**
[68]*University of Michigan, Ann Arbor, Michigan 48109, USA**
[69]*University of Minnesota, Minneapolis, Minnesota 55455, USA**
[70]*University of Oregon, Eugene, Oregon 97403, USA**
[71]*University of Rochester, Rochester, New York 14627, USA**
[72]*University of Salerno, I-84084 Fisciano (Salerno), Italy** *and INFN*
[73]*University of Sannio at Benevento, I-82100 Benevento, Italy** *and INFN*
[74]*University of Southampton, Southampton, SO17 1BJ, United Kingdom**
[75]*University of Strathclyde, Glasgow, G1 1XQ, United Kingdom**
[76]*University of Western Australia, Crawley, Washington 6009, Australia, USA**
[77]*University of Wisconsin–Milwaukee, Milwaukee, Wisconsin 53201, USA**
[78]*Washington State University, Pullman, Washington 99164, USA**
(Received 4 March 2010; published 5 May 2010)

We present results from an all-sky search for unmodeled gravitational-wave bursts in the data collected by the LIGO, GEO 600 and Virgo detectors between November 2006 and October 2007. The search is performed by three different analysis algorithms over the frequency band 50–6000 Hz. Data are analyzed for times with at least two of the four LIGO-Virgo detectors in coincident operation, with a total live time of 266 days. No events produced by the search algorithms survive the selection cuts. We set a frequentist upper limit on the rate of gravitational-wave bursts impinging on our network of detectors. When combined with the previous LIGO search of the data collected between November 2005 and November 2006, the upper limit on the rate of detectable gravitational-wave bursts in the 64–2048 Hz band is 2.0 events per year at 90% confidence. We also present event rate versus strength exclusion plots for several types of plausible burst waveforms. The sensitivity of the combined search is expressed in terms of the root-sum-squared strain amplitude for a variety of simulated waveforms and lies in the range 6×10^{-22} $\mathrm{Hz}^{-1/2}$ to 2×10^{-20} $\mathrm{Hz}^{-1/2}$. This is the first untriggered burst search to use data from the LIGO and Virgo detectors together, and the most sensitive untriggered burst search performed so far.

DOI: 10.1103/PhysRevD.81.102001 PACS numbers: 04.80.Nn, 07.05.Kf, 95.30.Sf, 95.85.Sz

I. INTRODUCTION

The LIGO Scientific Collaboration (LSC) and the Virgo Collaboration operate a network of interferometric gravitational-wave (GW) detectors with the goal of detecting gravitational waves from astrophysical sources. Some of these sources may produce transient ''bursts'' of GW radiation with relatively short duration ($\lesssim 1$ s). Plausible burst sources [1] include merging compact binary systems consisting of black holes and/or neutron stars [2,3], core-collapse supernovae [4], neutron star collapse [5], star-quakes associated with magnetar flares [6] or pulsar glitches [7], cosmic string cusps [8], and other violent events in the Universe.

During the most recent data-taking run five GW detectors were operational. The three LIGO detectors [9] started their Science Run 5 (S5) in November 2005, and the GEO 600 detector [10] joined the S5 run in January 2006. The Virgo detector [11] began its Virgo Science Run 1 (VSR1) in May 2007. All five instruments took data together until the beginning of October 2007.

An all-sky search for GW burst signals has already been conducted on the first calendar year of the LIGO S5 data (referred to as ''S5y1'') in a wide frequency band of 64–6000 Hz [12,13]. In this paper, we report on a search for GW burst signals in the frequency band 50–6000 Hz for the rest of the S5/VSR1 run, referred to as ''S5y2/VSR1.'' It

*The LIGO Scientific Collaboration.
†The Virgo Collaboration.

includes data collected by the LIGO and Virgo detectors, which had comparable sensitivities, and uses three different search algorithms. In comparison with the S5y1 analysis, the network of LIGO and Virgo detectors, spread over three sites, provides better sky coverage as well as improved capabilities to reject spurious signals. S5y2/VSR1 is also the first long-term observation with the worldwide network of interferometric detectors. This is a major step forward with respect to previous observations led by the network of resonant detectors [14,15], since, as we will show in this paper, the performance is improved by more than 1 order of magnitude both in the analyzed frequency bandwidth and the level of instrumental noise.

This paper is organized as follows. In Sec. II we describe the LSC and Virgo instruments. In Sec. III we give a brief overview of the search procedure. In Sec. IV we present the search algorithms. Simulations are described in Sec. V, and the error analysis in Sec. VI. The results of the search are presented in Sec. VII, and astrophysical implications are discussed in Sec. VIII. The appendices provide additional details on data characterization and the analysis pipelines.

II. DETECTORS

A. LIGO

LIGO consists of three detectors at two observatories in the United States. Each detector is a large Michelson-type interferometer with additional mirrors forming Fabry-Perot cavities in the arms and a power-recycling mirror in the input beam path. Interferometric sensing and feedback is used to ''lock'' the mirror positions and orientations to keep all of the optical cavities on resonance. A gravitational wave is sensed as a quadrupolar strain, measured interferometrically as an effective difference between the lengths of the two arms. The LIGO Hanford Observatory, in Washington, houses independent detectors with the arm lengths of 4 km and 2 km, called H1 and H2, respectively. The LIGO Livingston Observatory, in Louisiana, has a single detector with 4-km arms, called L1. The detector instrumentation and operation are described in detail elsewhere [9], and the improvements leading up to the S5 run which are most relevant for GW burst searches have been described in the first-year search [12].

The best achieved sensitivities of the LIGO detectors during the second year of S5, as a function of signal frequency, are shown in Fig. 1. The detectors are most sensitive over a band extending from about 40 Hz to a few kHz. Seismic noise dominates at lower frequencies since the effectiveness of the seismic isolation system is a very strong function of frequency. Above ~200 Hz, laser shot noise corrected for the Fabry-Perot cavity response yields an effective strain noise that rises linearly with frequency. The sensitivity at intermediate frequencies is determined mainly by thermal noise, with contributions from other sources. The peaks at ~350 Hz and harmonics are the thermally-excited vibrational modes of the wires from

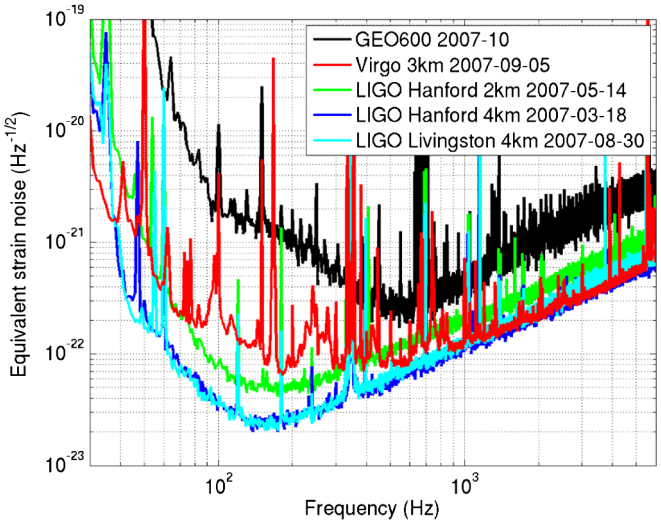

FIG. 1 (color online). Best noise amplitude spectral densities of the five LSC/Virgo detectors during S5/VSR1.

which the large mirrors are suspended. Smaller peaks are due to other mechanical resonances, power line harmonics, and calibration signals.

Commissioning periods during the second year of S5 led to incremental improvements in the detector sensitivities. The most significant of these were in January 2007, when the seismic isolation systems at both sites were improved to reduce the coupling of microseismic noise to the mirror suspensions, thereby mitigating noise from the nonlinear Barkhausen effect [16] in the magnets used to control the mirror positions; and in August 2007, when the L1 frequency stabilization servo was retuned. Overall, the average sensitivities of the H1 and L1 detectors during the second year were about 20% better than the first-year averages, while the H2 detector (less sensitive to begin with by a factor of ~2) had about the same average sensitivity in both years. The operational duty cycles for all three detectors also improved as the run progressed, from (72.8%, 76.7%, 61.0%) averaged over the first year to (84.0%, 80.6%, 73.6%) averaged over the second year for H1, H2, and L1, respectively.

B. GEO 600

The GEO 600 detector, located near Hannover, Germany, also operated during S5, though with a lower sensitivity than the LIGO and Virgo detectors. The GEO 600 data are not used in the initial search stage of the current study as the modest gains in the sensitivity to GW signals would not offset the increased complexity of the analysis. The GEO 600 data are held in reserve, and used to follow up any detection candidates from the LIGO-Virgo analysis.

GEO 600 began its participation in S5 on January 21 2006, acquiring data during nights and weekends.

Commissioning work was performed during the daytime, focussing on gaining a better understanding of the detector and improving data quality. GEO switched to full-time data taking from May 1 to October 6, 2006, then returned to night-and-weekend mode through the end of the S5 run. Overall GEO 600 collected about 415 days of science data during S5, for a duty cycle of 59.7% over the full S5 run.

C. Virgo

The Virgo detector [11], also called V1, is an interferometer with 3 km arms located near Pisa in Italy. One of the main instrumental differences with respect to LIGO is the seismic isolation system based on superattenuators [17], chains of passive attenuators capable of filtering seismic disturbances in 6 degrees of freedom with sub-Hertz corner frequencies. For VSR1, the Virgo duty cycle was 81% and the longest continuous period with the mirror positions interferometrically controlled was more than 94 hours. Another benefit from superattenuators is a significant reduction of the detector noise at very low-frequency (< 40 Hz) where Virgo surpasses the LIGO sensitivity.

Above 300 Hz, the spectral sensitivity achieved by Virgo during VSR1 is comparable to that of LIGO (see Fig. 1). Above 500 Hz the Virgo sensitivity is dominated by shot noise. Below 500 Hz there is excess noise due to environmental and instrumental noise sources, and below 300 Hz these produce burstlike transients.

Because of the different orientation of its arms, the antenna pattern (angular sensitivity) of Virgo is complementary to that of the LIGO detectors, with highest response in directions of low LIGO sensitivity. Virgo therefore significantly increases the sky coverage of the network. In addition, simultaneous observations with the three LIGO-Virgo sites improve rejection of spurious signals and allow reconstruction of the sky position and waveforms of detected GW sources.

III. SEARCH OVERVIEW

The analysis described in this paper uses data from the LIGO detectors collected from 14 November 2006 through 1 October 2007 (S5y2), and Virgo data from VSR1, which started on 18 May 18 2007 and ended at the same time as S5 [18]. The procedure used for this S5y2/VSR1 search is the same as that used for S5y1 [12]. In this section we briefly review the main stages of the analysis.

A. Data quality flags

The detectors are occasionally affected by instrumental or data acquisition artifacts as well as by periods of degraded sensitivity or an excessive rate of transient noise due to environmental conditions such as bad weather. Low-quality data segments are tagged with data quality flags (DQFs). These DQFs are divided into three categories depending on their seriousness. Category 1 DQFs are used to define the data segments processed by the analysis algorithms. Category 2 DQFs are unconditional data cuts applied to any events generated by the algorithms. Category 3 DQFs define the clean data set used to calculate upper limits on the GW rates.

We define DQFs for S5y2/VSR1 following the approach used for S5y1 [12]. More details are given in Appendix A. After category 2 DQFs have been applied, the total available time during this period is 261.6 days for H1, 253.4 days for H2, 233.7 days for L1 and 106.2 days for V1 [19].

B. Candidate event generation

As discussed in Sec. IV, three independent search algorithms are used to identify possible GW bursts: exponential Gaussian correlator (EGC), Ω-pipeline (Ω), and coherent waveBurst (cWB). We analyze data from time intervals when at least two detectors were operating in coincidence. Altogether, eight networks, or sets of detectors, operating during mutually exclusive time periods are analyzed by at least one algorithm. Table I shows the time available for analysis (''live time'') for the different network configurations after application of category 1 and 2 DQFs. The actual times searched by each algorithm for each network (''observation times'') reflect details of the algorithms, such as the smallest analyzable data block, as well as choices about which networks are most suitable for each algorithm. The three- and two-detector network configurations not shown in Table I have negligible live time and are not considered in this search.

LIGO and GEO 600 data are sampled at 16 384 Hz, yielding a maximum bandwidth of 8192 Hz, while Virgo

TABLE I. Exclusive live time in days for each detector network configuration after category 2 DQFs (second column) and the observation time analyzed by each of the search algorithms (last three columns). The cWB algorithm did not process the L1V1 network because the coherent likelihood regulator used in this analysis was suboptimal for two detectors with very different orientations. Omega used a coherent combination of H1 and H2 as an effective detector and thus analyzed networks either with both or with neither. EGC analyzed only data with three or more interferometers during the part of the run when Virgo was operational.

network	live time	cWB	Ω	EGC
H1H2L1V1	68.9	68.2	68.7	66.6
H1H2L1	124.6	123.2	123.4	16.5
H1H2V1	15.8	15.7	15.1	15.3
H1L1V1	4.5	4.2	···	4.4
H1H2	35.4	35.2	34.8	···
H1L1	7.2	5.9	···	···
L1V1	6.4	···	6.3	···
H2L1	3.8	3.5	···	···

data are sampled at 20000 Hz. Because of the large calibration uncertainties at high frequency, only data below 6000 Hz are used in the search. Also, because of high seismic noise, the frequency band below 50 Hz is excluded from the analysis. Furthermore, the EGC search was limited to the 300–5000 Hz band over which Virgo's sensitivity was comparable to LIGO's. In Sec. VI we describe the influence of the calibration uncertainties on the results of the search.

C. Vetoes

After gravitational-wave candidate events are identified by the search algorithms, they are subject to additional ''veto'' conditions to exclude events occurring within certain time intervals. These vetoes are based on statistical correlations between transients in the GW channel (data stream) and the environmental and interferometric auxiliary channels.

We define vetoes for S5y2/VSR1 following the approach used for S5y1 [12]. More details are given in Appendix B.

D. Background estimation and tuning

To estimate the significance of candidate GW events, and to optimize event selection cuts, we need to measure the distribution of events due to background noise. With a multidetector analysis one can create a sample of background noise events and study its statistical properties. These samples are created by time-shifting data of one or more detectors with respect to the others by ''unphysical'' time delays (i.e. much larger than the maximum time-of-flight of a GW signal between the detectors). Shifts are typically in the range from $\sim$1 s to a few minutes. Any triggers that are coincident in the time-shifted data cannot be due to a true gravitational-wave signal; these coincidences therefore sample the noise background. Background estimation is done separately for each algorithm and network combination, using hundreds to thousands of shifts. To take into account possible correlated noise transients in the H1 and H2 detectors, which share a common environment and vacuum system, no time-shifts are introduced between these detectors for any network combination including another detector.

The shifted and unshifted data are analyzed identically. A portion of the background events are used together with simulations (see below) to tune the search thresholds and selection cuts; the remainder is used to estimate the significance of any candidate events in the unshifted data after the final application of the selection thresholds. All tuning is done purely on the time-shifted data and simulations prior to examining the unshifted data set. This ''blind'' tuning avoid any biases in our candidate selection. The final event thresholds are determined by optimizing the detection efficiency of the algorithms at a fixed false alarm rate.

E. Hardware and software injections

At pseudorandom times during the run, simulated burst signals were injected (added) into the interferometers by sending precalculated waveforms to the mirror position control system. These ''hardware injections'' provided an end-to-end verification of the detector instrumentation, the data acquisition system and the data analysis software. The injection times were clearly marked in the data with a DQF. Most of hardware injections were incoherent, i.e., performed into a single detector with no coincident injection into the other detectors. Some injections were performed coherently by taking into account a simulated source location in the sky and the angle-dependent sensitivity of the detectors to the two wave polarization states.

In addition to the flagged injections, a ''blind injection challenge'' was undertaken in which a small number (possibly zero) of coherent hardware injections were performed *without* being marked by a DQF. Information about these blind injections (including whether the number was nonzero) was hidden from the data analysis teams during the search, and revealed only afterward. This challenge was intended to test our data analysis procedures and decision processes for evaluating any candidate events that might be found by the search algorithms.

To determine the sensitivity of our search to gravitational waves, and to guide the tuning of selection cuts, we repeatedly reanalyze the data with simulated signals injected in software. The same injections are analyzed by all three analysis pipelines. See Sec. V for more details.

IV. SEARCH ALGORITHMS

Anticipated sources of gravitational wave bursts are usually not understood well enough to generate waveforms accurate and precise enough for matched filtering of generic signals. While some sources of GW bursts are being modeled with increasing success, the results tend to be highly dependent on physical parameters which may span a large parameter space. Indeed, some burst signals, such the white-noise burst from turbulent convection in a core-collapse supernova, are stochastic in nature and so are inherently not templatable. Therefore usually more robust excess-power algorithms [20–23] are employed in burst searches. By measuring power in the data as a function of time and frequency, one may identify regions where the power is not consistent with the anticipated fluctuations of detector noise. To distinguish environmental and instrumental transients from true GW signals, a multidetector analysis approach is normally used, in which the event must be seen in more than one detector to be considered a candidate GW.

The simplest multidetector analysis strategy is to require that the events identified in the individual detectors are coincident in time. The time coincidence window which should be chosen to take into account the possible time delays of a GW signal arriving at different sites, calibration

and algorithmic timing biases, and possible signal model dependencies. Time coincidence can be augmented by requiring also an overlap in frequency. One such time-frequency coincidence method used in this search is the EGC algorithm [24] (see also Appendix C). It estimates the signal-to-noise ratio (SNR) ρ_k in each detector k and uses the combined SNR $\rho_{\rm comb} = \sqrt{\sum_k \rho_k^2}$ to rank candidate events.

A modification of the time-frequency coincidence approach is used in the Ω search algorithm [25] (also see Appendix D). In Ω, the identification of the H1H2 network events is improved by coherently combining the H1 and H2 data to form a single pseudodetector data stream H_+. This algorithm takes an advantage of the fact that the colocated and coaligned H1 and H2 detectors have identical responses to a GW signal. The performance of the Ω algorithm is further enhanced by requiring that no significant power is left in the H1 $-$ H2 null stream, H_-, where GW signals cancel. This veto condition helps to reduce the false alarm rate due to random coincidences of noise transients, which typically leave significant power in the null stream. Network events identified by Ω are characterized by the strength $Z = \rho^2/2$ of the individual detector events, and by the correlated H1H2 energy $Z_{H_+}^{\rm corr}$.

A different network analysis approach is used in the cWB search algorithm [26] (see also [12] and Appendix E). The cWB algorithm performs a least-squares fit of a common GW signal to the data from the different detectors using the constrained likelihood method [27]. The results of the fit are estimates of the h_+ and $h_\times$ waveforms, the most probable source location in the sky, and various likelihood statistics used in the cWB selection cuts. One of these is the maximum likelihood ratio L_m, which is an estimator of the total SNR detected in the network. A part of the L_m statistic depending on pairwise combinations of the detectors is used to construct the network correlated amplitude η, which measures the degree of correlation between the detectors. Random coincidences of noise transients typically give low values of η, making this statistic useful for background rejection. The contribution of each detector to the total SNR is weighted depending on the variance of the noise and angular sensitivity of the detectors. The algorithm automatically marginalizes a detector with either elevated noise or unfavorable antenna patterns, so that it does not limit the sensitivity of the network.

V. SIMULATED SIGNALS AND EFFICIENCIES

The detection efficiencies of the search algorithms depend on the network configuration, the selection cuts used in the analysis, and the GW morphologies which may span a wide range of signal durations, frequencies and amplitudes. To evaluate the sensitivity of the search and verify that the search algorithms do not have a strong model dependency, we use several sets of ad-hoc waveforms. These include

(i) Sine-Gaussian waveforms:

$$h_+(t) = h_0 \sin(2\pi f_0 t) \exp[-(2\pi f_0 t)^2/2Q^2], \quad (5.1)$$

$$h_\times(t) = 0. \quad (5.2)$$

We use a discrete set of central frequencies f_0 from 70 Hz to 6000 Hz and quality factors Q of 3, 9, and 100; see Table II and Fig. 2 (top). The amplitude factor h_0 is varied to simulate GWs with different strain amplitudes. For definition of the polarizations, see Eq. (5.8) and text below it.

(ii) Gaussian waveforms:

$$h_+(t) = h_0 \exp(-t^2/\tau^2), \quad (5.3)$$

$$h_\times(t) = 0, \quad (5.4)$$

where the duration parameter τ is chosen to be one of (0.1, 1.0, 2.5, 4.0) ms; see Fig. 2 (middle).

(iii) Harmonic ringdown signals:

$$h_+(t) = h_{0,+} \cos(2\pi f_0 t) \exp[-t/\tau], \quad t > 1/(4f_0), \quad (5.5)$$

$$h_\times(t) = h_{0,\times} \sin(2\pi f_0 t) \exp[-t/\tau], \qquad t > 0. \quad (5.6)$$

We use several central frequencies f_0 from 1590 Hz to 3067 Hz, one long decay time, $\tau = 200$ ms, and two short decay times, 1 ms and 0.65 ms; see Table III and Fig. 2 (bottom). Two polarization states are used: circular ($h_{0,+} = h_{0,\times}$), and linear ($h_{0,+} = 0$). The quarter-cycle delay in h_+ is to avoid starting the waveform with a large jump.

(iv) Band-limited white noise signals:
These are bursts of Gaussian noise which are white over a frequency band $[f_{\rm low}, f_{\rm low} + \Delta f]$ and which have a Gaussian time profile with standard deviation decay time τ; see Table IV. These signals are unpolarized in the sense that the two polarizations h_+ and $h_\times$ have equal RMS amplitudes and are uncorrelated with each other. The strengths of the *ad hoc* waveform injections are characterized by the root-square-sum amplitude $h_{\rm rss}$,

$$h_{\rm rss} = \sqrt{\int_{-\infty}^{+\infty} dt(|h_+(t)|^2 + |h_\times(t)|^2)}. \quad (5.7)$$

The parameters of these waveforms are selected to coarsely cover the frequency range of the search from $\sim$50 Hz to $\sim$6 kHz, and duration of signals up to a few hundreds of milliseconds. The Gaussian, sine-Gaussian and ringdown waveforms explore the space of GW signals with small time-frequency volume, while the white noise

TABLE II. Values of $h_{\rm rss}^{50\%}$ and $h_{\rm rss}^{90\%}$ (for 50% and 90% detection efficiency), in units of 10^{-22} Hz$^{-1/2}$, for sine-Gaussian waveforms with the central frequency f_0 and quality factor Q. Three columns in the middle are the $h_{\rm rss}^{50\%}$ measured with the individual search algorithms for the H1H2L1V1 network. The next column is the $h_{\rm rss}^{50\%}$ of the logical OR of the cWB and Ω algorithms for the H1H2L1V1 network. The last two columns are the $h_{\rm rss}^{50\%}$ and the $h_{\rm rss}^{90\%}$ of the logical OR of the algorithms and networks (H1H2L1V1 or H1H2L1 or H1H2). All $h_{\rm rss}$ values take into account statistical and systematic uncertainties as explained in Sec. VI.

f_0	Q	H1H2L1V1, $h_{\rm rss}^{50\%}$				all networks	
[Hz]		cWB	Ω	EGC	cWB or Ω	$h_{\rm rss}^{50\%}$	$h_{\rm rss}^{90\%}$
70	3	17.9	26.7	···	17.6	20.4	96.6
70	9	20.6	34.4	···	20.6	25.0	120
70	100	20.5	35.0	···	20.0	25.1	121
100	9	9.2	14.1	···	9.1	10.6	49.7
153	9	6.0	9.1	···	6.0	6.5	29.3
235	3	6.5	6.6	···	5.9	6.1	28.8
235	9	6.4	5.8	···	5.6	5.6	26.8
235	100	6.5	6.7	···	6.2	6.0	26.1
361	9	10.5	10.2	60.1	9.5	10.0	42.0
554	9	11.1	10.5	18.8	9.9	10.9	47.1
849	3	19.2	15.8	30.0	15.3	15.8	73.8
849	9	17.7	15.3	28.5	14.6	15.8	71.5
849	100	16.0	16.2	31.3	14.5	15.3	66.7
1053	9	22.4	19.0	33.8	18.3	19.4	86.9
1304	9	28.1	23.6	41.0	22.6	24.7	115
1451	9	28.6	···	43.3	28.6	30.2	119
1615	3	39.6	32.1	48.4	31.7	33.8	146
1615	9	33.7	28.1	51.1	27.3	29.5	138
1615	100	29.6	30.6	53.8	27.6	28.6	126
1797	9	36.5	···	57.8	36.5	38.3	146
2000	3	42.6	···	···	42.6	47.1	191
2000	9	40.6	···	58.7	40.6	44.0	177
2000	100	34.9	···	···	34.9	38.4	153
2226	9	46.0	···	68.6	46.0	51.1	187
2477	3	61.9	···	···	61.9	65.6	262
2477	9	53.5	···	76.7	53.5	56.1	206
2477	100	44.5	···	···	44.5	48.9	201
2756	9	60.2	···	82.2	60.2	64.4	248
3067	3	86.9	···	···	86.9	87.0	343
3067	9	69.0	···	96.6	69.0	75.0	286
3067	100	55.4	···	···	55.4	61.1	273
3413	9	75.9	···	108	75.9	82.9	323
3799	9	89.0	···	116	89.0	97.7	386
4225	9	109	···	138	109	115	575
5000	3	207	···	···	207	187	1160
5000	9	126	···	155	126	130	612
5000	100	84.7	···	···	84.7	100	480
6000	9	182	···	···	182	196	893

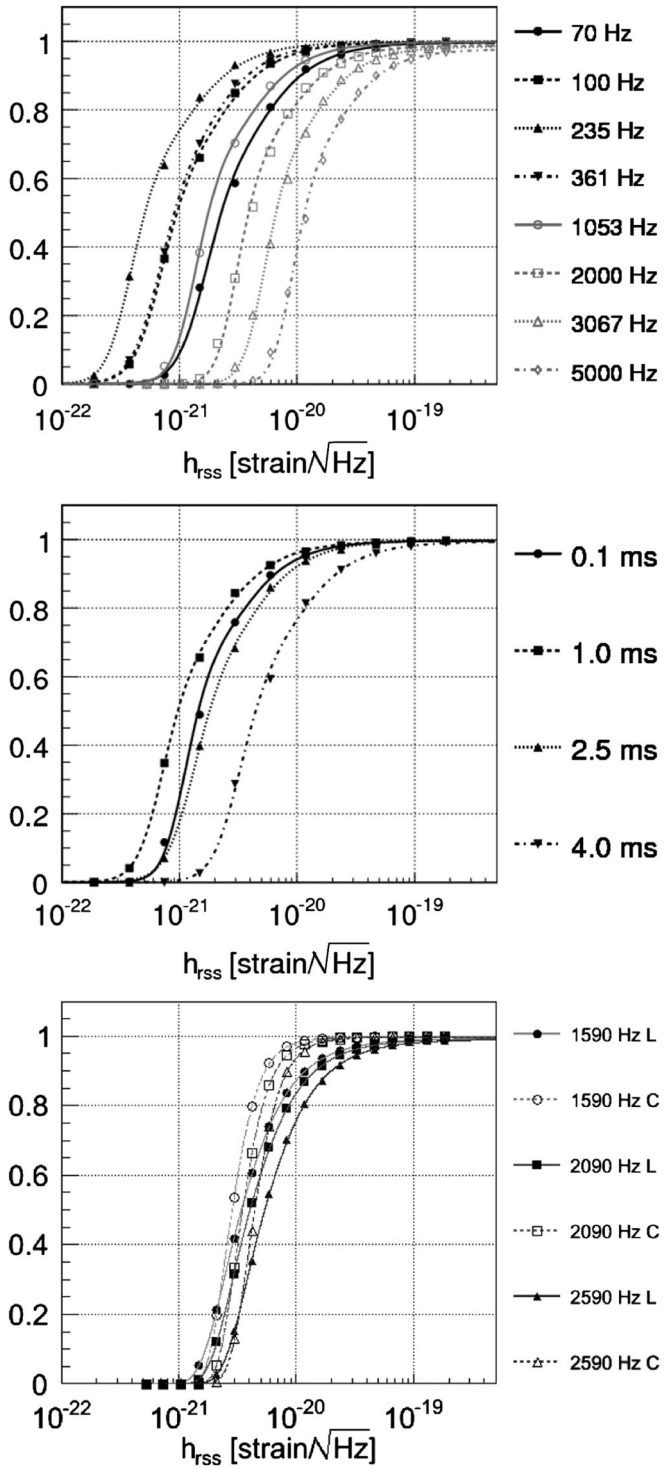

FIG. 2. Efficiency for selected waveforms as a function of signal amplitude $h_{\rm rss}$ for the logical OR of the H1H2L1V1, H1H2L1, and H1H2 networks. Top: sine-Gaussians with $Q = 9$ and central frequency spanning between 70 and 5000 Hz. Middle: Gaussians with τ between 0.1 and 4.0 ms. Bottom: linearly (L) and circularly (C) polarized ringdowns with $\tau = 200$ ms and frequencies between 1590 and 2590 Hz.

TABLE III. Values of $h_{\rm rss}^{50\%}$ and $h_{\rm rss}^{90\%}$ (for 50% and 90% detection efficiency using cWB), in units of 10^{-22} Hz$^{-1/2}$, for linearly and circularly polarized ringdowns characterized by parameters f and τ. All $h_{\rm rss}$ values take into account statistical and systematic uncertainties as explained in Sec. VI.

f	τ	all networks, $h_{\rm rss}^{50\%}$		all networks, $h_{\rm rss}^{90\%}$	
[Hz]	[ms]	Lin.	Circ.	Lin.	Circ.
1590	200	34.7	30.0	131	60.0
2000	1.0	49.5	43.8	155	81.1
2090	200	43.3	36.5	155	72.9
2590	200	58.6	46.0	229	88.8
3067	0.65	88.2	73.3	369	142

bursts explore the space of GW signals with relatively large time-frequency volume. Although the simulated waveforms are not physical, they may be similar to some waveforms produced by astrophysical sources. For example, the sine-Gaussian waveforms with few cycles are qualitatively similar to signals produced by the mergers of two black holes [2]. The long-timescale ringdowns are similar to signals predicted for excitation of neutron-star fundamental modes [28]. Some stellar collapse and core-collapse supernova models predict signals that resemble short ringdown waveforms (in the case of a rapidly rotating progenitor star) or band-limited white-noise waveforms with random polarizations. In the context of the recently proposed acoustic mechanism for core-collapse supernova explosions, quasiperiodic signals of $\gtrsim 500$ ms duration have been proposed [4].

TABLE IV. Values of $h_{\rm rss}^{50\%}$ and $h_{\rm rss}^{90\%}$ (for 50% and 90% detection efficiency), in units of 10^{-22} Hz$^{-1/2}$, for band-limited noise waveforms characterized by parameters $f_{\rm low}$, Δf, and τ. Two columns in the middle are the $h_{\rm rss}^{50\%}$ for the individual search algorithms for the H1H2L1V1 network. The next column is the $h_{\rm rss}^{50\%}$ of the logical OR of the cWB and Ω algorithms for the H1H2L1V1 network. The last two columns are the $h_{\rm rss}^{50\%}$ and the $h_{\rm rss}^{90\%}$ of the logical OR of the algorithms and networks (H1H2L1V1 or H1H2L1 or H1H2). All $h_{\rm rss}$ values take into account statistical and systematic uncertainties as explained in Sec. VI.

$f_{\rm low}$	Δf	τ	H1H2L1V1, $h_{\rm rss}^{50\%}$			all networks	
[Hz]	[Hz]	[ms]	cWB	Ω	cWB or Ω	$h_{\rm rss}^{50\%}$	$h_{\rm rss}^{90\%}$
100	100	0.1	7.6	13.6	7.6	8.4	19.6
250	100	0.1	9.1	10.2	8.8	8.6	18.7
1000	10	0.1	20.9	28.6	21.0	21.8	52.6
1000	1000	0.01	36.8	38.2	35.0	36.3	74.7
1000	1000	0.1	60.3	81.7	60.7	63.5	140
2000	100	0.1	40.4	···	40.4	44.1	94.4
2000	1000	0.01	60.7	···	60.7	62.4	128
3500	100	0.1	74.3	···	74.3	84.8	182
3500	1000	0.01	103	···	103	109	224
5000	100	0.1	101	···	101	115	255
5000	1000	0.01	152	···	152	144	342

To test the range for detection of gravitational waves from neutron-star collapse, two waveforms were taken from simulations by Baiotti *et al.* [5]. These waveforms, denoted D1 and D4, represent the extremes of the parameter space in mass and spin considered in that work. They are linearly polarized ($h_\times = 0$), with the waveform amplitude varying with the inclination angle ι (between the wave propagation vector and symmetry axis of the source) as $\sin^2\iota$.

The simulated detector responses $h_{\rm det}$ are constructed as

$$h_{\rm det} = F_+(\theta, \phi, \psi)h_+ + F_\times(\theta, \phi, \psi)h_\times. \tag{5.8}$$

Here F_+ and $F_\times$ are the detector antenna patterns, which depend on the direction to the source (θ, ϕ) and the polarization angle ψ. (The latter is defined as in Appendix B of [20].) These parameters are chosen randomly for each injection. The sky direction is isotropically distributed, and the polarization angle is uniformly distributed on $[0, \pi)$. For the ad-hoc waveforms no dependence on the inclination angle ι is simulated. The injections are distributed uniformly in time across the S5y2/VSR1 run, with an average separation of 100 s.

The detection efficiency after application of all selection cuts was determined for each waveform type. All waveforms were evaluated using cWB, while subsets were evaluated using Ω and EGC, due mainly to the limited frequency bands covered by those algorithms as they were used in this search (48–2048 Hz and 300–5000 Hz, respectively). Figure 2 shows the combined efficiency curves for selected sine-Gaussian, Gaussian and ringdown simulated signals as a function of the $h_{\rm rss}$ amplitude. Figure 3 shows the detection efficiency for the astrophysical signals D1 and D4 as a function of the distance to the source.

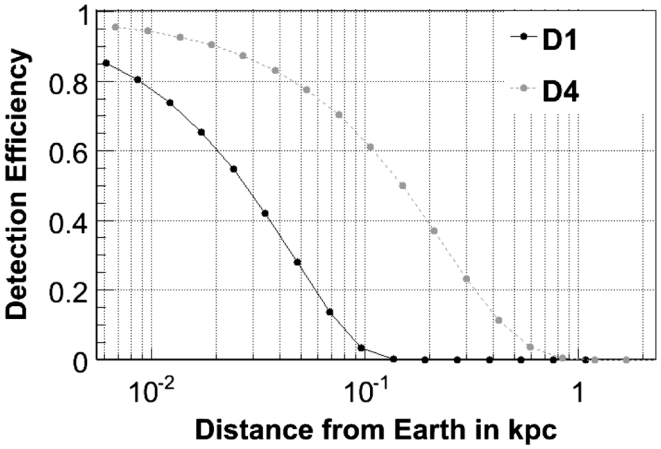

FIG. 3. Efficiency of the H1H2L1V1 network as a function of distance for the D1 and D4 waveforms of Baiotti *et al.* [5] predicted by polytropic general-relativistic models of neutron star collapse. These efficiencies assume random sky location, polarization and inclination angle.

Each efficiency curve is fitted with an empirical function and the injection amplitude for which that function equals 50% is determined. This quantity, $h_{\rm rss}^{50\%}$, is a convenient characterization of the sensitivity of the search to that waveform morphology. Tables II, III, and IV summarize the sensitivity of the search to the sine-Gaussian, ringdown, and band-limited white noise burst signals. Where possible, we also calculate the sensitivity of the logical OR of the cWB and Ω algorithms (since those two are used for the upper limit calculation as described in Sec. VII), and for the appropriately weighted combination of all networks (some of which are less sensitive) contributing to the total observation time. In general, the efficiency of the combination of the search algorithms is slightly more sensitive than the individual algorithms.

VI. UNCERTAINTIES

The amplitude sensitivities presented in this paper, i.e. the $h_{\rm rss}$ values at 50% and 90% efficiency, have been adjusted upward to conservatively reflect statistical and systematic uncertainties. The statistical uncertainty arises from the limited number of simulated signals used in the efficiency curve fit, and is typically a few percent. The dominant source of systematic uncertainty comes from the amplitude calibration: the single detector amplitude calibration uncertainties is typically of order 10%. Negligible effects are due to phase and timing uncertainties.

The amplitude calibration of the interferometers is less accurate at high frequencies than at low frequencies, and therefore two different approaches to handling calibration uncertainties are used in the S5y2/VSR1 search. In the frequency band below 2 kHz, we use the procedure established for S5y1 [13]. We combine the amplitude uncertainties from each interferometer into a single uncertainty by calculating a combined root-sum-square amplitude SNR and propagating the individual uncertainties assuming each error is independent: as a conservative result, the detection efficiencies are rigidly shifted towards higher $h_{\rm rss}$ by 11.1%. In the frequency band above 2 kHz, a new methodology, based on Monte Carlo simulations has been adopted to marginalize over calibration uncertainties: basically, we inject signals whose amplitude has been jittered according to the calibration uncertainties. The effect of miscalibration resulted in the increase of the combined $h_{\rm rss}^{50\%}$ by 3% to 14%, depending mainly on the central frequency of the injected signals.

VII. SEARCH RESULTS

In Sec. III we described the main steps in our search for gravitational-wave bursts. In the search all analysis cuts and thresholds are set in a blind way, using time-shifted (background) and simulation data. The blind cuts are set to yield a false-alarm rate of approximately 0.05 events or less over the observation time of each search algorithm, network configuration, and target frequency band. Here we describe the results.

A. Candidate events

After these cuts are fixed, the unshifted events are examined and the various analysis cuts, DQFs, and vetoes are applied. Any surviving events are considered as candidate gravitational-wave events and subject to further examination. The purpose of this additional step is to go beyond the binary decision of the initial cuts and evaluate additional information about the events which may reveal their origin. This ranges from ''sanity checks'' to deeper investigations on the background of the observatory, detector performances, environmental disturbances and candidate signal characteristics.

Examining the unshifted data, we found one foreground event among all the different search algorithms and detector combinations that survives the blind selection cuts. It was produced by cWB during a time when all five detectors were operating simultaneously. As the possible first detection of a gravitational-wave signal, this event was examined in great detail according to our follow-up checklist. We found no evident problem with the instruments or data, and no environmental or instrumental disturbance detected by the auxiliary channels. The event was detected at a frequency of 110 Hz, where all detectors are quite nonstationary, and where both the GEO 600 and Virgo detectors had poorer sensitivity (see Fig. 1). Therefore, while the event was found in the H1H2L1V1 analysis, we also reanalyzed the data using cWB and the H1H2L1 network. Figure 4 (top) shows the event above the blind selection cuts and the comparison with the measured H1H2L1 background of cWB in the frequency band below 200 Hz.

No foreground event passes the blind selection cuts in the Ω H1H2L1 analysis [see Fig. 4 (bottom)]; moreover, there is no visible excess of foreground events with respect to the expected background. The cWB event is well within the tail of the Ω foreground and does not pass the final cut placed on correlated energy of the Hanford detectors. Furthermore, the event is outside of the frequency band (300–5000 Hz) processed by the EGC algorithm. Figure 5 (top) shows the corresponding EGC foreground and background distributions for the H1H2L1V1 network. For comparison, Fig. 5 (bottom) shows similar distributions from cWB, with no indication of any excess of events in the frequency band 1200–6000 Hz.

To better estimate the significance of the surviving cWB event, we performed extensive background studies with cWB for the H1H2L1 network, accumulating a background sample with effective observation time of approximately 500 years. These studies indicate an expected false alarm rate for similar events of once per 43 years for the cWB algorithm and the H1H2L1 network. The statistical significance of the event must take into account a ''trials factor'' arising from multiple analyses using different

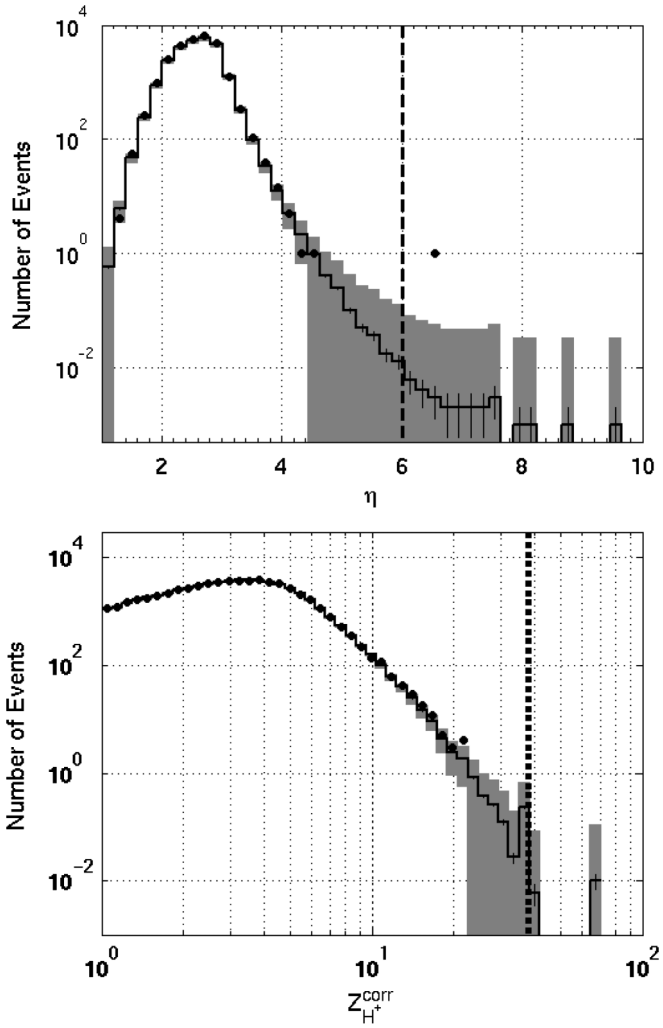

FIG. 4. Distribution of background (solid line) and foreground (solid dots) events from the search below 200 Hz in the H1H2L1 network, after application of category 2 data quality and vetoes: cWB (top), Ω (bottom). The event-strength figures of merit on the horizontal axes are defined in the appendices on the search algorithms. The small error bars on the solid line are the 1σ statistical uncertainty on the estimated background, while the wider gray belt represents the expected root-mean-square statistical fluctuations on the number of background events in the foreground sample. The loudest foreground event on the top plot is the only event that survived the blind detection cuts of this search, shown as vertical dashed lines. This event was later revealed to have been a blind injection.

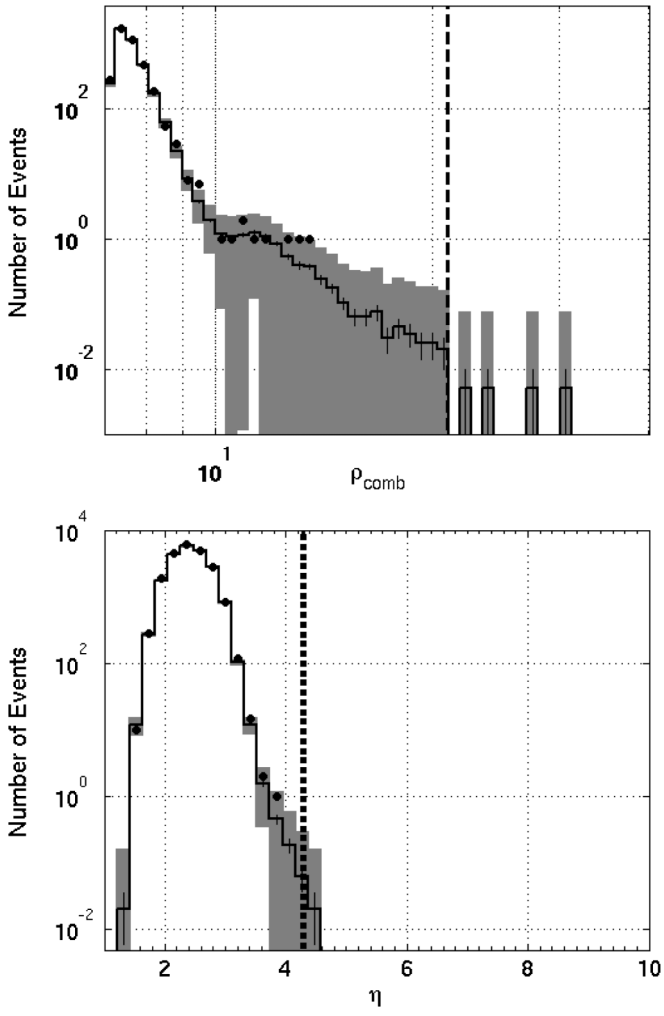

FIG. 5. Distribution of background (solid line) and foreground (solid dots) H1H2L1V1 events after category 2 data quality and vetoes: EGC events in the frequency band 300–5000 Hz (top), cWB events in the frequency band 1200–6000 Hz (bottom). The event-strength figures of merit on the horizontal axes are defined in the appendices on the search algorithms. The small error bars on the solid line are the 1σ statistical uncertainty on the estimated background, while the wider gray belt represents the expected root-mean-square statistical fluctuations on the number of background events in the foreground sample.

search algorithms, networks and frequency bands. Neglecting a small correlation among the backgrounds, this factor can be estimated by considering the total effective analyzed time of all the independent searches, which is 5.1 yr. The probability of observing one event at a background rate of once per 43 years or less in any of our searches is then on the order of 10%. This probability was considered too high to exclude a possible accidental origin of this event, which was neither confirmed nor ruled out as a plausible GW signal. This event was later revealed to be a hardware injection with $h_{\rm rss} = 1.0 \times 10^{-21}$ Hz$^{-1/2}$. It was the only burst injection within the ''blind injection challenge.'' Therefore it was removed from the analysis by the cleared injection data quality flag. We can report that cWB recovered the injection parameters and waveforms faithfully, and the exercise of treating the event as a real GW candidate was a valuable learning experience.

Although no other outstanding foreground events were observed in the search, we have additionally examined events in the data set with relaxed selection cuts, namely, before applying category 3 DQFs and vetoes. In this set we find a total of three foreground events. One of these is produced by the EGC algorithm (0.16 expected from the

background) and the other two are from the Ω-pipeline (1.4 expected). While an exceptionally strong event in the enlarged data set could, in principle, be judged to be a plausible GW signal, none of these additional events is particularly compelling. The EGC event occurred during a time of high seismic noise and while the H2 interferometer was reacquiring lock (and thus could occasionally scatter light into the H1 detector), both of which had been flagged as category 3 data quality conditions. The Ω-pipeline events fail the category 3 vetoes due to having corresponding glitches in H1 auxiliary channels. None of these three events passes the cWB selection cuts. For these reasons, we do not consider any of them to be a plausible gravitational-wave candidate. Also, since these events do not pass the predefined category 3 data quality and vetoes, they do not affect the calculation of the upper limits presented below.

B. Upper limits

The S5y2/VSR1 search includes the analysis of eight network configurations with three different algorithms. We use the method presented in [29] to combine the results of this search, together with the S5y1 search [12], to set frequentist upper limits on the rate of burst events. Of the S5y2 results, we include only the networks H1H2L1V1, H1H2L1 and H1H2, as the other networks have small observation times and their contribution to the upper limit would be marginal. Also, we decided *a priori* to use only the two algorithms which processed the data from the full S5y2 run, namely, cWB and Ω. (EGC only analyzed data during the ∼5 months of the run when Virgo was operational.) We are left therefore with six analysis results to combine with the S5y1 results to produce a single upper limit on the rate of GW bursts for each of the signal morphologies tested.

As discussed in [29], the upper limit procedure combines the sets of surviving triggers according to which algorithm(s) and/or network detected any given trigger, and weights each trigger according to the detection efficiency of that algorithm and network combination. For the special case of no surviving events, the 90% confidence upper limit on the total event rate (assuming a Poisson distribution of astrophysical events) reduces to

$$R_{90\%} = \frac{2.3}{\epsilon_{\rm tot} T}, \tag{7.1}$$

where $2.3 = -\log(1 - 0.9)$, $\epsilon_{\rm tot}$ is the detection efficiency of the union of all search algorithms and networks, and T is the total observation time of the analyzed data sets.

In the limit of strong signals in the frequency band below 2 kHz, the product $\epsilon_{\rm tot} T$ is 224.0 days for S5y1 and 205.3 days for S5y2/VSR1. The combined rate limit for strong GW signals is thus 2.0 $\rm yr^{-1}$. For the search above 2 kHz, the rate limit for strong GW signals is 2.2 $\rm yr^{-1}$. This slightly weaker limit is due to the fact that less data was analyzed in the S5y1 high-frequency search than in the S5y1 low-frequency search (only 161.3 days of H1H2L1 data [13]). Figure 6 shows the combined rate limit as a function of amplitude for selected Gaussian and sine-Gaussian waveforms.

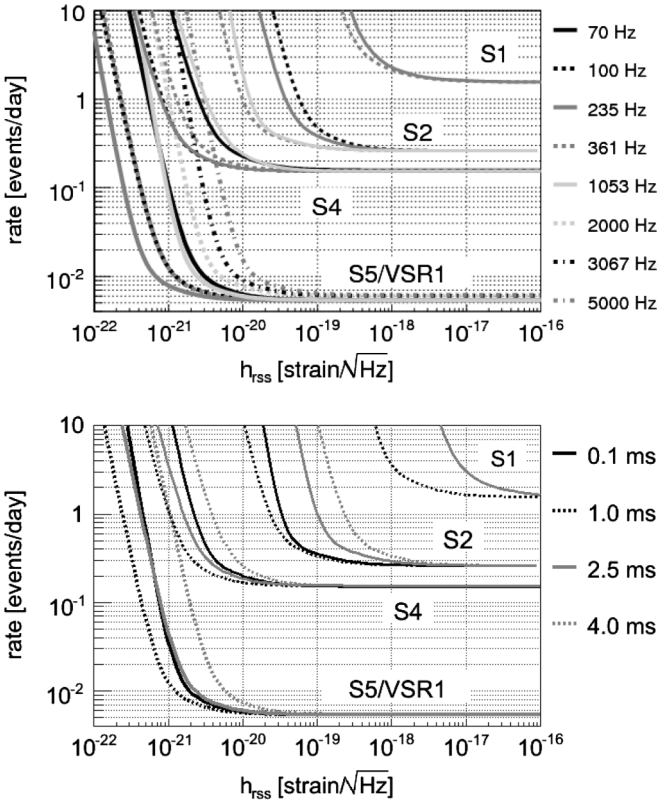

FIG. 6. Selected exclusion diagrams showing the 90% confidence rate limit as a function of signal amplitude for $Q = 9$ sine-Gaussian (top) and Gaussian (bottom) waveforms for the results of the entire S5 and VSR1 runs (S5/VSR1) compared to the results reported previously (S1, S2, and S4).

The results can also be interpreted as limits on the rate density (number per time per volume) of GWBs assuming a standard-candle source. For example, given an isotropic distribution of sources with amplitude $h_{\rm rss}$ at a fiducial distance r_0, and with rate density $\mathcal{R}$, the rate of GWBs at the Earth with amplitudes in the interval $[h, h + dh]$ is

$$dN = \frac{4\pi \mathcal{R} (h_{\rm rss} r_0)^3}{h^4} dh. \tag{7.2}$$

(Here we have neglected the inclination angle ι; equivalently we can take h^2 to be averaged over $\cos\iota$.) The expected number of detections given the network efficiency $\epsilon(h)$ (for injections without any ι dependence) and the observation time T is

$$\begin{aligned} N_{\rm det} &= T \int_0^\infty dh \left(\frac{dN}{dh}\right) \epsilon(h) \\ &= 4\pi \mathcal{R} T (h_{\rm rss} r_0)^3 \int_0^\infty dh h^{-4} \epsilon(h). \end{aligned} \tag{7.3}$$

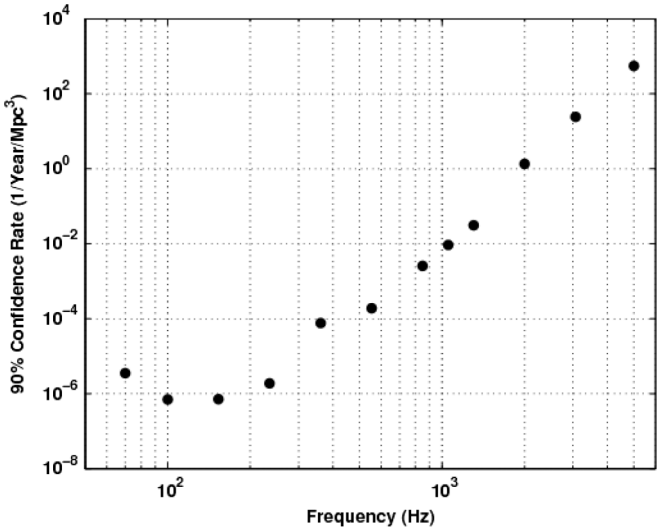

FIG. 7. Rate limit per unit volume at the 90% confidence level for a linearly polarized sine-Gaussian standard-candle with $E_{\rm GW} = M_\odot c^2$.

For linearly polarized signals distributed uniformly in $\cos\iota$, the efficiency is the same with h rescaled by a factor $\sin^2\iota$ divided by that factor's appropriately averaged value $\sqrt{8/15}$. Thus the above expression is multiplied by $\int_0^1 d\cos\iota (15/8)^{3/2}\sin^6\iota \approx 1.17$. The lack of detection candidates in the S5/VSR1 data set implies a 90% confidence upper limit on rate density $\mathcal{R}$ of

$$\mathcal{R}_{90\%} = \frac{2.0}{4\pi T (h_{\rm rss} r_0)^3 \int_0^\infty dh h^{-4} \epsilon(h)}. \qquad (7.4)$$

Assuming that a standard-candle source emits waves with energy $E_{\rm GW} = M_\odot c^2$, where $M_\odot$ is the solar mass, the product $h_{\rm rss} r_0$ is

$$h_{\rm rss} r_0 = \sqrt{\frac{G M_\odot}{c}} (\pi f_0)^{-1}. \qquad (7.5)$$

Figure 7 shows the rate density upper limits as a function of frequency. This result can be interpreted in the following way: given a source with a characteristic frequency f and energy $E_{\rm GW} = Mc^2$, the corresponding rate limit is $\mathcal{R}_{90\%}(f)(M_\odot/M)^{3/2}$ yr^{-1} Mpc^{-3}. For example, for sources emitting at 150 Hz with $E_{\rm GW} = 0.01 M_\odot c^2$, the rate limit is approximately 6×10^{-4} yr^{-1} Mpc^{-3}.

The bump at 361 Hz reflects the effect of the ''violin modes'' (resonant frequencies of the wires suspending the mirrors) on the sensitivity of the detector.

VIII. SUMMARY AND DISCUSSION

In this paper we present results of new all-sky untriggered searches for gravitational wave bursts in data from the first Virgo science run (VSR1 in 2007) and the second year of the fifth LIGO science run (S5y2 in 2006–2007). This data set represented the first long-term operation of a worldwide network of interferometers of similar performance at three different sites. Data quality and analysis algorithms are significantly improved since similar searches of the previous LIGO run (S4 in 2004) [30] and even since the first year of S5 (S5y1 in 2005–2006) [12,13]. This is reflected in an improved strain sensitivity with $h_{\rm rss}^{50\%}$ as low (good) as 5.6×10^{-22} Hz$^{-1/2}$ for certain waveforms (see Table II), compared to best values of 1.3×10^{-21} Hz$^{-1/2}$ and 6.0×10^{-22} Hz$^{-1/2}$ for S4 and S5y1, respectively. The new searches also cover an extended frequency band of 50–6000 Hz.

No plausible gravitational wave candidates have been identified in the S5y2/VSR1 searches. Combined with the S5y1 results, which had comparable observation time, this yields an improved upper limit on the rate of bursts (with amplitudes a few times larger than $h_{\rm rss}^{50\%}$) of 2.0 events per year at 90% confidence for the 64–2048 Hz band, and 2.2 events per year for higher-frequency bursts up to 6 kHz. Thus the full S5/VSR1 upper limit is better than the S5y1 upper limits of 3.75 per year (64–2000 Hz) and 5.4 per year (1–6 kHz), and is more than an order of magnitude better than the upper limit from S4 of 55 events per year.

We note that the IGEC network of resonant bar detectors set a slightly more stringent rate limit, 1.5 events per year at 95% confidence level [14]. However, those detectors were sensitive only around their resonant frequencies, near 900 Hz, and achieved that rate limit only for signal amplitudes (in $h_{\rm rss}$ units) of a few times 10^{-19} Hz$^{-1/2}$ or greater, depending on the signal waveform. (See Sec. X of [31] for a discussion of this comparison.) Further IGEC observations during 6 months of 2005 [15] improved the rate limit to $\simeq 8.4$ per year for bursts as weak as a few times 10^{-20} Hz$^{-1/2}$ but did not change the more stringent rate limit for stronger bursts. The current LIGO-Virgo burst search is sensitive to bursts with $h_{\rm rss}$ one to 2 orders of magnitude weaker than those which were accessible to the IGEC detectors.

To characterize the astrophysical sensitivity achieved by the S5y2/VSR1 search, we calculate the amount of mass, converted into GW burst energy at a given distance r_0, that would be sufficient to be detected by the search with 50% efficiency ($M_{\rm GW}$). Inverting Eq. (7.5), we obtain a rough estimate assuming an average source inclination angle (i.e. $h_{\rm rss}^2$ is averaged over $\cos\iota$):

$$M_{\rm GW} = \frac{\pi^2 c}{G} r_0^2 f_0^2 h_{\rm rss}^2. \qquad (8.1)$$

For example, consider a sine-Gaussian signal with $f_0 = 153$ Hz and $Q = 9$, which (from Table II) has $h_{\rm rss}^{50\%} = 6.0 \times 10^{-22}$ Hz$^{-1/2}$ for the four-detector network. Assuming a typical Galactic distance of 10 kpc, that $h_{\rm rss}$ corresponds to $M_{\rm GW} = 1.8 \times 10^{-8} M_\odot$. For a source in the

Virgo galaxy cluster, approximately 16 Mpc away, the same $h_{\rm rss}^{50\%}$ would be produced by a mass conversion of roughly $0.046M_{\odot}$. These figures are slightly better than for the S5y1 search and a factor of ~5 better than the S4 search.

We also estimate in a similar manner a detection range for GW signals from core-collapse supernovae and from neutron star collapse to a black hole. Such signals are expected to be produced at a much higher frequency (up to a few kHz) and also with a relatively small GW energy output (10^{-9}–$10^{-5}M_{\odot}c^2$). For a possible supernova scenario, we consider a numerical simulation of core collapse by Ott *et al.* [32]. For the model s25WW, which undergoes an acoustically driven explosion, as much as $8 \times 10^{-5}M_{\odot}$ may be converted to gravitational waves. The frequency content produced by this particular model peaks around ~940 Hz and the duration is of order 1 s. Taking this to be similar to a high-Q sine-Gaussian or a long-duration white noise burst, from our detection efficiency studies we estimate $h_{\rm rss}^{50\%}$ of 17–22 $\times 10^{-22}$ Hz$^{-1/2}$, i.e. that such a signal could be detected out to a distance of around 30 kpc. The axisymmetric neutron star collapse signals D1 and D4 of Baiotti *et al.* [5] have detection ranges (at 50% confidence) of only about 25 pc and 150 pc (see Fig. 3, due mainly to their lower energy ($M_{\rm GW} < 10^{-8}M_{\odot}$) and also to emitting most of that energy at 2–6 kHz, where the detector noise is greater.

The Advanced LIGO and Virgo detectors, currently under construction, will increase the detection range of the searches by an order of magnitude, therefore increasing by ~1000 the monitored volume of the universe. With that sensitivity, GW signals from binary mergers are expected to be detected regularly, and other plausible sources may also be explored. Searches for GW burst signals, capable of detecting unknown signal waveforms as well as known ones, will continue to play a central role as we increase our understanding of the universe using gravitational waves.

ACKNOWLEDGMENTS

The authors gratefully acknowledge the support of the United States National Science Foundation for the construction and operation of the LIGO Laboratory, the Science and Technology Facilities Council of the United Kingdom, the Max-Planck-Society and the State of Niedersachsen/Germany for support of the construction and operation of the GEO 600 detector, and the Italian Istituto Nazionale di Fisica Nucleare and the French Centre National de la Recherche Scientifique for the construction and operation of the Virgo detector. The authors also gratefully acknowledge the support of the research by these agencies and by the Australian Research Council, the Council of Scientific and Industrial Research of India, the Istituto Nazionale di Fisica Nucleare of Italy, the Spanish Ministerio de Educación y Ciencia, the Conselleria d'Economia Hisenda i Innovació of the Govern de les Illes Balears, the Foundation for Fundamental Research on Matter supported by the Netherlands Organisation for Scientific Research, the Polish Ministry of Science and Higher Education, the FOCUS Programme of Foundation for Polish Science, the Royal Society, the Scottish Funding Council, the Scottish Universities Physics Alliance, the National Aeronautics and Space Administration, the Carnegie Trust, the Leverhulme Trust, the David and Lucile Packard Foundation, the Research Corporation, and the Alfred P. Sloan Foundation. This document has been assigned LIGO Laboratory document number LIGO-P0900108-v6.

APPENDIX A: DATA QUALITY FLAGS

The removal of poor-quality LIGO data uses the data quality flag (DQF) strategy described in the first year analysis [12]. For the second year there are several new DQFs. New category 2 flags mark high currents in the end test-mass side coils, discontinuous output from a tidal compensation feed-forward system, periods when an optical table was insufficiently isolated from ground noise, and power fluctuations in lasers used to thermally control the radius of curvature of the input test masses. A flag for overflows of several of the main photodiode readout sensors that was used as a category 3 flag in the first year was promoted to category 2. New category 3 flags mark noise transients from light scattered from H1 into H2 and vice versa, large low-frequency seismic motions, the optical table isolation problem noted above, periods when the roll mode of an interferometer optic was excited, problems with an optical level used for mirror alignment control, and one period when H2 was operating with degraded sensitivity. The total "dead time" (fraction of live time removed) during the second year of S5 due to category 1 DQFs was 2.4%, 1.4%, and <0.1% for H1, H2, and L1, respectively. Category 2 DQF dead time was 0.1%, 0.1%, and 0.6%, and category 3 DQF dead time was 4.5%, 5.5%, and 7.7%. Category 4 flags, used only as additional information for follow-ups of candidate events (if any), typically flag one-time events identified by Collaboration members on duty in the observatory control rooms, and thus are quite different between the first and second years.

Virgo DQFs are defined by study of the general behavior of the detector, daily reports from the control room, online calibration information, and the study of loud transient events generated online from the uncalibrated Virgo GW channel by the Qonline [33] program. Virgo DQFs include out-of-science mode, hardware injection periods, and saturation of the current flowing in the coil drivers. Most of them concern a well identified detector or data acquisition problem, such as the laser frequency stabilization process being off, photodiode saturation, calibration line dropouts,

and loss of synchronization of the longitudinal and angular control. Some loud glitches and periods of higher glitch rate are found to be due to environmental conditions, such as increased seismic noise (wind, sea, and earthquakes), and 50 Hz power line ground glitches seen simultaneously in many magnetic probes. In addition, a faulty piezoelectric driver used by the beam monitoring system generated glitches between 100 and 300 Hz, and a piezo controlling a mirror on a suspended bench whose cabling was not well matched caused glitches between 100 and 300 Hz and between 600 and 700 Hz. The total dead time in VSR1 due to category 1 DQFs was 1.4%. Category 2 DQF dead time was 2.6%, and category 3 DQF dead time was 2.5% [34].

APPENDIX B: EVENT-BY-EVENT VETOES

Event-by-event vetoes discard gravitational-wave channel noise events using information from the many environmental and interferometric auxiliary channels which measure non-GW degrees of freedom. Our procedure for identifying vetoes in S5y2 and VSR1 follows that used in S5y1 [12]. Both the GW channels and a large number of auxiliary channels are processed by the KleineWelle (KW) [35] algorithm, which looks for excess power transients. Events from the auxiliary channels which have a significant statistical correlation with the events in the corresponding GW channel are used to generate the veto time intervals. Candidate events identified by the search algorithms are rejected if they fall inside the veto time intervals.

Veto conditions belong to one of two categories which follow the same notation used for data quality flags. Category 2 vetoes are a conservative set of vetoes targeting known electromagnetic and seismic disturbances at the LIGO and Virgo sites. These are identified by requiring a coincident observation of an environmental disturbance across several channels at a particular site. The resulting category 2 data selection cuts are applied to all analyses described in this paper, and remove $\sim$0.2% of analyzable coincident live time. Category 3 vetoes make use of all available auxiliary channels shown not to respond to gravitational waves. An iterative tuning method is used to maximize the number of vetoed noise events in the gravitational-wave channel while removing a minimal amount of time from the analysis. The final veto list is applied to all analyses below 2048 Hz, removing $\sim$2% of total analyzable coincident live time.

An additional category 3 veto condition is applied to Virgo triggers, based on the ratio of the amplitude of an event as measured in the in-phase (P) and quadrature (Q) dark port demodulated signals. Since the Q channel should be insensitive to a GW signal, large Q/P ratio events are vetoed. This veto has been verified to be safe using hardware signal injections [36], with a loss of live time of only 0.036%.

APPENDIX C: EGC BURST SEARCH

The exponential Gaussian correlator (EGC) pipeline is based on a matched filter using exponential Gaussian templates [37,38],

$$\Phi(t) = \exp\left(-\frac{t^2}{2\tau_0^2}\right)e^{2\pi i f_0 t}, \tag{C1}$$

where f_0 is the central frequency and τ_0 is the duration. Assuming that real GWBs are similar to sine-Gaussians, EGC cross-correlates the data with the templates,

$$C(t) = \frac{1}{N}\int_{-\infty}^{+\infty}\frac{\tilde{x}(f)\tilde{\Phi}^*(f)}{S(f)}e^{2\pi i f t}df. \tag{C2}$$

Here $\tilde{x}(f)$ and $\tilde{\Phi}(f)$ are the Fourier transforms of the data and template, and $S(f)$ is the two-sided noise power spectral density. N is a template normalization factor, defined as

$$N = \sqrt{\int_{-\infty}^{+\infty}\frac{|\Phi(f)|^2}{S(f)}df}. \tag{C3}$$

We tile the parameter space (f_0, $Q_0 \equiv 2\pi\tau_0 f_0$) using the algorithm of [39]. The minimal match is 72%, while the average match between templates is 96%. The analysis covers frequencies from 300 Hz to 5 kHz, where LIGO and Virgo have comparable sensitivity. Q_0 varies from 2 to 100, covering a large range of GW burst durations.

The quantity $\rho = \sqrt{2|C|^2}$ is the signal-to-noise ratio (SNR), which we use to characterize the strength of triggers in the individual detectors. The analysis is performed on times when at least three of the four detectors were operating. Triggers are generated for each of the four detectors and kept if the SNR is above 5. In order to reduce the background, category 2 DQFs and vetoes are applied, followed by several other tests. First, triggers must be coincident in both time and frequency between a pair of detectors. The time coincidence window is the light travel time between the interferometers plus a conservative 10 ms allowance for the EGC timing accuracy. The frequency coincidence window is selected to be 350 Hz. Second, events seen in coincidence in H1 and H2 with a unexpected ratio in SNR are discarded (the SNR in H1 should be approximately 2 times that in H2). Surviving coincident triggers are ranked according to the combined SNR, defined as

$$\rho_{\mathrm{comb}} = \sqrt{\rho_1^2 + \rho_2^2}, \tag{C4}$$

where ρ_1 and ρ_2 are the SNR in the two detectors. Third, a threshold is applied on ρ_1 and ρ_2 to reduce the trigger rate in the noisier detector. This lowers the probability that a detector with a large number of triggers will generate many coincidences with a few loud glitches in the other detector. Finally, for each coincident trigger we compute the SNR disbalance measure

TABLE V. Thresholds and background tuning information for all the networks studied by the EGC pipeline.

Network	Obs. time [days]	# lags	FAR	ρ_{comb}
H1H2L1V1	66.6	200	<400 Hz: 1 event in 10 years	69.8
			>400 Hz: 0.05 events	21.0
H1H2L1	18.3	1000	<400 Hz: 1 event in 10 years	80.9
			>400 Hz: 0.05 events	10.0
H1H2V1	15.9	1000	<400 Hz: 1 event in 10 years	89.6
			>400 Hz: 0.05 events	15.4
H1L1V1	4.5	2000	<400 Hz: 1 event in 10 years	67.9
			>400 Hz: 0.01 events	24.2

$$\Lambda = \frac{\rho_{\mathrm{comb}}}{\rho_{\mathrm{comb}} + |\rho_1 - \rho_2|}. \tag{C5}$$

This variable is useful in rejecting glitches in a pair of coaligned detectors with similar sensitivity, and so is used primarily for pairs of triggers from the LIGO detectors.

The background is estimated for each detector pair by time shifting the trigger lists. 200 time slides are done for H1H2L1V1, and more for the three-detector networks due to their shorter observation times (see Table V). The thresholds applied to ρ_1, ρ_2 and Λ are tuned for each detector pair to maximize the average detection efficiency for sine-Gaussian waveforms at a given false alarm rate. Once the ρ_1, ρ_2 and Λ thresholds are applied, all trigger pairs from the network are considered together and ρ_{comb} is used as the final statistic to rank the triggers. A threshold is placed on ρ_{comb}, chosen to give a low false alarm rate. More precisely, as we observe an excess of loud glitches with $f_0 < 400$ Hz, we use different thresholds depending on the frequency of the coincident triggers. Below 400 Hz, the false alarm rate is tuned to 1 event per 10 years. Above, the threshold for each network is set to give a maximum of 0.05 events expected from background for that network. An exception is made for H1L1V1, where the maximum number is chosen to be 0.01 events because of its shorter observation time. The final thresholds for each network are given in Table V.

APPENDIX D: Ω-PIPELINE BURST SEARCH

The Ω-Pipeline is essentially identical to QPipeline, which was used in previous LIGO S5 searches [12,13]. QPipeline has since been integrated into a larger software suite, with a change in nomenclature but no significant change in methodology. Since this approach is discussed in detail in [12,21], we provide only a summary here.

The Ω-Pipeline, like EGC, functions as a matched-filter search on a single-interferometer basis. The data stream is whitened by linear predictive filtering [40], then projected onto a template bank of complex exponentials. These templates are similar to those used by EGC, parametrized by central time τ_0, central frequency f_0, and quality factor Q_0, but use bisquare windows rather than Gaussian windows. The template spacing is also different, selected for computational speed, rather than for strict mathematical optimization as in EGC. The Ω template bank has a minimal match of 80%, and covers a frequency range from 48 Hz to 2048 Hz and a Q range from 2.35 to 100.

The significance of a single-interferometer trigger is given by its normalized energy Z, defined as the ratio of the squared magnitude of X (the projection onto the best-matched template) for that trigger to the mean-squared magnitude of other templates with the same f_0 and Q_0. For Gaussian white noise, Z is exponentially distributed and related to the matched filter SNR ρ by

$$Z = |X|^2/\langle |X|^2 \rangle = \rho^2/2. \tag{D1}$$

Z is used to rank L1 and V1 triggers.

For H1 and H2, Ω-Pipeline takes advantage of their colocated nature to form two linear combinations of the data streams. The first of these, the *coherent* stream H_+, is the sum of the strains in the two interferometers weighted by their noise power spectral densities. We define the coherent energy Z_{H_+} following (D1). We also define the correlated energy $Z^{\mathrm{corr}}_{\mathrm{H}_+}$, which is obtained by removing the contribution to Z_{H_+} from H1 and H2 individually and leaving only the cross-correlation term [41]. The H1H2 cuts are based on $Z^{\mathrm{corr}}_{\mathrm{H}_+}$, because it is less susceptible than Z_{H_+} to instrumental glitches, so providing better separation between signal and noise. The second stream, the *null* stream H_-, is the difference between the strains in H1 and H2. The normalized energy Z_{H_-} should be small for a gravitational wave, but generally much larger for an instrumental glitch. We therefore veto coherent stream triggers which are coincident in time and frequency with null stream triggers.

We require triggers to be coincident in at least two detectors. The interferometer combinations analyzed are shown in Table VI. (Note that because of the coherent analysis of H1 and H2, both must be operating for data from either to be analyzed.) Triggers are required to be coincident in both time and frequency as follows:

$$|T_1 - T_2| < T_c + \tfrac{1}{2}\max(\sigma_1, \sigma_2) \tag{D2}$$

TABLE VI. Thresholds on normalized energy for the various detector combinations.

Detector combination and frequency band	threshold	events in 1000 timeslides
H1H2L1 <200 Hz	$Z^{\rm corr}_{\rm H_+} > 37$, $Z_{L1} > 13$	14
H1H2L1 >200 Hz	$Z^{\rm corr}_{\rm H_+} > 13$, $Z_{L1} > 13$	16
H1H2V1 <200 Hz	$Z^{\rm corr}_{\rm H_+} > 22$, $Z_{V1} > 13$	9
H1H2V1 >200 Hz	$Z^{\rm corr}_{\rm H_+} > 14$, $Z_{V1} > 13$	0
L1V1 <200 Hz	$Z_{L1} > 32$ and $Z_{V1} > (4.7 \times 10^{-13} Z_{L1})^{-0.3}$	4
L1V1 >200 Hz	$Z_{L1} > 30$ and $Z_{V1} > (6.9 \times 10^{-12} Z_{L1})^{-0.27}$	5
H1H2 <200 Hz	$Z^{\rm corr}_{\rm H_+} > 80$	0 (10 slides)
H1H2 >200 Hz	$Z^{\rm corr}_{\rm H_+} > 30$	0 (10 slides)
total events		48

$$|F_1 - F_2| < \tfrac{1}{2}\max(b_1, b_2). \quad \text{(D3)}$$

Here T and F are the central time and frequency of the triggers, σ and b are their duration and bandwidth, and T_c is the light travel time between the interferometers.

The background for each detector pair is determined by time-shifting the triggers from one detector. We use 1000 shifts for each pair, except H1-H2. Only 10 shifts between H1 and H2 are used because the coherent analysis requires each shift to be processed independently, substantially increasing the computational cost. Also, time shifts between H1 and H2 are less reliable because they miss correlated background noise from the common environment. For all pairs, triggers below and above 200 Hz are treated separately because of the different characteristics of the glitch populations at these frequencies.

Normalized energy thresholds are set separately for each detector combination and frequency range such that there is less than a 5% probability of a false alarm after category 3 DQFs and vetoes. Table VI shows the thresholds and surviving events in timeslides for each combination. Figure 8 shows background and injection triggers and the energy thresholds for one interferometer pair.

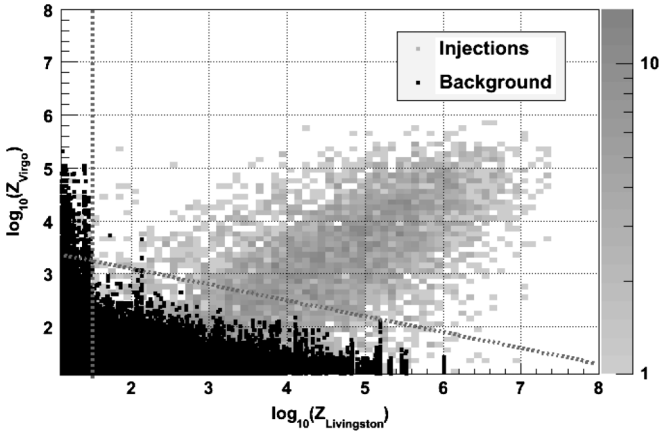

FIG. 8. Distribution of background and injection triggers below 200 Hz after category 3 DQFs and vetoes for L1-V1 pair. The dashed lines show the final normalized energy thresholds.

APPENDIX E: COHERENT WAVEBURST SEARCH

Coherent waveBurst (cWB) is a coherent algorithm for detecting gravitational-wave bursts. It constructs a least-squares fit of the two GW polarizations to the data from the different detectors using the constraint likelihood method [27]. The cWB algorithm was first used in search for gravitational wave bursts in the LIGO-GEO network [42]. More recently it has been used in the LIGO S5 first-year low-frequency search [12], and detailed descriptions of the algorithm can be found there and in [26,27].

The cWB analysis in this search covers frequencies from 64 Hz to 6.0 kHz, with the data processing split into two bands. The low-frequency (LF) band (64 Hz to 2.0 kHz) contains the most sensitive (but also the most nonstationary) data. The high-frequency (HF) band (1.28 kHz to 6.0 kHz) is dominated by the shot noise of the detectors and is much less polluted by environmental and instrumental transients. Splitting the analysis into two bands is convenient for addressing the different noise characteristics in these bands. It also eases the computational cost. The overlap of the bands is used to cross-check the results and to preserve the sensitivity to wide-band signals near the boundary between the bands.

The cWB analysis is performed in several steps. First, the data are decomposed into Meyer wavelets. Time-frequency resolutions of ($8 \times 1/16$, $16 \times 1/32$, $32 \times 1/64$, $64 \times 1/128$, $128 \times 1/256$, $256 \times 1/512$ [Hz $\times$ s]) are used for the low-frequency search and ($12.5 \times 1/25$, $25 \times 1/50$, $50 \times 1/100$, $100 \times 1/200$, $200 \times 1/400$, $400 \times 1/800$ [Hz $\times$ s]) for the high-frequency search. The data are processed with a linear predictor error filter to remove power lines, violin modes and other predictable data components. Triggers are identified as sets of wavelet pixels among the detectors containing excess power at time delays consistent with a gravitational wave from a physical sky position. For each trigger, trial incoming sky locations are sampled with 1° resolution, and various coherent statistics are computed. These include the maximum likelihood ratio L_m (a measure of the sum-squared matched-filter SNR detected in the network), the network correlated amplitude η, the network correlation coefficient (cc), the

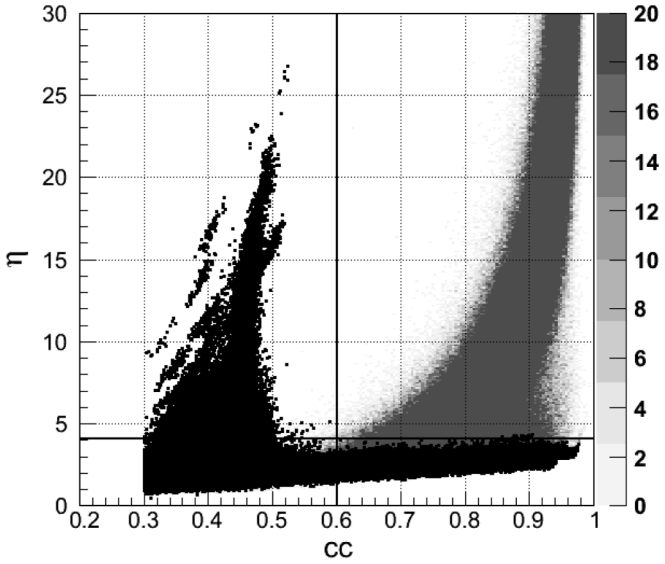

FIG. 9. Distribution of background triggers (black dots) after category 2 DQFs and vetoes for the L1H1H2 network for the high-frequency search, with $Q = 9$ sine-Gaussians injections (gray dots). The dashed lines show the thresholds on η and cc chosen for this network.

TABLE VII. Thresholds for each network for the cWB low- and high-frequency searches. Different thresholds on η are used for triggers below 200 Hz (η_1) and above 200 Hz (η_2) due to the different characteristics of the LIGO background noise in these frequency ranges. No energy disbalance cuts (Λ_{NET}, Λ_{HH}) are applied in the high-frequency search. In addition, a penalty factor cut of $P_f > 0.6$ is applied to all network configurations and searches.

	cWB LF						cWB HF		
	cc	η_1	η_2	Λ_{HH}	Λ_{NET}	P_f	cc	η	P_f
H1H2L1V1	0.5	4.5	4.1	0.3	0.35	0.6	0.6	4.3	0.6
H1H2L1	0.6	6.0	4.2	0.3	0.35	0.6	0.6	4.1	0.6
H1H2V1	⋯	⋯	⋯	⋯	⋯	⋯	0.7	4.6	0.6
H1L1V1	0.5	5.0	5.0	⋯	0.7	0.6	0.6	6.0	0.6
H1H2	0.6	6.0	4.1	0.3	0.35	0.6	0.5	5.0	0.6
H1L1	0.6	9.0	5.5	⋯	0.35	0.6	⋯	⋯	⋯
H2L1	0.6	6.5	5.5	⋯	0.35	0.6	⋯	⋯	⋯

energy disbalance statistics Λ, Λ_{HH} and the penalty factor P_f. (Each of these statistics is described in detail in [12].) The trial sky position giving the largest $cc \cdot L_m$ is selected as the best-guess incident direction, and the coherent statistics for this position are recorded. Finally, several post-production selection cuts are applied to the triggers to reduce the background.

Two groups of selection cuts are used in cWB. First, cuts on cc, Λ, Λ_{HH} and P_f are used to distinguish noise outliers from genuine GW signals. The most powerful consistency cut is based on the network correlation coefficient cc. For example, Fig. 9 shows a scatter plot of background triggers as a function of η and cc. Strong outliers (with large values of η) are characterized by low values of cc and are well separated from simulated signals. Additional selection cuts are based on the energy disbalance statistics Λ_{NET}, Λ_{HH}, and P_f. They are used to reject specific types of background events, such as H1-H2 correlated transients.

The second, final cut is on the network correlated amplitude η, which characterizes the significance of the triggers. Because of different characteristics of the background noise during the run and in the different frequency bands, the threshold on η is selected separately for each network configuration and frequency band to give false alarm probabilities of a few percent. In particular, in the low-frequency search separate η thresholds are used for triggers below and above 200 Hz. Table VII shows the thresholds used in the analysis.

The background is estimated separately on each segment of data processed. The cWB algorithm forms circular data buffers and shifts one detector with respect to the others, repeating the analysis hundreds of times on the time-shifted data. Table VIII shows the number of lags and accumulated background observation time for the various cWB searches and network configurations. The background data sets are used for tuning of the cWB selection cuts and also for estimation of the significance of the foreground events. For example, to estimate the significance of the blind injection identified by cWB, we generated a background sample with observation time equivalent to approximately 1000 H1H2L1 S5y2/VSR1 data sets.

TABLE VIII. Background observation time and false alarm rates for each network for the cWB low- and high-frequency searches.

	cWB LF Background			cWB HF Background		
	# lags	Obs time [year]	FAR year^{-1}	# lags	Obs time [year]	FAR year^{-1}
H1H2L1V1	200	34.8	0.3	96	17.6	0.17
H1H2L1	1000	499.9	0.1	96	31.7	0.09
H1H2V1	⋯	⋯	⋯	96	3.7	0.27
H1L1V1	200	1.8	3.3	288	3.0	0.33
H1H2	200	28.2	0.04	192	17.2	0.06
H1L1	200	4.6	2.0	⋯	⋯	⋯
H2L1	200	1.6	0.6	⋯	⋯	⋯

[1] C. Cutler and K. S. Thorne, in *Proc. of GR16*, edited by N. T. Bishop and S. D. Maharaj (World Scientific, Singapore, 2002).

[2] F. Pretorius, in *Physics of Relativistic Objects in Compact Binaries: from Birth to Coalescence*, edited by M. Colpi *et al.* (Springer Verlag, Berlin, 2009).

[3] Z. B. Etienne *et al.*, Phys. Rev. D **77**, 084002 (2008).

[4] C. D. Ott, Classical Quantum Gravity **26**, 063001 (2009).

[5] L. Baiotti *et al.*, Classical Quantum Gravity **24**, S187 (2007).

[6] S. Mereghetti, Astron. Astrophys. Rev. **15**, 225 (2008).

[7] N. Andersson and G. L. Comer, Phys. Rev. Lett. **87**, 241101 (2001).

[8] T. Damour and A. Vilenkin, Phys. Rev. D **64**, 064008 (2001).

[9] B. P. Abbott *et al.*, Rep. Prog. Phys. **72**, 076901 (2009).

[10] H. Grote (for the LIGO Scientific Collaboration), Classical Quantum Gravity **25**, 114043 (2008).

[11] F. Acernese *et al.*, Classical Quantum Gravity **25**, 114045 (2008).

[12] B. P. Abbott *et al.*, Phys. Rev. D **80**, 102001 (2009).

[13] B. P. Abbott *et al.*, Phys. Rev. D **80**, 102002 (2009).

[14] P. Astone *et al.*, Phys. Rev. D **68**, 022001 (2003).

[15] P. Astone *et al.*, Phys. Rev. D **76**, 102001 (2007).

[16] B. Alessandro, C. Beatrice, G. Bertotti, and A. Montorsi, J. Appl. Phys. **68**, 2908 (1990).

[17] S. Braccini *et al.*, Astropart. Phys. **23**, 557 (2005).

[18] This search includes several hours of data collected on 1 October 2007, after the official end of the S5 and VSR1 runs at 0:00 UTC on that day.

[19] For reference, a list of all time intervals included in the search may be found at https://dcc.ligo.org/cgi-bin/DocDB/ShowDocument?docid=T1000099&version=1.

[20] W. G. Anderson, P. R. Brady, J. D. Creighton, and É. É. Flanagan, Phys. Rev. D **63**, 042003 (2001).

[21] S. K. Chatterji, Ph.D. thesis, Massachusetts Institute of Technology, 2005.

[22] J. W. C. McNabb *et al.*, Classical Quantum Gravity **21**, S1705 (2004).

[23] S. Klimenko, I. Yakushin, M. Rakhmanov, and G. Mitselmakher, Classical Quantum Gravity **21**, S1685 (2004).

[24] F. Beauville *et al.*, Classical Quantum Gravity **25**, 045002 (2008).

[25] S. Chatterji, L. Blackburn, G. Martin, and E. Katsavounidis, Classical Quantum Gravity **21**, S1809 (2004).

[26] S. Klimenko *et al.*, Classical Quantum Gravity **25**, 114029 (2008).

[27] S. Klimenko, S. Mohanty, M. Rakhmanov, and G. Mitselmakher, Phys. Rev. D **72**, 122002 (2005).

[28] O. Benhar, V. Ferrari, and L. Gualtieri, Phys. Rev. D **70**, 124015 (2004).

[29] P. J. Sutton, Classical Quantum Gravity **26**, 245007 (2009).

[30] B. Abbott *et al.*, Classical Quantum Gravity **24**, 5343 (2007).

[31] B. Abbott *et al.*, Phys. Rev. D **72**, 062001 (2005).

[32] C. D. Ott, A. Burrows, L. Dessart, and E. Livne, Phys. Rev. Lett. **96**, 201102 (2006).

[33] L. Blackburn *et al.*, Classical Quantum Gravity **25**, 184004 (2008).

[34] N. Leroy *et al.*, Classical Quantum Gravity **26**, 204007 (2009).

[35] L. Blackburn *et al.* Report No. LIGO-G050158-00-Z, 2005, http://www.ligo.caltech.edu/docs/G/G050158-00.

[36] T. Ballinger *et al.*, Classical Quantum Gravity **26**, 204003 (2009).

[37] A. C. Clapson *et al.*, Classical Quantum Gravity **25**, 035002 (2008).

[38] F. Acernese *et al.*, Classical Quantum Gravity **26**, 085009 (2009).

[39] N. Arnaud *et al.*, Phys. Rev. D **67**, 102003 (2003).

[40] J. Makhoul, Proc. IEEE **63**, 561 (1975).

[41] This statement is actually only approximately correct due to complications related to normalization. See [12] for more details.

[42] B. Abbott *et al.*, Classical Quantum Gravity **25**, 245008 (2008).

Bayesian reconstruction of gravitational wave burst signals from simulations of rotating stellar core collapse and bounce

Christian Röver,[1] Marie-Anne Bizouard,[2] Nelson Christensen,[3] Harald Dimmelmeier,[4] Ik Siong Heng,[5] and Renate Meyer[6]

[1]*Max-Planck-Institut für Gravitationsphysik (Albert-Einstein-Institut), 30167 Hannover, Germany*
[2]*Laboratoire de l'Accélérateur Linéaire, Université Paris Sud, 91898 Orsay, France*
[3]*Physics and Astronomy, Carleton College, Northfield, Minnesota 55057, USA*
[4]*Department of Physics, Aristotle University of Thessaloniki, 54124 Thessaloniki, Greece*
[5]*Department of Physics and Astronomy, University of Glasgow, Glasgow G12 8QQ, United Kingdom*
[6]*Department of Statistics, The University of Auckland, Auckland 1142, New Zealand*

(Received 6 September 2009; published 17 November 2009)

Presented in this paper is a technique that we propose for extracting the physical parameters of a rotating stellar core collapse from the observation of the associated gravitational wave signal from the collapse and core bounce. Data from interferometric gravitational wave detectors can be used to provide information on the mass of the progenitor model, precollapse rotation, and the nuclear equation of state. We use waveform libraries provided by the latest numerical simulations of rotating stellar core collapse models in general relativity, and from them create an orthogonal set of eigenvectors using principal component analysis. Bayesian inference techniques are then used to reconstruct the associated gravitational wave signal that is assumed to be detected by an interferometric detector. Posterior probability distribution functions are derived for the amplitudes of the principal component analysis eigenvectors, and the pulse arrival time. We show how the reconstructed signal and the principal component analysis eigenvector amplitude estimates may provide information on the physical parameters associated with the core collapse event.

DOI: 10.1103/PhysRevD.80.102004 PACS numbers: 04.80.Nn, 02.70.Uu, 05.45.Tp, 97.60.Bw

I. INTRODUCTION

The detection of gravitational radiation will likely come in the near future. LIGO [1–3] is at its initial target sensitivity, and the detection of an event from an astrophysical source could come at any time. Around the globe a worldwide network of detectors is emerging; VIRGO in Italy [4,5], GEO in Germany [6], and TAMA in Japan [7] are operating alongside the LIGO detectors in the U.S. in the quest for gravitational wave detection. In a few years advanced LIGO and advanced VIRGO will come online, with a sensitivity increase of 10 over initial LIGO [8–11], increasing the prospective detection rate significantly. It will be a great day for physics when gravitational waves are finally directly detected, but it will also be the birth of a new way of observing the Universe and conducting astronomy and astrophysics.

The observations of expected sources should be dramatic: stellar collapse, pulsars, the inspiral of binary neutron stars followed by black hole formation, or even the stochastic background from the big bang. Gravitational wave astronomy will soon enter a regime where parameter estimation work will provide the means to make important astrophysical statements. Gravitational wave burst signals from rotating stellar core collapse and bounce, resulting in the formation of a protoneutron star, are one of the more promising and potentially extremely valuable sources for ground based interferometric detectors. Gravitational wave burst events are typically characterized by their short duration (from a few milliseconds to about one second) and the absence of accurate theoretical predictions for their waveforms (as opposed to e.g. waveform templates for binary inspiral). If these events happen sufficiently close by, the ground based gravitational wave detectors will be able to observe them. Detection searches for gravitational wave bursts typically use methods that can identify unmodeled but short duration events [12]. LIGO [13–15], VIRGO [16], GEO [14], and TAMA [15,17] have all recently conducted searches for gravitational wave bursts.

The prediction of the exact burst signal to be expected from a rotating stellar core collapse event depends on the complex interplay of general relativity, nuclear, and particle physics. Furthermore, it is anticipated that the signal is produced by various emission mechanisms, first from the coherent motion of the collapsing and rebounding core during the protoneutron star formation and then the ringing down of the nascent hot protoneutron star (all in cases when the core rotates). This is then possibly followed by emission due to prompt convective motion behind the hydrodynamic shock in the central part of the star due to nonaxisymmetric rotational instabilities for rapid rotation, as well as due to pulsations of the protoneutron star, for instance, triggered by fallback of matter onto it (see e.g. [18] for a comprehensive review). Only recently, the full complexity of the prospective emission mechanisms for gravitational waves in a stellar core collapse has become appreciated. Previously, research mainly concentrated on

the signal contribution from the collapse, core bounce, and ring-down phase, and therefore this is the gravitational wave signal that is now by far most comprehensively and accurately investigated using numerical studies. Recently, a series of calculations of core collapse models with unprecedented physical realism has been performed [19–21]. These studies provide strong evidence that the predictions of gravitational wave signals from the collapse and bounce phase are now robust. The gravitational wave results from these investigations have been made publicly available in the form of electronic waveform catalogs. If detected, such a gravitational wave signal can then ideally provide information on the mass of the progenitor model, the precollapse rotation, the density of the collapsed core, and the nuclear equation of state.

However, even for the collapse and core-bounce signal (not to mention the possible signal contributions from other emission mechanisms in a stellar core collapse event), one cannot conduct a template based search as is done when looking for coalescing compact binary signals, since it would be computationally impossible to completely cover the signal parameter space, and therefore various other methods have been developed to efficiently perform the search for gravitational wave burst signals in the detectors. Bayesian inferential methods provide a means to use data from interferometric gravitational wave detectors in order to extract information on the physical parameters associated with an event [22]. Markov chain Monte Carlo (MCMC) methods are a powerful computation technique for parameter estimation within this framework; they are especially useful in applications where the number of parameters is large [23]. Good descriptions of the positive aspects of a Bayesian analysis of scientific and astrophysical data are provided in [22,24,25]. MCMC routines have been developed that will produce parameter estimates for gravitational wave signals from binary inspiral [26–31] and pulsars [32–34]. Accurate parameter estimation of observed gravitational radiation events is the necessary pathway to understanding important problems in astrophysics and cosmology. In this paper we present methods which are the starting point in the process of using MCMC methods to extract and estimate parameters associated with rotating stellar core collapse events from their gravitational wave signals emitted during the collapse, core bounce, and ringdown phase.

Unfortunately, due to the complexity of the event (in particular, its intrinsic multidimensional nature), the computational time required to derive these signals in numerical simulations of rotating stellar core collapse is significant, and thus the waveform generation cannot be performed instantly while fitting a signal template to the data, and additional techniques to simplify the analysis are required. Instead of using waveforms corresponding to arbitrarily picked locations within parameter space, we reduce the complexity of the problem by simplifying the waveform space to the span of a small number of basis vectors. The basis vectors are derived from a representative catalog of numerically computed signal waveforms through the use of principal component analysis (PCA) [35]. The waveforms used in our present analysis are from the most recent, advanced, and comprehensive general relativistic study of rotating stellar core collapse by Dimmelmeier *et al.* [21] and depend on the mass of the progenitor model, the precollapse rotation, and the nuclear equation of state.

In this study we make use of a catalog that is smaller than eventually required in an extensive and accurate analysis of signals in real data, but with its nontrivial number of elements spanning a large portion of the interesting parameter space we expect it nevertheless to be sufficiently complex to probe and to demonstrate the method qualitatively. The MCMC algorithm essentially fits a superposition of derived basis vectors to the data, providing parameter estimates as well as associated uncertainties. We also demonstrate how PCA and MCMC then allow the reconstruction of the time series of a gravitational wave burst signal, including confidence bands. We present initial results showing that these PCA basis vectors are actually physically meaningful, and that we can extract astrophysical parameters from the measured core collapse burst signal. The ultimate goal is to be able to extract information on the nuclear equation of state from the gravitational wave signal as it is observed by a network of interferometers, as well as other relevant physical parameters associated with the event, as far as this is possible from the collapse, bounce, and ringdown signal alone.

There have been other approaches to signal reconstruction and parameter estimation with burst signals from stellar core collapse. The discipline essentially starts with the work of Gürsel and Tinto [36], who presented a method for reconstructing the time series for gravitational wave bursts. Rakhmanov [37] developed a general scheme of Tikhonov regularization to be applied on a network of detectors in order to extract the signal. MCMC methods have also been applied to parameter estimation for burst events from cosmic string cusps [38]. Searle *et al.* [39] have recently worked out the Bayesian framework to the coherent detection and analysis of burst signals, including a wide range of special cases like white noise burst signals, but also signals constituting linear combinations of some set of basis vectors, like the ones used in this present study. Summerscales *et al.* [40] proposed a maximum entropy technique in order to infer the time-dependent gravitational wave burst signals detected by a network of interferometric detectors; they then calculated the correlation between their reconstructed waveform and the entries in a catalog of rotating core collapse waveforms [41] in order to infer the physical parameters from the event. Our work is different in that we use waveforms from physical models (the table of rotating core collapse signals) as our means of

reconstructing the signal. PCA basis vectors are initially created from the table of waveforms, and the MCMC estimate of the amplitudes for the PCA basis vectors provides the reconstructed waveform. A linearly polarized gravitational wave signal can be reconstructed from the data of a single interferometer. The estimate of the physical parameters comes from an association of the reconstructed waveform with the elements of the catalog. The results in this paper are derived only using data from a single detector (signals embedded in simulated noise matching that of LIGO at its target sensitivity).

The organization of the paper is as follows. In Sec. II we describe the methods by which LIGO, VIRGO, GEO, and TAMA are searching for burst events; the parameter estimation technique we describe in this paper would be applied to event candidates from such a burst search. The method by which the catalog of stellar core collapse burst signals is established is described in Sec. III. A summary of the PCA method used in our study is presented in Sec. IV, while our analysis strategy is described in Sec. V. We illustrate how the analysis method works when applied to simulated example data in Sec. VI, and in Sec. VII we demonstrate that the PC basis vectors and the inferred corresponding coefficients actually carry physically meaningful information. In Sec. VIII we provide a summary, and discuss the direction of future work.

II. BURST SEARCH PIPELINES

All collaborations associated with ground based interferometric gravitational wave detectors have developed burst search pipelines in order to look for events [13–17]. Although some gravitational wave burst sources are well modeled, the burst pipelines search for very general types of waveforms. The only assumption which is usually made concerns the duration of the signal (less than a few hundred of ms) and the frequency bandwidth of the search, which can be as large as the detector bandwidth (from a few dozen of Hz up to the Nyquist frequency). Burst pipelines typically reduce the frequency bandwidth to a few kHz to focus on specific types of sources.

Most of the gravitational wave burst pipelines look for an excess of energy in a time-frequency map using different multiresolution time-frequency transforms. Anderson *et al.* [42] initially considered the energy given by the Fourier transform in a frequency band. More recent methods [43] make use of a wavelet decomposition of the data stream. In contrast, in [44–46] a gravitational wave burst signal represented as a sine Gaussian is implemeted.

Usually the gravitational wave burst searches are performed using data from a network of detectors. Demanding that a gravitational wave burst event is seen simultaneously in several detectors allows one to reduce the false alarm rate, which is rather high in a burst search due to the short duration of the signal. This is also the only way to disentangle a real gravitational wave signal from transient noise events. There exist two kinds of network analysis: coincident or coherent filtering. In a coincidence analysis [44,46], each interferometer output is analyzed, providing a list of triggers. A coincidence in time and frequency is then required. A coherent analysis [36,47–52] uses all interferometers' information by combining the input data streams or the filtered data streams into one single output which takes into account the detectors' antenna response function assuming the source is at a given position in the sky. A coherent analysis more efficienctly suppresses nonstationarities that are expected to be incoherent in the different detectors.

When using data from a network of detectors, burst pipelines can reconstruct the position in the sky of the source [36,53–55]. The accuracy of the source sky position depends on the time resolution of the pipeline. It is usually estimated for a set of different waveforms. Depending on the complexity of the signal waveform the time resolution can vary from a fraction of ms up to several ms [12]. The frequency content (central frequency and bandwidth) of the event is also estimated by the burst pipelines. The frequency information can give some hints concerning the possible astrophysical source. For instance, a central frequency of a few hundred Hz would point toward the event of a core collapse in a massive star resulting in the formation of a protoneutron star [21] (in particular, if the detection is accompanied by a neutrino trigger following shortly after) while a higher frequency content at about 10 kHz could suggest that the event could be due to a neutron star collapsing to a black hole [56]. Besides, coherent pipelines can also extract from the data an estimation of the waveform without assuming any model for the triggers with sufficient amplitude [36,57].

The work presented in this paper intends to extract even more information from the most significant events found by a gravitational wave burst pipeline assuming an astrophysical source model. The estimation of the parameters could also be used to reject a possible gravitational wave event candidate; the idea of distinguishing a real stellar core collapse signal from an instrumental glitch is briefly discussed in Secs. VII and VIII. The starting point for our technique would be the list of candidate triggers produced by a burst all-sky search pipeline, or times provided by electromagnetic and/or neutrino observations (external triggers). In both cases, the MCMC will search for the event over some relatively small time span. The trigger times provide a relatively small number of data periods to be examined by our method. The MCMC would attempt to produce a reconstruction of the signal based on a waveform catalog for stellar core collapse models.

III. GRAVITATIONAL WAVE SIGNALS FROM ROTATING CORE COLLAPSE AND BOUNCE

In stellar core collapse, the (possibly rotating) unstable iron core of a massive star at the end of its life contracts to

supernuclear density on a dynamical time scale of the order of 100 ms. As the core material stiffens due to repulsive nuclear forces, the collapse is halted abruptly, and the inner part of the core undergoes a rebound (the core bounce). After a period of ring-down oscillations, the hot protoneutron star settles down, while the remainder of the star is possibly (mainly depending on the mass of the progenitor) blown off in a supernova explosion.

If the precollapse stellar core is rotating, the dynamics of the evolution are reflected in the gravitational wave signal waveform with a slow rise during the core collapse, a large negative peak around bounce, and damped oscillations in the ring-down phase. If rotational effects become important for rapidly rotating models, the core collapse can even be stopped by centrifugal forces alone at subnuclear density. However, in contrast to previous, less sophisticated studies of the stellar core collapse scenario (see e.g. [58] and references therein), Dimmelmeier *et al.* [20] have shown that the signal waveform remains qualitatively unaltered and is thus generic for a wide range of initial rotation strength.

The gravitational radiation waveforms analyzed in this article are the burst signals from the most recent, advanced, and comprehensive general relativistic study of rotating stellar core collapse models [21]. These simulations were performed with a computational code that utilizes accurate Riemann solvers to evolve the general relativistic hydrodynamic equations and a nonlinear elliptic solver based on spectral methods [59] for the fully coupled metric equations in the conformal flatness approximation of general relativity [60]. The precollapse iron core models were taken from recent stellar evolutionary calculations by Heger *et al.* [61,62], either with an intrinsic or an artificially added rotation profile. These initial models were then evolved with a nonzero-temperature nuclear equation of state (EoS), either the one by Shen *et al.* [63,64] (Shen EoS) or the one by Lattimer and Swesty [65,66] (LS EoS, with a bulk incompressibility $K = 180$ MeV), both in the implementation of Marek *et al.* [67], including contributions from baryons, electrons, positrons, and photons. Deleptonization by electron capture on nuclei and free protons during the collapse phase is realized as proposed and tested by Liebendörfer [68].

Of the 136 models investigated in the study by Dimmelmeier *et al.* [21], 128 models have an analytic initial rotation profile. Their collapse behavior is determined by the following parameters:

(i) The strength of rotation is specified by the precollapse central angular velocity, which varies from $\Omega_{\mathrm{c,i}} = 0.45$ to $13.31\ \mathrm{rad\,s^{-1}}$ (with the individual range depending on the differentiality of rotation). The influence of rotation strength on the collapse dynamics and on the burst signal via rotational flattening is very pronounced.
For a wide range of slow to intermediate initial rotation strengths, the peak $|h|_{\max}$ of the gravitational wave amplitude is almost proportional to the ratio $T_{\mathrm{b}}/|W|_{\mathrm{b}}$ of rotational energy to gravitational energy at bounce (which in turn increases approximately linear with $\Omega_{\mathrm{c,i}}$ in this regime if all other model parameters are kept constant).
For very rapid rotation, however, $|h|_{\max}$ reaches a maximum and declines again, when the centrifugal barrier slows down the contraction considerably, preventing the core from collapsing to high supernuclear density. In such a case the frequency of the burst signal, which is practically constant for slow or moderate rotation, decreases significantly. Note that the trend to lower frequencies for very slowly rotating models shown in [20,21], which spoils the constancy of the signal frequency for such models, is due to a (possibly artificial) low-frequency contribution originating from postbounce convection in the protoneutron star, which superimposes the signal from the core bounce and protoneutron star ring-down.

(ii) The differentiality of the precollapse rotation profile is set by a length scale with values $A = 50\,000$, 1000, or 500 km, ranging from almost uniform to strongly differential rotation. For a fixed initial strength of rotation (as set by $\Omega_{\mathrm{c,i}}$), a change in A alone has no strong effect on the gravitational wave signal, neither on the amplitude nor on the frequency. However, rapid rotation can only be achieved for comparably small values of A.

(iii) The set of precollapse cores encompasses models with a progenitor mass of $M_{\mathrm{prog}} = 11.2$, 15.0, 20.0, or $40.0\mathrm{M}_{\odot}$ (masses at zero-age main sequence). The choice of the progenitor mass has a direct impact on the mass of the inner core during the collapse and at bounce (and thus on the mass of the protoneutron star). Already without rotation, the different progenitors produce an inner core at bounce with a mass that depends nonmonotonously on the mass of the progenitor (with the inner core mass increasing on the order of $M_{\mathrm{prog}} = 11.2$, 20.0, 15.0, and $40.0\mathrm{M}_{\odot}$). This variation is considerably amplified by rotation, which itself increases the mass on the inner core at bounce (approximately linear with $\Omega_{\mathrm{c,i}}$ at slow rotation and roughly quadratically at rapid rotation; see [21]). Nevertheless, the reflection of that effect on the peak signal amplitude $|h|_{\max}$ is practically negligible, as the effect of a high inner core mass (which causes a large quadrupole moment and thus a strong resulting gravitational wave signal) is canceled by strong centrifugal support, resulting in slower collapse dynamics and, consequently, a weaker gravitational wave signal.
The main frequency of the gravitational wave burst signal is also not influenced significantly by the mass

of the progenitor model, except that in models with the least massive progenitor ($M_{\rm prog} = 11.2{\rm M}_\odot$) even strong initial rotation does not decelerate the relatively small collapsing inner core enough to make it bounce at subnuclear densities. Hence the signal frequencies of such models remain comparably high. We also point out that the approximate nature of the deleptonization scheme during the collapse phase up to core bounce employed in these models could actually be responsible for overemphasizing the variation in the mass of the inner core at bounce with respect to the mass of the progenitor.

(iv) The microphysical equation of state during the evolution is chosen to be either the Shen EoS or the LS EoS. In the subnuclear density regime, the two EoSs are rather similar, with the LS EoS being a bit softer on average. However, at supernuclear density, the differences are more pronounced. Here the adiabatic index γ of the LS EoS jumps to $\sim$2.5, while in the Shen EoS γ reaches values of $\sim$3.0, making the nuclear material described by that EoS significantly stiffer. Consequently, the models with the Shen EoS consistently exhibit lower central densities at bounce and after ring-down.

Still, with respect to the peak waveform amplitude $|h|_{\rm max}$ of the burst signal, this does not translate into an unequivocal trend due to a complicated interplay in the protoneutron star between central compactness and density structure at intermediate radii. The peak frequency of the waveform spectrum, on the other hand, is almost always lower if the Shen EoS is used, which is a direct consequence of the lower central densities in the bounce and postbounce period due to the nuclear material stiffness from that EoS if all other parameters are identical and only the EoS is varied.

In Fig. 1 we present a representative sample of waveforms which illustrate the impact of a model's initial rotation state on the gravitational wave signal from core bounce, from slow and almost uniform initial rotation (model s20a1o05_shen), moderately fast and modestly differential initial rotation (model s20a2o09_shen), to rapid and very differential initial rotation (model s20a3o15_shen). While the effect of varying the initial rotation state is clearly reflected in the waveform for the models shown here, the influence of the progenitor model's mass and also the EoS for a fixed initial rotation state is much less apparent, and thus analogous pictorial waveform comparisons are not presented.

We note that 8 progenitor models of [21] are from a stellar evolutionary calculation that includes rotation in an approximate way. Hence, these models already have an initial angular velocity profile; no artificial rotation according to the simple analytic relation, like in the other models, is added prior to evolution. Consequently, as initial rotation

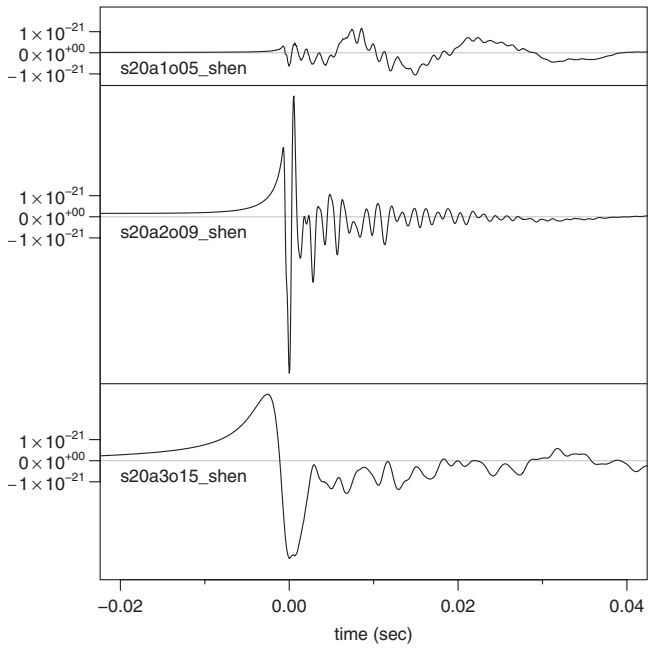

FIG. 1. Sample waveforms of the core-bounce signal for three models with varying initial rotation states while the mass of the progenitor model and EoS are fixed. Note the relatively small signal peak at the time of core bounce and the significant late-time contribution from postbounce convection for the slowly rotating model s20a1o05_shen, and the overall lower signal frequency for the rotation-dominated and centrifugally bouncing model s20a3o15_shen. The three signals presented here adequately cover the waveform morphology of our signal catalog.

is not parametrized, these models are not of use for this study. However, the collapse dynamics and associated signal waveforms of these models are well represented by models with artificially added precollapse rotation in terms of both signal amplitude and frequency, and therefore it is justified to not separately consider their behavior here. The different influences of the various model parameters, which are summarized here only briefly, are discussed in detail in [21]. The respective signal data can be downloaded freely from an online waveform template catalog [69].

We emphasize that the parameter selection for the models in [21] is fairly complete in that it accounts for all known relevant parameters which could have an impact on the burst signal from a core bounce (although, for instance in the case of neutrino effect, in an approximate way). Furthermore, the astrophysically meaningful range of the parameters has been reasonably exhausted (in the case of rotation, the expected strength of rotation for the bulk of stellar core collapse events is even at the lower end of the investigated range; see [70]). Only the selection of EoS is limited to two due to a lack of access to alternative nonzero-temperature nuclear equations of state for stellar core collapse at the time when the study by Dimmelmeier *et al.* [21] was performed. However, with the Shen EoS and

the LS EoS the two extremes of a rather stiff nuclear material and a somewhat soft one are probably well covered.

The range of frequencies and amplitudes of the signals is quite broad for the model sample of [21], with the integrated characteristic frequency f_c spanning from about 100 to 700 Hz (as opposed to the peak frequency f_{max} of the spectrum which lies in a narrow interval around 700 Hz; see Fig. 16 in [21]) and the integrated dimensionless characteristic amplitude h_c ranging from 6×10^{-22} to 7×10^{-21} for e.g. initial LIGO and a distance to the source of 10 kpc (for the definition of these quantities, see the references in e.g. [21]).

Still, the main factor of influence causing this variation is the rotation of the core (as measured by $\Omega_{c,i}$ and A, and rather well resolved in the models of [21]), while the mass of the progenitor, precollapse differentiality of rotation, and microphysical EoS hardly affect both f_c and h_c (see Fig. 17 in [21]). This partial degeneracy regarding the model parameters makes it very difficult to infer the unknown parameters from a detection of the gravitational wave burst signal emitted by a rotating stellar core collapse. In reverse, this means that parameters of little impact on the gravitational wave signal may be resolved only coarsely in a parameter study aiming at providing signal templates.

For an event with at most moderate rotation, in practice only the strength of rotation can be extracted from the waveform with confidence, provided the distance to the source and the orientation with respect to the rotation axis can also be determined. Only if a multitude of core collapse events can be detected via gravitational waves can systematic effects of e.g. the nuclear material stiffness (as described by the EoS) on the frequency also be analyzed with more certainty.

While the independent parameters $\Omega_{c,i}$, A, M_{prog}, and EoS uniquely specify each collapse model, from the actual numerical simulation of the collapse a number of important quantities can be obtained which characterize the evolution of each individual model; these are typically presented as results for rotating stellar core collapse calculations. Among these are the maximum density $\rho_{max,b}$ at the time of core bounce, the ratio $T_b/|W|_b$ of rotational energy to gravitational energy at bounce, and the corresponding value $T_{pb}/|W|_{pb}$ late after bounce.

These quantities provide information about the collapse dynamics and, for instance, permit one to distinguish between a core bounce that is mostly caused by the nuclear material stiffening at supernuclear densities to one that is dominated by centrifugal forces, which is again reflected by the waveform. Thus, in reverse the waveform encodes not only information about the independent model parameters, but also about these evolution quantities. Consequently, in the analysis on the correspondence between PCs and physical parameters presented in Sec. VII, we not only consider the parameters for the model setup but also the evolution of the quantities $\rho_{max,b}$, $T_b/|W|_b$, and $T_{pb}/|W|_{pb}$. However, in contrast to these "robust" parameters reflecting the global collapse dynamics we refrain from analyzing other quantities (like e.g. entropy at a specific off-center location or the time span of contraction) which are prone to depend more sensitively on the numerical evolution scheme or grid setup used for the model simulation.

IV. SINGULAR VALUE DECOMPOSITION

The signal waveforms used in the analysis reported here are originally generated at a higher sampling rate. Each waveform is subsequently resampled at a rate of 16 384 Hz (the LIGO and GEO data sampling rate). The waveforms are then buffered with zeros so that they are of the same length. Finally, the waveforms are time shifted so that the first (negative) peak in each waveform (which occurs shortly after the time of core bounce) is aligned.

For modeling purposes, the set of signal waveforms will be decomposed into an orthonormal basis. Following the method prescribed by [35], we create a matrix $\mathbf{H}$ so that each column corresponds to a signal waveform from the catalog after subtracting the overall mean of the waveforms. For m waveforms, each n samples long, $\mathbf{H}$ is a matrix with dimensions $n \times m$. Using singular value decomposition [71], $\mathbf{H}$ is factorized such that

$$\mathbf{H} = \mathbf{USV}', \tag{1}$$

where $\mathbf{U}$ and $\mathbf{V}$ are orthonormal $n \times r$ and $m \times r$ matrices, respectively, and $\mathbf{S}$ is a diagonal $r \times r$ matrix containing the singular values of $\mathbf{H}$ in decreasing order, i.e. $\mathbf{S} = \mathrm{diag}(s_1, \ldots, s_r)$ with $s_1 \geq \cdots \geq s_r > 0$, $r = \mathrm{rank}(\mathbf{H}) \leq \min(m, n)$. The columns of $\mathbf{U}$ are the eigenvectors of the empirical covariance matrix $\mathbf{HH}'$, and similarly, the columns of $\mathbf{V}$ are the eigenvectors of $\mathbf{H}'\mathbf{H}$. Additionally, the singular values in $\mathbf{S}$ are the square roots of the eigenvalues λ_i of either $\mathbf{HH}'$ or $\mathbf{H}'\mathbf{H}$, i.e. $s_i = \sqrt{\lambda_i}$.

The columns of $\mathbf{U}$, i.e. $\boldsymbol{u}_1, \ldots, \boldsymbol{u}_r$, form an orthonormal basis of the linear space spanned by the columns of $\mathbf{H}$, i.e. the signal waveform space, and each signal waveform can now be uniquely represented as a linear combination of these eigenvectors. A measure of multivariate scatter about the mean is the trace of the empirical covariance matrix, $\mathrm{tr}(\mathbf{HH}')$, also called total variation, which equals $\sum_i^r \lambda_i$. So the sum of the first $k \leq r$ largest eigenvalues, $\sum_{i=1}^k \lambda_i$, measures how much of the total variability of the waveforms is explained by the first k eigenvectors. These are referred to as the first k PCs and they achieve an optimal dimension reduction from the r-dimensional signal waveform space to a k-dimensional subspace.

Note that each waveform is n samples long and $\mathbf{U}$ has dimensions $n \times r$. For the waveforms considered in this article, n is typically 1000 to 10 000 samples long, so computing the eigenvectors of $\mathbf{HH}'$ in $\mathbf{U}$ can be computa-

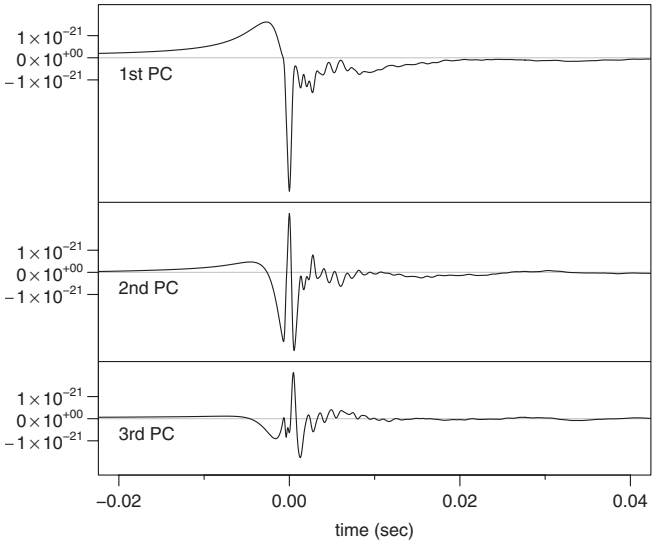

FIG. 2. The top three principal components (PCs) derived from the catalog of waveforms described in Sec. III.

tionally expensive. On the other hand, the number m of waveforms in the catalog is of the order of 100. So, computing the eigenvectors of $\mathbf{H}'\mathbf{H}$ in $\mathbf{V}$ is much less demanding, and they can be used to compute the eigenvectors in $\mathbf{U}$ by first noting that

$$\mathbf{H}'\mathbf{H}\boldsymbol{v}_i = \lambda_i \boldsymbol{v}_i, \tag{2}$$

where $\boldsymbol{v}_i$ is the eigenvector of $\mathbf{H}'\mathbf{H}$ corresponding to the ith largest eigenvalue λ_i. By premultiplying both sides with $\mathbf{H}$, we obtain

$$\mathbf{H}\,\mathbf{H}'\mathbf{H}\boldsymbol{v}_i = \lambda_i \mathbf{H}\boldsymbol{v}_i. \tag{3}$$

From this, we can see that $\mathbf{H}\boldsymbol{v}_i = \boldsymbol{u}_i$, i.e. $\mathbf{H}\boldsymbol{v}_i$ is the eigenvector corresponding to the ith largest eigenvalue of $\mathbf{H}\mathbf{H}'$ and thus equals the ith column of $\mathbf{U}$. Figure 2 illustrates the resulting first three PCs when applying this procedure to an actual waveform catalog.

V. ANALYSIS STRATEGY

A. Definitions

The starting point of our analysis is a waveform catalog, i.e. a catalog of time series (of equal lengths) describing the gravitational wave signal of core collapse events corresponding to different input parameter settings. Let n denote the number of samples (discrete time points) in each waveform vector and m the number of waveform vectors in the catalog. As detailed in Sec. IV, for these m time series we derive the first $k < r$ eigenvectors, $\boldsymbol{x}_1, \ldots, \boldsymbol{x}_k$, corresponding to the k largest eigenvalues [35]. Each of these eigenvectors again is of length n.

The data to be analyzed (the noisy measurement) are given in the form of a time series vector $\boldsymbol{y}$ of length N ($N > n$). This vector consists of additive nonwhite Gaussian noise with known (one-sided) power spectral density denoted by $S_1(f)$, superimposed by a core-bounce burst signal of length n located at an unknown instant T along the time axis.

Our aim is to model the core-bounce burst signal observation in terms of the basis of the k eigenvectors described above. To this end, we assume that the mean of the y_i's is a linear combination $\beta_1 x_{i,1} + \cdots + \beta_k x_{i,k}$ of the k eigenvectors, and zero before and after the burst signal. In matrix notation, this can be expressed in terms of the expectation value $\mathrm{E}[\boldsymbol{y}] = \boldsymbol{X}_{(T)}\boldsymbol{\beta}$, where $\boldsymbol{\beta} = (\beta_1, \ldots, \beta_k)'$ denotes the vector of regression coefficients, and the $N \times k$ matrix $\boldsymbol{X}_{(T)}$ has column vectors formed by the zero-padded k largest eigenvectors $\boldsymbol{x}_1, \ldots, \boldsymbol{x}_k$ which are cyclically time shifted by a lag T.

The signal reconstruction is eventually accomplished based on the Fourier domain representations of data and signal; in the following we will be referring to the conventions explicated in Appendix A. Let $\tilde{\boldsymbol{y}}$ denote the Fourier transformed data vector and $\tilde{\boldsymbol{x}}_i$, $i = 1, \ldots, k$, denote the discretely Fourier transformed eigenvectors after zero padding each to length N. The real and imaginary parts of these form the columns of the $N \times k$ real-valued matrix $\tilde{\boldsymbol{X}}$ (neglecting the redundant elements due to Hermitian symmetry).

One of the unknown parameters to be estimated is the signal's location T along the time axis, and in order to match data and signal, one needs to be able to shift both against each other in time. Let $\tilde{\boldsymbol{X}}_{(T)}$ be the matrix of Fourier domain basis vectors shifted in time so that these correspond to a particular signal arrival time T (with respect to some pivotal time point). Time shifting of $\tilde{\boldsymbol{X}}$ by some lag T can be done directly in the frequency domain by multiplying the original Fourier transform by a factor of $\exp(-2\pi \mathrm{i} f T)$.

B. Model 1: Basic linear regression model

If the data were an exact linear combination of first k principal components plus measurement noise, then the following standard linear model would adequately model the situation:

$$\boldsymbol{y} = \boldsymbol{X}_{(T)}\boldsymbol{\beta} + \boldsymbol{\varepsilon}, \tag{4}$$

where $\boldsymbol{\varepsilon}$ is the (Gaussian) noise vector with given (one-sided) spectral density $S_1(f)$. In the frequency domain this corresponds to

$$\tilde{\boldsymbol{y}} = \tilde{\boldsymbol{X}}_{(T)}\boldsymbol{\beta} + \tilde{\boldsymbol{\varepsilon}}, \tag{5}$$

where $\tilde{\boldsymbol{\varepsilon}}$ now is the Fourier transformed noise vector. In the Fourier domain, the real and imaginary components of the noise vector $\tilde{\boldsymbol{\varepsilon}}$ then simply are independently zero-mean Gaussian distributed with variances proportional to the power spectral density $S_1(f)$ [72,73] (see also Appendix B).

What is known here are the data (measurement) $\boldsymbol{y}$, the matrix $\boldsymbol{X}$ of basis vectors (derived from the waveform catalog through PCA), and the noise's power spectral density. The unknowns are the coefficients $\boldsymbol{\beta}$ and the time parameter T. The *a priori* information about these is expressed in the prior distribution $\mathrm{P}(\boldsymbol{\beta}, T)$, which is assumed to be uniform, i.e. any value is assumed equally likely.

C. Model 2: Random effects regression model

In general, the basis vectors will not allow one to completely reconstruct the original signal; there will always be a certain mismatch left unexplained when simplifying the problem to the reduced set of PCs as in (5). Neglecting the mismatch term would result in overconfidence in the reconstructed waveform and parameters. However, the simplified model introduced above will still be of interest, as it provides good approximations that are useful in the eventual implementation.

Adding an extra mismatch error component $\boldsymbol{m}$ to the model, a random effect in statistical terminology, the model is now

$$\tilde{\boldsymbol{y}} = \tilde{\boldsymbol{X}}_{(T)}\boldsymbol{\beta} + \tilde{\boldsymbol{m}} + \tilde{\boldsymbol{\varepsilon}}. \tag{6}$$

In the following, we expect the original catalog to be sufficiently densely populated, so that the mismatch is primarily due to the effect of neglecting PCs, and not due to the signal being much unlike the ones in the catalog. All we assume to be known about the mismatch is that it contributes a certain fractional amount to the signal's power. That amount was expressed in [35] in terms of the match parameter μ. Taking the difference between reconstructed and actual signal to be zero on average, and then expecting a certain (fractional) power for the mismatch, we use a Gaussian distribution with corresponding mean and variance for modeling the mismatch,

$$\mathrm{P}(m_i|\sigma_m^2) = \mathrm{N}(0, \sigma_m^2) \Leftrightarrow \mathrm{P}(\tilde{m}_j|\sigma_m^2) = \mathrm{N}\left(0, \frac{N}{2}\sigma_m^2\right), \tag{7}$$

i.e. the mismatch $\boldsymbol{m}$ enters the model as an additional white noise component with a one-sided power spectral density of $2\Delta_t\sigma_m^2$. The assumption of a Gaussian distribution is a simple and convenient choice here, and according to maximum entropy theory it also constitutes the most conservative possible choice [74]. It also seems to perform well in practice, despite the fact that the actual mismatch follows a rather heavy-tailed distribution with many near zero and also a substantial number of extreme values. Since the mismatch is supposed to scale with the signal (i.e. the "relative mismatch" is assumed constant), the mismatch's variance parameter σ_m^2 is set such that

$$\sigma_m^2 \approx \gamma^2 \frac{1}{N}\|\boldsymbol{X}\boldsymbol{\beta}\|^2, \tag{8}$$

depending on the PC coefficients $\boldsymbol{\beta}$ via the implied sum of squares (or power) of the PC contribution to the signal,

$$\frac{1}{N}\|\boldsymbol{X}\boldsymbol{\beta}\|^2 = \frac{1}{N}\sum_{i=1}^{N}\left(\sum_{j=1}^{Z}\beta_j x_{i,j}\right)^2, \tag{9}$$

and the scaling factor $\gamma^2 = \frac{1-\mu^2}{\mu^2}$ is set so that it corresponds to a particular match μ as in [35]. The above relationship between μ and γ^2 results from assuming the PC and mismatch contributions to the signal $\boldsymbol{s} = \boldsymbol{X}\boldsymbol{\beta} + \boldsymbol{m}$ to be (approximately) orthogonal: $\boldsymbol{m} \perp \boldsymbol{X}\boldsymbol{\beta}$ (i.e. the mismatch is defined as what is not spanned by the set of PCs).

The actual amount of mismatch is another unknown, and the (approximate) scaling of σ_m^2 with the signal power as in Eq. (8) is ensured through the definition of the prior distribution, which is set up as

$$\mathrm{P}(\boldsymbol{\beta}, T, \sigma_m^2) = \mathrm{P}(T) \times \underbrace{\mathrm{P}(\boldsymbol{\beta}, \sigma_m^2)}_{=\mathrm{P}(\boldsymbol{\beta})\times\mathrm{P}(\sigma_m^2|\boldsymbol{\beta})}. \tag{10}$$

As in the previous Sec. V B, the priors $\mathrm{P}(T)$ and $\mathrm{P}(\boldsymbol{\beta})$ are set to be independent and uniform, but the conditional prior distribution $\mathrm{P}(\sigma_m^2|\boldsymbol{\beta})$ is taken to be a scaled inverse χ^2 distribution:

$$\mathrm{P}_{\nu,\gamma^2}(\sigma_m^2|\boldsymbol{\beta}) = \text{Inv-}\chi^2\left(\nu, \gamma^2\frac{1}{N}\|\boldsymbol{X}\boldsymbol{\beta}\|^2\right), \tag{11}$$

with degrees-of-freedom parameter ν and scale parameter $(\gamma^2\frac{1}{N}\|\boldsymbol{X}\boldsymbol{\beta}\|^2)$, so that the prior certainty in the scale of $\sigma_m^2|\boldsymbol{\beta}$ is defined through ν. For example, a specification of $\gamma^2 = 0.1$ and $\nu = 3$ implies for the prior that $\mathrm{P}(0.038 < \sigma^2/(\frac{1}{N}\|\boldsymbol{X}\boldsymbol{\beta}\|^2) < 0.85) = 90\% = \mathrm{P}(0.73 < \mu < 0.98)$, and a conditional prior mean of $\mathrm{E}[\sigma_m^2|\boldsymbol{\beta}] = \frac{\nu}{\nu-2}\gamma^2\frac{1}{N}\|\boldsymbol{X}\boldsymbol{\beta}\|^2$. Setting $\nu = 0$ yields the (improper) Jeffreys prior, which does not depend on its prior scale parameter [75]. The Inv-χ^2 distribution was chosen here because it constitutes the conjugate prior distribution for this problem [75], which makes it a "natural" choice and makes the eventual implementation particularly simple, as will be seen in Sec. V D. The parameters γ^2 and ν may now be set so that the prior distribution reflects the reconstruction accuracy to be expected from the given set of k basis vectors derived from the waveform catalog at hand.

D. Monte Carlo integration

Inference on waveforms and parameters usually requires integrating the parameters' posterior distribution, as one is interested in figures like posterior expectations, quantiles, or marginal distributions. These are here determined using stochastic (Monte Carlo) integration, i.e. by generating samples from the posterior probability distribution and then approximating the desired integrals by sample statistics (means by averages, etc.). The generation of samples from the posterior distribution is done using MCMC methods, that is, by designing a Markov process whose stationary distribution is the posterior probability distribution

of interest, and which may then be numerically simulated step by step to produce the desired posterior samples. The generated samples then allow one to explore marginal or joint distributions of individual parameters, or of functions of the parameters as in the case of signal reconstruction, where the posterior distribution of $\tilde{\boldsymbol{X}}_{(T)}\boldsymbol{\beta} + \tilde{\boldsymbol{m}}$ is of interest, and T, $\boldsymbol{\beta}$, and $\tilde{\boldsymbol{m}}$ are random variables.

In the case of the basic linear model (see Sec. V B), the set of unknown parameters consists of the vector of PC coefficients $\boldsymbol{\beta}$ and the time shift parameter T. An MCMC algorithm here may be implemented as a Gibbs sampler [75], since the conditional posterior distribution $\mathrm{P}(\boldsymbol{\beta}|T, \boldsymbol{y})$ of coefficients $\boldsymbol{\beta}$ for a given time T is already known and easy to sample from [see Eq. (12)]. In a Gibbs sampler, generating samples from the joint distribution is carried out by alternately sampling from the two conditional distributions $\mathrm{P}(\boldsymbol{\beta}|T, \boldsymbol{y})$ and $\mathrm{P}(T|\boldsymbol{\beta}, \boldsymbol{y})$ [75]. Samples from $\mathrm{P}(\boldsymbol{\beta}|T, \boldsymbol{y})$ can be generated straight away, while a simple ''Metropolis-within-Gibbs'' step, i.e. a nested Metropolis sampler implementation [75], may be utilized for sampling from the (one-dimensional) distribution $\mathrm{P}(T|\boldsymbol{\beta}, \boldsymbol{y})$.

For the basic linear regression model (see Sec. V B), the conditional posterior distribution of the PC coefficients $\boldsymbol{\beta}$ for a given time shift T is a multivariate Gaussian distribution:

$$\mathrm{P}(\boldsymbol{\beta}|T, \boldsymbol{y}) = \mathrm{N}(\hat{\boldsymbol{\mu}}_T, \hat{\boldsymbol{\Sigma}}_T), \tag{12}$$

where

$$\hat{\boldsymbol{\Sigma}}_T = (\tilde{\boldsymbol{X}}'_{(T)} D^{-1} \tilde{\boldsymbol{X}}_{(T)})^{-1}, \tag{13}$$

$$\hat{\boldsymbol{\mu}}_T = (\tilde{\boldsymbol{X}}'_{(T)} D^{-1} \tilde{\boldsymbol{X}}_{(T)})^{-1} \tilde{\boldsymbol{X}}'_{(T)} D^{-1} \tilde{\boldsymbol{y}}, \tag{14}$$

and $D = \mathrm{diag}(\sigma^2(f_j))$ is the noise's covariance matrix, a diagonal matrix of the individual variances, as given in Eq. (B1) [75].

Sampling from the posterior distribution works similarly for the extended model (see Sec. V C), in addition to $\boldsymbol{\beta}$ and T, the mismatch $\tilde{\boldsymbol{m}}$ and mismatch variance σ_m^2 need to be sampled from. Note that the conditional posterior distribution $\mathrm{P}(\boldsymbol{\beta}|T, \tilde{\boldsymbol{m}}, \sigma_m^2, \boldsymbol{y})$ is not simply multivariate Gaussian any more, since changes in $\boldsymbol{\beta}$ lead to different prior density values (via its effect on the signal's sum-of-squares value). The expression in Eq. (12) still is an excellent approximation and is useful for defining a proposal distribution within the Metropolis step of the algorithm. The conditional distribution of the mismatch vector $\tilde{\boldsymbol{m}}$ is independent Gaussian:

$$\mathrm{P}(\tilde{\boldsymbol{m}}|\boldsymbol{\beta}, T, \sigma_m^2, \boldsymbol{y}) = \mathrm{N}(\check{\boldsymbol{\mu}}, \check{\boldsymbol{\Sigma}}), \tag{15}$$

where

$$\check{\mu}_{j,\mathrm{Re}} = \mathrm{Re}((\tilde{\boldsymbol{y}} - \tilde{\boldsymbol{X}}_{(T)}\boldsymbol{\beta})_j) \frac{\frac{N}{2}\sigma_m^2}{\frac{N}{2}\sigma_m^2 + \frac{N}{4\Delta_t} S_1(f_j)}, \tag{16}$$

$$\check{\sigma}^2_{jj,\mathrm{Re}} = \frac{\frac{N}{2}\sigma_m^2 \frac{N}{4\Delta_t} S_1(f_j)}{\frac{N}{2}\sigma_m^2 + \frac{N}{4\Delta_t} S_1(f_j)}, \tag{17}$$

and analogously for the imaginary parts $\mathrm{Im}(\tilde{m}_j)$. For the mismatch variance σ_m^2 the conditional posterior is

$$\mathrm{P}(\sigma_m^2|\boldsymbol{y}, \boldsymbol{\beta}, T, \tilde{\boldsymbol{m}}) = \mathrm{Inv}\text{-}\chi^2(\kappa, s^2), \tag{18}$$

where the degrees of freedom κ and scale s^2 are

$$\kappa = \nu + N, \tag{19}$$

$$s^2 = \frac{\nu\gamma^2 \frac{1}{N}\|\boldsymbol{X}\boldsymbol{\beta}\|^2 + \sum_{i=0}^{N} m_i^2}{\nu + N} \tag{20}$$

(see also Appendix C).

The MCMC sampler was eventually implemented as a Gibbs sampler, alternately sampling from the three conditional distributions of

(1) $\boldsymbol{\beta}, T|\boldsymbol{y}, \tilde{\boldsymbol{m}}, \sigma_m^2$,
(2) $\tilde{\boldsymbol{m}}|\boldsymbol{y}, \boldsymbol{\beta}, T, \sigma_m^2$, and
(3) $\sigma_m^2|\boldsymbol{y}, \boldsymbol{\beta}, T, \tilde{\boldsymbol{m}}$.

The first step is done in a Metropolis-within-Gibbs step, using a symmetric proposal distribution for T, the approximated posterior of $\boldsymbol{\beta}|T, \ldots$ from Eq. (12) for the corresponding $\boldsymbol{\beta}$ proposal, and accepting/rejecting as in a usual Metropolis-Hastings sampler based on corresponding posterior and proposal probability density values. Samples for the second and third step may be generated directly.

VI. IMPLEMENTATION AND APPLICATION

A. Setup

In the following examples we are using the waveform catalog described in Sec. III, containing 128 gravitational radiation waveforms from rotating core collapse and bounce [21,69]. The basis vectors to be used for signal reconstruction are generated through a PCA (see Sec. IV) [35]. Utilizing the same code and general setup for calculating the models described in [21,69], we then compute three new rotating stellar core collapse models with input parameter values that did not appear in the original catalog (but lie within the range of the catalog parameter space) and their associated waveforms. The aim is then to reconstruct these waveforms using the PCA method.

The simulated data used here are 1 s in length and sampled at 16 384 Hz, superimposed with (simulated) non-white Gaussian noise, and Tukey windowed. The shape of the noise curve is here taken to correspond to LIGO at its initial sensitivity as stated in [76]; this is the definition that is also implemented in the LIGO scientific collaboration's LSC algorithm library (LAL) [77]. The noise's spectral density $S_1(f)$ is estimated by averaging over a thousand ''empirical'' periodograms of identically generated data (same size and resolution, same windowing applied), more closely resembling a realistic case in which the noise spectrum would need to be estimated as well. In addition,

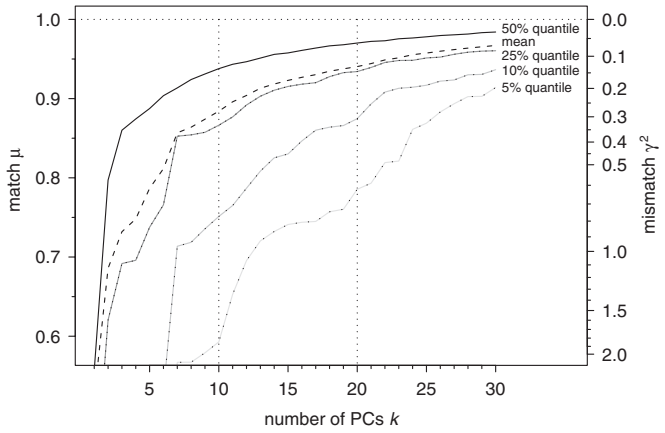

FIG. 3. Achievable match μ and scaling factor γ^2 for given numbers k of PCs across the whole catalog used here. A particular number k of PC basis vectors yields a certain match μ for each of the 128 waveforms in the catalog. Shown here is the distribution of matches across the catalog for increasing values of k, as characterized by mean, median, and some more quantiles.

this way convolution effects on the spectrum due to the finite data size and windowing are compensated.

The prior distribution for the mismatch parameter σ_m^2 is set by determining what match μ would be achievable for the given number k of PCs. This is done by projecting each single waveform in the catalog onto the span of the PCs, and then (for any given number k of PCs) considering the distribution of achieved mismatch values across the catalog. Figure 3 illustrates the mean, median, and some more quantiles of the mismatch distribution for increasing numbers of PCs (in analogy to Fig. 2 in Ref. [35]). We chose the prior's parameters (scale γ^2 and degrees of freedom ν) so that it matched the distribution of computed matches across the catalog. For the two example settings of $k = 10$ and $k = 20$ considered in the following, this leads to maximum likelihood estimates of ($\gamma^2 = 13.3\%$, $\nu = 2.82$) and ($\gamma^2 = 5.70\%$, $\nu = 2.96$). The resulting prior density for $k = 10$ PCs is also shown in Fig. 4.

B. Examples

The first example illustrated here, labeled signal A in the following, has a signal-to-noise ratio (SNR) of $\rho = 10$, where the SNR is defined as

$$\rho = \sqrt{4 \sum_j \frac{\frac{\Delta_t}{N} |\tilde{h}(f_j)|^2}{S_1(f_j)}}.$$

It was generated assuming the Shen EoS, a mass $M_{\mathrm{prog}} = 20 M_\odot$ for the progenitor, a precollapse central angular velocity $\Omega_{\mathrm{c,i}} = 5.48\ \mathrm{rad\,s^{-1}}$, a differentiality of the precollapse rotation profile given by $A = 1000$ km, and an effective distance of $d_{\mathrm{e}} = 5.17$ kpc. The effective distance depends on the actual distance to the source, and also reflects the effect on the amplitude of the gravitational wave signal from other parameters (such as the geometry of the detector with respect to the source), and is in general greater than the actual distance. The signal is embedded within simulated interferometer noise, and, using the model with $k = 10$ basis vectors, the posterior distributions of the model parameters are derived using an MCMC implementation as described in Sec. V D. The maximum achievable match for this example waveform (for $k = 10$ and varying time shift T) is $\mu = 0.97$.

The marginal posterior distributions of some individual parameters are illustrated in Fig. 4. Note the timing accu-

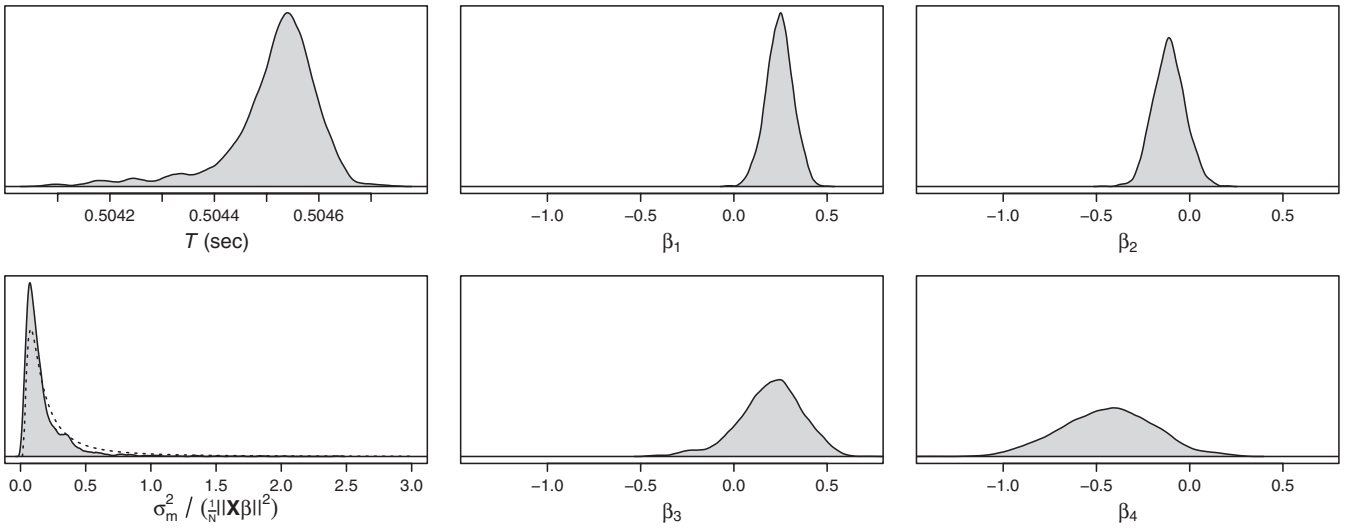

FIG. 4. Marginal posterior probability distributions of the parameters of example signal A with SNR $\rho = 10$, indicating the values and uncertainties of the model parameters as inferred from the data. Only the first four coefficients β_1 to β_4 corresponding to the top four principal components are shown here; there are $k = 10$ coefficients in total. The dashed line in the top right plot shows the prior probability distribution in comparison to the (very similar) posterior.

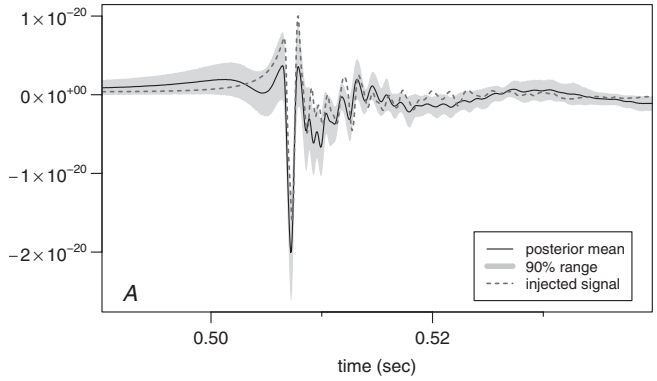

FIG. 5. Reconstruction of the example signal A with SNR $\rho = 10$ using $k = 10$ PCs.

racy, which has a standard error of 0.1 ms in this case; in the following examples (for the same SNR), these are also of the order of submilliseconds. The parameters' joint posterior distribution provides the posterior probability distribution of the waveform at any given time t_i. Figure 5 shows the posterior mean and a 90% confidence band in comparison with the originally injected waveform.

The example signal B illustrates how the signal recovery changes with differing numbers of PCs included in the model. This signal was generated assuming the LS EoS, a mass $M_{\rm prog} = 15.0{\rm M}_\odot$ for the progenitor, a precollapse central angular velocity $\Omega_{\rm c,i} = 2.825\ {\rm rad\,s^{-1}}$, a differentiality of the precollapse rotation profile of $A = 1000$ km, and an effective distance of $d_{\rm e} = 3.24$ kpc. The signal's match is $\mu = 0.89$ when using 10 PCs, and $\mu = 0.95$ for 20 PCs. The same data are analyzed twice, once using $k =$

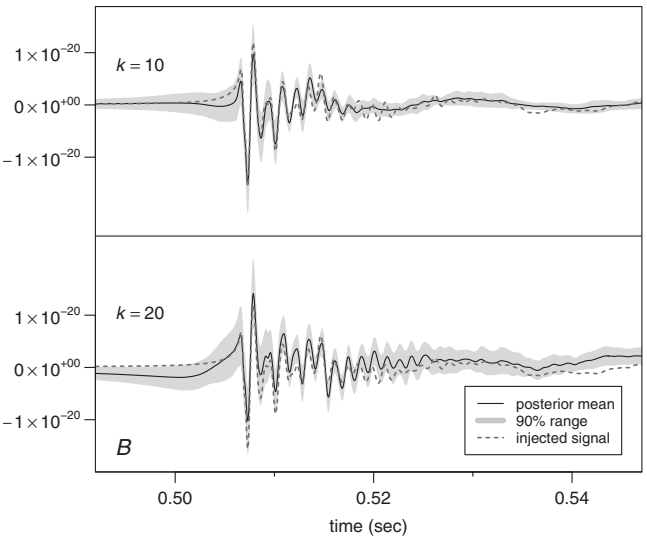

FIG. 6. A repeated analysis and reconstruction of the same example signal B with SNR $\rho = 10$ using different numbers of PCs ($k = 10$ and $k = 20$). Note that a larger number of basis vectors in the model does not necessarily improve signal recovery.

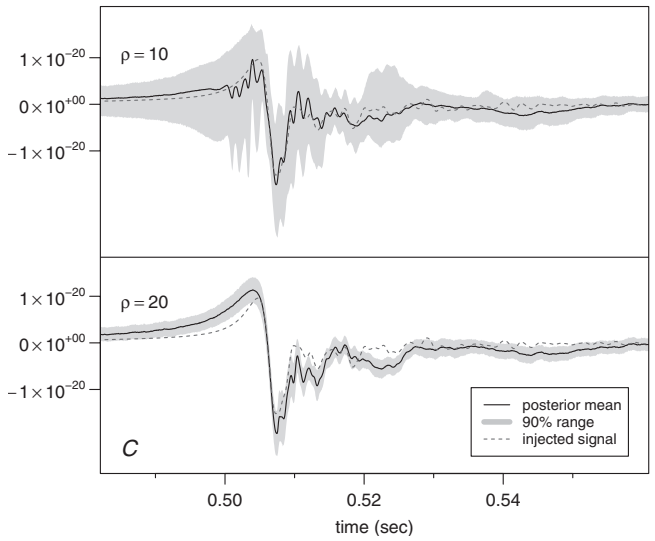

FIG. 7. Reconstruction of the same example signal C at different overall amplitudes (and, with that, SNRs $\rho = 10$ and $\rho = 20$), both times using $k = 10$ PCs.

10 and then using $k = 20$ PCs; the resulting recovered waveforms are shown in Fig. 6. The enlarged model in principle allows for a better match of the signal, but on the other hand the larger number of parameters also decreases the certainty in parameter estimates, so that the recovery does not necessarily improve. In this example, the posterior variances of the PC parameters common to both models ($\beta_1, \ldots, \beta_{10}$) as well as the time parameter T increased for the $k = 20$ case. In the resulting signal reconstruction (see Fig. 6) the confidence band is wider, and the discrepancy between injected signal and posterior mean also increases.

The reconstruction of signals at different SNRs can be seen in the following example signal C in Fig. 7; here the same signal is injected at different overall amplitudes and hence SNRs ($\rho = 10$ and $\rho = 20$). The injected signal was generated using the LS EoS, a mass $M_{\rm prog} = 40.0{\rm M}_\odot$ for the progenitor, a precollapse central angular velocity $\Omega_{\rm c,i} = 9.596\ {\rm rad\,s^{-1}}$, a differentiality of the precollapse rotation profile given by $A = 500$ km, and effective distances of $d_{\rm e} = 8.32$ and 4.16 kpc, respectively. The resulting signal waveform's match is $\mu = 0.97$. As expected, a higher SNR yields a more accurate recovery, and the resulting posterior variances are correspondingly smaller.

VII. CORRESPONDENCE BETWEEN PRINCIPAL COMPONENTS AND PHYSICAL PARAMETERS

The analysis performed above not only allows one to reconstruct the waveform, but the posterior distribution of the PC coefficients actually also contains information on the signal's physical parameters ($\Omega_{\rm c,i}$, A, $M_{\rm prog}$, and EoS) as well as other evolution parameters (like $\rho_{\rm max,b}$, $T_{\rm b}/|W|_{\rm b}$, and $T_{\rm pb}/|W|_{\rm pb}$). In the present study we are only able to choose between two specific EoSs, but as this work pro-

gresses the goal is to make estimates from a wider selection of EoSs. Considering the catalog of waveforms alone, one can project each waveform onto the span of the PCs (as was done in the construction of Fig. 3) and inspect the resulting fitted PC coefficients. Figure 8 illustrates the values of the first three coefficients (β_1, β_2, and β_3) for all the signals in the catalog. Obviously the distribution of coefficients in parameter space exhibits some structure. This structure can now be exploited, the idea being that the posterior means and variances of the coefficients β_i for a measured signal expose a pattern that is characteristic for the type of signal. For illustration, in the following we describe a simple approach involving the three example waveforms from the previous section. The coefficients' posterior distribution can be related back to the sets of coefficients for reconstructing every signal in the original catalog, in order to identify similarities. A simple *ad hoc* measure of similarity is a χ^2 match that relates a set of best-matching coefficients $\hat{\beta}_i$ $(i = 1, \ldots, k)$ associated with each catalog entry to the posterior distribution of the coefficients $\mathrm{P}(\beta_i|y)$ of the inferred signal. Such a match may be defined as

$$\chi^2 = \min_{c\in\mathbb{R}} \sum_{i=1}^{k} \frac{(c\hat{\beta}_i - \mathrm{E}[\beta_i|\boldsymbol{y}])^2}{\mathrm{Var}(\beta_i|\boldsymbol{y})}, \tag{21}$$

considering only posterior means and variances of individual coefficients β_i, and allowing for a scaling factor c in the overall amplitude of the matched signal. Computing the match for each signal from the catalog allows one to rank all signals and then determine those that fit the best. A mapping scheme set up this way combines elements of nearest-neighbor and naive-Bayes classification techniques [78].

For the initial example signal *A* shown above (see Figs. 4 and 5), the posterior means and standard deviations (error bars) are illustrated in a parallel coordinates plot [79] in Fig. 9, together with the five best-matching catalog entries. More details on the injected and the ten best-matching signals are given in Table I. Table II lists the closest correspondents for the other example signals (examples *B* and *C*) in comparison with the injection values. In the case of signal *A*, the best-matching waveform from the catalog and the injected signal have very similar physical parameters. For signals *B* and *C* this simple method still provides a good estimation of the physical parameters, although admittedly not as accurate as case *A*; note that the reconstruction of the waveform is quite accurate for all three signals. We think that through the use of techniques such as Procrustes rotation [80] we will be able to provide a more direct link to the physical parameters. The posterior mean values for the first three PC coefficients (β_1 to β_3) for all five examples are also illustrated in Fig. 8. Reconstruction of the measured signals through the PC basis vectors not only allows one to capture the waveforms' appearances, but also yields information on the underlying physical parameters.

The information available from matching a signal candidate against a set of basis vectors may not only facilitate a classification within a set of possible astrophysical sources (as illustrated in Fig. 8), but may also help in distinguishing it from signals of different origin, like instrumental glitches, etc. Different types of potential signals may also be partly reconstructible in terms of a linear combination of PCs, but a poor match, an unusual combi-

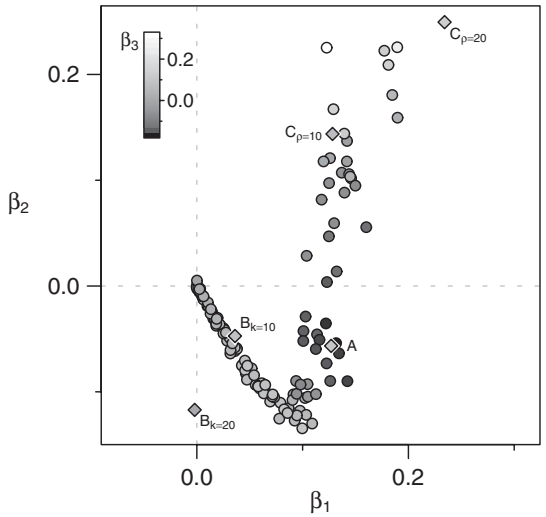

FIG. 8. The resulting first three PC coefficients β_1, β_2, and β_3 when matching each of the 128 waveforms in the catalog against the set of PCs (no noise involved). The waveforms in the catalog all correspond to a signal from a fixed distance (10 kpc). Note that the coefficients only occupy a very restricted region in parameter space. The diamonds show the posterior mean values of the PC coefficients for the three examples (labeled *A*, *B*, and *C*) discussed in the text. For comparison they are scaled down (by their known distance) to the same magnitude.

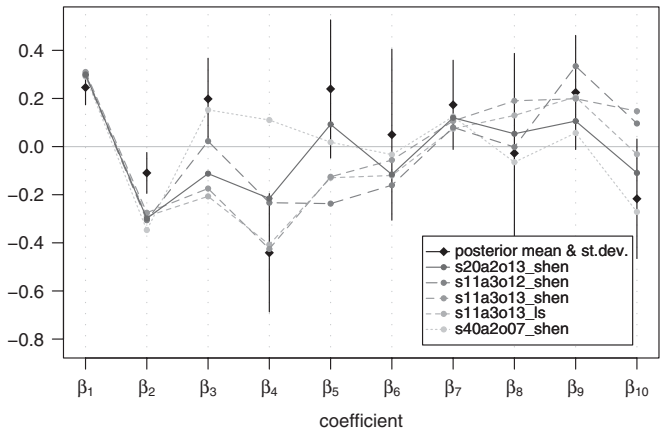

FIG. 9. Comparison of the distributions of all PC coefficients β_i to the best-matched sets of coefficients found in the original catalog. Posterior means and standard deviations (error bars) are shown in black, the (scaled) sets of the top five best-matching coefficients are shown in different shades of gray.

TABLE I. The injected example signal A and the corresponding top 10 best-matching catalog entries. The column labeled with "Model" identifies the signal from the original catalog [69]. The following columns state achieved χ^2 match [according to Eq. (21)], the corresponding EoS, mass of the progenitor model ($M_{\rm prog}$), precollapse angular velocity at the center ($\Omega_{\rm c,i}$), precollapse differential rotation length scale (A), rotation rates initially ($T_{\rm i}/|W|_{\rm i}$), at the time of bounce ($T_{\rm b}/|W|_{\rm b}$), and late after bounce ($T_{\rm pb}/|W|_{\rm pb}$), and the maximum density in the core at the time of bounce ($\rho_{\rm max,b}$) [21]. The corresponding best-matching effective distance $d_{\rm e}$ results from inverting the amplitude c [see Eq. (21)] that yields the optimal match.

Rank	Model	χ^2	EoS	$M_{\rm prog}$ ($M_\odot$)	$\Omega_{\rm c,i}$ (rad s^{-1})	A (km)	$\frac{T_{\rm i}}{\lvert W\rvert_{\rm i}}\lvert\frac{T_{\rm b}}{\lvert W\rvert_{\rm b}}\lvert\frac{T_{\rm pb}}{\lvert W\rvert_{\rm pb}}$ (%)	$\rho_{\rm max,b}$ (10^{14} g cm^{-3})	$d_{\rm e}$ (kpc)
Example signal A (injected)			Shen	20.0	5.48	1000	1.27|11.9|10.5	2.62	5.17
1	s20a2o13_shen	10.8	Shen	20.0	6.45	1000	1.80|14.8|12.8	2.42	3.50
2	s11a3o12_shen	12.8	Shen	11.2	10.65	500	1.28|14.9|12.3	2.46	3.46
3	s11a3o13_shen	13.7	Shen	11.2	11.30	500	1.44|16.1|13.2	2.36	3.37
4	s11a3o13_ls	13.8	LS	11.2	11.30	500	1.44|15.8|13.2	2.64	3.10
5	s40a2o07_shen	14.6	Shen	40.0	3.40	1000	0.72|11.8|9.9	2.58	3.75
6	s11a3o12_ls	15.4	LS	11.2	10.65	500	1.28|14.7|12.3	2.75	3.12
7	s15a2o09_shen	15.4	Shen	15.0	4.56	1000	1.09|11.8|10.3	2.58	3.42
8	s20a3o09_shen	15.7	Shen	20.0	8.99	500	0.90|15.7|12.5	2.38	3.58
9	s20a3o07_shen	17.4	Shen	20.0	5.95	500	0.50|10.1|8.0	2.70	3.24
10	s20a2o13_ls	20.6	LS	20.0	6.45	1000	1.80|14.4|12.9	2.75	2.94
⋮	⋮	⋮	⋮	⋮	⋮	⋮	⋮	⋮	⋮

TABLE II. The injected signal example signals B and C, and the corresponding best-matching catalog entries when varying k or ρ, respectively; see also Sec. VI B and Table I.

PCs/SNR	model	χ^2	EoS	$M_{\rm prog}$ ($M_\odot$)	$\Omega_{\rm c,i}$ (rad s^{-1})	A (km)	$\frac{T_{\rm i}}{\lvert W\rvert_{\rm i}}\lvert\frac{T_{\rm b}}{\lvert W\rvert_{\rm b}}\lvert\frac{T_{\rm pb}}{\lvert W\rvert_{\rm pb}}$ (%)	$\rho_{\rm max,b}$ (10^{14} g cm^{-3})	$d_{\rm e}$ (kpc)
Example signal B (injected)			LS	15.0	2.82	1000	0.41|5.5|5.2	3.61	3.24
$k = 10$	s11a3o07_shen	1.9	Shen	20.0	5.95	500	0.40|5.9|5.1	2.89	3.41
$k = 20$	s15a1o13_ls	47.4	LS	15.0	2.71	50 000	3.26|6.1|6.6	3.56	1.28
Example signal C (injected)			LS	40.0	9.60	500	1.46|22.1|19.0	0.73	8.32|4.16
$\rho = 10$	s40a3o13_ls	5.8	LS	40.0	11.30	500	2.07|23.4|20.7	0.28	5.38
$\rho = 20$	s40a2o15_shen	19.6	Shen	40.0	7.60	1000	3.62|21.1|20.3	0.27	2.32

nation of coefficients, or a better match from an alternative set of basis vectors may then provide evidence in favor or against certain signal origins.

VIII. CONCLUSIONS AND OUTLOOK

In this paper we have described initial work on implementing a scheme by which the physical parameters associated with a rotating collapse and bounce in a stellar core collapse event can be estimated through the observation of gravitational waves by detectors such as LIGO, VIRGO, GEO, or TAMA. We have presented a technique which allows one to reconstruct the detected signal through the use of numerically calculated gravitational radiation waveforms, principal component analysis, and Markov chain Monte Carlo methods; we have then compared the reconstructed signals to the table of numerically calculated waveforms and inferred the physical parameters.

The results displayed in this paper were achieved through the application of a number of different and difficult analysis techniques. We are encouraged that in this initial study we have displayed the fact that these methods can be combined in a way such that physical information about the supernova event can be extracted from the detected gravitational wave data. We have found that our method is quite successful in the reconstruction of the detected waveform, and this is displayed in the three examples. In the present analysis we have used the output from a single detector, and we expect that the accuracy of the signal reconstruction will only get better as we expand the application of this work to the coherent analysis of multiple interferometers. We were able to make a fairly good association with the physical parameters; however, we think that we will be able to greatly improve on our ability to make parameter estimation estimates. In the present study we worked with a relatively small signal catalog, where each physical parameter took on only a handful of different values; for example, there were only two EoS to choose from. Our parameter estimation demonstration was pretty good within these constraints, but we expect the accuracy to increase with expanded signal catalogs. In addition, Procrustes rotation [80] is an example of one technique that we intend to apply in order to make better statistical estimates of the physical parameters based on the eigenstates provided by the PCA.

Our eventual goal is to apply the method to the output from a network of detectors, which will provide an even better ability to discriminate signal and noise, reconstruct the signal, plus allow us to estimate the source position on the sky. This would necessitate the use of catalogs for stellar core collapse waveforms which are both quantitatively more extensive and qualitatively improved, so that the parameter space of likely events can be completely covered and very finely resolved. For instance, a larger selection of available equation of state tables will extend the phase space in that respective direction, while a more accurate inclusion of neutrino effects will both improve the quality of the burst signal from core bounce and as well yield a much more appropriate characterization of the low-frequency signal from postbounce convective bulk motion in the postshock region and in the protoneutron star. In addition, other prospective emission mechanisms for gravitational waves in a core collapse event, like protoneutron star pulsations or nonaxisymmetric rotational instabilities, could be also considered (for a comprehensive review on various such mechanisms, see [18]).

The method presented in this paper will provide a better way to produce statistical and probabilistic statements about the physical parameters associated with a stellar core collapse event, and the ability to make statements about actual signals observed by interferometric detectors. The data from multiple interferometers will be coherently analyzed; this will allow the estimation of parameters associated with the location of the source on the sky, similar to what can be achieved with coherent MCMC analysis of binary inspiral gravitational wave data [29,30]. As noted previously in our examples, the timing accuracy is better than 1 ms for a single interferometer observation; a multiple interferometer coherent MCMC should provide very good sky localization estimation, and the use of principal components within the framework of Searle *et al.* [39] also shows great promise. In addition, a coherent analysis will also allow us to better distinguish mismatch ($\boldsymbol{m}$, common to all detectors) from noise ($\boldsymbol{\varepsilon}$, different between different detectors) and hence should improve the waveform reconstruction. We also plan to incorporate a flexible model for the detector noise spectrum, as described in [73]. A proper accounting for the noise spectral densities of the interferometers could also be applied in producing the PCA eigenvectors and eigenvalues, i.e. these would not simply be the result of a least-squares fit, but rather a noise-weighted least-squares fit. The resulting basis vectors should then better reflect what is actually ''visible'' to an interferometric detector within its limited sensitivity band.

An important part of our long-term research program will be to ensure that the catalog of waveforms truly spans and encompasses those from physically possible rotating stellar core collapses; it will be critical for us to consult closely with experts in the field [18–21] to assure that the physical parameters for the waveforms we will use cover the range of natural possibilities. Typically when initially constructing the initial models one already has some idea about how many intermediate steps per free parameters are required. When the waveforms are generated as the output from the calculations (along with the other output data), then the variations of the waveforms and the other data give some indication if the original choice of model construction and parameter division are sensible. While the signal catalog needs to stretch over the extreme limits of the values for the physical parameters, a strength of our method is that the table need not be densely populated (as is the case with the template bank for coalescing binary signals); this is the advantage provided by the use of the PCA. For example, when the PCA eigenvalues are derived, their variation provides guidance about the quality of our catalog. We can test whether the waveform table contains enough entries by successfully reconstructing additional (off-table) signals placed within the parameter space; this was essentially the method used for verifying the results presented in this article.

The technique described in this paper could prove to be advantageous for signal reconstruction and parameter estimation when numerical techniques are required in order to produce the waveforms. For example, we can imagine our method as being useful for estimating parameters for complicated binary inspiral signals; numerical relativity calculations are producing a wide array of complicated inspiral signals [81]. We have already shown in Sec. VII that the fitted PC coefficients can be related to the original physical parameters of the signals in the catalog. Future research will explore how the joint posterior distribution of the PC coefficients can be employed for statistical inference on the physical parameters by linking the different parameter spaces via Procrustes rotation [80].

This method should also prove to be useful in distinguishing a real stellar core collapse event from a common noise glitch in the data. As displayed in Fig. 8, there is a characteristic pattern to be found with PCA values associated with a real signal. A glitch produced by noise, when reconstructed via PCA, will likely fall outside the pattern formed by stellar core collapse signals. Alternatively, one could set up an alternative glitch model, which, instead of using numerical simulations for the (PCA) basis vector generation, is trained on sets of measured waveforms that are known to be instrumental artifacts. We intend to test this potential veto technique.

In this paper we have reduced the table of 128 waveforms to 10 or 20 of the most important PC eigenvectors. Instead of arbitrarily choosing the number of eigenvectors to use, we plan to have our MCMC optimize the signal reconstruction through the use of a reversible jump MCMC, similar to the method described in [82], thereby treating the number or subset of PCs as another unknown. In this Bayesian approach the optimal number of eigenvectors is

determined by weighing the benefit of a good signal fit with a large number of eigenvectors against the Ockham's Razor penalization when the model gets overly complex.

ACKNOWLEDGMENTS

It is a pleasure to thank Christian D. Ott and Patrick J. Sutton for a careful reading of the script. H. D. acknowledges a Marie Curie Intra-European Fellowship within the 6th European Community Framework Programme (IEF 040464). This work was supported by the Max-Planck-Society, The Royal Society of New Zealand Marsden Fund Grant No. UOA-204, National Science Foundation Grants No. PHY-0553422 and No. PHY-0854790, the Fulbright Scholar Program, the DAAD and IKY (IKYDA German-Greek research travel grant), by the European Network of Theoretical Astroparticle Physics ENTApP ILIAS/N6 under Contract No. RII3-CT-2004-506222, and by the Science and Technology Facilities Council of the United Kingdom and the Scottish Universities Physics Alliance.

APPENDIX A: DEFINITION OF DISCRETE FOURIER TRANSFORM

The discrete Fourier transform is defined for a real-valued function h of time t, sampled at N discrete time points at a sampling rate of $\frac{1}{\Delta_t}$.

The transform maps from

$$\{h(t) \in \mathbb{R}\colon\ t = 0, \Delta_t, 2\Delta_t, \ldots, (N-1)\Delta_t\} \tag{A1}$$

to a function of frequency f

$$\{\tilde{h}(f) \in \mathbb{C}\colon\ f = 0, \Delta_f, 2\Delta_f, \ldots, (N-1)\Delta_f\}, \tag{A2}$$

where $\Delta_f = \frac{1}{N\Delta_t}$ and

$$\tilde{h}(f) = \sum_{j=0}^{N-1} h(j\Delta_t)\exp(-2\pi \mathrm{i} j\Delta_t f). \tag{A3}$$

Since h is real valued, the elements of $\tilde{h}$ are symmetric in the sense that $\tilde{h}(i\Delta_f)$ and $\tilde{h}((N-i)\Delta_f)$ are complex conjugates; this allows one to restrict attention to the non-redundant elements indexed by $i = 0, \ldots, N/2$.

APPENDIX B: FOURIER DOMAIN MODEL

A Gaussian distribution of a (time-domain) random vector also implies Gaussianity for the Fourier transformed vector. In particular, if $n(t)$ is (zero mean, stationary) Gaussian noise with one-sided power spectral density $S_1(f)$, then in the limit of large N and small Δ_t the real and imaginary components of the discrete Fourier transformed time series are independently zero-mean Gaussian distributed:

$$\mathrm{P}(\mathrm{Re}(\tilde{n}(f_j))) = \mathrm{N}(0, \sigma^2_{f_j}), \qquad \mathrm{P}(\mathrm{Im}(\tilde{n}(f_j))) = \mathrm{N}(0, \sigma^2_{f_j}), \tag{B1}$$

where the variance parameter is $\sigma^2_{f_j} = \frac{N}{4\Delta_t} S_1(f_j)$ [72,73,83].

APPENDIX C: JOINT AND CONDITIONAL POSTERIORS

For the random effects model from Sec. V C the joint distribution of data and parameters may be factored out into

$$p(\boldsymbol{y}, \boldsymbol{\beta}, T, \sigma_m^2, \tilde{\boldsymbol{m}}) = p(\boldsymbol{y}|\boldsymbol{\beta}, T, \sigma_m^2, \tilde{\boldsymbol{m}}) \times p(\tilde{\boldsymbol{m}}|\boldsymbol{\beta}, T, \sigma_m^2) \times p(\sigma_m^2|\boldsymbol{\beta}, T) \times p(\boldsymbol{\beta}, T) \tag{C1}$$

$$\propto \exp\left(-2\sum_{j=1}^{N/2} \frac{\frac{\Delta_t}{N}|\tilde{y}_j - (\tilde{\boldsymbol{X}}_{(T)}\boldsymbol{\beta})_j - \tilde{m}_j|^2}{S_1(f_j)}\right) \tag{C2}$$

$$\times (\sigma_m^2)^{-N/2} \exp\left(-\sum_{i=1}^{N} \frac{m_i^2}{2\sigma_m^2}\right) \tag{C3}$$

$$\times \left(\frac{1}{N}\|\boldsymbol{X}\boldsymbol{\beta}\|^2\right)^{\nu/2} (\sigma_m^2)^{-1-(\nu/2)} \exp\left(\frac{-\nu\gamma\frac{1}{N}\|\boldsymbol{X}\boldsymbol{\beta}\|^2}{2\sigma_m^2}\right), \tag{C4}$$

where the proportionality here refers to keeping the data and known parameters constant. In the above equation, the first term (C2) is the "usual" time-domain likelihood from Appendix B, the term (C3) is the likelihood of the mismatch (random effect), and the term (C4) is a conditional prior of the mismatch variance parameter. By fixing the values for different subsets of parameters, one can determine conditional posterior distributions that are useful for the Gibbs sampling implementation (see Sec. V D).

[1] A. Abramovici *et al.*, Science **256**, 325 (1992).

[2] B. C. Barish, in *Gravitational Wave Detection: Proceedings of the Tama International Workshop on Gravitational Wave Detection*, edited by K. Tsubono *et al.* (Universal Academy Press, Tokyo, 1997), pp. 155–161.

[3] B. Abbott *et al.*, Nucl. Instrum. Methods Phys. Res., Sect. A **517**, 154 (2004).

[4] B. Caron *et al.*, Nucl. Phys. B, Proc. Suppl. **48**, 107 (1996).
[5] A. Brillet, in *Gravitational Wave Detection: Proceedings of the Tama International Workshop on Gravitational Wave Detection* (Ref. [2]), pp. 163–173.
[6] J. Hough *et al.*, in *Gravitational Wave Detection: Proceedings of the Tama International Workshop on Gravitational Wave Detection* (Ref. [2]), pp. 175–182.
[7] K. Tsubono *et al.*, in *Gravitational Wave Detection: Proceedings of the Tama International Workshop on Gravitational Wave Detection* (Ref. [2]), pp. 183–191.
[8] J. R. Smith *et al.*, Class. Quantum Grav. **26**, 114013 (2009).
[9] http://www.ligo.caltech.edu/advLIGO/.
[10] F. Acernese *et al.*, J. Opt. A **10**, 064009 (2008).
[11] http://wwwcascina.virgo.infn.it/advirgo/.
[12] F. Beauville *et al.*, Class. Quantum Grav. **25**, 045002 (2008).
[13] B. Abbott *et al.*, Class. Quantum Grav. **24**, 5343 (2007).
[14] B. Abbott *et al.*, Class. Quantum Grav. **25**, 245008 (2008).
[15] B. Abbott *et al.*, Phys. Rev. D **72**, 122004 (2005).
[16] F. Acernese *et al.*, Class. Quantum Grav. **26**, 085009 (2009).
[17] M. Ando *et al.*, Phys. Rev. D **71**, 082002 (2005).
[18] C. D. Ott, Class. Quantum Grav. **26**, 063001 (2009).
[19] C. D. Ott, H. Dimmelmeier, A. Marek, H.-T. Janka, I. Hawke, B. Zink, and E. Schnetter, Phys. Rev. Lett. **98**, 261101 (2007).
[20] H. Dimmelmeier, C. D. Ott, H. T. Janka, A. Marek, and E. M. Müller, Phys. Rev. Lett. **98**, 251101 (2007).
[21] H. Dimmelmeier, C. D. Ott, A. Marek, and H.-T. Janka, Phys. Rev. D **78**, 064056 (2008).
[22] L. S. Finn, arXiv:gr-qc/9709077.
[23] W. R. Gilks, S. Richardson, and D. J. Spiegelhalter, *Markov Chain Monte Carlo in Practice* (Chapman&Hall/CRC, Boca Raton, FL, 1996).
[24] T. J. Loredo, in *Statistical Challenges in Modern Astronomy*, edited by E. D. Feigelson and G. J. Babu (Springer-Verlag, New York, 1992), Chap. 12, pp. 275–297.
[25] P. C. Gregory, in *Bayesian Inference and Maximum Entropy Methods in Science and Engineering*, edited by A. Mohammad-Djafari, AIP Conf. Proc. No. 568 (AIP, New York, 2001), pp. 557–568.
[26] N. Christensen and R. Meyer, Phys. Rev. D **64**, 022001 (2001).
[27] N. Christensen, R. Meyer, and A. Libson, Class. Quantum Grav. **21**, 317 (2004).
[28] C. Röver, R. Meyer, and N. Christensen, Class. Quantum Grav. **23**, 4895 (2006).
[29] C. Röver, R. Meyer, and N. Christensen, Phys. Rev. D **75**, 062004 (2007).
[30] C. Röver, R. Meyer, G. M. Guidi, A. Viceré, and N. Christensen, Class. Quantum Grav. **24**, S607 (2007).
[31] M. V. van der Sluys, C. Röver, A. Stroeer, N. Christensen, V. Kalogera, R. Meyer, and A. Vecchio, Astrophys. J. Lett. **688**, L61 (2008).
[32] N. Christensen, R. J. Dupuis, G. Woan, and R. Meyer, Phys. Rev. D **70**, 022001 (2004).
[33] R. Umstätter, R. Meyer, R. Dupuis, J. Veitch, G. Woan, and N. Christensen, Class. Quantum Grav. **21**, S1655 (2004).
[34] J. Veitch, R. Umstätter, R. Meyer, N. Christensen, and G. Woan, Class. Quantum Grav. **22**, S995 (2005).
[35] I. S. Heng, Class. Quantum Grav. **26**, 105005 (2009).
[36] Y. Gürsel and M. Tinto, Phys. Rev. D **40**, 3884 (1989).
[37] M. Rakhmanov, Class. Quantum Grav. **23**, S673 (2006).
[38] J. S. Key and N. J. Cornish, Phys. Rev. D **79**, 043014 (2009).
[39] A. C. Searle, P. J. Sutton, and M. Tinto, Class. Quantum Grav. **26**, 155017 (2009).
[40] T. Z. Summerscales, A. Burrows, L. S. Finn, and C. D. Ott, Astrophys. J. **678**, 1142 (2008).
[41] C. D. Ott, A. Burrows, E. Livne, and R. Walder, Astrophys. J. **600**, 834 (2004).
[42] W. G. Anderson, P. R. Brady, J. D. E. Creighton, and E. E. Flanagan, Phys. Rev. D **63**, 042003 (2001).
[43] S. Klimenko and G. Mitselmakher, Class. Quantum Grav. **21**, S1819 (2004).
[44] S. Chatterji, L. Blackburn, G. Martin, and E. Katsavounidis, Class. Quantum Grav. **21**, S1809 (2004).
[45] S. Chatterji, Ph.D. thesis, Massachussetts Institute of Technology, 2005.
[46] A.-C. Clapson, M. Barsuglia, M.-A. Bizouard, V. Brisson, F. Cavalier, M. Davier, P. Hello, N. Leroy, and M. Varvella, Class. Quantum Grav. **25**, 035002 (2008).
[47] J. Sylvestre, Phys. Rev. D **68**, 102005 (2003).
[48] N. Arnaud, M. Barsuglia, M.-A. Bizouard, V. Brisson, F. Cavalier, M. Davier, P. Hello, S. Kreckelbergh, and E. K. Porter, Phys. Rev. D **67**, 102003 (2003).
[49] L. Wen and B. Schutz, Class. Quantum Grav. **22**, S1321 (2005).
[50] S. Mohanty, M. Rakhmanov, S. Klimenko, and G. Mitselmakher, Class. Quantum Grav. **23**, 4799 (2006).
[51] S. Klimenko, I. Yakushin, A. Mercer, and G. Mitselmakher, Class. Quantum Grav. **25**, 114029 (2008).
[52] P. Sutton *et al.*, arXiv:0908.3665.
[53] F. Cavalier *et al.*, Phys. Rev. D **74**, 082004 (2006).
[54] J. Markowitz, M. Zanolin, L. Cadonati, and E. Katsavounidis, Phys. Rev. D **78**, 122003 (2008).
[55] S. Fairhurst, arXiv:0908.2356.
[56] L. Baiotti, I. Hawke, L. Rezzolla, and E. Schnetter, Phys. Rev. Lett. **94**, 131101 (2005).
[57] E. E. Flanagan and S. A. Hughes, Phys. Rev. D **57**, 4566 (1998).
[58] H. Dimmelmeier, J. A. Font, and E. Müller, Astron. Astrophys. **393**, 523 (2002).
[59] H. Dimmelmeier, J. Novak, J. A. Font, J. M. Ibáñez, and E. Müller, Phys. Rev. D **71**, 064023 (2005).
[60] J. A. Isenberg, Int. J. Mod. Phys. D **17**, 265 (2008).
[61] A. Heger, N. Langer, and S. E. Woosley, Astrophys. J. **528**, 368 (2000).
[62] A. Heger, S. E. Woosley, and H. C. Spruit, Astrophys. J. **626**, 350 (2005).
[63] H. Shen, H. Toki, K. Oyamatsu, and K. Sumiyoshi, Prog. Theor. Phys. **100**, 1013 (1998).
[64] H. Shen, H. Toki, K. Oyamatsu, and K. Sumiyoshi, Nucl. Phys. **A637**, 435 (1998).
[65] J. M. Lattimer, C. J. Pethick, D. G. Ravenhall, and D. Q. Lamb, Nucl. Phys. **A432**, 646 (1985).
[66] J. M. Lattimer and F. D. Swesty, Nucl. Phys. **A535**, 331 (1991).

[67] A. Marek, H.-T. Janka, R. Buras, M. Liebendörfer, and M. Rampp, Astron. Astrophys. **443**, 201 (2005).
[68] M. Liebendörfer, Astrophys. J. **633**, 1042 (2005).
[69] www.mpa-garching.mpg.de/rel_hydro/wave_catalog.shtml.
[70] S. E. Woosley and A. Heger, Astrophys. J. **637**, 914 (2006).
[71] G. Strang, *Introduction to Linear Algebra* (Wellesley Cambridge Press, Wellesley, MA, 1993).
[72] L. S. Finn, Phys. Rev. D **46**, 5236 (1992).
[73] C. Röver, R. Meyer, and N. Christensen, arXiv:0804.3853.
[74] G. L. Bretthorst, in *Maximum Entropy and Bayesian Methods*, edited by W. v. d. Linden *et al.* (Kluwer Academic Publishers, Dordrecht, The Netherlands, 1999), pp. 21–46.
[75] A. Gelman, J. B. Carlin, H. Stern, and D. B. Rubin, *Bayesian Data Analysis* (Chapman&Hall/CRC, Boca Raton, FL, 1997).
[76] T. Damour, B. R. Iyer, and B. S. Sathyaprakash, Phys. Rev. D **63**, 044023 (2001).
[77] J. Creighton *et al.*, LAL Software Documentation, 2007, http://www.lsc-group.phys.uwm.edu/daswg/projects/lal.html.
[78] T. Hastie, R. Tibshirani, and J. Friedman, *The Elements of Statistical Learning; Data Mining, Inference, and Prediction* (Springer-Verlag, New York, 2001).
[79] A. Inselberg, Visual Computer **1**, 69 (1985).
[80] K. V. Mardia, J. T. Kent, and J. M. Bibby, *Multivariate Analysis* (Academic Press, London, 1979).
[81] B. Aylott *et al.*, Class. Quantum Grav. **26**, 165008 (2009).
[82] R. Umstätter, N. Christensen, M. Hendry, R. Meyer, V. Simha, J. Veitch, S. Vigeland, and G. Woan, Phys. Rev. D **72**, 022001 (2005).
[83] D. R. Brillinger, *Time Series: Data Analysis and Theory* (McGraw-Hill, New York, 1981).

All-sky search for long-duration gravitational wave transients with initial LIGO

B. P. Abbott,[1] R. Abbott,[1] T. D. Abbott,[2] M. R. Abernathy,[1] F. Acernese,[3,4] K. Ackley,[5] C. Adams,[6] T. Adams,[7] P. Addesso,[8] R. X. Adhikari,[1] V. B. Adya,[9] C. Affeldt,[9] M. Agathos,[10] K. Agatsuma,[10] N. Aggarwal,[11] O. D. Aguiar,[12] A. Ain,[13] P. Ajith,[14] B. Allen,[9,15,16] A. Allocca,[17,18] D. V. Amariutei,[5] S. B. Anderson,[1] W. G. Anderson,[15] K. Arai,[1] M. C. Araya,[1] C. C. Arceneaux,[19] J. S. Areeda,[20] N. Arnaud,[21] K. G. Arun,[22] G. Ashton,[23] M. Ast,[24] S. M. Aston,[6] P. Astone,[25] P. Aufmuth,[16] C. Aulbert,[9] S. Babak,[26] P. T. Baker,[27] F. Baldaccini,[28,29] G. Ballardin,[30] S. W. Ballmer,[31] J. C. Barayoga,[1] S. E. Barclay,[32] B. C. Barish,[1] D. Barker,[33] F. Barone,[3,4] B. Barr,[32] L. Barsotti,[11] M. Barsuglia,[34] D. Barta,[35] J. Bartlett,[33] I. Bartos,[36] R. Bassiri,[37] A. Basti,[17,18] J. C. Batch,[33] C. Baune,[9] V. Bavigadda,[30] M. Bazzan,[38,39] B. Behnke,[26] M. Bejger,[40] C. Belczynski,[41] A. S. Bell,[32] C. J. Bell,[32] B. K. Berger,[1] J. Bergman,[33] G. Bergmann,[9] C. P. L. Berry,[42] D. Bersanetti,[43,44] A. Bertolini,[10] J. Betzwieser,[6] S. Bhagwat,[31] R. Bhandare,[45] I. A. Bilenko,[46] G. Billingsley,[1] J. Birch,[6] R. Birney,[47] S. Biscans,[11] A. Bisht,[9,16] M. Bitossi,[30] C. Biwer,[31] M. A. Bizouard,[21] J. K. Blackburn,[1] C. D. Blair,[48] D. Blair,[48] R. M. Blair,[33] S. Bloemen,[10,49] O. Bock,[9] T. P. Bodiya,[11] M. Boer,[50] G. Bogaert,[50] C. Bogan,[9] A. Bohe,[26] P. Bojtos,[51] C. Bond,[42] F. Bondu,[52] R. Bonnand,[7] R. Bork,[1] V. Boschi,[18,17] S. Bose,[53,13] A. Bozzi,[30] C. Bradaschia,[18] P. R. Brady,[15] V. B. Braginsky,[46] M. Branchesi,[54,55] J. E. Brau,[56] T. Briant,[57] A. Brillet,[50] M. Brinkmann,[9] V. Brisson,[21] P. Brockill,[15] A. F. Brooks,[1] D. A. Brown,[31] D. Brown,[5] D. D. Brown,[42] N. M. Brown,[11] C. C. Buchanan,[2] A. Buikema,[11] T. Bulik,[41] H. J. Bulten,[58,10] A. Buonanno,[26,59] D. Buskulic,[7] C. Buy,[34] R. L. Byer,[37] L. Cadonati,[60] G. Cagnoli,[61] C. Cahillane,[1] J. Calderón Bustillo,[62,60] T. Callister,[1] E. Calloni,[63,4] J. B. Camp,[64] K. C. Cannon,[65] J. Cao,[66] C. D. Capano,[9] E. Capocasa,[34] F. Carbognani,[30] S. Caride,[67] J. Casanueva Diaz,[21] C. Casentini,[68,69] S. Caudill,[15] M. Cavaglià,[19] F. Cavalier,[21] R. Cavalieri,[30] G. Cella,[18] C. Cepeda,[1] L. Cerboni Baiardi,[54,55] G. Cerretani,[17,18] E. Cesarini,[68,69] R. Chakraborty,[1] T. Chalermsongsak,[1] S. J. Chamberlin,[15] M. Chan,[32] S. Chao,[70] P. Charlton,[71] E. Chassande-Mottin,[34] H. Y. Chen,[72] Y. Chen,[73] C. Cheng,[70] A. Chincarini,[44] A. Chiummo,[30] H. S. Cho,[74] M. Cho,[59] J. H. Chow,[75] N. Christensen,[76] Q. Chu,[48] S. Chua,[57] S. Chung,[48] G. Ciani,[5] F. Clara,[33] J. A. Clark,[60] F. Cleva,[50] E. Coccia,[68,77] P.-F. Cohadon,[57] A. Colla,[78,25] C. G. Collette,[79] M. Constancio, Jr.,[12] A. Conte,[78,25] L. Conti,[39] D. Cook,[33] T. R. Corbitt,[2] N. Cornish,[27] A. Corsi,[80] S. Cortese,[30] C. A. Costa,[12] M. W. Coughlin,[76] S. B. Coughlin,[81] J.-P. Coulon,[50] S. T. Countryman,[36] P. Couvares,[1] D. M. Coward,[48] M. J. Cowart,[6] D. C. Coyne,[1] R. Coyne,[80] K. Craig,[32] J. D. E. Creighton,[15] J. Cripe,[2] S. G. Crowder,[82] A. Cumming,[32] L. Cunningham,[32] E. Cuoco,[30] T. Dal Canton,[9] S. L. Danilishin,[32] S. D'Antonio,[69] K. Danzmann,[16,9] N. S. Darman,[83] V. Dattilo,[30] I. Dave,[45] H. P. Daveloza,[84] M. Davier,[21] G. S. Davies,[32] E. J. Daw,[85] R. Day,[30] D. DeBra,[37] G. Debreczeni,[35] J. Degallaix,[61] M. De Laurentis,[63,4] S. Deléglise,[57] W. Del Pozzo,[42] T. Denker,[9,16] T. Dent,[9] H. Dereli,[50] V. Dergachev,[1] R. DeRosa,[6] R. De Rosa,[63,4] R. DeSalvo,[8] S. Dhurandhar,[13] M. C. Díaz,[84] L. Di Fiore,[4] M. Di Giovanni,[78,25] A. Di Lieto,[17,18] I. Di Palma,[26,9] A. Di Virgilio,[18] G. Dojcinoski,[86] V. Dolique,[61] F. Donovan,[11] K. L. Dooley,[19] S. Doravari,[6] R. Douglas,[32] T. P. Downes,[15] M. Drago,[9,87,88] R. W. P. Drever,[1] J. C. Driggers,[33] Z. Du,[66] M. Ducrot,[7] S. E. Dwyer,[33] T. B. Edo,[85] M. C. Edwards,[76] A. Effler,[6] H.-B. Eggenstein,[9] P. Ehrens,[1] J. M. Eichholz,[5] S. S. Eikenberry,[5] W. Engels,[73] R. C. Essick,[11] T. Etzel,[1] M. Evans,[11] T. M. Evans,[6] R. Everett,[89] M. Factourovich,[36] V. Fafone,[68,69,77] H. Fair,[31] S. Fairhurst,[81] X. Fan,[66] Q. Fang,[48] S. Farinon,[44] B. Farr,[72] W. M. Farr,[42] M. Favata,[86] M. Fays,[81] H. Fehrmann,[9] M. M. Fejer,[37] I. Ferrante,[17,18] E. C. Ferreira,[12] F. Ferrini,[30] F. Fidecaro,[17,18] I. Fiori,[30] R. P. Fisher,[31] R. Flaminio,[61] M. Fletcher,[32] J.-D. Fournier,[50] S. Franco,[21] S. Frasca,[78,25] F. Frasconi,[18] Z. Frei,[51] A. Freise,[42] R. Frey,[56] V. Frey,[21] T. T. Fricke,[9] P. Fritschel,[11] V. V. Frolov,[6] P. Fulda,[5] M. Fyffe,[6] H. A. G. Gabbard,[19] J. R. Gair,[90] L. Gammaitoni,[28,29] S. G. Gaonkar,[13] F. Garufi,[63,4] A. Gatto,[34] G. Gaur,[91,92] N. Gehrels,[64] G. Gemme,[44] B. Gendre,[50] E. Genin,[30] A. Gennai,[18] J. George,[45] L. Gergely,[93] V. Germain,[7] A. Ghosh,[14] S. Ghosh,[10,49] J. A. Giaime,[2,6] K. D. Giardina,[6] A. Giazotto,[18] K. Gill,[94] A. Glaefke,[32] E. Goetz,[67] R. Goetz,[5] L. Gondan,[51] G. González,[2] J. M. Gonzalez Castro,[17,18] A. Gopakumar,[95] N. A. Gordon,[32] M. L. Gorodetsky,[46] S. E. Gossan,[1] M. Gosselin,[30] R. Gouaty,[7] C. Graef,[32] P. B. Graff,[64,59] M. Granata,[61] A. Grant,[32] S. Gras,[11] C. Gray,[33] G. Greco,[54,55] A. C. Green,[42] P. Groot,[49] H. Grote,[9] S. Grunewald,[26] G. M. Guidi,[54,55] X. Guo,[66] A. Gupta,[13] M. K. Gupta,[92] K. E. Gushwa,[1] E. K. Gustafson,[1] R. Gustafson,[67] J. J. Hacker,[20] B. R. Hall,[53] E. D. Hall,[1] G. Hammond,[32] M. Haney,[95] M. M. Hanke,[9] J. Hanks,[33] C. Hanna,[89] M. D. Hannam,[81] J. Hanson,[6] T. Hardwick,[2] J. Harms,[54,55] G. M. Harry,[96] I. W. Harry,[26] M. J. Hart,[32] M. T. Hartman,[5] C.-J. Haster,[42] K. Haughian,[32] A. Heidmann,[57] M. C. Heintze,[5,6] H. Heitmann,[50] P. Hello,[21] G. Hemming,[30] M. Hendry,[32] I. S. Heng,[32] J. Hennig,[32] A. W. Heptonstall,[1] M. Heurs,[9,16] S. Hild,[32] D. Hoak,[97] K. A. Hodge,[1] D. Hofman,[61] S. E. Hollitt,[98] K. Holt,[6] D. E. Holz,[72] P. Hopkins,[81] D. J. Hosken,[98] J. Hough,[32] E. A. Houston,[32] E. J. Howell,[48] Y. M. Hu,[32] S. Huang,[70] E. A. Huerta,[99] D. Huet,[21] B. Hughey,[94] S. Husa,[62] S. H. Huttner,[32] T. Huynh-Dinh,[6] A. Idrisy,[89] N. Indik,[9] D. R. Ingram,[33] R. Inta,[80] H. N. Isa,[32] J.-M. Isac,[57] M. Isi,[1] G. Islas,[20] T. Isogai,[11] B. R. Iyer,[14] K. Izumi,[33] T. Jacqmin,[57] H. Jang,[74] K. Jani,[60] P. Jaranowski,[100] S. Jawahar,[101] F. Jiménez-Forteza,[62] W. W. Johnson,[2] D. I. Jones,[23] R. Jones,[32] R. J. G. Jonker,[10] L. Ju,[48] K. Haris,[102] C. V. Kalaghatgi,[22] V. Kalogera,[103] S. Kandhasamy,[19] G. Kang,[74] J. B. Kanner,[1] S. Karki,[56] M. Kasprzack,[2,21,30] E. Katsavounidis,[11] W. Katzman,[6] S. Kaufer,[16] T. Kaur,[48] K. Kawabe,[33] F. Kawazoe,[9] F. Kéfélian,[50] M. S. Kehl,[65]

[99]West Virginia University, Morgantown, West Virginia 26506, USA
[100]University of Białystok, 15-424 Białystok, Poland
[101]SUPA, University of Strathclyde, Glasgow G1 1XQ, United Kingdom
[102]IISER-TVM, CET Campus, Trivandrum Kerala 695016, India
[103]Northwestern University, Evanston, Illinois 60208, USA
[104]Institute of Applied Physics, Nizhny Novgorod, 603950, Russia
[105]Pusan National University, Busan 609-735, Korea
[106]Hanyang University, Seoul 133-791, Korea
[107]NCBJ, 05-400 Świerk-Otwock, Poland
[108]IM-PAN, 00-956 Warsaw, Poland
[109]Rochester Institute of Technology, Rochester, New York 14623, USA
[110]Monash University, Victoria 3800, Australia
[111]Seoul National University, Seoul 151-742, Korea
[112]ESPCI, CNRS, F-75005 Paris, France
[113]Università di Camerino, Dipartimento di Fisica, I-62032 Camerino, Italy
[114]Southern University and A&M College, Baton Rouge, Louisiana 70813, USA
[115]College of William and Mary, Williamsburg, Virginia 23187, USA
[116]Instituto de Física Teórica, University Estadual Paulista/ICTP South American Institute for Fundamental Research, São Paulo, São Paulo 01140-070, Brazil
[117]IISER-Kolkata, Mohanpur, West Bengal 741252, India
[118]Rutherford Appleton Laboratory, HSIC, Chilton, Didcot, Oxon OX11 0QX, United Kingdom
[119]Whitman College, 280 Boyer Ave, Walla Walla, Washington 9936, USA
[120]National Institute for Mathematical Sciences, Daejeon 305-390, Korea
[121]Hobart and William Smith Colleges, Geneva, New York 14456, USA
[122]Institute of Astronomy, 65-265 Zielona Góra, Poland
[123]Andrews University, Berrien Springs, Michigan 49104, USA
[124]Università di Siena, I-53100 Siena, Italy
[125]Trinity University, San Antonio, Texas 78212, USA
[126]University of Washington, Seattle, Washington 98195, USA
[127]Abilene Christian University, Abilene, Texas 79699, USA

(Received 30 November 2015; published 12 February 2016)

We present the results of a search for long-duration gravitational wave transients in two sets of data collected by the LIGO Hanford and LIGO Livingston detectors between November 5, 2005 and September 30, 2007, and July 7, 2009 and October 20, 2010, with a total observational time of 283.0 days and 132.9 days, respectively. The search targets gravitational wave transients of duration 10–500 s in a frequency band of 40–1000 Hz, with minimal assumptions about the signal waveform, polarization, source direction, or time of occurrence. All candidate triggers were consistent with the expected background; as a result we set 90% confidence upper limits on the rate of long-duration gravitational wave transients for different types of gravitational wave signals. For signals from black hole accretion disk instabilities, we set upper limits on the source rate density between 3.4×10^{-5} and 9.4×10^{-4} $\mathrm{Mpc}^{-3}\,\mathrm{yr}^{-1}$ at 90% confidence. These are the first results from an all-sky search for unmodeled long-duration transient gravitational waves.

DOI: 10.1103/PhysRevD.93.042005

I. INTRODUCTION

The goal of the Laser Interferometer Gravitational-Wave Observatory (LIGO) [1] and the Virgo detectors [2] is to directly detect and study gravitational waves (GWs). The direct detection of GWs holds the promise of testing general relativity in the strong-field regime, of providing a new probe of objects such as black holes and neutron stars, and of uncovering unanticipated new astrophysics.

LIGO and Virgo have jointly acquired data that have been used to search for many types of GW signals: unmodeled bursts of short duration (<1 s) [3–7], well-modeled chirps emitted by binary systems of compact objects [8–12], continuous signals emitted by asymmetric neutron stars [13–20], as well as a stochastic background of GWs [21–24]. For a complete review, see Ref. [25]. While no GW sources have been observed by the first-generation network of detectors, first detections are expected with the next generation of ground-based detectors: advanced LIGO [26], advanced Virgo [27], and the cryogenic detector KAGRA [28]. It is expected that the advanced detectors,

*Deceased.
†publication@ligo.org; publication@ego-gw.it

operating at design sensitivity, will be capable of detecting approximately 40 neutron star binary coalescences per year, although significant uncertainties exist [29].

Previous searches for unmodeled bursts of GWs [3–5] targeted source objects such as core-collapse supernovae [30], neutron-star-to-black-hole collapse [31], cosmic string cusps [32], binary black hole mergers [33–35], star-quakes in magnetars [36], pulsar glitches [37], and signals associated with gamma-ray bursts (GRBs) [38]. These burst searches typically look for signals of duration 1 s or shorter.

At the other end of the spectrum, searches for persistent, unmodeled (stochastic) GW backgrounds have also been conducted, including isotropic [21], anisotropic and point-source backgrounds [22]. This leaves the parameter space of unmodeled transient GWs not fully explored; indeed, multiple proposed astrophysical scenarios predict long-duration GW transients lasting from a few seconds to hundreds of seconds, or even longer, as described in Sec. II. The first search for unmodeled long-duration GW transients was conducted using LIGO data from the S5 science run, in association with long GRBs [39]. In this paper, we apply a similar technique [40] in order to search for long-lasting transient GW signals over all sky directions and for all times. We utilize LIGO data from the LIGO Hanford and Livingston detectors from the S5 and S6 science runs, lasting from November 5, 2005 to September 30, 2007 and from July 7, 2009 to October 20, 2010, respectively.

The organization of the paper is as follows: In Sec. II, we summarize different types of long-duration transient signals which may be observable by LIGO and Virgo. In Sec. III, we describe the selection of the LIGO S5 and S6 science run data that have been used for this study. We discuss the search algorithm, background estimation, and data quality methods in Sec. IV. In Sec. V, we evaluate the sensitivity of the search to simulated GW waveforms. The results of the search are presented in Sec. VI. We conclude with possible improvements for a long-transient GW search using data from the advanced LIGO and Virgo detectors in Sec. VII.

II. ASTROPHYSICAL SOURCES OF LONG GW TRANSIENTS

Some of the most compelling astrophysical sources of long GW transients are associated with extremely complex dynamics and hydrodynamic instabilities following the collapse of a massive star's core in the context of core-collapse supernovae and long GRBs [30,40,41]. Soon after core collapse and the formation of a protoneutron star, convective and other fluid instabilities (including standing accretion shock instability [42]) may develop behind the supernova shock wave as it transitions into an accretion shock. In progenitor stars with rapidly rotating cores, long-lasting, nonaxisymmetric rotational instabilities can be triggered by corotation modes [43–46]. Long-duration GW signals are expected from these violently aspherical dynamics, following within tens of milliseconds of the short-duration GW burst signal from core bounce and protoneutron star formation. Given the turbulent and chaotic nature of postbounce fluid dynamics, one expects a stochastic GW signal that could last from a fraction of a second to multiple seconds, and possibly even longer [30,40,47–50].

After the launch of an at least initially successful explosion, fallback accretion onto the newborn neutron star may spin it up, leading to nonaxisymmetric deformation and a characteristic upward chirp signal (700 Hz–few kHz) as the spin frequency of the neutron star increases over tens to hundreds of seconds [51,52]. GW emission may eventually terminate when the neutron star collapses to a black hole. The collapse process and formation of the black hole itself will also produce a short-duration GW burst [53,54].

In the collapsar model for long GRBs [55], a stellar-mass black hole forms, surrounded by a massive, self-gravitating accretion disk. This disk may be susceptible to various nonaxisymmetric hydrodynamic and magnetohydrodynamic instabilities which may lead to fragmentation and inspiral of fragments into the central black hole (e.g., Refs. [56,57]). In an extreme scenario of such accretion disk instabilities (ADIs), magnetically "suspended accretion" is thought to extract spin energy from the black hole and dissipate it via GW emission from nonaxisymmetric disk modes and fragments [58,59]. The associated GW signal is potentially long lasting (10–100 s) and predicted to exhibit a characteristic downward chirp.

Finally, in magnetar models for long and short GRBs (e.g., Refs. [60,61]), a long-lasting post-GRB GW transient may be emitted by a magnetar undergoing rotational or magnetic nonaxisymmetric deformation (e.g., Refs. [62,63]).

III. DATA SELECTION

During the fifth LIGO science run (S5, November 5, 2005 to September 30, 2007), the 4 km and 2 km detectors at Hanford, Washington (H1 and H2), and the 4 km detector at Livingston, Louisiana (L1), recorded data for nearly two years. They were joined on May 18, 2007 by the Virgo detector (V1) in Pisa, Italy, which was beginning its first science run. After a two-year period of upgrades to the detectors and the decommissioning of H2, the sixth LIGO and second and third Virgo scientific runs were organized jointly from July 7, 2009 to October 10, 2010.

Among the four detectors, H1 and L1 achieved the best strain sensitivity, reaching $\approx 2 \times 10^{-23}/\sqrt{\text{Hz}}$ around 150 Hz in 2010 [64,65]. Because of its reduced arm length, H2 sensitivity was at least a factor of 2 lower than H1 on average. V1 sensitivity varied over time, but was always lower than the sensitivity of H1 and L1 by a factor between

1.5 and 5 at frequencies higher than 60 Hz. Moreover, the H1-L1 pair live time was at least a factor 2 longer than the live time of the H1-V1 and L1-V1 pairs added together. Using Virgo data, however, could help with sky localization of source candidates; unfortunately, the sky localization was not implemented at the time of this search. Consequently, including Virgo data in this analysis would have increased the overall search sensitivity by only a few percent or less at the cost of analyzing two additional pairs of detectors. As a result, we have analyzed only S5 and S6 data from the H1-L1 pair for this search.

In terms of frequency content, we restrict the analysis to the 40–1000 Hz band. The lower limit is constrained by seismic noise, which steeply increases at lower frequencies in LIGO data. The upper limit is set to include the most likely regions of frequency space for long-transient GWs, while keeping the computational requirements of the search at an acceptable level. We note that the frequency range of our analysis includes the most sensitive band of the LIGO detectors, namely 100–200 Hz.

Occasionally, the detectors are affected by instrumental problems (data acquisition failures, misalignment of optical cavities, etc.) or environmental conditions (bad weather, seismic motion, etc.) that decrease their sensitivity and increase the rate of data artifacts, or glitches. Most of these periods have been identified and can be discarded from the analysis using data quality flags [66–69]. These are classified by each search into different categories depending on how the GW search is affected.

Category 1 data quality flags are used to define periods when the data should not be searched for GW signals because of serious problems, like invalid calibration. To search for GW signals, the interferometers should be locked and there should be no evidence of environmental noise transients corrupting the measured signal. For this search, we have used the category 1 data quality flags used by searches for an isotropic stochastic background of GWs [21,23]. This list of flags is almost identical to what has been used by the unmodeled all-sky searches for short-duration GW transients [3,4]. We also discard times when simulated signals are injected into the detectors through the application of a differential force onto the mirrors.

Category 2 data quality flags are used to discard triggers which pass all selection cuts in a search, but are clearly associated with a detector malfunction or an environmental condition [68]. In Sec. IV C, we explain which category 2 flags have been selected and how we use them in this search.

Overall, we discard 5.8% and 2.2% of H1-L1 coincident data with our choices of category 1 data quality flags for S5 and S6, respectively. The remaining coincident strain time series are divided into 500 s intervals with 50% overlap. Intervals smaller than 500 s are not considered. For the H1-L1 pair, this results in a total observation time of 283.0 days during S5 and 132.9 days for S6.

IV. LONG TRANSIENT GW SEARCH PIPELINE

A. Search algorithm

The search algorithm we employ is based on the cross-correlation of data from two GW detectors, as described in Ref. [40]. This algorithm builds a frequency-time map (ft-map) of the cross power computed from the strain time series of two spatially separated detectors. A pattern recognition algorithm is then used to identify clusters of above-threshold pixels in the map, thereby defining candidate triggers. A similar algorithm has been used to search for long-lasting GW signals in coincidence with long GRBs in LIGO data [39]. Here we extend the method to carry out an untriggered (all-sky, all-time) search, considerably increasing the parameter space covered by previous searches.

Following Ref. [40], each 500 s interval of coincident data is divided into 50% overlapping, Hann-windowed, 1 s long segments. Strain data from each detector in the given 1 s segment are then Fourier transformed, allowing formation of ft-maps with a pixel size of 1 s × 1 Hz. An estimator for GW power can be formed [40]:

$$\hat{Y}(t;f;\hat{\Omega}) = \frac{2}{\mathcal{N}}\mathrm{Re}[Q_{IJ}(t;f;\hat{\Omega})\tilde{s}_I^{\star}(t;f)\tilde{s}_J(t;f)]. \quad (1)$$

Here t is the start time of the pixel, f is the frequency of the pixel, $\hat{\Omega}$ is the sky direction, $\mathcal{N}$ is a window normalization factor, and $\tilde{s}_I$ and $\tilde{s}_J$ are the discrete Fourier transforms of the strain data from GW detectors I and J. We use the LIGO H1 and L1 detectors as the I and J detectors, respectively. The optimal filter Q_{IJ} takes into account the phase delay due to the spatial separation of the two detectors, $\Delta\vec{x}_{IJ}$, and the direction-dependent efficiency of the detector pair, $\epsilon_{IJ}(t;\hat{\Omega})$:

$$Q_{IJ}(t;f;\hat{\Omega}) = \frac{e^{2\pi i f \Delta\vec{x}_{IJ}\cdot\hat{\Omega}/c}}{\epsilon_{IJ}(t;\hat{\Omega})}. \quad (2)$$

The pair efficiency is defined by

$$\epsilon_{IJ}(t;\hat{\Omega}) = \frac{1}{2}\sum_A F_I^A(t;\hat{\Omega})F_J^A(t;\hat{\Omega}), \quad (3)$$

where $F_I^A(t;\hat{\Omega})$ is the antenna factor for detector I and A is the polarization state of the incoming GW [40]. An estimator for the variance of the $\hat{Y}(t;f,\hat{\Omega})$ statistic is then given by

$$\hat{\sigma}_Y^2(t;f;\hat{\Omega}) = \frac{1}{2}|Q_{IJ}(t;f;\hat{\Omega})|^2 P_I^{\mathrm{adj}}(t;f)P_J^{\mathrm{adj}}(t;f), \quad (4)$$

where $P_I^{\mathrm{adj}}(t;f)$ is the average one-sided power spectrum for detector I, calculated by using the data in eight nonoverlapping segments on each side of time segment t [40]. We can then define the cross-correlation signal-to-noise ratio (SNR) in a single pixel, ρ:

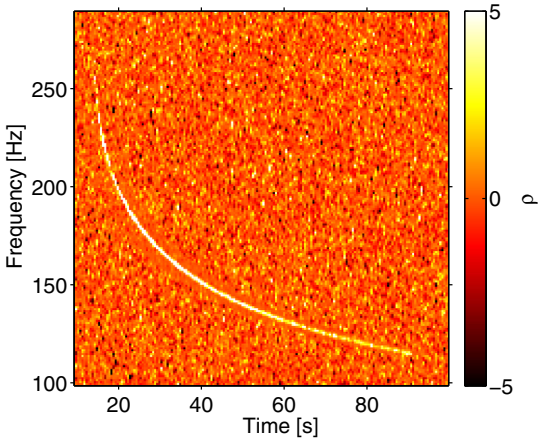

FIG. 1. ft-map of ρ (cross-correlation signal-to-noise ratio) using simulated Gaussian data. A simulated GW signal from an accretion disk instability [58,59] (model waveform ADI-E, see Table I) with known sky position is added to the data stream and is visible as a bright, narrow-band track. Blurring around the track is due to the usage of adjacent time segments in estimating $\hat{\sigma}_Y$; the estimate of $\hat{\sigma}_Y$ in these bins is affected by the presence of the GW signal.

$$\rho(t;f;\hat{\Omega}) = \hat{Y}(t;f;\hat{\Omega})/\hat{\sigma}_Y(t;f;\hat{\Omega}). \tag{5}$$

Because this is proportional to strain squared, it is an energy SNR, rather than an amplitude SNR.

This statistic is designed such that true GW signals should induce positive definite ρ when the correct filter is used (i.e., the sky direction $\hat{\Omega}$ is known). Consequently, using a wrong sky direction in the filter results in reduced or even negative ρ for real signals. Figure 1 shows an example ft-map of ρ containing a simulated GW signal with a known sky position.

Next, a seed-based clustering algorithm [70] is applied to the ρ ft-map to identify significant clusters of pixels. In particular, the clustering algorithm applies a threshold of $|\rho| \geq 1$ to identify seed pixels, and then groups these seed pixels that are located within a fixed distance (two pixels) of each other into a cluster. These parameters were determined through empirical testing with simulated long-transient GW signals similar to those used in this search (discussed further in Sec. V A). The resulting clusters (denoted Γ) are ranked using a weighted sum of the individual pixel values of $\hat{Y}$ and $\hat{\sigma}_Y$:

$$\mathrm{SNR}_\Gamma(\hat{\Omega}) = \frac{\sum_{t;f\in\Gamma} \hat{Y}(t;f;\hat{\Omega})\hat{\sigma}_Y^{-2}(t;f;\hat{\Omega})}{\left(\sum_{t;f\in\Gamma}\hat{\sigma}_Y^{-2}(t;f;\hat{\Omega})\right)^{1/2}}. \tag{6}$$

$\mathrm{SNR}_\Gamma(\hat{\Omega})$ represents the signal-to-noise ratio of the cluster Γ.

In principle, this pattern recognition algorithm could be applied for every sky direction $\hat{\Omega}$, since each sky direction is associated with a different filter $Q_{IJ}(t;f;\hat{\Omega})$. However, this procedure is prohibitively expensive from a computational standpoint. We have therefore modified the seed-based clustering algorithm to cluster both pixels with positive ρ and those with negative ρ (arising when an incorrect sky direction is used in the filter). Since the sky direction is not known in an all-sky search, this modification allows for the recovery of some of the power that would normally be lost due to a suboptimal choice of sky direction in the filter.

The algorithm is applied to each ft-map a certain number of times, each iteration corresponding to a different sky direction. The sky directions are chosen randomly, but are fixed for each stretch of uninterrupted science data. Different methods for choosing the sky directions were studied, including using only sky directions where the detector network had high sensitivity and choosing the set of sky directions to span the set of possible signal time delays. The results indicated that sky-direction choice did not have a significant impact on the sensitivity of the search.

We also studied the effect that the number of sky directions used had on the search sensitivity. We found that the search sensitivity increased approximately logarithmically with the number of sky directions, while the computational time increased linearly with the number of sky directions. The results of our empirical studies indicated that using five sky directions gave the optimal balance between computational time and search sensitivity.

This clustering strategy results in a loss of sensitivity of $\approx$10%–20% for the waveforms considered in this search as compared to a strategy using hundreds of sky directions and clustering only positive pixels. However, this strategy increases the computational speed of the search by a factor of 100 and is necessary to make the search computationally feasible.

We also apply two data-cleaning techniques concurrently with the data processing. First, we remove frequency bins that are known to be contaminated by instrumental and environmental effects. This includes the violin resonance modes of the suspensions, power line harmonics, and sinusoidal signals injected for calibration purposes. In total, we removed 47 1 Hz–wide frequency bins from the S5 data, and 64 1 Hz–wide frequency bins from the S6 data. Second, we require the waveforms observed by the two detectors to be consistent with each other, so as to suppress instrumental artifacts (glitches) that affect only one of the detectors. This is achieved by the use of a consistency-check algorithm [71] which compares the power spectra from each detector, taking into account the antenna factors.

B. Background estimation

An important aspect of any GW search is understanding the background of accidental triggers due to detector noise; this is crucial for preventing false identification of noise triggers as GW candidates. To estimate the false alarm rate (FAR), i.e. the rate of accidental triggers due to detector

noise, we introduce a nonphysical time shift between the H1 and L1 strain data before computing ρ. Analysis of the time-shifted data proceeds identically to that of unshifted data (see Sec. IV A for more details). With this technique, and assuming the number of hypothetical GW signals is small, the data should not contain a correlated GW signal, so any triggers will be generated by the detector noise. We repeat this process for multiple time shifts in order to gain a more accurate estimate of the FAR from detector noise.

As described in Sec. III, each analysis segment is divided into 500 s–long intervals which overlap by 50% and span the entire data set. For a given time shift i, the H1 data from interval n are correlated with L1 data from the interval $n + i$. Since the time gap between two consecutive intervals may be nonzero, the actual time shift applied in this process is at least $500 \times i$ seconds. The time shift is also circular: if for a time shift i, $n + i > N$ (where N is the number of overlapping intervals required to span the data set), then H1 data from the interval n are correlated with L1 data from the interval $n + i - N$. It is important to note that the minimum time-shift duration is much longer than the light travel time between the two detectors and also longer than the signal models we consider (see Sec. V for more information) in order to prevent accidental correlations.

Using this method, 100 time shifts have been processed to estimate the background during S5, amounting to a total analyzed live time of 84.1 years. We have also studied 100 time shifts of S6 data, with a total analyzed live time of 38.7 years. The cumulative rates of background triggers for the S5 and S6 data sets can be seen in Figs. 2 and 3, respectively.

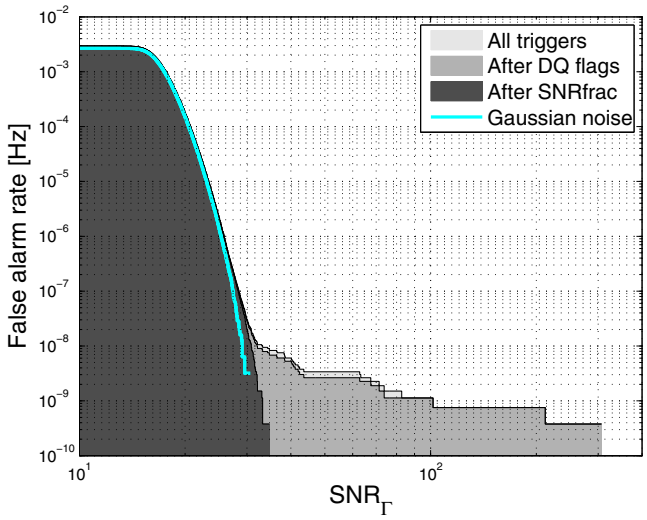

FIG. 2. The false alarm rate is shown as a function of the trigger SNR_Γ, for 100 time shifts of data from the S5 science run. Distributions are shown before and after applying the postprocessing cuts. Here, SNRfrac refers to a postprocessing cut based on how a trigger's power is distributed in time (described further in Sec. IV C). Also shown is the FAR distribution generated by a Monte Carlo simulation assuming Gaussian detector noise. Recall that this is an energy SNR, rather than an amplitude SNR.

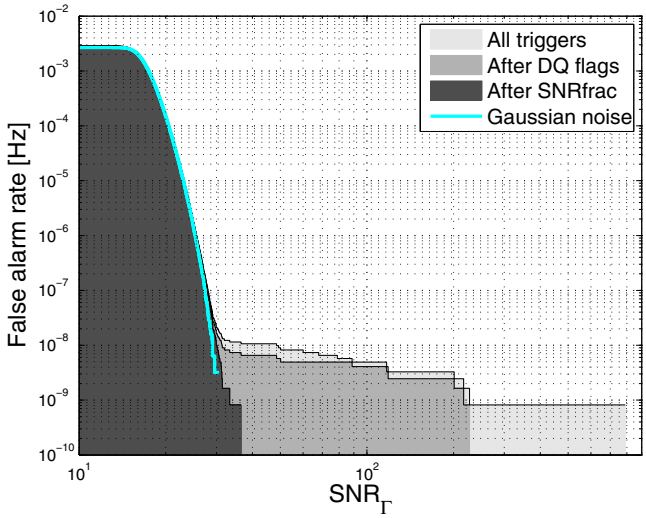

FIG. 3. The false alarm rate is shown as a function of the trigger signal-to-noise ratio, SNR_Γ, for 100 time shifts of data from the S6 science run. See caption of Fig. 2 for all details.

C. Rejection of loud noise triggers

As shown in Figs. 2 and 3, the background FAR distribution has a long tail extending to $\mathrm{SNR}_\Gamma > 100$; this implies that detector noise alone can generate triggers containing significant power. Many of these triggers are caused by short bursts of nonstationary noise (glitches) in H1 and/or L1, which randomly coincide during the time-shifting procedure. It is important to suppress these types of triggers so as to improve the significance of true GW signals in the unshifted data.

These glitches are typically much less than 1 s in duration, and as a result, nearly all of their power is concentrated in a single 1 s segment. To suppress these glitches, we have defined a discriminant variable, SNRfrac, that measures the fraction of SNR_Γ located in a single time segment. The same SNRfrac threshold of 0.45 was found to be optimal for all simulated GW waveforms using both S5 and S6 data. This threshold was determined by maximizing the search sensitivity for a set of simulated GW signals (see Sec. V); we note that this was done before examining the unshifted data, using only time-shifted triggers and simulated GW signals. The detection efficiency is minimally affected (less than 1%) by this SNRfrac threshold choice.

We also utilize LIGO data quality flags to veto triggers generated by a clearly identified source of noise. We have considered all category 2 data quality flags used in unmodeled or modeled transient GW searches [68]. These flags were defined using a variety of environmental monitors (microphones, seismometers, magnetometers, etc.) and interferometer control signals to identify stretches of data which may be compromised due to local environmental effects or instrumental malfunction. Since many of these data quality flags are not useful for rejecting noise triggers in this analysis, we select a set of effective data

quality flags by estimating the statistical significance of the coincidence between these data quality flags and the 100 loudest triggers from the time-shifted background study (no SNRfrac selection applied). The significance is defined by comparing the number of coincident triggers with the accidental coincidence mean and standard deviation. Given the small number of triggers we are considering (100), and in order to avoid accidental coincidence, we have applied a stringent selection: only those data quality flags which have a statistical significance higher than 12 standard deviations (as defined above) and an efficiency-over-dead-time ratio larger than 8 have been selected. Here, efficiency refers to the fraction of noise triggers flagged, while dead time is the amount of science data excluded by the flag.

For both the S5 and S6 data sets, this procedure selected data quality flags which relate to malfunctions of the longitudinal control of the Fabry-Perot cavities and those which indicate an increase in seismic noise. The total dead time which results from applying these data quality (DQ) flags amounts to ≈12 hours in H1 and L1 (0.18%) for S5, and ≈4 hours in H1 (0.13%) and ≈7 hours in L1 (0.22%) for S6.

As shown in Figs. 2 and 3, these two data quality cuts (SNRfrac and DQ flags) are useful for suppressing the high-SNR_Γ tail of the FAR distribution. More precisely, the SNRfrac cut is very effective for cleaning up coincident glitches with high SNR_Γ, while the DQ flags are capable of removing less extreme triggers occurring due to the presence of a well-identified noise source. We have thus decided to look at the unshifted (zero-lag) triggers after the SNRfrac cut is applied and to reserve the DQ flags for the exclusion of potential GW candidates that are actually due to a well-understood instrumental problem.

After the application of the SNRfrac cut, the resulting FAR distribution can be compared with that of a Monte Carlo simulation using a Gaussian noise distribution (assuming an initial LIGO noise sensitivity curve). A discrepancy of ≈10% in the total number of triggers and a slight excess of loud triggers are observed for both the S5 and S6 data sets when compared to Gaussian noise.

V. SEARCH SENSITIVITY

A. GW signal models

To assess the sensitivity of our search to realistic GW signals, we use 15 types of simulated GW signals. Four of these waveforms are based on an astrophysical model of a black hole accretion disk instability [58,59]. The other 11 waveforms are not based on a model of an astrophysical GW source, but are chosen to encapsulate various characteristics that long-transient GW signals may possess, including duration, frequency content, bandwidth, and rate of change of frequency. These *ad hoc* waveforms can be divided into three families: sinusoids with a time-dependent frequency content, sine-Gaussians, and band-limited white noise bursts. All waveforms have 1 s–long Hann-like tapers applied to the beginning and end of the waveforms in order to prevent data artifacts which may occur when the simulated signals have high intensity. In this section, we give a brief description of each type of GW signal model.

1. Accretion disk instabilities

In this study, we include four variations on the ADI model (see Sec. II for more details). Although this set of waveforms does not span the entire parameter space of the ADI model, it does encapsulate most of the possible variations in the signal morphology in terms of signal durations, frequency ranges and derivatives, and amplitudes (see Table I for a summary of the waveforms). While these waveforms may not be precise representations of realistic signals, they capture the salient features of many proposed models and produce long-lived spectrogram tracks.

2. Sinusoids

The sinusoidal waveforms are characterized by a sine function with a time-dependent frequency content. The waveforms are described by

$$h_+(t) = \frac{1+\cos^2\iota}{2}\cos 2\psi \cos\phi(t) - \cos\iota \sin 2\psi \sin\phi(t), \tag{7}$$

$$h_\times(t) = \frac{1+\cos^2\iota}{2}\sin 2\psi \cos\phi(t) + \cos\iota \cos 2\psi \sin\phi(t), \tag{8}$$

where ι is the inclination angle of the source, ψ is the source polarization, and $\phi(t)$ is a phase time series, given by

$$\phi(t) = 2\pi\left(f_0 t + \frac{1}{2}\left(\frac{df}{dt}\right)t^2 + \frac{1}{6}\left(\frac{d^2f}{dt^2}\right)t^3\right). \tag{9}$$

Two of the waveforms are completely monochromatic, two have a linear frequency dependence on time, and two

TABLE I. List of ADI waveforms [58,59] used to test the sensitivity of the search. Here, M is the mass of the central black hole, a^* is the dimensionless Kerr spin parameter of the black hole, and ϵ is the fraction of the disk mass that forms clumps. Frequency refers to the ending and starting frequencies of the GW signal, in that order. All waveforms have an accretion disk mass of 1.5 $M_\odot$.

Waveform	$M[M_\odot]$	a^*	ϵ	Duration [s]	Frequency [Hz]
ADI-A	5	0.30	0.050	39	135–166
ADI-B	10	0.95	0.200	9	110–209
ADI-C	10	0.95	0.040	236	130–251
ADI-E	8	0.99	0.065	76	111–234

TABLE II. List of sinusoidal waveforms used to test the sensitivity of the search. Here, f_0 is the initial frequency of the signal, df/dt is the frequency derivative, and d^2f/dt^2 is the second derivative of the frequency.

Waveform	Duration [s]	f_0 [Hz]	$\frac{df}{dt}$ [Hz/s]	$\frac{d^2f}{dt^2}$ [Hz/s^2]
MONO-A	150	90	0.0	0.00
MONO-B	250	505	0.0	0.00
LINE-A	250	50	0.6	0.00
LINE-B	100	900	−2.0	0.00
QUAD-A	30	50	0.0	0.33
QUAD-B	70	500	0.0	0.04

have a quadratic frequency dependence on time. This family of waveforms is summarized in Table II.

3. Sine-Gaussians

The sine-Gaussian waveforms are essentially monochromatic signals (see Eqs. (7) and (8)) multiplied by a Gaussian envelope:

$$e^{-t^2/\tau^2}. \tag{10}$$

Here, τ is the decay time, which defines the width of the Gaussian envelope. This set of waveforms is summarized in Table III.

4. Band-limited white noise bursts

We have generated white noise and used a sixth-order Butterworth band-pass filter to restrict the noise to the desired frequency band. Each polarization component of the simulated waveforms is generated independently; thus, the two components are uncorrelated. This family of waveforms is summarized in Table IV.

B. Sensitivity study

Using the waveforms described in the previous section, we performed a sensitivity study to determine the overall detection efficiency of the search as a function of waveform amplitude. First, for each of the 15 models, we generated 1500 injection times randomly between the beginning and the end of each of the two data sets, such that the injected waveform was fully included in a group of at least one 500 second–long analysis window. A minimal time lapse of 1000 s between two injections was enforced. For each of the 1500 injection times, we generated a simulated signal with random sky position, source inclination, and waveform polarization angle. The time-shifted data plus simulated signal was then analyzed using the search algorithm described in Sec. IV. The simulated signal was considered recovered if the search algorithm found a trigger fulfilling the following requirements:

(1) The trigger was found between the known start and end times of the simulated signal.
(2) The trigger was found within the known frequency band of the signal.
(3) The SNR_Γ of the trigger exceeded a threshold determined by the loudest trigger found in each data set (using the unshifted data).

This was repeated with 16 different signal amplitudes (logarithmically spaced) for each waveform and injection time in order to fully characterize the search's detection efficiency as a function of signal strength.

In Fig. 4, we show the efficiency, or ratio of recovered signals to the total number of simulations, as a function of either the distance to the source or the root-sum-squared strain amplitude (h_{rss}) arriving at the Earth, defined as

$$h_{\mathrm{rss}} = \sqrt{\int (|h_+(t)|^2 + |h_\times(t)|^2)dt}. \tag{11}$$

Among each family of waveforms, the pipeline efficiency has a frequency dependence that follows the data strain sensitivity of the detectors. The duration of the signal also plays a role, but to a lesser extent. We also note that the search efficiency for monochromatic waveforms (MONO and SG) is significantly worse than for the other waveforms. This is due to the usage of adjacent time segments to compute $\hat{\sigma}_Y$ (see Eq. (4)), which is affected by the presence of the GW signal.

TABLE III. List of sine-Gaussian waveforms used to test the sensitivity of the search. Here, τ is the decay time of the Gaussian envelope.

Waveform	Duration [s]	f_0 [Hz]	τ [s]
SG-A	150	90	30
SG-B	250	505	50

TABLE IV. List of band-limited white noise burst waveforms used to test the sensitivity of the search.

Waveform	Duration [s]	Frequency band [Hz]
WNB-A	20	50–400
WNB-B	60	300–350
WNB-C	100	700–750

VI. RESULTS

Having studied the background triggers and optimized the SNRfrac threshold using both background and simulated signals, the final step in the analysis is to apply the search algorithm to the unshifted (zero-lag) data (i.e. zero time shift between the H1 and L1 strain time series) in order to search for GW candidates. The resulting distributions of SNR_Γ for the zero-lag S5 and S6 data sets are compared to the corresponding background trigger distributions in Fig. 5. A slight deficit of triggers is present in the S6 zero

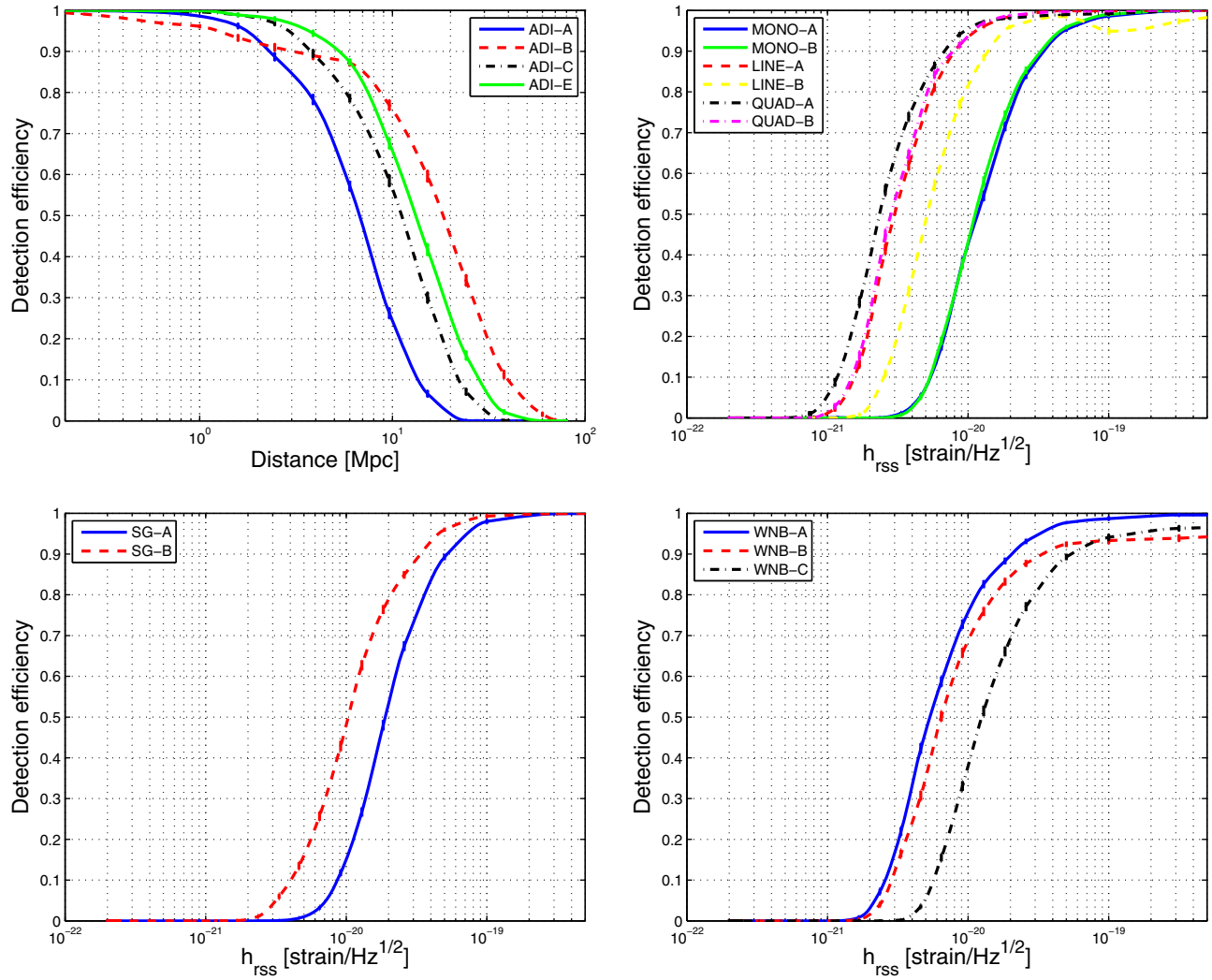

FIG. 4. Efficiency of the search pipeline at recovering different waveforms as a function of the distance to the source (for ADI waveforms) or the signal strength $h_{\rm rss}$ (all others). All results shown here used data from the S6 science run. The SNRfrac threshold is set at 0.45, and the recovery threshold is set at $\mathrm{SNR}_\Gamma = 27.13$. The error bars are computed using binomial statistics. Top left: ADI waveforms. Top right: sinusoidal waveforms. Bottom left: sine-Gaussian waveforms. Bottom right: white noise burst waveforms.

lag, but it remains within one standard deviation of what is expected from the background.

A. Loudest triggers

Here, we consider the most significant triggers from the S5 and S6 zero-lag analyses. We check the FAR of each trigger, which is the number of background triggers with SNR_Γ larger than a given threshold $\mathrm{SNR}^\star_\Gamma$ divided by the total background live time, $T_{\rm bkg}$. We also consider the false alarm probability (FAP), or the probability of observing at least N background triggers with SNR_Γ higher than $\mathrm{SNR}^\star_\Gamma$:

$$\mathrm{FAP}(N) = 1 - \sum_{n=0}^{n=N-1} \frac{\mu_{\rm bkg}^n}{n!} \times e^{-\mu_{\rm bkg}}, \qquad (12)$$

where $\mu_{\rm bkg}$ is the number of background triggers expected from a Poisson process (given by $\mu_{\rm bkg} = T_{\rm obs} \times \mathrm{FAR}(\mathrm{SNR}^\star_\Gamma)$, where $T_{\rm obs}$ is the observation time). For the loudest triggers in each data set, we take $N = 1$ to estimate the FAP.

The most significant triggers from the S5 and S6 zero-lag analyses occurred with false alarm probabilities of 54% and 92%, respectively. They have respective false alarm rates of 1.00 yr^{-1} and 6.94 yr^{-1}. This shows that triggers of this significance are frequently generated by detector noise alone, and thus, these triggers cannot be considered GW candidates.

Additional follow-up indicated that no category 2 data quality flags in H1 nor L1 were active at the time of these triggers. The examination of the ft-maps, the whitened time series around the time of the triggers, and the monitoring records indicate that these triggers were due to a small excess of noise in H1 and/or L1, and are not associated with a well-identified source of noise.

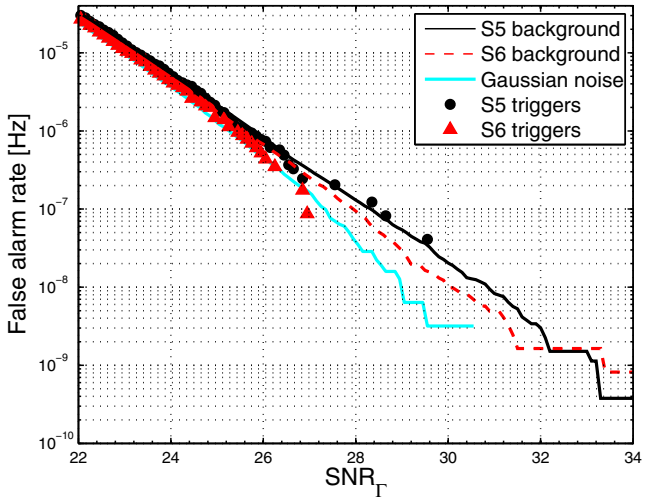

FIG. 5. FAR distribution of unshifted triggers from S5 (black circles) and S6 (red triangles) as a function of the trigger signal-to-noise ratio, SNR_Γ. The distributions are compared to the estimated background distributions for the S5 (solid black) and S6 (dashed red) data sets. We observe a slight deficit of triggers in S6 that remains within one standard deviation of what is expected from the time-shifted triggers. Also shown is the FAR distribution generated by a Monte Carlo simulation assuming Gaussian detector noise (solid cyan).

More information about these triggers is provided in Table V.

B. Rate upper limits

Since no GW candidates were identified, we proceed to place upper limits on the rate of long-duration GW transients assuming an isotropic and uniform distribution of sources. We use two implementations of the loudest event statistic [72] to set upper limits at 90% confidence. The first method uses the false alarm density (FAD) formalism [6,10], which accounts for both the background detector noise and the sensitivity of the search to simulated GW signals. For each simulated signal model, one calculates the efficiency of the search as a function of source distance at a given threshold on SNR_Γ, then integrates the efficiency over volume to gain a measure of the volume of space which is accessible to the search (referred to as the visible volume). The threshold is given by the SNR_Γ of the "loudest event," or in this case, the trigger with the lowest FAD. The 90% confidence upper limits are calculated (following Ref. [72]) as

$$R_{90\%,\mathrm{VT}} = \frac{2.3}{\sum_k V_{\mathrm{vis},k}(\mathrm{FAD}^\star) \times T_{\mathrm{obs},k}}. \quad (13)$$

Here, the index k runs over data sets, $V_{\mathrm{vis},k}(\mathrm{FAD}^\star)$ is the visible volume of search k calculated at the FAD of the loudest zero-lag trigger ($\mathrm{FAD}^\star$), and $T_{\mathrm{obs},k}$ is the observation time, or zero-lag live time of search k. The factor of 2.3 in the numerator is the mean rate (for zero observed triggers) which should give a nonzero number of triggers 90% of the time; it can be calculated by solving Eq. (12) for μ_{bkg} with $N = 1$ and a FAP of 0.9 (i.e., $1 - e^{-\mu_{\mathrm{bkg}}} = 0.9$). The subscript VT indicates that these upper limits are in terms of number of observations per volume per time.

Due to the dependence of these rate upper limits on distance to the source, they cannot be calculated for the *ad hoc* waveforms without setting an arbitrary source distance. A full description of the FAD and visible volume formalism is given in Appendix A; in Table VI, we present these upper limits for the four ADI waveforms.

Statistical and systematic uncertainties are discussed further in Appendix A, but we note here that the dominant source of uncertainty is the amplitude calibration uncertainty of the detectors. During the S5 science run, the amplitude calibration uncertainty was measured to be 10.4% and 14.4% for the H1 and L1 detectors, respectively, in the 40–2000 Hz frequency band [73]. Summing these uncertainties in quadrature gives a total calibration uncertainty of 17.8% on the amplitude, and thus, an uncertainty of 53.4% on the visible volume. For S6, the amplitude calibration uncertainty was measured at 4.0% for H1 and 7.0% for L1 in the 40–2000 Hz band, resulting in a total calibration uncertainty of 8.1% on the amplitude and 24.2% on the visible volume [74]. These uncertainties are marginalized over using a Bayesian method discussed in Appendix B. The upper limits presented in Table VI are conservative and include these uncertainties.

TABLE V. The most significant triggers from the S5 and S6 data sets. GPS times given correspond to trigger start times; both triggers had durations of 23.5 seconds.

Data set	SNR_Γ	FAR [yr^{-1}]	FAP	GPS time	Freq. [Hz]
S5	29.65	1.00	0.54	851136555.0	129–201
S6	27.13	6.94	0.92	958158359.5	537–645

TABLE VI. Rate upper limits on ADI waveforms calculated with Eq. (13). The visible volume of each search is shown to illustrate relative search sensitivities. Uncertainties on the visible volumes are not included, but are primarily due to calibration uncertainty, and are 53% and 24% for all waveforms in S5 and S6, respectively. 1σ uncertainties on the upper limits are marginalized over using the Bayesian method described in Appendix B.

	V_{vis} [Mpc^3]		
Waveform	S5	S6	$R_{90\%,\mathrm{VT}}$ [$\mathrm{Mpc}^{-3}\,\mathrm{yr}^{-1}$]
ADI-A	1.8×10^3	3.6×10^3	9.4×10^{-4}
ADI-B	5.7×10^4	9.1×10^4	3.4×10^{-5}
ADI-C	7.8×10^3	1.6×10^4	2.2×10^{-4}
ADI-E	1.6×10^4	3.2×10^4	1.1×10^{-4}

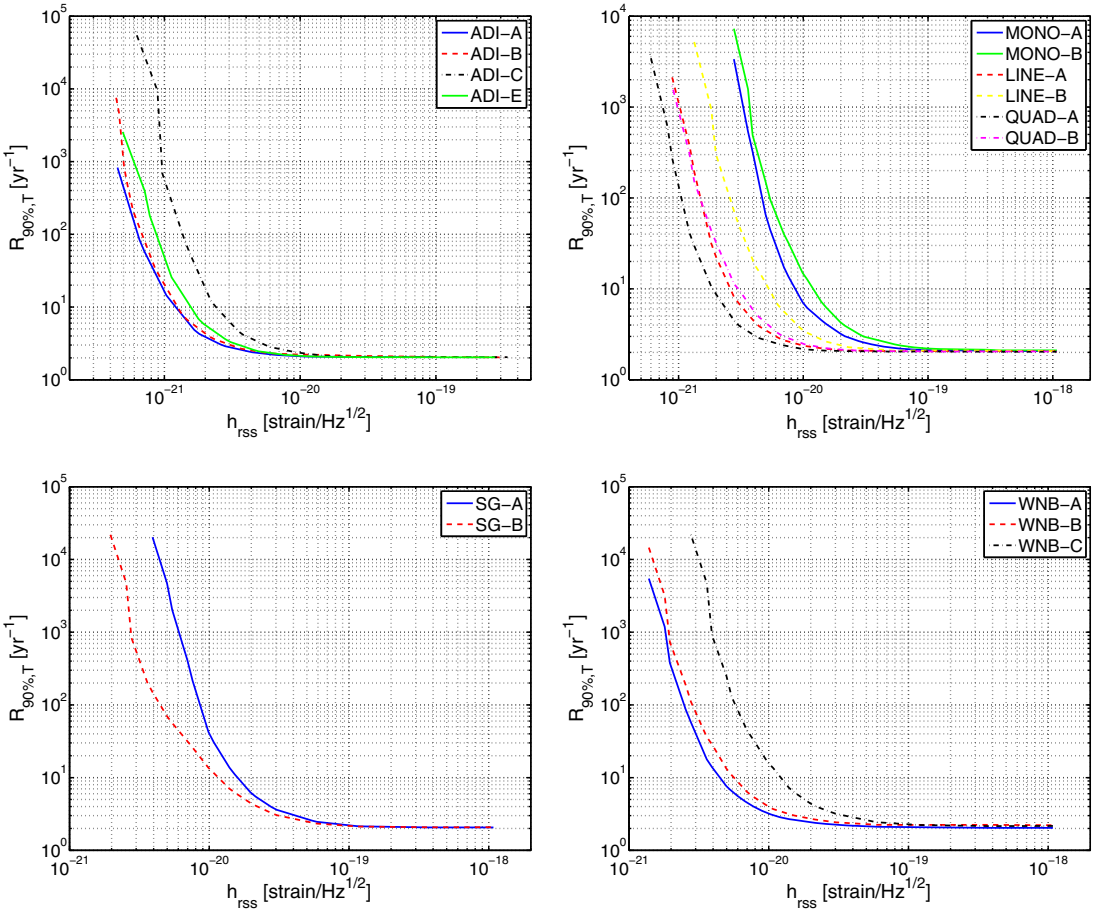

FIG. 6. Loudest event statistic upper limits for the 15 simulated GW signals used to test the sensitivity of the search (calculated with Eq. (14)). 1σ uncertainties are included by adjusting the signal amplitudes upward. Top left: ADI waveforms. Top right: sinusoidal waveforms. Bottom left: sine-Gaussian waveforms. Bottom right: white noise burst waveforms.

For signal models without a physical distance calibration, we use the loudest event statistic to calculate rate upper limits at 90% confidence based on the search pipeline's efficiency:

$$R_{90\%,\mathrm{T}} = \frac{2.3}{\sum_k \epsilon_k(\mathrm{SNR}^{\star}_{\Gamma,k}) T_{\mathrm{obs},k}}. \tag{14}$$

Here, ϵ_k is the efficiency of search k at a detection threshold $\mathrm{SNR}^{\star}_{\Gamma,k}$ corresponding to the loudest zero-lag trigger from search k. The resulting upper limits are in terms of the number of observations per time, as indicated by the subscript T. They are a function of signal strength in the form of root-sum-squared strain, h_{rss}, and are presented in Fig. 6.

Again, systematic uncertainty in the form of amplitude calibration uncertainty is the main source of uncertainty for these upper limits. This uncertainty is accounted for by adjusting the signal amplitudes used in the sensitivity study (and shown in the efficiency curves in Fig. 4) upward by a multiplicative factor corresponding to the respective 1σ amplitude calibration uncertainty; this results in conservative upper limits.

In Fig. 7, we show the $R_{90\%,\mathrm{T}}$ upper limits in terms of source distance for the ADI waveforms. To compare these upper limits to the $R_{90\%,\mathrm{VT}}$ upper limits, one would integrate the inverse of the $R_{90\%,\mathrm{T}}$ curves (shown in Fig. 7) over volume to obtain an overall estimate of the signal rate. The two methods have been compared, and the results are consistent within ≈25% for all four of the ADI waveforms. Differences between the two methods arise from the usage of different trigger ranking statistics (FAD vs. SNR_{Γ}), and the fact that the uncertainties are handled differently in each case.

C. Discussion

Given the absence of detection candidates in the search, we have reported upper limits on the event rate for different GW signal families. Specifically, Fig. 6 shows that, along with signal morphology, both the frequency and the duration of a signal influence the search sensitivity. The h_{rss} values for a search efficiency of 50%

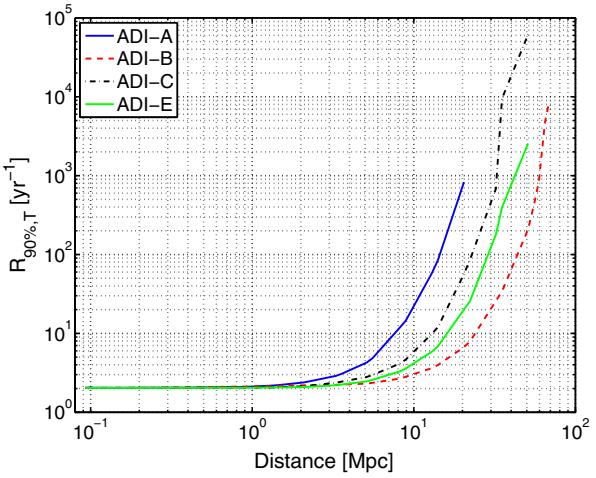

FIG. 7. Loudest event statistic upper limits for the four ADI waveforms used to test the sensitivity of the search. Here, the upper limits are plotted in terms of distance rather than $h_{\rm rss}$.

obtained with S5 and S6 data are reported in Table VII. For the ADI waveforms, the 50% efficiency distance is also given. Although these limits cannot be precisely compared to the results of unmodeled short transient GW searches [4] because different waveforms were used by the two searches, it is clear that in order for long transient GW signals to be observed, it is necessary for the source to be more energetic: the total energy radiated is spread over hundreds of seconds instead of a few hundred milliseconds.

One can also estimate the amount of energy emitted by a source located at a distance r where the search efficiency drops below 50% ($h_{\rm rss}^{50\%}$) using the quadrupolar radiation approximation to estimate the energy radiated by a pair of rotating point masses:

$$E_{\rm GW} \approx (h_{\rm rss}^{50\%})^2 r^2 \pi^2 f_{\rm GW}^2 \frac{c^3}{G}. \quad (15)$$

Considering the mean frequency of each GW waveform, we obtain an estimate of the energy that would have been released by a source that would be detected by this search. For the ADI waveforms, the corresponding energy is between 9×10^{-8} $M_\odot c^2$ and 6×10^{-7} $M_\odot c^2$. For the *ad hoc* waveforms, one must fix a fiducial distance at which one expects to observe a signal. For instance, considering a Galactic source at 10 kpc, the emitted energy would be in the range 2×10^{-7}–2×10^{-4} $M_\odot c^2$. This is still 2–4 orders of magnitude larger than the amount of energy estimated in Ref. [47] for a 10 kpc protoneutron star developing matter convection over 30 s: 4×10^{-9} $M_\odot c^2$.

Finally, we note that the search for long-duration transient signals is also closely related to the effort by LIGO and Virgo to observe a stochastic background of GWs. One or more long-lived transient GW events, with a duration of days or longer, could produce an apparent signal in either the isotropic [21,23,24] or directional [22] stochastic GW searches. It was for this reason that this long-duration transient detection pipeline was originally developed [40]. The methods for detecting these long-duration transients have been adapted, in the study described in this present paper, to search for signals in the 10 s–to–500 s regime. A dedicated search for long-duration transient GW signals which last for days or longer will be a necessary component in the effort to understand the origin of apparent stochastic background signals which may be observed by LIGO and Virgo in the future [75].

TABLE VII. Values of $h_{\rm rss}$ and distance where the search achieves 50% efficiency for each of the simulated GW signals studied and each of the two data sets. $E_{\rm GW}$ is an estimate of the energy released (given by Eq. (15)) by a source located at the detection distance for the ADI waveforms, or at 10 kpc for the *ad hoc* waveforms.

Run	S5			S6		
Waveform	$h_{\rm rss}^{50\%}$ [Hz$^{-1/2}$]	distance$^{50\%}$ [Mpc]	$E_{\rm GW}$ [$M_\odot c^2$]	$h_{\rm rss}^{50\%}$ [Hz$^{-1/2}$]	distance$^{50\%}$ [Mpc]	$E_{\rm GW}$ [$M_\odot c^2$]
ADI-A	1.8×10^{-21}	5.4	1.5×10^{-7}	1.4×10^{-21}	6.8	9.4×10^{-8}
ADI-B	1.9×10^{-21}	16.3	1.9×10^{-7}	1.7×10^{-21}	18.6	1.5×10^{-7}
ADI-C	3.6×10^{-21}	8.9	9.9×10^{-7}	2.9×10^{-21}	11.3	6.3×10^{-7}
ADI-E	2.3×10^{-21}	11.5	3.3×10^{-7}	2.0×10^{-21}	13.4	2.4×10^{-7}
LINE-A	3.9×10^{-21}	…	4.9×10^{-7}	3.1×10^{-21}	…	3.1×10^{-7}
LINE-B	8.5×10^{-21}	…	9.6×10^{-5}	5.2×10^{-21}	…	3.7×10^{-5}
MONO-A	1.3×10^{-20}	…	3.1×10^{-6}	1.2×10^{-20}	…	2.4×10^{-6}
MONO-B	2.1×10^{-20}	…	2.3×10^{-4}	1.1×10^{-20}	…	7.0×10^{-5}
QUAD-A	2.7×10^{-21}	…	2.4×10^{-7}	2.4×10^{-21}	…	1.9×10^{-7}
QUAD-B	5.1×10^{-21}	…	1.6×10^{-5}	2.9×10^{-21}	…	5.3×10^{-6}
SG-A	2.4×10^{-20}	…	1.0×10^{-5}	1.9×10^{-20}	…	6.2×10^{-6}
SG-B	2.1×10^{-20}	…	2.5×10^{-4}	1.0×10^{-20}	…	5.9×10^{-5}
WNB-A	7.2×10^{-21}	…	5.5×10^{-6}	5.5×10^{-21}	…	3.2×10^{-6}
WNB-B	9.1×10^{-21}	…	1.8×10^{-5}	6.4×10^{-21}	…	9.2×10^{-6}
WNB-C	2.1×10^{-20}	…	5.0×10^{-4}	1.3×10^{-20}	…	1.7×10^{-4}

VII. CONCLUSIONS

In this paper, we have presented an all-sky search for long-lasting GW transients with durations between a few seconds and a few hundred seconds. We performed the search on data from the LIGO H1 and L1 detectors collected during the S5 and S6 science runs. We used a cross-correlation pipeline to analyze the data and identify potential GW candidate triggers. To reject high-SNR_Γ triggers due to detector noise, we defined a discriminant cut based on the trigger morphology. We have also used data quality flags that veto well-identified instrumental or environmental noise sources to remove significant outliers. No GW candidates were identified in this search, and as a consequence, we set upper limits on several types of simulated GW signals. These are the first upper limits from an unmodeled all-sky search for long-transient GWs. The upper limits are given in Table VI and Figs. 6 and 7.

After 2010, the LIGO and Virgo interferometers went through a series of upgrades [26,27]. LIGO has just started its first observational campaign with its advanced configuration and will be joined by Virgo in 2016 [29]. The strain sensitivity of the advanced detectors is expected to eventually reach a factor of 10 better than the first-generation detectors. This development alone should increase the distance reach of our search by a factor of 10, the energy sensitivity by a factor of 100, and the volume of space which we can probe by a factor of 1000.

Improvements are also being made to this search pipeline; a technique for generating triggers called "seedless clustering" has been shown to increase the sensitivity of the search by 50% or more in terms of distance [76–81]. The improvements to the search pipeline described in this paper, coupled with the increased sensitivity of LIGO and Virgo, will drastically improve the probability of detecting long-duration transient GWs and pave the way for an exciting future in GW astronomy.

ACKNOWLEDGMENTS

The authors gratefully acknowledge the support of the United States National Science Foundation (NSF) for the construction and operation of the LIGO Laboratory; the Science and Technology Facilities Council (STFC) of the United Kingdom, the Max-Planck-Society (MPS), and the State of Niedersachsen/Germany for support of the construction and operation of the GEO600 detector; and the Italian Istituto Nazionale di Fisica Nucleare (INFN) and the French Centre National de la Recherche Scientifique (CNRS) for the construction and operation of the Virgo detector and the creation and support of the EGO consortium. The authors also gratefully acknowledge research support from these agencies as well as by the Australian Research Council; the International Science Linkages program of the Commonwealth of Australia; the Council of Scientific and Industrial Research of India; the Department of Science and Technology, India; the Science & Engineering Research Board (SERB), India; the Ministry of Human Resource Development, India; the Spanish Ministerio de Economía y Competitividad; the Conselleria d'Economia i Competitivitat and Conselleria d'Educaci, Cultura i Universitats of the Govern de les Illes Balears; the Foundation for Fundamental Research on Matter supported by the Netherlands Organisation for Scientific Research; the National Science Centre of Poland; the European Union; the Royal Society; the Scottish Funding Council; the Scottish Universities Physics Alliance; the National Aeronautics and Space Administration; the Hungarian Scientific Research Fund (OTKA); the Lyon Institute of Origins (LIO); the National Research Foundation of Korea; Industry Canada and the Province of Ontario through the Ministry of Economic Development and Innovation; the Natural Science and Engineering Research Council, Canada; the Brazilian Ministry of Science, Technology, and Innovation; the Carnegie Trust; the Leverhulme Trust; the David and Lucile Packard Foundation; the Research Corporation; and the Alfred P. Sloan Foundation. The authors gratefully acknowledge the support of the NSF, STFC, MPS, INFN, CNRS and the State of Niedersachsen/Germany for provision of computational resources.

APPENDIX A: VISIBLE VOLUME AND FALSE ALARM DENSITY

In order to constrain the rate and source density of the GW signals studied in this search, we estimate the volume of the sky in which the search algorithm is sensitive to these signals. For this, we use the visible volume [6,10]

$$V_{\mathrm{vis}}(\mathrm{SNR}_\Gamma) = \sum_i 4\pi r_i^2 \left(\frac{dN_{\mathrm{inj}}}{dr}(r_i)\right)^{-1}. \quad \text{(A1)}$$

Here the index i runs over detected injections, r_i is the distance to the ith injection, and dN_{inj}/dr is the radial density of injections. The SNR_Γ parameter sets the threshold which determines whether an injection is recovered or not. To calculate the visible volume, we require distance-calibrated waveforms, so this method is not practical for the *ad hoc* waveforms discussed previously.

Our estimate of the visible volume is affected by both statistical and systematic uncertainties. We can estimate the statistical uncertainty on the visible volume using binomial statistics [6,10]:

$$\sigma_{\mathrm{stat}} = \sqrt{\sum_i \left[4\pi r_i^2 \left(\frac{dN_{\mathrm{inj}}}{dr}(r_i)\right)^{-1}\right]^2}. \quad \text{(A2)}$$

Systematic uncertainty on the visible volume comes from the amplitude calibration uncertainties of the detectors:

$$\sigma_{\rm sys} = 3 \times V_{\rm vis} \times \sigma_{\rm calibration}. \quad \text{(A3)}$$

These uncertainties are discussed further in Sec. VI B. We can estimate the total uncertainty on the visible volume by summing the statistical and systematic uncertainties in quadrature:

$$\sigma_{V_{\rm vis}} = \sqrt{\sigma^2_{\rm stat} + \sigma^2_{\rm sys}}. \quad \text{(A4)}$$

We note that the statistical uncertainty is negligible for this search compared to the systematic uncertainty from the amplitude calibration uncertainty of the detectors.

The false alarm density (FAD) statistic is useful for comparing the results of searches over different data sets or even using different detector networks [6,10,82]. It provides an estimate of the number of background triggers expected given the visible volume and background live time of the search. The classical FAD is defined in terms of the FAR divided by the visible volume:

$$\mathrm{FAD_c}(\mathrm{SNR}_\Gamma) = \frac{\mathrm{FAR}(\mathrm{SNR}_\Gamma)}{V_{\rm vis}(\mathrm{SNR}_\Gamma)}. \quad \text{(A5)}$$

In this way, the FAD accounts for the network sensitivity to GW sources as well as the detector noise level and the accumulated live time.

We follow Ref. [82] to define a FAD which produces a monotonic ranking of triggers:

$$\mathrm{FAD}(\mathrm{SNR}_{\Gamma,i}) = \min(\mathrm{FAD_c}(\mathrm{SNR}_{\Gamma,i}), \mathrm{FAD_c}(\mathrm{SNR}_{\Gamma,i-1})), \quad \text{(A6)}$$

where the index i runs over triggers in increasing order of SNR_Γ.

One then uses the FAD to combine results from searches over different data sets or with different detector networks by calculating the time-volume productivity of the combined search:

$$\nu(\mathrm{FAD}) = \sum_k V_{{\rm vis},k}(\mathrm{FAD}) \times T_{{\rm obs},k}. \quad \text{(A7)}$$

Here the index k runs over data sets or detector networks. We note that the denominator in Eq. (13) is equal to ν as described here. The uncertainty on ν can be calculated as

$$\sigma_\nu(\mathrm{FAD}) = \sqrt{\sum_k T^2_{{\rm obs},k} \sigma^2_{V_{{\rm vis},k}}(\mathrm{FAD})}. \quad \text{(A8)}$$

The combined time-volume product is then used to calculate final upper limits (see Eqs. (13) and (B1)).

APPENDIX B: BAYESIAN FORMALISM FOR FAD UPPER LIMIT CALCULATION

The observed astrophysical rate of triggers is given by

$$R = \frac{N}{\nu(\mathrm{FAD}^\star)}, \quad \text{(B1)}$$

where N is the number of triggers observed by the search, ν is the time-volume product described in Eq. (A7), and $\mathrm{FAD}^\star$ is the false alarm density of the most significant zero-lag trigger. Although this search found no GW candidates, N is Poisson distributed, with some underlying mean and variance μ. To properly handle the uncertainty associated with the time-volume product, we utilize a Bayesian formalism to account for uncertainties in both quantities in the calculation of rate upper limits. Here, our goal is to constrain the rate using the mean expected number of triggers, μ.

Given an observation of N triggers with a time-volume product of $\bar{\nu}$, we can define a posterior distribution for μ and ν in terms of Bayes' theorem:

$$P(\mu, \nu | N, \bar{\nu}) = \frac{P(N, \bar{\nu} | \mu, \nu) P(\mu, \nu)}{P(N, \bar{\nu})}, \quad \text{(B2)}$$

where $P(\mu, \nu | N, \bar{\nu})$ is the posterior distribution, $P(N, \bar{\nu} | \mu, \nu)$ is the likelihood, $P(\mu, \nu)$ are the priors, and $P(N, \bar{\nu})$ is the evidence.

We may disregard the evidence since it is simply a normalization factor, and use uniform priors on μ and ν:

$$\mu \in [0, \mu_{\rm max}], \quad \text{(B3a)}$$

$$\nu \in [0, \nu_{\rm max}]. \quad \text{(B3b)}$$

Here $\mu_{\rm max}$ and $\nu_{\rm max}$ are defined to be large enough that all of the significant posterior mass is enclosed.

The likelihood function can be framed as the product of two separate distributions: a Poisson distribution with mean μ and a Gaussian distribution with mean $\bar{\nu}$ and sigma σ_ν (see Eq. (A8)).

$$P(N, \bar{\nu} | \mu, \nu) = \frac{e^{-\mu} \mu^N}{N!} \frac{e^{-(\nu - \bar{\nu})^2/(2\sigma^2_{\bar{\nu}})}}{\sqrt{2\pi}\sigma_\nu}. \quad \text{(B4)}$$

Using this formalism, we can calculate the posterior distribution as a function of μ and ν. However, we are primarily interested in setting limits on the rate, given as the ratio of μ and ν. We can transform the posterior distribution to be a function of two new variables by multiplying the original posterior by the Jacobian determinant of the transformation:

$$P(R, \nu | N, \bar{\nu}) = P(\mu, \nu | N, \bar{\nu}) \times |J|. \quad \text{(B5)}$$

Choosing the new variables to be R and ν (for simplicity), we obtain a Jacobian determinant of

$$|J| = \left| \begin{matrix} \frac{\partial \mu}{\partial R} & \frac{\partial \mu}{\partial \nu} \\ \frac{\partial \nu}{\partial R} & \frac{\partial \nu}{\partial \nu} \end{matrix} \right| = \nu. \tag{B6}$$

This gives a posterior distribution of

$$P(R, \nu | N, \bar{\nu}) = \nu \frac{e^{-\mu} \mu^N}{N!} \frac{e^{-(\nu-\bar{\nu})^2/(2\sigma_\nu^2)}}{\sqrt{2\pi}\sigma_\nu}. \tag{B7}$$

Finally, we marginalize over ν to get the posterior distribution of R:

$$P(R|N, \bar{\nu}) = \int_0^{\nu_{\max}} P(R, \nu | N, \bar{\nu}) d\nu. \tag{B8}$$

Using this distribution, we can find the 90% limit on R, $R_{90\%,\mathrm{VT}}$, such that 90% of the posterior mass is enclosed, by numerically solving Eq. (B9):

$$0.9 = \int_0^{R_{90\%,\mathrm{VT}}} P(R|N, \bar{\nu}) dR. \tag{B9}$$

[1] B. Abbott *et al.* (LIGO Scientific Collaboration), Rep. Prog. Phys. **72**, 076901 (2009).
[2] T. Accadia *et al.* (Virgo Collaboration), J. Instrum. **7**, P03012 (2012).
[3] J. Abadie *et al.* (LIGO Scientific Collaboration and Virgo Collaboration), Phys. Rev. D **81**, 102001 (2010).
[4] J. Abadie *et al.* (LIGO Scientific Collaboration and Virgo Collaboration), Phys. Rev. D **85**, 122007 (2012).
[5] J. Aasi *et al.* (LIGO Scientific Collaboration and Virgo Collaboration), Phys. Rev. Lett. **112**, 131101 (2014).
[6] J. Abadie *et al.* (LIGO Scientific Collaboration and Virgo Collaboration), Phys. Rev. D **85**, 102004 (2012).
[7] J. Aasi *et al.* (LIGO Scientific Collaboration and Virgo Collaboration), Phys. Rev. D **89**, 122003 (2014).
[8] J. Abadie *et al.* (LIGO Scientific Collaboration and Virgo Collaboration), Phys. Rev. D **82**, 102001 (2010).
[9] J. Abadie *et al.* (LIGO Scientific Collaboration and Virgo Collaboration), Phys. Rev. D **85**, 082002 (2012).
[10] J. Abadie *et al.* (LIGO Scientific Collaboration and Virgo Collaboration), Phys. Rev. D **83**, 122005 (2011).
[11] J. Aasi *et al.* (LIGO Scientific Collaboration and Virgo Collaboration), Phys. Rev. D **87**, 022002 (2013).
[12] J. Aasi *et al.* (LIGO Scientific Collaboration and Virgo Collaboration), Phys. Rev. D **89**, 102006 (2014).
[13] B. Abbott *et al.* (LIGO Scientific Collaboration), Astrophys. J. **683**, L45 (2008).
[14] J. Aasi *et al.* (LIGO Scientific Collaboration and Virgo Collaboration), Phys. Rev. D **87**, 042001 (2013).
[15] J. Abadie *et al.* (LIGO Scientific Collaboration and Virgo Collaboration), Phys. Rev. D **85**, 022001 (2012).
[16] J. Aasi *et al.* (LIGO Scientific Collaboration and Virgo Collaboration), Astrophys. J. **785**, 119 (2014).
[17] J. Aasi *et al.* (LIGO Scientific Collaboration and Virgo Collaboration), Phys. Rev. D **88**, 102002 (2013).
[18] J. Aasi *et al.* (LIGO Scientific Collaboration and Virgo Collaboration), Phys. Rev. D **90**, 062010 (2014).
[19] J. Aasi *et al.* (LIGO Scientific Collaboration and Virgo Collaboration), Classical Quantum Gravity **31**, 085014 (2014).
[20] J. Aasi *et al.* (LIGO Scientific Collaboration and Virgo Collaboration), Classical Quantum Gravity **31**, 165014 (2014).
[21] B. Abbott *et al.* (LIGO Scientific Collaboration and Virgo Collaboration), Nature (London) **460**, 990 (2009).
[22] B. Abbott *et al.* (LIGO Scientific Collaboration and Virgo Collaboration), Phys. Rev. Lett. **107**, 271102 (2011).
[23] J. Aasi *et al.* (LIGO Scientific Collaboration and Virgo Collaboration), Phys. Rev. Lett. **113**, 231101 (2014).
[24] J. Aasi *et al.* (LIGO Scientific Collaboration and Virgo Collaboration), Phys. Rev. D **91**, 022003 (2015).
[25] M. A. Bizouard and M. A. Papa, C.R. Phys. **14**, 352 (2013).
[26] J. Aasi *et al.* (LIGO Scientific Collaboration), Classical Quantum Gravity **32**, 074001 (2015).
[27] F. Acernese *et al.* (Virgo Collaboration), Classical Quantum Gravity **32**, 024001 (2015).
[28] T. Uchiyama, K. Furuta, M. Ohashi, S. Miyoki, O. Miyakawa, and Y. Saito, Classical Quantum Gravity **31**, 224005 (2014).
[29] J. Aasi *et al.* (LIGO Scientific Collaboration and Virgo Collaboration), arXiv:1304.0670.
[30] C. D. Ott, Classical Quantum Gravity **26**, 063001 (2009).
[31] L. Baiotti, I. Hawke, and L. Rezzolla, Classical Quantum Gravity **24**, S187 (2007).
[32] T. Damour and A. Vilenkin, Phys. Rev. D **64**, 064008 (2001).
[33] K. Belczynski, A. Buonanno, M. Cantiello, C. L. Fryer, D. E. Holz, I. Mandel, M. C. Miller, and M. Walczak, Astrophys. J. **789**, 120 (2014).
[34] M. Shibata and K. Taniguchi, Living Rev. Relativity **14**, 6 (2011).
[35] Z. B. Etienne, J. A. Faber, Y. T. Liu, S. L. Shapiro, K. Taniguchi, and T. W. Baumgarte, Phys. Rev. D **77**, 084002 (2008).
[36] S. Mereghetti, Astron. Astrophys. Rev. **15**, 225 (2008).
[37] N. Andersson and G. L. Comer, Phys. Rev. Lett. **87**, 241101 (2001).
[38] M. Briggs *et al.* (LIGO Scientific Collaboration and Virgo Collaboration), Astrophys. J. **760**, 12 (2012).
[39] J. Aasi *et al.* (LIGO Scientific Collaboration and Virgo Collaboration), Phys. Rev. D **88**, 122004 (2013).
[40] E. Thrane, S. Kandhasamy, C. D. Ott, W. G. Anderson, N. L. Christensen *et al.*, Phys. Rev. D **83**, 083004 (2011).
[41] K. Kotake, C.R. Phys. **14**, 318 (2013).

[42] J. M. Blondin, A. Mezzacappa, and C. DeMarino, Astrophys. J. **584**, 971 (2003).
[43] C. D. Ott, S. Ou, J. E. Tohline, and A. Burrows, Astrophys. J. **625**, L119 (2005).
[44] C. D. Ott, H. Dimmelmeier, A. Marek, H.-T. Janka, I. Hawke, B. Zink, and E. Schnetter, Phys. Rev. Lett. **98**, 261101 (2007).
[45] S. Scheidegger, R. Käppeli, S. C. Whitehouse, T. Fischer, and M. Liebendörfer, Astron. Astrophys. **514**, A51 (2010).
[46] T. Kuroda, T. Takiwaki, and K. Kotake, Phys. Rev. D **89**, 044011 (2014).
[47] E. Mueller, M. Rampp, R. Buras, H. T. Janka, and D. H. Shoemaker, Astrophys. J. **603**, 221 (2004).
[48] K. Kotake, W. Iwakami, N. Ohnishi, and S. Yamada, Astrophys. J. **697**, L133 (2009).
[49] B. Müller, H.-T. Janka, and A. Marek, Astrophys. J. **766**, 43 (2013).
[50] K. N. Yakunin, A. Mezzacappa, P. Marronetti, S. Yoshida, S. W. Bruenn, W. R. Hix, E. J. Lentz, O. E. B. Messer, J. A. Harris, E. Endeve *et al.*, Phys. Rev. D **92**, 084040 (2015).
[51] A. L. Piro and C. D. Ott, Astrophys. J. **736**, 108 (2011).
[52] A. L. Piro and E. Thrane, Astrophys. J. **761**, 63 (2012).
[53] C. D. Ott, C. Reisswig, E. Schnetter, E. O'Connor, U. Sperhake, F. Löffler, P. Diener, E. Abdikamalov, I. Hawke, and A. Burrows, Phys. Rev. Lett. **106**, 161103 (2011).
[54] T. Dietrich and S. Bernuzzi, Phys. Rev. D **91**, 044039 (2015).
[55] S. E. Woosley, Astrophys. J. **405**, 273 (1993).
[56] A. L. Piro and E. Pfahl, Astrophys. J. Lett. **658**, 1173 (2007).
[57] K. Kiuchi, M. Shibata, P. J. Montero, and J. A. Font, Phys. Rev. Lett. **106**, 251102 (2011).
[58] M. H. P. M. van Putten, Phys. Rev. Lett. **87**, 091101 (2001).
[59] M. H. P. M. van Putten, A. Levinson, H. K. Lee, T. Regimbau, M. Punturo, and G. M. Harry, Phys. Rev. D **69**, 044007 (2004).
[60] B. Metzger, D. Giannios, T. Thompson, N. Bucciantini, and E. Quataert, Mon. Not. R. Astron. Soc. **413**, 2031 (2011).
[61] A. Rowlinson, P. T. O'Brien, B. D. Metzger, N. R. Tanvir, and A. J. Levan, Mon. Not. R. Astron. Soc. **430**, 1061 (2013).
[62] A. Corsi and P. Mészáros, Astrophys. J. **702**, 1171 (2009).
[63] L. Gualtieri, R. Ciolfi, and V. Ferrari, Classical Quantum Gravity **28**, 114014 (2011).
[64] J. Abadie *et al.* (LIGO Scientific Collaboration and Virgo Collaboration), LIGO Report No. T1100338.
[65] J. Abadie *et al.* (LIGO Scientific Collaboration and Virgo Collaboration), LIGO Report No. T0900499.
[66] N. Christensen (LIGO Scientific Collaboration and Virgo Collaboration), Classical Quantum Gravity **27**, 194010 (2010).
[67] J. Slutsky, L. Blackburn, D. Brown, L. Cadonati, J. Cain *et al.*, Classical Quantum Gravity **27**, 165023 (2010).
[68] J. Aasi *et al.* (LIGO Scientific Collaboration and Virgo Collaboration), Classical Quantum Gravity **32**, 115012 (2015).
[69] J. Aasi *et al.* (LIGO Scientific Collaboration and Virgo Collaboration), Classical Quantum Gravity **29**, 155002 (2012).
[70] T. Prestegard and E. Thrane, LIGO Report No. L1200204.
[71] T. Prestegard, E. Thrane, N. L. Christensen, M. W. Coughlin, B. Hubbert, S. Kandhasamy, E. MacAyeal, and V. Mandic, Classical Quantum Gravity **29**, 095018 (2012).
[72] R. Biswas, P. R. Brady, J. D. E. Creighton, and S. Fairhurst, Classical Quantum Gravity **26**, 175009 (2009).
[73] J. Abadie *et al.* (LIGO Scientific Collaboration), Nucl. Instrum. Methods Phys. Res., Sect. A **624**, 223 (2010).
[74] I. Bartos *et al.*, LIGO Report No. T1100071.
[75] E. Thrane, V. Mandic, and N. Christensen, Phys. Rev. D **91**, 104021 (2015).
[76] E. Thrane and M. Coughlin, Phys. Rev. D **88**, 083010 (2013).
[77] E. Thrane and M. Coughlin, Phys. Rev. D **89**, 063012 (2014).
[78] M. Coughlin, E. Thrane, and N. Christensen, Phys. Rev. D **90**, 083005 (2014).
[79] M. Coughlin, P. Meyers, E. Thrane, J. Luo, and N. Christensen, Phys. Rev. D **91**, 063004 (2015).
[80] M. Coughlin, P. Meyers, S. Kandhasamy, E. Thrane, and N. Christensen, Phys. Rev. D **92**, 043007 (2015).
[81] E. Thrane and M. Coughlin, Phys. Rev. Lett. **115**, 181102 (2015).
[82] S. Klimenko, C. Pankow, and G. Vedovato, LIGO Report No. L1300869.

Chapter 4

Detector characterization for transient gravitational wave searches during Virgo Science run VSR1 – VSR4

4.1 Introduction

Real GW detector data are still far from being stationary and Gaussian. As a consequence the trigger rate and the amplitude of the louder triggers are larger than what would be expected from a Gaussian distribution. Multi-detector coincidence and/or coherence techniques allow one to reduce a large fraction of noise triggers coming from one detector. But it is now a established fact with ground based GW detector analyses that suppressing, as much as possible, all periods of data that are known to be spoiled by disturbances is mandatory in order to decrease the false alarm rate required for a discovery. On the other hand, one does not want to reduce the observation time when the glitches are harmless for the GW search (for instance when they have low SNR). As we will see, a certain trade off between observation time and excess noise reduction is necessary, but a good understanding of the sources of noises is always mandatory.

Different sources of disturbances[1] will generate different effects in the GW strain amplitude data. GW search pipelines run on all science periods yield triggers whose main characteristics – duration, frequency and strength (SNR, energy or significance) – give a way to classify the effect of noise disturbance in GW searches. A "glitch" refers to a short disturbance in time, typically shorter than a second. They can be as short as one sample (digital error). But not all excess noise triggers are as short as glitches. Non stationary data over a larger time scale (up to few dozens of seconds) will generate an excess of triggers in GW burst searches. The frequency information provides clues to identify the origin of the noise disturbance. An eventual periodicity in time of the triggers can also help to find out their origin. Thousands of auxilliary signals are recorded along with the GW strain amplitude channel h(t). These channels provide lots of information about the status of the detector and are heavily used in order to understand the noise path and develop vetoes, as we will see later.

In many occasions, one uses the word glitch to refer to any short effect in non stationary data. But in a broader acceptance, the word glitch covers any non stationary data features, which are responsible of an excess of triggers in transient GW searches compared to what is expected from Gaussian noise. To select glitches in the main GW channel (or in any other channels), one uses burst search algorithms that cover a given frequency range. For historical reasons, 48-2048 Hz is the privileged frequency band for glitch studies because it overlaps rather well with the best sensitivity region of ground-based detectors and it reveals already a large number of problems. One generally starts from a list of background triggers that do not contain any GW signal triggers (for instance time shifted triggers seen in coincidence in different interferometers). Originally, GW unmodelled burst searches were thought to suffer the most from glitches in the data because of the similarity between glitches and a generic burst signal. It turns out that all GW searches benefit from the detector characterization effort. This is particularly true for high mass CBC searches

[1] Disturbances include noise generated by the detector environment as well as the detector's components, such as the laser beams, the mirrors, the control loops, etc.

for which templates can be as short as a few seconds, and can match easily low frequency glitches. Both CBC and burst LSC-Virgo groups put a large common effort in understanding the main sources of noise excess and develop efficient vetoes that reject noise in excess.

Although many efforts are constantly done by the commissioning and the noise hunting teams to improve the quality of data, glitch investigation is a daily endeavor during data taking runs, as many noise disturbances come from the experiment environment: wind, airplanes, earthquakes, acoustic and magnetic noises, human presence in buildings, etc). Some also come from the detector itself: electronic failure, control failure, dust, optical default, diffused light, imperfect alignment configuration, laser frequency noise, laser jitter, etc). The distinction between the two categories is not really important as many sources of noise couple with each other. Change of running conditions (new software/hardware, new control, etc) can also be a source of new noises.

Since the first Virgo commissioning runs (back in 2002), I have studied Virgo data, looking for the origin of the excess of triggers (originally for burst searches). Glitch studies have been carried out in the Virgo Data Quality (VDQ) group, and the next sections are report work done in Virgo runs where data were acquired in searching for GW signals. C7 was the 7^{th} commissioning run lasting 5 days in 2005 from September 14^{th} to September 19^{th}. It was the first run with a power recycling Virgo interferometer in science conditions. Then Virgo conducted four science data acquisition runs that were interlaced with commissioning and upgrades periods: VSR1 (136 days from May 18^{th} to October 1^{st} 2007), VSR2 (186 days from July 7^{th} 2009 to January 8^{th} 2010), VSR3 (69 days from August 11^{th} 2010 to October 19^{th} 2010) and VSR4 (108 days from May 20^{th} 2011 to September 5^{th} 2011).

Other disturbances, such as quasi-periodic noise, appear as narrow band spectral features (lines) in the frequency spectrum. Noise lines affect mainly the search of continuous waves emitted by neutron stars and the GW stochastic background search. But when lines are non stationary, the amplitude and/or the frequency modulation can generate glitches.

The detector characterization work for burst and CBC GW searches consists in the identification of the main sources of glitches, the understanding of how the noise couples to the GW strain amplitude time series and finally the generation of data quality information that can be used by GW transient searches. The last step consists of the generation of the vetoes to be applied by GW searches such that the background events rate follows as much as possible a Gaussian statistic.

In Section 4.2, I provide some definitions and describe the pieces of hardware that are later mentioned in the rest of the chapter. In Section 4.3, I give a brief summary of the evolution of the Virgo detector between 2005 and 2011, date of the shutdown for advanced Virgo installation. I also describe how the sensitivity has improved over the years. In Section 4.4, I describe a rather exhaustive list of all identified families of glitches in the Virgo data taken between 2005 and 2011. When this has been understood, I explain how the noise source couples with the dark fringe. The last Section 4.5 contains a brief description of the Virgo data quality monitoring system, and a more complete summary of the veto developments. The way we estimate the veto performance is explained along with the impact of the vetoes on GW burst searches.

What is contained in the next sections goes well beyond my own investigations with Virgo and LIGO data. It is fair to say that this is the work of a dozens of Virgo/LIGO students and colleagues. However, this has been a regular and active research activity for me over my entire time with the Virgo Collaboration.

4.2 Definitions

The Virgo detector is equipped with many probes that monitor its status. A few thousands of channel time series are acquired continuously [354], even when Virgo is not locked. At any moment, the detector is assigned a given status that gives rough indication about its behavior. It also indicates whether any particular operation (regular or not like commissioning work) is currently being performed from the control room or in an experimental hall [355]. Mode or status can be: "Adjusting", "Calibration", "Commissioning", "Injecting", "Locked", "Locking", "Maintenance", "Not Locked", "Science", "Troubleshooting", "Upgrading". **"Locked"** and **"Science"** are the 2 modes for which we consider the data for detector characterization. During a "Commissioning" time, although Virgo is kept locked, some noise can be generated by the activity of the commissioners. We are of course not interested by these glitches.

A **glitch** is a short fluctuation of the amplitude of a channel that is not described by a Gaussian process. It can be as small as 1 ms or last for several seconds. If this lasts longer than a few seconds, it is usually referred as non-stationary

data. A glitch can be well localized in frequency or wide band.

An **auxiliary channel** is any channel except the photodiode channels that collect light coming out from the interferometer dark port (beam B1 as shown on Figure 4.1). Among the auxiliary channels, some contain measurements of the detector's environment (magnetic fields, acoustic noise, temperature, etc). Others record the signals of photodiodes used for the longitudinal and angular control of the optical components. For instance, useful signals are obtained by detecting the light in the transmission of the arm cavities (beams B7 and B8) and in reflection of the power recycling cavity (beam B2), as well as detecting the reflection at the secondary surface of the beam splitter (beam B5) and the light reflected by the output Mode-Cleaner (beam B1p). The GW channel signal that results from a detuning of the carrier resonance in the arms is extracted from the dark port channel demodulated and sampled at 20 kHz. The dark port channel is called the **dark fringe** and the reconstructed and calibrated GW signal is called **h(t)**. On the simplified optical layout of Figure 4.1, the main photodiodes are indicated.

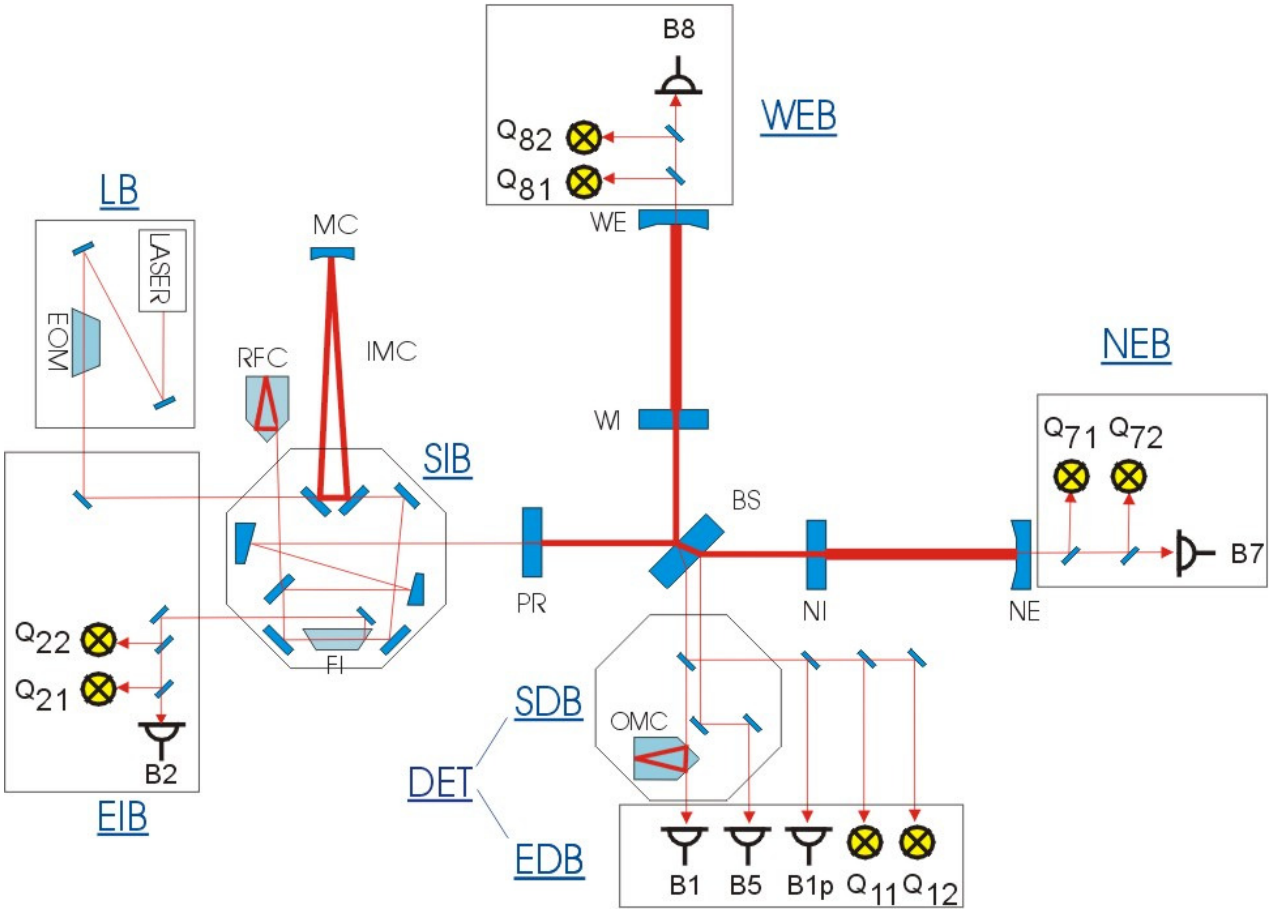

Figure 4.1: The Virgo optical layout. The main optical components are drawn in blue. The photodiodes which are used for the longitudinal and angular control of the mirrors are represented on the different benches.

To monitor the environment of the detector, all buildings are equipped with different types of probes: microphones, accelerometers, thermometers, humidity probes, anemometer on top of buildings [356]. The most critical buildings that host optical components are the two arms' end: North End (**NE**) and West End (**WE**) buildings, Central building (**CE**) and the Mode-Cleaner building (**MC**). All channels are digitized (ADC). The sampling frequency depends on the probe and varies from 500 Hz up to 20 kHz in Virgo.

4.3 Reaching the sensitivity

The commissioning of Virgo started in 2003. This has been a long and not always adiabatic process during which the initial design of the detector has been downgraded or upgraded many times, each time new problems were discovered. Detector sensitivity progresses are rather well visible in the noise spectrum measured in the data acquired during commissioning and science runs which are important markers. Not only do runs provide data for GW searches, but they also contribute to the detector commissioning: over the years it became more and more clear that improvements of the noise spectrum required the identification of all sources of noise (transient or permanent) that contribute directly and indirectly to the average sensitivity. Here feedback from data analysis is crucial. GW searches are indeed limited by many sorts of noise (glitches, lines, micro-seismic noise up-conversion, ...), and understanding the noise sources and their propagation mechanisms to the GW channel may require months of noise hunting and detector characterization.

Figure 4.2 shows the evolution of the Virgo sensitivity since 2005, year of the last commissioning runs, C7, which was the first run where Virgo was almost in its final optical configuration but still far from its nominal sensitivity. Virgo was then operating with a reduced laser power (0.7 W instead of 10 W) to avoid instabilities due to backscattering light in the mode-cleaner cavity. the back-scattering light problem was fixed by installing a Faraday isolator on the input bench [357]. VSR1, in 2007, was the first long science run with ~ 11 W entering into the detector and a prototype of the thermal compensation system (TCS) to manage thermally deformed mirrors. It took place in the last months of the LIGO 2-year long S5 run. While the VSR1 sensitivity at high frequency was very close to the design sensitivity (10 W laser), there was still more than an order of magnitude to gain at low frequency. The sensitivity below 150 Hz was dominated by noise introduced by the alignment control systems. In order to prepare for advanced Virgo and continue to mitigate the limiting technical noise sources, a series of upgrades have been decided: Amplified 25 W laser with a new injection system able to cope with thermal effects, improved TCS, new electronics and monolithic suspensions to fight against the thermal noise in the 100 – 300 Hz band. The Virgo+ project started just after VSR1 and after 18 months of commissioning followed by a very successful noise mitigation campaign, Virgo almost reached its nominal sensitivity at the start up of VSR2/S6 mid 2009. Similarly to Virgo, LIGO engaged a series of upgrades (enhanced LIGO) to gain a factor 2 in the overall sensitivity with respect to the LIGO nominal sensitivity reached at the end of S5 (2007). VSR2 was interrupted for 6 months to allow the installation of the monolithic suspensions of the Fabry Perot cavity mirrors. More commissioning time would have been needed to fix all new sources of noise that show up after this upgrade. However Virgo had to re-join the scientific data taking with LIGO to participate to a test campaign of the low latency GW transient searches coupled with prompt electromagnetic follow-up of the main GW candidates. The VSR3 run started mid August 2010, with a high noise level that improved a bit before the end of S6/VSR3 in October 2010. While the end of S6 signaled the beginning of advanced LIGO installation, Virgo went back to commissioning for 10 months to better understand and mitigate the limiting sources of noise. In the meantime the design of advanced Virgo was finalized. Given the progress at low frequency (gain of a factor 3) the 3 month long VSR4 run in coincidence with the GEO detector has been organized mid 2011 [358]. VSR4 data are the most sensitive data taken ever below 50 Hz. The Virgo sensitivity achieved during each run is shown in Figure 4.2. Table 4.1 summarizes the main features of the Virgo runs. Figure 4.3 illustrates the LIGO-GEO-Virgo runs schedule between 2005 and 2011 while Figure 4.4 shows the sensitivity evolution of the Virgo detector during that period quoting the horizon distance which is the distance at which a binary neutron star coalescence would be detected with a SNR of 8 assuming the binary system is optimally oriented and optimally located [359].

Virgo Runs	C7	VSR1	VSR2	VSR3	VSR4
Date	14 Sep. 2005 → 19 Sep. 2005	18 May 2007 → 1 Oct. 2007	7 Jul. 2009 → 8 Jan. 2010	11 Aug. 2010 → 20 Oct. 2010	3 Jun. 2011 → 5 Sep. 2011
Science time	4.5 days	108 days	149 days	50 days	76 days
Science duty cycle	66%	81%	80%	73%	82%
Average lock duration	1.3 h	10 h	10 h	9 h	11 h
Maximal lock duration	14.3 h	94 h	143 h	63 h	71 h
Average short transient trigger rate (SNR>5)^2	-	2.1 Hz	0.6 Hz	1.8 Hz	1.1 Hz
Horizon	$\sim$ 2 Mpc	$\sim$ 8.5 Mpc	$\sim$ 20 Mpc	$\sim$ 13 Mpc	$\sim$ 23 Mpc

Table 4.1: Duty cycles of the different science runs taken by Virgo between 2005 and 2011(C7 is not *per se* a science run, but the data taking conditions were these of a science run).

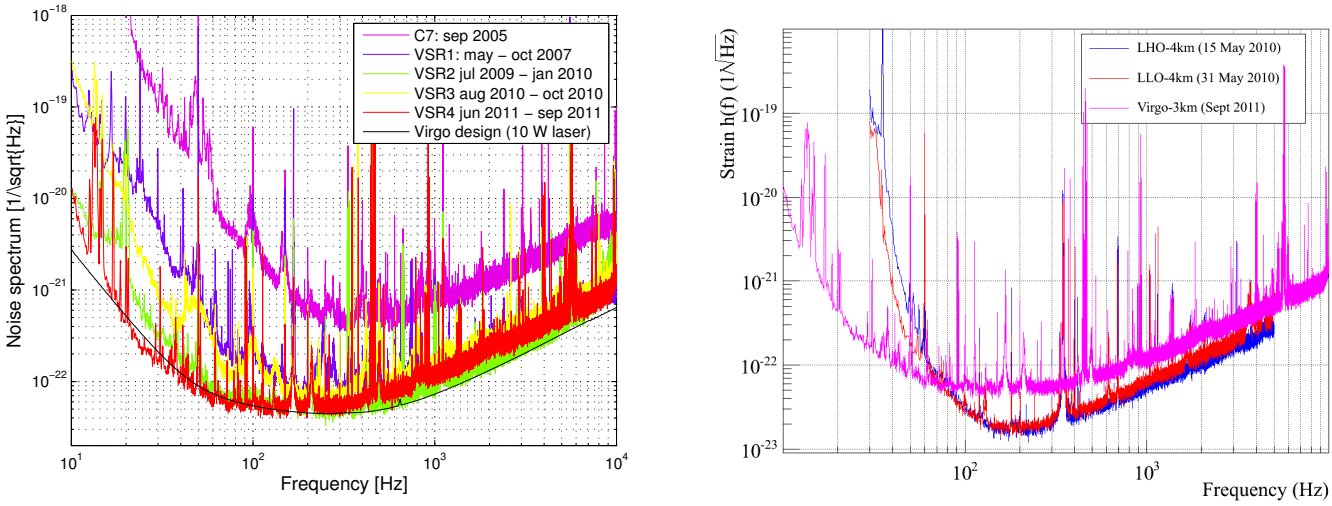

Figure 4.2: Left: Evolution of the Virgo sensitivity between 2005 and 2011. Right: Comparison between the best sensitivities reached by LIGO Hanford (blue), LIGO Livingston (red) and Virgo (magenta).

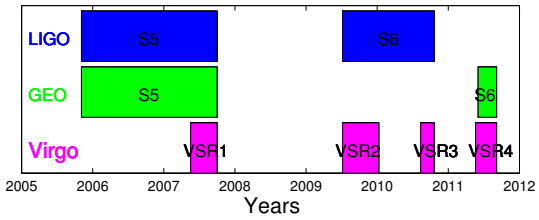

Figure 4.3: Virgo, LIGO and GEO science runs schedule between 2005 and 2011.

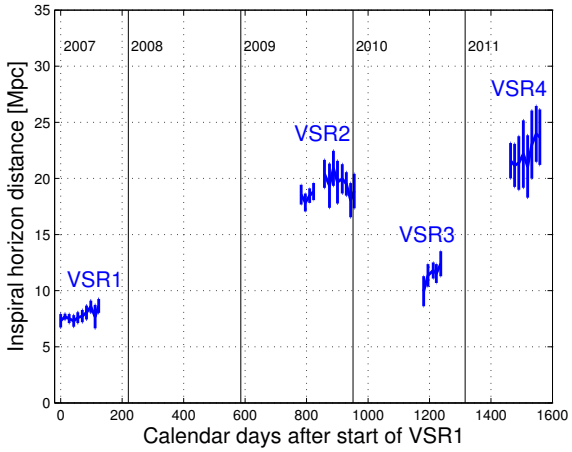

Figure 4.4: Virgo horizon distance evolution between 2005 and 2011. The horizon is the distance at which an optimally oriented and located binary neutron star is detected with SNR>8.

4.4 Glitches and couplings

In the following we give examples of the most representative non Gaussian noise disturbances that couple with the laser light that transports the GW signal and we explain their origin and the noise path. For some of them, we indicate how the affected periods can be flagged. This list of examples is not exhaustive.

4.4.1 Acoustic glitches

Acoustic noise in the experimental buildings will generate extra noise in the dark fringe signal, despite the acoustic enclosures that have been installed over the years around the most critical optical components. One of the most popular example are the airplanes or helicopters flying over Virgo (Pisa airport, 15 km away from Virgo, hosts military aircrafts that fly at rather low altitude over Virgo). In Figure 4.5 the glitch frequency modulation due to the Doppler mechanism is clearly visible in the dark fringe in an acoustic and a seismic channels. In this example, the coupling between the external disturbance and the dark fringe is rather clear (frequency and duration match in the dark fringe, acoustic and seismic channels).

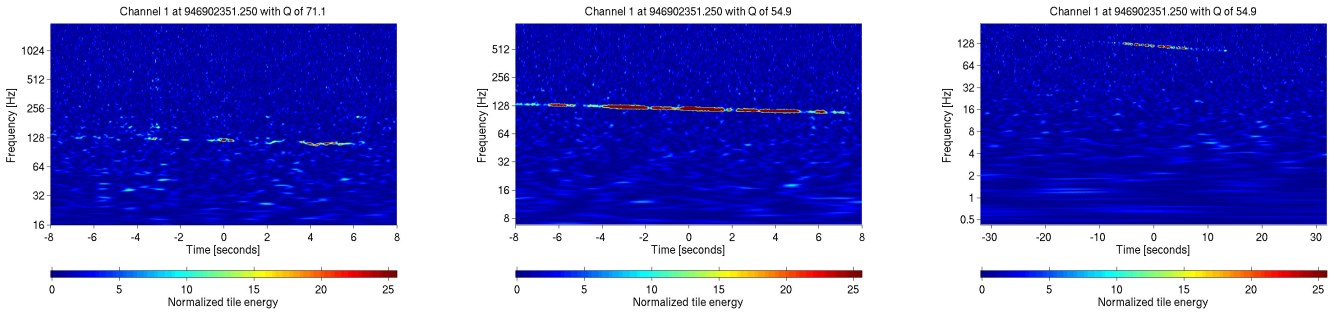

Figure 4.5: Spectrogram of dark fringe (left), central building acoustic (middle) and seismic (right) channels.

But this is not always as clear. For instance it is not uncommon that glitches in the dark fringe are much shorter than the glitches seen in the auxiliary channel. Sometimes frequencies do not match. It depends on the coupling path that can sometimes induce up-conversion. That is one of the reasons why only time coincidence (2 events must overlap in time) is usually requested to associate a glitch in an auxiliary channel to a dark fringe glitch.

Airplanes are detected in acoustic and seismic probes. Several acoustic and seismic probes are recording data in each building. Usually many probes simultaneously see the airplane event, which is rather well detected by just computing the root mean square (RMS) in several frequency band (64 – 128 Hz, 128 – 256 Hz and 256 – 512 Hz). Glitches due to an airplane are thus easily vetoed. Glitches due to acoustic noise in buildings different from airplanes (it seems that sometimes objects drop from platforms or benches) are also easily and well efficiently flagged.

4.4.2 Magnetic glitches

Both in VSR1 and VSR2, rather loud glitches were observed at $\sim$ 50 Hz in coincidence in the dark fringe and in many magnetic probes. As the rate of these glitches in VSR2 was rather high (up to several dozens per day), some investigations by the commissioning team have been carried out to understand their origin. It turns out that glitches observed in the Mode-Cleaner, central and arms' end buildings are of different origin.

The most frequent glitches visible up to 3 times an hour in winter months had their origin located in the Mode-Cleaner building. The source has been identified to be the compressor machine which cools down water for the building air conditioning (water chiller) or the heater [360]. The compressor is located outside the Mode-Cleaner building. This is a triphased engine, connected to the isolated power supply (IPS) line. When the water temperature exceeds a given threshold, the engine starts from rest; it draws an intense electric current which causes a drop in the IPS line voltage, about 10 V drop lasting about 20ms that generates an intense magnetic transient visible in magnetic probes. Glitches are not visible in UPS line voltage but in some error signals related to the injection system and used for the control

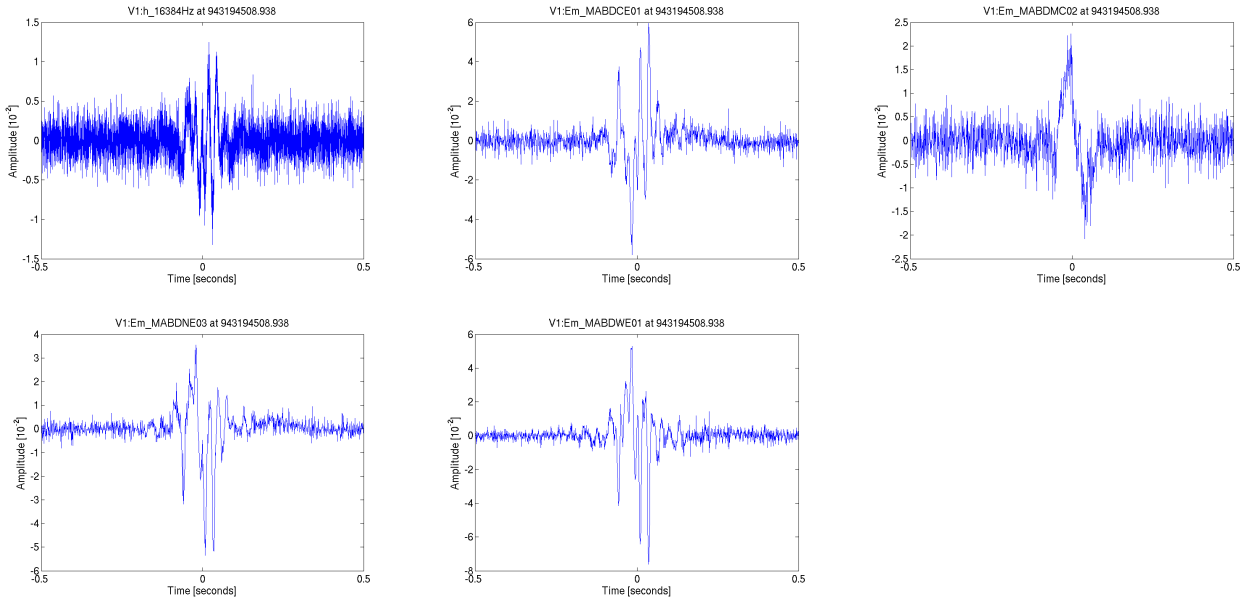

Figure 4.6: Magnetic glitch seen in the time series of h(t) and some magnetic probes located in all buildings (CE, MC, NE and WE).

of Virgo. The electronic crates of the injection system are in the laser laboratory room that hosts the laser and all benches with optical components that prepare the laser beam injected into Virgo. Two hypotheses to explain how this couples to the dark fringe have been proposed:

1. The glitch travels to the Central Building via IPS (a voltage drop is detected in Central Building IPS sniffers and magnetometers), and is picked up through ground loop currents by the injection system electronics. Glitchy error signals are used to control the interferometer that hence transmit glitches.

2. The dark fringe glitch is actually due to a real variation of Virgo arms' length (thus found in error signals). This variation could be caused by the Mode-Cleaner mirror moving because of magnetic force exerted on it by magnetic transient in the Mode-Cleaner building.

In the first scenario, which is privileged, electronic crates have to be better isolated not to pick up magnetic glitches.

Magnetic glitches generated by an air conditioning water chiller have also been observed in the WE building magnetic probes but, contrary to the MC building case, these glitches are not transmitted into the dark fringe. On the contrary, magnetic glitches observed simultaneously in WE, NE, and CE building magnetic probes are observed in the dark fringe channel, most probably because of some ground loop pick ups in some electronic components. These glitches observed in VSR1 and VSR2 are rarer than the MC magnetic glitches, and so far no action has been taken to track them down. In both cases, as the signature of these glitches are rather clear (huge glitch in magnetometer channels), vetoes based on band RMS of 3 magnetometer probes in each building (MC, WE, NE and CE) have been designed. As magnetometers can be noisy, the veto is active when the band RMS of at least two channels exceeds the threshold. This redundancy greatly avoids to veto periods of good data. Figure 4.6 shows a magnetic glitch seen in dark fringe and in magnetic probes (time series) of all buildings (NE, WE, CE and MC).

4.4.3 Seismic glitches / scattered light (VSR2)

Seismic noise limits the sensitivity of Virgo below a few Hz, but it also reduces the searches sensitivity because it indirectly generates a large amount of noise triggers at higher frequencies. These triggers are most of the time not as loud as, for instance, magnetic glitches, but they are very numerous and hence coincident analyses fail at reducing their background rate as the coincident rate is proportional to each individual detector trigger rate.

The Virgo site ground motion between 0.1 and 1 Hz has a typical peak frequency of 0.3 Hz which is mainly due to sea waves (Cascina is located roughly at 20 km from the sea coast). In case of quiet sea conditions, the peak amplitude is 0.3 μm. In case of rough sea, the peak amplitude can be 30 times larger. These moments are rare but more frequent during winter and will last from few hours up to few days during which the trigger rate is high (see Figure 4.7) with glitches with frequency up to $\sim$ 150 Hz. The arch shape in the time-frequency plane (see Figure 4.7) gives a very clear signature to these glitches [361] as explained below.

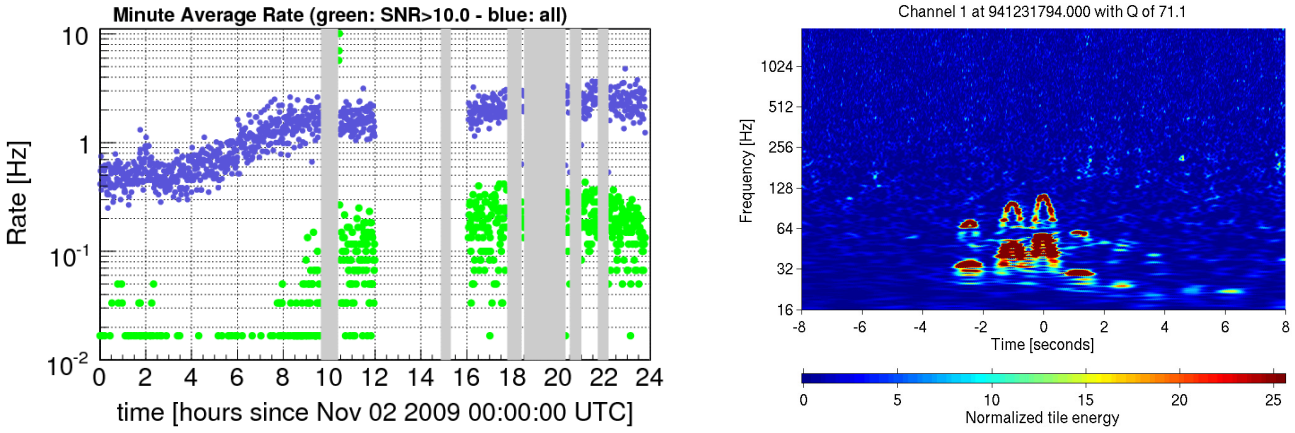

Figure 4.7: Left: Increase of the Omega burst trigger rate on November 2nd after 6:00 UTC. Triggers' rate is in blue while trigger rate for triggers with SNR>10 are represented in green. Right: Example of a glitch responsible for the trigger rate increase due to micro-seismic noise that couples with diffused light on the WE optical bench. The duration of the arch corresponds to the sea activity frequency ($\sim$ 0.3 Hz). The frequency of the glitch got up-converted. A second harmonic due to light that scatters two times in the bench is also visible.

One way low frequency seismic noise get up-converted into the dark fringe was through scattered light. For instance the optical benches located behind the 2 arms' end mirrors host many optical components that are not seismically isolated (the bench is set on the ground). Spurious beams, due to multiple reflections, can hit a component that is excited by the seismic noise and then scatter back into the main beam. The consequence is a phase modulation by the displacement noise of the scattering surface. The phase modulation of a very small fraction (few ppm) of scattered light is strong enough to spoil the dark fringe. That generates glitches at higher frequency (up to 100 Hz) while the seismic excitation is below 1 Hz, illustrating the up-conversion mechanism [362, 363]. The optical benches are the main sources of back scattering light, but the Brewster window, the baffles, the cryogenic trap and the suspended benches are also locations where seismic noise couples with dark fringe through scattering light. The number of visible arches depends on the number of reflections. In Virgo VSR3 data up to 3 arches have been observed on time-frequency plots.

The problem has been reduced (by less than an order of magnitude) after VSR1 by dumping spurious beams, cleaning optics, damping mechanical resonances of optical mounts on optical benches, but is still a major source of glitches when the micro-seismic activity is high. VSR2 data thus required the development of a specific veto to reduce the disturbance of these micro-seismic glitches. It turns out that computing band RMS of the auxiliary seismic channels was not providing a good veto (lots of false dismissal periods). A better way to define a veto was to compute the velocity of the top stage of the suspension using position sensor channels. The velocity of the top stage is a good measurement of the displacement noise that generates phase noise. Furthermore, it can be shown that the glitch frequency is proportional to the displacement noise velocity. The higher the velocity, the higher is the glitch frequency [363]. A threshold on the velocity of the top stage (15 $\mu m/s$) provides a very efficient veto (see section 4.5.6).

The problem of diffused light during all Virgo runs was mostly important for the WE external bench because of the larger transmission factor of the WE mirror (40 ppm) with respect to NE mirror (10 ppm).

4.4.4 Seismic glitches / alignment control looseness (VSR2)

When the micro-seismic noise around 700 mHz becomes important, it worsens the angular control accuracy. Angular degrees of freedom, Θ_x (pitch) and Θ_y (yaw) of the mirrors are controlled with low bandwidth control loops and low gain to avoid to spoil the dark fringe with control noise. Θ_x control is especially affected by high frequency micro-seismic noise where Θ_x control loop gain is low.

The coupling with the dark fringe is quite interesting; when the angular control correction signals are far away their nominal values, glitches at well precise frequencies (165, 210 and 420 Hz) show up in the dark fringe as shown in Figure 4.8. These frequencies correspond to known resonances of the suspended detection bench [364]. The glitch rate is around 1.5 Hz (2 times 700 mHz) when micro-seismic noise is high. It has been shown that these glitches occur when Θ_x, and to a lesser degree, Θ_y control signals sensitive to the differential angular movement of the cavities get extremal values (in both edges). A veto is then easily designed by just thresholding the alignment control signals.

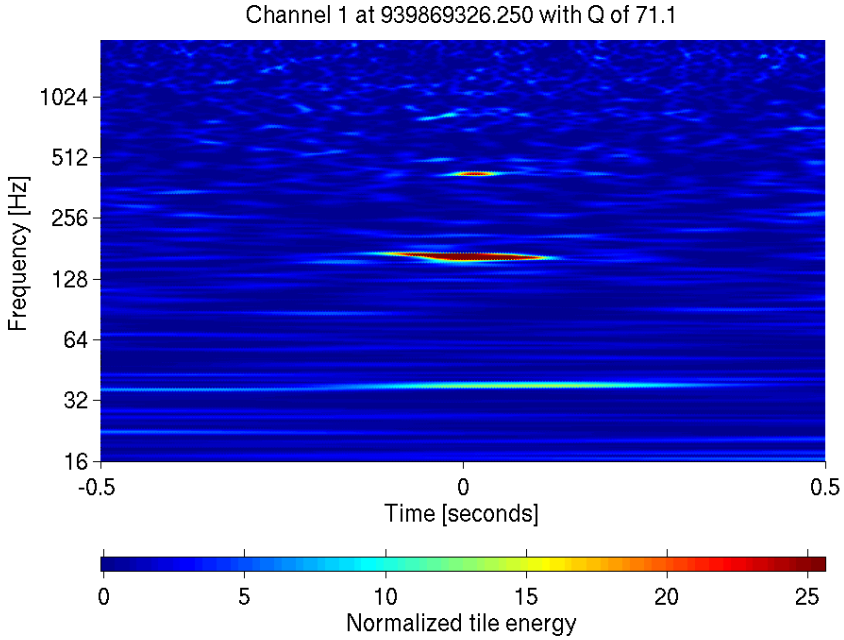

Figure 4.8: Example of a glitch due to a coupling between micro-seismic noise and the misalignment of the Fabry-Perot cavities (extremal values of the angular degrees of freedom control signals).

4.4.5 Default of the alignment control in C7 data

The 7$^{\text{th}}$ commissioning run of Virgo in September 2005 gives another nice illustration of non stationary data due to an alignment control default. Burst analyses [1] noticed that triggers are not uniformly distributed over time but seem to show up in bunches lasting up to a few seconds. Figure 4.9 shows the whitened GW strain channel's amplitude and its spectrogram during a data period that contains a bunch of burst triggers (around t=13 s). These events have been called Bursts of Bursts (BoBs).

The spectrogram shows that the event has a broadband frequency content contrary to most of the events caused by external disturbances (see for example the glitches due to acoustic or magnetic noise). This broadband spectral signature gave clues that helped to identify the BoBs as local increases of the noise level due to an increase of the coupling factor between the frequency noise (which is dominant at high frequency for C7 [365]) and the dark fringe channel.

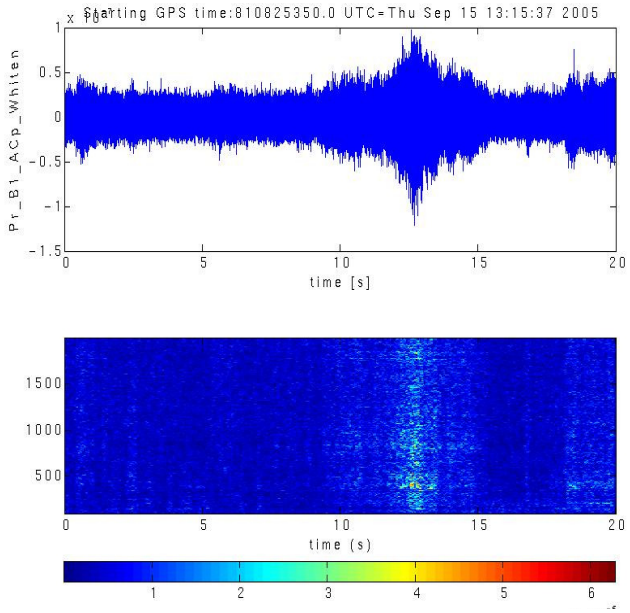

Figure 4.9: An example of a non stationary period in C7 data (Burst of Burst) around t=13 s. The upper plot shows the whitened dark fringe channel amplitude as function of time, while he bottom plot is the corresponding spectrogram.

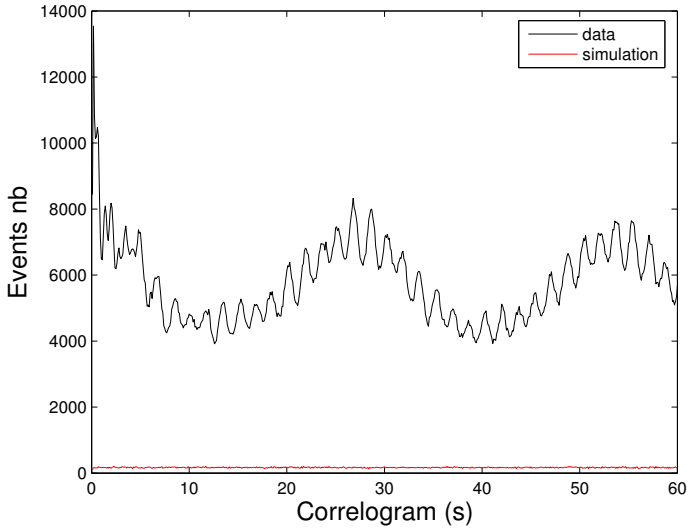

Figure 4.10: The correlogram of the events detected by the burst algorithm MeanFilter [344] with a 1 ms window. A peak around T=27 s is present, with a replica at 54 s. A 0.6 Hz modulation is also visible; this frequency corresponds to the pendulum mode of the last stage of the Virgo suspension.

We then tried to identify the cause of the variations of the coupling factor. The presence of a peak around t=27s in the correlogram of the burst events (see Figure 4.10) provided evidence that the residual angular motion of the mirrors could be playing a role. Indeed, 27 s corresponds to the frequency of a mechanical resonance between Filter 7 and the marionetta of the suspension that, if excited, may induce mirror angular degrees of freedom excitation.

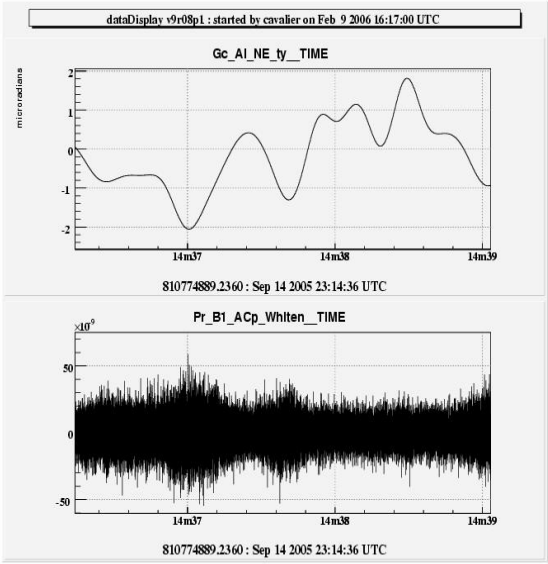

Figure 4.11: Above: The θ_y angular position of the North End mirror. Bottom: The corresponding whitened dark fringe signal. Each time the NE mirror takes an extreme negative value the RMS of the dark fringe increases.

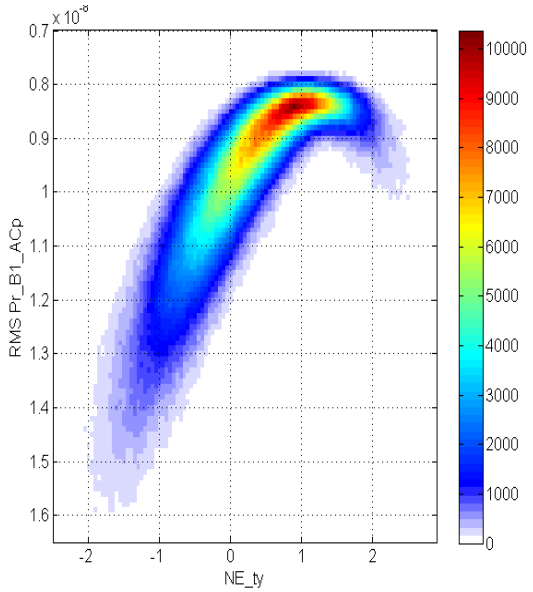

Figure 4.12: RMS (computed over 2 ms) of the dark fringe signal as function of the θ_y value of the North End mirror.

The correlation between BoB events and extremal (negative) values of the θ_y angular tilt of the NE mirror appears clearly on Figures 4.11 and 4.12 where the RMS (computed over 2 ms) of the dark fringe signal is plotted as function of the θ_y value of the NE mirror. This quadratic dependence is also present with a lower significance for the other angular degrees of freedom (θ_x and θ_y for all mirrors).

One way to monitor the dark fringe noise increase due to the laser frequency coupling variation is to consider the amplitude of the 1111 Hz line which is introduced at the level of the laser frequency control system to monitor the

coupling of the laser frequency noise in the dark fringe. There is also a clear time coincidence between the 1111 Hz line amplitude height and the NE mirror large tilt. This has been used to define a veto for the C7 run burst analyses [2].

4.4.6 Phase noise glitches

High frequency glitches (> 2 kHz) have not attracted lots of attention. One of the reasons is that the most promising sources of GW transient are below 2 kHz. Furthermore the glitch rate at high frequency and the glitch variety is lower than in the low frequency region. However, the high frequency spectrum of Virgo exhibits various phenomena of non stationary data characterized by the presence of glitches at well identified frequencies[3]. For instance, Figure 4.13 shows the presence of glitches at ~ 2930 Hz. The spectrogram of the dark fringe signal shows clearly that this frequency region is highly non stationary. A clear dependence with alignment control signal has been shown. More interestingly, the glitch modulation observed in the dark fringe seems perfectly correlated with the extremal values of the other quadrature of the demodulated signal at the dark port supporting the idea that the glitches observed at high frequency are due to phase noise whose coupling is changing with time through a mechanism that has not been identified [366].

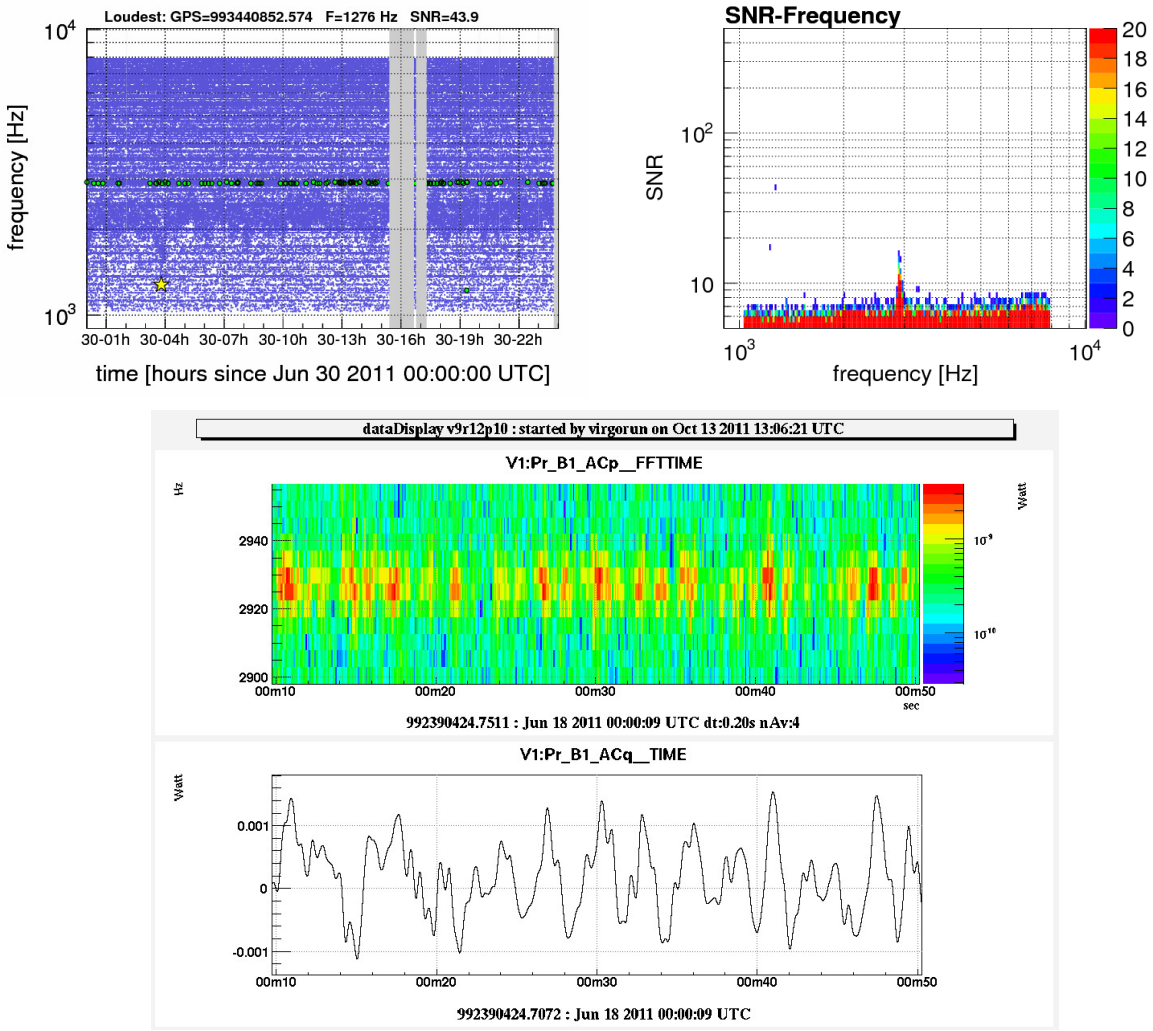

Figure 4.13: Upper: Distribution of high frequency glitches as function of time and frequency. Lower: Spectrogram of the dark fringe and times series of the other quadrature of the demodulated signal at the dark port.

[3]This is also true for LIGO Livingston to a lesser extent

4.4.7 Dust glitches

Most of the laser beams carrying the GW signal travel through high quality vacuum vessels that guarantee the absence of dust falling down through the laser beams. Yet, the laser source and the detection optical benches are in air. In [367] one shows that a $10 - 100\,\mu$m size dust particles crossing the beam inside a cavity generates large amplitude transient signals. The presence of dust particles in many parts of the detectors (towers, laser and detection labs, brewster windows, mirrors, ...) has been known since the beginning of the detector installation, but it became more and more clear that dust crossing beams were visible in the GW channel [368]. Experimentally, this has been confirmed before VSR2 in 2009 around the detection bench [369]: the number of glitches visible in the GW channel increased after opening the detection lab door for less than 1 minute as shown in Figure 4.14. On average 5 large glitches per minute were visible for almost 1 hour before the dust settled in the room. After this demonstration, Plexiglas covers over the main beam paths have been installed in order to reduce the dust contamination. Dust storms, as visible in Figure 4.14, no longer occur. From time to time glitches that have the signature of a dust crossing a beam are visible and a specific veto based on the fact that dusts crossing a beam generate similar amplitude glitch in both quadrature and in-phase channels of the interferometer dark port output has been developed (see section 4.5.5).

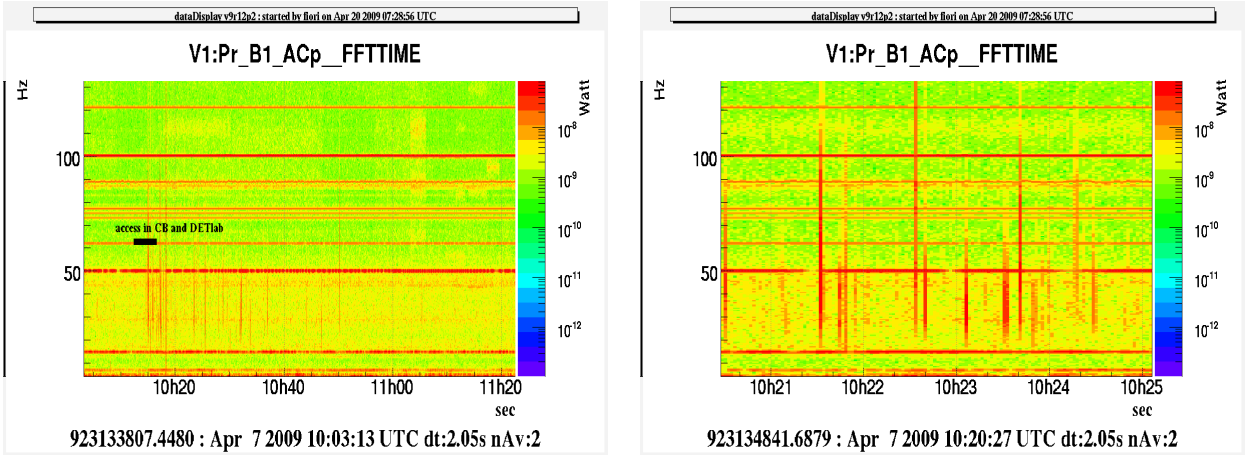

Figure 4.14: Spectrogram of the GW channel showing a storm glitches due to dust crossing beams on the detection bench after the door of the detection laboratory was opened for a dozen of seconds. It took roughly 1 hour for dust to settle down. The right figure is a zoom of the left panel.

4.4.8 Main laser glitches

The main laser is a rather complex system as the laser must be stabilized in power and frequency at a very stringent level: the laser frequency noise couples with asymmetries in the interferometer arms' cavities to generate phase fluctuations. The frequency stabilization requirements ($4 \times 10^{-6} Hz/\sqrt{Hz}$ [370]) can only be achieved by using the arm Fabry-Perot cavities as a reference. A complex control system has been implemented to maintain the laser noise below the specifications. Failures or malfunctioning of control loops have been found to be a source of loud glitches in almost all runs. For instance, when the matching of the pre mode-cleaner cavity worsens, the actuation range of the power stabilization loop is too small and saturation generates glitches in the laser power after the input mode-cleaner. The glitches are broad-band as illustrated in Figure 4.15

4.4.9 Thermo-mechanical glitches

The temperature inside the central building and the end arms' building is controlled accurately to avoid thermal elongation/contraction of the mechanical structures. This is not the case of the input mode cleaner tunnel. For many years, a series of glitches have been observed predominantly around noon and midnight. They are coincident with glitches in seismometer probes around the injection and the mode cleaner towers and sound like a metallic membrane

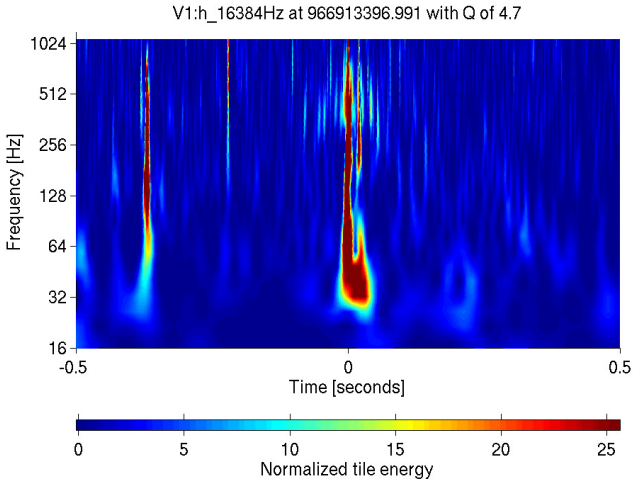

Figure 4.15: Example of broad-band glitches due to the main laser power stabilization failures during VSR3 run.

that buckles [371]. During VSR4, the noise path mechanism has been understood: When the external temperature gradients are the largest, elongation/contraction forces can exceed the static friction that maintains the tube on its support. When this happens a mechanical shock occurs and propagates along the tube up to the injection and mode cleaner towers. These glitches are easily vetoed thanks to a seismometer probe installed on the input mode-cleaner tube.

4.4.10 Thermal compensation control glitches (VSR2)

The absorption of a few ppm of the laser power in core optics distorts the surface of mirrors (thermal lensing effect) and hence changes the optical properties of the Fabry-Perot cavities. Increasing the laser power to decrease, for instance, the shot noise requires the ability to compensate the deformation such that lock acquisition is still possible. Between VSR1 and VSR2 (2008), a thermal compensation system (TCS) has been installed for the 2 input mirror of the Fabry-Perot cavities to be able to operate Virgo with injecting $\sim$17 W inside Virgo during VSR2. This consists of two CO_2 annulus laser, DC pre-stabilized, installed on benches located around each input mirror tower. Unfortunately, the TCS can introduce displacement noise through its CO_2 laser intensity fluctuations which were found to be the origin of some glitches in the dark fringe channel. Figure 4.16 gives an illustration of such glitches. The SNR are usually moderate, smaller than 30, but the glitch rate can be dominated by TCS glitches.

In October 2009, in the middle of VSR2, an active control system has been installed to reduce the laser intensity fluctuation by a factor $\sim$10 [372]. The number of glitches decreased nicely afterwards. A veto has been developed based on the auxiliary channels that record the North Input and West Input mirror CO_2 laser power.

4.4.11 Missing samples in control correction (VSR1)

In August 2007, during VSR1, some very loud glitches have been identified to be due to a loss of synchronization between the Global Control and the photodiodes that provide input signals for the 10 kHz longitudinal correction. Usually a loss of synchronization leads to a lock loss. In this particular case, when it happened concomitantly with the presence of a strong 5 kHz line in the longitudinal correction signals, strong transients were generated in the dark fringe. The 5 kHz line (which is harmless for transient searches) is not always present. Fortunately some Global Control monitoring channels gave each second the number of samples lost per second. When this information is not available, a simple check of correction signal consecutive samples has been done to define a veto (when a sample is lost, the correction signal samples have the same value). Figure 4.17 shows the SNR of these glitches (marked by a blue cross) as function of time.

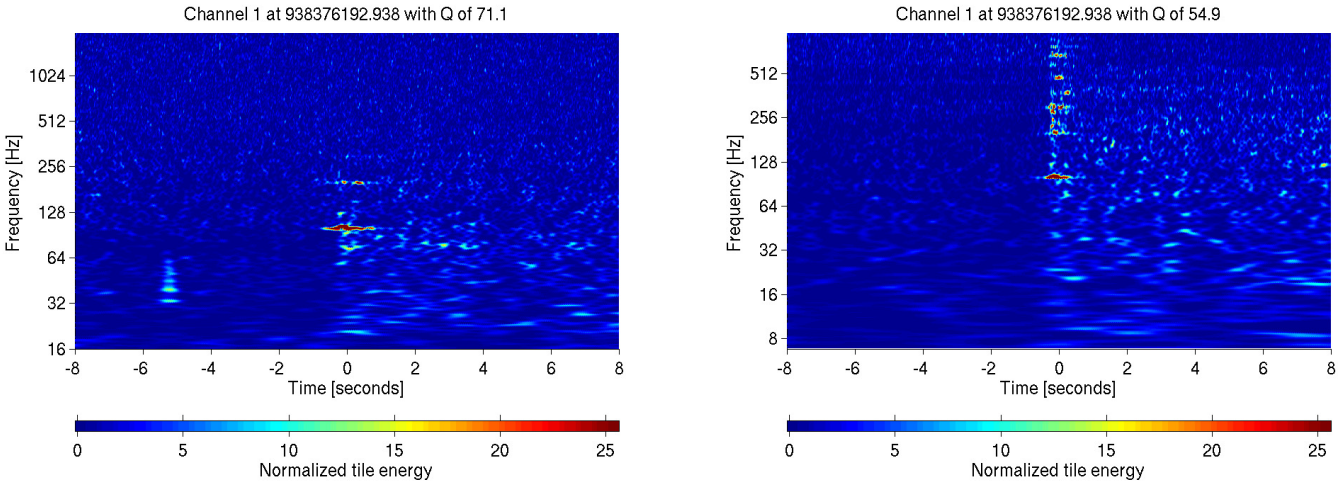

Figure 4.16: Example of a glitch due to the TCS CO_2 laser intensity fluctuation. Left: Dark fringe channel. Right: TCS North Input mirror laser power monitoring channel.

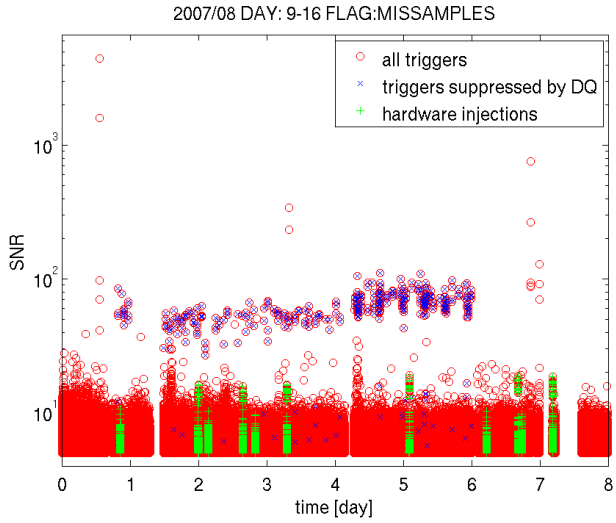

Figure 4.17: SNR of Omega triggers as function of time (first week of August 2007) showing the loud glitches generated by a loss of synchronization between the Global Control and the photodiodes. All loud glitches due to the loss of synchronization are vetoed.

4.4.12 Piezo malfunctioning (VSR1)

During VSR1, many piezo electrical devices moving or controlling mirrors on optical benches have been found responsible for the introduction of noise in the dark fringe. This was especially the case of a piezo involved in the control of the beam entering into the reference cavity that is used to stabilize the laser frequency and lock the common mode of Virgo. A "dirty" voltage (not filtered at high frequency) applied to the piezo introduced mechanical noise on the injection bench that induced phase noise inside the input Mode Cleaner cavity that then propagated to the dark fringe. The source of the noise has been reduced by simply filtering the voltage (a resistance has been added). Unfortunately this happened only 2 weeks before the end of VSR1. The glitch reduction was substantial as seen on Figure 4.18,

especially around 600 Hz but also around 250 Hz. All piezo devices and more generally all control actuators, were regularly incriminated for the presence of glitches in the GW channel. In many cases, manual tests are necessary to identify the glitch generation mechanism as it is hard to monitor all possible sources of malfunctioning.

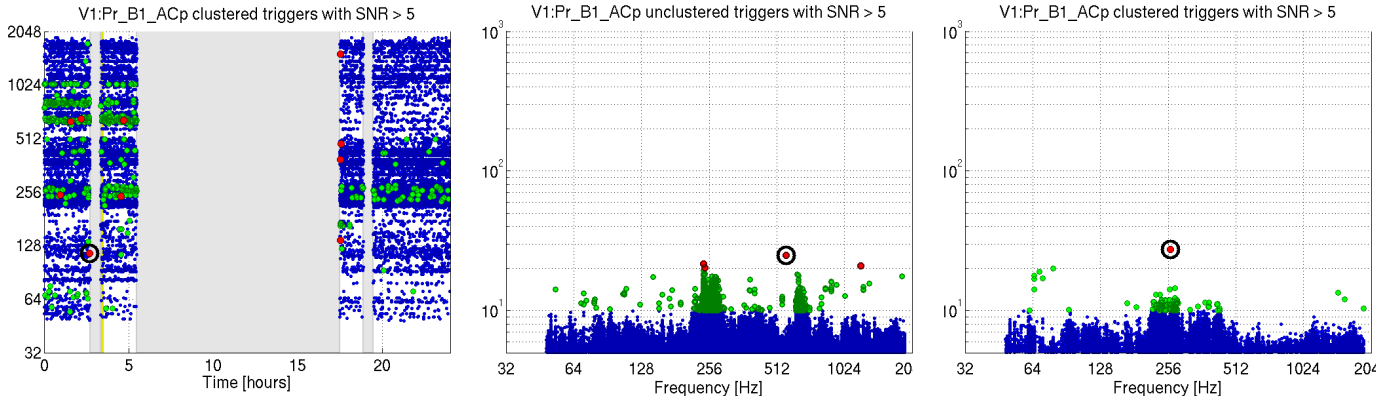

Figure 4.18: Left: Distribution of Omega triggers in time and frequency during the day when the Input Bench piezo has been fixed. The grey zone corresponds to the time of intervention. Middle and right: Distribution of Omega trigger SNR as function of their frequency before the intervention (middle) and after (right).

4.4.13 Mirror glitches

Some glitches with a very clear signature (sharp step in the GW channel as shown in Figure 4.19) have been observed few hundreds of times per run. They have been associated with the excitation of NI and WI mirrors internal modes (5.5 kHz drum and 3.9 kHz butterfly modes). They correspond to a sudden change of the surface of the mirror (relaxation process). In the case of the WI mirror, these glitches have been observed for the first time in 2008 a few weeks after the magnets and some spacers were glued with water-glass instead of a ceramic glue [373]. For the NI mirror, the glitch amplitude and the glitch rate were lower, but as only ceramic glue was used for magnets, there is still some uncertainty about the exact mechanism of glitch generation. As no auxiliary information is available to monitor what is happening, no veto could be developed. However, the signature of these glitches in the GW channel is clear and the glitch rate was low enough to decide that if by accident one of the glitches passes all the selection criteria, it would be easy and safe to discard confidently a GW trigger that would have had the signature of a mirror glitch.

4.4.14 Radio frequency glitches

High frequency electromagnetic noise overlapping the 6.26 MHz modulation frequency can be picked up in photodiode signals before demodulation and thus be visible in the GW channel below 20 kHz [374]. The perturbation is usually not stable in frequency nor in amplitude and an excess of glitches are generated as shown in Figure 4.20. Radio frequency noise is suspected to be sniffed by some Virgo electronic equipments and transmitted through communication serial links. It is not always simple to identify the radio frequency source to mitigate the noise or suppress the coupling, but sometimes, by changing an external condition, the problem is attenuated. This is what happened during VSR3 for the RF glitches; it has been discovered that by decreasing the data acquisition room temperature by 1 degree, the modulation frequency band pollution could be reduced as show in Figure 4.20.

4.4.15 Saturation glitches

Correction signals in control loops that saturate the electronics (ADC, DAC, coil drivers, ...) can generate very loud glitches. This is especially the case of the photodiode signals that must remain within their nominal range ($\pm$ 10 V). When saturation happens in the photodiode pre-amplifiers the situation is more tricky, as other effects (harmonics) than a simple glitch can happen.

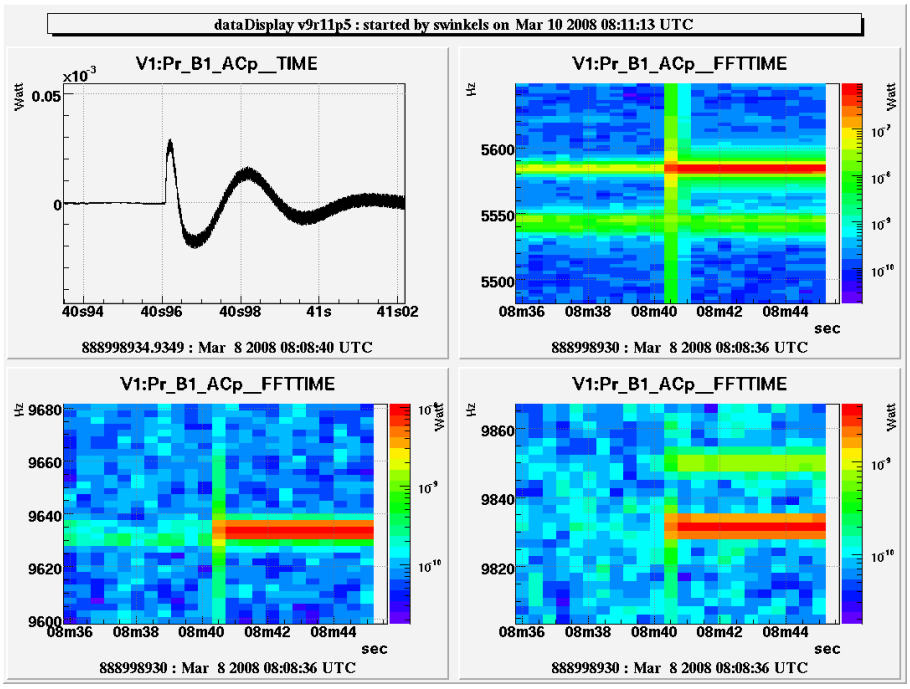

Figure 4.19: Dark fringe time series exhibiting a huge deviation from Gaussian noise. It looks like the response to an delta function excitation. The time frequency maps show different high frequency resonances excited by a sharp change of the mirror surface.

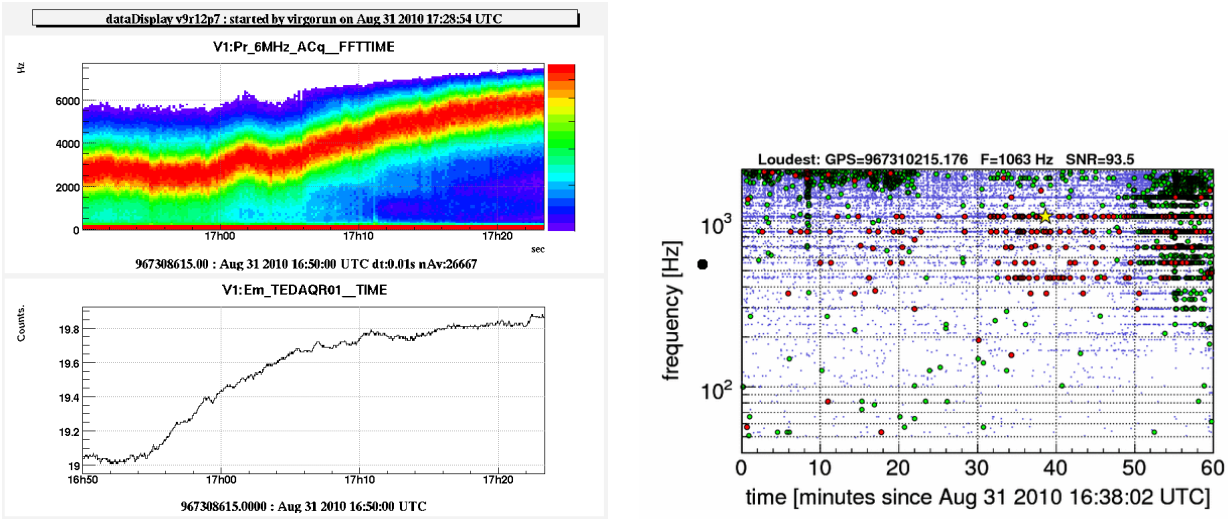

Figure 4.20: Left: Spectrogram of 30 minutes of data showing an excess of noise between 2 and 6 kHz that drifts over time following the data acquisition room temperature increase. The excess of loud glitches (SNR $>$ 10 glitches in red) at high frequency (between 1 and 4 kHz) is visible on the right plot. The correlation between the glitch excess at high frequency and the temperature in the DAQ room has been observed but has never been understood.

4.5 Virgo data quality monitoring

4.5.1 General description

So far we have discussed glitches investigations because this is a major concern for many short GW signal searches, but this is only one part of the Virgo detector characterization endeavors. Despite the huge effort of the commissioning teams, ground based GW detectors' noise is strongly non Gaussian and non stationary. Permanent care and monitoring is needed. Over the years, Virgo has improved its monitoring system to be able to detect as quickly as possible problems and long term drifts that deteriorate the quality of the data, both in terms of sensitivity and glitch rate [375]. In the following we will sketch briefly what are the main components of the detector characterization in Virgo in order to put into a context the work presented here about glitch investigations and vetoes for data analysis. Figure 4.21 sketches the different activities that are carried out to estimate the detector sensitivity, to hunt any source of extra noise, to identify noise lines, to generate vetoes against known sources of glitches, and to determine new coupling between the dark fringe and a noise recorded in the auxiliary channels.

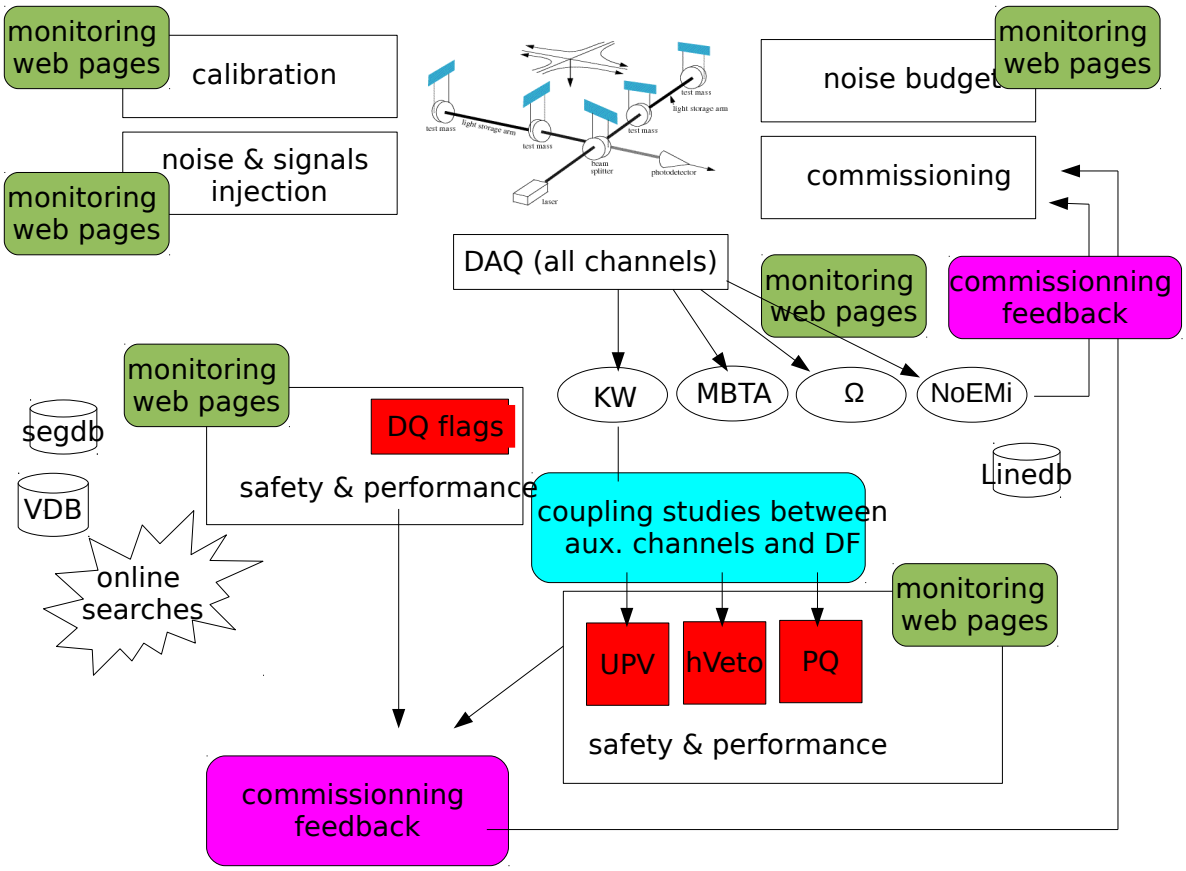

Figure 4.21: Virgo detector characterization elements. Each of them correspond to an activity or a piece of software that processes Virgo raw data. Most of the activities generate automatically web pages that are useful for commissioning and shifters.

The role of the commissioning which includes a team hunting for any source of noise that shows up and limits the sensitivity of Virgo is crucial. Much of the detector characterization is done a posteriori, but using monitoring information produced online. The environment (seismic, acoustic and magnetic noise, temperature in buildings, wind outside) is monitored thanks to many probes installed around the detector, alarms are raised in the control room whenever one of them detects something unusual. An important aspect of the work carried out by the commissioning

team is the understanding of the sensitivity noise curve in the frequency domain. The goal is to determine which sources of noise contribute and thus limit the detector's sensitivity. From a theoretical point of view, if the environment of the interferometer was perfect, the power spectrum should be limited by "fundamental" noises: Seismic noise below 10 Hz [376, 377]. Then thermal noise of the last stage (wires, mirror substrate and coating) of the suspension should be the dominant source of noise until 300 Hz. The high frequency part of the noise power spectrum is expected to be limited by shot noise. In reality the Virgo noise spectrum is much more complicated (see Figure 4.2). For instance, above 100 Hz, the only visible resonances should be the violin vibration modes of the mirrors. Many more structures are present in the Virgo noise power spectrum, and each of them needs to be identified. Usually, noise sources are gathered unto two categories:

- environmental: For instance magnetic fields in building can induce forces on mirrors. Seismic noise can be re-injected because of the presence of diffused light on external benches, etc
- technical: Laser frequency noise, oscillator phase noise, shot noise, electronic noise, actuator noise, longitudinal and angular control noise.

For many of these known sources of noise, methods to measure their level of coherence in the dark fringe have been developed [378]. The incoherent sum of all known sources of noise can be compared to the measured noise power spectrum. If most of the measured sensitivity curve is explained by the contribution of a given source, such "noise budget" figures reveal structures that are not yet modelled by any known noise source (see Figure 4.22). For instance during VSR2, in the frequency band between 150 and 300 Hz there was some non explained structures. Noise investigation and mitigation are constantly made. When the noise coupling mechanism is discovered, if it cannot be suppressed or attenuated, it will be modelized and added to the automatic noise budget which is updated regularly.

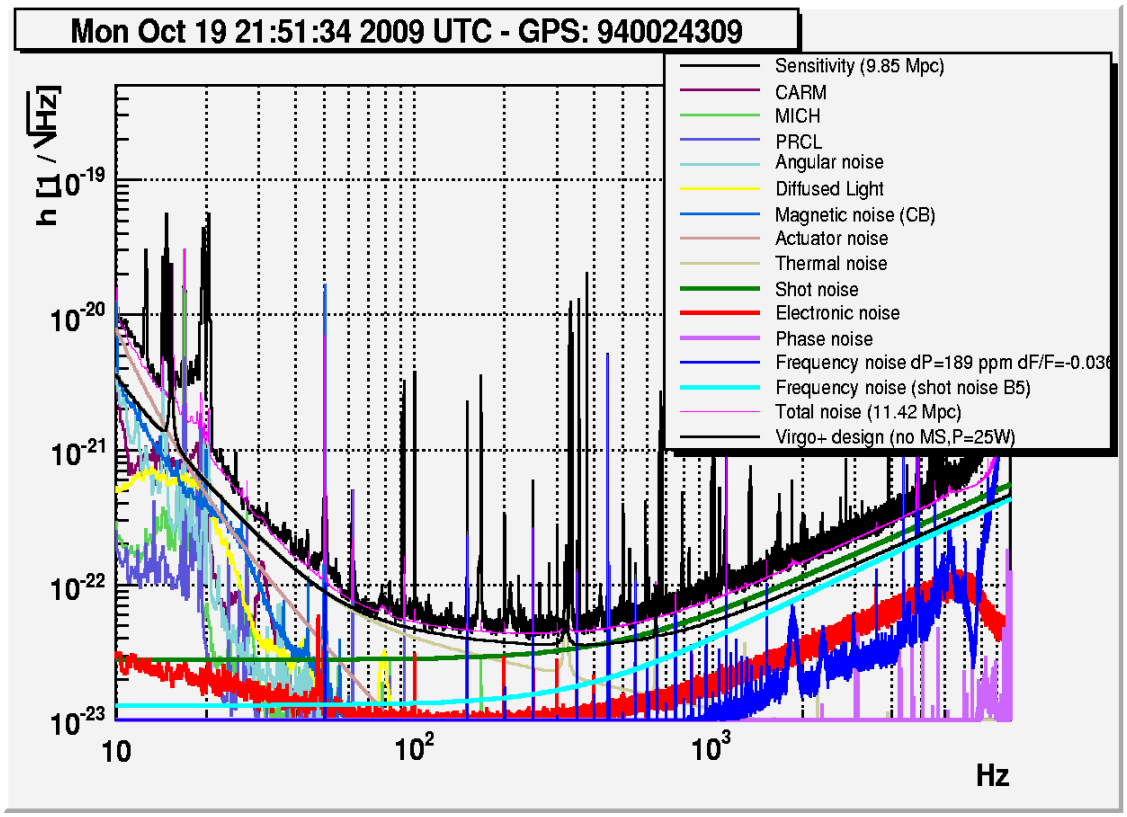

Figure 4.22: VSR2 noise budget (October 2009): Each estimated or measured noise contribution to the Virgo sensitivity curve is shown in addition to their incoherent sum (pink) which can be compared directly to the measured sensitivity curve (black).

Calibration is also an important task that requires the monitoring and performance measurements rather regularly in order to follow changes in gains and the actuators' parameters. Calibration ultimately allows one to estimate the sensitivity curve shown many times in this report. It consists in measuring the frequency response of the mirror actuation system and in converting the output power into a strain amplitude [379, 380].

Both noise budget measurements and calibration require the injection of well known monochromatic signals or white noise. To inject a GW strain signal into the interferometer, a force is applied upon one of the mirrors of the interferometer's arms. In case of a well defined signal (defined for instance with an analytical waveform), the force is derived from the signal by taking the second derivative and applying the right scaling factor. That generates a differential change of the arms' length which mimics the path of a GW signal. GW hardware injections are also useful for data analysis to test the capability of the pipelines to recover GW signals. It is also useful to check if a veto is safe. Section 4.5.3 gives more details about the hardware injections of transient signals done during the runs.

To describe a spectral line, one usually uses the frequency and the amplitude of the peak maximum. The line width is the peak width at half maximum. Other parameters like the persistence that gives the fraction of time the line is visible and the critical ratio which is the difference of the peak amplitude and the mean value of the spectrum divided by the spectrum standard deviation are also important to fully characterize spectral lines in Virgo. As already mentioned, the line hunting focus is on those which do not have a well-known origin. Non stationary lines are particularly troublesome since they are likely producing transient events or can cross the frequency bands of a known pulsar of interest. A dedicated tool has been developed in Virgo: NoEMi (Noise Event Miner) is able to analyze Virgo h(t) and a subset of auxiliary channels in real time. On a daily basis, it looks for time and frequency coincidences between the dark fringe and the auxiliary channels. It especially raises an alarm when noise lines are detected within the frequency band of a known pulsar. Many noise lines present in Virgo data have been identified. Most of them are generated by motors and electronic devices operating in a periodic working cycle. This includes machines for air conditioning, vacuum pumps, cooling fans for electronic devices, digital clocks regulating data exchange between electronic devices and the mains power supply [211].

The last element of the Virgo data quality activities is the generation of vetoes that will be used by GW transient searches. The description of these vetoes and their performance to reduce the loudest glitches is explained in the next sections. Since VSR2, most of the vetoes are produced online with a latency for online GW searches of less than 1 minute. This strong requirement comes from burst online searches that aim at sending alerts to optical telescopes and satellites to follow-up the most significant GW candidates within few minutes up to few hours [381]. This implies that the performance of the Data Quality (DQ) flags are estimated online such that any problem is detected by people on shift. For instance an abnormally large deadtime should immediately be reported and investigated. It may correspond to a real worsening of the quality of the data. It may also corresponds to a computing failure. The performance of the DQ flags is estimated using GW triggers produced with a very low latency; two transient search pipelines are generated triggers: MBTA[382, 383] for a standard template based compact binary coalescence (CBC) search and Omega[337] for short transient unmodelled signal search. A third transient signal pipeline, KleineWell (KW), is used to process not only the GW strain channel, but all auxiliary channels (in Virgo it amounts to ~ 500 channels sampled between 500 Hz up to 20 kHz). To be able to process thousands of channels online using few computing nodes, one requires a fast computing algorithm. KW[337] has been developed by LSC colleagues for that goal. MBTA and Omega triggers are used to estimate the performance of vetoes. KW triggers are used to build vetoes as explained in the next sections.

4.5.2 Vetoes

4.5.2.1 Introduction

Once a source of glitches is identified, one wants to veto the corresponding periods. There are different ways to define vetoes useful for burst and inspiral analyses [384, 385, 386, 387]. As already stated, there are two main categories of disturbances: Environmental and instrumental. In the first case, there are now well identified phenomena (seismic, magnetic and acoustic noise) that couple with the dark fringe. Usually, probes that measure the environmental conditions of the detector are well tuned to allow for the capture of the moments of noise excess. In the case of instrumental disturbances, each detector configuration change can bring new sources of noise[4] and more systematic studies are helpful to highlight new phenomena. For that purpose, one will use "blindly" all auxiliary channels to bring out which channels have a statistically significant correlation with the dark fringe. Several algorithms have been

[4]especially after a long period of commissioning.

developed in LIGO and we have adapted them for Virgo purposes. Two of them are looking at time coincidence between dark fringe and auxiliary channels triggers: UPV (Used Percentage Veto) [388] and hVeto (for hierarchical Veto) [389] (see section 4.5.4). BCV [390] is searching for non linear coupling between the dark fringe and auxiliary channels and Excavator [391] is looking for correlation between glitches and auxiliary channels value.

Besides, the way vetoes are defined is entangled with the way they are applied by GW searches. There are periods that are known not to be analyzable (even in science times). It means that pipelines should not process h(t). For instance h(t) is so glitchy or h(t) is few order of magnitudes larger than the usual values, that pipelines fail at processing data. It's usually easy to find out these periods, to identify the problem and to define the corresponding veto segments which are generally long (from several seconds up to several hours). These veto segments are used to redefine the science segments. The other vetoes are used to discard triggers.

For historical reasons, environmental vetoes are called DQ flags. or DQ whereas KW based vetoes are called event by event vetoes. This is rather arbitrary, especially in Virgo, where many "instrumental" DQs are created during a run after the noise coupling has been identified using daily KW veto results. In Virgo, the difference between DQs and event by event vetoes is actually more technical: DQs are generated automatically with a very low latency while KW based vetoes are generated within 1 day or 1 week.

Furthermore, some DQ segments are defined after some observations reported by investigators who recommend not to use some periods of data for data analysis because a rather severe problem occurred while the interferometer was still in science mode. These observations are translated into special DQ called SciMon (scientist monitoring) DQ.

Since VSR2, most of the DQ are generated with a very short latency, shorter than 1 minute. This request comes from low latency searches which need to take a decision about sending or not on alert to telescopes or satellites within few minutes/hours after the potential GW event has been recorded. This is not the case of event by event vetoes that are generated with at least 1 day of delay and thus are not used in any online searches but are very useful for detecting new sources of noise. The main reason is that these vetoes require to consider a large set of data to obtain results statistically significant.

Once vetoes are defined (segment lists are generated), their performance is studied. For that, several quantities are computed:

- **dead time** dt: Fraction of science times that are vetoed.
- **efficiency** ϵ(SNR): Fraction of GW triggers that are vetoed. Usually this fraction is estimated for triggers whose SNR is higher than a given value.
- **use percentage** UP(SNR): Fraction of veto segments that veto at least 1 GW trigger. This quantity is also computed for GW triggers above a given value and hence is a function of SNR.

Efficiency and use percentage make use of triggers of a specific search. We consider triggers from a burst pipeline (Omega) and those from an inspiral pipeline (MBTA) to evaluate the performance of vetoes for a typical burst search and an inspiral one respectively. Once these quantities are defined, vetoes can be "qualified" and use recommendation can be given. Unfortunately, there is not a unique figure of merit that automatically ranks vetoes. Applying a veto implies a risk to veto a genuine GW trigger, even if the veto is safe (see section 4.5.3). This risk is proportional to the veto deadtime. That is why it is important to check that vetoes do not discard good quality data periods. Not all DQs and event by event vetoes that are defined will be applied in searches. The list of selected vetoes is the result of careful performance studies to estimate the benefit over risk ratio for each veto.

If there is no unique figure of merit to measure the quality of a veto, there are criteria that should be fulfilled: a veto of good quality should have a large use percentage (UP). That means that each veto segment is suppressing at least 1 glitch in the GW channel and hence indicates the level of coupling between the source of noise on which the veto is based and the GW glitches. If the UP is low, this is an indication that a large fraction of good quality data are falsely dismissed. However, the UP can be biased by a large number of GW triggers vetoed by chance due to a large deadtime. The number of accidental vetoed GW triggers can be estimated by the number of GW triggers times the deadtime. If this number is similar or larger than the number of vetoed GW triggers, the veto is not sound. Checking $\epsilon(\mathrm{SNR})/dt$ is thus important. Finally, as a sanity check, dt must correspond to the fraction of time where data are really affected by a noise source. For instance, a veto against the periodic magnetic glitches in the mode-cleaner building must have a deadtime that corresponds to the well known duration of the noisy periods. A smaller or larger dt might indicate that the veto segment size is not properly covering the right noisy periods. All the quantities help at

classifying the vetoes into categories. This classification is not absolute but depends however on the search for which vetoes are developed as UP and ϵ depend on GW triggers.

The categories indicate how the pipelines should use each of the vetoes. They indicate the degree of severity of a problem and how well the coupling with the dark fringe is understood. Table 4.2 gives the definition of each category and how most of GW transient searches are using them.

Category	Definition	Prescription for searches
CAT1	Flags obvious and severe malfunctions of the detector.	Offline analysis pipeline should run on data only after removing CAT1 time periods. Science data are redefined after removing CAT1 segments.
CAT2	Flags noisy periods where the coupling between the noise source and the GW channel is well established.	Triggers should be removed if flagged by a CAT2 veto. A significant trigger surviving the CAT2 vetoes is a good candidate for detection follow-up.
CAT3	Flags noisy periods where the coupling between the noise source and the GW channel is not well established.	CAT3 vetoes should not be applied blindly. Triggers flagged by a CAT3 veto should be followed up carefully. CAT3 vetoes are applied to compute upper-limits.
CAT4	Flags periods where hardware injections are performed.	Periods flagged by a CAT4 veto are used for specific studies. This category is applied for any search analysis.
CAT5	Advisory flag to keep track of problems for which no (or very low) impact was seen in the GW channel.	CAT5 can be useful for follow-up studies of interesting GW candidates. The validity of the flagging must be carefully checked by experts.

Table 4.2: Definition of the categories used to qualify the DQ flags and prescription for GW searches

4.5.2.2 Data Quality flags

Before VSR2, most of the DQ flags were produced offline by different algorithms developed by a few people. Some were run online with a latency smaller than 1 minute. As most of the algorithms that produce the DQ vetoes process data quicker than data acquisition rate, all DQ flags are now produced in quasi real time.

The first DQs that have been developed were checking whether an electronic channel was saturated. For some channels involved in the optical controls, electronic saturation is the source of very loud glitches in the dark fringe.

Environmental DQs (anti-seismic, anti-magnetic and anti-acoustic noise DQs) are built using the RMS of a environmental probe channel in a given frequency band (BRMS). It allows one to pick up rapid and short increases in a channel that is found coincident in time with a glitch in the dark fringe. But the BRMS of some channels can change abruptly (step function). These changes are not associated with any glitches in the dark fringe and hence the veto should not be "on" during the corresponding time. This has been observed mainly with magnetometer probes and ground issues are suspected to be the cause. It turns out to be rather difficult to detect these sharp changes online. The only way to disentangle these fake glitches from normal ones, for which the BRMS might exceed the threshold for few seconds and then come back to its average value, is to wait for at least few dozen of seconds before deciding that the BRMS increase should not be considered. This is of course in contradiction with low latency vetoes. Fortunately these events are not frequent and the best way to reduce the impact on the quality of the veto is to have adaptative thresholds (threshold is recomputed each 10 seconds with an estimation of the mean and standard deviation of the BRMS). Although most of the channels we use are not affected by the problem, for many DQs we use an adaptative thresholds. Note that when DQs are reprocessed, we can check and eliminate veto segments that are due to the sharp but harmless change of the channel.

The glitches described in Section 4.4.4 due to angular misalignments have required the development of special DQs. These DQ flags are built by setting a threshold on the (down-sampled) angular control correction channels of the arms' end mirrors. Extremal values of the correction channels correspond to strong misalignment that then generate high order modes coupling in the dark fringe. Three different flags corresponding to different thresholds are defined to be able to tackle glitches of different amplitudes. These "angular" glitches have a rather low SNR, and some searches might not be affected by the lowest SNR glitches. Having different DQs with different thresholds allows one to choose later what is the most efficient veto for a given search.

Another DQ flag to eliminate diffused light coupled with micro-seismic noise is obtained by setting a threshold on the velocity of the top-stage of the WE and NE suspensions. The velocity is computed by just taking the first derivative of the channel that monitors the position of the top stage [386].

Periods of time during which hardware injections (see Section 4.5.3) are done are flagged with some specific DQ flags (final results of GW searches must exclude hardware injection times). The complete lists of DQs defined during VSR1, VSR2 and VSR3 are given in [392].

4.5.2.3 Data Quality flags software architecture

The software architecture of all processes involved in the generation of online DQ flags is given in Figure 4.23. To summarize, input data (auxiliary channels) are read in a shared memory filled by data acquisition processes by each "monitor" process. A monitor is a process that filters the data (BRMS computation for instance) and generates binary information "0", "1" or "-1" for each second of data. As explained in [393], "0" means that veto is off, "-1" means that no info is available to decide the status of the veto, and "1" means that the veto is on. At that level, the information is stored in C structures and written in another shared memory. The process "SegOnline" reads each of the vectors that have been generated by the monitors and transforms the information defined for each second of data into veto segments with value "0", "1" or "-1". Segments are then written on disk in ASCII and XML format.

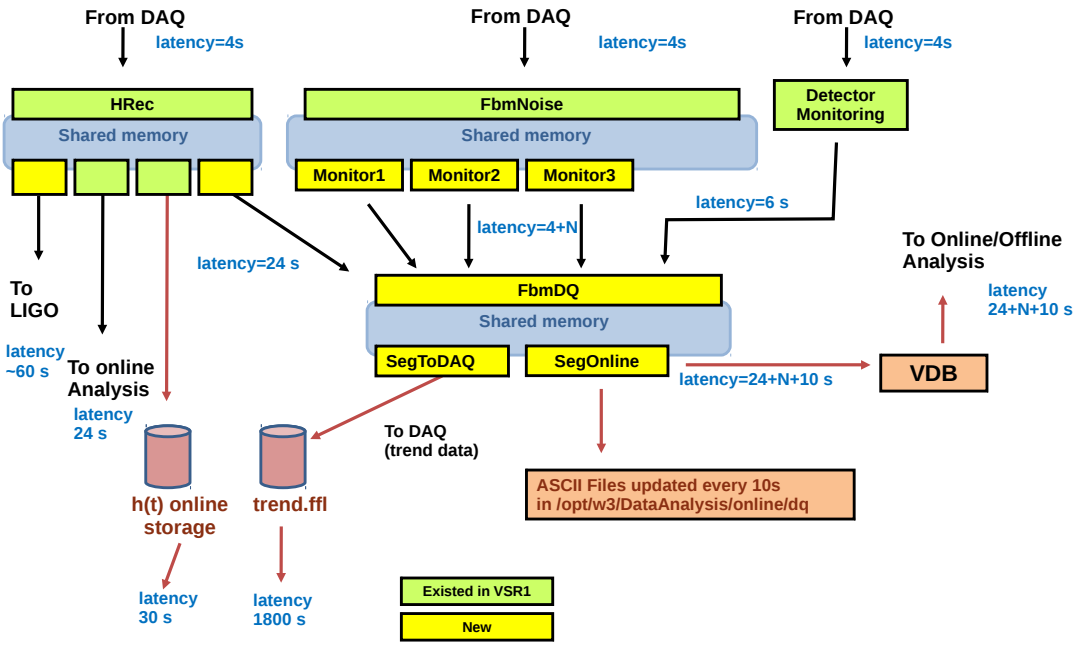

Figure 4.23: Software architecture of the DQ flags generation [394].

Another process inserts each 30 seconds the newly created segments in the Virgo database (VDB) [395]. The XML files covering 16 s long periods are sent using rsync protocol to Caltech that broadcasts them to Livingston and Hanford clusters. They are also inserted in the LIGO segment database (segdb). With such a mechanism during VSR2, the average latency of Virgo DQ availability in LIGO clusters where online GW searches are performed was less than 1 minute.

Frequency (Hz)	50	70	100	153	235	393	554	850	1304	2000
Nominal SNR in Virgo	100	100	100	100	100	100	100	100	50	25

Table 4.3: Frequency and nominal SNR of the "loud" and incoherent Sine-Gaussian (quality factor of 9) hardware injections performed in Virgo. At high frequency, the SNR is reduced because this is not possible to injection loud signal without taking the risk of saturating the actuators. For the same reason the highest frequency cannot be larger than ∼2 kHz.

4.5.3 Veto safety and hardware injections

Veto safety is an important issue as we cannot take the risk to discard a genuine GW event. More precisely, assuming that both veto segments and GW events are randomly distributed in time, a GW trigger might be vetoed with a certain probability. This probability will be high if the deadtime of the veto is large, but a veto is declared "unsafe" when it suppresses more GW triggers than what is expected from a pure accidental coincidence of two random processes.

All vetoes, except PQ (see section 4.5.5) are built using channels that are assumed to be free of gravitational wave content[5], but to really check vetoes are safe we use the ficticious GW signals injected inside the interferometer acting directly on the mirrors (see section 4.5.1). Hardware injections (HIs) mimic the path of a real gravitational wave through the detector and one expects that all the effects of a real gravitational wave inside the detector will take place and be recorded in all probes. This is the key hypothesis for using HIs to test that a veto built on auxiliary channels is safe.

Several types of waveforms are used to derive the force applied on mirrors. All transient search groups have defined a set of waveforms to be injected. Burst, inspiral and stochastic background signals are injected coherently[6] in all detectors at well determined instants. On the contrary, to mimic the presence of a continuous source, permanent sinusoidal but Doppler modulated waveforms are injected in each detector independently, with an amplitude which is much smaller than the noise floor at that frequency. In addition to coherent signal injections, burst signals are injected with high SNR (nominal values of 50 and 100). These are the hardware injections (HI) that we use to check veto safety. The potential coupling of a GW signal with the auxiliary signal that is used to build a veto is assumed to be linear. As these high amplitude hardware injections are causing troubles for CBC and burst GW searches (they are similar to loud glitches and thus bias the power spectrum density estimation), they cannot be too frequent. On average, they are performed randomly a dozen of times per week and Sine Gaussian waveforms are used to scan a large frequency range inside the detector frequency bandwidth as described in Table 4.3.

As injection GPS times and all other parameters are determined in advance (update each ∼ 2 months), the SNR value will vary according to the sensitivity change of the detector. Each hour the list of successful HIs is updated. Not all foreseen HIs are effectively done as Virgo might be unlocked when injections are scheduled. Each veto segment list v_i is then applied to the successful HIs. One determines $N^{v_i}_{vetoed}$ the number of vetoed HIs by the veto v_i. This number is then compared to the expected number $N^{v_i}_{exp}$ of vetoed HIs. If one assumes there is no correlation between HIs and the veto segments, this number is just

$$N^{v_i}_{exp} = N_{HI} \times \frac{T^{v_i}_{veto}}{T_{science}} = N_{HI} \times dt^{v_i} \tag{4.1}$$

where $T^{v_i}_{veto}$ is the total duration of the veto, $T_{science}$ is the science time duration and dt^{v_i} is the deadtime of the veto v_i. To compare $N^{v_i}_{exp}$ and $N^{v_i}_{vetoed}$, and assuming that hardware injections are randomly performed[7], we compute the

[5]Some auxiliary channels used for the control of the suspended elements contain a fraction of the GW signal and are thus explicitly excluded for the veto generation.

[6]The amplitude and the arrival time in each detector is computed assuming a given position in the sky. A uniform distribution of sources over the sky is considered to generate all injections.

[7]For most of the vetoes, we can also assume that veto segments are randomly distributed in time. This is not always true as sometimes the noise source has known occurrence frequency.

Poisson probability to have $N^{v_i}_{vetoed}$ or more events when $N^{v_i}_{exp}$ are expected. This probability is given by

$$p^{v_i}(N \geq N^{v_i}_{vetoed}) = \sum_{n=N^{v_i}_{vetoed}}^{n=\infty} P(N^{v_i}_{exp}, n) \tag{4.2}$$

$$= 1 - \sum_{n=0}^{n=N^{v_i}_{vetoed-1}} P(N^{v_i}_{exp}, n) \tag{4.3}$$

$$= 1 - \Gamma(N^{v_i}_{exp}, N^{v_i}_{vetoed}) \tag{4.4}$$

where $P(n, \lambda)$ is the Poisson distribution of mean λ and Γ is the incomplete Gamma function[396]. By setting a threshold on this probability we have an automatic possibility to determine which veto is unsafe.

4.5.3.1 Online veto safety checks during VSR2, VSR3 and VSR4

During science times, hundreds of veto segment lists are produced online. As some of these vetoes are used by low latency searches to vet good GW candidate alerts, veto safety is checked online. Each hour, one checks if new HIs have been performed. If yes, all the quantities described above ($N^{v_i}_{exp}$, $N^{v_i}_{vetoed}$, dt_{v_i} and p^{v_i}) are updated and displayed on a web page [397].

The distribution of the safety probability is shown for VSR2, VSR3 and VSR4 runs in Figure 4.24. In these histograms, for each run we consider all veto lists generated regardless of their interest in GW transient searches. A large fraction (96%) of the safety probability are above 1%, but there are a few veto lists with very low safety probability. A priori, if the veto is safe, one expects that the safety probability stays above 1%. A safety probability lower than 10^{-3} indicates that the veto is discarding too many HIs to be considered safe. The veto lists with an probability lower than 1% have been checked individually (9 for VSR2, 3 for VSR3 and 2 for VSR4). For all vetoed HIs, there was no direct link between the veto and the HIs, the veto being justified by the presence of a loud glitch few seconds before or after the injection happened. This should, a priori, be encompassed in the definition of $p^{v_i}(N \geq N^{v_i}_{vetoed})$. Actually the problem is to estimate accurately $N^{v_i}_{exp}$. In Eq. (4.1), the deadtime of the veto is computed over the full run and we assume it remains constant over the full run. Yet, we know that this hypothesis is not true for all vetoes (seasonal variation of the anti-seismic noise vetoes). Another source of deviation from the random process hypothesis comes from the fact that loud HIs are performed in bunches of 10 with a time interval of 2 or 3 seconds[8]. For many low safety probability vetoes, the excess of vetoed HIs came from multi-second long segments that veto more than 1 loud HIs by chance. As an illustration, Figure 4.25 shows a time frequency map of 30 seconds of data during which a bunch of loud injections has been performed during a period with many micro-seismic/scattered light glitches (see 4.4.3). 4 of 10 hardware injections were vetoed by a 260 s long veto segment. This is clearly an extreme case for which Eq. (4.1) gives an inaccurate estimation of $N^{v_i}_{exp}$.

Knowing these problems, in the online veto safety monitoring system we have implemented an alert system with 2 thresholds: when the probability p^{v_i} is lower than 10^{-3}, a warning signal is raised. Below 10^{-5}, the veto is declared unsafe online and a manual analysis is immediately organized thanks to the online generation of time-frequency maps for all recorded channels which are generated for each HI.

The number of vetoes with probability lower than 10^{-3} and 10^{-5} is reported in Table 4.4 for each run. None of these vetoes were confirmed to be unsafe after hand-made cross-checks. We especially checked whether the vetoed HI could have induced a signal in the auxiliary channel used to generate the veto. In all cases we have been able to exclude this hypothesis and all DQs used for GW transient searches (after a selection process described in 4.5.6) have been declared safe.

[8]To minimize the deadtime for GW searches generated by the loud HIs

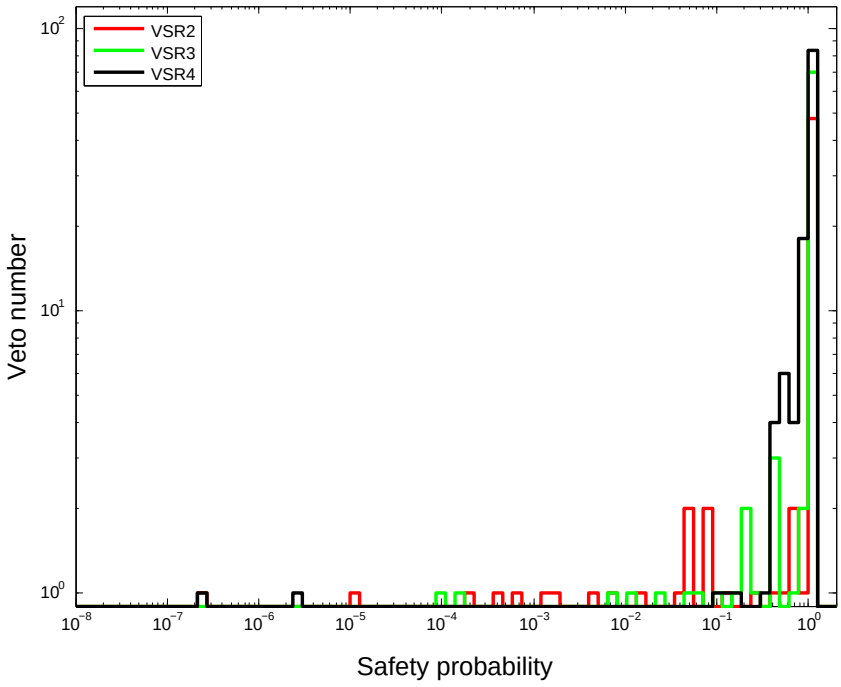

Figure 4.24: Histogram of the safety probability of all veto lists produced during VSR2 (red), VSR3 (green) and VSR4 (black) runs.

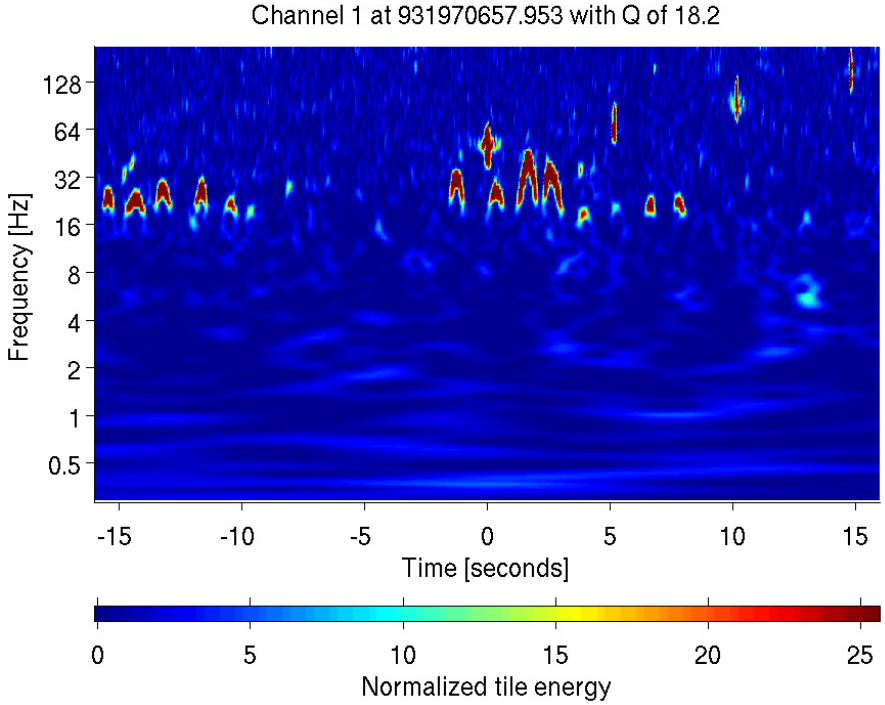

Figure 4.25: Time frequency map showing 3 loud hardware injections (time 0, 5 and 10 second) surrounded by scattered light glitches with their arch-like signature.

Run	Veto name	deadtime (%)	vetoed HI / successful HI	$N_{exp}^{v_i}$	p^{v_i}	Comments
VSR2	V1:SE_NE_0.25_1_TIGHT	12.7	144/720	91.5	2.4e-07	Long veto
	V1:SE_WE_0.25_1_MEDIUM	4.1	49/711	29.4	4.5e-04	segments due
	V1:SE_WE_0.25_1_TIGHT	12.7	135/720	91.4	1.2e-05	to scattered
	V1:SEISMIC_NE_ZLVDT	0.9	18/711	6.7	2.0e-04	light glitches.
	V1:SEISMIC_WE_ZLVDT	1.8	26/720	12.7	6.9e-04	
VSR3	V1:PR_OMC_200_500_LOW	0.6	7/207	1.1	1.7e-04	Local deadtime is higher.
	V1:SEBREWINJ_4_1024	0.1	5/390	0.4	8.8e-05	Local deadtime is higher.
VSR4	V1:B5_1024_4096_FULL	0.1	8/702	.6	2.5e-07	Local deadtime is higher.
	V1:B5_1024_4096	0.2	9/702	1.1	2.9e-06	Local deadtime is higher.

Table 4.4: List of low safety probability veto segments lists during VSR2, VSR3 and VSR4 Virgo runs. During VSR2, these are vetoes based on seismic monitoring channels. V1:SEBREWINJ_4_1024 and V1:PR_OMC_200_500_LOW are monitoring seismic noise near the detection tower Brewster window and the output mode cleaner on the detection bench respectively. Finally VSR4 unsafe vetoes are related to an excess of noise seen in the photodiode B5.

Another example is given by the V1:SEBREWINJ_4_1024 veto during VSR3: 6 loud injections (out of the same series of 10) are vetoed by 4 veto segments of 2, 11, 3 and 101 s. These three veto segments are correctly flagging seismic noise measured around the injection tower. At the time of the hardware injections, the deadtime is not 0.1% but much higher. If we had used a more realistic deadtime estimation, the probability of vetoing 6 events would have been higher than 2.5×10^{-6}.

4.5.3.2 Veto safety probability improvement

With the experience of past Virgo runs, we know that the estimate of the expected number of vetoed HI is sometimes incorrect. The main reason is that loud HI are performed in bunches of 10 separated by few seconds each. When a veto segments last only a few seconds, the same segment may veto more than 1 HI. This would be harmless if the deadtime was well estimated to compute the number of expected vetoed HI. The standard method we used during past science runs assumed that the deadtime was constant over the full run. This hypothesis was not fulfilled for DQ flags having seasonal or daily variations. If the deadtime is underestimated when a bunch of 10 loud HIs is performed, the number of expected vetoed HI would be underestimated.

One way to attenuate this problem would be to consider randomly only one of the HIs in each bunch. This should improve the safety probability computation, as HIs used to compute the veto safety probability could be considered randomly distributed. Another possibility is to abandon the random distribution hypothesis, but try to estimate $N_{exp}^{v_i}$ considering the deadtime variations when HIs are performed. For VSR2, VSR3 and VSR4, we have compared different safety probability estimates. Eqs. (4.1) and (4.4) are unchanged. What is modified is either the number of loud HI (reduction by selecting randomly 1 loud HI in each group of 10), or the deadtime which is estimated around each HI inside a time window. We have tested 3 different time window sizes: $\pm$ 1 mn, $\pm$ 10 mns and $\pm$ 1 hour. The time ($\pm$ 5s) around each injection is excluded from the deadtime calculation to avoid bias if the veto is unsafe. The comparison of the different probabilities as shown in Figure 4.26 for VSR2, VSR3 and VSR4 runs shows that low probability tail is nicely reduced by the 2 alternative probability calculations. Another way to compare the methods performance is to draw the histogram of the difference of the number of expected vetoed HIs and the number of vetoed HIs. Figure 4.27 shows that, the tail of the $N_{exp}^{v_i} - N_{vetoed}^{v_i}$ distribution is reduced, the distribution is almost symmetrical and the number of events in the bin "0" is the highest when one compares the probability with a local deadtime estimation with the averaged deadtime.

More precisely, tables 4.5, 4.6 and 4.7 report all probabilities. Randomly selecting one loud HI in each bunch of 10 one obtains safety probability systematically higher than 1% which is what we expect if one assumes that all DQ flags are safe. The drawback of this method is to reduce by a factor ~ 9 the number of loud HIs used to compute the probability. For some vetoes, the number of loud HIs is too small (<100) to produce statistically sound results at any time during a data taking acquisition. The probability using the local deadtime estimation is, on the contrary, not affected by this problem and as reported in tables 4.5, 4.6 and 4.7, all safety probabilities are higher than 1%. From

the tables one can also conclude that the probability values are consistent for all the three window sizes considered here except for few DQ flags. For most of these exceptions, the smallest window size gives the highest probabilities.

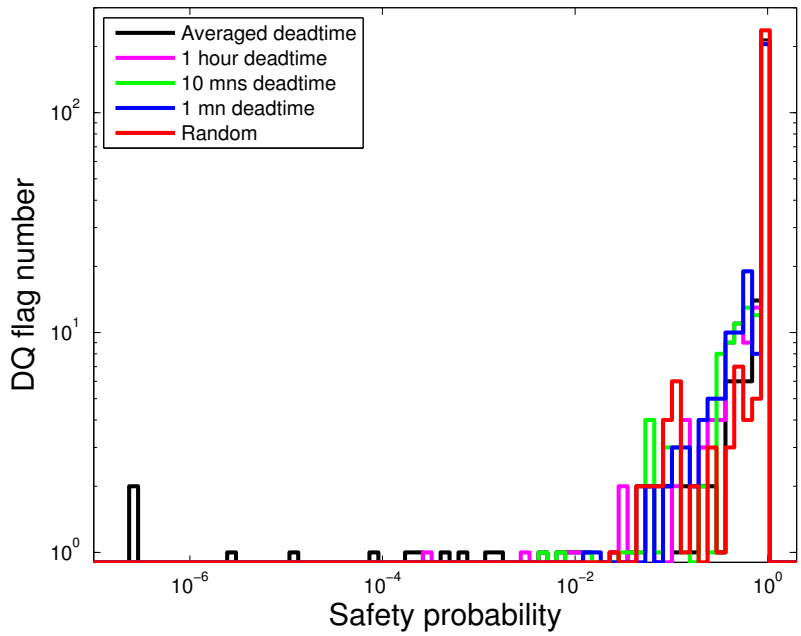

Figure 4.26: Comparison of the different safety probability estimations for all a priori safe vetoes defined during VSR2, VSR3 and VSR4 runs.

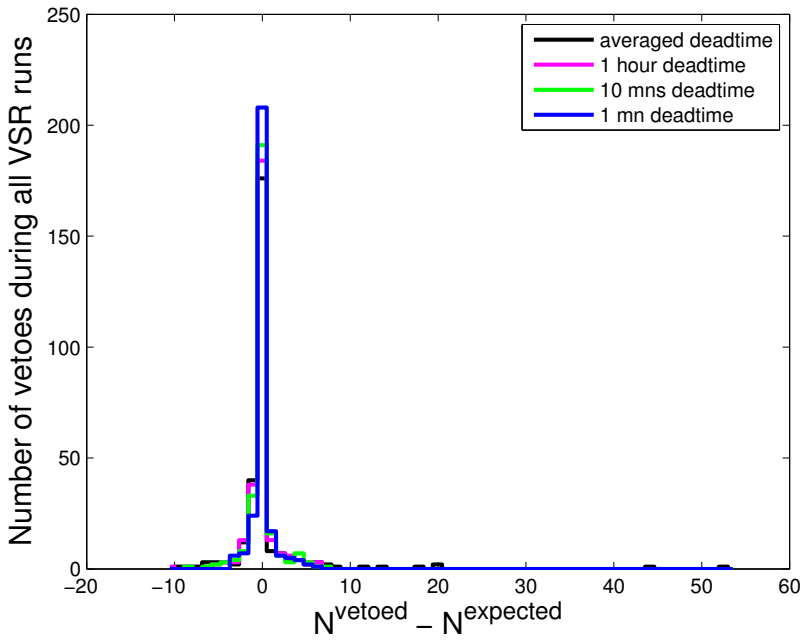

Figure 4.27: Difference between the number of vetoed loud hardware injections and the expected number of vetoed hardware injections for all vetoes defined during VSR2, VSR3 and VSR4.

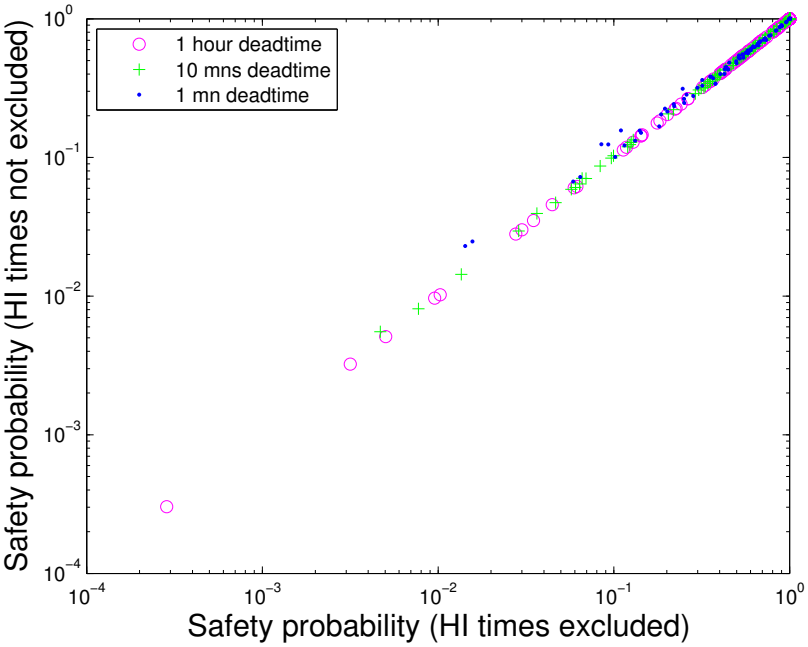

Figure 4.28: Comparison of the safety probability computed excluding the time around each HIs (x-axis) or without exclusion (y-axis) for all vetoes during VSR2, VSR3 and VSR4.

There is also an overlap of the DQ flags with those for which computing the local deadtime without excluding the time around each HI injection gives a slightly higher probability (see Figure 4.28). None of these DQ flags are unsafe, but veto segments are long and using a minute long window to compute the deadtime is not adapted. If computing the deadtime locally seems to be a good way to obtain accurate safety probability, we can still be affected by the fact that HIs are not randomly distributed. That is the reason why, for advanced Virgo, all different safety probabilities (averaged deadtime, local deadtime and randomly chosen HI in each bunch) will be computed, such that we can easily monitor if a veto is or becomes unsafe.

DQ flag name	Deadtime (%)	Probability averaged deadtime	Probability deadtime over 1 mn	Probability deadtime over 10 mns	Probability deadtime over 1 hour	Probability 1 loud injection per bunch
V1:B5_LOW_FREQ	0.60	8.1e-01	6.0e-01	7.0e-01	8.1e-01	5.3e-01
V1:B5_LOW_FREQ_TIGHT	1.37	1.2e-01	1.0e-01	6.9e-02	1.1e-01	2.5e-01
V1:MAB_MC_16_64	0.13	6.1e-01	4.3e-01	5.1e-01	5.2e-01	1.0e+00
V1:PR_6MHZ	0.53	4.0e-02	1.1e-01	4.7e-02	6.2e-02	4.9e-01
V1:SE_CE_1_4	0.27	1.4e-02	1.4e-02	7.7e-03	5.0e-03	2.8e-01
V1:SE_CE_2_8	0.14	7.5e-02	1.1e-01	1.3e-01	6.0e-02	1.6e-01
V1:SE_MC_1_4	0.11	4.5e-02	9.3e-02	8.4e-02	2.8e-02	1.3e-01
V1:SE_MC_2_8	0.05	5.0e-03	1.6e-02	1.4e-02	3.2e-03	5.8e-02
V1:SE_NE_0.25_1_LOOSE	0.68	7.1e-01	4.3e-01	6.7e-01	8.7e-01	5.7e-01
V1:SE_NE_0.25_1_MEDIUM	3.32	2.7e-01	7.4e-01	9.4e-01	9.6e-01	4.0e-01
V1:SE_NE_0.25_1_TIGHT	12.70	2.4e-07	3.6e-01	3.5e-01	3.6e-01	9.0e-02
V1:SE_NE_1_4	0.07	3.9e-01	2.6e-01	4.8e-01	4.0e-01	1.0e+00
V1:SE_WE_0.25_1_LOOSE	1.02	8.0e-03	2.5e-01	1.3e-01	2.6e-01	7.2e-01
V1:SE_WE_0.25_1_MEDIUM	4.08	4.5e-04	3.0e-01	3.1e-01	4.3e-01	4.0e-01
V1:SE_WE_0.25_1_TIGHT	12.69	1.2e-05	5.8e-01	6.4e-01	6.7e-01	8.9e-02
V1:SE_WE_4_16	0.10	5.0e-01	2.0e-01	3.3e-01	3.2e-01	1.1e-01
V1:SEISMIC_AL_DIFFEND_TX	1.08	5.5e-02	5.9e-02	4.2e-01	2.0e-01	7.4e-01
V1:SEISMIC_AL_DIFFEND_TY1	5.37	1.4e-03	4.4e-01	6.4e-01	6.1e-01	8.0e-01
V1:SEISMIC_AL_DIFFEND_TY2	4.10	1.8e-03	4.0e-01	5.8e-01	5.1e-01	2.6e-01
V1:SEISMIC_AL_DIFFEND_TY3	2.40	7.3e-02	7.6e-01	8.4e-01	8.0e-01	9.5e-01
V1:SEISMIC_NE_ZLVDT	0.94	2.3e-04	6.3e-01	6.4e-01	6.4e-01	3.3e-01
V1:SEISMIC_WE_ZLVDT	1.76	6.9e-04	6.2e-01	5.3e-01	5.4e-01	6.5e-01

Table 4.5: Different estimations of the safety probability for all VSR2 DQ flags with safety probability lower than 1.

DQ flag name	Dead-time (%)	Probability averaged deadtime	Probability deadtime over 1 mn	Probability deadtime over 10 mns	Probability deadtime over 1 hour	Probability 1 loud injection per bunch
V1:B5_1024_4096	0.41	4.7e-01	9.1e-01	9.3e-01	8.7e-01	1.0e+00
V1:B5_1024_4096_FULL	0.30	7.0e-01	9.6e-01	9.7e-01	9.4e-01	1.0e+00
V1:BS_IMC_POWERSTAB_HIGH	0.79	1.7e-01	7.8e-01	9.4e-01	8.2e-01	1.0e+00
V1:BS_IMC_POWERSTAB_LOW	1.35	2.4e-01	8.3e-01	9.5e-01	8.6e-01	1.0e+00
V1:PR_6MHZ	0.14	4.2e-01	3.2e-01	3.4e-01	3.5e-01	1.0e+00
V1:PR_OMC_200_500_MEDIUM	0.08	1.1e-02	6.1e-01	3.0e-01	2.6e-01	1.0e+00
V1:PR_OMC_200_500_LOW	0.55	1.7e-04	2.5e-01	2.9e-01	2.6e-01	1.2e-01
V1:PR_OMC_4_200_MEDIUM	0.37	7.9e-03	5.2e-01	2.0e-01	2.3e-01	8.2e-02
V1:SEBREWINJ_4_1024	0.11	8.8e-05	5.8e-01	4.7e-03	2.9e-04	5.0e-02
V1:SEBREWINJ_40_1024	0.06	2.1e-01	5.2e-01	2.2e-01	1.8e-01	1.0e+00
V1:SEBREWINJ_LARGEBAND	0.01	4.6e-02	3.2e-01	6.6e-02	4.5e-02	1.0e+00
V1:SE_CE_1_4	0.27	9.0e-02	8.4e-01	5.5e-01	2.2e-01	1.2e-01
V1:SEISMIC_AL_DIFFEND_ELLIPTIC2	1.58	2.4e-02	1.4e-01	5.7e-02	9.6e-03	1.0e+00
V1:SEISMIC_AL_DIFFEND_ELLIPTIC3	2.24	6.1e-02	2.2e-01	1.0e-01	3.5e-02	8.6e-02
V1:SEISMIC_WE_ZLVDT	2.71	8.9e-01	3.5e-01	4.3e-01	4.6e-01	1.2e-01
V1:SE_NE_0.25_1_TIGHT	6.34	4.3e-01	8.5e-02	9.7e-02	1.2e-01	1.7e-01
V1:SE_WE_0.25_1_TIGHT	7.21	9.6e-01	6.7e-01	7.8e-01	7.1e-01	6.3e-01
V1:TCS_NI_POWER_GLITCH	1.69	2.2e-01	5.8e-01	3.7e-02	1.0e-02	5.4e-01

Table 4.6: Comparison of different estimations of the safety probability for all VSR3 DQ flags with safety probability lower than 1.

DQ flag name	Deadtime (%)	Probability averaged deadtime	Probability deadtime over 1 mn	Probability deadtime over 10 mns	Probability deadtime over 1 hour	Probability 1 loud injection per bunch
V1:B1ACQ_POS_0	4.86	8.3e-01	6.0e-01	5.3e-01	5.3e-01	5.2e-01
V1:B1ACQ_POS_1	1.86	9.9e-01	9.0e-01	8.5e-01	8.4e-01	7.7e-01
V1:B1ACQ_POS_2	0.58	9.1e-01	5.0e-01	3.8e-01	4.1e-01	1.0e+00
V1:B5_1024_4096	0.16	2.9e-06	5.4e-01	5.4e-01	2.4e-01	1.2e-01
V1:B5_1024_4096_FULL	0.09	2.6e-07	6.6e-01	4.8e-01	1.4e-01	6.5e-02
V1:B5_LOW_FREQ	0.44	9.6e-01	5.9e-01	6.2e-01	6.7e-01	1.0e+00
V1:B5_LOW_FREQ_TIGHT	0.83	9.3e-01	6.8e-01	6.4e-01	6.9e-01	4.8e-01
V1:BSBMSNFV_16_64	0.82	1.3e-01	2.2e-01	1.2e-01	1.4e-01	2.7e-02
V1:BS_IMC_POWERSTAB_LOW	0.17	6.7e-01	3.7e-01	4.8e-01	5.3e-01	1.0e+00
V1:GLITCH_2930HZ_CA	0.64	8.2e-01	7.2e-01	8.2e-01	8.2e-01	3.9e-01
V1:MAB_MC_16_64	0.17	6.9e-01	7.1e-01	7.2e-01	6.9e-01	1.0e+00
V1:PR_OMC_200_500_LOW_OLD	0.61	9.3e-01	8.8e-01	8.1e-01	8.7e-01	1.0e+00
V1:PR_OMC_200_500_MEDIUM_OLD	0.26	8.4e-01	6.7e-01	7.6e-01	7.4e-01	1.0e+00
V1:PR_OMC_4_200_LOW	0.42	9.5e-01	9.0e-01	8.1e-01	8.8e-01	1.0e+00
V1:RECYCLING_GLITCH_LOW	0.83	9.8e-01	9.5e-01	9.9e-01	9.9e-01	4.8e-01
V1:RECYCLING_GLITCH_LOW_OLD	0.26	8.4e-01	5.6e-01	7.6e-01	8.5e-01	1.0e+00
V1:RECYCLING_GLITCH_MID	0.26	8.4e-01	5.6e-01	7.6e-01	8.5e-01	1.0e+00
V1:SAWEF7TYCORR_2_8	0.88	5.8e-01	5.0e-01	3.9e-01	5.4e-01	1.0e+00
V1:SAWEF7TYLVDT_4_150	0.15	6.4e-01	5.5e-01	6.1e-01	5.5e-01	1.0e+00
V1:SEBREWINJ_40_1024	0.13	5.9e-01	4.5e-01	5.6e-01	5.9e-01	1.0e+00
V1:SEBREWINJ_40_1024_OLD	0.08	4.3e-01	3.8e-01	4.0e-01	4.3e-01	1.0e+00
V1:SEBREWINJ_4_1024	0.13	5.9e-01	4.5e-01	5.6e-01	5.9e-01	9.4e-02
V1:SEBREWINJ_4_1024_OLD	0.08	4.3e-01	3.8e-01	4.0e-01	4.3e-01	1.0e+00
V1:SEBREWINJ_LARGEBAND	0.02	1.5e-01	1.3e-01	1.2e-01	1.3e-01	1.0e+00
V1:SEISMIC_AL_DIFFEND_ELLIPTIC3	5.60	9.5e-01	6.3e-01	4.8e-01	6.6e-01	9.3e-01
V1:SEISMIC_AL_DIFFEND_TX1	3.60	4.7e-01	1.4e-01	6.0e-02	1.5e-01	9.4e-01
V1:SEISMIC_AL_DIFFEND_TX2	1.55	5.3e-01	1.9e-01	6.4e-02	1.8e-01	1.0e+00
V1:SEISMIC_AL_DIFFEND_TX3	0.67	8.5e-01	2.0e-01	4.0e-01	5.8e-01	1.0e+00
V1:SEISMIC_AL_DIFFEND_TY1	6.99	8.4e-01	6.8e-01	7.3e-01	8.0e-01	6.0e-01
V1:SEISMIC_AL_DIFFEND_TY2	2.43	8.7e-01	6.5e-01	6.7e-01	6.9e-01	8.5e-01
V1:SEISMIC_AL_DIFFEND_TY3	0.78	8.0e-01	6.0e-01	6.0e-01	5.8e-01	1.2e-01
V1:SEISMIC_AL_DIFFEND_TY4	0.26	5.4e-01	5.1e-01	3.8e-01	3.3e-01	1.0e+00
V1:SETOIN01_128_256	0.07	4.0e-01	2.8e-01	3.6e-01	4.0e-01	1.0e+00
V1:SETOIN01_128_256_OLD	0.06	3.6e-01	1.8e-01	3.3e-01	3.7e-01	4.8e-02
V1:SE_NE_0.25_1_MEDIUM	0.17	6.9e-01	2.5e-01	4.6e-01	4.9e-01	1.0e+00
V1:SE_NE_0.25_1_TIGHT	3.16	8.9e-01	4.3e-01	3.5e-01	4.1e-01	9.1e-01
V1:SE_WE_0.25_1_MEDIUM	1.25	9.9e-01	7.3e-01	8.9e-01	9.3e-01	1.0e+00
V1:SE_WE_0.25_1_TIGHT	7.47	8.3e-01	5.4e-01	3.6e-01	4.2e-01	5.3e-01
V1:SSFS_1200_4000	0.01	9.4e-02	6.4e-02	2.9e-02	3.0e-02	1.0e+00
V1:TCS_WI_POWER_GLITCH	0.37	9.3e-01	4.5e-01	6.2e-01	5.0e-01	1.0e+00
V1:TCS_WI_POWER_GLITCH_NEW	0.11	5.3e-01	4.5e-01	5.2e-01	4.8e-01	8.1e-02

Table 4.7: Comparison of different estimations of the safety probability for all VSR4 DQ flags with safety probability lower than 1.

4.5.4 Auxiliary channel vetoes

Auxiliary channels are used in several ways for both detector characterization and vetoes for GW searches. Being able to correlate an excess of glitches in the GW channel with a set of auxiliary channels usually brings interesting clues to understand the sources of noise. Here, correlation could mean that an excess of glitches in some auxiliary channels are coincident with the GW channel glitches or that the auxiliary probes are recording unusual values (for instance control signals vary within a range when all control loops are at their working point). Several algorithms are used to identify and to rank the few interesting channels have been developed. UPV (Used Percentage Veto) [388] and hVeto [389] are two algorithms selecting auxiliary channels based on time coincidence between glitches in the GW and the auxiliary channels. Both have been run with low latency during VSR2, VSR3 and VSR4 and LIGO S6 runs, providing interesting hints to commissioners. They also generate automatically veto lists whose performance are studied like the other DQ flags in order to decide if they are useful for GW searches (see section 4.5.6). The main inputs of UPV and hVeto are auxiliary channel triggers generated by the KleineWelle algorithm [337] which is a quick short transient algorithm, based on the Haar wavelet transform, able to process hundred of channels with only a few processors. UPV and hVeto assume that the coupling between the noise source and the GW channel is linear. Yet, it is well-known that there are many sources of non-linear noise coupling in interferometric detectors. For instance the scattered light problem described in section 4.4.3 depends on the angular movement of the suspended mirrors. Actually the slow angular motions of the mirrors, the beam position, contrast defect, etc ... are generating many changing coupling conditions. The BCV algorithm (Bi-linear Coupling Veto) [390] considers a simple model of bi-linear coupling mechanism by just associating (multiplication operation) a slow monitoring (mirror angular position) channel with a fast (control) channel. Glitch time coincidence between the GW and the "pseudo" channel is then considered. The Excavator algorithm [391] compares auxiliary channel values at times of glitches and in absence of glitches. All these algorithms target linear and non-linear noise coupling in the GW channel and have proven to be very efficient and useful for identifying the running conditions that generate background events for GW searches. The next section describes another veto algorithm that has been able to veto another class of glitches. The text is adapted from [398].

4.5.5 The PQ veto

4.5.5.1 Introduction

After applying all the vetoes we described so far, we found in VSR1/S5 GW transient searches that many of the remaining loud triggers were observed with nearly equal size in both the in-phase (ACp) and quadrature (ACq) Virgo interferometer output channels, while we expect the ACq channel to be much less sensitive to a GW signal, provided that the demodulation phase is well tuned. A phase modulation on the laser light is applied before it enters the interferometer by an electro-optical modulator, generating sidebands on the carrier. As a consequence the signal associated with a relative arm length change will be detected as an event at the modulation frequency that is high enough (6.3 MHz) such that it will prevent the GW signal from being spoiled by laser power and electronic noises that dominate at low frequency. The photodiode currents are then subsequently demodulated in phase and in quadrature, and the signal from an arm length change is observed at its correct frequency in the recorded data. An error in the demodulation phase induces a small coupling of the GW signal with the quadrature channel. However, the ratio of the GW energy coupled into the two phases is expected to remain high. In other words, a real GW event will be seen with a SNR in ACp much higher than in ACq. On the contrary, ACq will be sensitive to glitches in signals which are related to interferometer common mode noise. It may happen that some source of noise can affect both quadrature signals with similar strength. This is especially the case for a dust particle crossing the laser beam before the output dark port photodiode where the beam is especially small in width.

The ratio between the two amplitude channels is expected to be proportional to $\frac{1}{sin(\delta\phi)}$, where $\delta\phi$ is the error on the demodulation phase [399]. Usually, the ratio of signal amplitudes ACp/ACq, which can be estimated using calibration signal at a fixed frequency, is in between 10 and a few hundreds. It has been previously proposed in GEO [400] and LIGO [399, 401] to use the ratio of energy seen in the two quadrature channels to reject false alarm events. I developed the technique for Virgo data, starting with VSR1 data. The veto has then been generated and studied for the next science runs (VSR2, VSR3 and VSR4). We also studied LIGO S5 data, but the veto was found less trustable and less interesting than with Virgo data as the phase shift between the two quadrature signals was not fully monitored during S5. Indeed, a critical point is to assure that no real GW events would be suppressed; therefore one should develop a

veto with a rather good security factor. To do so, we used the hardware signal injections to verify safety and develop the characteristics of this veto. With Virgo data, differences from one run to another have been found as shown in the next sections

4.5.5.2 Development with VSR1 data

Veto definition KleineWelle (KW) [337] triggers generated for both the ACp and ACq channels have been used. Each trigger list contains the peak time and the significance of the trigger. The KW significance is defined through the assumption that the energy in a cluster composed of N wavelet coefficients follows a χ^2 distribution with N degrees of freedom. The threshold on KW significance has been chosen rather low in order to be able to detect the residual component of GW in the ACq channel when looking at high SNR hardware injections. Data quality vetoes have been applied such that we do not consider in this study periods of time where known and identified problems occurred. Coincidence between ACp and ACq triggers within some time window, Δt, is required. A sharp coincidence between noise triggers in ACp and ACq is expected. However a 10 ms time window has been used in order to take into account the KW timing accuracy (a few ms). Furthermore, $\Delta t = 10$ ms maintains the coincidence of rather long (in time) and large (in SNR) triggers in ACp and/or ACq; for a long glitch the peak time might not be well defined. The ratio between the KW significance in the two demodulation phase channels, measured in coincidence, is

$$\kappa = \frac{SNR_{ACq}}{SNR_{ACp}}$$

For a real GW signal we expect to have $\kappa << 1$. On the contrary, coincident triggers with κ higher than a given threshold Σ should be considered as noise glitches. A veto is then defined by considering the time around coincident KW triggers whose κ is higher than Σ. Yet, since this *PQ veto* is designed to suppress high SNR events in the ACq channel that induce a transient in the GW channel, it is reasonable to consider only high significance ACq triggers. A threshold $\Theta > 100$ is applied on the ACq significance of the coincident triggers.

Validation using injected signals in the data In order to both validate the safety hypothesis and decide which thresholds to apply on κ, data segments containing hardware signal injections were studied. The hardware injections that have been used were Sine Gaussian waveforms of all strengths; during VSR1, seven different frequencies associated with the Sine Gaussians have been used (70, 105, 235, 393, 554, 850, 914 and 1304 Hz). The SNR of the injected waveforms were 7.5, 15, 75 and 150. In total, 2559 hardware injections have been performed and used in this analysis. The low SNR injections (7.5) were not expected to produce a signal in the ACq channel detectable by KW despite the very low threshold applied on the KW triggers' significance. 76% of the hardware injections have been detected by KW in the ACp channel, but only 6% are seen in coincidence in the ACp and ACq channels.

We first look for hardware injection signals in the coincident ACp-ACq KW triggers by requesting that the time difference between the injected signal and the ACp trigger be smaller than 20 ms. Given the coincident ACp-ACq trigger rate, the number of accidental coincidence events due to the size of the coincidence time window is about 15 for the entire VSR1. This number is rather large due to the high coincident ACp-ACq trigger rate. That means that we expect, on average, 15 hardware injections that are accidently associated to an ACp-ACq coincident trigger. This is especially true for low amplitude ACp-ACq triggers that dominate the triggers rate. Figure 4.29 shows the KW significance in ACp versus ACq of coincident triggers. On the same plot, triggers associated with a hardware injection are displayed. None of the hardware injection triggers have a KW significance higher in ACq than in ACp. The hardware injections whose reconstructed ACp significance is higher than 100 correspond to signals injected with a SNR of 75 and 150. Below an ACp significance of 100, some hardware injections of rather low SNR (15) are associated with a trigger in ACq. Those 19 triggers are compatible with the expected 15 accidental associations due to the high ACp-ACq coincident trigger rate in the low KW significance region. They should not be considered in this study. Only the loudest hardware injections, with a SNR of 75 or 150, are strong enough to generate a signal in the quadrature ACq signal. The highest value of the ratio κ is 0.45, as shown in Figure 4.30. This is higher than what is expected (8%) if one assumes an error on the demodulation phase of 5 degrees. We noticed that the highest κ values correspond to some of the loudest hardware injections (SNR = 150) whose ACp KW significance is ~ 5 times smaller than the average value. We do not have a satisfactory explanation for these observations. However, we noticed that the ACp KW significance distribution is rather wide for the loudest hardware injections. Given that result, we determined that

vetoing periods of time during which an excess of energy is seen in coincidence in the ACp and ACq channels with a ratio κ higher than 1 is safe and would not suppress a genuine GW event.

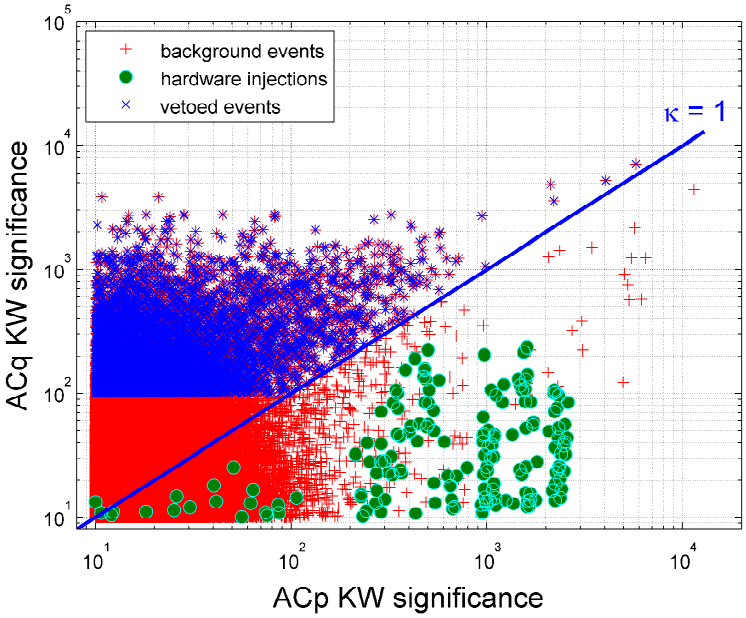

Figure 4.29: SNR of the coincident KW triggers in the two quadrature demodulated channels of the output dark port signal: ACp (in phase) and ACq (in quadrature). The time coincidence window of the triggers seen in the two channels is 10 ms. All other data quality flags have already been applied. The hardware injection signals, which were seen in both of the two demodulation phase channels, are indicated by the circles.

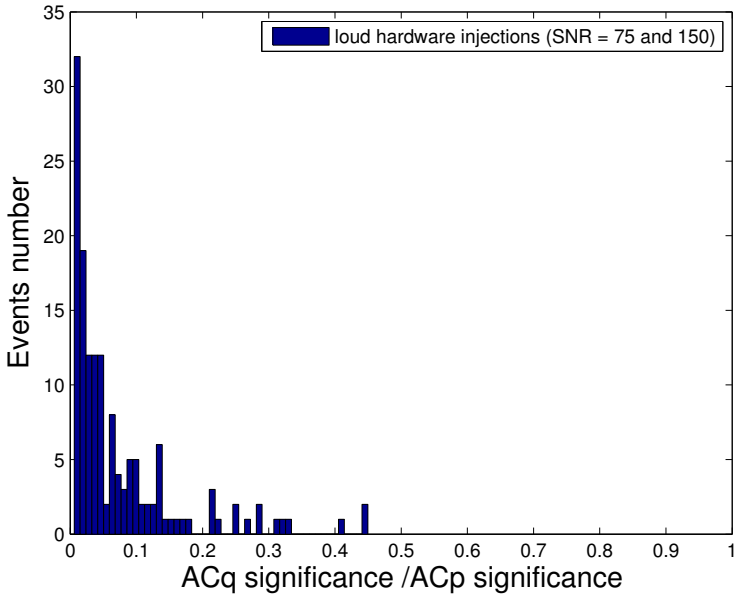

Figure 4.30: Ratio of the KW significance of coincident triggers seen in the in-phase GW channel ACp and the quadrature channel ACq. These KW triggers have been associated to the high SNR (75 & 150) hardware injections.

Veto construction For the definition of the PQ veto, we considered all coincident ACp-ACq KW triggers whose ratio κ is higher than 1. Furthermore, only coincident triggers with an ACq significance higher than a given threshold (100) have been considered. This is admittedly arbitrary, but it allows us to focus only on the periods of data where significant glitches in the ACq channel are observed. We are only interested in studying and suppressing periods with large amplitude glitches in ACq and in ACp and not those just above the noise floor. We tested different values of the ACq KW significance threshold; 100 has been found to be a good compromise between keeping the deadtime low and vetoing moderate amplitude glitches. The third parameter that has been considered is the veto time window size about the ACp-ACq coincidence time. The size of this window has to be large enough such that all glitches connected to a PQ event are really suppressed. Actually, we have noticed that some of the very large amplitude glitches are so long (several hundreds of ms) that a large veto window is needed; Looking at the time duration of the largest glitches seen in coincidence in ACp and ACq, we found that a fixed 800 ms veto window needs to be applied in the definition of the PQ veto to suppress the entire glitch period and not only a small fraction around the peak time. It turns out that this veto window was large enough so that it could be adapted both for the burst and CBC searches. We considered several values of the threshold on the KW significance of the ACq triggers, and decided to choose 100 and $\kappa = 1$. $\kappa = 1$ is the minimal value that we could consider given the safety results obtained in Section 4.5.5.2. The threshold on ACq has been chosen considering the ratio efficiency/deadtime. It should be noted, that keeping a high threshold on the KW significance of the ACq triggers allows one to concentrate the application of this veto on the loudest events, and thereby keeping the deadtime (and accidental coincidences) relatively low. This corresponds to a veto dead time of 0.036%, which is small.

Application to burst and CBC analyses Once defined, the PQ veto has been applied to triggers of several burst and CBC pipelines. We estimate the fraction of triggers louder than a given SNR that are effectively vetoed. In Table 4.8 we report the PQ veto efficiency for KW [337] Virgo triggers (burst analysis) and MBTA (Multi-band Template Analysis) [382] Virgo triggers (CBC analysis) For large SNR triggers, this veto has a very high efficiency. Furthermore, the deadtime is much smaller than the efficiency, demonstrating the significance of the veto. Despite the fact that the PQ veto only corresponds to a relatively small number of triggers, almost half of the loudest remaining triggers after all other data quality flags and vetoes have been applied can be suppressed by this veto. This demonstrates its usefulness for the burst and CBC analyses. Figure 4.31 shows the SNR distribution of the MBTA triggers before and after the application of the PQ veto.

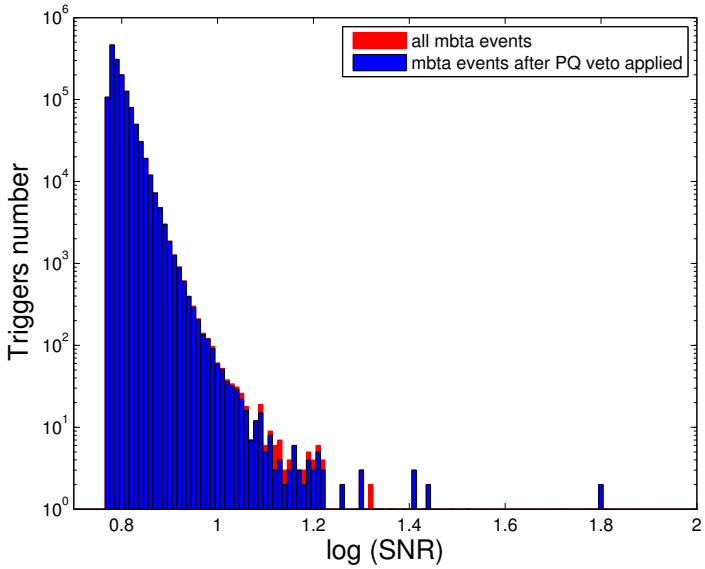

Figure 4.31: Distribution of the SNR of the MBTA Virgo triggers before the application of the PQ veto (red) and after the veto is applied (blue). All other data quality flags and vetoes have been applied.

Burst	h(t) significance higher than			50	100	200	
	PQ veto efficiency (%)			13	25	40	
CBC	h(t) SNR higher than	8	9	10	11	12	13
	PQ veto efficiency (%)	9	21	33	38	43	45

Table 4.8: Fraction of KW burst triggers and MBTA triggers suppressed by the PQ veto during VSR1. The deadtime is 0.036 %, much smaller than the efficiency.

4.5.5.3 Results with VSR2, VSR3 and VSR4 data

Similar studies have been performed with the successive runs. The main changes were the use of SNR instead of significance for the KW triggers and the reduction of KW triggers that were generated for SNR>7.5 instead of SNR>4 as during VSR1. This reduces the accidental coincidence rate between ACq triggers and hardware injections. Figure 4.32 shows the results from all the runs. Note that VSR1 data have been reprocessed for comparison. Table 4.9 reports numbers about triggers and hardware injections coincidence. One thing to note is that the number of ACp and ACq triggers vary greatly from one run to another. It is also much higher than the accidental number of coincident events given the size of the coincidence window (2 ms) as the two signals in quadrature see common noise sources. Each run had very different experimental conditions with different control systems. The control of the demodulation phase improved over the four science runs. From one run to another, the number of loud HI associated to coincident ACp/ACq triggers is changing. But more importantly, Figure 4.33 shows that this number is not constant as function of time. For VSR1 and VSR2, there are days that have obvious excesses. We did not know the origin, but can suspect phase mis-tuning during these days. Following the same hypothesis, one can note that the phase during VSR4 was particularly well controlled. During VSR4 a servo loop was in running to control the phase well within 1 degre [402]. In any case, all loud hardware injections were found outside the ACp/ACq region that was considered for the veto.

	VSR1	VSR2	VSR3	VSR4
SNR> 7.5 ACp triggers nb	162089	119000	358800	41561
SNR> 7.5 ACq triggers nb	303351	3649878	123975	56065
Science duration [s]	9.49×10^6	12.85×10^6	4.33×10^6	7.22×10^6
SNR< 20 injections nb	2244	645	215	244
SNR> 20 injections nb	315	720	390	702
ACp/ACq coincident nb	32392	32874	77459	10044
ACp/ACq accidental nb	10	67	21	1
ACp/injections (SNR> 20) nb	315/315	720/720	380/390	701/702
ACp/ACq/injections (SNR>20) nb	45/315	50/720	66/390	4/702
ACp/ACq/injections (SNR>20) accidental nb	0.9	0.35	1.1	0.15

Table 4.9: ACp and ACq triggers, coincident rate and accidental coincident rate of the PQ veto for all Virgo science runs.

4.5.5.4 Conclusions

We have developed for the VSR1 data a veto to suppress glitches that show up with more energy in the quadrature than in the in-phase interferometer output channel. We demonstrated using hardware injections that the veto is safe with respect to a real GW event. Furthermore, the deadtime of the veto is very small and it suppresses half of the remaining loudest Virgo triggers in the burst and CBC pipelines after all the other data quality flags and vetoes have been applied. This veto is being considered as a powerful way to reduce loud glitches in Virgo and thus the rate of the LIGO-Virgo accidental coincidences.

But because of its inherent potentially unsafe nature the PQ veto was applied as a cat 3 flag by many searches, despite its high efficiency to suppress loud glitches not vetoed by any other veto.

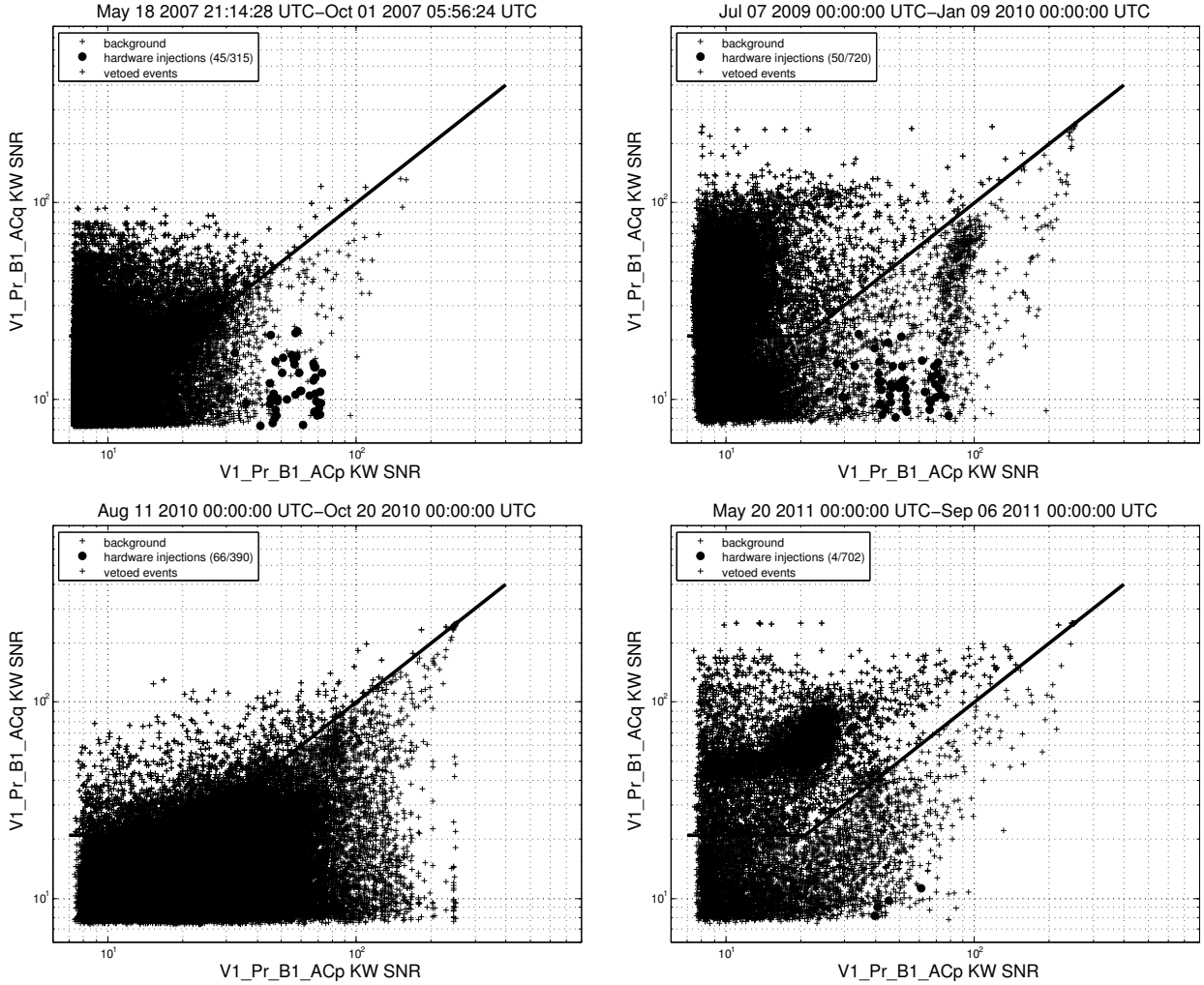

Figure 4.32: SNR of the coincident KW triggers in the two quadrature demodulated channels of the output dark port signal: ACp (in phase) and ACq (in quadrature) for VSR1, VSR2, VSR3 and VSR4. The time coincidence window of the triggers seen in the two channels is 10 ms. All other data quality flags have already been applied. The hardware injection signals, which were seen in both of the two demodulation phase channels, are indicated by the circles.

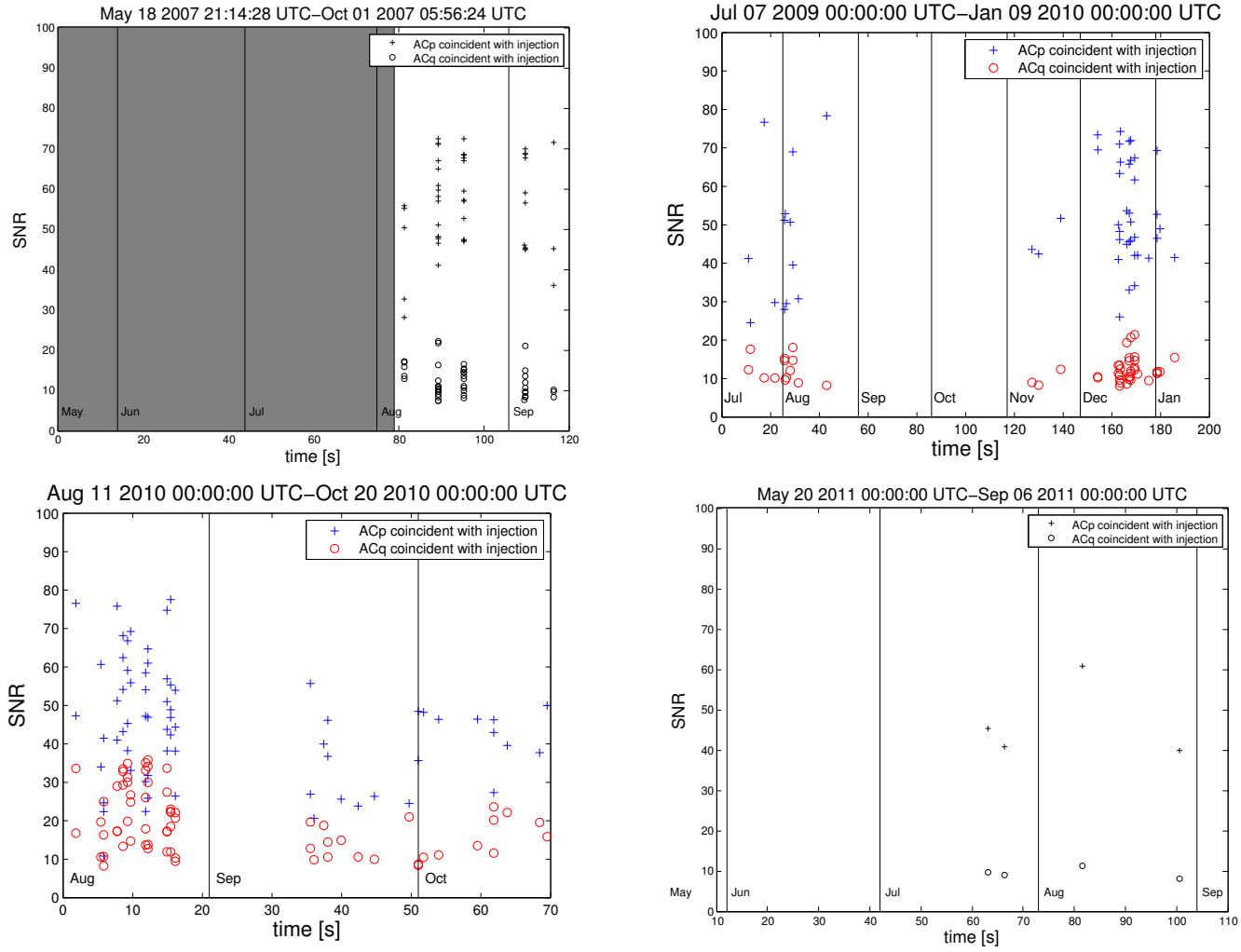

Figure 4.33: SNR of the coincident ACp and ACq triggers that are coincident with an hardware injections as function of time for VSR1, VSR2, VSR3 and VSR4 run. The grey area indicate periods during which no hardware injections were performed.

4.5.6 Veto tuning, veto performance and impact on GW searches

As explained in 4.5.2.1, vetoes' performance were blindly evaluated using GW triggers generated from two GW transient searches, one targeting very short transients (Omega), the other one targeting CBC signals (MBTA). In the following, we will report on results concerning only the Omega triggers. The goal of the veto performance study is to provide recommendations for burst and CBC searches whether and how vetoes should be used. Use percentage, deadtime, efficiency and efficiency/deadtime were computed for all vetoes. These quantities were computed for different triggers of different strengths. It may also happen that the veto segment boundaries were not correctly defined. To fix this, segments' boundaries can be modified. A given segment list and its padding window were then assigned to a category (see section 4.5.2.1). The assignment was done by hand, and was based on the efficiency of the veto to suppress specific type of triggers. For instance the presence of extremely loud glitches was an indication that the data should not be analyzed at all (category 1 veto). The difference between category 2 and 3 was not as precise. Category 2 vetoes contained mainly flags that had a high efficiency and a low dead-time (efficiency/deadtime is thus large). Most of the category 3 vetoes concerned glitches of moderate SNR (< 10) that were numerous but not always problematic for a genuine GW event to show up in the tail of the distributions. Some of the category 3 vetoes had large deadtimes

or low use percentages. As the probability to veto a GW genuine event is given by the total deadtime of all vetoes applied, the selection of vetoes and their category assignment is a compromise between the capability to disentangle genuine GW events and background events and keeping the veto deadtime as low as possible. In the end, for each run, a list of category 1, 2 and 3 vetoes were provided for burst and CBC generic GW searches. Note that a segment list can be assigned to 2 different categories with different padding windows. The padding window is determined among all possible combinations of $\pm$ 10 seconds, by maximizing the ratio efficiency/deadtime for triggers with SNR > 8.

Figure 4.34 supports the fact that the goal of category 1 vetoes is to suppress all the periods of time that are highly affected by large noise perturbance. The performance of the category 2 and 3 vetoes are represented in Figure 4.35. The efficiency depends on the SNR of the glitches that also tend to gather in families with similar properties (SNR, frequency and duration). One should note that from one run to another, glitch families are not identical. This is the reason why the vetoes' efficiency at a given noise event SNR varies a lot from one run to another: For instance VSR1 category 2 (category 3) vetoes efficiency was 49% (54%) for SNR$>$ 10 glitches, while it reached 75% (85%) for VSR2 vetoes, as shown on Figure 4.35. As the interferometer configuration is different from one run to another, the glitch rate can vary significantly: 2.1 Hz for VSR1 and 0.6 Hz for VSR2 for triggers with SNR > 5 after category 1. The VSR2 run start was proceeded by an important campaign of noise hunting that fixed problems and optimized several optical control loops. A large fraction of the remaining glitches were due to scattered light effects for which efficient vetoes could be defined. Many of these glitches had a moderate SNR. The VSR2 vetoes thus have an excellent efficiency for low SNR triggers, but as these glitches were numerous the deadtime is not negligible.

As already mentioned, the category 2 and 3 vetoes assignment is a rather subjective process, based on the efficiency, the deadtime and the use percentage of each veto for different categories of glitches (small, moderate or large SNR). As the quality of data varies during a run, veto performance results will vary. For VSR1, VSR2 and VSR3 the vetoes' performance was checked by splitting the full data in month-long periods and then compared to the results obtained on the full run period. That allowed one to specify time limits for the application of a few vetoes and their category assignment. That concerned only few vetoes that were especially useful to suppress very specific noise perturbance, that was not present during the full run. For VSR4, we selected and assigned a category to each veto looking at the veto performance over week long periods. That had the great advantage to really follow the variation of the rate of the different families of glitches. The glitch rate can vary quickly, and optimizing the veto selection over 1 week long periods has been found to be more efficient than a selection done looking at the whole run data set. The comparison between the two ways to select vetoes and categories is not straightforward as the resulting deadtime is rather different: Category 1 and 2 vetoes deadtime was 12.9% for the whole run optimization and only 4.5% when the selection was done week after week. However, one can note that, except for the Omega triggers whose SNR was below 10, the week-long selection was more efficient while the overall deadtime was much lower (see Figure 4.36). The efficiency/deadtime comparison showed that for any category of triggers the week-long selection was more appropriate. This should be remembered for advanced Virgo veto selection.

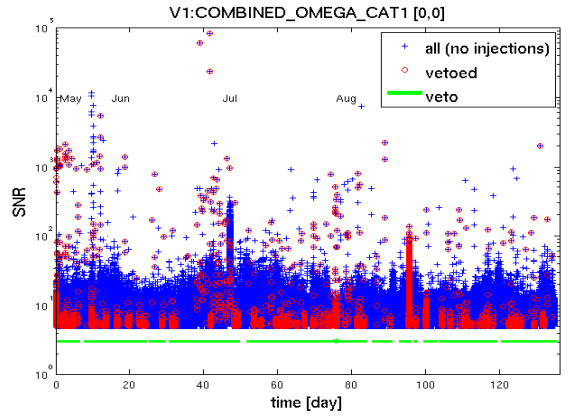

	eff	use perc.	eff/dt
SNR> 5	38992 / 20035307=0.20%	52.7%	0.1
SNR> 8	2310 / 668345=0.35%	41.1%	0.2
SNR> 15	606 / 59235=1.02%	32.4%	0.7
SNR> 30	278 / 17095=1.63%	29.2%	1.2

deadtime: 133903 / 9487112=1.41%

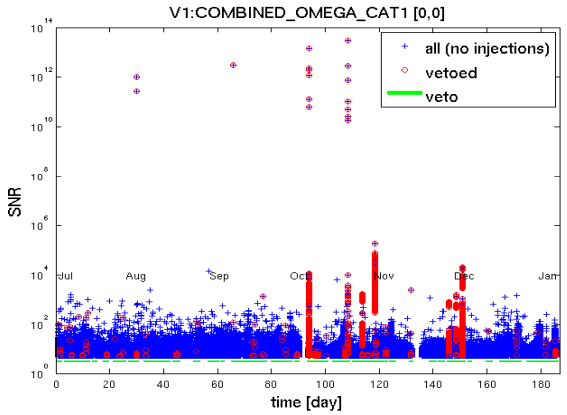

	eff	use perc.	eff/dt
SNR> 5	5716 / 8123418= 0.1%	21.5%	0.8
SNR> 8	4461 / 205717= 2.2%	15.4%	24.6
SNR> 15	4120 / 31966=12.9%	13.3%	146.5
SNR> 30	2788 / 5484=50.9%	10.8%	577.7

deadtime: 11355 / 12903027=0.088%

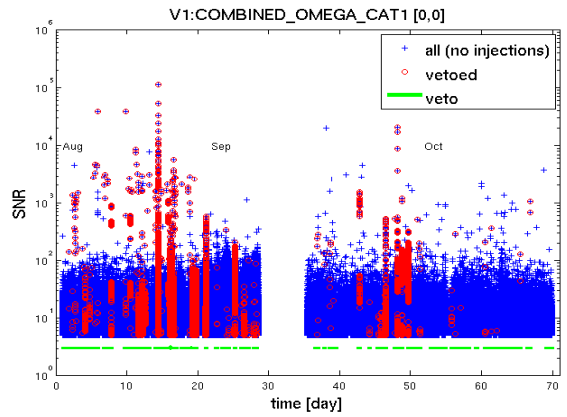

	eff	use perc.	eff/dt
SNR> 5	145359 / 7856834=1.9%	81.7%	1.4
SNR> 8	54799 / 696800=7.9%	77.3%	5.8
SNR> 15	35443 / 114220=31.0%	60.4%	23.0
SNR> 30	19360 / 39979=48.4%	47.8%	35.9

deadtime: 58762 / 4355153=1.35%

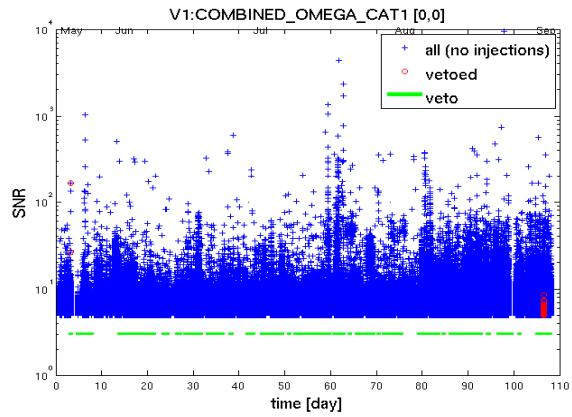

	eff	use perc.	eff/dt
SNR> 5	95 / 7075002=0.001%	1.2%	0.02
SNR> 8	3 / 114582=0.003%	1.2%	0.04
SNR> 15	2 / 10332=0.019%	0.6%	0.28
SNR> 30	1 / 1798=0.056%	0.6%	0.81

deadtime: 4948 / 7226139=0.068%

Figure 4.34: Left: SNR of all Omega triggers as function of time for the four Virgo science runs. The red circles indicate which triggers are eliminated if all defined category 1 vetoes are applied. Right: Figure of merits of the category 1 vetoes.

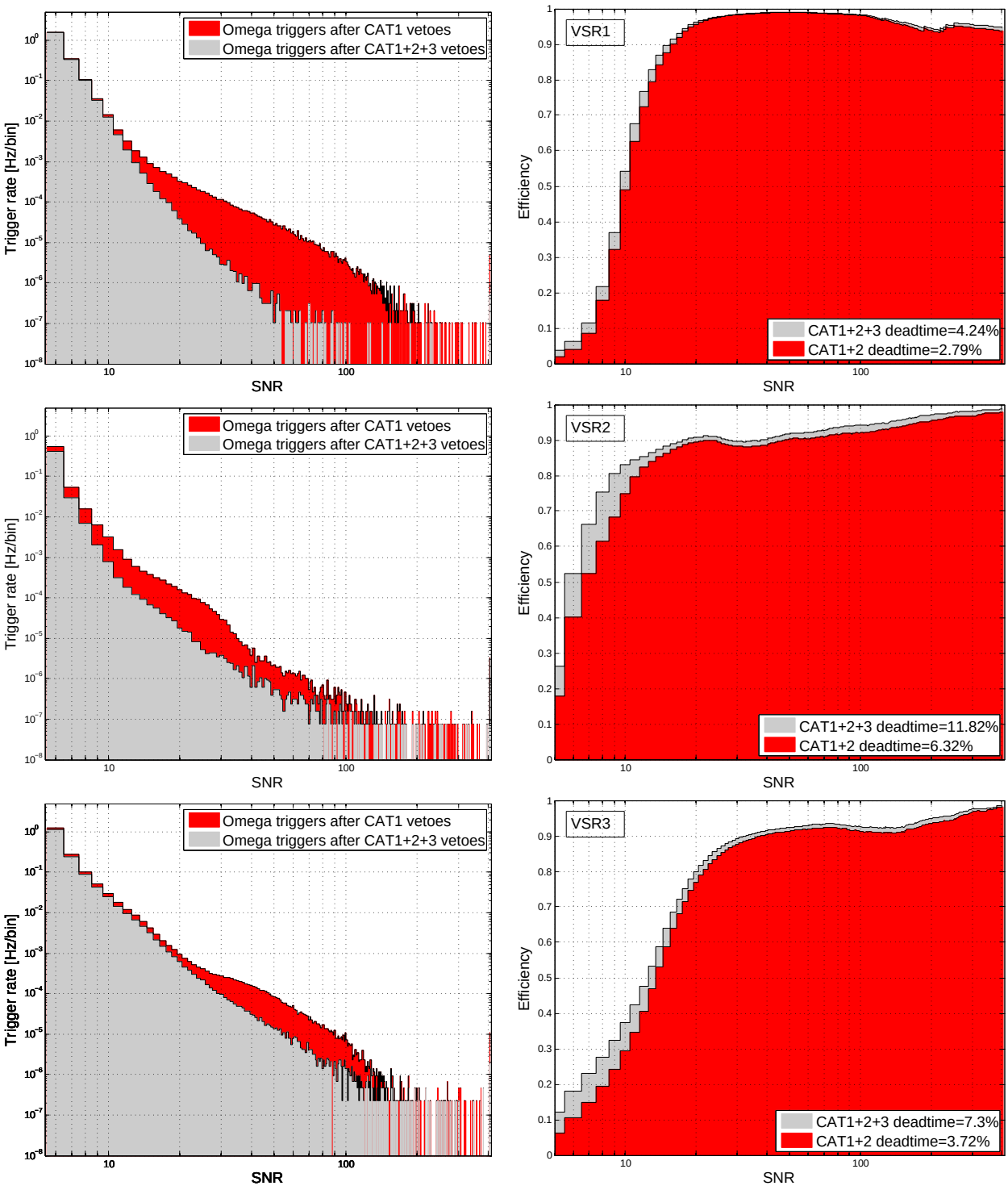

Figure 4.35: Left: Virgo Omega triggers' rate as function of the triggers' SNR after category 1 vetoes are applied (red) and after category 1, 2 and 3 vetoes are applied (grey) for VSR1, VSR2 and VSR3 runs. Right: Vetoes' efficiency as function of the SNR of the Omega triggers. The red histograms are for category 1 and 2 vetoes. The grey histograms concern all category vetoes.

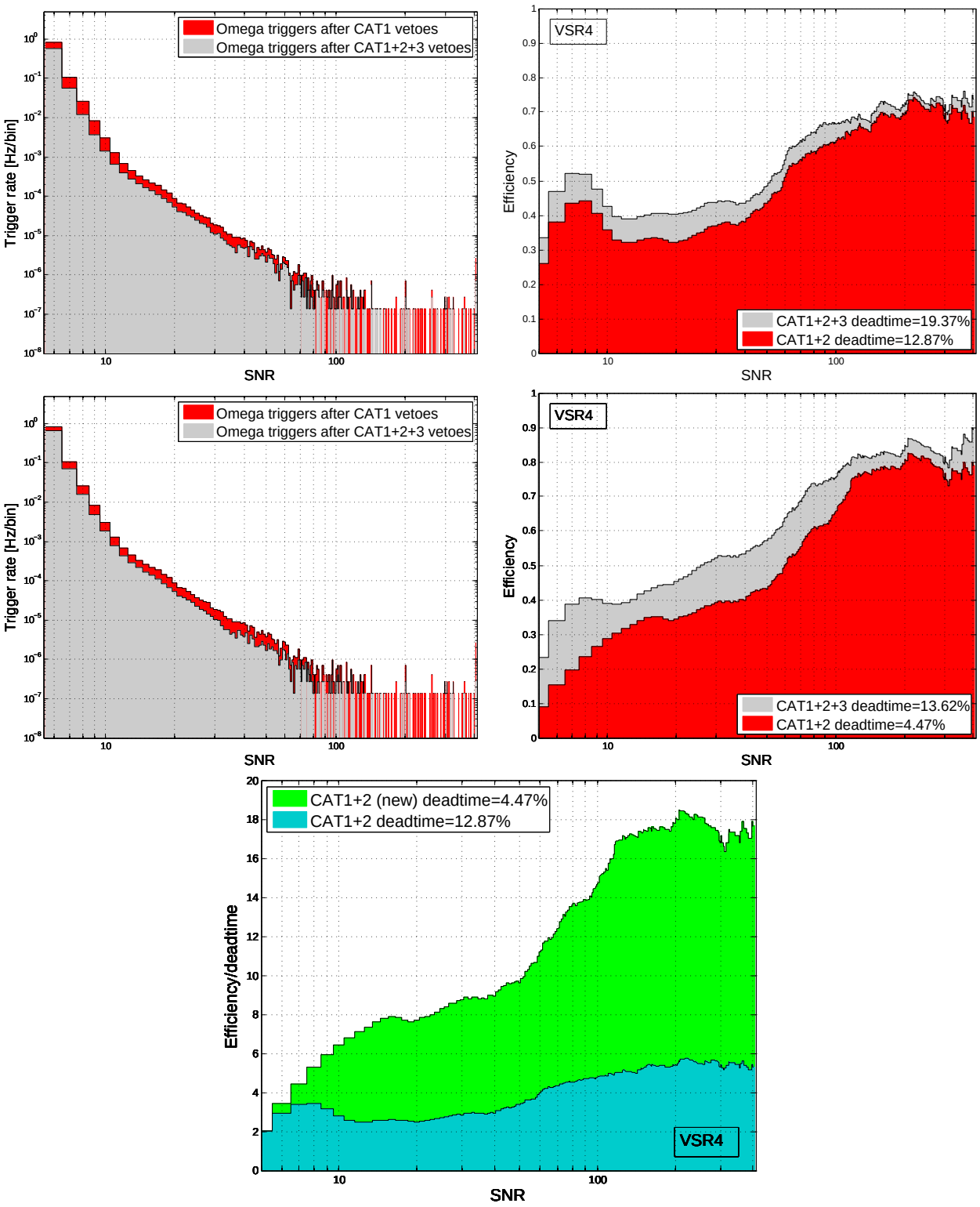

Figure 4.36: Left: Virgo Omega triggers' rate as function of their SNR after category 1 vetoes are applied (red) and after category 1, 2 and 3 vetoes are applied (grey) for the VSR4 run. Right: Vetoes' efficiency as function of the SNR of the Omega triggers. The red histograms are for category 1 and 2 vetoes. The grey histograms concern all category vetoes. Top row: The selection of vetoes has been done as for the other runs (looking at the veto performance over the whole data set). Middle row: The list of vetoes and their assignment is defined for each week. Lower row: Efficiency/deadtime for category 1 and 2 vetoes selected using vetoes' performance over week-long periods (green) or the whole run (light blue).

4.5.6.1 Use of UPV and hVeto vetoes

As described in Section 4.5.4, vetoes using KW triggers have been generated by two algorithms (UPV and hVeto). Both algorithms used the time coincidence between transients in an auxiliary channel and the strain amplitude channel. UPV vetoes have been generated either for CBC triggers (online low mass CBC search triggers) and burst-like triggers, using the online non calibrated strain amplitude KW triggers. The selection of channels differed only slightly. UPV and hVeto vetoes have been applied as category 3 vetoes for rather arbitrary reasons as for many of those vetoes the performance in terms of efficiency/deadtime are rather good. UPV and hVeto have been useful to identify automatically and quickly (all auxiliary channels are considered and results are generated daily and weekly) the channels that reveal a significant coincidence rate with glitches in the strain amplitude channel. In Virgo, we have adopted a strategy that consisted of implementing a data quality flag based on the most significant auxiliary channels revealed by UPV or hVeto. These data quality flags can then be promoted as a category 2 veto. That is the reason why for Virgo data, the remaining UPV and hVeto vetoes were only marginally interesting as they veto events already vetoed by a data quality flag as shown in Figure 4.37. One should mention that UPV and hVeto vetoes were performing better for LIGO data because the most significant auxiliary channels found by UPV and hVeto were not "transformed" into a DQ flag like in Virgo.

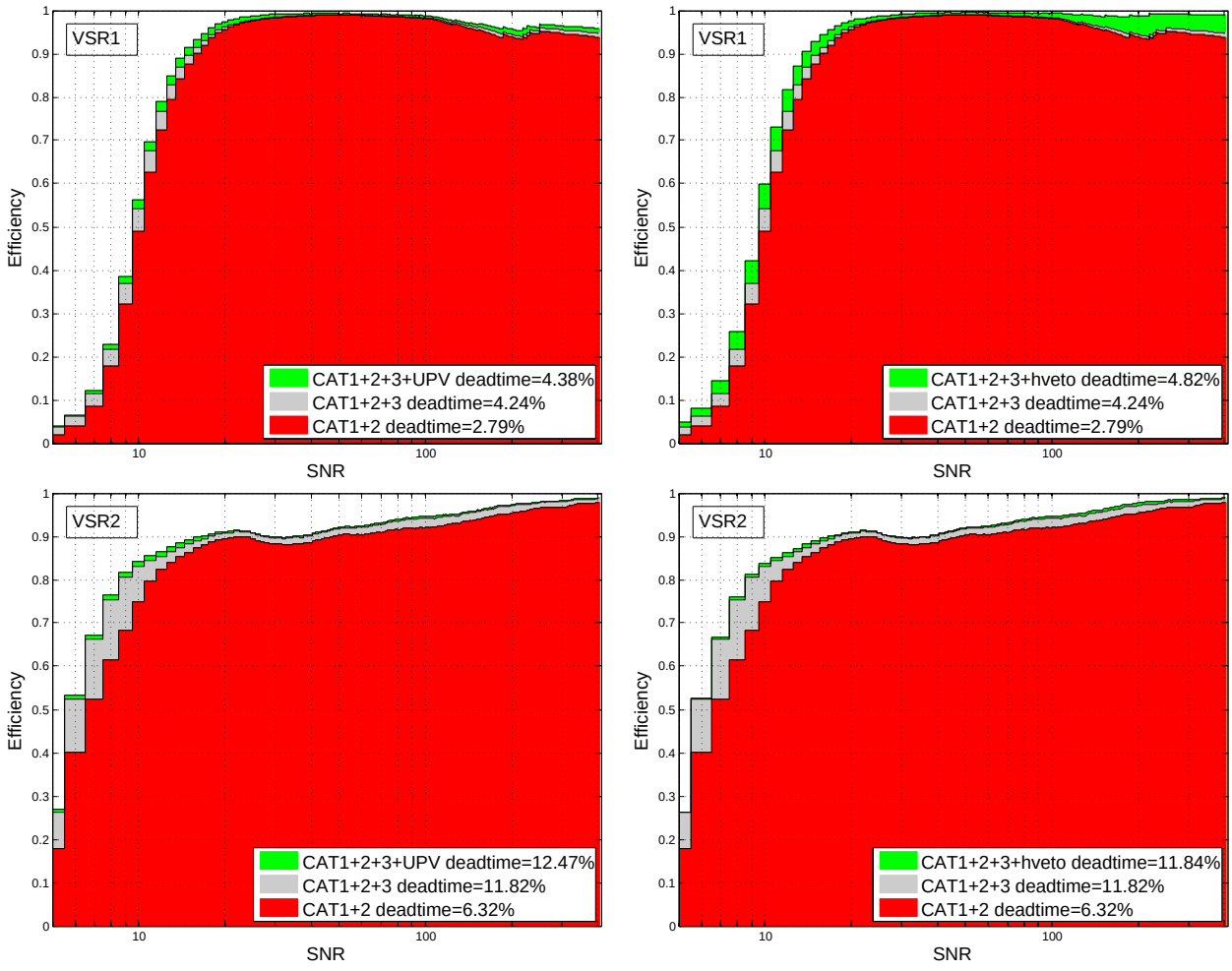

Figure 4.37: Efficiency of the UPV (left) and hVeto (right) vetoes as function of the SNR of the Omega triggers for VSR1 and VSR2 runs. The grey histogram shows category 1+2+3 efficiency while the light green histogram shows the contribution of the UPV and hVeto vetoes.

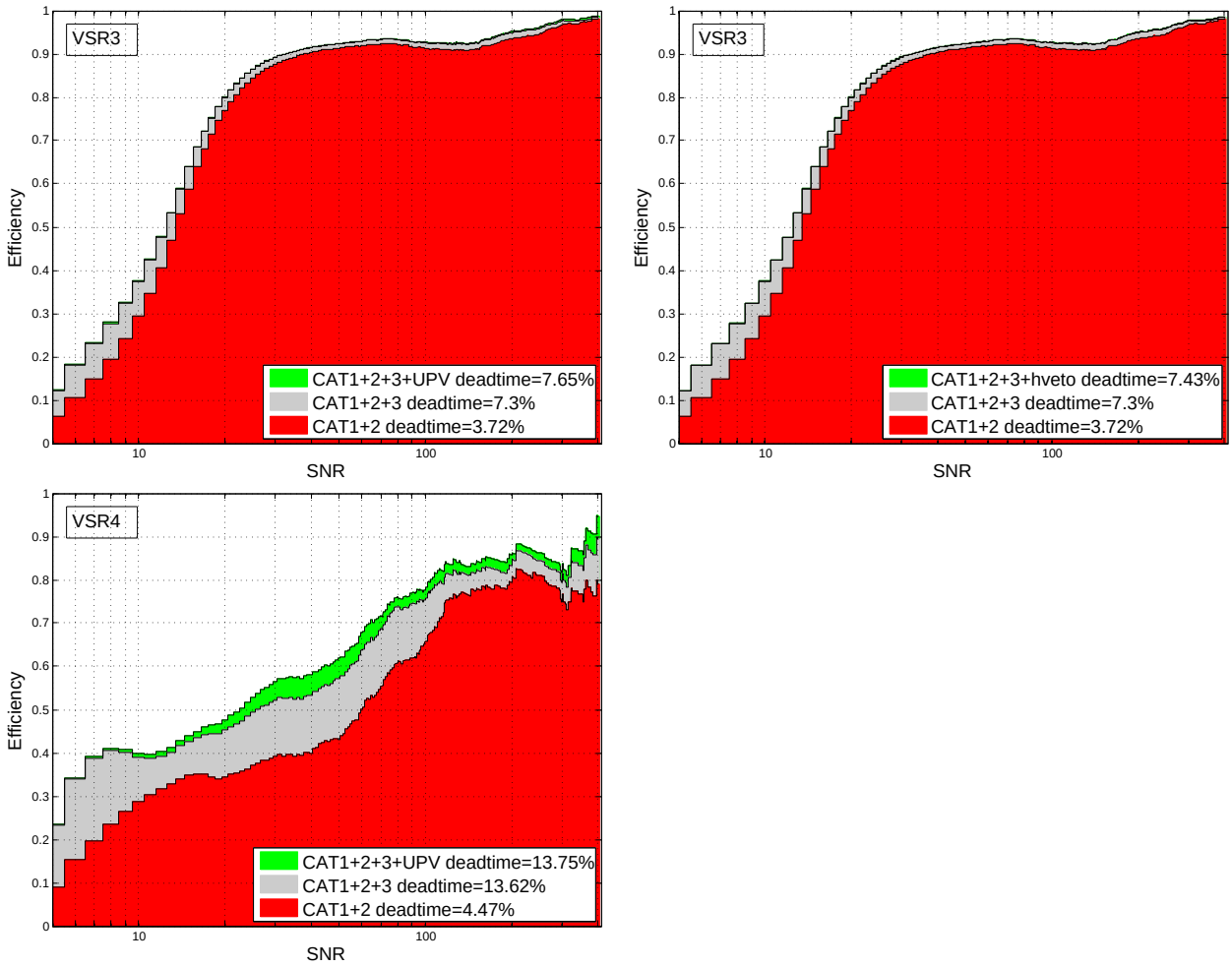

Continued Figure 4.37: Efficiency of the UPV (left) and hVeto (right) vetoes as function of the SNR of the Omega triggers for VSR3 and VSR4 runs. The grey histogram shows category 1+2+3 efficiency while the light green histogram shows the contribution of the UPV and hVeto vetoes. For VSR4, only UPV vetoes have been generated.

4.5.6.2 Impact on GW burst search

There is no reliable way to predict the effect of the vetoes on a multi-detector transient search from the vetoes performance for single detector triggers. It especially depends on the weight assigned to each detector when data streams are processed. In a simple time coincident search, all detectors' triggers have the same weight, regardless of the sensitivity difference between each detector. When data streams are coherently combined, data streams of the low sensitivity detectors are, a priori, naturally suppressed. One thus expects that loud glitches from such low sensitivity data streams are playing a minor role in the overall background triggers tail. Following [211] two months[9] of coherent WaveBurst (cWB) triggers involving Virgo data (H1L1V1, H1V1 and L1V1 exclusive coincident time) have been considered to estimate the effect of the Virgo vetoes on the false alarm rate reduction. Figure 4.38 shows the evolution of the false alarm rate using two different ways to rank cWB triggers: the SNR in Virgo data and the ρ variable that measures the degree of correlation between several data streams. The latter is used to rank cWB triggers. To measure the Virgo vetoes overall interest for GW transient searches, one needs to consider triggers after cWB selection cuts. The false alarm rate as function of the SNR measured in Virgo data showed that Virgo CAT2 vetoes were rather efficient for all 3 network configurations (H1V1, L1V1 and L1H1V1). For instance, between 73%

[9]November and December 2009 during VSR2 run.

and 92% of the cWB triggers having an SNR higher than 10 were vetoed by Virgo vetoes. Those efficiency results were comparable with the vetoes performance obtained with single detector Omega triggers.

However, what really matters for a search is the reduction of the tail of the background events ranked with ρ as the less events at high ρ, the greater the detection volume to estimate the impact of the Virgo vetoes. One can also consider, for a fixed false alarm rate, how much the corresponding ρ value changed when Virgo vetoes were applied. The present study with only 2 months of data did not reliably answer to the question, but if one considers a false alarm rate of 3×10^{-9} Hz (1 event in 10 years) the corresponding ρ threshold is improved by Virgo vetoes by 11% and 18% for H1V1 and L1V1 network configuration, but only 2% for the triple L1H1V1 network configuration[10]. If the difference between H1V1 and L1V1 is not understood (Virgo vetoes efficiency is at least twice more efficient for the H1V1 network configuration), Virgo vetoes have an overall greater impact on two-fold network combinations than on the three-fold. LIGO vetoes were not applied in this study, but we have checked that LIGO CAT1+2+3 vetoes have a similar impact than Virgo vetoes. Vetoes are contributing to the reduction of the background outliers but were far from being sufficient to get rid of the huge excess of outliers compared to what was expected if S6/VSR2 data were Gaussian (see Figure 4.38).

4.5.6.3 Non identified problems

As shown in Figures 4.35 and 4.36 vetoes have suppressed almost all loud glitches seen in Virgo data for all runs. Figure 4.39 shows the distribution in time and frequency of Omega triggers that pass Virgo vetoes. The comparison from one run to another was not straightforward as the trigger rate for each run was different (during VSR3 the glitch rate was $\sim$ 1 order of magnitude higher than the other run). After all the vetoes were applied, VSR2 and VSR4 runs were dominated by low frequency glitches.

All remaining glitches with SNR > 100 have been checked (5 for VSR1, 73 for VSR2, 181 for VSR3 and 39 for VSR4). Most of them show an isolated and very short glitch with no significant coincident transients in an auxiliary channel. None of them have revealed that a veto based on coincidence with a glitch in an auxiliary channel could have been defined. The only family of remaining glitches that has been identified is characterized by glitches with energy deposited in both the in-phase (ACp) and quadrature (ACq) interferometer output channels. They passed the PQ veto because the SNR reconstructed in the ACq channel was lower than the ACp SNR. A fraction of these glitches were characterized by a low frequency (< 100 Hz). KW algorithm is known to poorly recover a transient signal whose content is at low frequency[344]. Replacing KW with a transient finder algorithm capable of reconstructing low frequency transients, such as the Omicron trigger generator derived from the Omega pipeline [403], should increase the efficiency of Virgo vetoes.

4.6 Conclusions

Vetoes studies have already started with advanced LIGO. Among the improvements one can cite the use of trigger generators providing more accurate frequency information [403, 404] and the use of the frequency for the UPV vetoes [403]. Much of the data quality information used by GW searches is based on glitches visible in auxiliary channels. Other types of non linear couplings between a noise source and the GW strain channel are not revealed this way and other algorithms looking at deviations of the optical elements from their nominal positions should be very useful (Excavator [391] and BCV [390] are two examples).

Past GW searches with LIGO and Virgo data have shown that the use of vetoes, and more generally, data quality is fundamental to cleaning the data and can improve the searches' sensitivity considerably. Yet, an effort to simplify the use of data quality information in GW searches is needed. Ideas to combine the data quality information into a time series quantity that would give a "data quality" weight to any GW trigger instead of defining veto segments of different categories will be investigated.

The data quality information must also be generated with a maximal latency of a few minutes to allow low latency GW searches to send alerts to other partners for rapid follow-up of the GW candidates. This effort of making data quality information generation automatic has already started, but the past experience has shown that building an error-free system requires time and human effort.

[10] 20% of reduction of the ρ threshold correspond roughly into a sensitivity gain of a factor 2.

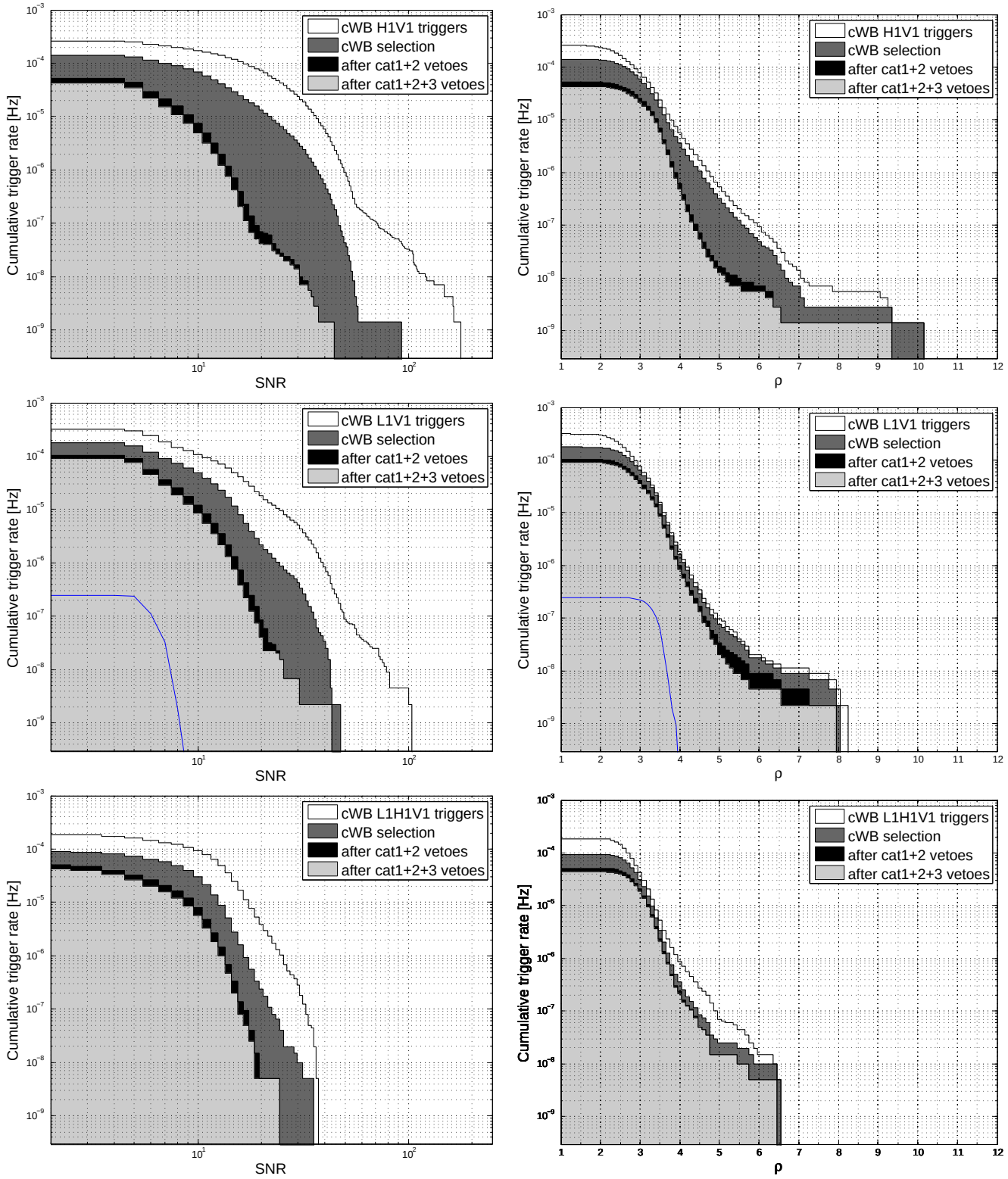

Figure 4.38: cWB triggers' rate as function of the SNR reconstructed in Virgo data (left) and the correlated energy ρ (right) after cWB selection and Virgo vetoes selection. The blue thin line histogram for the L1V1 network configuration is obtained with Gaussian simulated data.

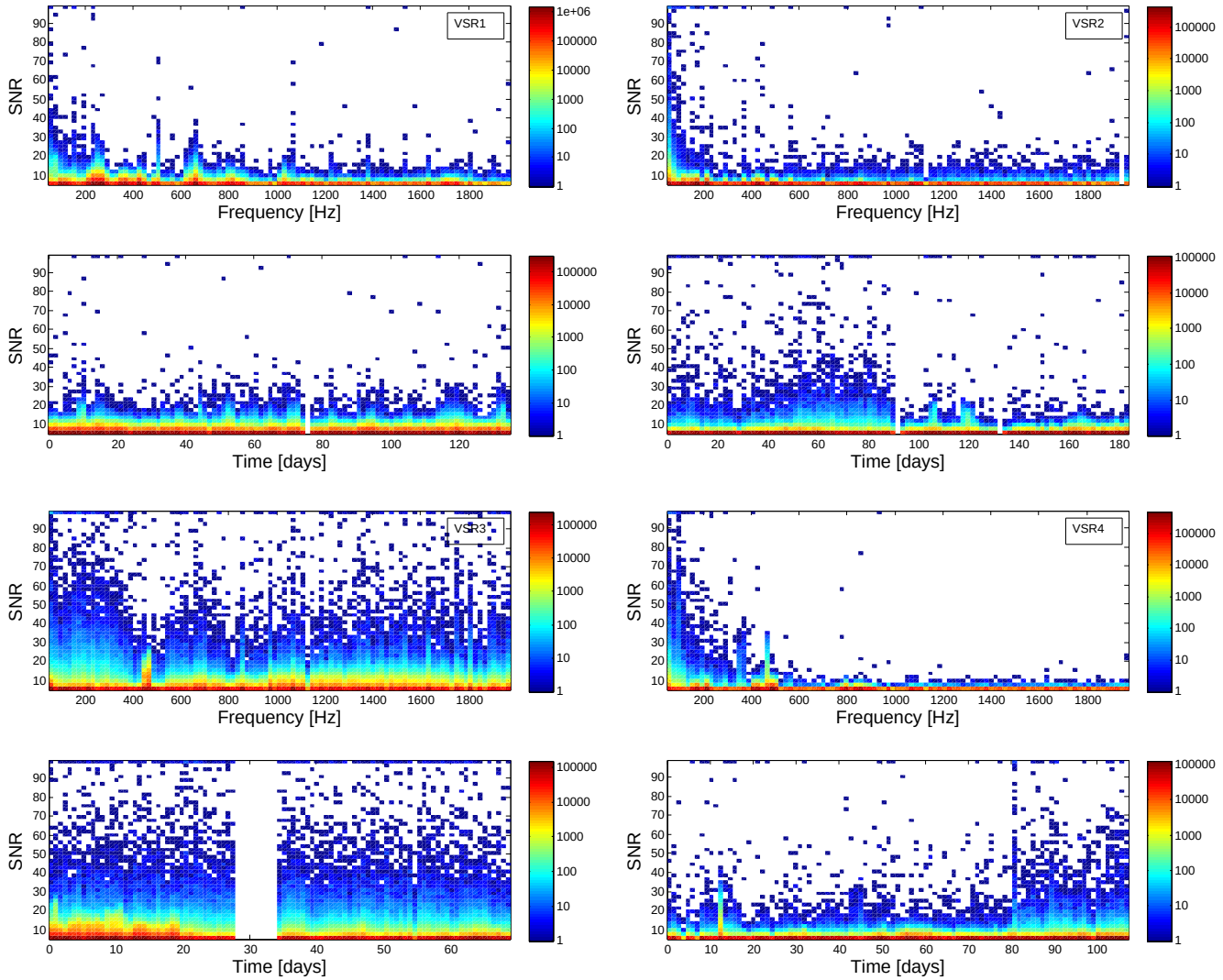

Figure 4.39: Density of Omega triggers passing all vetoes (category 1+2+3 and UPV) in the frequency versus SNR and time versus SNR plans for the 4 Virgo runs.

Chapter 5

Epilogue

5.1 Virgo joining LIGO detectors in Summer 2017

After the end of the first observing run (O1), the LIGO detectors underwent a ten month long commissioning and upgrade campaign. In the meantime advanced Virgo installation completed and the commissioning of the detector started in November 2016. As planned in [271] the second observing run (O2) started end of November 2016 with two LIGO detectors but without Virgo whose commissioning was just starting. The Michelson degree of freedom of Virgo got locked at half fringe (while maintaining its recycled laser power) just before the end of the year. Eight more months were needed for Virgo to reach a binary neutron star (BNS) inspiral range of 28 Mpc, a factor 2-4 less than LIGO Hanford (BNS range of $\sim$ 50 Mpc) and LIGO Livingston (BNS range of $\sim$ 100 Mpc) in August 2017. In fact, once the major control systems (longitudinal and angular controls of the suspended mirrors and the laser frequency stabilization) were routinely controlled after April 2017, the Virgo sensitivity improved quickly as a solid noise mitigation campaign could take place. The Virgo sensitivity evolution after May 2017 is shown in Figure 5.1. Thanks to this unprecedented sensitivity, Virgo joined the LIGO detectors in the last month of the O2 obvserving run for the most exquisite and rewarding science run ever. The best advanced Virgo sensitivity obtained in 2017 is shown in Figure 5.2. The next paragraphs aim at summarizing the main steps of the advanced Virgo installation that took a bit more than four years to complete.

Like advanced LIGO, a major upgrade of Virgo concerned the reduction of the thermal noise, the most offending noise in the 40 Hz – 300 Hz frequency band. The major source of thermal noise comes from the coatings. To reduce the mirror coating thermal noise, the beam size on the test-masses has been enlarged by a factor 2.5 to lower the impact of the dynamical deformations. Coating materials and substrate materials of the core optics have been improved with the new test-masses. Each pair of test-masses (either the two input mirrors or the two end mirrors) have been coated at the same time to provide identical properties and symmetry, that is mandatory to cancel common noises in the interferometer when operated at dark fringe.

The second source of thermal noise is due to the vibrations of the last stage of the suspension (mirror, wires and mirror hangers). To reduce the friction and mechanical energy dissapation one uses fused silica monolithic suspensions to hang the test-masses to the suspensions' mechanical filters. The increase in size of the laser beam on the test-masses is probably the upgrade to advanced Virgo which provided the largest impact on the initial Virgo infrastructure and topology. Indeed, in order to accomodate this larger beam, most of the vacuum link pipes in the central area had to be replaced with larger ones. More demanding mode matching telescopes had to be developed and more difficult-to-operate, quasi-symmetrical Fabry-Perot cavities were installed in the arms.

The largest impact is on the power recycling cavity which, to be accomodated in the existing buildings, had to be designed with a very small Gouy phase, of the order of few milliradians, becoming marginally stable [405]. To cope with cavity instabilities, a thermal compensation system (TCS) to control the optical aberrations is expected to play a major role to keep the interferometer at the nominal working point.

To eliminate stray light due to ghost beams and scattered light additional baffles and diaphragms have been installed in different locations in the vacuum chamber. The residual gas pressure noise has been also mitigated by further reducing the vacuum pressure in the 3km-long tubes from 10^{-7} mbar of initial Virgo to 10^{-9} mbar. New optical benches, some of them suspended under vacuum, have been also installed during the advanced Virgo upgrade.

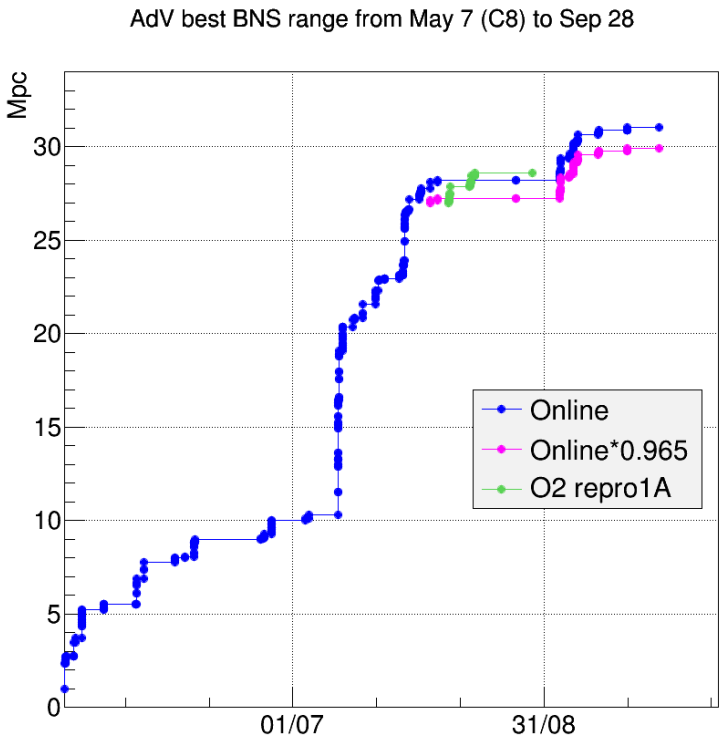

Figure 5.1: Advanced Virgo BNS range evolution From May to September 2017. The large gain around July 14th is due to a Data Acquisition upgrade that fixed aliasing issues. The magenta curve is the most accurate BNS range estimated by the Virgo calibration group in October 2017 [406]. The green curve is derived from the h(t) reprocessing that has been performed at the end of August for GW170814 and GW170817 related publications.

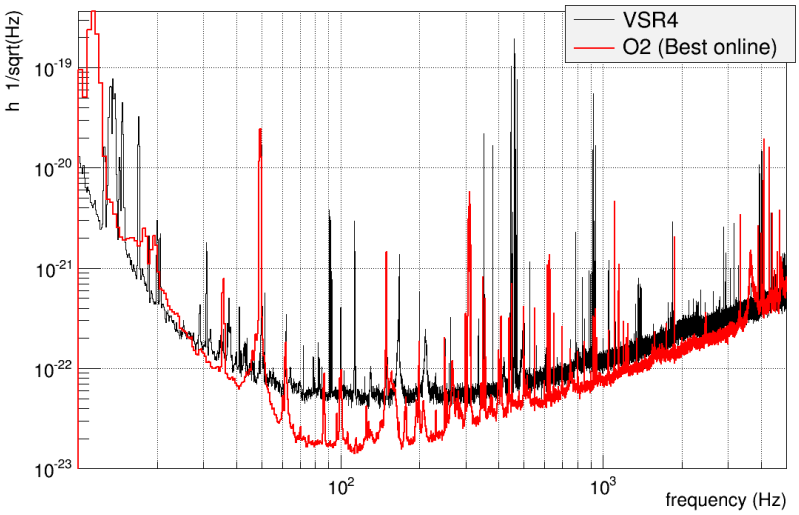

Figure 5.2: Best advanced Virgo sensitivity in 2017 (O2) compared to the best Virgo sensitivity in 2011 (VSR4).

In the frequency range 300 Hz – 10 kHz, the quantum nature of light is limiting the interferometer's sensitivity[1] In order to reduce the impact of quantum noise above 300 Hz the finesse of the arm cavities has been increased by a factor ~ 3 and a new laser power (~ 16 times more powerful than the initial Virgo laser) will be installed in the coming year[2].

The integration of the different components of advanced Virgo took several years and has been peppered with problems. To quote a few of them: the suspension anti-spring maraging steel blades breaking and the monolithic suspensions breaking too. The former was an ageing problem of an element that functionned optimally for more than 10 years (the failure was linked to embrittlement due to Hydrogen contamination during the machining process). More than 80% of the blades have been replaced. The later was not expected as monolithic suspensions had been successfully used in 2010-2011 (Virgo Science Runs 3 and 4). Yet, advanced Virgo monolithic suspensions fibers broke while under vaccuum during advanced Virgo installation in 2015 – 2016. It has been identified that the breaking always happened at the level of the wires. Tests in air had previously demonstrated that these silica fibers are super-resistant to heavy loads. On the contrary, when fast dust particles hit a fiber they produce fractures, that evolve with different time scale to a full break. The presence of dust particules has been later found to be due to some primary dirty scroll pumps. These pumps will be replaced soon with multi-stage root dry pumps. A temporary solution, driven mainly by schedule considerations, was to fall back to steel wires for payloads in the beginning of 2017 in such a way Virgo could join LIGO before the end of O2. The sensitivity with steel wires was calculated to be still compatible with the goal for the early stage of advanced Virgo.

5.2 The second observing run of LIGO and Virgo

Virgo joined the LIGO detectors on August 1$^{\text{st}}$ 2017 and ran until the end of O2 (August 25$^{\text{th}}$ 2017). The duty cycle of the Virgo detector approached 85% during this month such that the triple detector livetime reached 62% during the last month of the run. As shown in Figure 5.3, the LIGO Livingston sensitivity smoothly increased during O2 while LIGO Hanford had a sensitivity drop in July 2017 related to an earthquake in the Montana state. The Hanford sensitivity was then limited by the alignment control performance that never came back as good as before the earthquake.

Until August, two stellar-mass black hole mergers had been observed in LIGO O2 data, GW170104, GW170608 confirming the rate of binary black hole (BBH) merger, $9 - 240\,\text{Gpc}^{-3}\text{yr}^{-1}$, measured with O1 events [407]. In both cases, alerts were sent to EM follow-up partners who did not report any significant counterpart. In August 2017, Virgo commissioning efforts have been rewarded by the observation of the first triple detector BBH merger, GW170814, 14 days after Virgo came online. The parameters of GW170814 are similar to the other BBH events observed so far, but for the first time, the sky map of the source that has been sent to the EM follow up partners was reduced by a factor ten thanks to the triple detector network: the 90% credible region was reduced from $1160\,\text{deg}^2$ using only the two LIGO detectors to $60\,\text{deg}^2$ using all three detectors [408]. The other interest of a triple detector detection is the possibility to measure gravitational-wave polarizations from the antenna response of the LIGO-Virgo[3] network. We could show that the data of this event strongly favored pure tensor polarization of gravitational waves, over pure scalar or pure vector polarizations, but additional events observed in the LIGO-Virgo network will allow more interesting tests of gravitational-wave polarizations. Figure 5.4 shows the mass distribution of all known black holes, either through electromagnetic or through gravitational-wave observations.

Amazingly, only three days later, the low-latency compact binary searches detected a loud signal corresponding to a low mass binary system with component masses very close to neutron star mass [409]. The stricking additional information that came immediately was that at the same time Fermi-GBM had detected a weak GRB trigger (GRB 170817A). The Fermi-GBM trigger was 1.7 s after the gravitational-wave merger and the spatial coincidence of the two events made the probability that the two events appear by chance smaller than 5.0×10^{-8} [410]. Thanks to the fact the event has been observed by 3 detectors and despite the low SNR recorded in the Virgo detector, the source was localized in a sky region of $31\,\text{deg}^2$ at 90% and its luminosity distance was estimated to 40^{+8}_{-14} Mpc. GRB 170817A is the closest short GRB with a known distance, but is between 2 and 6 orders of magnitude less energetic

[1] The quantum noise is also responsible for radiation pressure noise at low frequency but many other technical noises dominate the noise floor below 40 Hz. Yet, twice heavier test-masses are now in place such that the safety margin against radiation pressure noise is larger.

[2] The 100 W laser will be installed for O3, but the power will not exceed 50 W in O3 because specific issues such as parametric instabilities that show up with high power in cavities need to be first addressed. For O4, a possible 200 W laser will be considered.

[3] And in a near future in the LIGO-Virgo-KAGRA network.

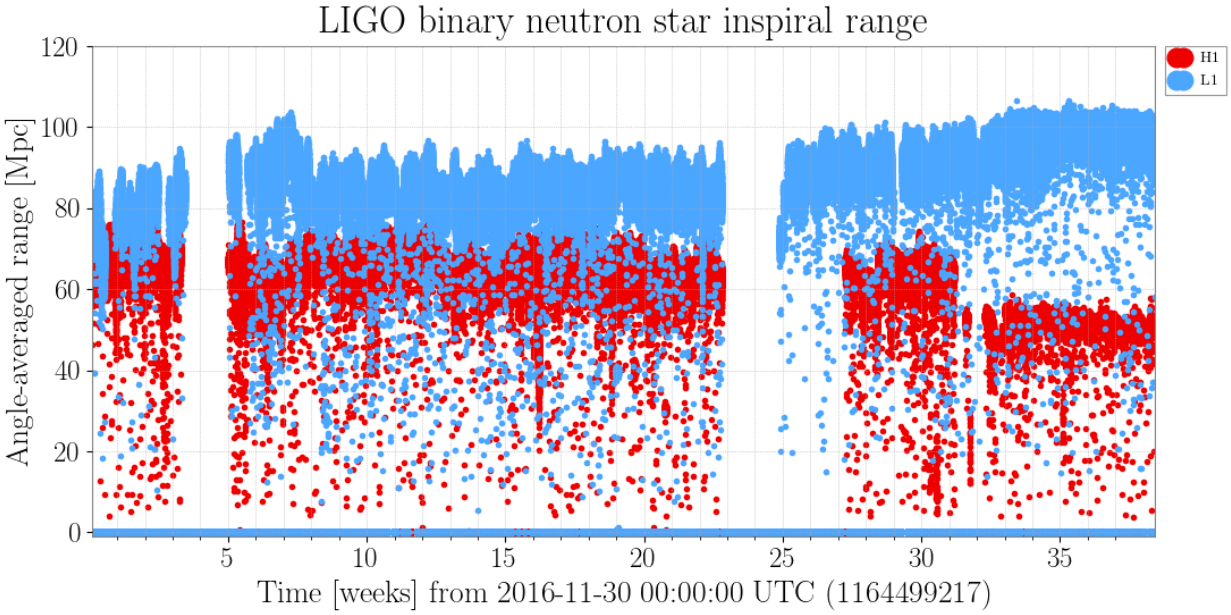

Figure 5.3: Time evolution of the LIGO detectors BNS range over the O2 run. The absence of data are due to periodes of commissioning, maintenance or interferometer unlocks.

than other bursts with measured redshift [410]. This is the first direct confirmation of binary neutron star merger being the progenitor of short GRB [411]. The nearly simultaneous observation of the merger and the GRB allowed for a constraint on the difference between the speed of gravity and the speed of light to be between -3×10^{-15} and $+7 \times 10^{-16}$ times the speed of light. New bounds on the violation of Lorentz invariance have been placed and a new test of the equivalence principle by constraining the Shapiro delay between gravitational and electromagnetic radiation is also now possible. The time delay is also used to constrain the emission region size and bulk Lorentz factor of the region emitting the gamma rays [410].

Realizing quickly the importance of the observation of GW170817, an initial alert has been sent within 30 minutes, mentioning the very likely observation of a very nearby binary neutron star merger. In a few hours the LIGO-Virgo skymap was available. As illustrated in Figure 5.5, the $\sim 31\,\mathrm{deg}^2$ obtained with three detectors has been extremely useful for the rapid response optical telescopes to find out the host Galaxy of GW170817. More than 80 groups have followed up GW170817 in the following hours to weeks after of its discovery. A bright optical transient named SSS17a[4] has been found in NGC 4993 (at ~ 40 Mpc) less than 11 hours after the merger by the One-Meter, Two Hemisphere (1M2H) team using the 1-m Swope Telescope [412]. The optical transient was independently detected by multiple teams within an hour [413]. Subsequent observations targeted the object and its environment. Early ultraviolet observations revealed a blue transient that faded within 48 hours. Optical and infrared observations showed a redward evolution over ~ 10 days. Following early non-detections, X-ray and radio emission were discovered at the optical transients position ~ 9 and ~ 16 days, respectively, after the merger. Both the X-ray and radio emission likely arise from a physical process that is distinct from the one that generates the UV/optical/near-infrared emission. No ultra-high-energy gamma rays and no neutrino candidates consistent with the source were found in follow-up searches. These observations support the hypothesis that GW170817 was produced by the merger of two neutron stars in NGC 4993 followed by a short gamma-ray burst (GRB170817A) and a kilonova/macronova powered by the radioactive decay of r-process nuclei synthesized in the ejecta [411, 413, 414].

[4]now named AT2017gfo according to the IAU convention.

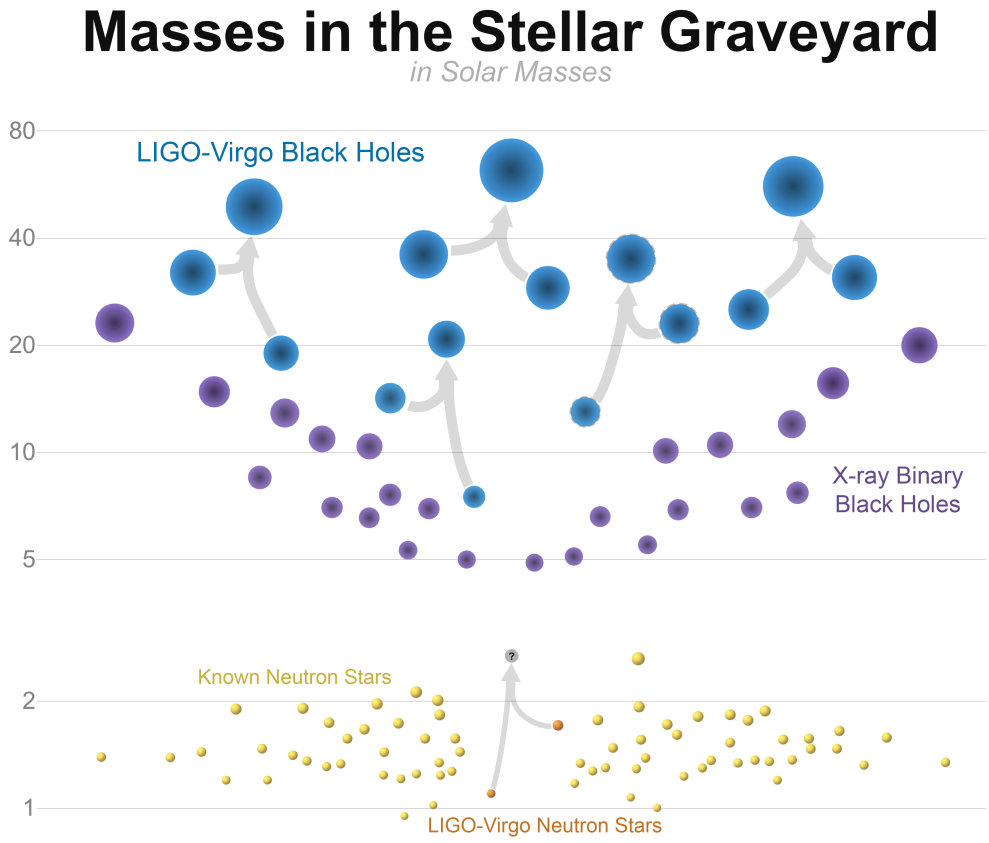

Figure 5.4: A representation of the masses of the different black holes and neutron stars known either through electromagnetic or gravitational-wave observations. Note the gap of a few solar masses between the heaviest neutron stars and the lighest black holes. Credit Visualization: LIGO/Frank Elavsky/Northwestern.

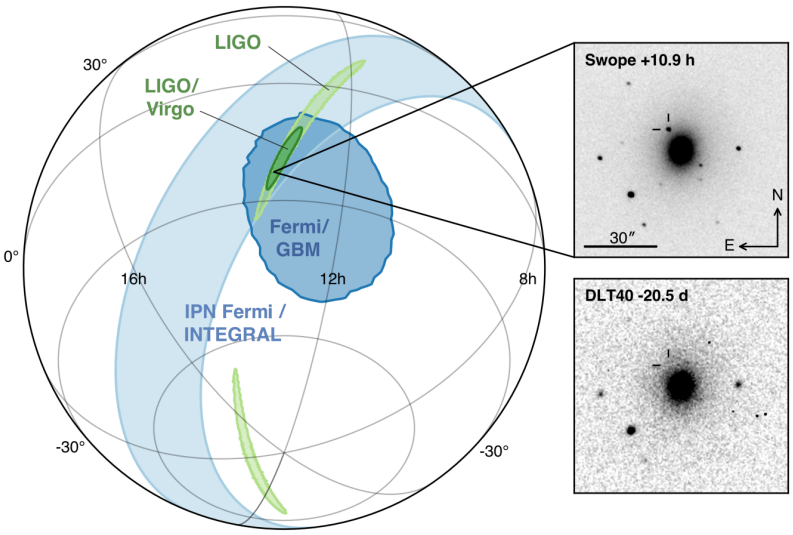

Figure 5.5: Skymap of GW170817 (green) and GRB170817A (blue). The LIGO only (light green) skymap 90% area is reduced from 190 deg^2 to 31 deg^2 when Virgo data are used. The inset shows the location of the apparent host galaxy NGC4993 seen by the Swope telescope 10.9 hours after GW170817 and an image of the same sky region taken by DLT40 20.5 days before.

The determination of the position of the source within ~ 10 arcsec of the galaxy NGC 4993 has also qualified GW170817 to be the first standard siren of a new type to measure the Hubble constant, the local expansion rate of the universe [415]. Gravitational waves allow for the estimation of the luminosity distance of the source while the electromagnetic observations determine the recession velocity (redshift) of the source and the peculiar velocity of the source with respect to the host galaxy. Combining all estimates, we obtain H_0=70^{+12}_{-8} km s^{-1} Mpc^{-1} at 68% credible interval [416]. This value is consitent with CMB Planck (67.74 ± 0.46 [417]) and type Ia supernovae WFC3/HST survey (73.24 ± 1.74 [418]) while being completely independent. The main source of uncertainty of the LIGO-Virgo Hubble constant comes from the 2-D joint posterior distribution for luminosity distance and binary plane inclination which is the angle between the line of sight source-detector and the total angular momentum vector. This angle is highly degenerate with the distance. More binary neutron star mergers and more precise measurements of the inclination angle using the electromagnetic observations will reduce the uncertainty in the coming years.

Assuming the binary is composed of two neutron stars, GW170817 is providing a new way to study the extreme state of nuclear matter inside a very exotic type of star. Inside a neutron star, matter is much denser than in any matter on Earth. What is known from neutron stars comes from its interaction with its environment and the resulting electromagnetic emission. Because gravitational waves provide information about the dynamics of the merger, they are a new way to probe how matter is bound and resists to its own gravity. The effects of one neutron star on the other in a binary system are expected to be visible in the late part of the inspiral phase through the tidal deformation of the two neutron stars. Tidal deformations are expected to be measurable in the gravitational-wave phase above 400 Hz, and this phase correction can be described in terms of a single tidal deformability parameter Λ which is the ratio of each star's induced mass quadrupole to the tidal field of its companion. The tidal deformability tells us how much the star deforms because of the presence of a companion and its composition. The parameter Λ depends on the equation of state via the neutron star radius. The less compact is the neutron star, the larger is its radius and the larger is Λ. Analyzing the phase evolution in the very last instants of the inspiral, and taking into account the uncertainties on the neutron star spins measurement, the most extreme values of Λ authorized by soft equation of state models have been excluded at 90% with GW170817 [409].

The fate of the compact object created during the merger is of primary importance as it also provides information on neutron star matter. First of all, using numerical simulation one can predict the amount of matter ejected during the merger. These simulations including relativistic hydrodynamic equations, magnetic fields and neutrino transport, show that the ejecta depends on many parameters (the masses of the two stars, their sizes, the stars' compactness, their spins and their binding energies). These predictions only consider the matter ejected dynamically. Additional matter may be ejected on longer timescales after the merger by winds from a disk of matter around the merger remnant. The estimated ejecta mass ranges between 10^{-3} and $10^{-2}\,\mathrm{M}_\odot$ over the wide range of possible equation of state.

The other fundamental topic is related to the nature of the compact object formed and the dynamics of the formation process. Gravitational waves are providing unique information about this. The nature of the remnant depends primarily on the masses of the binary components and on the equation of state of nuclear matter. This could be either a black hole (direct black hole formation or hypermassive neutron star that collapse to a black hole in less than 1 s) or a neutron star, with the latter being either long-lived or too massive for stability implying delayed collapse to a black hole (supramassive neutron star) [419].

A hypermassive neutron star is one that has mass greater than the maximum mass of a uniformly rotating star, but is prevented from collapse through support from differential rotation and thermal gradients. Rapid cooling mechanisms through neutrino emission and magnetic braking causes such merger remnants to collapse < 1 s after formation. If the star is less massive but still supramassive (its mass is larger than the maximum for a non-rotating neutron star) it will spin down through electromagnetic and gravitational-wave emission, eventually collapsing to a black hole between ~ 10 and 5×10^4 s after merger. Considering the posterior distribution for the progenitor masses of GW170817 [409], one can derive the posterior distribution for the gravitational mass of the post-merger remnant assuming conservation of baryonic mass (and neglecting mass loss to the ejecta). For a broad range of equations of state, this post-merger mass lies in the hypermassive neutron star regime [410].

A search for gravitational waves from the remnant of the binary neutron star merger GW170817 using data from advanced LIGO and advanced Virgo has been carried out. We search for short (1 s) and intermediate-duration (500 s) signals[5], which includes gravitational-wave emission from a hypermassive neutron star or supramassive neutron star, respectively [420]. We find no signal from the post-merger remnant. Our derived strain upper limits are more than

[5]Our all-sky long transient search algorithm *STAMP-AS* described in chapter 3 has has been quickly adapted to search a ~ 500 s long signal just after GW170817.

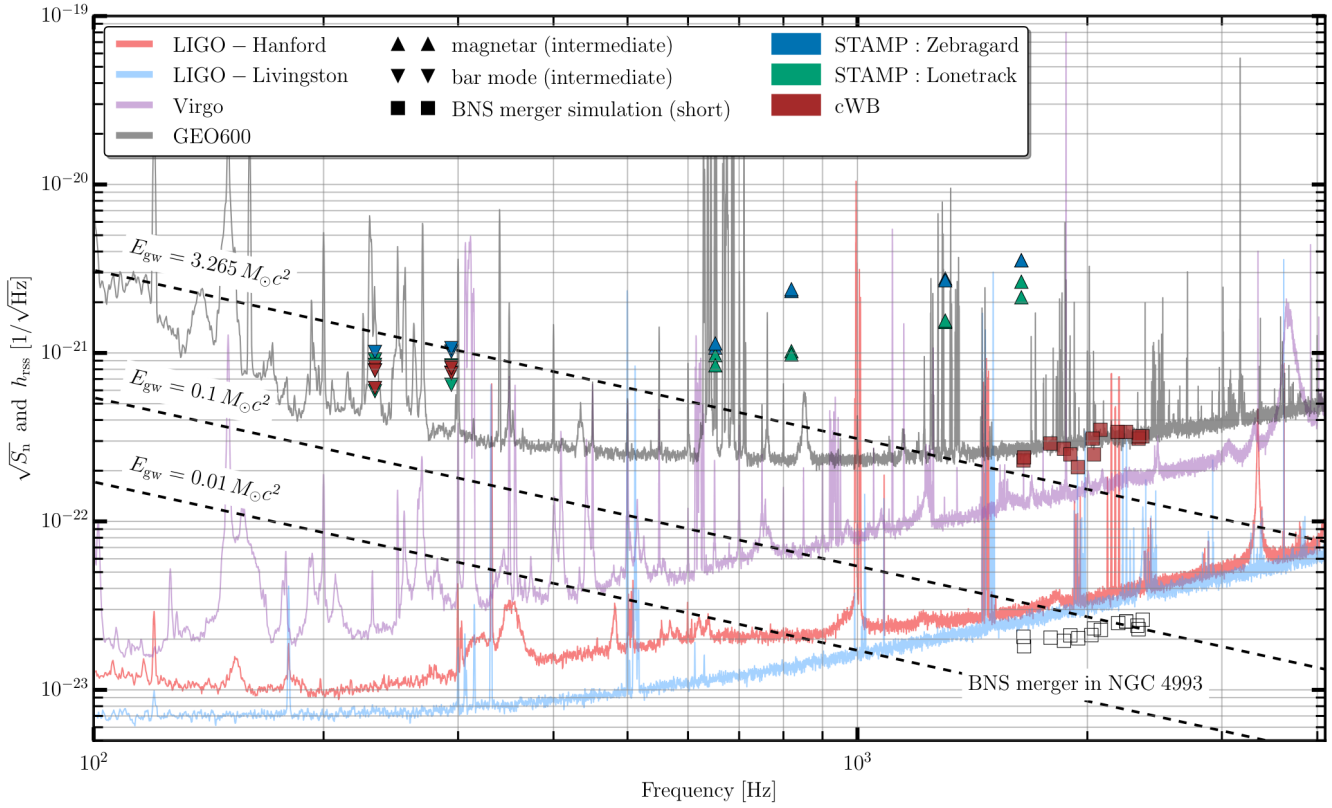

Figure 5.6: Noise amplitude spectral density of LIGO, Virgo and GEO detectors at the time of GW170817, and the root-sum-squared strain amplitude h_{rss} at 50% false dismissal probability for various waveforms in the short and intermediate duration searches performed by *STAMP-AS* (blue and green) and cWB (red). The dashed lines indicate the maximum h_{rss} possible for a narrow-band gravitational-wave signal with fixed energy content under the most optimistic assumption that all available energy is emitted in gravitational waves after the merger [420].

an order of magnitude larger than those predicted by most models. We set limits on h_{rss}, the root-sum-squared strain amplitude at 50% false dismissal probability for various waveforms as shown on Figure 5.6. These limits can be translated into limits on the amount of energy emitted during the post merger phase. In the best cases, these limits are still 1 or 2 orders of magnitude larger than realistic predictions.

5.3 Perspectives

5.3.1 LIGO-Virgo network evolution

The LIGO and Virgo detectors sensitivity improvements in the 2015-2020 years are described in a living document that is regularly updated [271]. A recent update that includes KAGRA will soon be published. KAGRA will be operational in its full configuration by early 2019. The LIGO-Virgo-KAGRA observing scenario describes a sucession of data taking periods separated with detector upgrades and commissioning periods to reach the detectors' target sensitivities. Figure 5.7 shows the evolution of the strain amplitude spectral densities for the three detectors in the next five years. The advanced LIGO detectors are expected to reach a 200 Mpc BNS range circa 2019. The target advanced Virgo sensitivity is slightly lower, with a BNS range of 130 Mpc circa 2021. Further, the dual recycling locking scheme that allows a better sensitivity at high frequency will be applied in advanced Virgo not before 2019. So far, the LIGO-Virgo run planning is respected but with advanced Virgo sensitivity slightly worse than anticipated.

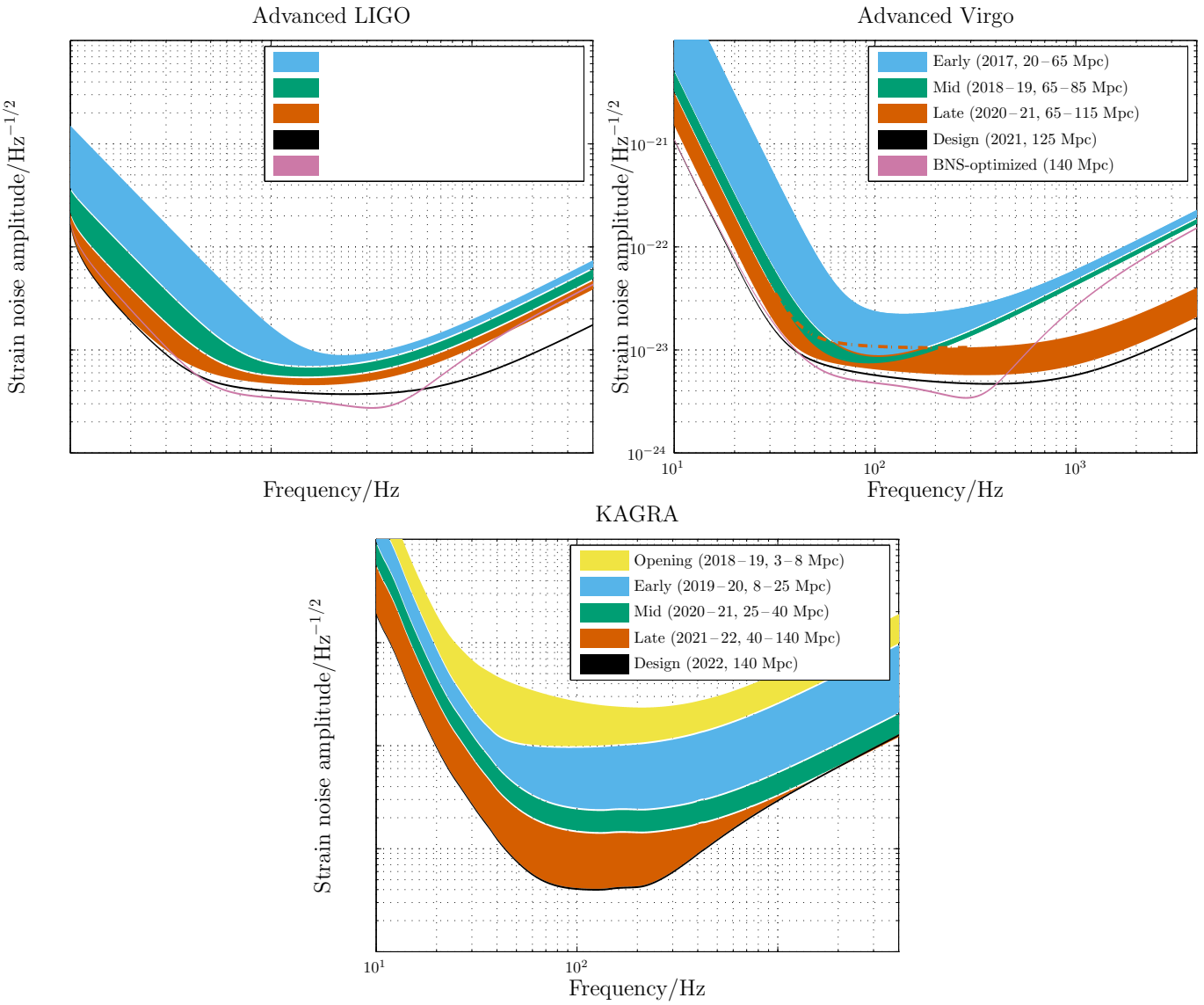

Figure 5.7: Advanced LIGO (top left), advanced Virgo (top right) and KAGRA (bottom) target strain sensitivities as a function of frequency. The binary neutron star inspiral range is given in Mpc. The (best guess) detector sensitivity evolution is defined for three periods as the detectors progress (early, mid and late) as well as the final design sensitivity target and the binary neutron star optimized sensitivities.

This is explained by all the difficulties summarized in section 5.1. KAGRA will reach its design sensitivity (140 Mpc) a bit after LIGO and Virgo but the addition of a fourth detector is anticipated to improve the sky localization of the sources before KAGRA reaches its design sensitivity, as GW170817 has demonstrated with Virgo. Note that India is building a site infrastructure to host the former 2 km-long LIGO Hanford detector. Operation at the same level as the LIGO detectors is anticipated for no earlier than 2024. Right now, advanced LIGO and advanced Virgo are in a commissioning phase until end of 2018 where the third observing run should start and last for approximately one year. The observing runs planning is presented in Figure 5.8. The runs will be longer and longer for detectors reaching their target sensitivities.

For a given source, the number of detectable events scales with the search time-volume, VT, where T is the observing run duration and $V = (4\pi/3)R^3$ is the time-averaged volume of universe that is surveyed. This rule of thumb assumes a uniform distribution of sources in this volume. For weak gravitational-wave signals, such as core-

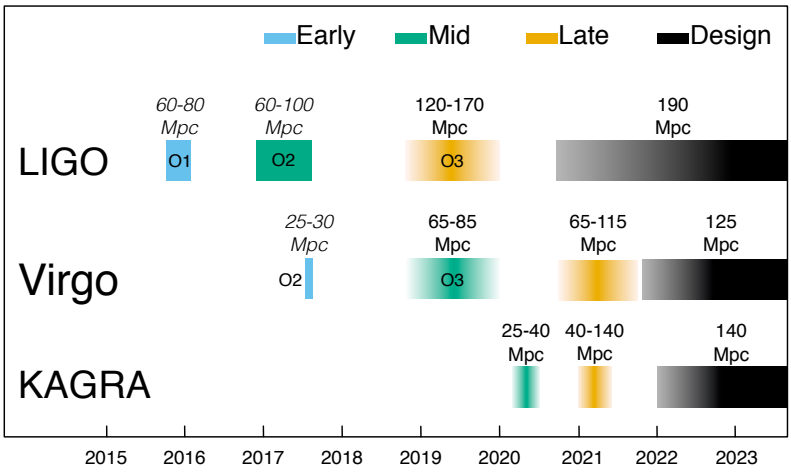

Figure 5.8: The planned sensitivity evolution and observing runs for the advanced LIGO, advanced Virgo and KAGRA detectors over the coming years. The colored bars show the observing runs, with the expected sensitivities given by the data in Figure 5.7 for future runs, and the achieved sensitivities in O1 and in O2.

collapse supernova for which the current detection range does not exceed few kpc for the standard GW emission mechanisms, this rule of thumb is not valid as the galaxies' distribution in a radius smaller than 1 Mpc is far from being uniform. On the contrary, for the BNS inspiral source case[6], VT is providing reasonable estimates of what will likely be detectable in the future by the LIGO-Virgo-KAGRA network and is reported in Table 5.1. The O2 GW170817 observation matches very well the prediction and allows to affirm that a few of BNS inspirals should be detected in 2018 –2019 observing run.

For un-modelled transient sources such as core-collapse supernova, the estimation of the number of events that could be observed in the next five years is unfortunately limited by the fact that the density of galaxies within 100 kpc is rather low. To do a precise estimate, one needs to consider the catalogue of galaxies surrounding us as done in [421] and illustrated in Figure 5.9 extracted from [421]. It includes information about the morphology type of the galaxies (luminosity), the optical absorption of the galactic plane and an estimate of failed supernovae. One obtains ~ 4 events per year within a distance of 20 Mpc. This distance corresponds to the most optimistic gravitational-wave emission mechanism (such as the long-lasting bar mode or the torus fragmentation instability driven models). It is maybe more realistic to consider the core bounce phase and non-axisymmetric gravitational-wave emission due to rotational instabilities and convection instabilities inside and above the proto-neutron coupled with neutrino heating and standing accretion shock instability mechanisms. In that case, the gain of a factor 10 in range for the target sensitivity of the advanced detectors is not going to provide many more detectable core-collapse supernovae than what we expect in the Milky-way (2 – 3 per century).

[6]Similar statement could be done for the BBH source case, but we are now able to make a measurement of the rate using gravitational waves.

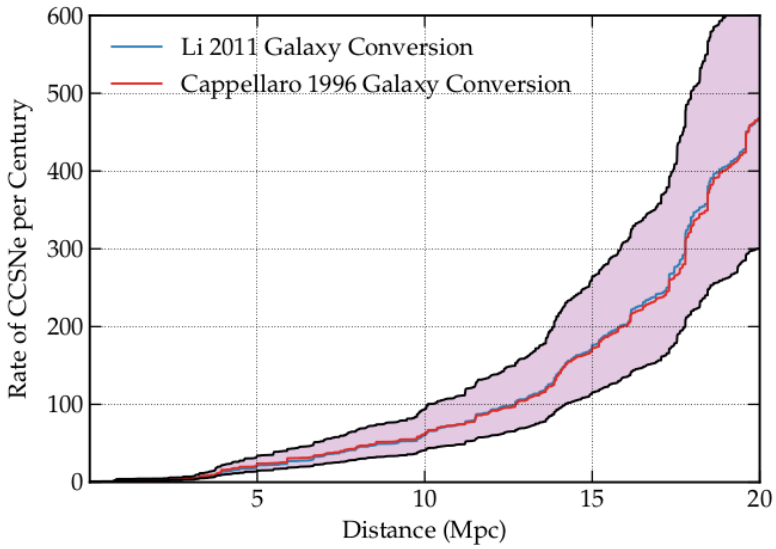

Figure 5.9: Cumulative core-collapse supernova rate as a function of distance within 20 Mpc. This figure is from [421] and by courtesy of Jasmine Gill.

Epoch		2015 – 2016	2016 – 2017	2018 – 2019	2020+	2024+
Planned run duration		4 months	9 months	12 months	(per year)	(per year)
Expected BNS range/Mpc	LIGO	40 – 80	80 – 120	120 – 170	190	190
	Virgo	—	20 – 65	65 – 85	65 – 115	125
	KAGRA	—	—	—	140	—
Achieved BNS range/Mpc	LIGO	60 – 80	60 – 100	—	—	—
	Virgo	—	25 – 30	—	—	—
	KAGRA	—	—	—	—	—
Estimated BNS detections		0.002 – 2	0.007 – 30	0.04 – 100	0.1 – 200	0.4 – 400
Actual BNS detections		0	1	—	—	—

Table 5.1: Expected sensitivities, observing run durations, and number of expected BNS sources discovered by the advanced LIGO, advanced Virgo and KAGRA detectors, in the next decade []. Future planned runs assume a 70 –75% duty cycle for each instrument. The BNS detection numbers also account for the uncertainty in the BNS source rate density [422]. This is extracted from [271].

5.3.2 Personal perspectives for the next five years

Having participated to the fantastic discovery of compact binary system mergers is making me more optimistic about the chances to discover a new types of gravitational-wave transients. Core-collapse supernovae would be a major discovery and would open another new era in astrophysics to understand the fate of old stars and thus the content of the universe. In the last few years, I have turned my research activities on an extension of the gravitational-wave burst search domain, historically focused on short transient signals lasting a few milli-seconds as expected from the gravitational-wave emission when the core density exceeds that of nuclear matter and then bounces in core-collapse supernova. In collaboration with the stochastic background search group, I have participated to the developement of the *STAMP-AS* pipeline to search coherent long-duration transient signals of any morphology[7]. The target sources are associated to stellar mass black holes and binary neutron stars, objects that LIGO-Virgo have discovered recently. The perspective to discover possible new mecanisms of gravitational-wave emission is exciting as understanding stellar

[7]Any morphology but assuming basic features as signal continuity in time-frequency and rather smooth variations.

mass black holes and neutron stars is fundamental to understanding the content of our universe and thus being able to answer to fundamental questions such as stars formation and the distribution of matter in the universe. Looking for long duration transient signals will be my main contribution to the new source search effort of the LIGO-Virgo collaboration. Pipelines improvement and extensions to signals of longer ($> 500\,\mathrm{s}$) duration are under way. Bridging the gap between transient signals and continuous waves is important as many astrophysical phenomena are related to gravitational-wave predictions of signals as long as several hours, to days[345, 133]. Another important task that has been neglected so far in our search with *STAMP-AS* is to include the third detector Virgo in the pipeline, in a way that despite Virgo's lower sensitivity on average brings signal significance without deterioring the search sensitivity on average. Having a search algorithm like *STAMP-AS* that takes into account the detectors' sensitivity is fundamental when dealing with the realistic case of non equal sensitivity detectors's network.

GW170817 has demonstrated that an unexpected surprise is always possible. Looking for gravitational-wave events means to first identify the most significant events in the data, which means that they cannot be explained by a noise artefact. The second important step is to identify the source that emitted gravitational waves. Many algorithms have been developed and applied to gravitational-wave data using the strain amplitude of all detectors or reduced information like the time delay between detectors and the SNR of the event in each detector [253, 208, 423, 424]. The difficulty here is that apart from compact binary coalescence the signal waveforms of the burst transient sources are not analytically available. It is thus a difficult problem to infer the different parameters that describe the source without a precise model. One way that has been explored by different groups is to assume that the exact signal can be completly represented with a linear combination of a set of known functions. These functions can be based on a catalog of numerical simulations transformed into a basis of components (principal components analysis) or just sine-gaussian waveforms. These methods have been tested for different types of sources [126, 425, 426]. So far, nothing specific to long transient signals has been applied to LIGO-Virgo data. This is an excellent subject that could be very useful in cases where we have good candidates. With the identification, using these methods, of the post-merger remnant with future BNS sources our discoveries will bring tremendious information for understanding the effects of the matter in binary neutron systems.

Bibliography

[1] F. Acernese et al., *Gravitational wave burst search in the Virgo C7 data*, Class. Quantum Grav. 26 (2009) 085009. arXiv:0812.4870.

[2] M.-A. Bizouard et al., *Data quality and veto studies for the all-sky gravitational wave burst search in Virgo C7 Run data*, Tech. Rep. VIR-0013D-07, Virgo Project (2007). https://tds.virgo-gw.eu/ql/?c=1526.

[3] K. G. Arun and M.-A. Bizouard, *Search for binary black hole merger signals in the Virgo C7 data*, Tech. Rep. VIR-011A-08, Virgo Project (2008). https://tds.virgo-gw.eu/ql/?c=1969.

[4] J. Abadie et al., *All-sky search for gravitational-wave bursts in the first joint LIGO-GEO-Virgo run*, Phys. Rev. D **81** (2010) 102001. arXiv:1002.1036.

[5] A. Einstein, *Die Grundlage der allgemeinen Relativitäts theorie*, Annalen der Physik **49** (1916) 769.

[6] U. Le Verrier, *Lettre de M. Le Verrier à M. Faye sur la théorie de Mercure et sur le mouvement du périhélie de cette planète*, Comptes rendus hebdomadaires des séances de l'Académie des sciences (Paris) **49** (1859) 379.

[7] G. Clemence, *The Relativity Effect in Planetary Motions*, Rev. Mod. Phys. **19** (1947) 361.

[8] S. Weinberg, *Gravitation and Cosmology*, John Wiley and Sons, New York, 1972. http://www-spires.fnal.gov/spires/find/books/www?cl=QC6.W431.

[9] C. M. Will, *The Confrontation between General Relativity and Experiment*, Living Rev. Relativity **9**. http://www.livingreviews.org/lrr-2006-3.

[10] F. Dyson and A. Eddington, *A determination of the deflection of light by the Sun's gravitational field, from observations made at the total eclipse of 29 May 1919*, Phil. Trans. R. Soc. Lond. A **220** (1920) 291–333.

[11] M. Bartelmann, *Gravitational Lensing*, Class. Quantum Grav. 27 (2010) 233001. arXiv:1010.3829.

[12] R. Pound and G. Rebka, *Gravitational Red-Shift in Nuclear Resonance*, Phys. Rev. Lett. **3** (1959) 439–441.

[13] R. Pound and G. Rebka, *Apparent Weight of Photons*, Phys. Rev. Lett. **4** (1960) 337–341.

[14] C. Chou et al., *Optical Clocks and Relativity*, Science **329** (2010) 1630–1633. http://www.sciencemag.org/content/329/5999/1630.full.pdf.

[15] C. Everitt et al., *Gravity Probe B: Final Results of a Space Experiment to Test General Relativity*, Phys. Rev. Lett. **106** (2011) 221101.

[16] I. Shapiro, *Fourth Test of General Relativity*, Phys. Rev. Lett. **13** (1964) 789–791.

[17] I. Shapiro et al., *Fourth Test of General Relativity: New Radar Result*, Phys. Rev. Lett. **26** (1971) 1132–1135.

[18] B. Bertotti and L. Iess, *A test of general relativity using radio links with the Cassini spacecraft*, Nature **425** (2003) 374–376.

[19] E. B. Fomalont and S. M. Kopeikin, *The Measurement of the Light Deflection from Jupiter: Experimental Results*, Astrophys. J. **598** (2003) 704.

[20] S. L. Shapiro and S. A. Teukolsky, *Black holes, white dwarfs, and neutron stars: The physics of compact objects*, New York, USA: Wiley (1983), 1983.

[21] J. M. Lattimer and M. Prakash, *The Physics of Neutron Stars*, Science **304** (2004) 536–542. arXiv:astro-ph/0405262. http://www.sciencemag.org/content/304/5670/536.full.pdf.

[22] K. Thorne and S. Hawking, *Black Holes and Time Warps: Einstein's Outrageous Legacy*, W. W. Norton & Company, 1995.

[23] J. M. Weisberg and D. J. Nice, *Timing Measurements of the Relativistic Binary Pulsar PSR B1913+16*, Astrophys. J. **722** (2010) 1030–1034.

[24] S. Weinberg, *Cosmology*, Oxford University Press, 2008.

[25] P. A. R. Ade et al., *Planck 2013 results. XVI. Cosmological parameters*, A&A **571** (2014) A16.

[26] A. Einstein, *Sitzungsberichte der physikalisch-mathematischen Klasse*, Preuss. Akad. Wiss. Berlin **1** (1916) 688.

[27] A. Einstein, *Sitzungsberichte der physikalisch-mathematischen Klasse*, Preuss. Akad. Wiss. Berlin **1** (1918) 154.

[28] J. Taylor and J. Weisberg, *Further experimental tests of relativistic gravity using the binary pulsar PSR 1913+16*, Astrophys. J. **345** (1989) 434.

[29] M.-A. Bizouard et al., *Pulsar timing arrays*, Class. Quantum Grav. **30** (2013) 220301.

[30] L. Grishchuk, *Amplification of gravitational waves in an istropic universe*, Sov. Phys. JETP **40** (1975) 409–415.

[31] M. Kamionkowski and A. Kosowsky, *Statistics of cosmic microwave background polarization*, Phys. Rev. D **55** (1997) 7368–7388. arXiv:astro-ph/9611125.

[32] International year of light and light-based technologies (2015). http://www.light2015.org/Home.html.

[33] M.-A. Bizouard and M. A. Papa, *Searching for gravitational waves with the LIGO and Virgo interferometers*, Comptes Rendus Physique **14** (2013) 352.

[34] M. A. Bizouard, *Observational results from the LIGO and Virgo detectors*, General Relativity and Gravitation **46**.

[35] B. Abbott et al., *LIGO: The Laser Interferometer Gravitational-Wave Observatory*, Rept. Prog. Phys. **72** (2009) 076901. arXiv:0711.3041.

[36] H. Grote et al., *The GEO 600 status*, Class. Quantum Grav. **27** (2010) 084003.

[37] T. Accadia et al., *Virgo: a laser interferometer to detect gravitational waves*, JINST **7** (2012) P03012.

[38] F. Acernese et al., *Status of Virgo*, Class. Quantum Grav. **25** (2008) 114045.

[39] G. M. Harry, *Advanced LIGO: the next generation of gravitational wave detectors*, Class. Quantum Grav. **27** (2010) 084006.

[40] B. P. Abbott et al., *Observation of Gravitational Waves from a Binary Black Hole Merger*, Phys. Rev. Lett. **116** (2016) 061102. arXiv:1602.03837.

[41] B. P. Abbott et al., *GW151226: Observation of Gravitational Waves from a 22-Solar-Mass Binary Black Hole Coalescence*, Phys. Rev. Lett. **116** (2016) 241103. arXiv:1606.04855.

[42] T. Accadia et al., Plans for the upgrade of the gravitational wave detector virgo: Advanced virgo, in: T. Damour and R. Jantzen (Eds.), Proceedings of the Twelfth Marcel Grossmann Meeting on General Relativity, World Scientific, Paris, 2012, p. 1738.

[43] K. Kuroda, *Large-scale gravitational wave telescope (LCGT)*, Int. J. Mod. Phys. D **20** (2011) 1755–1770.

[44] Y. Aso et al., *Interferometer design of the KAGRA gravitational wave detector*, Phys. Rev. D **88** (D4) (2013) 043007. arXiv:1306.6747.

[45] J. Aasi et al., *Prospects for Localization of Gravitational Wave Transients by the Advanced LIGO and Advanced Virgo Observatories.* arXiv:1304.0670.

[46] N. Christensen, *Multimessenger Astronomy*, in *Proceedings of the The Rencontres de Moriond and GPhyS colloquium, La Thuile, Italy, 20-27 March 2011*arXiv:1105.5843.

[47] B. P. Abbott et al., *Localization and broadband follow-up of the gravitational-wave transient GW150914*, Astrophys. J. Lett. **826** (2016) L13. arXiv:1602.08492.

[48] F. Tisserand, *Les travaux de Le Verrier*, Annales de l'Observatoire de Paris **15** (1880) 23–43.

[49] U. L. Verrier, *Lettre de M. Le Verrier à M. Faye sur la théorie de Mercure et sur le mouvement du périhélie de cette planète*, Comptes rendus hebdomadaires des séances de l'Académie des sciences (Paris) **49** (1859) 379–383. https://archive.org/stream/comptesrendusheb49acad#page/378/mode/2up.

[50] J. C. Maxwell, *A Dynamical Theory of the Electromagnetic Field*, Phil. Trans. R. Soc. Lond. **155** (1865) 459.

[51] J. C. Maxwell, *A treatise on electricity and magnetism*, no. 1 à 2 in A Treatise on Electricity and Magnetism, Dover Publications, 1954. https://books.google.fr/books?id=HbUPAQAAMAAJ.

[52] H. Hertz, *Über die Ausbreitungsgeschwindigkeit der electrodynamischen Wirkungen*, Annalen der Physik **270** (1888) 551–569.

[53] H. Hertz, *Über elektrodynamische Wellen im Luftraume und deren Reflexion*, Wiedemanns Ann. **34** (1888) 610.

[54] H. Hertz and D. Jones, *Electric Waves: Being Researches on the Propagation of Electric Action with Finite Velocity Through Space*, Macmillan and Company, 1893. https://books.google.fr/books?id=EJdAAAAAIAAJ.

[55] A. Michelson and E. Morley, *On the relative motion of the Earth and the luminiferous ether*, American Journal of Science **34** (1887) 333–345.

[56] F. Arago, *Œuvres Complètes de François Arago*, Œuvres Complètes, Tome 7, **4** (1858) 548–568. http://gallica.bnf.fr/ark:/12148/bpt6k92713k.

[57] H. Lorentz, *La théorie électromagnétique de Maxwell et son application aux corps mouvants*, Extrait des Archives néerlandaises des sciences exactes et naturelles, E. J. Brill, 1892. https://books.google.fr/books?id=FJ49mAEACAAJ.

[58] H. Lorentz, *Versuch einer Theorie der electrischen und optischen Erscheinungen in bewegten Körpern*, Cambridge Library Collection - Physical Sciences, Cambridge University Press, 2013. https://books.google.fr/books?id=vY6HAAAAQBAJ.

[59] H. A. Lorentz, *The Relative Motion of the Earth and the Aether*, Zittingsverlag Akad. V. Wet. **1** (1892) 74–79.

[60] G. Fras. Fitz Gerald, *The Ether and the Earth's Atmosphere*, Science **13** (1889) 390.

[61] H. Lorentz, *Electromagnetic phenomena in a system moving with any velocity smaller than that of light*, Proceedings of the Royal Netherlands Academy of Arts and Sciences **6** (1904) 809–831.

[62] H. Poincaré, *Les géométries non euclidiennes*, Revue générale des sciences pures et appliquées **2** (1891) 769–774.

[63] H. Poincaré, *La mesure du temps*, Revue de métaphysique et de morale **6** (1898) 1–13.

[64] H. Poincaré, *La science et l'hypothèse*, Flammarion, Paris, 1902. http://www.worldcat.org/title/oeuvres-philosophiques-1-la-science-et-lhypothese/oclc/314619140&referer=brief_results.

[65] H. Poincaré, *Sur la dynamique de l'électron*, Comptes Rendus **140** (1905) 1504–1508.

[66] H. Poincaré, *Sur la dynamique de l'électron*, Rendiconti del Circolo matematico di Palermo **21** (1906) 129–176.

[67] A. Einstein, *Zur Elektrodynamik bewegter Körper*, Annalen der Physik **322** (1905) 891–921.

[68] A. Einstein, *Ist die Trägheit eines Körpers von seinem Energieinhalt abhängig?*, Annalen der Physik **323** (1905) 639–641.

[69] H. Minkowski, *Raum und Zeit*, Physikalische Zeitschrift **10** (1905) 75–88.

[70] N. Christensen and T. Moore, *Teaching general relativity to undergraduates*, Physics Today **65** (2012) 41.

[71] T. A. Moore, *A General Relativity Workbook*, University Science Books, 2013.

[72] J. W. Moffat, *A new nonsymmetric gravitational theory*, Physics Letters B **355** (1995) 447–452. arXiv:gr-qc/9411006.

[73] A. Riess et al., *Observational Evidence from Supernovae for an Accelerating Universe and a Cosmological Constant*, Astrophys. J. **116** (1998) 1009.

[74] S. Perlmutter et al., *Measurements of* Ω *and* Λ *from 42 High-Redshift Supernovae*, Astrophys. J. **517** (1999) 565.

[75] L. Knox and N. Christensen, *The Age of the Universe and the Cosmological Constant Determined from Cosmic Microwave Background Anisotropy Measurements*, Astrophys. J. Lett. **563** (2001) L95.

[76] N. Jarosik et al., *Seven-year Wilkinson Microwave Anisotropy Probe (WMAP) Observations: Sky Maps, Systematic Errors, and Basic Results*, Astrophys. J. Suppl. **192** (2011) 14.

[77] N. Christensen et al., *Bayesian methods for cosmological parameter estimation from cosmic microwave background measurements*, Class. Quantum Grav. **18** (2001) 2677.

[78] L. Blanchet, *Gravitational radiation from post-Newtonian sources and inspiralling compact binaries*, Living Rev. Relativity **9** (2006) 3. arXiv:gr-qc/0202016. http://www.livingreviews.org/lrr-2006-4.

[79] M. Maggiore, *Gravitational Waves: Volume 1: Theory and Experiments*, Gravitational Waves, OUP Oxford, 2007. https://books.google.com/books?id=AqVpQgAACAAJ.

[80] J. Creighton and W. Anderson, *Gravitational-Wave Physics and Astronomy: An Introduction to Theory, Experiment and Data Analysis*, Wiley series in cosmology, Wiley, 2012. https://books.google.com/books?id=n75zEK98WDsC.

[81] P. R. Saulson, *Gravitational wave detection: Principles and practice*, Comptes Rendus Physique **14** (2013) 288–305.

[82] J. H. Taylor and J. M. Weisberg, *A new test of general relativity - Gravitational radiation and the binary pulsar PSR 1913+16*, Astrophys. J. **253** (1982) 908–920.

[83] J. M. Weisberg and D. J. Nice, *Timing Measurements of the Relativistic Binary Pulsar PSR B1913+16*, Astrophys. J. **722** (2010) 1030–1034. arXiv:arXiv:1011.0718.

[84] M. Maggiore, *Gravitational wave experiments and early universe cosmology*, Phys. Rep. **331** (2000) 283–367. arXiv:gr-qc/9909001.

[85] R. Prix, Gravitational waves from spinning neutron stars, in: W. Becker (Ed.), Neutron Stars and Pulsars, Springer-Verlag, Berlin Heidelberg, 2009, pp. 651–683.

[86] C. D. Ott, *The Gravitational Wave Signature of Core-Collapse Supernovae*, Class. Quantum Grav. **26** (2009) 063001. arXiv:0809.0695.

[87] R. Apreda et al., *Gravitational waves from electroweak phase transitions*, Nucl. Phys. B **631** (2002) 342–368. arXiv:gr-qc/0107033.

[88] T. Damour and A. Vilenkin, *Gravitational radiation from cosmic (super)strings: Bursts, stochastic background, and observational windows*, Phys. Rev. D **71** (2005) 063510. arXiv:hep-th/0410222.

[89] M. Burgay et al., *An Increased estimate of the merger rate of double neutron stars from observations of a highly relativistic system*, Nature **426** (2003) 531–533. arXiv:astro-ph/0312071.

[90] V. Kalogera et al., *Formation of Double Compact Objects*, Phys. Rep. **442** (2007) 75–108. arXiv:astro-ph/0612144.

[91] K. Postnov and L. Yungelson, *The Evolution of Compact Binary Star Systems*, Living Rev. Relativity **9** (2007) 6. http://www.livingreviews.org/lrr-2006-6.

[92] K. Belczynski et al., *The coalescence rates of double black holes*, in *Proceedings of the The Rencontres de Moriond and GPhyS colloquium, La Thuile, Italy, 20-27 March 2011*arXiv:1106.0397.

[93] O. Godet et al., *First evidence for spectral state transitions in the ESO243-49 hyper luminous X-ray source HLX-1*, Astrophys. J. **705** (2009) L109–L112. arXiv:0909.4458.

[94] P. Madau and M. J. Rees, *Massive black holes as Population III remnants*, Astrophys. J. **551** (2001) L27–L30. arXiv:astro-ph/0101223.

[95] S. F. Portegies Zwart and S. L. McMillan, *The Runaway growth of intermediate-mass black holes in dense star clusters*, Astrophys. J. **576** (2002) 899–907. arXiv:astro-ph/0201055.

[96] A. Bohé and S. Marsat, *Next-to-next-to-leading order spinorbit effects in the gravitational wave flux and orbital phasing of compact binaries*, Class. Quantum Grav. **30** (2013) 135009. arXiv:1303.7412.

[97] J. M. Centrella et al., *The Final Merger of Black-Hole Binaries*, Ann. Rev. Nucl. Part. Sci. **60** (2010) 75–100. arXiv:1010.2165.

[98] M. Shibata and K. Taniguchi, *Coalescence of Black Hole-Neutron Star Binaries*, Living Rev. Relativity **14** (2011) 6. http://www.livingreviews.org/lrr-2011-6.

[99] L. Baiotti and B. Giacomazzo, *Accurate evolutions of inspiralling neutron-star binaries: prompt and delayed collapse to black hole*, Phys. Rev. D **78** (2008) 084033. arXiv:0804.0594.

[100] J. Aasi et al., *Search for Gravitational Waves from Binary Black Hole Inspiral, Merger and Ringdown in LIGO-Virgo Data from 2009-2010*, Phys. Rev. D **87** (2013) 022002. arXiv:1209.6533.

[101] J. Abadie et al., *Search for gravitational waves from intermediate mass binary black holes*, Phys. Rev D **85** (2012) 102044. arXiv:1201.5999.

[102] N. Christensen and R. Meyer, *Using Markov chain Monte Carlo methods for estimating parameters with gravitational radiation data*, Phys. Rev. D **64** (2001) 022001. arXiv:gr-qc/0102018.

[103] S. Babak and A. Taracchini, *Validating the effective-one-body model of spinning, precessing binary black holes against numerical relativity*, Phys. Rev. D **95** (2017) 024010. arXiv:1607.05661.

[104] L. Bildsten, *Gravitational radiation and rotation of accreting neutron stars*, Astrophys. J. **501** (1998) L89. arXiv:astro-ph/9804325.

[105] G. Ushomirsky and C. Cutler, *Deformations of accreting neutron star crusts and gravitational wave emission*, Mon. Not. R. Astron. Soc. **319** (2000) 902. arXiv:astro-ph/0001136.

[106] C. Cutler, *Gravitational waves from neutron stars with large toroidal B fields*, Phys. Rev. D **66** (2002) 084025. arXiv:gr-qc/0206051.

[107] N. Andersson, *A New class of unstable modes of rotating relativistic stars*, Astrophys. J. **502** (1998) 708–713. arXiv:gr-qc/9706075.

[108] J. Friedman and B. F. Schutz, *Secular instability of rotating Newtonian stars*, Astrophys. J. **222** (1978) 281.

[109] N. Chamel and P. Haensel, *Physics of Neutron Star Crusts*, Living Rev. Relativity **11** (2008) 10. http://www.livingreviews.org/lrr-2008-10.

[110] L. Wade et al., *Continuous Gravitational Waves from Isolated Galactic Neutron Stars in the Advanced Detector Era*, Phys. Rev. D **86** (2012) 124011. arXiv:1209.2971.

[111] N. Andersson et al., *R mode runaway and rapidly rotating neutron stars*, Astrophys. J. **534** (2000) L75. arXiv:astro-ph/0002114.

[112] A. L. Watts and B. Krishnan, *Detecting gravitational waves from accreting neutron stars*, Adv. Space Res. **43** (2009) 1049–1054. arXiv:0901.1680.

[113] R. Brustein et al., *Relic gravitational waves from string cosmology*, Phys. Lett. B **361** (1995) 45–51. arXiv:hep-th/9507017.

[114] A. Buonanno and M. Maggiore, *Spectrum of relic gravitational waves in string cosmology*, Phys. Rev. D **55** (1997) 3330–3336. arXiv:gr-qc/9605072.

[115] T. Kibble, *Topology of Cosmic Domains and Strings*, J. Phys. A **9** (1976) 1387–1398.

[116] X. Siemens and V. Mandic, *Gravitational wave stochastic background from cosmic (super)strings*, Phys. Rev. Lett. **98** (2007) 111101. arXiv:astro-ph/0610920.

[117] B. P. Abbott et al., *GW150914: Implications for the stochastic gravitational wave background from binary black holes*, Phys. Rev. Lett. **116** (2016) 131102. arXiv:1602.03847.

[118] J. Aasi et al., *Searching for stochastic gravitational waves using data from the two colocated LIGO Hanford detectors*, Phys. Rev. D. **91** (2015) 022003.

[119] I. Sendra and T. Smith, *Improved limits on short-wavelength gravitational waves from the cosmic microwave background*, Phys. Rev. D **85** (2012) 123002.

[120] S. Henrot-Versillé et al., *Improved constraint on the primordial gravitational-wave density using recent cosmological data and its impact on cosmic string models*, Class. Quantum Grav. **32** (2015) 045003. arXiv:1408.5299.

[121] J. Aasi et al., *Improved Upper Limits on the Stochastic Gravitational-Wave Background from 2009˘2010 LIGO and Virgo Data*, Phys. Rev. Lett. **113** (2014) 231101.

[122] B. Abbott et al., *An upper limit on the stochastic gravitational-wave background of cosmological origin*, Nature **460** (2009) 990–994.

[123] C. L. Fryer and K. C. New, *Gravitational Waves from Gravitational Collapse*, Living Rev. Relativity **14** (2011) 1. http://www.livingreviews.org/lrr-2011-1.

[124] K. Kotake, *Multiple physical elements to determine the gravitational-wave signatures of core-collapse supernovae*, Comptes Rendus Physique **14** (2013) 318–351. arXiv:1110.5107.

[125] H. Dimmelmeier and J. A. Font, *Relativistic simulations of rotational core collapse. 2. Collapse dynamics and gravitational radiation*, A&A **393** (2002) 523. arXiv:astro-ph/0204289.

[126] C. Röver et al., *Bayesian reconstruction of gravitational wave burst signals from simulations of rotating stellar core collapse and bounce*, Phys. Rev. D **80** (2009) 102004.

[127] S. Mereghetti, *The strongest cosmic magnets: Soft Gamma-ray Repeaters and Anomalous X-ray Pulsars*, Astron. Astrophys. Rev. **15** (2008) 225. arXiv:0804.0250.

[128] A. Vilenkin and E. P. S. Shellard, *Cosmic Strings and Other Topological Defects*, Cambridge University Press, Cambridge, 1994.

[129] R. Caldwell and B. Allen, *Cosmological constraints on cosmic string gravitational radiation*, Phys. Rev. D **45** (1992) 3447–3468.

[130] T. Damour and A. Vilenkin, *Gravitational wave bursts from cusps and kinks on cosmic strings*, Phys. Rev. D **64** (2001) 064008. arXiv:gr-qc/0104026.

[131] A. Burrows et al., *Simulations of Magnetically-Driven Supernova and Hypernova Explosions in the Context of Rapid Rotation*, Astrophys. J. **664** (2007) 416–434. arXiv:astro-ph/0702539.

[132] S. Scheidegger et al., *The Influence of Model Parameters on the Prediction of Gravitational wave Signals from Stellar Core Collapse*, A&A **514** (2010) A51. arXiv:1001.1570.

[133] A. Corsi and P. Mészáros, *Gamma-ray Burst Afterglow Plateaus and Gravitational Waves: Multi-messenger Signature of a Millisecond Magnetar?*, Astrophys. J. **702** (2009) 1171.

[134] L. Lindblom and B. J. Owen, *Gravitational radiation instability in hot young neutron stars*, Phys. Rev. Lett. **80** (1998) 4843–4846. arXiv:gr-qc/9803053.

[135] B. J. Owen and L. Lindblom, *Gravitational radiation from the r mode instability*, Class. Quantum Grav. **19** (2002) 1247–1254. arXiv:gr-qc/0111024.

[136] S. E. Woosley, *Gamma-ray bursts from stellar mass accretion disks around black holes*, Astrophys. J. **405** (1993) 273.

[137] A. L. Piro and E. Pfahl, *Fragmentation of Collapsar Disks and the Production of Gravitational Waves*, Astrophys. J. Lett. **658** (2006) 1173. arXiv:astro-ph/0610696.

[138] M. van van Putten, *Proposed source of gravitational radiation from a torus around a black hole*, Phys. Rev. Lett. **87** (2001) 091101.

[139] M. H. M. van van Putten et al., *Gravitational radiation from gamma-ray bursts as observational opportunities for LIGO and Virgo*, Phys. Rev. D **69** (2004) 044007. arXiv:gr-qc/0308016.

[140] M. H. P. M. van van Putten, *Gravitational Waveforms of Kerr Black Holes Interacting with High-Density Matter*, Astrophys. J. Lett. **684** (2008) L91.

[141] E. E. Flanagan and S. A. Hughes, *The basics of gravitational wave theory*, New Journal of Physics **7** (2005) 204.

[142] A. Einstein and N. Rosen, *On gravitational waves*, Journal of the Franklin Institute **1** (1937) 43.

[143] D. Kennefick, *Einstein versus the Physical Review*, Physics Today **58** (2005) 43.

[144] A. Eddington, *"The propagation of gravitational waves"*, Proc. R. Soc. A **102** (1922) 268.

[145] L. Landau and E. Lifshitz, *The Classical Theory of Fields*, Course of theoritical physics, Elsevier Science, 2013. https://books.google.com/books?id=HudbAwAAQBAJ.

[146] J. Preskill and K. Thorne, Foreword to feynman lectures on gravitation, in: B. Hatfield (Ed.), Feynman Lectures On Gravitation, Addison-Wesley, Reading MA, 1995. http://www.theory.caltech.edu/~preskill/pubs/preskill-1995-feynman.pdf.

[147] C. DeWitt, WADC Technical Report 57-216, in: C. DeWitt (Ed.), Conference on the Role of Gravitation in Physics at the University of North Carolina, 1957.

[148] P. Saulson, *Josh Goldberg and the physical reality of gravitational waves*, General Relativity and Gravitation **43** (2011) 3289–3299.

[149] F. Pirani, *On the physical significance of the Riemann tensor*, Acta Phys. Polon. **15** (1956) 389.

[150] F. Pirani, *Invariant formulation of gravitational radiation theory*, Phys. Rev. **105** (1957) 1089.

[151] H. Bondi, *Plane Gravitational Waves in General Relativity*, Nature **179** (1957) 1072–1073.

[152] J. Weber and J. A. Wheeler, *Reality of the Cylindrical Gravitational Waves of Einstein and Rosen*, Rev. Mod. Phys. **29** (1957) 509–515.

[153] J. Weber, *Gravitational Waves*, Crown Publishers, New York, 1979.

[154] J. Weber, *Detection and Generation of Gravitational Waves*, Phys. Rev. **117** (1960) 306–313.

[155] J. Weber, *Observation of the Thermal Fluctuations of a Gravitational-Wave Detector*, Phys. Rev. Lett. **17** (1966) 1228–1230.

[156] J. Weber, *Evidence for Discovery of Gravitational Radiation*, Phys. Rev. Lett. **22** (1969) 1320–1324.

[157] J. Weber, *Gravitational Radiation Experiments*, Phys. Rev. Lett. **24** (1970) 276–279.

[158] J. Weber, *Anisotropy and Polarization in the Gravitational-Radiation Experiments*, Phys. Rev. Lett. **25** (1970) 180–184.

[159] P. R. Saulson, *Physics of gravitational wave detection: resonant and interferometric detectors*, XXVI SLAC Summer Institute on Particle Physics. `http://www.slac.stanford.edu/gen/meeting/ssi/1998/media/saulson.pdf`.

[160] G. W. Gibbons and S. W. Hawking, *Theory of the Detection of Short Bursts of Gravitational Radiation*, Phys. Rev. D **4** (1971) 2191–2197.

[161] W. H. Press and K. S. Thorne, *Gravitational-Wave Astronomy*, Annual Review of Astronomy and Astrophysics **10** (1972) 335–374.

[162] D. J. Hegyi, *Sixth Texas Symposium on Relativistic Astrophysics*, New York Academy of Sciences, 1973. `http://trove.nla.gov.au/work/21562893`.

[163] P. Kafka and L. Schnupp, *Final Result of the Munich-Frascati Gravitational Radiation Experiment*, A&A **70** (1978) 97.

[164] J. Weber et al., *Topics in Theoretical and Experimental Gravitation Physics*, Cambridge University Press, Plenum Press, New York, 1977, proceedings of the International School of Cosmology and Gravitation held in Erice, Trapani, Sicily, March 13-25 1975.

[165] J. Weber, *Gravitational radiation detector observations in 1973 and 1974*, Nature **266** (1977) 243.

[166] S. P. Boughn et al., *Observations with a low-temperature, resonant mass, gravitational radiation detector*, Astrophys. J. Lett. **261** (1982) L19–L22.

[167] P. Astone et al., *IGEC2: A 17-month search for gravitational wave bursts in 2005-2007*, Phys. Rev. D **82** (2010) 022003. `arXiv:1002.3515`.

[168] M. Gertsenshtein and V. Pustovoit, *Detection of low frequency gravitational waves* **43** (1962) 605–607.

[169] V. Pustovoit and M. Gertsenshtein, *On The Detection Of Low Frequency Gravitational Waves*, Sov. Phys. JETP-USSR **16** (1963) 433–435.

[170] G. Moss and L. Miller, *Photon-Noise-Limited Laser Transducer for Gravitational Antenna*, Appl. Opt. **10** (1971) 2495–2498.

[171] R. L. Forward, *Wideband laser-interferometer graviational-radiation experiment*, Phys. Rev. D **17** (1978) 379–390.

[172] R. Weiss, *Gravitation Research: Electromagnetically Coupled Broadband Gravitational Antennaact*, Quarterly Progress Report - MIT Research Lab of Electronics **105** (1972) 54. `http://hdl.handle.net/1721.1/56271`.

[173] D. R. Herriott and H. J. Schulte, *Folded Optical Delay Lines*, Appl. Opt. **4** (1965) 883–889.

[174] H. Billing et al., *An argon laser interferometer for the detection of gravitational radiation*, J. Phys. E **12** (1979) 1043–1050.

[175] D. Shoemaker et al., *Noise Behavior of the Garching 30-meter Prototype Gravitational Wave Detector*, Phys. Rev. D **38** (1988) 423–432.

[176] H. Ward et al., *The Glasgow Gravitational Wave Detector*, IEEE Transactions on Instrumentation and Measurement **34** (1985) 261–265.

[177] R. W. P. Drever et al., *Optical Cavity Laser Interferometers for Gravitational Wave Detection*, Springer Berlin Heidelberg, Berlin, Heidelberg, 1981, pp. 33–40.

[178] R. W. P. Drever et al., *A Gravity Wave Detector Using Optical Cavity Sensing*, in: 9th International Conference on General Relativity and Gravitation Jena, Germany, July 14-19, 1980,pp. 265–267.

[179] R. Spero, *The Caltech laser-interferometric gravitational wave detector*, in: Fourth Marcel Grossmann Meeting on General Relativity, Roma, Italy, July, 1985 pp. 615–620.

[180] A. Abramovici et al., *LIGO: The Laser Interferometer Gravitational-Wave Observatory*, Science **256** (1992) 325–333.

[181] C. Bradaschia et al., *The Virgo Project: A wide band antenna for gravitational wave detection*, Nuclear Instruments and Methods in Physics Research Section A **289** (1990) 518 – 525.

[182] B. Willke et al., *The GEO 600 gravitational wave detector*, Class. Quantum Grav. **19** (2002) 1377–1387.

[183] C. Affeldt et al., *Advanced techniques in GEO 600*, Class. Quantum Grav. **31** (2014) 224002.

[184] T. Uchiyama et al., *Excavation of an underground site for a km-scale laser interferometric gravitational-wave detector*, Class. Quantum Grav. **31** (2014) 224005.

[185] J. Faller et al., *An antenna for laser gravitational-wave observations in space*, Adv. Space Res. **9** (1989) 107111.

[186] P. Amaro-Seoane et al., *eLISA/NGO: Astrophysics and cosmology in the gravitational-wave millihertz regime*, GW Notes **6** (2013) 4–110. `arXiv:1201.3621`.

[187] S. Kawamura et al., *The Japanese space gravitational wave antenna: DECIGO*, Class. Quantum Grav. **28** (2011) 094011.

[188] K. Danzmann and A. Rüdiger, *LISA technology-concept, status, prospects*, Class. Quantum Grav. **20** (2003) S1.

[189] S. Vitale, *Space-borne gravitational wave observatories*, General Relativity and Gravitation **46** (2014) 1730.

[190] P. Amaro-Seoane et al., *Laser Interferometer Space Antenna (submitted to ESA on January 13th in response to the call for missions for the L3 slot in the Cosmic Vision Programme)* `arXiv:1702.00786`.

[191] F. B. Estabrook and H. D. Wahlquist, *Response of Doppler spacecraft tracking to gravitational radiation*, General Relativity and Gravitation **6** (1975) 439–447.

[192] S. Detweiler, *Pulsar timing measurements and the search for gravitational waves*, Astrophys. J. Lett. **234** (1979) 1100–1104.

[193] R. W. Hellings and G. S. Downs, *Upper limits on the isotropic gravitational radiation background from pulsar timing analysis*, Astrophys. J. Lett. **265** (1983) L39–L42.

[194] G. Hobbs, *The Parkes Pulsar Timing Array*, Class. Quantum Grav. **30** (2013) 224007.

[195] M. A. McLaughlin, *The North American Nanohertz Observatory for Gravitational Waves*, Class. Quantum Grav. **30** (2013) 224008.

[196] M. Kramer and D. J. Champion, *The European Pulsar Timing Array and the Large European Array for Pulsars*, Class. Quantum Grav. **30** (2013) 224009.

[197] R N Manchester (for the IPTA), *The International Pulsar Timing Array*, Class. Quantum Grav. **30** (2013) 224010.

[198] T. J. W. Lazio, *The Square Kilometre Array pulsar timing array*, Class. Quantum Grav. **30** (2013) 224011.

[199] C. Moore and R. Cole, *Gravitational Wave Sensitivity Curve Plotter*, Project homepage, University of Cambridge. `http://www.ast.cam.ac.uk/~cjm96/noise_curve.pdf`.

[200] S. Dimopoulos et al., *Atomic gravitational wave interferometric sensor*, Phys. Rev. D **78** (2008) 122002.

[201] P. W. Graham et al., *New Method for Gravitational Wave Detection with Atomic Sensors*, Phys. Rev. Lett. **110** (2013) 171102.

[202] B. P. Abbott et al., *LIGO: the Laser Interferometer Gravitational-Wave Observatory*, Reports on Progress in Physics **72** (2009) 076901.

[203] F. Acernese et al., *Advanced Virgo: a second-generation interferometric gravitational wave detector*, Class. Quantum Grav. **32** (2015) 024001.

[204] *LIGO-India,*. `http://gw-indigo.org/tiki-index.php?page=LIGO-India`.

[205] M. C. Edwards and R. Meyer, *Bayesian parameter estimation of core collapse supernovae using gravitational wave simulations*, Inverse Problems **30** (2014) 114008.

[206] J. Aasi et al., *Parameter estimation for compact binary coalescence signals with the first generation gravitational-wave detector network*, Phys. Rev. D **88** (2013) 062001. `arXiv:1304.1775`.

[207] S. Klimenko et al., *Localization of gravitational wave sources with networks of advanced detectors*, Phys. Rev. D **83** (2011) 102001. `arXiv:1101.5408`.

[208] F. Cavalier et al., *Reconstruction of source location in a network of gravitational wave interferometric detectors*, Phys. Rev. D **74** (2006) 082004. `arXiv:gr-qc/0609118`.

[209] S. Fairhurst, *Triangulation of gravitational wave sources with a network of detectors*, New J. Phys. **11** (2009) 123006. `arXiv:0908.2356`.

[210] J. Abadie et al., *Sensitivity Achieved by the LIGO and Virgo Gravitational Wave Detectors during LIGO's Sixth and Virgo's Second and Third Science Runs.* , Tech. rep. (2012). `arXiv:1203.2674`. `https://dcc.ligo.org/LIGO-T1100338/public`.

[211] J. Aasi et al., *Virgo data characterization and impact on gravitational wave searches*, Class. Quantum Grav. **29** (2012) 155002. `arXiv:1203.5613`.

[212] J. Slutsky et al., *Methods for Reducing False Alarms in Searches for Compact Binary Coalescences in LIGO Data*, Class. Quantum Grav. **27** (2010) 165023. `arXiv:1004.0998`.

[213] N. Christensen, *LIGO S6 detector characterization studies*, Class. Quantum Grav. **27** (2010) 194010.

[214] N. Christensen, *Measuring the stochastic gravitational radiation background with laser interferometric antennas*, Phys. Rev. D **46** (1992) 5250–5266.

[215] E. Thrane and N. Christensen, *Correlated magnetic noise in global networks of gravitational-wave interferometers: observations and implications*, Phys. Rev. D **87** (2013) 123009. `arXiv:1303.2613`.

[216] Y. Guersel and M. Tinto, *Near optimal solution to the inverse problem for gravitational wave bursts*, Phys. Rev. D **40** (1989) 3884–3938.

[217] S. Nissanke et al., *Localizing compact binary inspirals on the sky using ground-based gravitational wave interferometers*, Astrophys. J. **739** (2011) 99. arXiv:1105.3184.

[218] T. Sidery et al., *Reconstructing the sky location of gravitational-wave detected compact binary systems: methodology for testing and comparison*, Phys. Rev. D **89** (2014) 084060. arXiv:1312.6013.

[219] B. Abbott et al., *Implementation and testing of the first prompt search for electromagnetic counterparts to gravitational wave transients*, A&A **539** (2012) A124. arXiv:1109.3498.

[220] J. Abadie et al., *First low-latency LIGO+Virgo search for binary inspirals and their electromagnetic counterparts*, A&A **541** (2012) A155. arXiv:1112.6005.

[221] B. F. Schutz and M. Tinto, *Antenna patterns of interferometric detectors of gravitational waves. I - Linearly polarized waves*, Mon. Not. R. Astron. Soc. **224** (1987) 131–154.

[222] B. F. Schutz, *A first course in general relativity*, Cambridge University Press, 1985.

[223] L. Rolland, *Etalonnage de l'interféromètre et reconstruction du signal d'onde gravitationnelle: de Virgo à Advanced Virgo*, Habiliation à diriger des recherches, Université de Savoie Mont-Blanc (2015). https://tel.archives-ouvertes.fr/tel-01163891v2/document.

[224] F. Acernese et al., *Virgo: a large interferometer for gravitational wave detection started its first scientific run*, J. Phys. Conf. Ser. **120** (2008) 032007.

[225] E. Hirose et al., *Sapphire mirror for the KAGRA gravitational wave detector*, Phys. Rev. D **89** (2014) 062003.

[226] E. Hirose et al., *Update on the development of cryogenic sapphire mirrors and their seismic attenuation system for KAGRA*, Class. Quantum Grav. **31** (2014) 224004.

[227] Y. Levin, *Internal thermal noise in the LIGO test masses: A direct approach*, Phys. Rev. D **57** (1998) 659–663.

[228] G. Harry and T. Bodiya, *Optical Coatings and Thermal Noise in Precision Measurement*, Cambridge University Press, 2012. http://books.google.com/books?id=770n4QLmBrMC.

[229] T. T. Fricke et al., *DC readout experiment in Enhanced LIGO*, Class. Quantum Grav. **29** (2012) 065005.

[230] E. Tournefier, *Technical noises for Virgo+: DC and AC readout*, Tech. Rep. VIR-NOT-LAP-1390-338, Virgo Project (2007). https://tds.virgo-gw.eu/ql/?c=1818.

[231] J. Aasi et al., *Enhanced sensitivity of the LIGO gravitational wave detector by using squeezed states of light*, Nature Photonics **7** (2013) 613–619.

[232] B. Zhang, *Open Questions in GRB Physics*, Comptes Rendus Physique **12** (2011) 206–225. arXiv:1104.0932.

[233] C. L. Fryer and S. E. Woosley, *Formation Rates of Black Hole Accretion Disk Gamma-Ray Bursts*, Astrophys. J. **526** (1999) 152–177. arXiv:astro-ph/9904122.

[234] B. Metzger et al., *The protomagnetar model for gamma-ray bursts*, Mon. Not. R. Astron. Soc. **413** (2011) 2031–2056.

[235] E. Nakar, *Short-hard gamma-ray bursts*, Phys. Rep. **442** (2007) 166–236. arXiv:astro-ph/0701748.

[236] L. Rezzolla et al., *The missing link: Merging neutron stars naturally produce jet-like structures and can power short Gamma-Ray Bursts*, Astrophys. J. **732** (2011) L6. arXiv:1101.4298.

[237] N. Tanvir et al., *A "kilonova" associated with short-duration gamma-ray burst 130603B*, Nature **500** (2013) 547–549. arXiv:1306.4971.

[238] E. Nakar et al., *The Distances of short-hard GRBs and the SGR connection*, Astrophys. J. **640** (2006) 849–853. arXiv:astro-ph/0502148.

[239] J. A. de de Freitas Pacheco, *Do soft gamma repeaters emit gravitational waves?*, A&A **336** (1998) 397–401. arXiv:astro-ph/9805321.

[240] A. Corsi and B. J. Owen, *Maximum gravitational-wave energy emissible in magnetar flares*, Phys. Rev. D **83** (2011) 104014. arXiv:1102.3421.

[241] F. Stecker and M. Salamon, *High-energy neutrinos from quasars*, Space Sci. Rev. **75** (1996) 341–355. arXiv:astro-ph/9501064.

[242] S. Ando et al., *Multimessenger astronomy with gravitational waves and high-energy neutrinos*, Rev. Mod. Phys. **85** (2013) 1401–1420. arXiv:1203.5192.

[243] I. Bartos and C. Finley, *Observational Constraints on Multi-messenger Sources of Gravitational Waves and High-energy Neutrinos*, Phys. Rev. Lett. **107** (2011) 251101. arXiv:1108.3001.

[244] M. Aartsen et al., *Evidence for High-Energy Extraterrestrial Neutrinos at the IceCube Detector*, Science **342** (2013) 1242856. arXiv:1311.5238.

[245] C. Kochanek et al., *A Survey About Nothing: Monitoring a Million Supergiants for Failed Supernovae*, Astrophys. J. **684** (2008) 1336–1342. arXiv:0802.0456.

[246] B. Baret et al., *Multimessenger Science Reach and Analysis Method for Common Sources of Gravitational Waves and High-energy Neutrinos*, Phys. Rev. D **85** (2012) 103004. arXiv:1112.1140.

[247] M. Was, *Searching for gravitational waves associated with gamma-ray bursts in 2009-2010 LIGO-Virgo data*, Ph.D. thesis, Université de Paris-Sud (2011).

[248] J. Barnes and D. Kasen, *Effect of a High Opacity on the Light Curves of Radioactively Powered Transients from Compact Object Mergers*, Astrophys. J. **775** (2013) 18. arXiv:1303.5787.

[249] D. Grossman et al., *The long-term evolution of neutron star merger remnants - II. Radioactively powered transients*, Mon. Not. R. Astron. Soc. **439** (2013) 757–770. arXiv:1307.2943.

[250] F. Mannucci et al., *The Supernova rate per unit mass*, A&A **433** (2005) 807. arXiv:astro-ph/0411450.

[251] J. Abadie et al., *Predictions for the Rates of Compact Binary Coalescences Observable by Ground-based Gravitational-wave Detectors*, Class. Quantum Grav. **27** (2010) 173001.

[252] F. Ozel et al., *The Black Hole Mass Distribution in the Galaxy*, Astrophys. J. **725** (2010) 1918–1927. arXiv:1006.2834.

[253] N. Christensen and R. Meyer, *Markov chain Monte Carlo methods for Bayesian gravitational radiation data analysis*, Phys. Rev. D **58** (1998) 082001.

[254] V. Raymond et al., *The Effects of LIGO detector noise on a 15-dimensional Markov-chain Monte-Carlo analysis of gravitational-wave signals*, Class. Quantum Grav. **27** (2010) 114009. arXiv:0912.3746.

[255] J. Antoniadis et al., *The millisecond pulsar mass distribution: Evidence for bimodality and constraints on the maximum neutron star mass*arXiv:1605.01665.

[256] A. Buonanno et al., *Toward faithful templates for non-spinning binary black holes using the effective-one-body approach*, Phys. Rev. D **76** (2007) 104049. arXiv:0706.3732.

[257] Y. Pan et al., *Inspiral-merger-ringdown multipolar waveforms of nonspinning black-hole binaries using the effective-one-body formalism*, Phys. Rev. D **84** (2011) 124052. arXiv:1106.1021.

[258] B. Abbott et al., *Search for gravitational wave ringdowns from perturbed black holes in LIGO S4 data*, Phys. Rev. D **80** (2009) 062001. arXiv:0905.1654.

[259] S. Klimenko et al., *Method for detection and reconstruction of gravitational wave transients with networks of advanced detectors*, Phys. Rev. D **93** (2016) 042004. arXiv:1511.05999.

[260] A.-C. Clapson et al., *EGC: A time-frequency augmented template-based method for gravitational wave burst search in ground-based interferometers*, Class. Quantum Grav. **25** (2008) 035002.

[261] R. Lynch et al., *Information-theoretic approach to the gravitational-wave burst detection problem*, Phys. Rev. D **95** (10) (2017) 104046. arXiv:1511.05955.

[262] J. Abadie et al., *All-sky search for gravitational-wave bursts in the second joint LIGO-Virgo run*, Phys. Rev. D **85** (2012) 122007. arXiv:1202.2788.

[263] J. Aasi et al., *Constraints on cosmic strings from the LIGO-Virgo gravitational-wave detectors*, Phys. Rev. Lett. **112** (2014) 131101. arXiv:1310.2384.

[264] S. A. Usman et al., *The PyCBC search for gravitational waves from compact binary coalescence*, Class. Quantum Grav. **33** (21) (2016) 215004. arXiv:1508.02357.

[265] K. Cannon et al., *Toward Early-Warning Detection of Gravitational Waves from Compact Binary Coalescence*, Astrophys. J. **748** (2012) 136. arXiv:1107.2665.

[266] B. P. Abbott et al., *Properties of the Binary Black Hole Merger GW150914*, Phys. Rev. Lett. **116** (24) (2016) 241102. arXiv:1602.03840.

[267] B. P. Abbott et al., *Observation of binary black-hole mergers in advanced LIGO's first run*arXiv:tobesubmitted.

[268] V. Kalogera and G. Baym, *The maximum mass of a neutron star*, Astrophys. J. **470** (1996) L61. arXiv:astro-ph/9608059.

[269] J. Casares and P. G. Jonker, *Mass Measurements of Stellar and Intermediate Mass Black-Holes*, Space Sci. Rev. **183** (2014) 223–252. arXiv:1311.5118.

[270] B. E. Tetarenko et al., *WATCHDOG: A Comprehensive All-Sky Database of Galactic Black Hole X-ray Binaries*, Astrophys. J. Suppl. **222** (2016) 15. arXiv:1512.00778.

[271] B. P. Abbott et al., *Prospects for Observing and Localizing Gravitational-Wave Transients with Advanced LIGO and Advanced Virgo*, Living Rev. Relativity **19**. http://www.livingreviews.org/lrr-2016-1.

[272] B. P. Abbott et al., *Tests of general relativity with GW150914*, Phys. Rev. Lett. **116** (22) (2016) 221101. arXiv:1602.03841.

[273] M. Modjaz, *Stellar Forensics with the Supernova-GRB Connection*, Astron. Nachr. **332** (2011) 434. arXiv:1105.5297.

[274] T. Galama et al., *Discovery of the peculiar supernova 1998bw in the error box of GRB 980425*, Nature **395** (1998) 670. arXiv:astro-ph/9806175.

[275] A. Rowlinson et al., *Discovery of the afterglow and host galaxy of the low redshift short GRB 080905A*, Mon. Not. R. Astron. Soc. **408** (2010) 383–391. arXiv:1006.0487.

[276] J. Aasi et al., *Search for gravitational waves associated with γ-ray bursts detected by the Interplanetary Network*, Phys. Rev. Lett. **113** (2014) 011102. arXiv:1403.6639.

[277] J. Aasi et al., *Search for long-lived gravitational-wave transients coincident with long gamma-ray bursts*, Phys. Rev. D **88** (2013) 122004. arXiv:1309.6160.

[278] M. Briggs et al., *Search for gravitational waves associated with gamma-ray bursts during LIGO science run 6 and Virgo science runs 2 and 3*, Astrophys. J. **760** (2012) 12. arXiv:1205.2216.

[279] J. Abadie et al., *Search for gravitational-wave inspiral signals associated with short Gamma-Ray Bursts during LIGO's fifth and Virgo's first science run*, Astrophys. J. **715** (2010) 1453–1461. arXiv:1001.0165.

[280] B. Abbott et al., *Search for gravitational-wave bursts associated with gamma-ray bursts using data from LIGO Science Run 5 and Virgo Science Run 1*, Astrophys. J. **715** (2010) 1438–1452. arXiv:0908.3824.

[281] B. Abbott et al., *Search for gravitational waves associated with 39 gamma-ray bursts using data from the second, third, and fourth LIGO runs*, Phys. Rev. D **77** (2008) 062004. arXiv:0709.0766.

[282] J. Abadie et al., *Implications For The Origin Of GRB 051103 From LIGO Observations*, Astrophys. J. **755** (2012) 2. arXiv:1201.4413.

[283] B. Abbott et al., *Implications for the Origin of GRB 070201 from LIGO Observations*, Astrophys. J. **681** (2008) 1419–1428. arXiv:0711.1163.

[284] P. B. Cameron et al., *Discovery of a radio afterglow following the 27 December 2004 giant flare from SGR 1806-20*, Nature **434** (2005) 1112–1115. arXiv:astro-ph/0502428.

[285] J. Abadie et al., *Search for Gravitational Wave Bursts from Six Magnetars*, Astrophys. J. **734** (2011) L35. arXiv:1011.4079.

[286] B. Abbott et al., *Stacked Search for Gravitational Waves from the 2006 SGR 1900+14 Storm*, Astrophys. J. **701** (2009) L68–L74. arXiv:0905.0005.

[287] J. Abadie et al., *A search for gravitational waves associated with the August 2006 timing glitch of the Vela pulsar*, Phys. Rev. D **83** (2011) 042001. arXiv:1011.1357.

[288] S. Adrian-Martinez et al., *A First Search for coincident Gravitational Waves and High Energy Neutrinos using LIGO, Virgo and ANTARES data from 2007*, Journal of Cosmology and Astroparticle Physics **1306** (2013) 008. arXiv:1205.3018.

[289] M. G. Aartsen et al., *Multimessenger search for sources of gravitational waves and high-energy neutrinos: Initial results for LIGO-Virgo and IceCube*, Phys. Rev. D **90** (2014) 102002. arXiv:1407.1042.

[290] S. Adrian-Martinez et al., *High-energy Neutrino follow-up search of Gravitational Wave Event GW150914 with ANTARES and IceCube*, Phys. Rev. D **93** (12) (2016) 122010. arXiv:1602.05411.

[291] J. Aasi et al., *First Searches for Optical Counterparts to Gravitational-wave Candidate Events*, Astrophys. J. Suppl. **211** (2014) 7. arXiv:1310.2314.

[292] M. van van Haarlem et al., *LOFAR: The LOw-Frequency ARray*, A&A **556** (2013) A2. arXiv:1305.3550.

[293] V. Connaughton et al., *Fermi GBM Observations of LIGO Gravitational Wave event GW150914*, Astrophys. J. **826** (1) (2016) L6. arXiv:1602.03920.

[294] P. Jaranowski and A. Krolak, *Data analysis of gravitational - wave signals from spinning neutron stars. 1. The Signal and its detection*, Phys. Rev. D **58** (1998) 063001. arXiv:gr-qc/9804014.

[295] C. Cutler and B. F. Schutz, *The Generalized F-statistic: Multiple detectors and multiple GW pulsars*, Phys. Rev. D **72** (2005) 063006. arXiv:gr-qc/0504011.

[296] R. J. Dupuis and G. Woan, *Bayesian estimation of pulsar parameters from gravitational wave data*, Phys. Rev. D **72** (2005) 102002. arXiv:gr-qc/0508096.

[297] P. Astone et al., *A method for detection of known sources of continuous gravitational wave signals in non-stationary data*, Class. Quantum Grav. **27** (2010) 194016.

[298] B. Abbott et al., *Setting upper limits on the strength of periodic gravitational waves using the first science data from the GEO 600 and LIGO detectors*, Phys. Rev. D **69** (2004) 082004. arXiv:gr-qc/0308050.

[299] B. Abbott et al., *Limits on gravitational wave emission from selected pulsars using LIGO data*, Phys. Rev. Lett. **94** (2005) 181103. arXiv:gr-qc/0410007.

[300] B. Abbott et al., *Upper limits on gravitational wave emission from 78 radio pulsars*, Phys. Rev. D **76** (2007) 042001. arXiv:gr-qc/0702039.

[301] B. Abbott et al., *Searches for gravitational waves from known pulsars with S5 LIGO data*, Astrophys. J. **713** (2010) 671–685. arXiv:0909.3583.

[302] J. Aasi et al., *Gravitational waves from known pulsars: results from the initial detector era*, Astrophys. J. **785** (2014) 119. arXiv:1309.4027.

[303] J. Aasi et al., *Narrow-band search of continuous gravitational-wave signals from Crab and Vela pulsars in Virgo VSR4 data*, Phys. Rev. D **91** (2015) 022004. arXiv:1410.8310.

[304] B. Abbott et al., *Beating the spin-down limit on gravitational wave emission from the Crab pulsar*, Astrophys. J. **683** (2008) L45–L50. arXiv:0805.4758.

[305] J. Abadie et al., *First search for gravitational waves from the youngest known neutron star*, Astrophys. J. **722** (2010) 1504–1513. arXiv:1006.2535.

[306] J. Aasi et al., *Searches for continuous gravitational waves from nine young supernova remnants*, Astrophys. J. **813** (2015) 39. arXiv:1412.5942.

[307] B. Abbott et al., *Coherent searches for periodic gravitational waves from unknown isolated sources and Scorpius X-1: Results from the second LIGO science run*, Phys. Rev. D **76** (2007) 082001. arXiv:gr-qc/0605028.

[308] B. P. Abbott et al., *Upper Limits on Gravitational Waves from Scorpius X-1 from a Model-Based Cross-Correlation Search in Advanced LIGO Data*, Astrophys. J. **847** (1) (2017) 47. arXiv:1706.03119.

[309] B. P. Abbott et al., *Directional Limits on Persistent Gravitational Waves from Advanced LIGOs First Observing Run*, Phys. Rev. Lett. **118** (2017) 121102. arXiv:1612.02030.

[310] J. Aasi et al., *Directed search for gravitational waves from Scorpius X-1 with initial LIGO data*, Phys. Rev. D **91** (2015) 062008. arXiv:1412.0605.

[311] J. Aasi et al., *Search of the Orion spur for continuous gravitational waves using a loosely coherent algorithm on data from LIGO interferometers*, Phys. Rev. D **93** (2016) 042006. arXiv:1510.03474.

[312] Einstein@home. http://einstein.phys.uwm.edu.

[313] J. Abadie et al., *All-sky Search for Periodic Gravitational Waves in the Full S5 LIGO Data*, Phys. Rev. D **85** (2012) 022001. arXiv:1110.0208.

[314] J. Aasi et al., *Einstein@Home all-sky search for periodic gravitational waves in LIGO S5 data*, Phys. Rev. D **87** (2013) 042001. arXiv:1207.7176.

[315] J. Aasi et al., *Application of a Hough search for continuous gravitational waves on data from the 5th LIGO science run*, Class. Quantum Grav. **31** (2014) 085014. arXiv:1311.2409.

[316] J. Aasi et al., *Implementation of an $\mathcal{F}$-statistic all-sky search for continuous gravitational waves in Virgo VSR1 data*, Class. Quantum Grav. **31** (2014) 165014. arXiv:1402.4974.

[317] B. P. Abbott et al., *Comprehensive all-sky search for periodic gravitational waves in the sixth science run LIGO data*, Phys. Rev. D **94** (4) (2016) 042002. arXiv:1605.03233.

[318] B. P. Abbott et al., *Results of the deepest all-sky survey for continuous gravitational waves on LIGO S6 data running on the Einstein@Home volunteer distributed computing project*, Phys. Rev. D **94** (10) (2016) 102002. arXiv:1606.09619.

[319] P. Jaranowski and A. Krolak, *Data analysis of gravitational wave signals from spinning neutron stars. 3. Detection statistics and computational requirements*, Phys. Rev. D **61** (2000) 062001. arXiv:gr-qc/9901013.

[320] J. Aasi et al., *First low frequency all-sky search for continuous gravitational wave signals*, Phys. Rev. D **93** (2016) 042007. arXiv:1510.03621.

[321] E. Goetz and K. Riles, *An all-sky search algorithm for continuous gravitational waves from spinning neutron stars in binary systems*, Class. Quantum Grav. **28** (2011) 215006. arXiv:1103.1301.

[322] J. Aasi et al., *First all-sky search for continuous gravitational waves from unknown sources in binary systems*, Phys. Rev. D **90** (2014) 062010. arXiv:1405.7904.

[323] J. Aasi et al., *Improved Upper Limits on the Stochastic Gravitational-Wave Background from 20092010 LIGO and Virgo Data*, Phys. Rev. Lett. **113** (2014) 231101. arXiv:1406.4556.

[324] J. Abadie et al., *Upper limits on a stochastic gravitational-wave background using LIGO and Virgo interferometers at 600-1000 Hz*, Phys. Rev. D **85** (2012) 122001. arXiv:1112.5004.

[325] B. Abbott et al., *First Cross-Correlation Analysis of Interferometric and Resonant-Bar Gravitational-Wave Data for Stochastic Backgrounds*, Phys. Rev. D **76** (2007) 022001. arXiv:gr-qc/0703068.

[326] J. Aasi et al., *Searching for stochastic gravitational waves using data from the two colocated LIGO Hanford detectors*, Phys. Rev. D **91** (2015) 022003. arXiv:1410.6211.

[327] B. Abbott et al., *Directional Limits on Persistent Gravitational Waves Using LIGO S5 Science Data*, Phys. Rev. Lett. **107** (2011) 271102.

[328] F. Pretorius, *Evolution of binary black hole spacetimes*, Phys. Rev. Lett. **95** (2005) 121101. arXiv:gr-qc/0507014.

[329] A. Buonanno and T. Damour, *Effective one-body approach to general relativistic two-body dynamics*, Phys. Rev. D **59** (1999) 084006. arXiv:gr-qc/9811091.

[330] A. Buonanno and T. Damour, *Transition from inspiral to plunge in binary black hole coalescences*, Phys. Rev. D **62** (2000) 064015. arXiv:gr-qc/0001013.

[331] A. Taracchini et al., *Effective-one-body model for black-hole binaries with generic mass ratios and spins*, Phys. Rev. D **89** (2014) 061502. arXiv:1311.2544.

[332] P. Ajith et al., *Inspiral-merger-ringdown waveforms for black-hole binaries with non-precessing spins*, Phys. Rev. Lett. **106** (2011) 241101. arXiv:0909.2867.

[333] S. Husa et al., *Frequency-domain gravitational waves from nonprecessing black-hole binaries. I. New numerical waveforms and anatomy of the signal*, Phys. Rev. D **93** (2016) 044006. arXiv:1508.07250.

[334] S. Khan et al., *Frequency-domain gravitational waves from nonprecessing black-hole binaries. II. A phenomenological model for the advanced detector era*, Phys. Rev. D **93** (2016) 044007. arXiv:1508.07253.

[335] M. Middleton, *Black hole spin: theory and observation*, Springer: Astrophysics and Space Science Library, 2015. arXiv:1507.06153.

[336] S. Klimenko and G. Mitselmakher, *A wavelet method for detection of gravitational wave bursts*, Class. Quantum Grav. **21** (2004) S1819–S1830.

[337] S. Chatterji et al., *Multiresolution techniques for the detection of gravitational-wave bursts*, Class. Quantum Grav. **21** (2004) S1809–S1818. arXiv:0412119[gr-qc].

[338] S. K. Chatterji, *The search for gravitational-wave bursts in data from the second LIGO science run*, Thesis, MIT Physics department (2005). http://dspace.mit.edu/handle/1721.1/34388.

[339] A.-C. Clapson, *Impulsive signals search with the gravitational wave detector Virgo*, Thesis, Université Paris Sud - Paris XI, lAL 06-45 (Apr. 2006). https://tel.archives-ouvertes.fr/tel-00085885.

[340] S. Klimenko et al., *Constraint likelihood analysis for a network of gravitational wave detectors*, Phys. Rev. D **72** (2005) 122002. arXiv:gr-qc/0508068.

[341] S. Klimenko et al., *Coherent method for detection of gravitational wave bursts*, Class. Quantum Grav. **25** (2008) 114029. arXiv:0802.3232.

[342] T. B. Littenberg and N. J. Cornish, *A Bayesian Approach to the Detection Problem in Gravitational Wave Astronomy*, Phys. Rev. D **80** (2009) 063007. arXiv:0902.0368.

[343] N. J. Cornish and T. B. Littenberg, *BayesWave: Bayesian Inference for Gravitational Wave Bursts and Instrument Glitches*, Class. Quantum Grav. **32** (2015) 135012. arXiv:1410.3835.

[344] F. Beauville et al., *A comparison of methods for gravitational wave burst searches from LIGO and Virgo*, Class. Quantum Grav. **25** (2008) 045002. arXiv:0701026[gr-qc].

[345] E. Thrane et al., *Long gravitational-wave transients and associated detection strategies for a network of terrestrial interferometers*, Phys. Rev. D **83** (2011) 083004. arXiv:1012.2150.

[346] E. Mueller et al., *Towards gravitational wave signals from realistic core collapse supernova models*, Astrophys. J. **603** (2004) 221–230. arXiv:astro-ph/0309833.

[347] B. Müller and H.-T. Janka, *A New Multi-dimensional General Relativistic Neutrino Hydrodynamics Code of Core-collapse Supernovae. III. Gravitational Wave Signals from Supernova Explosion Models*, Astrophys. J. **766** (2013) 43. arXiv:1210.6984.

[348] K. N. Yakunin et al., *Gravitational Wave Signatures of Ab Initio Two-Dimensional Core Collapse Supernova Explosion Models for 12-25 Solar Masses Stars*, Phys. Rev. D **94** (2015) 084040. arXiv:1505.05824.

[349] K. Kiuchi et al., *Gravitational waves from the Papaloizou-Pringle instability in black hole-torus systems*, Phys. Rev. Lett. **106** (2011) 251102. arXiv:1105.5035.

[350] A. Rowlinson et al., *Signatures of magnetar central engines in short GRB light curves*, Mon. Not. R. Astron. Soc. **430** (2013) 1061. arXiv:1301.0629.

[351] L. Gualtieri and R. Ciolfi, *Structure, deformations and gravitational wave emission of magnetars*, Class. Quantum Grav. **28** (2011) 114014. arXiv:1011.2778.

[352] T. Prestegard, *Unmodeled searches for long-lasting gravitational-wave signals with LIGO and studies of underground seismic noise for future gravitational-wave detectors*, Thesis, University of Minnesota (2016).

[353] B. P. Abbott et al., *All-sky search for long-duration gravitational wave transients with initial LIGO*, Phys. Rev. D **93** (2016) 042005. arXiv:1511.04398.

[354] F. Acernese et al., *Data Acquisition System of the Virgo Gravitational wave Interferometric Detector*, in: XV^{th} IEEE NPSS Real Time Conference 2007, Fermilab, Batavia USA2007.

[355] Virgo operation group, http://wwwcascina.virgo.infn.it/DetectorOperations/index.htm.

[356] Virgo environmental sensors, http://wwwcascina.virgo.infn.it/EnvMon/sensors.htm.

[357] P. Lapenna, *Faraday isolator on the IB*, Tech. Rep. VIR-200A-06, Virgo Project (2006). https://tds.virgo-gw.eu/ql/?c=2856.

[358] Data Analysis groups, Virgo and GEO commissioning teams, *Joint GEO-Virgo science run in summer 2011: the science case*, Tech. Rep. VIR-0063C-11, Virgo Project (2011). https://tds.virgo-gw.eu/ql/?c=8114.

[359] J. Abadie et al., *Sensitivity to Gravitational Waves from Compact Binary Coalescences Achieved during LIGO's Fifth and Virgo's First Science Run*, Tech. rep. (2010). arXiv:1003.2481. https://dcc.ligo.org/LIGO-T0900499/public.

[360] Virgo logbook, https://logbook.virgo-gw.eu/virgo/?r=25395, https://logbook.virgo-gw.eu/virgo/?r=25476, https://logbook.virgo-gw.eu/virgo/?r=25386.

[361] Virgo logbook, https://logbook.virgo-gw.eu/virgo/?r=25500, https://logbook.virgo-gw.eu/virgo/?r=26288.

[362] E. Tournefier, *Back-scattering by the optical benches: results from Virgo and constraints for AdVirgo*, Tech. Rep. VIR-0070A-08, Virgo Project (2008). https://tds.virgo-gw.eu/ql/?c=2083.

[363] T. Accadia et al., *Noise from scattered light in Virgo's second science run data*, in: 14^{th} Gravitational Wave Data Analysis Workshop, 18-23 Januray 2010, Roma, Italy, Class. Quantum Grav. **27**, 2010, p. 194011.

[364] Virgo logbook, https://logbook.virgo-gw.eu/virgo/?r=25310.

[365] R. Flaminio and R. Gouaty, *Analysis of the sensitivity of the recycled interferometer during C5, C6 and C7 runs*, Tech. Rep. VIR-NOT-LAP-1390-313, Virgo Project (2006). https://tds.virgo-gw.eu/ql/?c=1618.

[366] Virgo logbook, https://logbook.virgo-gw.eu/virgo/?r=30413.

[367] J.-Y. Vinet, *Evaluation of gravitational events simulated by dust particles from the top of the tube through the beam*, Tech. Rep. VIR-NOT-LAS-1380-123, Virgo Project (1995). https://tds.virgo-gw.eu/ql/?c=508.

[368] Virgo logbook, https://logbook.virgo-gw.eu/virgo/?r=15475, https://logbook.virgo-gw.eu/virgo/?r=15456.

[369] Virgo logbook, https://logbook.virgo-gw.eu/virgo/?r=22756.

[370] F. Bondu, *L'interféromètre Virgo: propriétés optiques, stabilisation en fréquence du laser*, Habiliation à diriger des recherches, Université de Nice Sophia-Antipolis (2008). http://tel.archives-ouvertes.fr/tel-00284986.

[371] Virgo logbook, https://logbook.virgo-gw.eu/virgo/?r=29403.

[372] T. Accadia et al., *A Thermal Compensation System for the gravitational wave detector Virgo*, in: 12^{th} Marcel Grossman meeting, 12-18 July 2009, Paris, France2010.

[373] Virgo logbook, https://logbook.virgo-gw.eu/virgo/?r=20419.

[374] Virgo logbook, https://logbook.virgo-gw.eu/virgo/?r=27754, https://logbook.virgo-gw.eu/virgo/?r=27690.

[375] D. Verkindt, *Acquisition de données et surveillance en ligne du détecteur d'ondes gravitationnelles Virgo*, Habiliation à diriger des recherches, Université de Savoie (2007). http://tel.archives-ouvertes.fr/tel-00163735.

[376] F. Acernese et al., *Measurement of the seismic attenuation performance of the Virgo Superattenuator*, Astroparticle Physics **23** (2005) 557–565.

[377] F. Acernese et al., *Measurements of Superattenuator seismic isolation by Virgo interferometer*, Astroparticle Physics **33** (2010) 182–189.

[378] G. Vajente, *Measurements of control noise budgets*, Tech. Rep. VIR-003A-08, Virgo Project (2008). https://tds.virgo-gw.eu/ql/?c=1957.

[379] T. Accadia et al., *Calibration and sensitivity of the Virgo detector during its second science run*, Class. Quantum Grav. **28** (2011) 025005. arXiv:1009.5190[gr-qc].

[380] T. Accadia et al., *Reconstruction of the gravitational wave signal $h(t)$ during the Virgo science runs and independent validation with a photon calibrator*, Class. Quantum Grav. **31** (2014) 165013. arXiv:1401.6066.

[381] J. Abadie et al., *Observational method for seeking electromagnetic counterparts to gravitational wave triggers*, ApJ in preparation.

[382] F. Marion et al., *Multiband search of coalescing binaries applied to Virgo CITF data*, in: 38^{th} Rencontres de Moriond: Gravitational Waves and Experimental Gravitation, Les Arcs, France, 22-29 Mar 2003.

[383] T. Adams et al., *Low-latency analysis pipeline for compact binary coalescences in the advanced gravitational wave detector era*, Class. Quantum Grav. **33** (17) (2016) 175012. arXiv:1512.02864.

[384] J. Slutsky et al., *Methods for Reducing False Alarms in Searches for Compact Binary Coalescences in LIGO Data*, Class. Quantum Grav. **27** (2010) 165023. arXiv:1004.0998.

[385] N. Christensen, *LIGO S6 detector characterization studies*, in: 14^{th} Gravitational Wave Data Analysis Workshop, 18-23 Januray 2010, Roma, Italy, Class. Quantum Grav. **27**, 2010, p. 194010.

[386] F. Robinet, *Data quality in gravitational wave bursts and inspiral searches in the second Virgo Science Run*, in: 14^{th} Gravitational Wave Data Analysis Workshop, 18-23 Januray 2010, Roma, Italy, Class. Quantum Grav. **27**, 2010, p. 194012.

[387] N. Leroy, *Data quality and vetoes for the gravitational-wave burst and inspiral analyses in Virgo's first science run*, in: 13^{th} Gravitational Wave Data Analysis Workshop, 19-22 Januray 2010, San Juan, Puerto Rico, Class. Quantum Grav. **26**, 2009, p. 204007.

[388] T. Isogai, *Used percentage veto for LIGO and virgo binary inspiral searches*, in: 14^{th} Gravitational Wave Data Analysis Workshop, 18-23 January 2010, Roma, Italy, J. Phys.: Conf. Ser. **243**, 2010, p. 012005.

[389] J. R. Smith et al., *A Hierarchical method for vetoing noise transients in gravitational-wave detectors*, Class. Quantum Grav. **28** (2011) 235005. arXiv:1107.2948.

[390] Bi-linear coupling veto web site, https://virgo.physics.carleton.edu/trac/OmegaVeto-trac/.

[391] B. Swinkels, *Brute force search for vetoes*, Tech. Rep. VIR-0430A-12, Virgo Project (2012). https://tds.virgo-gw.eu/ql/?c=9253.

[392] The VDQ group web site, https://wwwcascina.virgo.infn.it/DataAnalysis/VDBdoc/index.html.

[393] The VDQ group, *Science, injection, and data quality segments for Virgo*, Tech. Rep. VIR-0010A-11, Virgo Project (2008). https://tds.virgo-gw.eu/ql/?c=8307.

[394] The VDQ group, *Virgo DQ and vetoes for VSR2/S6 online analysis*, Tech. Rep. VIR-0011A-11, Virgo Project (2008). https://tds.virgo-gw.eu/ql/?c=8061.

[395] The Virgo segment database, https://segments-web.ligo.org/.

[396] W. Press et al., *Numerical Recipes in C*, Cambridge University Press, 1998.

[397] The Virgo veto safety web site, https://wwwcascina.virgo.infn.it/MonitoringWeb/.

[398] T. Ballinger, *A powerful veto for gravitational wave searches using data from Virgo's first scientific run*, in: 13^{th} Gravitational Wave Data Analysis Workshop, 19-22 Januray 2010, San Juan, Puerto Rico, Class. Quantum Grav. **26**, 2009, p. 204003.

[399] C. Hanna, *Reducing gravitational wave false alarms using signals at the antisymmetric port in LIGO detectors*, in: 6^{th} Edoardo Amaldi Conference on Gravitational Waves, 20-24 June 2005, Okinawa, Japan, Class. Quantum Grav. **23**, 2006, p. S17.

[400] K. Kotter et al., *PQMon: A powerful veto for burst events*, in: 7^{th} Gravitational Wave Data Analysis Workshop, 17-19 Dec 2002. Kyoto, Japan, Class. Quantum Grav. **20**, 2003, p. S895.

[401] N. Christensen, *Veto studies for LIGO inspiral triggers*, in: 9^{th} Annual Gravitational Wave Data Analysis Workshop, 15-18 Dec 2004. Annecy, France, Class. Quantum Grav. **22**, 2005, p. S1059. arXiv:gr-qc/0504067.

[402] Virgo logbook, https://logbook.virgo-gw.eu/virgo/?r=28913.

[403] F. Robinet, *Omicron: Q-pipeline for detector characterization*, Tech. Rep. G1200194 (2012). https://dcc.ligo.org/LIGO-G1200194.

[404] C. Pankow, *ExcessPower: status update*, Tech. Rep. G1301022, LSC (2013). https://dcc.ligo.org/LIGO-G1301022.

[405] Accadia, T and others, *Advanced Virgo Technical Design Report*, Tech. Rep. VIR-0128A-12, Virgo Project (2012). https://tds.virgo-gw.eu/ql/?c=8940.

[406] Virgo logbook. https://logbook.virgo-gw.eu/virgo/?r=39617.

[407] B. P. Abbott et al., *Binary Black Hole Mergers in the first Advanced LIGO Observing Run*, Phys. Rev. X **6** (2016) 041015. arXiv:1606.04856.

[408] B. P. Abbott et al., *GW170814: A Three-Detector Observation of Gravitational Waves from a Binary Black Hole Coalescence*, Phys. Rev. Lett. **119** (2017) 141101. arXiv:1709.09660.

[409] B. P. Abbott et al., *GW170817: Observation of Gravitational Waves from a Binary Neutron Star Inspiral*, Phys. Rev. Lett. **119** (2017) 161101. arXiv:1710.05832.

[410] B. P. Abbott et al., *Gravitational Waves and Gamma-Rays from a Binary Neutron Star Merger: GW170817 and GRB 170817A*, Astrophys. J. **848** (2017) L13. arXiv:1710.05834.

[411] B. D. Metzger, *Kilonovae*, Living Rev. Relativity **20** (2017) 3. arXiv:1610.09381.

[412] D. A. Coulter et al., *Swope Supernova Survey 2017a (SSS17a), the optical counterpart to a gravitational wave source*, Science. http://science.sciencemag.org/content/early/2017/10/13/science.aap9811.full.pdf.

[413] B. P. Abbott et al., *Multi-messenger Observations of a Binary Neutron Star Merger*, Astrophys. J. **848** (2017) L12. arXiv:1710.05833.

[414] B. P. Abbott et al., *Estimating the Contribution of Dynamical Ejecta in the Kilonova Associated with GW170817*, Accepted in: Astrophys. J.arXiv:1710.05836.

[415] B. F. Schutz, *Determining the Hubble Constant from Gravitational Wave Observations*, Nature **323** (1986) 310–311.

[416] B. P. Abbott et al., *A gravitational-wave standard siren measurement of the Hubble constant*, Nature **551** (7678) (2017) 85–88. arXiv:1710.05835.

[417] P. A. R. Ade et al., *Planck 2015 results. XIII. Cosmological parameters*, A&A **594** (2016) A13. arXiv:1502.01589.

[418] A. G. Riess et al., *A 2.4% Determination of the Local Value of the Hubble Constant*, Astrophys. J. **826** (2016) 56. arXiv:1604.01424.

[419] A. L. Piro and B. Giacomazzo, *The Fate of Neutron Star Binary Mergers*, Astrophys. J. **844** (2017) L19. arXiv:1704.08697.

[420] B. P. Abbott et al., *Search for post-merger gravitational waves from the remnant of the binary neutron star merger GW170817*arXiv:1710.09320.

[421] K. Gill et al., *Gravitational Wave Astronomy Prospectives for Core-Collapse Supernovae Populations*. https://dcc.ligo.org/LIGO-P1500232.

[422] J. Abadie et al., *Predictions for the Rates of Compact Binary Coalescences Observable by Ground-based Gravitational-wave Detectors*, Class. Quantum Grav. **27** (2010) 173001. arXiv:1003.2480.

[423] J. Markowitz et al., *Gravitational Wave Burst Source Direction Estimation using Time and Amplitude Information*, Phys. Rev. D **78** (2008) 122003. arXiv:0810.2264.

[424] S. Fairhurst, *Source localization with an advanced gravitational wave detector network*, Class. Quantum Grav. **28** (2011) 105021. arXiv:1010.6192.

[425] J. Powell and M. Szczepanczyk, *Inferring the core-collapse supernova explosion mechanism with three-dimensional gravitational-wave simulations.* arXiv:1709.00955.

[426] B. Bécsy et al., *Parameter estimation for gravitational-wave bursts with the BayesWave pipeline*, Astrophys. J. **839** (2017) 15. arXiv:1612.02003.